



ADDRESS OF PUBLISHER
& EDITOR'S OFFICE:

GDAŃSK UNIVERSITY
OF TECHNOLOGY

Institute
of Naval Architecture
and Ocean Engineering
G. Narutowicza 11/12
80-233 Gdańsk, POLAND

EDITORIAL STAFF:

Wiesław Tarełko
| Editor in Chief
Janusz Kozak
| Deputy Editors-in-Chief
Wojciech Litwin
| Deputy Editors-in-Chief

Price:
single issue: 25 PLN

Prices for abroad
single issue:
- in Europe EURO 15
- overseas USD 20

WEB:
pg.edu.pl/pmr

e-mail : pmr@pg.edu.pl

ISSN 1233-2585

CONTENS

- 4 **Oleksandr Kanifolskyi**
GENERAL STRENGTH, ENERGY EFFICIENCY (EEDI), AND ENERGY WAVE CRITERION (EWC) OF DEADRISE HULLS FOR TRANSITIONAL MODE
- 11 **Marek Kraskowski**
CFD OPTIMISATION OF THE LONGITUDINAL VOLUME DISTRIBUTION OF A SHIP'S HULL BY CONSTRAINED TRANSFORMATION OF THE SECTIONAL AREA CURVE
- 21 **Jingze Lv, Yiqun Lin, Rui Zhang, Boyang Li, Hualin Yang**
ASSISTED PROPULSION DEVICE OF A SEMI-SUBMERSIBLE SHIP BASED ON THE MAGNUS EFFECT
- 35 **Jinglei Yang, Han-bing Sun, Xiao-wen Li, Xin Liu**
FLOW FIELD CHARACTERISTIC ANALYSIS OF CUSHION SYSTEM OF PARTIAL AIR CUSHION SUPPORT CATAMARAN IN REGULAR WAVES
- 47 **Zaopeng Dong, Shijie Qi, Min Yu, Zhengqi Zhang, Haisheng Zhang, Jiakang Li, Yang Liu**
AN IMPROVED DYNAMIC SURFACE SLIDING MODE METHOD FOR AUTONOMOUS COOPERATIVE FORMATION CONTROL OF UNDERACTUATED USVS WITH COMPLEX MARINE ENVIRONMENT DISTURBANCES
- 61 **Zhenghua Xiong, Bo Xiang, Ye Chen, Bin Chen**
RESEARCH ON THE RISK CLASSIFICATION OF CRUISE SHIP FIRES BASED ON AN ATTENTION-BP NEURAL NETWORK
- 69 **Viktor Yalama, Olga Yakovleva, Volodymyr Trandafilov, Mykhailo Khmelniuk**
FUTURE SUSTAINABLE MARITIME SECTOR: FISHING CARRIERS AND THEIR ADOPTION TO THE ENVIRONMENTAL REGULATIONS. PART I
- 78 **Viktor Yalama, Olga Yakovleva, Volodymyr Trandafilov, Mykhailo Khmelniuk**
FUTURE SUSTAINABLE MARITIME SECTOR: ENERGY EFFICIENCY IMPROVEMENT AND ENVIRONMENTAL IMPACT REDUCTION FOR FISHING CARRIERS OLDER THAN 20 YEARS IN THE FLEET PART II
- 89 **Viet-Dung Do, Xuan-Kien Dang, Tien-Dat Tran, Thi Duyen-Anh Pham**
JACKING AND ENERGY CONSUMPTION CONTROL OVER NETWORK FOR JACK-UP RIG: SIMULATION AND EXPERIMENT

**ADDRESS OF PUBLISHER
& EDITOR'S OFFICE:**

**GDAŃSK UNIVERSITY
OF TECHNOLOGY**

**Institute
of Naval Architecture
and Ocean Engineering
G. Narutowicza 11/12
80-233 Gdańsk, POLAND**

- 99** **Oleksandr Cherednichenko, Serhiy Serbin, Mykhaylo Tkach, Jerzy Kowalski, Daifen Chen**
MATHEMATICAL MODELLING OF MARINE POWER PLANTS WITH THERMOCHEMICAL FUEL TREATMENT
- 109** **Andrzej Adamkiewicz, Janusz Fydrych, Jan Drzewieniecki**
STUDIES ON THE EFFECTS OF COLD STARTS OF THE SHIP MAIN ENGINE
- 119** **Hong Shi, Qianwei Zhang, Meinan Liu, Kaijie Yang, Jie Yuan**
NUMERICAL STUDY OF THE EJECTION COOLING MECHANISM OF VENTILATION FOR A MARINE GAS TURBINE ENCLOSURE
- 128** **Meng Liang, Mingzhi Chen**
MONITORING THE PERFORMANCE OF A SHIP'S MAIN ENGINE BASED ON BIG DATA TECHNOLOGY
- 141** **Krzysztof Rudzki, Piotr Gomulka, Anh Tuan Hoang**
OPTIMIZATION MODEL TO MANAGE SHIP FUEL CONSUMPTION AND NAVIGATION TIME
- 154** **Paweł Dymarski, Czesław Dymarski, Piotr Grymajło**
AN INNOVATIVE METHOD OF MEASURING THE EXTENSION OF THE PISTON ROD IN HYDRAULIC CYLINDERS, ESPECIALLY LARGE ONES USED IN THE SHIPBUILDING AND OFFSHORE INDUSTRY
- 160** **Jakub Kowalski, Janusz Kozak**
INFLUENCE OF MATERIAL THICKNESS ON THE DUCTILE FRACTURE OF STEEL PLATES FOR SHIPBUILDING
- 167** **Krzysztof Emilianowicz, Milena Supernak, Agnieszka Ossowska**
APPLICATION OF THE CORROSION TESTER IN CORROSION TESTS USING THE ACOUSTIC EMISSION METHOD
- 176** **Mariusz Zieja, Wojciech Wawrzyński, Justyna Tomaszewska, Norbert Sigiel**
A METHOD FOR THE INTERPRETATION OF SONAR DATA RECORDED DURING AUTONOMOUS UNDERWATER VEHICLE MISSIONS

Editorial

POLISH MARITIME RESEARCH is the scientific journal with a worldwide circulation. This journal is published quarterly (four times a year) by Gdansk University of Technology (GUT). On September, 1994, the first issue of POLISH MARITIME RESEARCH was published. The main objective of this journal is to present original research, innovative scientific ideas, and significant findings and application in the field of :

Naval Architecture, Ocean Engineering and Underwater Technology,

The scope of the journal covers selected issues related to all phases of product lifecycle and corresponding technologies for offshore floating and fixed structures and their components.

All researchers are invited to submit their original papers for peer review and publications related to methods of the design; production and manufacturing; maintenance and operational processes of such technical items as:

- all types of vessels and their equipment,
- fixed and floating offshore units and their components,
- autonomous underwater vehicle (AUV) and remotely operated vehicle (ROV).

We welcome submissions from these fields in the following technical topics:

- ship hydrodynamics: buoyancy and stability; ship resistance and propulsion, etc.,
 - structural integrity of ship and offshore unit structures: materials; welding; fatigue and fracture, etc.,
 - marine equipment: ship and offshore unit power plants: overboarding equipment; etc.
-

Scientific Board

Chairman : Prof. JERZY GIRTLEK - Gdańsk University of Technology, Poland

Vice-chairman : Prof. CARLOS GUEDES SOARES, Universidade de Lisboa, Lisbon, Portugal

Vice-chairman : Prof. MIROSŁAW L. WYSZYŃSKI - University of Birmingham, United Kingdom

Prof. POUL ANDERSEN

Technical University of Denmark
Kongens Lyngby
Denmark

Prof. YORDAN GARBATOV

Universidade de Lisboa,
Lisbon
Portugal

Prof. JERZY MERKISZ

Poznan University of Technology
Poznan
Poland

Prof. JIAHN-HORNG CHEN

National Taiwan Ocean University
Keelung
Taiwan

Prof. STANISŁAW GUCMA

Maritime University of Szczecin
Szczecin
Poland

Prof. VALERI NIEKRASOV

Admiral Makarov National University
of Shipbuilding
Mikolaiv
Ukraine

Prof. VINCENZO CRUPI

University of Messina
Messina
Italy

Prof. JIAHN-HORNG CHEN

National Taiwan Ocean University
Keelung
Taiwan

Prof. SERHIY SERBIN

Admiral Makarov National
University of Shipbuilding
Mikolaiv
Ukraine

Prof. MAREK DZIDA

Gdansk University of Technology
Gdansk
Poland

Prof. ANTONI ISKRA

Poznan University of Technology
Poznan
Poland

Prof. JOZEF SZALA

UTP University of Science and
Technology
Bydgoszcz
Poland

Dr. KATRIEN ELOOT,

Flanders Hydraulics Research,
Antwerpen
Belgium

Prof. JAN KICINSKI

Institute of Fluid-Flow Machinery -
Polish Academy of Sciences
Gdansk
Poland

Prof. HOANG ANH TUAN

Ho Chi Minh City
University of Technology
(HUTECH)
Ho Chi Minh
Vietnam

Prof. ODD MAGNUS FALTINSEN

Norwegian University of Science and
Technology
Trondheim
Norway

Prof. ZBIGNIEW KORCZEWSKI

Gdansk University of Technology
Gdansk
Poland

Prof. TADEUSZ SZELANGIEWICZ

Maritime University of Szczecin
Szczecin
Poland

Prof. MASSIMO FIGARI

University of Genova
Genova
Italy

Prof. JOZEF LISOWSKI

Gdynia Maritime University
Gdynia
Poland

Prof. DRACOS VASSALOS

University of Strathclyde
Glasgow
United Kingdom

Prof. HASSAN GHASSEMI

Amirkabir University of Technology
Tehran
Iran

Prof. JERZY EDWARD MATUSIAK

Aalto University
Espoo
Finland

GENERAL STRENGTH, ENERGY EFFICIENCY (EEDI), AND ENERGY WAVE CRITERION (EWC) OF DEADRISE HULLS FOR TRANSITIONAL MODE

Oleksandr Kanifolskyi* 

Odesa National Maritime University, Odesa, Ukraine

Corresponding author: oleksandrkanifolskyi@gmail.com (Oleksandr Kanifolskyi)

ABSTRACT

In the modern world, environmental issues come to the fore. The document of MARPOL for reducing the emission of pollutants into the atmosphere relates to the energy efficiency coefficient EEDI. This coefficient is directly related to the power of the main engine and, accordingly, to the water resistance. The way to reduce the energy efficiency factor EEDI by increasing the relative length $\frac{L}{\sqrt[3]{V}}$ of the ship was proposed in this article. To determine the maximum value of the relative length, knowledge of the $\sqrt[3]{V}$ general strength of the vessel is required. The value of the relative section modulus of an equivalent girder for a small vessel of transitional mode is defined. The result of the graphic solution of two equations is the value of such a relative section modulus. This parameter is required to determine the limiting value of the relative length and to find solutions to reduce the coefficient EEDI. Comparative analysis of the obtained data with the data of the strength and weight of the H-girder with a length similar to the ship was conducted. The formula for determining the limiting value of the relative length was obtained from the equation of general strength. For a preliminary assessment of the future project of the ship, in terms of permissible design accelerations and the possibility of the ship moving against a sea wave of a certain height, a graph was built based on the application of the energy wave criterion EWC and the requirements of various classification societies.

Keywords: Energy wave criterion, energy efficiency factor, design accelerations

NOMENCLATURE

$\Delta = \gamma V$ – displacement of the ship

γ – density of water

β – deadrise angle, degrees

$Fr_V = \frac{v}{\sqrt{g\sqrt[3]{V}}}$ – volume Froude number

W – section modulus

$\frac{W}{\Delta}$ – relative section modulus

$\frac{L}{\sqrt[3]{V}}$ – relative length

$EEDI$ – energy efficiency index

D – depth of the ship

B – width of the ship

d – draft of the ship

c_b – block coefficient

$n = 1 + a_{CG}$ – summary acceleration

a_{CG} – design vertical acceleration (expressed in g)

σ_a – allowable compression stress for the material

t – thickness of the plating

Ω – area of the cross section of the ship

R – total resistance

$\frac{R}{\Delta}$ – relative total resistance

- R_o – residuary resistance
- $\frac{R_o}{\Delta}$ – relative residuary resistance
- EWC – energy wave criterion
- η – efficiency coefficient

INTRODUCTION

Three modes are distinguished in the theory of ship design. The character of these modes is determined by the nature of the forces of maintenance. If the weight of the vessel Δ is completely balanced by the hydrostatic force, this mode is called displacement $\Delta = \gamma V$, volume Froude number $Fr_V < 1$.

With further increase in the vessel speed, the bow rises and the bottom of the vessel will be moved with the angle of attack to the surface of the water. An additional force directed perpendicular to the bottom of the vessel develops. This force can be decomposed into two components: hydrodynamic resistance of water and the hydrodynamic lift force Y . The transitional mode begins. The weight of the ship is balanced by two forces: the hydrostatic and hydrodynamic $\Delta = \gamma V_1 + Y$, $1 < Fr_V < 3$. The hydrostatic force γV_1 is created by the part of the body of the craft V_1 that is submerged in the liquid. The transitional mode has not been extensively studied because the elements of displacement and planing are parts of the forces. Another difficulty for the study is a variable position of the vessel relative to the water at various speeds.

The increase in the speed leads to a further growth of the hydrodynamic force, emersion of the vessel, and accordingly a reduction in the hydrostatic force. The planing mode is the regime when the hydrodynamic lift forces Y fully support the weight of the craft $\Delta = Y$, $Fr_V > 3$.

When a high-speed vessel is moving in the transitional mode with a volume Froude number, loads increase from the interaction of the bottom of the vessel and the waves. Accelerations increase accordingly, which adversely affects the health of the passengers and crew. Hull structures and equipment may also be damaged. The acceleration that is considered to be acceptable from a physiological point of view is limited to a value of 0.2g. In reality, the acceleration on board the high-speed vessel reaches high values. Modern requirements of classification societies significantly raise the level for permissible accelerations on board high-speed vessels. Various methods are used to reduce shock loads. One of them is an increase in the deadrise angle β . Vessels with a deadrise angle $\beta > 20^\circ$ are often called “monohull deep V”. To evaluate the project of the ship in terms of design accelerations and the ability of the ship to move against the wave, it is possible to build a graph based on the energy wave criterion EWC and requirements of classification societies. This criterion is based on the energy of the sea wave and the kinetic energy of the vessel with the added masses of water. The problem of ship motion on the head wave is considered in [1]. In this work, the authors improved the existing methods of the theory of the ship but did not give an answer to the

question of whether a ship with kinetic energy can move towards the wave. In [2], the theoretical basis for describing the wave energy is considered in detail and the ship’s roll parameters are calculated, but there are no recommendations for assessing the decrease in the ship’s speed on a head wave.

In the transitional mode, the water resistance increases significantly. A decrease in resistance is possible by increasing the relative length $\frac{L}{\sqrt[3]{V}}$ of the vessel, which can lead to

problems in ensuring general strength. To determine the maximum possible value of the relative length, knowledge of the relative section modulus is required. There is a lack of information about the relative section modulus of an equivalent girder of the vessel $\frac{W}{\Delta}$ in various studies. The

choice of the relative length of the vessel is associated with such qualities as propulsion and many others. Sometimes, the shipbuilder’s desire to reduce water resistance by increasing this parameter is limited by the difficulties of ensuring general strength. There is a need to find the limiting values of the relative length, ensuring the strength of the vessel, while maintaining acceptable propulsion. The value $\frac{L}{\sqrt[3]{V}}$ is associated with propulsion or rather with the relative $\frac{R}{\Delta}$ resistance of water $\frac{R}{\Delta}$.

Also, this indicator has an impact on the energy efficiency index $EEDI$. Thus, in this study, an attempt will be made to combine the requirements for general strength, propulsion, and energy efficiency in order to create new and improved existing ships.

THE RELATIVE SECTION MODULUS OF AN EQUIVALENT GIRDER FOR A VESSEL

Values characterizing various types of girders are sometimes given in different literature. Some books propose a coefficient of the structural quality of a girder $\frac{W}{F}$ as the ratio of the section modulus W to the area of its cross section F . In other sources, the dependence of the weight of one linear meter of the girder on the section modulus is presented. From this information, it is clear that each type of beam is characterized by its own dependence. For research, it is possible to apply knowledge about the section modulus of the small vessel, as given in [3]. The minimum section modulus of a small vessel (with deadrise angle $\beta = 0$, depth D , width B , thickness of plating t) is described by the formula $W = D(B + \frac{D}{3})t = (0.33D^2 + DB)t$. As noted above, deadrise hulls are widely used in transitional motion. In this paper, the forms with deadrise angle will be considered, Fig. 1.

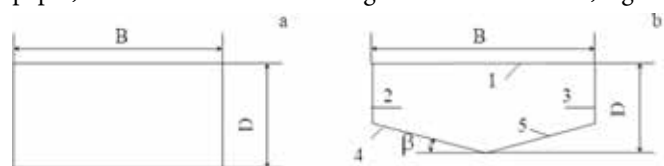


Fig. 1. Sections of the hull.

Writing the elements in Table 1, it is possible to obtain a formula for the section modulus of the hull with a deadrise angle $\beta = 25^\circ$.

$$W = (0.33D^2 + 0.015B^2 + 0.82DB - 0.028\frac{B^3}{D})t \quad (1)$$

When applying the value of the deadrise angle $\beta = 0^\circ$ in the calculations, the following formula was obtained

$$W_{\beta=0} = D(B + \frac{D}{3})t = (0.33D^2 + DB)t \quad (2)$$

This formula is similar to the formula presented in [3] and mentioned above in this article.

Equations of a similar type for deadrise angles from 0° to 30° can be obtained. The results of the calculations were used to determine the coefficient of the profile u in the formula $W = \frac{u}{2} D\Omega$, which includes the depth D and the area of the cross section of the ship Ω , after equating the right sides of the equations described above. Using this data, it is possible to find out how the section modulus of the deadrise hulls differs from the flat bottom, Fig. 2.

Sometimes, in the early stages of a project when there is no complete data on the projected vessel, there is a need to assess the general strength of the vessel. In such cases, some simplifications are applied in the calculation, and the cross-section of the vessel appears as the cross-section of an equivalent H-girder. In these cases, the formula $W = \frac{u}{2} D\Omega$ is usually used.

Tab. 1. Elements of the cross section of the vessel in Fig. 1b

Numbers of elements corresponding to Figure 1b	Area, F	The distance between the center of gravity of the element and the central axis, z
1	2	3
1	tB	$\frac{D}{2}$
2, 3	$(D - \frac{B}{2}tg\beta)t$	$\frac{B}{2}tg\beta$
4, 5	$\frac{Bt}{2\cos\beta}$	$\frac{D}{2} - \frac{B}{4}tg\beta$

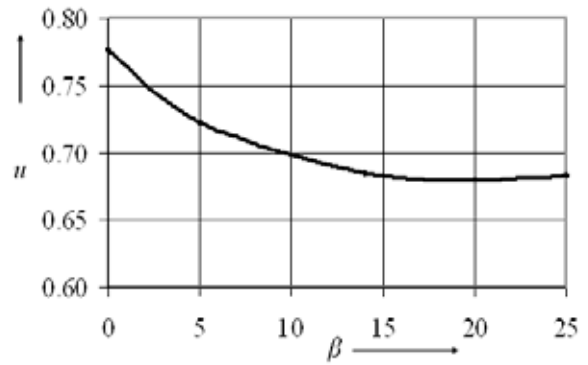


Fig. 2. The dependence of the coefficient of the profile u on the deadrise angle.

For the calculations, it is assumed that the position of the central axis passing through the centre of gravity of the cross section of the vessel is in the middle of the depth. This assumption is based on the fact that the bottom deadrise will shift the position of this axis towards the deck, and the stronger and heavier construction of the bottom will lower the axis towards the bottom. Sometimes in assessing the general strength, simplification is used to find the minimum acceptable value. The thickness of the girders is distributed over the thickness of the vessel plating. For further calculations, the thickness of the steel plating is assumed to be 6 mm, as an average value for transitional mode vessels with a length of about 30 m.

Information about the structural quality of a girder $\frac{W}{F}$ can be projected on the calculations of the relative section modulus of an equivalent girder for a vessel $\frac{W}{\Delta}$. In approximate calculations of strength, the shape of the profile, which corresponds to the equivalent girder of the vessel, is an H-girder, Fig. 3, and, taking into account the direct dependence of the cross-sectional area on the length of the vessel, we can assume the presence of such a value of the relative section modulus $\frac{W}{\Delta}$, which is characteristic for a specific type of ship. This value retains approximately the same value for ships of the same type; the same hull material and speed mode.

Formula (2) can be represented in the form,

$$\frac{W}{\Delta} = \frac{D(B + \frac{D}{3})t}{\gamma_c L B d} = \frac{k_D t (1 + 0.07k_D)}{\gamma_b L} \quad (3)$$

taking into account the geometry of the hull and the fact that $k_D = \frac{D}{d}$ and $\frac{B}{d} = 4.7$ (such a relative width value corresponds to the minimum water resistance in the speed range $2 \leq Fr_V \leq 3$).

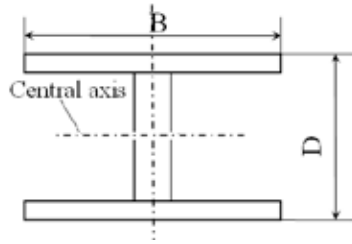


Fig. 3. The equivalent girder for calculating the section modulus of the ship (H-girder).

The relative section modulus, in m^3/t , can also be found from the equation of general strength based on the bending moment due to still water loads, wave induced loads, and impact loads, $M = W\sigma_a = \frac{\Delta L}{k} n$

$$\frac{W}{\Delta} = \frac{L}{k\sigma_a} n \quad (4)$$

where $n = 1 + a_{CG}$ is the summary acceleration, L is the vessel length in m, σ_a is the allowable compression stress for material of the hull in t/m^2 , and k is the coefficient characteristic for the type of vessel.

For crafts of different types of service (passenger, ferry, cargo), an acceleration greater than $a_{CG} = 1.0$ may not be adopted for the purpose of defining limit operating conditions [4]. In the calculations, a fixed value $n = 1 + a_{CG} = 2$ was adopted. In Rules [5], it is proposed the summary acceleration $n = 1 + a_{CG}$ for passenger ships $n = 2$ and $n = 1 + a_{CG} = 2.3$ for pleasure boats. In real conditions, the summary acceleration will be connected with the relative speed Fr_v .

The coefficient k for pleasure boats can be obtained from the formula for the bending moment due to still water loads, wave induced loads, and impact loads $M = \frac{\Delta}{2}(m - 0.17c_b L)(g + 1.3g)$ [5]. The value of $m = -0.05L$ is the average arm of the loaded ship, reference point is middle. For value of block coefficient $c_b = 0.55$, the formula will be in the form $M = -\frac{\Delta L}{20}(g + 1.3g)$ in kNm or $M = -\frac{\Delta L}{20}(1 + 1.3)$ in tm . Same considerations for passenger ships at $n = 2$. The value of the coefficient k is assumed to be equal 20.

The allowable compression stress is assumed to be equal to 0.8 of the yield strength of the material, in this case, steel. The researcher can apply the materials and the requirements of any rules chosen by him to solve the task in the proposed method.

After a joint graphical solution of two equations (3) and (4), as shown in Fig. 4, it is possible to determine a value $\frac{W}{\Delta} = 0.0003 \text{ m}^3/\text{t}$ for steel hull, satisfying the requirements of general strength and taking into account the geometry of the hull. It is interesting to note that the Bureau Veritas Rules are created specifically for vessels less than 65 m in length [5].

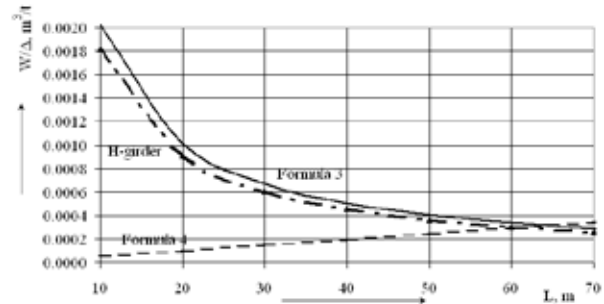


Fig. 4. The value of the relative section modulus.

The solution obtained by the graphical method does not take into account the case of deadrise. Next, an analysis will be made of how much the section modulus of hulls with different deadrise differs from the section modulus of the hull without deadrise. Based on the analysis of the coefficient of the profile u in the formula $W = \frac{u}{2} D\Omega$, which includes the depth D and the area of the cross section of the ship Ω , it can be assumed that the difference in the value of the section modulus for deadrise hull and for non-deadrise hull is, on average, about 10%, as shown in Fig. 2. Taking into account this fact, the value of the relative section modulus of the deadrise steel hull taken for further calculations can be considered to be about $\frac{W}{\Delta} = 0.00027 \text{ m}^3/\text{t}$. To check the obtained values $\frac{W}{\Delta}$, it is possible to conduct an additional calculation. As noted above, the type of the balk, which corresponds to the equivalent girder of the hull of the vessel, is the H-girder in the approximate calculations. Using the data on the dependence of the weight of 1 m of an H-girder on its section modulus and adopting various lengths of the beam, it is possible to get a value close to $0.0003 \text{ m}^3/\text{t}$ for a balk with a length of 64 m, as shown in Fig. 4.

THE MAXIMUM VALUE OF THE RELATIVE LENGTH OF THE SHIP AND THE ENERGY EFFICIENCY DESIGN INDEX

Using the obtained information about the value of $\frac{W}{\Delta}$, it is possible to determine the relative length $\frac{L}{\sqrt[3]{V}}$ of the vessel from the conditions of general strength $\sigma_a W \geq \frac{\Delta L}{k} n$.

The values of the summary acceleration n can be presented as the dependency on the Froude numbers in the speed range $2 \leq Fr_v \leq 3$, $n = 0.3 Fr_v^2 = 0.3 \frac{v^2}{g\sqrt[3]{V}}$. This formula was obtained on the basis of data from classification societies and data provided by various researchers.

After substituting the formula for summary acceleration n into the general strength condition $\sigma_a W \geq \frac{\Delta L}{k} n$, the inequality for relative length is

$$\sigma_a \frac{kgW}{0.3v^2\Delta} \geq \frac{L}{\sqrt[3]{V}} \quad (5)$$

The relative length $\frac{L}{\sqrt[3]{V}}$ depends on the relative residuary resistance $\frac{R_o}{\Delta}$. The relative total resistance of water $\frac{R}{\Delta}$ included in the simplified equation for the calculation of the energy efficiency design index $EEDI = \frac{aR}{k_1 k_2 \eta \Delta}$ [6], where the coefficient a depends on the type of ship. The way to obtain this formula is described below.

The MARPOL'S formula for the calculation of the attained $EEDI$, in its shortened form, is:

$$EEDI = \frac{(\prod_{j=1}^n f_j) (\sum_{i=1}^{nME} P_{ME(i)} C_{FME(i)} SFC_{ME(i)})}{f_i f_c Capacity f_w v_{ref}} \quad (6)$$

Other absent elements of this formula are connected with the power of the auxiliary engines, shaft motor, and engines with innovative technology. The factor f_j is related to the ice reinforcement of the hull and can take a value no greater than 1. The factor f_i is a capacity factor and must not be less than 1. The coefficient f_c depends upon the deadweight and volume of cargo tanks for gas carriers and chemical tankers, but for other types of ships, it is equal to 1. f_w is a weather factor and depends on the sea conditions. It can be taken as equal to 1.

The P_{ME} is taken as 75% of the power of the main engine $P_{ME} = 0.75N$, where $N = \frac{Rv}{\eta}$, so $P_{ME} = 0.75 \frac{Rv}{\eta}$.

For calculations using formula (6), the velocity of the ship v is taken as that when using 75% power of the main engine. To account for this fact, the factor $k_1 v_{ref} = k_1 v$ must be used in the equation.

The part of equation (6) *capacity* is the deadweight (for non-passenger ships) or gross capacity GT for passenger ships. Basically, ships of the transitional mode are used for transporting passengers (passenger craft, passenger ferries, etc.). The approximate formula for calculating the capacities is $GT = k_2 \Delta$.

The next factor is C_{FME} , which is termed the carbon emission coefficient. The last of the considered factors is SFC_{ME} , which is characterized by the specific fuel consumption of the engine. The values of these factors can be accepted as 3.1144 g CO₂/g fuel and 190 g/kWh, respectively.

After transformations, the formula $EEDI = \frac{aR}{k_1 k_2 \eta \Delta}$ is obtained.

For approximate estimation of $\frac{R}{\Delta}$, in transitional mode, data received from different Δ researchers were analyzed. The data from towing tanks at SSPA and NPL came from Brown, Volodin, Nordstrom, and Groot. The tests included a range of $\frac{L}{B}$, $\frac{B}{d}$, c_b values, different hull forms, and different angles B of entry for the waterlines [7]. The results of the study of the relationships of residuary resistance $\frac{R_o}{\Delta}$ against $l = \frac{L}{\sqrt[3]{V}}$ in transitional mode are shown in Fig. 5. The $\frac{R_o}{\Delta}$ residuary resistance R_o has most of the total resistance value in this mode.

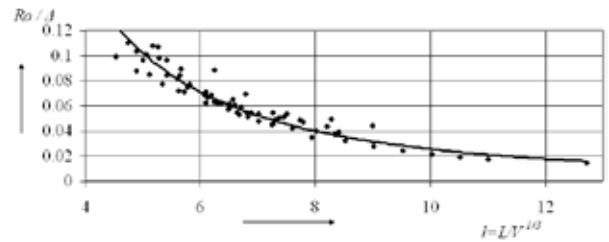


Fig. 5. The dependence of the relative residuary resistance on relative length at $Fr_v = 2$.

Using the least squares method and Fig. 5, formula 7 was derived for $Fr_v = 2$.

$$\left(\frac{R_o}{\Delta}\right) = 2.53 \left(\frac{L}{\sqrt[3]{V}}\right)^{-1.99} \quad (7)$$

The coefficient of determination for the data has a value of more than 0.83.

The following results were obtained after differentiation of equation (7)

$$d\left(\frac{R_o}{\Delta}\right) = -5.03 \left(\frac{L}{\sqrt[3]{V}}\right)^{-2.99} d\left(\frac{L}{\sqrt[3]{V}}\right) \quad (8)$$

Equation (8) helps to analyze the influence of the change in the relative length on the relative residuary resistance and $EEDI$.

THE ENERGY WAVE CRITERION EWC

In the previous sections of this article, the design accelerations and the determination of the relative length of the vessel have been described. When designing a vessel, it is already useful at the first stages to have information about the possibility of the vessel moving towards a wave of a certain height [1] and the permissible values of design accelerations that occur during such movement. To study these issues, it is possible to use the energy wave criterion EWC and formulas of classification societies.

The energy wave criterion $EWC = \frac{\gamma g k_w h_w^3 B}{4.4 m v^2}$ contains the

following parameters: water density γ ; acceleration of gravity g ; coefficient $k_w = \frac{L_w}{h_w}$ relating the length L_w and height h_w of the wave; ship width B ; speed v ; and mass displacement of the vessel m . This criterion was

derived from the inequality containing the wave energy $E_w = \frac{\gamma g k_w h_w^3 B}{8}$ and the kinetic energy of the ship (vessel

parameters: block coefficient c_b , length L , width B , and draft d) with the added masses of water

$E_s = 1.1 \frac{m v^2}{2} = 1.1 \frac{\gamma c_b L B d v^2}{2}$. The coefficient EWC is similar to

Newton's criterion $Ne = \frac{PL_N}{mv^2}$; in this equation, P is the force and L_N is the linear size [8].

This criterion EWC was applied to solve the task for determining the maximum value of the wave height at which the ship will be able to move against the wave. If the value of this criterion is close to 1 or exceeds the value of 1, then it is possible to predict a significant decrease in the speed of the vessel or its inability to move against the wave.

Accelerations arising from such a movement can be estimated using the recommendations of various classification societies. The relationship between design acceleration values, ship characteristics, and the maximum wave height that the ship can meet during the voyage is based on the GL [4] and RINA [9] formula $H_{sm} = 5 \frac{a_{CG}}{v} \frac{L^{1.5}}{6 + 0.14L}$. The calculation was made following the scheme. Froude number values and ship length options were given. The speed of the ship was then determined, which corresponds to these Froude numbers and the lengths of the ship. Using the iteration method, the length of the vessel and the Froude numbers were determined, which correspond to a given wave height and to the value of a_{CG} .

APPLICATION OF THE OBTAINED FORMULAS IN PRACTICE

So, the opportunity appeared to apply the presented formulas in practice on an example of a real ship. For the calculation, the high-speed small vessel "Length 28" was chosen, the length of ship is 28 m, the width is 7.2 m, the speed is 30 knots, $Fr_v = 2.2$. The material of the hull is glass reinforced plastic. The summary acceleration n of the vessel in the example has a value $n = 0.3 Fr_v^2 = 0.3 \frac{v^2}{g \sqrt[3]{V}} = 1.45$.

The researcher can apply the materials, value n , and the requirements of any rules chosen by him to solve the task in the proposed method. After the joint solution of formulas (3) and (4), the value $\frac{W}{\Delta} = 0.0009$ m3/t was obtained (glass reinforced plastic).

The real value of the relative length $\frac{L}{\sqrt[3]{V}}$ of this vessel is about 5.5. The maximum allowable value $\frac{L}{\sqrt[3]{V}}$ calculated by formula (5) is $\frac{L}{\sqrt[3]{V}} = 8.2$ (hull material and thickness were taken into account when performing the calculation). If we assume that this value will be increased by one unit, it will take the value $\frac{L}{\sqrt[3]{V}} = 6.5$, and then the relative residual resistance will decrease

$$d\left(\frac{R_o}{\Delta}\right) = -5.03 \left(\frac{L}{\sqrt[3]{V}}\right)^{-2.99} d\left(\frac{L}{\sqrt[3]{V}}\right) = -0.031 \text{ or about } 35\%,$$

as shown in Fig. 5. An increase in the relative length of the ship was achieved, for example, by increasing its length and reducing its block coefficient, and the displacement value will remain close to the original. This approach involves the choice of the relative length of the vessel at an early stage of the project. Considering the fact that the residual resistance at

$Fr_v = 2.2$ has a large part of the total resistance, the overall decrease in the relative total resistance $\frac{R}{\Delta}$ can be significantly

reduced. The residual resistance has a dominant part in the total resistance in the transitional mode. The residual resistance is about 70% of the total resistance in this mode. The friction resistance will also change after changing the relative length but will have less impact on the total resistance because the residual resistance is dominant.

An approximate formula for estimating the energy efficiency factor is $EEDI = \frac{aR}{k_1 k_2 \eta \Delta}$. Consequently, as

a result of the performed operations, a significant reduction in the carbon dioxide emissions into the atmosphere is possible.

The information in Fig. 6 shows the results of the calculation using the equation $1.1 \frac{\gamma_c L B d v^2}{2} = \frac{\gamma g k_w h_w^3}{8} B$, which is the

basis of the energy wave criterion EWC . This equation includes the kinetic energy of the vessel with the added masses of water (left part) and the full energy of the wave (right part). The energy of the vessel with the added masses of water is spent to overcome the barrier, and in accordance with the principle of change in kinetic energy, the speed of the vessel is reduced to zero.

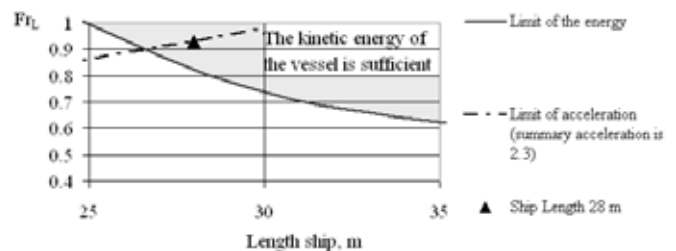


Fig. 6. Comparison of the energies of the ship and the energy of a wave with a height $h_{3\%} = 4.3$ m, $\frac{L_w}{h_{3\%}} = 20$.

The movement of the vessel "Length 28" towards a wave with a heights of $h_{3\%} = 4.3$ m is possible with a significant speed reduction. With a higher wave height $h_{3\%} = 4.5$ m, the ship will not be able to move against the wave. The points located above the curve characterize the vessels having enough kinetic energy for movement. The ship "Length 28" has the enough kinetic energy for movement with such a wave.

Fig. 6 shows the line for the limit of permissible design accelerations at such a wave. The line is built on the basis of the RINA and GL requirements for the maximum wave height that the ship can meet during the voyage $H_{sm} = 5 \frac{a_{CG}}{v} \frac{L^{1.5}}{6 + 0.14L}$. The length of the vessel and the Froude numbers were determined, which correspond to a wave height, subject to the condition $a_{CG} = 1.3$, for pleasure boats [5].

CONCLUSIONS

To solve the problem of determining the relative section modulus of an equivalent girder for a small vessel, the methods of structural mechanics and the theory ship design were applied: the equation of general strength, taking into account the summary acceleration, and the method of the preliminary calculation of the section modulus.

The joint solution of the above-mentioned equations gives the value of the relative section modulus of a transitional mode small vessel equal to $0.0003 \text{ m}^3/\text{t}$ for a steel hull. Taking into account the deadrise of the hull, a value of $\frac{W}{\Delta} = 0.00027 \text{ m}^3/\text{t}$ can be adopted. The data of the verification calculation of the relative section modulus for the H-girder confirmed the obtained results. When using other materials, the relative section modulus will take on different values, as shown in the example of a vessel with a glass reinforced plastic hull.

The maximum value of the relative length of a small high-speed vessel $\frac{L}{\sqrt[3]{V}}$, taking into account summary accelerations and $\frac{W}{\Delta}$, can be found from the inequality $\sigma_a \frac{kgW}{0.3v^2 \Delta} \geq \frac{L}{\sqrt[3]{V}}$

. Increasing the value of the relative length of the vessel leads to a decrease in water resistance, which in turn positively reduces the value of the factor *EEDI* and therefore reduces carbon dioxide emissions into the atmosphere.

Combining the three qualities of a ship: the general strength, propulsion, and energy efficiency presented in this article will help create safer and more energy efficient ships.

The use of the energy wave criterion *EWC* at an early stage of the project makes it possible to assess the possibility of a vessel moving towards a wave with a certain height or to predict a decrease in the vessel's speed. The proposed version of the graph, which demonstrates the relationship between the parameters of the future ship with the characteristics of sea waves and design accelerations, can be useful when creating a ship project. Such an assessment is extremely useful for certain categories of ships, such as rescue crafts. The criterion *EWC* contains ship data and sea wave characteristics, which allows the designer to evaluate various ship operation options.

REFERENCES

1. T. Zhang, J. Ren, and L. Liu, "Prediction of ship motions via a three-dimensional time-domain method following a quad-tree adaptive mesh technique," *Polish Marit. Res.*, vol. 27, no. 1, 2020, doi: 10.2478/pomr-2020-0003.
2. S. Bielicki, "Prediction of ship motions in irregular waves based on response amplitude operators evaluated experimentally in noise waves," *Polish Marit. Res.*, vol. 28, no. 1, 2021, doi: 10.2478/pomr-2021-0002.
3. N. Dormidontov and A. Kalmychkov, "On the concept of "small vessel" inland navigation" in *Experience in designing and construction, state and prospects of low-tonnage shipbuilding*, Technical Conference 1966, 1966.
4. Germanischer Lloyd, "Rules for classification and construction. High speed craft", 2012.
5. Bureau Veritas, "Rules and regulations for the classification of ships of less than 65 m in length. Part II-B. Hull Structure. Chapter 13. Light highspeed ships", 1990.
6. O. Kanifolskyi, "EEDI (energy efficiency design index) for small ships of the transitional mode," *Trans RINA, Intl J Small Craft Tech*, vol 156, Part B1, 2014, doi: 10.3940/rina.ijst.2014.b1.152tn.
7. M. Alivagabov and others, "Reference book on small shipbuilding", 1988.
8. O. Kanifolskyi and L. Krysiuk, "New area of application of the energy wave criterion (EWC): determination of the coastal navigation voyage", *Journal of Marine Science and Technology*. vol 27, issue 1, 2022, doi: 10.1007/s00773-021-00829-7.
9. Registro Italiano Navale. Rules for the classification of fast patrol vessels. Part B. Hull and Stability, 2007.

CONTACT WITH THE AUTHOR

Oleksandr Kanifolskyi

e-mail: oleksandrkanifolskyi@gmail.com

Odesa National Maritime University,
Faculty of Shipbuilding,
Information Technology and Systems Engineering, Odesa,
UKRAINE

CFD OPTIMISATION OF THE LONGITUDINAL VOLUME DISTRIBUTION OF A SHIP'S HULL BY CONSTRAINED TRANSFORMATION OF THE SECTIONAL AREA CURVE

Marek Kraskowski *

Maritime Advanced Research Centre S.A., Poland

* Corresponding author: marek.kraskowski@cto.gda.pl (M. Kraskowski)

ABSTRACT

The paper presents a proposal for a formalised approach to hull shape optimisation with respect to total resistance, by fine-tuning longitudinal volume distribution. An algorithm for automated modification of the hull is presented, allowing for varying the sectional area distribution with a negligible influence on the resulting displacement. Computational fluid dynamics (CFD) solver STAR-CCM+ and computer-aided design (CAD) software NX were used to search the optimal volume distribution of selected parent shapes, with respect to total resistance. The bow part and the aft part were optimised separately. The resulting resistances of the selected optimal shapes were then verified by means of scale model tests, realised in the towing tank at the Maritime Advanced Research Centre (CTO) S.A. A noticeable gain in total resistance was achieved and confirmed by experimental tests. The proposed approach seems to be a promising method for relatively quick parametric optimisation of the designed hull shapes; it is also applicable for generic CFD optimisation studies.

Keywords: parametric optimisation, CFD, model tests, resistance, wave pattern

INTRODUCTION

The trends observed in modern research focused on experimental and computational ship hydromechanics, reflect new possibilities provided by advanced software, high-performance computers and advanced control systems applied in experimental setups. Examples of state-of-the-art experimental techniques were presented by Lu et al. [1] and Bielicki [2]. In computational fluid dynamics, the focus is on simulating fully nonlinear dynamics [3] and on effective shape optimisation [4]. In terms of computational analyses, the last two decades have witnessed a revolution in the feasibility of computational fluid dynamics (CFD) analyses in engineering applications. In the early 2000's, viscous flow analyses were

carried out by full-time researchers, for relatively simple objects and with the use of coarse block-structured meshes. However, objects of arbitrary complexity can now be easily analysed by engineers. This progress has mainly been made possible due to the development of computers, automated unstructured meshing, and the ability to handle complex geometries and user-friendly graphic interfaces. Attempts to formalise the optimisation of analysed geometries were also made from the very beginning of the solvers development. Initially, the multi-variant analyses were possible with the use of potential codes [5] and for 2D cases [6]. Later on, the growing power of computers and efficiency of computer-aided design (CAD) software allowed for parametric optimisation of actual 3D geometries with the use of Reynolds-Averaged Navier-Stokes

(RANS) solvers. An example of the effective optimisation of a parametrised hull shape was presented by Gundelach [7]. His approach to hull modelling can be referred to as a Fully Parametric Model (FPM), in which the CAD surface is based on Non-Uniform Rational B-Spline (NURBS) curve surfaces defined from scratch. A foundation for this approach was prepared by Nowacki [8] and Harries [9,10]. Examples of the successful application of fully parametric models for hull shape optimisation were presented by Biliotti et al. [11], Han et al. [12] and Brenner et al. [13]. In order to make the optimisation process more efficient, surrogate models are also used [14]. However, parametrisation of a free form shape, like a ship's hull, usually requires careful selection of the regions to be modified and advanced coding, which makes the CAD preparation time-consuming, and so this approach is not very feasible in engineering practice. An alternative approach is the *a posteriori* transformation of an existing CAD file, which makes the possibilities for modification very limited, but the parametrisation itself can be realised relatively quickly [15]. Examples of such an approach were presented by Peri and Campana [16], Perez and Clemente [17] and Choi [18]. This paper also presents a variant of this approach; the optimisation is focused on finding the optimum balance between the angle of the ends of the waterplane and the fairness of the shoulders. This kind of optimisation is applicable for fine-tuning of pre-optimised shapes with no major faults. An example of the application of the proposed approach, to a selected shape, and the experimental verification of the results is presented.

PARENT HULL SHAPE

The presented analyses were carried out for the INSEAN 7000 DWT Tanker. Its shape is presented in Fig. 1 and its basic features are presented in Table 1.



Fig. 1. Parent hull shape

Tab. 1. Basic features of the parent hull shape

Length between perpendiculars	L_{pp} [m]	94.00
Breadth	B [m]	15.40
Draught	T [m]	6.00
Displacement	∇ [m ³]	6827
Wetted surface area	S [m ²]	2249
Block coefficient	C_B [-]	0.786
Design speed	V [kn]	14
Froude number	F_n [-]	0.237

POSSIBLE APPROACHES TO SHAPE PARAMETRISATION

Parametrisation of the CAD geometry consists of defining the dependencies between the locations of points and angles of curves etc. by introducing expressions, such that changing the value of one or more global variables modifies the whole geometry. This can be explained by the simple example of a cube. If the properties of this solid are not known, its unequivocal definition in a Cartesian coordinate system requires the specification of 24 figures, i.e. three coordinates for each of the eight corners of the cube. However, if we know the dependencies between the coordinates of the cube corners, we can define and modify its geometry by giving just one figure, i.e. the length of one side.

Two important observations can be made on the basis of this example:

1. Although the modification of the parametrised geometry is very fast, much more work is required to prepare the CAD definition, due to the need to define the dependencies between selected geometric features of the object.
2. Parametric definition of the object loses flexibility in introducing the modifications, e.g. changing the form of the regular cube into an arbitrary cuboid is not possible with parametric definition, while it is straightforward with a standard definition.

Several attempts have been made to achieve effective hull form parametrisation; it was found that two general approaches can be distinguished:

1. Building the parametrised hull definition from scratch, i.e. defining points, curves and surfaces so as to match the required basic shape, and then defining the dependencies between the locations of the points, curve angles etc. to enable efficient modifications.
2. Defining the control points and planes so as to control the surface provided in the form of a CAD exchange file, e.g. IGES, and then defining the dependencies between the locations of control points and planes to enable efficient modifications.

The 'pros and cons' of the described approaches can be easily pointed out, assuming that the task to be realised consists of optimising the initial proposal of the shape provided by the customer.

1. Building the parametrised definition from scratch.

Advantages:

- + allows much more accurate control of the details of the geometry;
- + provides full flexibility in deciding which regions will be modified and how.

Disadvantages:

- when the definition is relatively simple, i.e. based on a small number of points and curves, it is almost impossible to accurately match the basic shape required;
- on the other hand, if the shape is to be reproduced accurately, the complexity of the definition increases

dramatically, which makes it less useful in introducing modifications;

- defining the hull from scratch always requires a relatively long time, while the fast exchange of proposals is especially important at an early stage of the contract.

2. Defining the control points and planes allowing transformations of the existing shape.

Advantages:

- + full match between the basic shape and its parametrised definition;
- + the process of parametrisation is fast and easy.

Disadvantages:

- considerably limited control of the details of the geometry.

Both approaches were attempted and the results are presented in the following sections.

HULL PARAMETRISATION

As mentioned in the introduction, the selected approach is based on the *a-posteriori* transformation of existing hull surface definition; an attempt to model the shape with a fully parametric definition turned out to be inefficient. It was either very hard to obtain the required consistency with the parent shape, or the definition became extremely complex. Parametric transformation of the existing geometry was realised using the Global Shaping feature of the NX software. NX CAD is a very generic environment, designed for integrated computer aided engineering. It contains CAD, CAM, CFD, FEM and other tools; in the presented work, only the CAD module was used. Global Shaping is a feature dedicated to manipulating the features of an object imported as an external geometry file. The method of transformation is explained on the basis of Fig. 2 and can be described as a formalised global shaping.

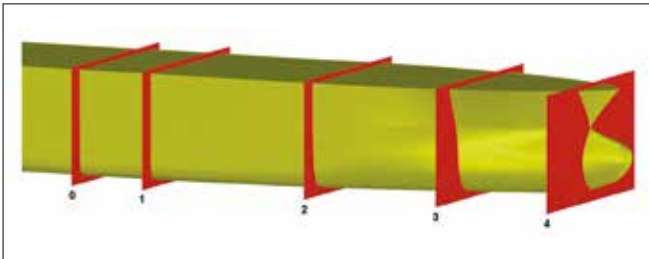


Fig. 2. Transformation with the use of control planes

An arbitrary number of control points is assigned to the transformed region. In the presented case, the transformation is applied to the region between the mid-ship section and the fore perpendicular. The locations of the points located at the ends of the region (0 and 3 in the presented case) remain unchanged. All of the control points located between them (1-2) can be shifted arbitrarily, which results in the continuous shift of the hull sections in the region between points 0 and 3. The resulting shift in individual sections, relative to their initial position, is evaluated using the Bézier curve formulation. This formulation is explained in detail below.

Let us define the vector of the initial locations of the control points:

$$X_{BASE} = [x_0 \ x_1 \ x_2 \ x_3 \ x_4]. \quad (1)$$

The transformation is realised by shifting the control points to new locations:

$$X_{TR} = [x_{0,TR} \ x_{1,TR} \ x_{2,TR} \ x_{3,TR} \ x_{4,TR}]. \quad (2)$$

In the presented case, $x_0 = x_{0,TR}$ and $x_4 = x_{4,TR}$; however, in a generic case, this does not necessarily hold true.

The difference between the initial and transformed location of the control points is denoted as:

$$\Delta X = X_{BASE} - X_{TR} = [\Delta x_0 \ \Delta x_1 \ \Delta x_2 \ \Delta x_3 \ \Delta x_4]. \quad (3)$$

Our goal is to evaluate the shift of an arbitrary point located between x_0 and x_4 , based on the values of ΔX . For this purpose, we introduce the parameter $t \in [0,1]$ and parametrise the length of the transformed region, so that x_0 corresponds to $t = 0$ and x_4 corresponds to $t = 1$. The shift of the arbitrary point between x_0 and x_4 is evaluated using the formula:

$$dx(t) = \sum_{i=0}^n \Delta x_i B_i^n(t) \quad (4)$$

where are so-called Bernstein polynomials [9] and defined as:

$$B_i^n(t) = \begin{cases} \binom{n}{i} t^i (1-t)^{n-i} & \text{for } i = 0 \dots n \\ 0 & \text{for } i < 0, i > n \end{cases} \quad (5)$$

Let us now present an example of shape transformation based on 4 control points ($n = 3$). The graph below (Fig. 3) shows the form of Bernstein polynomials for $i = 0 \dots 4$.

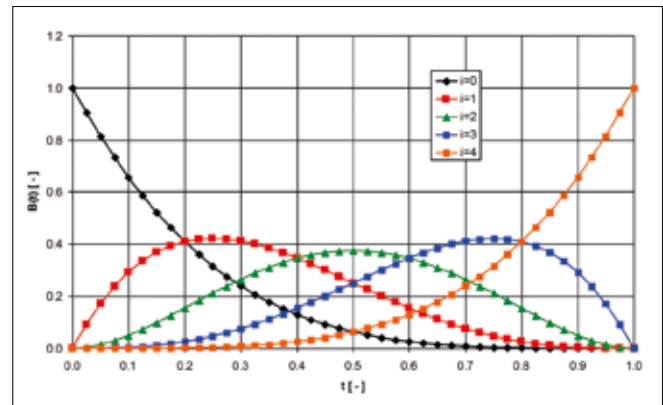


Fig. 3. Bernstein polynomials

The formulation of the transformation results show that the locations of the control points have no influence on the transformation results; it is only the number of control points which affects the transformation form. The control points are, thus, evenly distributed along the modified region, which results from the technical requirements of the applied NX software (we use mid-ship as the zero point and fore perpendicular as the end point, $x = 47$ m):

$$X_{BASE} = [0 \ 11.75 \ 23.50 \ 35.25 \ 47]. \quad (6)$$

We then introduce the following transformation based on a single parameter p (values of the vector ΔX):

$$\Delta X = [0 \quad -p \quad -p \quad a \cdot p \quad 0]. \quad (7)$$

According to Eq. (7), the result of shifting three control points on the transformation of the sectional area curve of the bow part is shown in Fig. 4 (modified – red). The contribution of subsequent control points, as well as the resulting shift dx , is presented in the second graph.

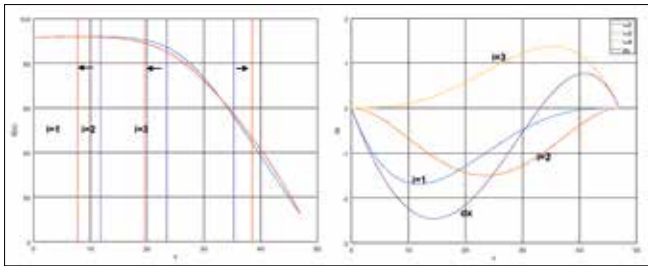


Fig. 4. Using Bernstein polynomials for shape transformation

The coefficient a is a constant which is used to calibrate the transformation procedure, so that the displacement volume remains constant within a considered range of variation of parameter p . The range of p is limited by the software requirements, i.e. the control planes must not swap places along the hull after transformation; in other words: if the x coordinate of plane i is larger than the x coordinate of plane $i-1$ before transformation, it must still be larger after transformation (this is not a limitation of the formulation itself). On the other hand, the transformed shape for extreme values of parameter p must still fit the ship-shape canon; however, this criterion has no mathematical formulation, it is only based on designer experience and intuition. The procedure for selecting the range of p and value of a can be described as follows:

- select an interval (usually symmetrical) of parameter p which meets the mentioned criteria; in the presented example, the range is from -4 to 4 ;
- set the value of p to the minimum of the assumed interval and set the value of a to 1 ;
- use the trapezoid rule to integrate the sectional area curve and compare the displacement volume before and after the transformation; vary the coefficient a to obtain a match;
- repeat the procedure for the maximum value of parameter p , using the value of a found in the previous step; in the presented example, a match was achieved without further iteration.

Using a MATLAB routine for the transformation and integration allows the correct value of a to be found in just a few steps, in a guess-and-check manner. In the presented example, a constant value of a allowed a constant displacement to be maintained with an accuracy of 0.2 m^3 , i.e. 0.006% .

The longitudinal centre of buoyancy (LCB) of the ship is not directly controlled in the described procedure. In the presented example, changing the parameter p between -4 and 4 , results

in shifting the centre of volume of the fore part by 0.113 m , which results in shifting the LCB of the ship by 0.057 m (0.06% of L_{pp}). If such a change in LCB is acceptable, as assumed in the presented study, the fore part and the aft part can be optimised independently. If not, then the aft part must be transformed in parallel with the fore part, so as to compensate any change in LCB. The resulting modifications of the sectional area curve for extreme values of parameter p are presented in Fig. 5.

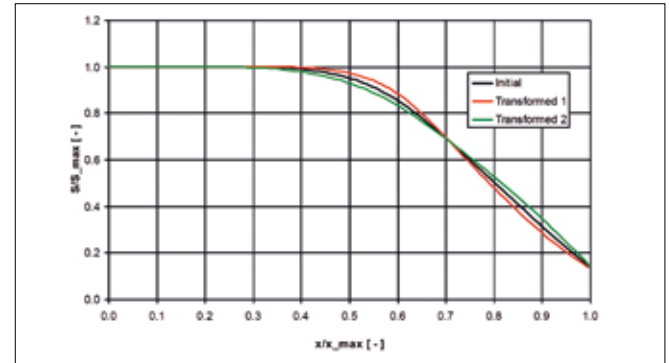


Fig. 5. Considered range of modifications of the longitudinal volume distribution

The described method of parametrised hull transformation is quite similar to the well-known Lackenby transformation [20], in the sense that existing hull sections are moved to new locations. The features of the method, in comparison with the studies presented by the cited authors, are as follows:

- shape is controlled by just one parameter;
- applied constraints imply that all of the modifications generated during the optimisation process are allowable (constant displacement volume);
- a very small number of cases are analysed in order to find the optimum.

The method is also easy to implement, using the commercial NX software in the presented study. On the other hand, its drawback is that, at the moment, it is dedicated to optimise a single geometric feature of the hull.

COMPUTATIONAL MODEL

The resistance for subsequent variants of the parent shape was computed with the use of STAR-CCM+ solver. The computations were carried out at full scale. The CFD solver was coupled with the NX CAD software and the computational procedure was executed in the following manner:

- a table of the required range of parameter p to be analysed, was pre-defined and imported to the CFD solver;
- the CFD solver managed the process by sending the command to the CAD software at the beginning of each analysis, to execute another modification;
- the modified shape was imported to CFD solver, which executed the re-meshing and analysis.

This procedure is presented in the form of the flowchart in Fig. 6.

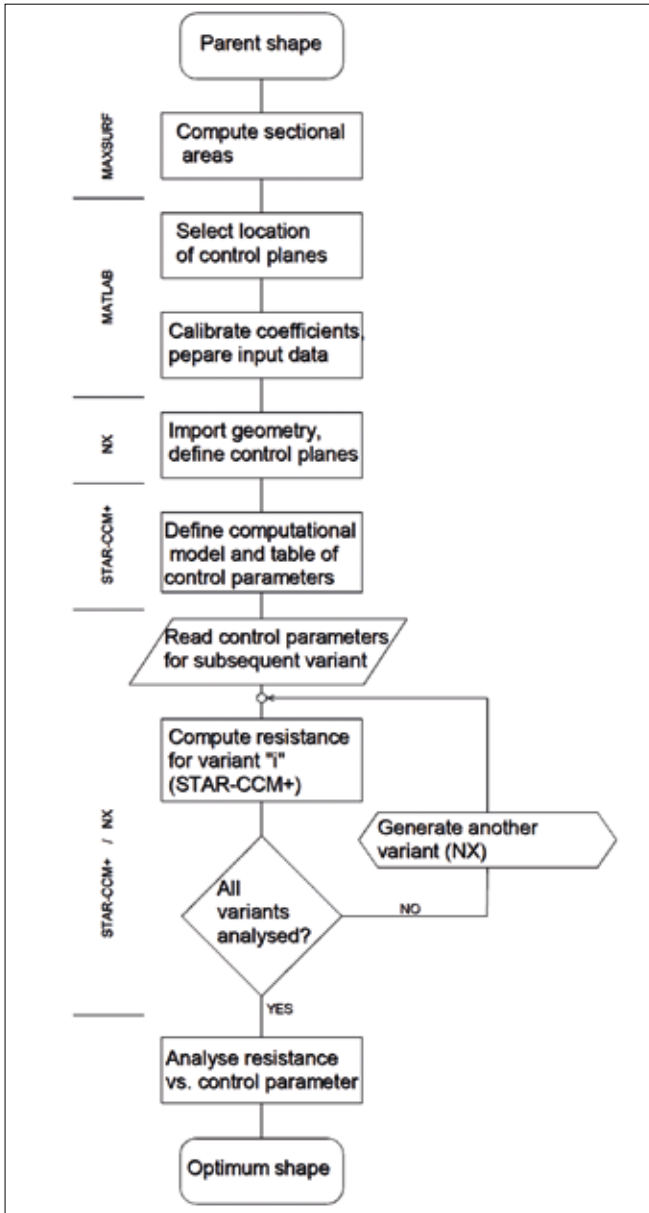


Fig. 6. Optimisation procedure - flowchart

As the low computational time is of high priority, and the focus was primarily on differences in resistance rather than absolute values of the resistance, a relatively coarse mesh was used and the dynamic trim and sinkage were neglected. Initial trim and draught were adjusted, based on the computations for the parent shape, and remained unchanged for all other variants, assuming that their variation would be small, due to constant displacement and LCB. The number of mesh cells for the optimisation process was 1.9×10^6 . Computations for variable mesh density confirmed that increasing the number of cells above this value does not influence the tendencies revealed in the optimisation process. The boundaries of the rectangular domain were located as follows: inlet - $2L$ upstream of the bow, outlet - $2L$ downstream of the stern, bottom - $2L$ below the hull base line, top $1L$ above the hull base line, lateral wall - $2L$ from the hull symmetry, where L is the overall ship length. The computational domain is presented in Fig. 7.

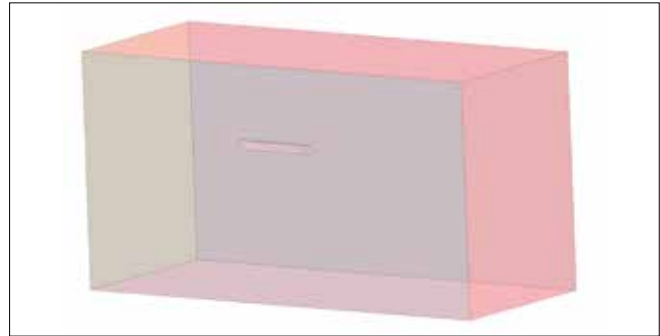


Fig. 7. Computational domain size

The types of boundary condition are as follows:

- upstream, top, bottom and side walls of the domain: prescribed velocity components and volume fraction of water;
- downstream: prescribed pressure;
- hull: no-slip wall.

The wave damping zone was used in the region close to the domain boundaries in order to speed up convergence by preventing the wave reflections inside the domain.

The settings of the computational model were as follows:

- free surface treatment: multiphase flow (Volume of Fluid);
- implicit unsteady model;
- turbulence model: k-epsilon;
- time step: 0.02 s;
- 5 outer iterations per time step.

The visualisations of the mesh are presented in Fig. 8 and Fig. 9.

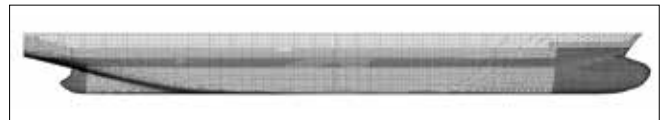


Fig. 8. Computational mesh - hull surface

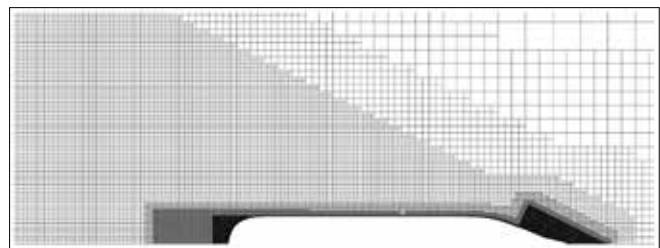


Fig. 9. Computational mesh - free surface region

The resulting y^+ values on the hull surface are presented in Fig. 10. Relatively large values of y^+ (above 100) enforce the application of wall functions.

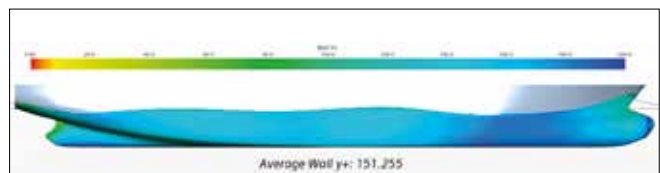


Fig. 10. Wall y^+ on the hull surface

Convergence of the continuity equations and convergence of the resistance value for the selected case are presented in Fig. 11 and Fig. 16, respectively.

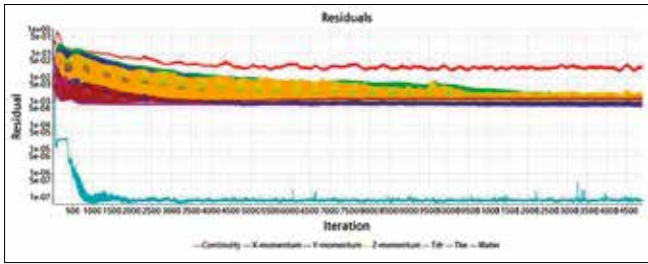


Fig. 11. Residuals

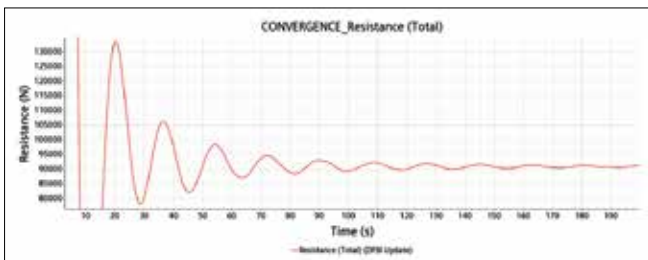


Fig. 12. Convergence of the resistance

RESULTS OF BOW PART OPTIMISATION

The bow part optimisation, with respect to resistance, was carried out in two steps. The first step was the optimisation of the longitudinal volume distribution between the mid-ship section and the fore perpendicular; the second step was the optimisation of the bow bulb length. Location of the control points, for the optimisation of longitudinal volume distribution, is presented in Fig. 13 (three variable control points).

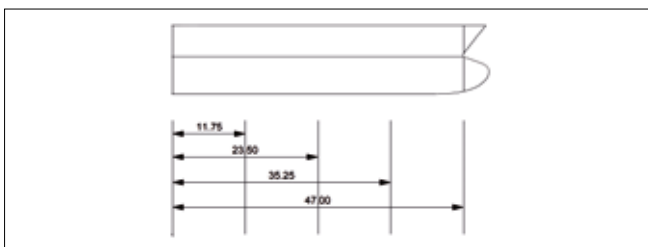


Fig. 13. Location of the control points for the bow part

Location of the control points for the optimisation of bow bulb length is presented in Fig. 14.

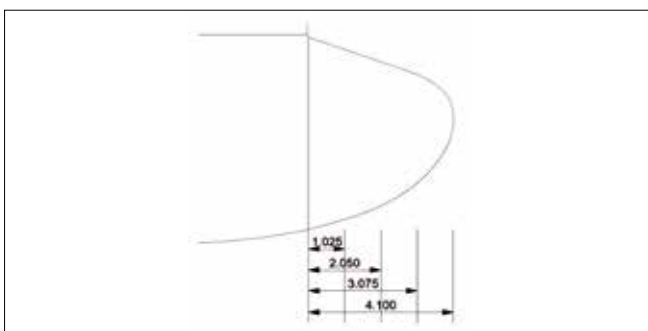


Fig. 14. Location of the control points for the bow bulb

The search for the optimum longitudinal volume distribution started with a quick analysis of global tendency. Five values of parameter p were used to generate the population of shapes: -4, -2, 0, 2 and 4 (5 variants), where $p = 0$ corresponds to parent shape. The resulting relative resistance values are presented in Fig. 15.

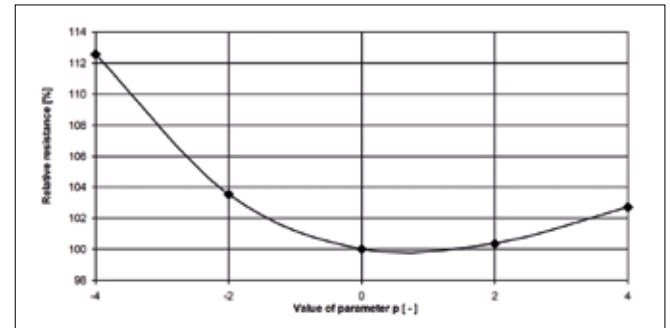


Fig. 15. Relative resistance for five variants of the bow part

The influence of the modifications on the bow pattern for two extreme variants as well as the optimal variant is presented in Fig. 16.

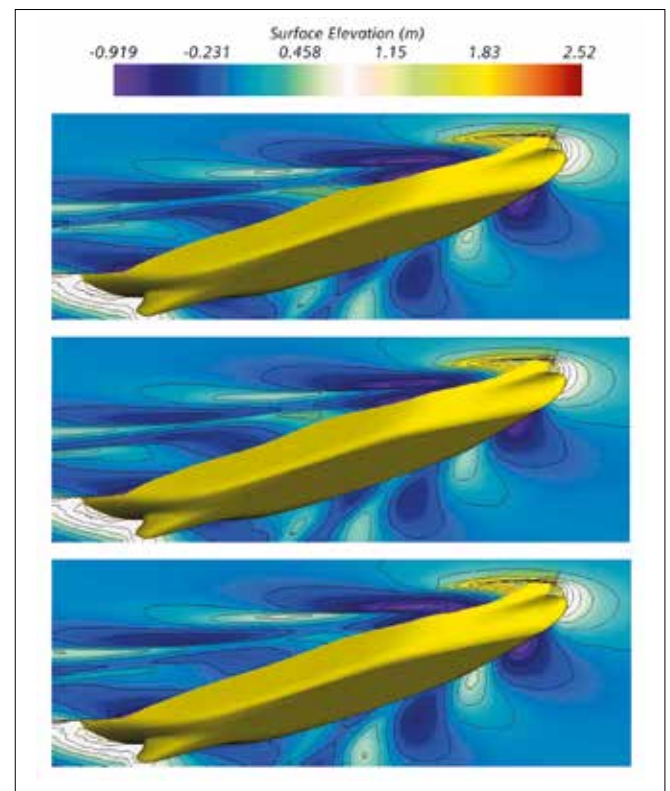


Fig. 16. Optimisation of the bow part - wave pattern: lowest waterplane entrance angle (top), optimum (middle) and fairest shoulder (bottom)

The quantitative results show that the computer resistance is lowest for the parent shape, i.e. no improvement was achieved in the first attempt. However, the shape of the curve suggests that the actual minimum resistance should be expected for the value of parameter p between 0 and 2. Thus, the computations were continued for three more variants of hull shape, corresponding to the values of parameter p equal to 0.4, 0.74 and 1.0. The results are presented in Fig. 17.

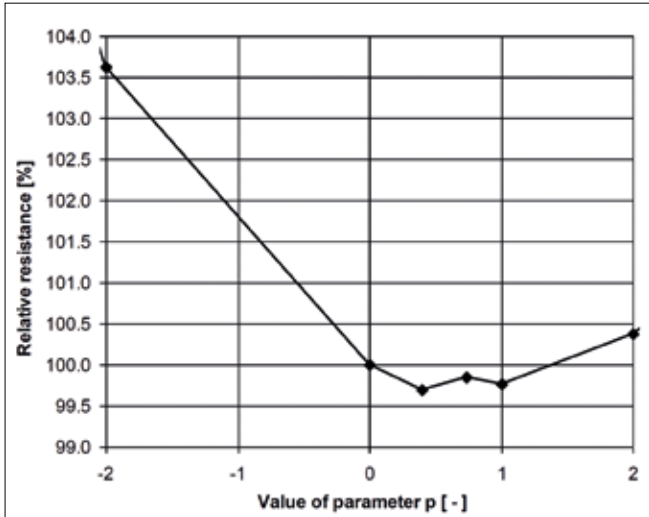


Fig. 17. Analysis of relative resistance for refined range of parameter p

A slight reduction in resistance was observed; however, it was almost negligible (approximately 0.25%).

The next step of the optimisation of the bow part was the optimisation of the bulb length. The length was changed within the range 4.1-6.1 m (the upper limit was selected arbitrarily). In the case of bulb optimisation, the influence of its size on total displacement volume was neglected; the actual increase of volume for the longest bulb was 16 m³, which corresponds to 0.2% of the total volume of the parent shape. A change in LCB also occurs, equal to 0.12% of L_{PP} . The location of the control points presented in Fig. 14 was changed, proportionally, i.e. the bulb was transformed by uniform 'stretching'. Five variants of the bulb were analysed. The resulting relative resistance values are presented in Fig. 18 (100% now corresponds to initial bulb length).

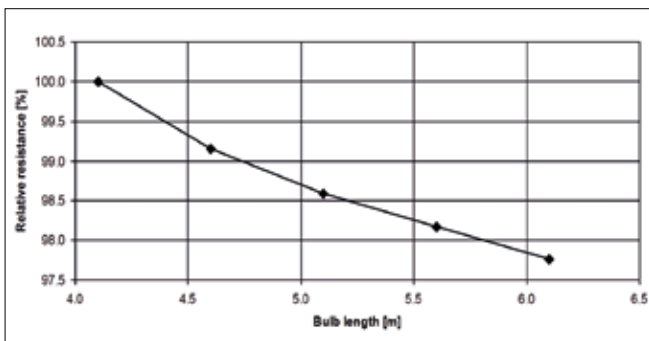


Fig. 18. Relative resistance as a function of bulb length

As can be seen, the resistance decreases monotonically with increasing bulb length. The total reduction of resistance due to optimisation of the bow part achieved is 2.54%, which is noticeable from the point of view of fuel consumption.

The influence of the bow bulb modifications on the wave pattern are presented in Fig. 19.

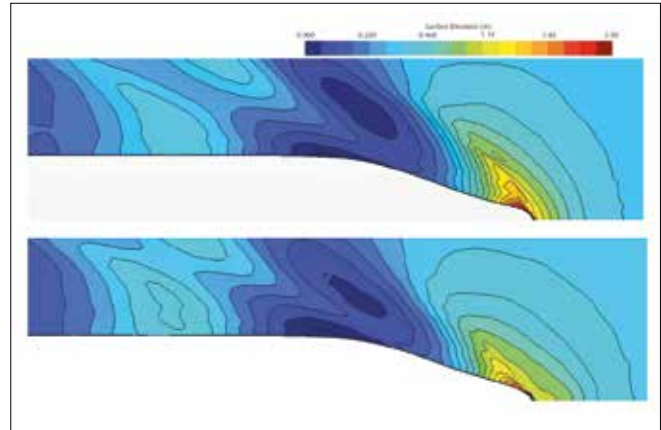


Fig. 19. Optimisation of the bow bulb - wave pattern: initial bulb (top) vs. optimised bulb (bottom)

Comparison between the bow parts of the parent shape and the optimised one is presented in Fig. 20.

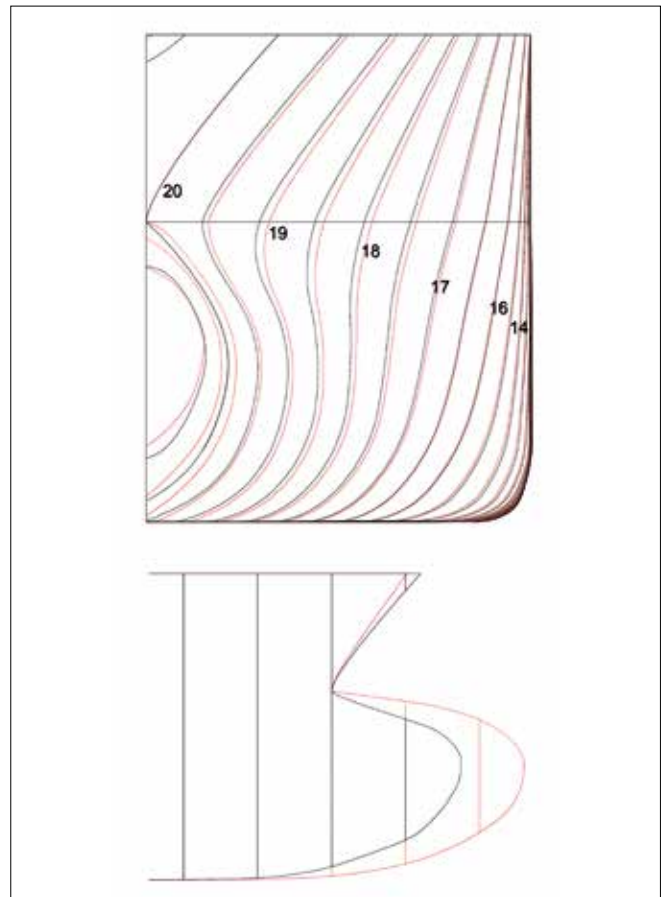


Fig. 20. Bow part - parent shape (black) vs. optimised one (red)

RESULTS OF STERN PART OPTIMISATION

Optimisation of the stern part only comprised the optimisation of the longitudinal volume distribution. The location of the control points is presented in Fig. 21 (four variable control points).

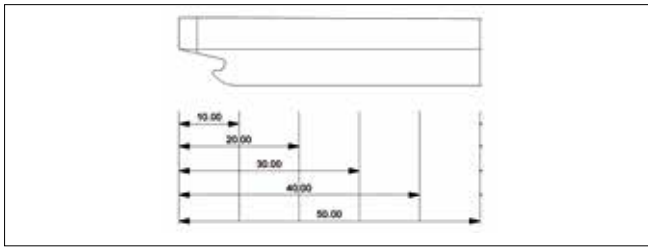


Fig. 21. Location of the control points for the stern part

In the case of a stern part, there are four intermediate control points: the values of the vector

$$\Delta X = [0 \quad -p \quad -p \quad a \cdot p \quad a \cdot p \quad 0]. \quad (8)$$

The considered values of parameter p were: -3, -1, 0, 1, 3, 5 and 6 (seven variants), where $p = 0$ corresponds to the parent shape. The relative resistance for the resulting hull shape variants is presented in Fig. 22.

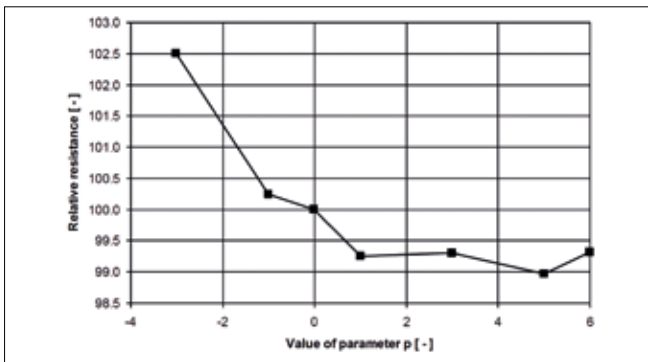


Fig. 22. Relative resistance for seven variants of the stern part

In the case of the stern, total resistance was reduced by 1.03%, according to CFD results. The influence of the stern part modifications is presented in Fig. 23.

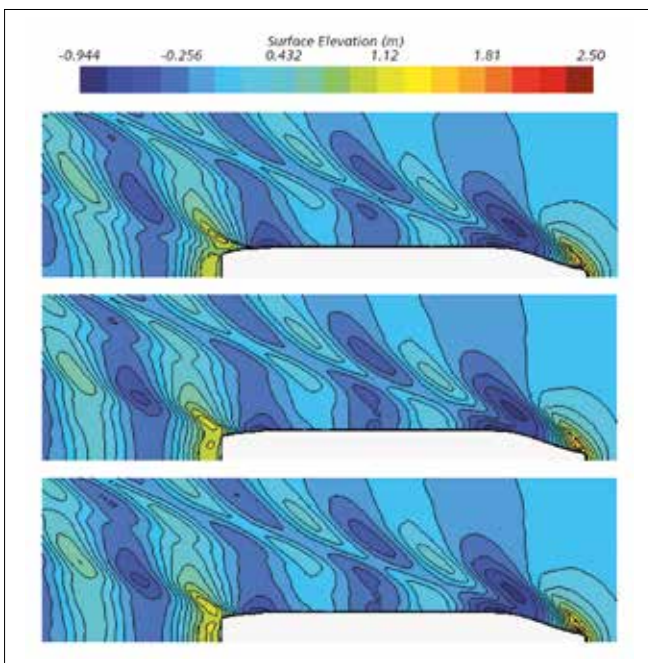


Fig. 23. Optimisation of the bow part - wave pattern: lowest waterplane entrance angle (top), optimum (middle) and fairest shoulder (bottom)

Comparison between the aft parts of the parent shape and the optimised one is presented in Fig. 24.

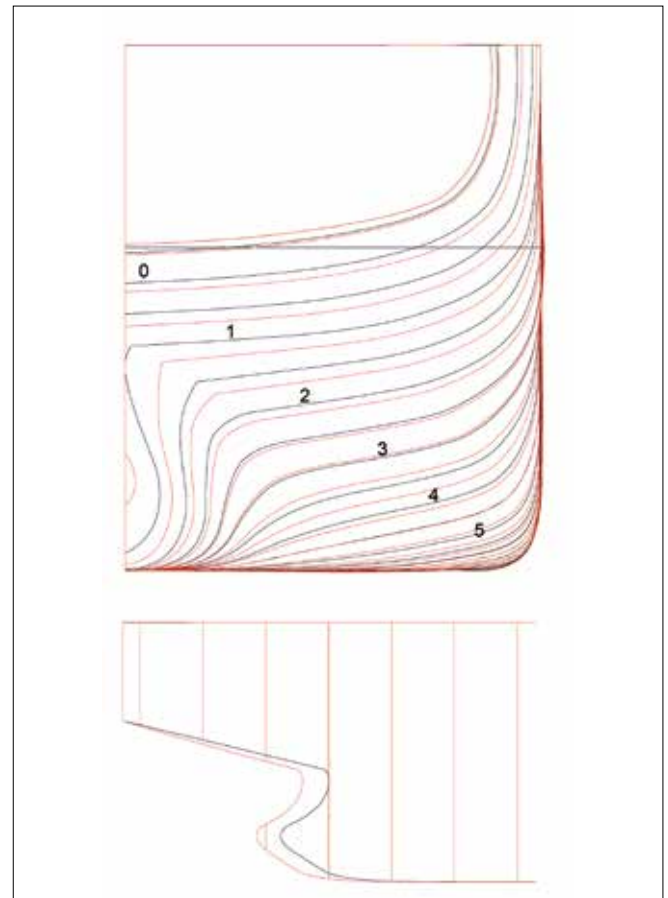


Fig. 24. Aft part - parent shape (black) vs. optimised one (red)

RESULTS OF EXPERIMENTAL VERIFICATION

The experiments were carried out on a model built at a scale 17.035, in the towing tank at CTO, S.A. The model was built in two parts, so that the influence of the bow part optimisation and stern part optimisation could be verified separately. Three configurations were tested:

- initial bow + initial stern
- optimised bow + optimised stern
- optimised bow + optimised stern.

The experimental model is presented in Fig. 25.



Fig. 25. Model testing

The resulting resistance (the direct results of the model tests) is presented in Fig. 26.

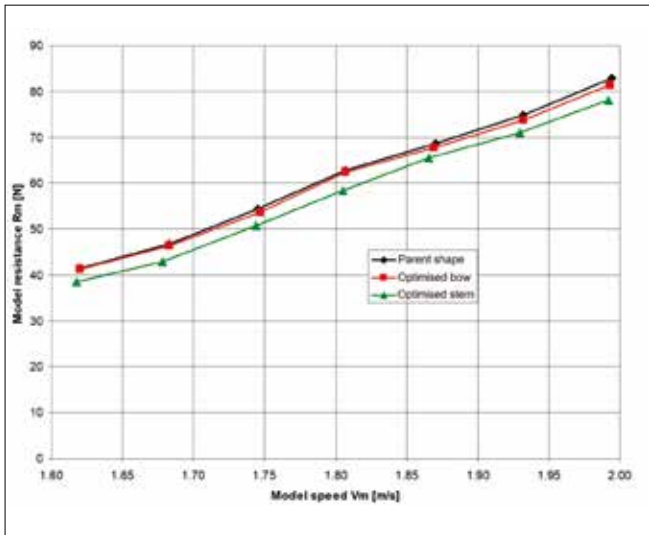


Fig. 26. Results of model tests

A quantitative comparison between the full scale resistance extrapolated from model tests and those computed with CFD for a design speed of 14 knots, is presented in Table 2.

Tab. 2. Comparison between model tests and CFD

	Experiment		CFD	
	Resist. [kN]	Reduct. [%]	Resist. [kN]	Reduct. [%]
Optim. Bow / orig. aft	211.4	–	183.4	–
Optim. Bow / orig. aft	207.9	1.7	178.7	2.5
Optim. Bow / orig. aft	200.8	5.0	176.8	3.6

A general underestimation of the total resistance in CFD computations can be observed, which is primarily explained by neglecting the dynamic trim and sinkage in CFD. Besides that, the resistance measurement results show different values of the gain in total resistance due to optimisation; however, the tendency observed in CFD computations was confirmed.

SUMMARY

This paper proposes an approach to parametric optimisation of a ship's hull, with respect to resistance, based on a *posteriori* transformation of an existing CAD file. The transformation is realised so that the volume of the submerged part remains unchanged. The optimisation is realised by coupling the CFD solver STAR-CCM+ with the NX CAD software. A prescribed set of parameters is considered and the resulting modifications are compared, with respect to total resistance. The bow part and the stern part were optimised separately. The conclusions are as follows:

- the parent shape is already well optimised, so that only a small reduction in resistance could be achieved;
- some reduction in resistance was obtained, both for the

bow part and for the stern part (in the case of the bow part, the reduction in resistance was mainly achieved by bow bulb elongation);

- the values resulting from model testing are not consistent with the values obtained from CFD; however, the correct tendency was shown with CFD computations;
- the possibility of modification with the presented method is extremely limited, but, on the other hand, it can be applied quite fast and the optimisation process is relatively short, as the optimum can be found for a small number of variants.

Further work should include taking into account the following issues:

- introducing the constraints in the stern shape transformation, so that the propeller space remains unchanged;
- verification of the influence of stern shape transformation on propulsive and cavitation characteristics, based on a study similar to the one presented, e.g. by Zhang et al. [21].

ACKNOWLEDGEMENTS

This research was financed by the National Centre for Research and Development of the Republic of Poland, within the framework of the Esthetics project (POLTUR3/ESTHETICS/1/2019).

BIBLIOGRAPHY

1. Y. Lu, J. Wu, W. Li and Y. Wu, 'A new six-dof parallel mechanism for captive model test', Polish Maritime Research, No. 3 (107), Vol. 27; pp. 4-15, 2020, DOI: 10.2478/pomr-2020-0041 27.
2. S. Bielicki, 'Prediction of ship motions in irregular waves based on response amplitude operators evaluated experimentally in noise waves', Polish Maritime Research, No. 1(109), Vol. 28, pp. 16-27, 2021, DOI: 10.2478/pomr-2021-0002.
3. Q. Wang, P. Yu, B. Zhang, G. Li, 'Experimental Study and Numerical Simulation of the Water Entry of a Ship-Like Symmetry Section with an Obvious Bulbous Bow', Polish Maritime Research, No. 3(111), Vol. 28, pp. 16-34, 2021, DOI: 10.2478/pomr-2021-0031.
4. A. Karczewski, M. Kunicka, 'Influence of the Hull Shape on the Energy Demand of a Small Inland Vessel with Hybrid Propulsion', Polish Maritime Research, No. 3(111), Vol. 28, pp. 16-34, 2021, DOI: 10.2478/pomr-2021-0032.
5. H.C. Raven, 'A solution method for the nonlinear ship wave resistance problem', Ph.D. dissertation, Delft Univ. Techn., 1996.
6. A. Stück, 'Adjoint Navier-Stokes Methods for Hydrodynamic Shape Optimisation', Ph.D. dissertation, Technische Universität Hamburg-Harburg, 2012.

7. M. Gundelach, 'Sketched Parametric Modeling in CFD Optimisation', Master thesis, Feb/2017, University of Rostock, Germany.
8. H. Nowacki, D. Liu, and X. Lü, 'Fairing bézier curves with constraints', *Computer Aided Geometric Design*, 7(1-4), 43-55 (1990).
9. S. Harries, 'Parametric Design and Hydrodynamic Optimisation of Ship Hull Forms', Mensch-und-Buch-Verlag, Berlin (1998).
10. S. Harries, C. Abt, 'Parametric curve design applying fairness criteria', *International Workshop on Creating Fair and Shape-Preserving Curves and Surfaces* (1998).
11. I. Biliotti, S. Brizzolara, M. Viviani, G. Vernengo, D. Ruscelli, M. Galliussi, D. Guadalupi, and A. Manfredini, 'Automatic parametric hull form optimisation of fast naval vessels', *Proceedings of the Eleventh International Conference on Fast Sea Transportation (FAST 2011)*, 2011.
12. S. Han, Y.-S. Lee, and Y.B. Choi, 'Hydrodynamic hull form optimisation using parametric models', *Journal of Marine Science and Technology*, 17(1), 1-17, 2012, DOI: 10.1007/s00773-011-0148-8.
13. M. Brenner, V. Zagkas, S. Harries, and T. Stein, 'Optimisation using viscous flow computations for retrofitting ships in operation', *Proceedings of the 5th International Conference on Computational Methods in Marine Engineering, MARINE*, 2013.
14. Y. Feng, O. el Moctar, and T.E. Schellin, 'Parametric Hull Form Optimisation of Containerships for Minimum Resistance in Calm Water and in Waves', *Journal of Marine Science and Application* 20, 670-693, 2021. DOI: 10.1007/s11804-021-00243-w.
15. G. Vernengo, D. Villa, S. Gaggero, and M. Viviani, 'Interactive design and variation of hull shapes: pros and cons of different CAD approaches', *International Journal on Interactive Design and Manufacturing*, 14, pp. 103-114, 2020. DOI: 10.1007/s12008-019-00613-3.
16. D. Peri, and E.F. Campana, 'Multidisciplinary design optimisation of a naval surface combatant', *Journal of Ship Research* 47(1), 1-12, 2003, DOI: 10.5957/jsr.2003.47.1.1.
17. F. Perez, and J.A. Clemente, 'Constrained design of simple ship hulls with b-spline surfaces', *Computer Aided Design* 43(12), 1829-1840, 2011, DOI:10.1016/j.cad.2011.07.008.
18. H.J. Choi, 'Hull-form optimisation of a container ship based on bell-shaped modification function', *International Journal of Naval Architecture and Ocean Engineering* 7(3), 478-489, 2015, DOI: 10.1515/ijnaoe-2015-0034.
19. G.G. Lorentz, 'Bernstein Polynomials', University of Toronto Press, 1953.
20. H. Lackenby, 'On the systematic geometrical variation of ship forms', *Trans. INA* 92, 289-315, 1950.
21. Y. Zhang, X. P. Wu, M. Y. Lai, G. P. Zhou and J. Zhang, 'Feasibility Study of Rans in Predicting Propeller Cavitation in Behind-Hull Conditions', *Polish Maritime Research*, No. 4(108), Vol. 27, pp. 26-35, 2020, DOI: 10.2478/pomr-2020-0063.

CONTACT WITH THE AUTHOR

Marek Kraskowski

e-mail: marek.kraskowski@cto.gda.pl

Maritime Advanced Research Centre S.A.
Ship Hydromechanics Division
Gdansk
POLAND

FLOW FIELD CHARACTERISTIC ANALYSIS OF CUSHION SYSTEM OF PARTIAL AIR CUSHION SUPPORT CATAMARAN IN REGULAR WAVES

Jinglei Yang ¹

Han-bing Sun ^{2*}

Xiao-wen Li ¹

Xin Liu ¹

¹ Jimei University, School of Marine Engineering, Xiamen, China

² Harbin Engineering University, College of shipbuilding engineering, Harbin, China

* Corresponding author: sunhanbing@hrbeu.edu.cn (H. Sun)

ABSTRACT

In order to study the flow field characteristics of cushion system of partial air cushion support catamaran (PACSCAT) in waves, an analysis was carried out involving flexible treatment on the bow and stern air seals to simulate air seal shape under test conditions by means of computational fluid dynamics method and fluid structure interaction (FSI) method. On this basis, the pressure conditions of the air cushion chamber and the pressurized chamber at different wavelengths and different speeds are studied and compared with experimental results. The experimental results show that: for the air cushion pressure, the nonlinear characteristics of the numerical calculation results are more subtle than the experimental values, after linear transformation, the amplitudes of the experimental values are obviously greater than the calculated values after linear transformation, but the average values are not much different; At low speed of 2.0m/s, the spatial pressure distribution of the pressurized chamber and the air cushion chamber are uniformly distributed, at high speed of 3.6m/s, except for a certain pressure jump occurred in the air cushion chamber near the stern air seal, the pressure in other spaces is also evenly distributed, it proves that the pressurized chamber type of air intake can effectively meet the air cushion pressure balance.

Keywords: regular waves; partial air cushion support catamaran (PACSCAT); cushion system; fluid structure interaction (FSI); flow field characteristics

INTRODUCTION

The partial air cushion support catamaran (PACSCAT) is a new type of high-performance ship, which is based on slender catamaran and supported by air cushion [1-2]. It not only can sail at high speed with the attitude of planning boat, but also has outstanding sailing stability and maneuverability. Due to the wide sidewall of the PACSCAT, propellers or water jets can be used as propulsion devices, allowing PACSCAT to have better maneuverability than air cushion vehicle (ACV).

The non-uniform distribution of air cushion is a difficulty in studying the motion characteristics of hovercraft. So,

it is necessary to establish a spatial non-uniform pressure distribution model of air cushion. In fact, the form of air cushion spatial distribution is closely related to the governing equation satisfied by aerodynamic force. The continuity equation is related to the spatial uniform distribution of the air cushion, the one-dimensional wave equation is related to the non-uniform distribution of the air cushion along the length direction, and the three-dimensional wave equation is related to the non-uniform pressure distribution of the air cushion in three dimensions. Obviously, it is the latter two governing equations that are more accurate to describe the spatial non-uniform pressure distribution characteristics of

air cushion. The hydrodynamic analysis software of the air cushion platform ACVSIM [3-4] and WAMIT [5], can be used to obtain the distribution characteristics of the air cushion in three-dimensional space. Of which, ACVSIM uses the three-dimensional wave equation directly as the governing equation of the air cushion flow field, and its numerical solution adopts the immersion boundary element method (IBM). The immersed boundary element method can allow the air cushion boundary to deform and is suitable for the air cushion with speed and arbitrary shape. On the other hand, WAMIT uses the method of transforming 3D wave equation into Helmholtz equation (assuming aerodynamic force as harmonic pulsation) as the governing equation of air cushion flow field, and its velocity potential is obtained by Fourier series solution which is applicable to rectangular air cushion (Lee and Neumann, (2016) [6]. Therefore, the establishment of the spatial non-uniform pressure distribution model can solve the heave, pitch and other motion problems of hovercraft, achieve accurate simulation of the aerodynamic force under any wave direction, and help to explain the unique resonance problems of hovercraft, such as “pebble” effect [7] or acoustic resonance phenomenon [8].

As a practical engineering method with wide application in the calculation of ship hydrodynamic, numerical method has been proved to be applicable to the simulation of hovercraft motion [9-11]. In the simulating calculation of PACSCAT motion, the mechanical models are considered nonlinear except the fan characteristic equation which cannot completely simulate the fan pumping up, and the motion characteristics are also considered strongly nonlinear [12-13], which are highly consistent with the strong nonlinear phenomenon caused by multiple factors of PACSCAT. When the hovercraft is sailing in the waves, the pressure and flow field of the air-cushion system will change to a certain extent due to the nonlinear discharge, which will not only affect the movement performance, but also seriously affect the normal use of the hovercraft. Due to the high speed of the local air-cushion catamaran, the pressure and flow field characteristics of the air-cushion system have a crucial impact on the navigation performance. Therefore, the purpose of this paper is to study the pressure characteristics and air-cushion space of the cushion lift system in waves. distribution characteristics. The author conducts fluid structure interaction treatment on bow and stern flexible air seals of PACSCAT based on the fluid structure interaction solver of commercial hydrodynamic calculation software STAR-CCM+, and analyses the flow field characteristics of the cushion system based on fluid structure interaction method.

NUMERICAL CALCULATION METHOD

GOVERNING EQUATIONS AND THEORIES

For traditional computational fluid dynamics, numerical calculation for incompressible viscous flow and multiphase flow theory follows the Reynolds-Averaged Navier-Stokes equation

[14-15], which is the most widely used in engineering. Ignoring the effect of density pulsation and considering the change of average density, the equation is as follows:

$$\frac{\partial \rho}{\partial t} + \frac{\partial}{\partial x_i} (\rho u_i) = 0 \quad (1)$$

$$\frac{\partial (\rho u_i)}{\partial t} + \frac{\partial}{\partial x_j} (\rho u_i u_j) = -\frac{\partial p}{\partial x_i} + \frac{\partial}{\partial x_j} \left[\mu \frac{\partial u_i}{\partial x_j} - \overline{\rho u_i' u_j'} \right] + S_i \quad (2)$$

(i, j = 1, 2)

Where, u_i, u_j is the time average value of the velocity component; $i, j = 1, 2$; ρ is fluid density; μ is hydrodynamic viscosity coefficient; u_i', u_j' is the pulsation value of the velocity component; p is the time average value of pressure; S_i is the generalized source term of momentum equation.

This study uses VOF free liquid surface method [16-18] as the numerical simulation method of motion interface capturing, which is characterized by defining the motion interface as a fluid volume function in the spatial grid, and establishing the development equation of this fluid volume function, which makes the interface capturing problem is how to accurately determine the position, shape and deformation direction of the moving interface through fluid transport.

The motion model adopts the motion mode of six degrees of freedom (DFBI). The following is its motion equation. First, the motion equation of its center of gravity is established by the overall coordinate system, and its equation is:

$$m \frac{dv}{dt} = \vec{f} \quad (3)$$

where m is the mass of the hull, \vec{f} is the various forces acting on the hull, and v is the speed.

The rotation equation is based on the local coordinate system with the center of gravity as the origin, and the equation is as follows:

$$M \frac{d\vec{\omega}}{dt} + \vec{\omega} \times M\vec{\omega} = \vec{n} \quad (4)$$

$$M = \begin{bmatrix} M_{xx} & M_{xy} & M_{xz} \\ M_{xy} & M_{yy} & M_{yz} \\ M_{xz} & M_{yz} & M_{zz} \end{bmatrix} \quad (5)$$

where M is the moment of inertia of the transient state, $\vec{\omega}$ is the angular velocity of the hull, and \vec{n} is the resultant moment acting on the hull.

In this study, the direct input method of boundary fluid velocity function is adopted for wave-making [19]. This boundary wave-making method is based on the velocity of wave water particle and the velocity of the inlet defined by the wave surface equation to achieve wave-making. This method can control wavelength, wave amplitude and wave frequency well, and the convergence of numerical simulation is good. For the target wave which is a planar linear sinusoidal regular wave in finite water depth, the relevant wave theoretical equation is expressed as follows, where the horizontal velocity equation is expressed as:

$$v_h = \zeta_a \omega \frac{chk(z + d_w)}{shkd_w} \cos k(x - ct) \quad (6)$$

The vertical velocity equation is:

$$v_v = \zeta_a \omega \frac{chk(z + d_w)}{shkd_w} \sin k(x - ct) \quad (7)$$

Where, ζ_a is wave amplitude; k is wave number; ω is circular frequency; d_w is water depth; c is velocity; t is time.

The wave period is defined as:

$$T = \frac{2\pi}{\omega} \quad (8)$$

The wavelength λ is defined as:

$$\lambda = \frac{2\pi}{K} \quad (9)$$

The relationship between wave period and wavelength under finite water depth is:

$$T = \left[\frac{g}{2\pi\lambda} \tanh\left(\frac{2\pi d}{\lambda}\right) \right]^{-1/2} \quad (10)$$

Where, λ is wavelength; g is gravitational acceleration; T is wave period.

For the processing of the flexible air seals at the bow and stern of the local air-cushion catamaran, this paper adopts the independent solver in STAR-CCM+, which is specially developed for the coupling effect of fluid and solid, namely fluid structure interaction (FSI), which makes it possible to calculate the linear or Nonlinear geometric deformation problems.

NUMERICAL CALCULATION MODEL

The traditional flexible device is used to seal the air at the bow and stern of the PACSCAT experimental model to achieve the purpose of lifting and reducing drag. The bow adopts bag-finger skirt, and the stern adopts double-bag skirt [1]. This configuration is able to not only ensure good airtightness of the air cushion, but also improve the obstacle-crossing performance and wave-breaking performance of PACSCAT. The sidewall is designed wide, the bow structure is similar to the gliding wall of a gliding boat [2] the cross structure is a pontoon structure used as a pressurized chamber. The schematic diagram of PACSCAT is shown in Fig. 1, and the principal dimension of the calculation model is shown in Table 1.

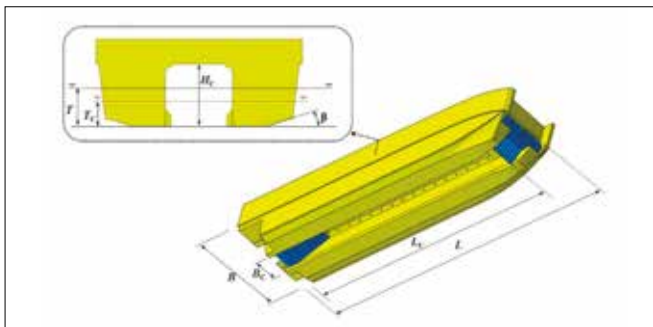


Fig. 1. Hull characteristics of PACSCAT

Tab. 1. The principal dimension of the calculation model.

Parameter	Model
Length L (m)	3
Breadth B (m)	0.7
Length of air cushion chamber L_c (m)	2.6
Breadth of sidewall B_1 (m)	0.22
Breadth of air cushion chamber B_c (m)	0.26
Height of cross structure H_c (m)	0.16

The air intake form of this study is pressurized chamber type, which is different from other hovercraft used air duct as high pressure air transmission method. The high pressure air enters into pressurized chamber directly after the fan pumping up, a part of air enters into air cushion chamber through a row of air hole in pressurized chamber, and the other part of high pressure air enters into air cushion chamber through the bow and stern air seals. The schematic diagram of air transportation of cushion system is shown in Fig. 2. When the air cushion system is numerically simulated, the air inlet is set at the top of the pressurized chamber, so that the high pressure air which is set as constant air flow will enter into pressurized chamber through the air hole connected with the air cushion chamber. The air intake form of numerical calculation is consistent with the experiment. To obtain the pressure situation of the air cushion chamber, pressure monitoring points P1, P2 and P3 are arranged at the fore, middle and rear positions of the air cushion chamber.

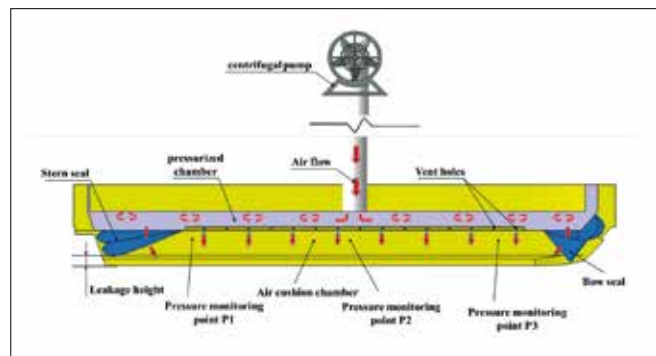


Fig. 2. Schematic diagram of cushion system in numerical calculation

CALCULATION DOMAIN AND GRID DIVISION

In order to represent correctly the experimental setup in the computational analyses, the hull in the computations was free to pitch and heave. In view of the hull characteristics of PACSCAT, the calculation domain adopts integral type to ensure the integrity of the air cushion system. For the simulation of flow field, the calculation domain is set to ensure the effective balance between calculation efficiency and accuracy as far as possible, and ensure that the wave-absorbing region is at least twice the wavelength. The selected wavelength in this study is 7 m. Therefore, the calculation domain is set as follows: The forward is 1 times the length of the ship, the aft is 3 times the

length of the ship, the side is 1 times the length of the ship, above the free liquid surface is 1 times the length of the ship, and below the free liquid surface is 1.5 times the length of the ship.

The inlet boundary condition of the calculation domain is Velocity inlet, and the outlet boundary condition is Pressure outlet. The top, bottom and both sides boundary condition of the calculation domain are set as slip wall, which named as Free slip wall. The calculated model is located near the free liquid surface as a 6-DOF rigid body. Fig. 3 shows calculation domain and boundary conditions. The VOF method is used to capture the movement of free liquid surface, and the wave pattern is first-order Stokes wave. The flow field in the calculation is Euler multiphase flow, continuum iteration is carried out by implicit unsteady state. The wave parameters in the calculation are exactly the same as those in the experiment, that is, the regular wave amplitude is 25 mm, and the ship speed is 2.0 m/s and 3.6 m/s, respectively.

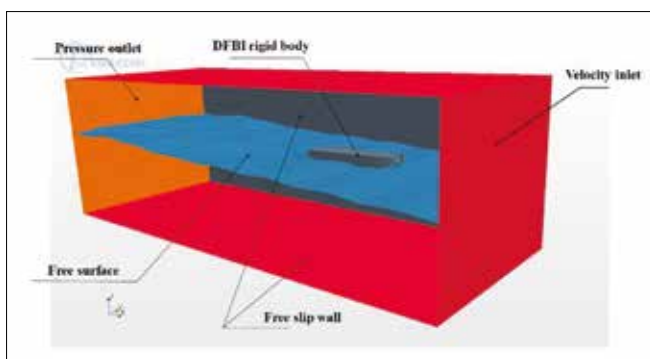


Fig. 3. Numerical calculation domain and boundary conditions

For the grid division, overlapping grid form is adopted in the study, and grid encryption is carried out at the area of free liquid surface, hull surrounding, cushion system and the bow and stern air seals. The wave height is set as 25 mm. The wavelengths of short wave and long wave to ship length ratio are quite different, so in order to capture the characteristics of wave better, the study adopts different division forms for grids at different wavelengths, so as to ensure that the number of grids per unit wavelength is not less than 70, and the number of grids per unit wave height is not less than 20 in the whole calculation domain [20]. Fig. 4 shows the division diagram of overlapping grids.

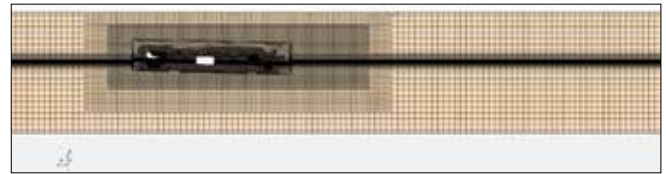


Fig. 4. The division diagram of overlapping grids

FLEXIBLE TREATMENT OF BOW AND STERN AIR SEAL

For flexible treatment of bow and stern air seals, fluid structure interaction method based on independent solver is used. However, mainly due to the high speed of the PACSCAT, flexible seals will cause the large deformation and the gas-liquid force changed, which makes the calculation impossible to be carried out, so the bow and stern gas seals needs some simplification. For the bow seals, rigid setting is carried out for the bow D type bag (shown as Fig. 5(a)), to simplify the force of the airbag and make numerical calculation more feasible, because in this study it cannot simulate the deformation of the flexible solid thin shell which has air and liquid on each side. The flexible finger skirts under real condition are composed of eight sets of independent skirt finger, as shown in Fig. 5(a). In the preliminary calculation, the author found that if the independent skirt fingers fit to each other nicely, the grid treatment will encounter mutual interference problems, especially at the junction, the limited fluid force cannot be obtained because of the extremely small gap, and the calculation cannot be performed. Based on the preliminary calculation results, the flexible finger skirts are processed that each independent finger does not stick, and each skirt has a gap of about 2.5 mm wide, with 2.28 mm thickness, as shown in Fig. 5(b). Usually, the skirts near the sidewall of PACSCAT will not deform in the real condition, besides that, the deformable treatment will lead to the non-convergence of numerical calculation, so the wall surface of finger skirt at the junction of sidewall is set as a rigid structure, which is made non-adhesion treatment with the rigid sidewall.

For the stern air seal structure, considering that it is currently impossible to couple the double airbags in the inflated state in the case of triple media such as gas, liquid, and solid, as shown in Fig. 6(a), so it is necessary to simplify the stern airbag by a flat

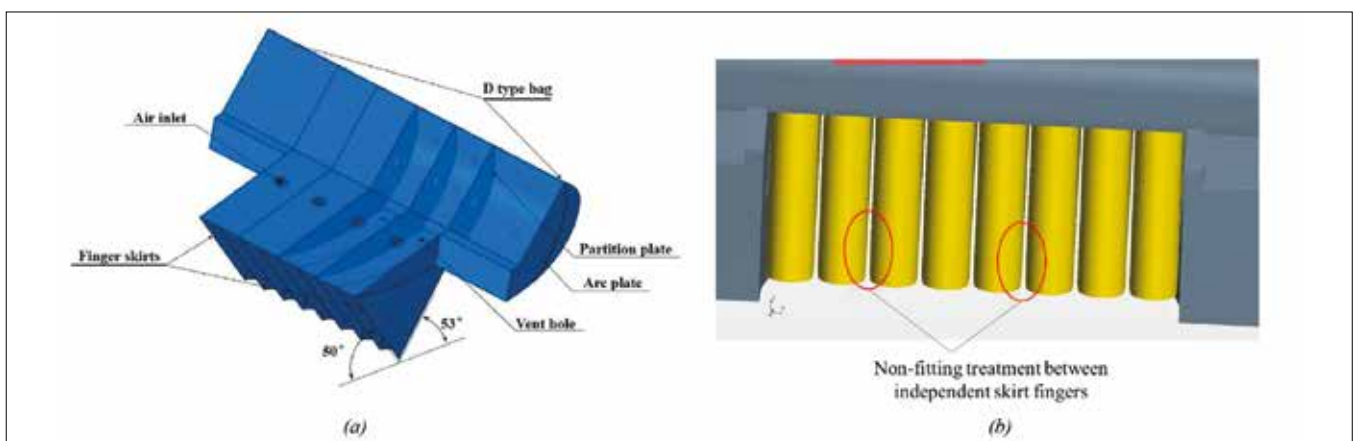


Fig. 5. Non-adherent treatment of bow skirt finger

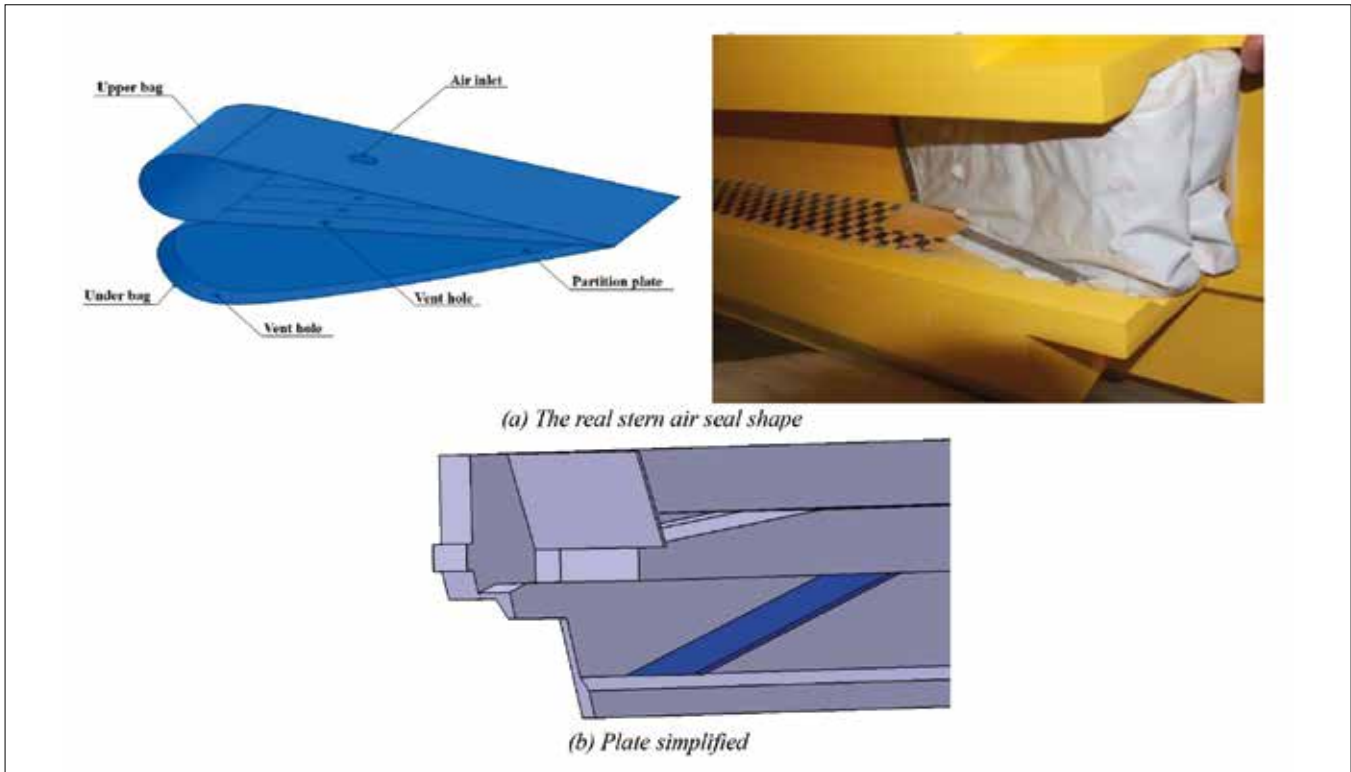


Fig. 6. The real and simplified of stern double bag air seal

plate in this study. In order to match the flexible characteristics of the double-bag stern seals, and according to the expression of the stiffness of the elastic material in the force analysis of the flexible air seal, this study carried out preliminary calculations to determine the optimal material characteristic parameters by comparing the resistance error in waves. The calculations were based on the same Poisson coefficient and model scale, for flexible plates with different Young's modulus and different densities. And then the properties of the bow and stern gas seal material used are selected as a density of 1300 kg/m³, a Young's modulus of 10 MPa, and a Poisson coefficient of 0.45. During the calculation, it is found that the stern flexible plate with uniform density and thickness is more conducive to the realization of numerical calculation, so the stern flexible plate air seal set here is uniform, and the thickness of the plate is 7mm, as shown in Fig. 6(b). It should be noted that the flat-type simplification of the double-bag stern seals can only achieve

the purpose of sealing the air-cushion cabin, and cannot fully simulate the double-bag seals in the real situation.

In contrast to the single flow field calculation domain for rigid air seals, fluid structure interaction calculation domain requires to define multiple domains for interactions and fluid motions between different fluids and solids. Due to the large increase of the number of flexible air seal grids, the balance of calculation and analysis between the grid number and calculated efficiency must be considered. The follow-up work of this paper is to study the number of grids which are used in the final calculation. Figs. 7 and 8 below show the grid form of the bow and stern air seal.

Because the hull of PACSCAT is a 6-DOF rigid body that is non-deformable solid, so the ship does not need a solid area, only the deformable bow and stern air seal need solid areas. These areas are connected by the following interfaces: A fluid-structure interface between the bow air seal and the fluid

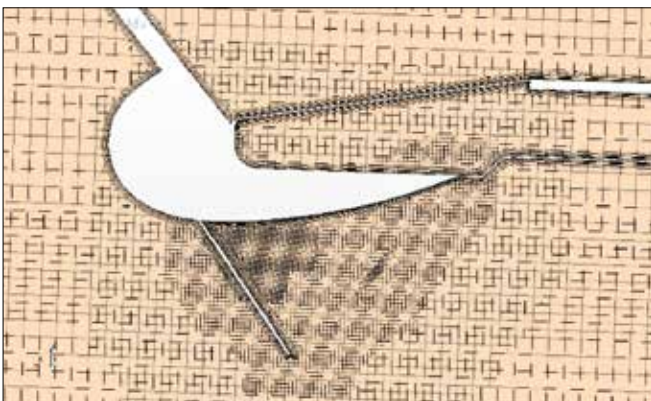


Fig. 7. The grid form of bow skirt

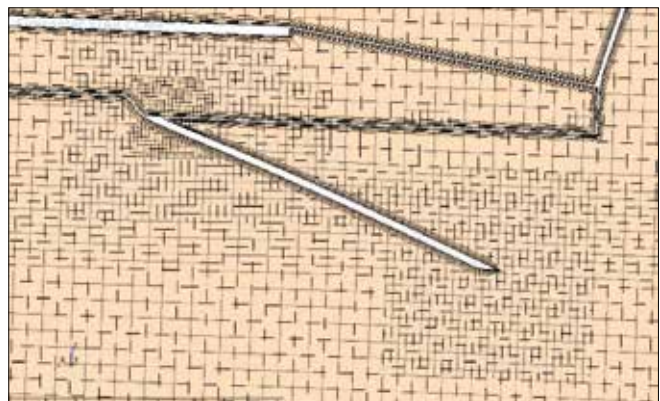


Fig. 8. The grid form of stern skirt

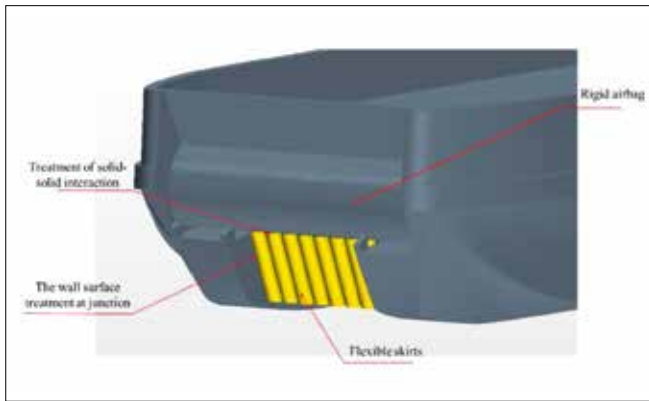


Fig. 9. Interface of bow air seal

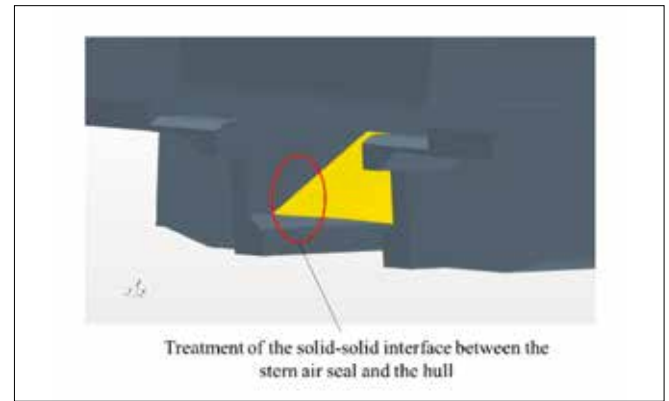


Fig. 10. Interface of stern air seal

surrounding the air seal; A fluid-structure interface between the stern air seal and the fluid surrounding the air seal; A fluid-fluid interface between the fluid area of main body and the fluid surrounding the bow and stern air seals; A solid-solid interface between different solid parts of bow and stern air seals. As shown in Figs. 9 and 10 below, the solid-solid interface treatment between the top of skirt finger and the rigid airbag of the bow skirt will be carried out; and the solid-solid interface treatment between the top of stern simplified plate and the wet deck of the air cushion chamber will be carried out.

CALCULATION RESULTS AND ANALYSIS

COMPARISON BETWEEN NUMERICAL CALCULATION AND EXPERIMENTAL DATA

Figures 11 to 12 are the time histories of the calculated values of heave and pitch compared with the experimental values in waves, when the speed is 3.6 m/s and the wavelength is 7.0 m. In order to analyze the calculation results, the calculation time histories are linearized by using the sine curve fitting method. It can be seen from Fig. 11 that the calculated value and the experimental value are relatively close in terms of amplitude and mean, and the curves have similar motion characteristics. From the Fig. 12, it can be seen that the calculated data and phase are basically consistent with the experimental results, and the calculated mean value is relatively close to the experimental value. Comparing the heave and pitch curves, the following conclusions can be drawn: In the numerical calculation of the PACSCAT with flexible seals based on the fluid structure

interaction (FSI), the motion characteristics of each motion parameter are close to the experimental values. Although there is a certain error in the amplitude, the motion of heave and pitch law have obvious similarity, and the mean error is small, indicating that the method is feasible to the study of flow field characteristic analysis of PACSCAT.

The air cushion pressure is an important parameter of the cushion system directly affects its performance, especially when the pressure jump is large due to the unsteady leakage. In this study, the accuracy of air cushion pressure numerical simulation is studied by comparing with the experimental data, meanwhile the pressurized chamber pressure and air cushion pressure at low speed are calculated extended, so that the pressure characteristics of PACSCAT in waves can be analysed.

Fig. 13 shows the comparison between the calculated values and the test values of air cushion pressure at the wavelength of 7.0 m and speed of 3.6 m/s. The pressure of pc_1 , pc_2 and pc_3 is the pressure value of P1, P2 and P3 mentioned above, EXP is the test data, and CAL is the numerical calculated data. As shown as the Fig. 13, the nonlinear characteristics of numerical calculation are not as obvious as the test values, and the oscillation amplitudes of the time histories of numerical calculation are quite slight, such as the calculation value at pc_1 , which is always around 0.8kpa. The oscillation patterns of the calculated data are close to each other at different longitudinal positions of the air cushion, especially the peak value and trough value of pc_2 are more obvious. The nonlinear oscillation characteristics of the test values are more prominent, the main reason is that the non-uniform leakage phenomenon caused by the flexible air seal of the bow and stern is more obvious, and the dynamic response of the simulated bow and stern flexible air seals is quite different from that of the actual air seals, so the

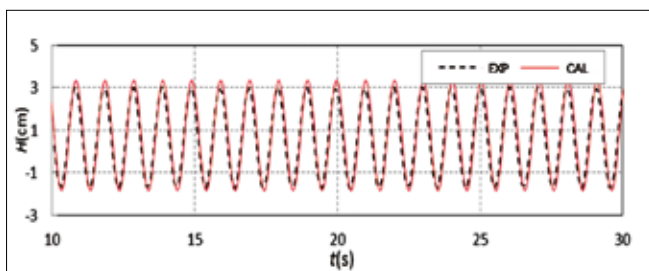


Fig. 11. Comparison of wave time histories curves between calculated heave values and test values

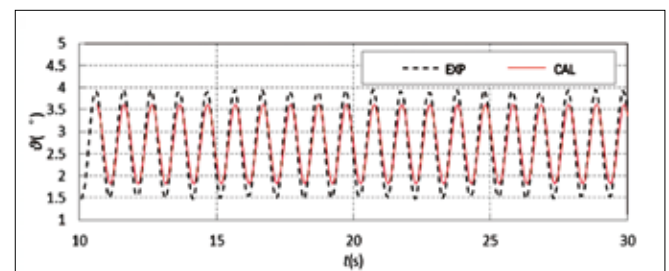


Fig. 12. Comparison of wave time histories curves between pitch values and test values

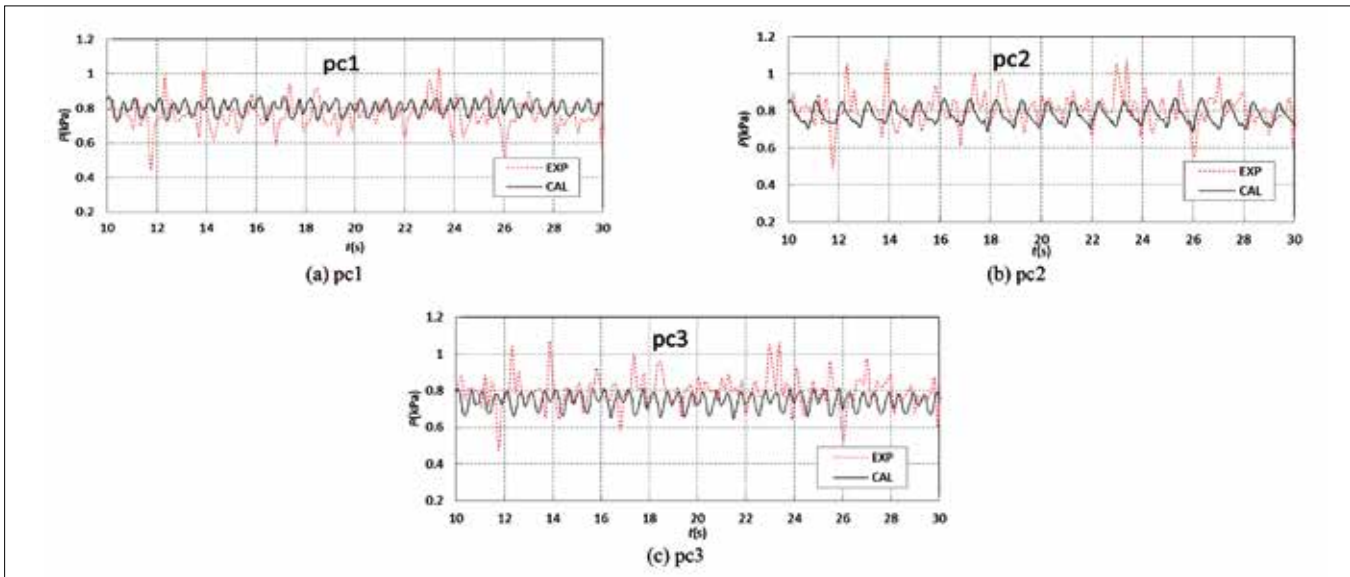


Fig. 13. Comparison of original test and calculated values of air cushion pressure at different positions of air cushion

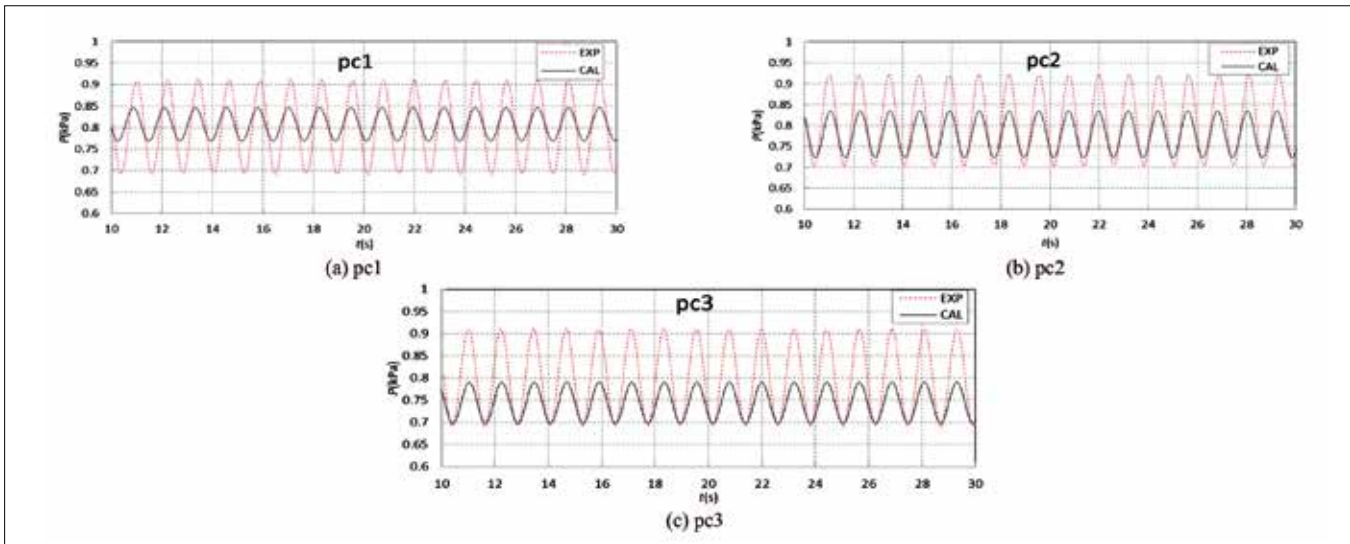


Fig. 14. Comparison of linearized test and calculated values of air cushion pressure at different positions of air cushion

flexible state of the bow and stern air seals cannot be completely simulated, which makes the oscillation relatively gentle. Fig. 14 shows the comparison of data after linear transformation. It can be seen that the oscillation amplitudes of the test values are significantly larger than the calculated values. The amplitudes of the test values at different positions are close to each other, and that of the calculated values are also close to each other. Compared with the amplitudes, the calculated average values are closer to the test values, especially at the longitudinal position p1 of the air cushion. With the moving forward of the air cushion pressure point, the calculated average values decrease gradually, and the errors between the calculated values and the test values increase gradually. The pressure data of the numerical calculation at the fore of the air cushion is lower than that at the aft. The main reason is that the air seal treatment at the bow based on fluid structure interaction adopts the form of independent skirt fingers, and there is a certain gap between each skirt finger, which leads to a certain amount of air cushion leakage, then affects the changes of pressure.

COMPARISON OF PRESSURE CALCULATION RESULTS AT DIFFERENT SPEEDS

According to the above introduction, the sailing attitude of PACSCAT at low speed is quite different from that at high speed, and the air cushion pressure is also quite different. In this section, the model at a wavelength of 7.0 m and a speed of 2.0 m/s is studied, the air cushion pressure is compared to that of speed at 3.6 m/s, and the characteristics of air cushion pressure at low speed and high speed are analysed. Fig. 15 shows the comparison of the original calculation data at different speeds and different pressure points, it can be seen that both average and amplitude of air cushion pressure at the speed of 2.0 m/s are significantly reduced than that at the speed of 3.6 m/s, the variation curves of pressure at low speeds and different positions are relatively consistent, and the air cushion pressure is evenly distributed in the air cushion space at low speed. It indicates that there is no obvious air leakage when the ship sails in the wave in this moment.

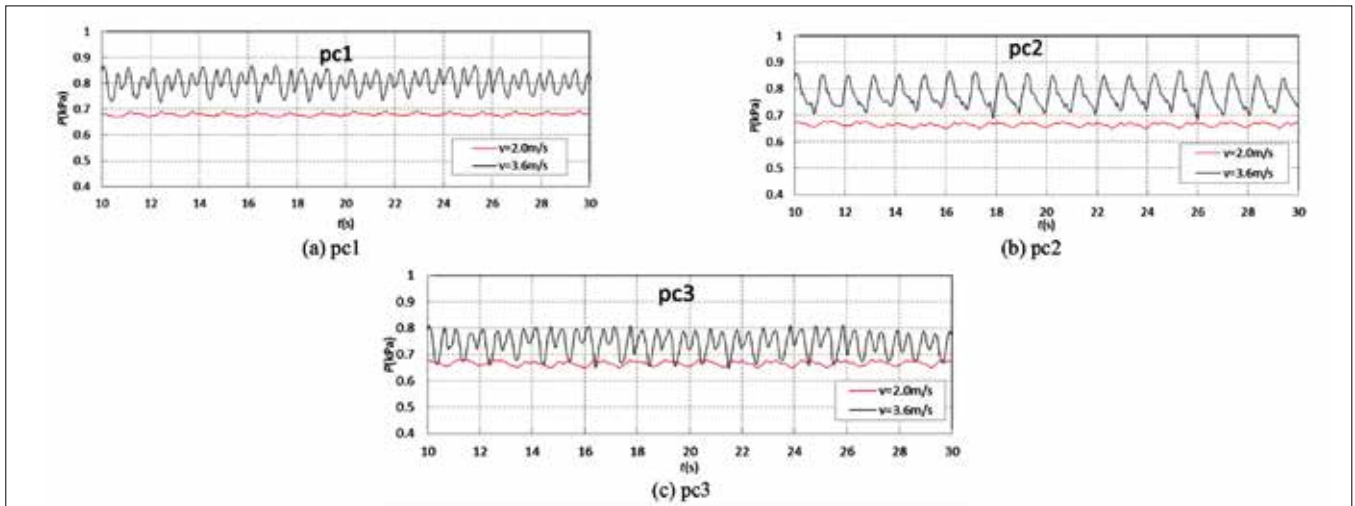


Fig. 15. Comparison of original calculated data of air cushion pressure at different speeds

PRESSURE CHARACTERISTIC ANALYSIS OF PRESSURIZED CHAMBER

As for the cushion system, the pressurized chamber mainly plays the role of combining and conveying high pressure air to the air cushion chamber. In general, different with the force exerted on the air cushion chamber when contacting with waves, the pressure fluctuation in the pressurized chamber is caused only by the reaction force of the air cushion pressure. This section studies the pressure fluctuation of the pressurized chamber in waves and analyses its diachronic characteristics at different speeds. The calculated pressure points are distributed at the three spatial points arranged at the fore, middle and rear of the pressurized chamber. The longitudinal coordinate positions are consistent with P1, P2 and P3 of the air cushion chamber, and the vertical positions are in the middle positions between the upper and lower decks of the pressurized chamber. The pressure is marked as Pt1, Pt2 and Pt3 respectively. There is no linearization treatment to the calculated data in order to analyse the pressure of the pressurized chamber from the perspective of the original calculated data. Figs. 16 and 17 respectively show the pressure monitoring condition in the pressurized chamber at the speed of 2.0 m/s and 3.6 m/s at different positions, and the air cushion pressure pc2 in the Figure is displayed for comparative analysis. It can be seen from Fig. 16 that the pressure duration of the three monitoring points in the pressurized chamber are almost the same in terms of amplitudes, average values, and oscillation patterns, indicating that the pressurized chamber pressure is little disturbed by the

change of air cushion pressure at low speed, and the amplitude of pressurized chamber pressure and air cushion pressure pc2 is basically the same. At this time, the average ratio of pressurized chamber pressure to air cushion pressure is 1.034. In Fig. 17, the time histories of pressurized chamber pressure at the three monitoring points are complex and do not show the same variation laws, but the amplitude is close to the average value, and there is no significant difference between the amplitude at pc2. At this time, the average ratio of pressurized chamber pressure to air cushion pressure is 1.303. Contrast with the condition at different speeds, the pressure curve characteristics of pressurized chamber have similarities with the air cushion pressure in previous section, but pressurized chamber pressure is closer to air cushion pressure at lower speed, and much greater than air cushion pressure obviously at higher speed, so that the ratio of pressurized chamber pressure to air cushion pressure up to 1.3. It follows that when PACSCAT sailing in waves, high speed will cause pressure changes in the pressurized chamber or the air flue, researchers need to pay more attention to the design of the pressurized chamber, so as to avoid the phenomenon of fan pumping due to excessive pressure.

No matter at low speed and high speed, the pressurized chamber pressure at three monitoring points is similar, so the pressurized chamber pressure in space is evenly distributed well, which has the effect of combining the high pressure air to a certain extent, thereby avoiding delivery timeliness reducing due to spatial non-uniform distribution of the air, and then affecting the lift performance.

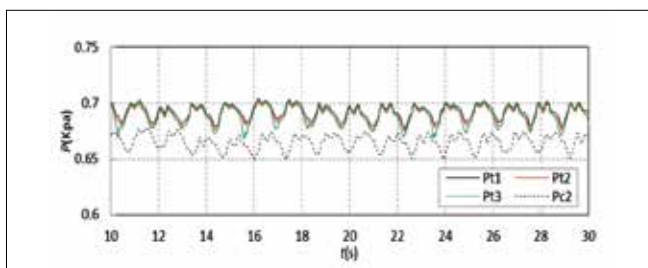


Fig. 16 Calculation data of pressure in pressurized chamber at different positions at speed $V = 2.0$ m/s

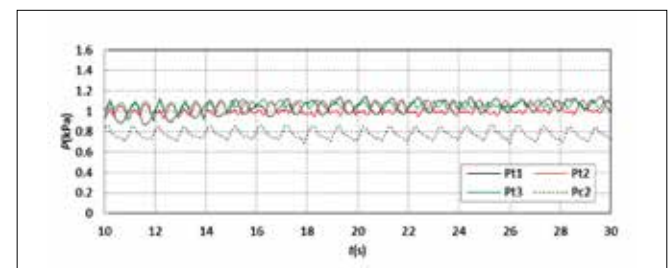


Fig. 17. Calculation data of pressure in pressurized chamber at different positions at speed $V = 3.6$ m/s

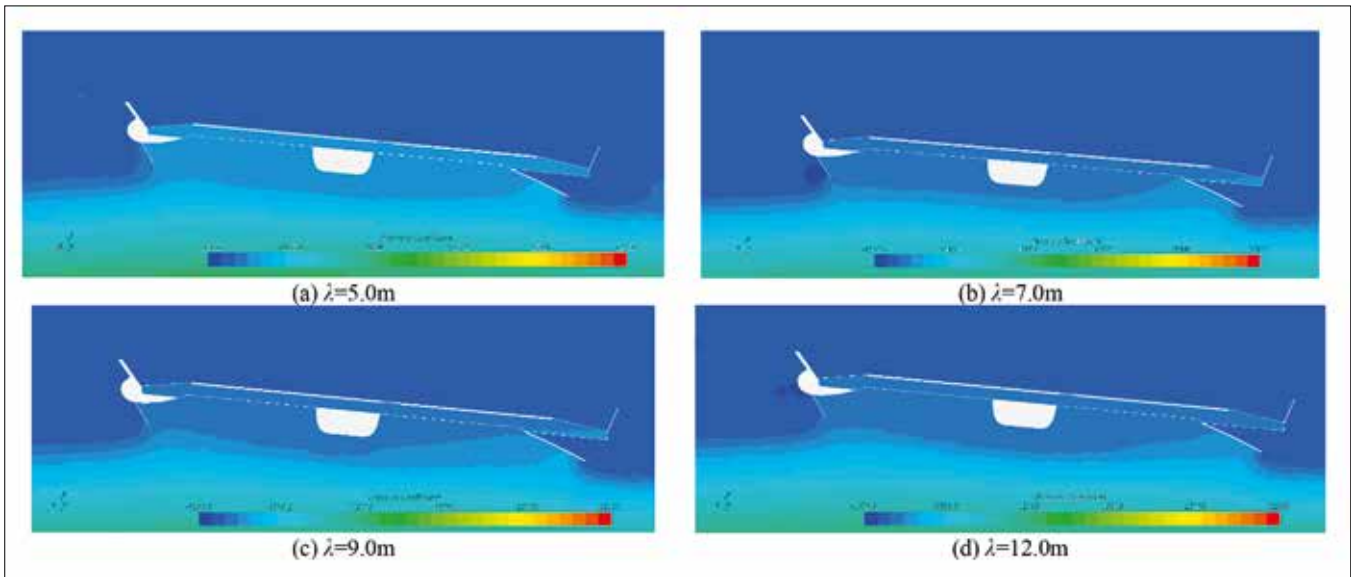


Fig. 18. Vertical spatial pressure distribution at speed $V = 3.6\text{m/s}$

SPATIAL PRESSURE DISTRIBUTION CHARACTERISTICS

The pressurized chamber and air cushion chamber pressure at different positions are analysed by monitoring points in the previous section, the spatial pressure in air cushion chamber will change with the waves and the attitude of hull, the air cushion of the system usually assume evenly distributed in space, this section will analyse the pressure nephogram of the system, and study the uniform distribution of air cushion in space at different speeds. Fig. 18 below shows the pressure nephogram of air cushion in vertical space at different wavelengths and at the speed of 3.6 m/s, the transverse position of nephogram is just at $Y = 0$. The air cushion pressure in the vertical direction has little change in the pressurized chamber and air cushion chamber, especially the pressure in the pressurized chamber. There is a certain pressure fluctuation at the rear of the air cushion

chamber, the fluctuation range is concentrated at the middle and rear of the longitudinal positions, the pressure fluctuation does not reach the wet deck of the air cushion chamber, so it can be considered that the pressure at the rear of the air cushion chamber is almost evenly distributed in space except at the stern air seal position.

Fig. 19 and 20 below respectively show the spatial pressure distribution in xy plane of pressurized chamber and air cushion chamber, it can be seen from the Fig. 17, the air cushion pressure of pressurized chamber in the xy plane is almost the same, according to the monitoring situation of pressure duration curve at different positions in the previous section, the air cushion pressure in the pressurized chamber is evenly distributed for sure, and the disturbance caused by wave force is small. It can be seen from Fig. 18 that the air cushion pressure has a sudden jump at the fore and rear positions, especially near the stern air seal. From the vertical spatial pressure distribution of the air

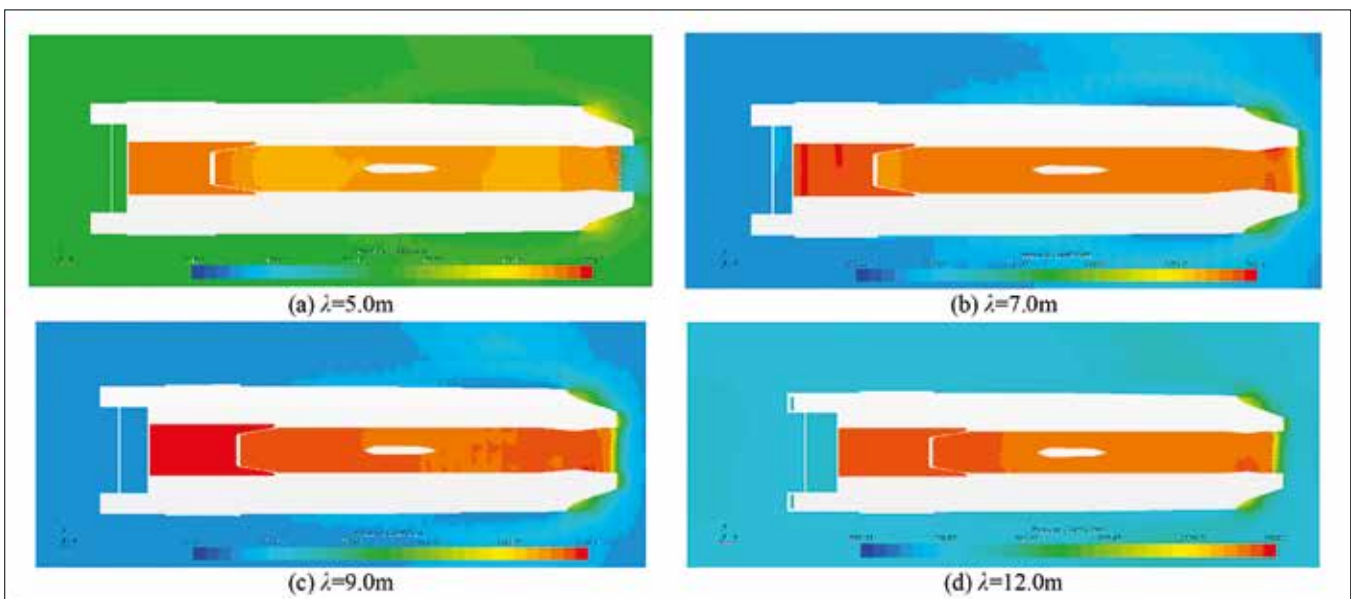


Fig. 19. Pressure distribution of pressurized chamber in the xy plane at the speed of $V = 3.6\text{m/s}$

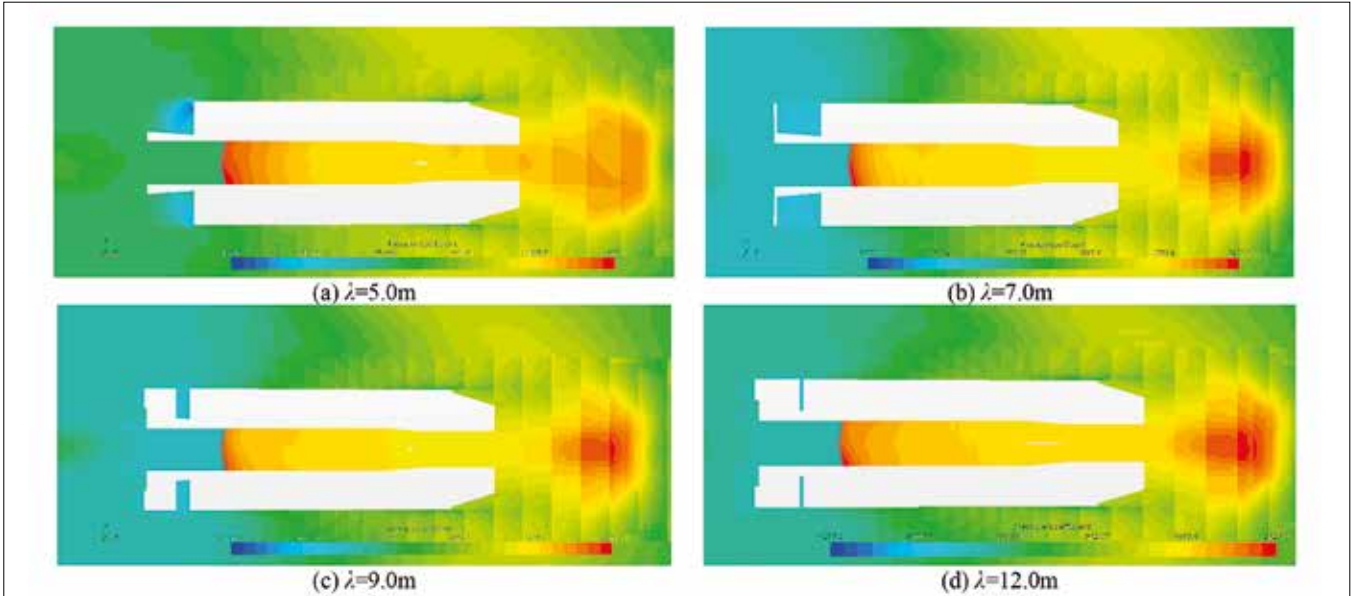


Fig. 20. Pressure distribution of air cushion chamber in the xy plane at the speed of $V = 3.6\text{ m/s}$

cushion chamber in Fig. 16, it is not difficult to understand that the pressure is obviously larger here. Therefore, the conclusion can be basically consistent with the above, that is, except for the position near the stern air seal, the pressure in most space of the air cushion chamber is evenly distributed.

Figs. 21 and 23 show the spatial pressure distribution at wavelength of 5.0 m and 7.0 m at the speed of $v = 2.0\text{ m/s}$, so as to study the characteristics of the spatial pressure characteristics in the air cushion chamber at low speed. From the comparative analysis of the vertical and xy plane pressure nephogram, it can

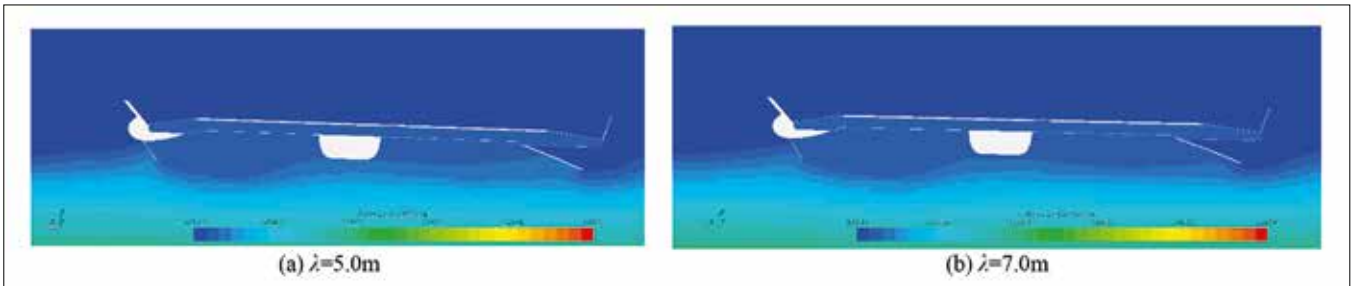


Fig. 21. Vertical spatial pressure distribution at speed of $V = 2.0\text{ m/s}$

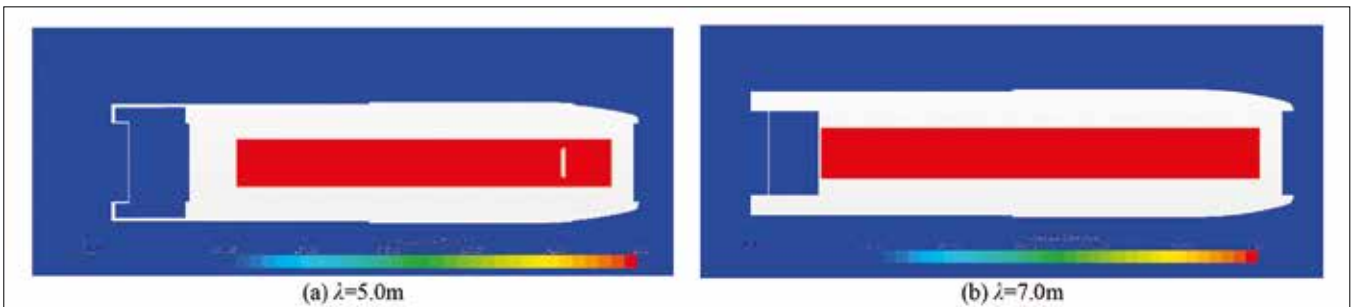


Fig. 22. Pressure distribution of pressurized chamber in the xy plane at speed of $V = 2.0\text{ m/s}$

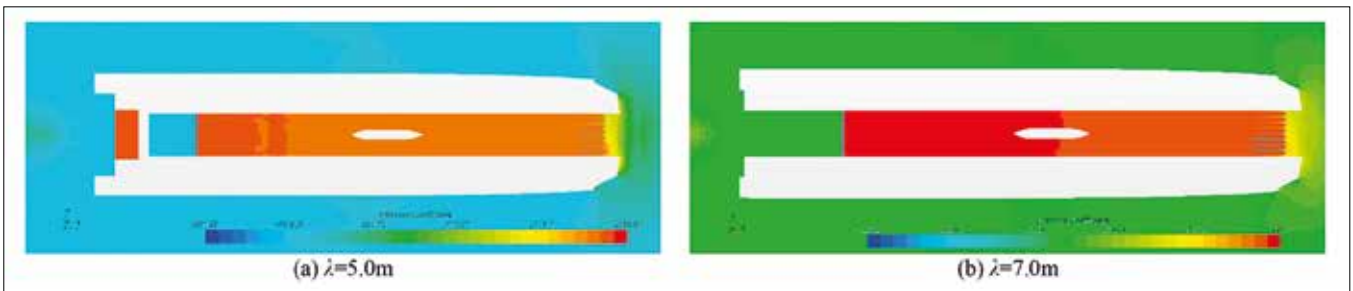


Fig. 23. Pressure distribution of air cushion chamber in the xy plane at speed of $V = 2.0\text{ m/s}$

be clearly seen that at this speed, the pressure no matter in the pressurized chamber or in the air cushion chamber is uniformly distributed in space, especially in the pressurized chamber, the pressure changes are slight. Therefore compared with the uniform distribution condition of air cushion space at speed of 3.6 m/s, a conclusion can be carried out as follows, when PACSCAT sailing in waves at low speed, the spatial pressure distribution is evenly distributed no matter in the pressurized chamber or in the air cushion chamber, and the wave disturbance is slight, but at high speed, the pressure in the pressurized chamber is evenly distributed, the pressure in air cushion chamber is also considered to be uniform distribution except near the stern air seal position where occurs a pressure jump. The spatial uniform distribution of pressure also indicates that the arrangement with gap between each skirt finger does not cause excessive leakage of air and a large change of air cushion pressure.

CONCLUSIONS

This study calculates the variation performance of the cushion system pressure, in waves at different wavelengths and speeds, based on the flow field characteristics of PACSCAT cushion system by using the fluid structure interaction method, and the conclusions are as follows:

- a) The nonlinear characteristics of the numerical calculation of the pressure in the air-cushion cabin are relatively low, the oscillation amplitudes of the time histories of numerical calculation are smaller. The oscillation patterns of the original calculated data at different longitudinal positions of the air cushion are similar, especially the peak value and trough value at pc2 are more prominent.
- b) After linear processing, the oscillation amplitudes of air cushion chamber pressure test values are larger than the calculated values, in comparison with the amplitudes, the average of calculated values are more close to the experimental values, especially at the longitudinal position P1 of air cushion, and with the air cushion pressure point moving forward, the average calculated values reduce gradually, and the calculation deviation also gradually increases.
- c) When PACSCAT sailing at low speed, the spatial pressure is uniformly distributed and less disturbed by waves no matter in the pressurized chamber or the air cushion chamber, while PACSCAT sailing at high speed, except for the pressure jump in the air cushion chamber near the stern air seal position, the pressure in other spaces is also considered to be uniformly distributed.

REFERENCES

1. L. Yun, and A. Bliault, *Theory and design of air cushion craft*. London: Bath Press, 2000.
2. J. Zou, Q.J. Meng, Z. Lin, and X.W. Li, "Research on the concept of PACSCAT," *Ship Science and Technology*, vol. 34, no. 7, pp. 30-34, July 2012, doi: 10.3404/j.issn.1672-7649.2012.07.006
3. B. Milewski, B. Connell, J. Wilson, and D. Kring, "Dynamics of ACV operating in a seaway," in *Proc. of the 9th Int. Con. on Numerical Ship Hydrodynamics, 5-8 August 2007, Ann Arbor, USA* [Online]. Available: <https://citeseerx.ist.psu.edu/viewdoc/summary?doi=10.1.1.547.1611>
4. W.M. Milewski, B. Connell, B. Petersen, and D. Kring, "Initial validation of the ACVSIM model for dynamics of air cushion vehicles," in *Proc. of the 27th Symposium on Naval Hydrodynamics, 5-10 October 2008, Seoul, Korea, 2008*. [Online]. Available: <https://citeseerx.ist.psu.edu/viewdoc/summary?doi=10.1.1.511.2009>
5. WAMIT Inc. *WAMIT User Manual-Version 7*. Chestnut Hill, 2016.
6. C.H. Lee, and J.N. Newman, "An extended boundary integral equation for structures with oscillatory free-surface pressure," *International Journal of Offshore and Polar Engineering*, vol. 26, no. 1, pp. 41-47, 26(1): 41-47, March 2016, doi: 10.17736/ijope.2016.mk44
7. N. Hirata, and O.M. Faltinsen, "Computation of cobblestone effect with unsteady viscous flow under a stern seal of a SES," *Journal of Fluids and Structures*, vol. 14, no. 7, pp.1053-1069, October 2000, doi: 10.1006/jflls.2000.0312
8. G.L. Li, "Analysis of heave characteristics of SES in short wave," *Jiangsu Ship*, vol. 13, no. 3, pp. 1-7, June 1996, doi: CNKI:SUN:JSCB.0.1996-03-000
9. Z.Q. You, *Numerical simulation and optimization of internal Flow field of ACV*. Harbin Engineering University, 2018.
10. K.J. Chen, *Research on CFD calculation method of cushion lift performance of hovercraft*. Dalian University of Technology, 2013.
11. B. Lan, *CFD calculation of hydrodynamic performance of cushion lift platform*. Harbin Engineering University, 2006.
12. W.Y. Duan, and S. Ma, "Comparison of two -, two - and half - and three - dimensional methods for hydrodynamic linear solutions of ship motion," in *Proc. of the 17th National Symposium on Hydrodynamics, 31 December 2003 - 2 January 2004, HongKong, China*. [Online] Available: <https://d.wanfangdata.com.cn/>
13. Z.Q. Guo, *Multi-domain 2.5D method with viscous effects and its application on a partial air cushion supported catamaran*. Harbin Engineering University, 2017.
14. W.Y. Wu, *Hydrodynamic*. Beijing: Peking University Press, 1982.
15. F.J. Wang, *Calculated hydrodynamic analysis*. Beijing: Tsinghua University Press, 2004.

16. C.S. Wu, and D.X. Zhu, "Numerical simulation of sailing ship radiation problem based on N-S equation," *Journal of Ship Mechanics*, vol. 12, no. 4, pp. 560-567, September 2008, doi: JournalArticle/5aed43dcc095d710d40a20e8
17. L. Lei, Z.X. Wang, P. Sun, and J.N. Nie, "Application research of ideal equation turbulence model for computational fluids," *Ship Engineering*, vol. 2010, no. 3, pp. 5-8, June 2010.
18. Y.B. Li, D.B. Huang, and Y. Liang, "A theoretical calculation method for far field waveform of hovercraft," *Journal of Harbin Engineering University*, vol. 23, no. 2, pp. 5-7, February 2002, doi: 10.3969/j.issn.1000-6982.2010.03.002
19. J.D Li, *Seakeeping*. Harbin: Harbin Institute of Ship Engineering Press, 1992.
20. R. Deng, *Numerical research on influence of the interceptor on catamaran hydrodynamic performances*. Harbin Engineering University, 2010.

CONTACT WITH THE AUTHORS

Jinglei Yang

e-mail: yangjinglei1220@126.com

Jimei University

School of Marine Engineering, Xiamen

CHINA

Han-bing Sun

Jimei University

School of Marine Engineering, Xiamen

CHINA

Xiao-wen Li

Jimei University

School of Marine Engineering, Xiamen

CHINA

Xin Liu

Jimei University

School of Marine Engineering, Xiamen

CHINA

ASSISTED PROPULSION DEVICE OF A SEMI-SUBMERSIBLE SHIP BASED ON THE MAGNUS EFFECT

Jingze Lv 

Yiqun Lin 

Rui Zhang 

Boyang Li * 

Hualin Yang 

College of Electromechanical Engineering, Qingdao University of Science and Technology, China

* Corresponding author: qdlby@126.com (Boyang Li)

ABSTRACT

The purpose of this study is to explore the potentiality of wind propulsion on semi-submersible ships. A new type of Flettner rotor (two rotating cylinders) system installed on a semi-submersible ship is proposed. The structure and installation of two cylinders with a height of 20 m and a diameter of 14 m are introduced. The numerical simulation of the cylinder is carried out in Fluent software. The influence of apparent wind angle and spin ratio on the two cylinders are analysed, when the distance between two cylinders is 3D-13D (D is cylinder diameter). When the distance between two cylinders is 3D, the performance of the system increases with an increase in spin ratio. Moreover, the apparent wind angle also has an effect on the system performance. Specifically, the thrust contribution of the system at the apparent wind angle of 120° is the largest at the spin ratio of 3.0. The maximum thrust reaches 500 kN. When the spin ratio is 2.5 and the apparent wind angle is 120°, the maximum effective power of the system is 1734 kW. In addition, the influence of the two cylinders distance on system performance cannot be ignored. When the distance between the two cylinders is 7D and the spin ratio is 2.5, the effective power of the system reaches a maximum, which is 1932 kW.

Keywords: Flettner rotor, Semi-submersible ship, Wind energy, Ship propulsion, Numerical simulation

NOMENCLATURE

Symbol	Denomination
D	Diameter of the rotating cylinder
H	Height of rotating cylinder
S	Cross-sectional area of rotating cylinder
ρ	Fluid density
ν	Kinematic viscosity is 1.45×10^{-5} pa/s
V_{ship}	Ship speed
V_{wind}	Environmental wind speed
V_a	Apparent wind speed
U_{tan}	Tangential velocity of rotating cylinder
$\alpha = \frac{U_{tan}}{V_a}$	Spin ratio
X	Distance between two cylinders
y^+	A non-dimensional wall distance
θ	Apparent wind angle

Symbol	Denomination
CL	Lift coefficient
CD	Drag coefficient
CT	Thrust coefficient
CH	Heel coefficient
FT	Thrust force
FH	Side force from heel
PT	Thrust power
CM	Moment coefficient
P_{motor}	Power consumption
P_{ef}	Effective power
P	Static pressure
P_{∞}	Free flow pressure
$C_p = \frac{P - P_{\infty}}{0.5 \cdot \rho \cdot V_a^2}$	Pressure coefficient

INTRODUCTION

With the exhaustion of oil resources and the deterioration of the environment, more and more countries are paying attention to the development of renewable energy. At the same time, stricter requirements for ship emissions have been put forward by the International Maritime Organization (IMO) [1-3]. Therefore, it is urgent to develop energy conservation & emission reduction technologies by using renewable energy or clean energy. Renewable energy is widely used in ships. Nowadays, the renewable energy used on ships mainly includes solar energy and wind energy [4,5]. Of these, wind energy is characterised by wide distribution and abundant reserves [6]. Besides this, flat sea levels have less resistance to the wind and so wind energy at sea is more abundant. The utilisation of wind energy in ships has unique advantages [7].

In order to realise the utilisation of wind energy in ships, scholars have studied a variety of devices to capture wind energy. The mature wind energy utilisation devices mainly include: traditional sails, airfoil sails, kite sails and Flettner rotors [8-10]. The Flettner rotor is an effective device for capturing wind energy on ships [11,12]. The device was first installed on ships one hundred years ago. The Flettner rotor relies on a drive system to achieve rotation. When the wind is coming from one side, the rotation of the rotor causes the wind speed on both sides of the rotor to be changed. Based on Bernoulli's principle, there will be a pressure difference between the two sides of the cylinder, so the lift generated by the cylinder can provide assisted thrust for the ship. The lift is also called a Magnus force and this phenomenon is known as the Magnus effect.

Flettner rotors have been installed on actual ships. The Flettner rotor was first installed and tested on the German ship 'Buckau' in 1924. Recently, an ore carrier also installed Flettner rotors to reduce fuel consumption. Related simulations and experiments on Flettner rotors have been studied by scholars [13-15]. Lu et al. [11] proposed three wind energy utilisation technologies (Flettner rotor, wingsail and DynaRig concept) and selected an Aframax Oil Tanker as a model to compare three kinds of technologies. They found that the three technologies contributed to saving 5.6-8.9% of fuel, the Flettner rotor having the best fuel-saving function. Tillig et al. [12] analysed a total of 11 different arrangements of Flettner rotors in the tanker and RoRo ship. The study showed that tankers saved 30% fuel and the RoRo ship saved 14% fuel. Thus, the Flettner rotor has become an effective propulsion device in ship navigation. In order to identify the most influencing parameters on Flettner rotor performance, De Marco et al. [16] analysed the influence of spin ratio, aspect ratio and end plate on the Flettner rotor. It was found that spin ratio is the most important factor affecting rotor performance. Li et al. [17] proposed that a deformed sail and a 300,000-ton oil tanker was used as the base ship. They found that the 16-sided sail had better performance and the peak value of lift for the sail was 590 kN. Bordogna et al. [18] studied the influence of Reynolds number on the performance of the cylinders through large wind tunnel tests. For the

performance of the cylinders, it was a key point for the spin ratio of 2.5. Bordogna et al. [19] studied the aerodynamic interaction effect of two Flettner rotors through wind tunnel test. The results showed that the distance and spin ratio are the most important factors affecting the aerodynamic performance of two cylinders. Li et al. [20] proposed a new Flettner rotor and, on the basis of not occupying the deck area, the device obtained a better performance than the Flettner rotor. They found that the maximum thrust can reach 750 kN for a 100,000-ton ship.

Flettner rotors usually work in side-winds and the performance of the rotor primarily depends on the environment, wind and ship speed. In practical installations, ships are usually equipped with multiple Flettner rotors to greater use wind energy. The diameter of the Flettner rotor is 1.5-5.0 m and its height is 15-40 m [21,22]. In addition, according to the condition of the Magnus effect, the wind-receiving area of the Flettner rotor affects its performance. The larger the wind-receiving area of the Flettner rotor, the greater the thrust [23,24]. However, the Flettner rotor has a larger wind-receiving area, which can occupy the deck area. This is a disadvantage for ships with high deck utilisation [25]. So, it will be of great significance to design a new Flettner rotor which can assist the navigation of ships but also save on deck area.

Currently, Flettner rotors are mostly installed in merchant ships, but a few have been installed in special ships. The semi-submersible ship is a kind of special ship which transports cargo, with a super large size that cannot be divided. Fig. 1 shows the semi-submersible ship 'Xin Guang Hua' of COSCO SHIPPING. When a semi-submersible ship is transporting cargo from one port to another, it is usually empty on the return journey: Port A to port B is free of cargo, or port B to port A is free of cargo. Half of the ship's working time is ballast voyage (ballast voyage means that there is no cargo on deck). An empty deck makes the Flettner rotors on a semi-submersible have a better chance of harnessing wind energy. Secondly, due to the low centre of gravity of the semi-submersible ship, the installation of Flettner rotors has little effect on the stability of the ship during the voyage. Therefore, the Flettner rotors installed on a semi-submersible ship have great advantages. However, if the Flettner rotors are installed directly on the deck, the deck area will be occupied, thus affecting the cargo transport of the semi-submersible ship. In addition, the semi-submersible ship has two pontoons on the deck to adjust the ship's draft. If the pontoons are combined with the Flettner rotors, the Flettner rotors can use the wind energy to provide part of the ship's thrust without occupying the deck area. Based on the above discussion, in this study, the installation and method of use of a new type of Flettner rotor is proposed. The new Flettner rotor system is an assisted propulsion device. The two pontoons of a semi-submersible ship and two rotating cylinders are cleverly combined. Two huge rotating cylinders were created without affecting the function of the pontoons. The advantage of these rotating cylinders is that they do not occupy the deck area and can increase the wind-receiving area of the rotating

cylinders, so that the rotor can better apply wind energy. In general, Flettner rotors have the potential to save 3% to 25% of engine fuel consumption. This is of economic value to semi-submersible ships.



Fig. 1. The semi-submersible ship 'Xin Guang Hua'

THE STRUCTURE AND INSTALLATION OF THE NEW TYPE OF FLETTNER ROTOR SYSTEM

In order to analyse the contribution of the new type of Flettner rotor system, the semi-submersible ship 'Xin Guang Hua' of COSCO SHIPPING was selected as an example. This is one of the largest semi-submersible ships in the world and is typical for its kind. The structure of the new type of Flettner rotor system is shown in Fig. 2(a). Two huge rotating cylinders are set on the outside of two pontoons, respectively. Fig. 2(b) shows the composition of one of the rotating cylinders. It is a circular hollow cylinder with an end plate, enveloped on the outside of the pontoon. A motor drives the rotating cylinder to achieve its function without affecting the function of the

pontoon. Moreover, in order to avoid interfering with the ship's crew passing the pontoon, the bottom of the rotating cylinder is placed 2 m away from the deck; the top of the rotating cylinder is placed on the upper of the pontoons. When the ship is sailing, the wind coming from one side of the rotating cylinder will generate the Magnus effect. Fig. 2(c) shows the installation position of the new Flettner rotor system on the semi-submersible ship. Fig. 2(c_1) shows two rotating cylinders installed side by side, in which the distance of the two rotating cylinders $X=3D$. This is a typical case, which will be described in detail in this study. In addition to this, the pontoons on the deck can move along the sliding rail. Therefore, the boosting effect of two rotating cylinders at different positions was studied when the ship is sailing with no load or transporting cargo of small size. Figs. 2(c_2)-(c_4) show two rotating cylinders installed in different positions; to be specific, the distance of the two rotating cylinders $X>3D$.

The new type of Flettner rotor system is superior in a number of ways. On the one hand, the rotating cylinders are installed on the pontoons, which can realise the utilisation of wind energy without occupying the area of the deck. On the other hand, due to the large size of the pontoons, the rotating cylinders installed on the outside of the pontoons have a larger wind-receiving area than the conventional Flettner rotor. The larger wind-receiving area increases the lift generated by the rotating cylinders.

In this analysis, a 100,000-ton semi-submersible ship, Xin Guang Hua, was selected as an example for simulation. Table 1 shows some of its parameters. The height of the pontoons on the semi-submersible ship was 20 m. In order not to affect the functions of the semi-submersible ship's transportation cargo, the diameter of the rotating cylinders should be as close to the pontoons as possible. The diameters of the rotating cylinders were 14 m. In addition, the height of the rotating cylinders was 20 m and the diameters of the end plate were 28 m.

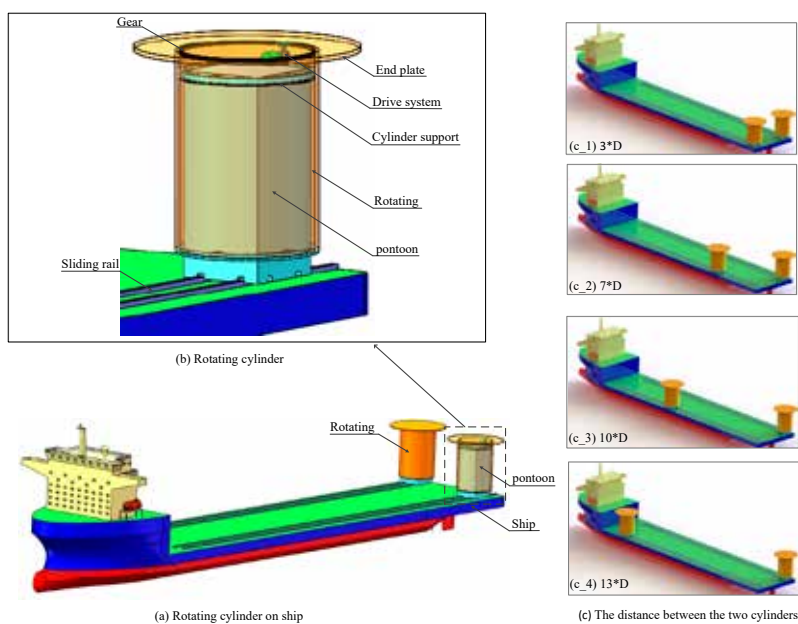


Fig. 2. The new Flettner rotor system and its installation position on the ship

Tab. 1. Parameters of 'Xin Guang Hua'

Parameter	Value (m)	Parameter	Value
Length overall	255.0	Deadweight (tonne)	98500
Breadth moulded	68.0	Main engine power (kw)	21300
Depth	14.5	Maximum speed (knots)	14.5
Draft	10.5	Effective deck area (m2)	14280

GEOMETRICAL CONFIGURATION

PHYSICAL MODELS

When the ship is affected by environmental wind (V_{wind}), the Magnus force generated by the rotating cylinder will provide part of the thrust for the ship. As shown in Fig. 3, when wind is coming from the port side of the ship, the two rotating cylinders rotate clockwise and generate a forward thrust. Similarly, when wind is coming from the starboard side of the ship, the two rotating cylinders rotate counter-clockwise and also produce a forward thrust, according to the Magnus effect. Therefore, in order to ensure that the thrust from the rotating cylinder reaches its peak value along the traveling direction of the ship, a wind direction sensor can be installed to obtain the wind direction at this time, so as to control the rotation of the rotating cylinders. In addition to this, the apparent wind acting on the rotating cylinders is an important factor for verifying the performance of the new type of Flettner rotor system. As shown in Fig. 3(a), the apparent wind acting on the rotating cylinders is the vector sum of the ship speed and the environmental wind speed. The apparent wind acting on the rotating cylinders can be obtained by Eq. (1). In the following simulation, the apparent winds in different directions were considered; the environmental wind speed was 10 m/s and the ship speed was 5 m/s.

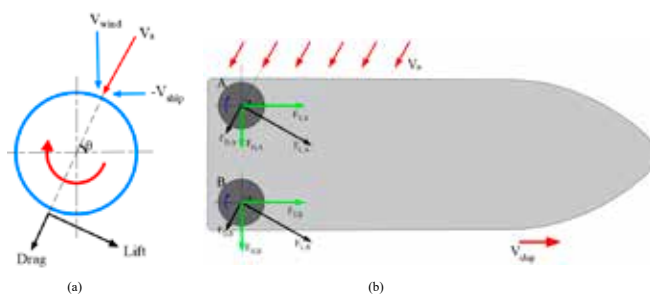


Fig. 3. The apparent wind (a) and force generated by the cylinders (b)

As shown in Fig. 3, in the course of the ship's voyage, the thrust (CT) and heel (CH) coefficients are determined by the lift (CL) and drag coefficients (CD) of the rotating cylinder and the apparent wind angle between the heading and the apparent wind speed. The equations of thrust coefficient and heel coefficient are given as follows [14]:

$$V_a = V_{wind} - V_{ship} \quad (1)$$

$$C_T = C_L * \sin(\theta) - C_D * \cos(\theta) \quad (2)$$

$$C_H = C_L * \cos(\theta) + C_D * \sin(\theta) \quad (3)$$

The thrust (FT) and side force from the heel (FH) are calculated according to thrust coefficient (CT), heel coefficient (CH), apparent wind speed (Va) air density (ρ) and Cross-sectional area of the rotating cylinder (S), according to the Eqs. (4) and (5). Fig. 3(b) shows the diagram of ship forces.

$$F_T = 0.5 * \rho * S * V_a^2 * C_T \quad (4)$$

$$F_H = 0.5 * \rho * S * V_a^2 * C_H \quad (5)$$

The thrust generated by the rotating cylinders is the vector sum of lift and drag. According to the thrust (FT), ship speed (V_{ship}), spin ratio (α), and torque coefficient (CM), the thrust power generated by the rotating cylinders and the power consumed by the motor are calculated in Eqs. (6) and (7) [26].

$$P_T = T * V_{ship} \quad (6)$$

$$P_{motor} = 0.5 * \rho * S * V_a^3 * C_M * \alpha \quad (7)$$

The effective power generated by the rotating cylinder is determined by the power consumed by the motor and the lift / drag acting on the rotating cylinder. The effective power P_{ef} is given by Eq. (8).

$$P_{ef} = P_T - P_{motor} \quad (8)$$

COMPUTATIONAL DOMAIN AND GRID GENERATION

In order to obtain lift coefficients, drag coefficients and propulsive power of the two rotating cylinders, the CFD (Computational Fluid Dynamics) software 'Fluent' was used to calculate the RANS equation, in conjunction with the Realisable k- ϵ turbulence model [27-29]. From Eqs. (9) and (10), the RANS equation included the continuity equation and momentum equation are given as:

$$\nabla \cdot U = 0 \quad (9)$$

$$\rho \bar{u}_j \frac{\partial \bar{u}_i}{\partial x_j} = \rho \bar{f}_i + \frac{\partial}{\partial x_i} \left[-\bar{p} \delta_{ij} + \mu \left(\frac{\partial \bar{u}_i}{\partial x_j} + \frac{\partial \bar{u}_j}{\partial x_i} \right) - \overline{\rho u_i' u_j'} \right] \quad (10)$$

where ρ is the density of the fluid; μ is fluid viscosity; δ_{ij} is Kronecker delta; U is the relative velocity; \bar{f}_i is the mass force term; \bar{p} is static pressure; and $-\overline{\rho u_i' u_j'}$ is the apparent stress resulting from the fluctuating velocity field, generally referred to as the Reynolds stress.

The computational domain and boundary condition for the two rotating cylinders are given in Fig. 4. The whole computational domain shape is a similar cylinder, which has

a diameter of $15X$. X is the distance between the centres of the two rotating cylinders. The thickness of the computational domain is four times that of the rotating cylinders. The two rotating cylinders are installed symmetrically in the central region of the computational domain. The two rotating cylinders are surrounded by two $2*D$ rotating domains (D is the diameter of the rotating cylinder), which are used to represent the wind field generated by the rotating cylinders [30]. The inlet boundary is set on the left side of the calculational domain, which adopts the Velocity-inlet; the outlet boundary is set on the right side of the calculational domain, which adopts the Pressure-outlet and the value is $1.103*10^5$ pa. The other four faces of the computational domain are defined as walls.

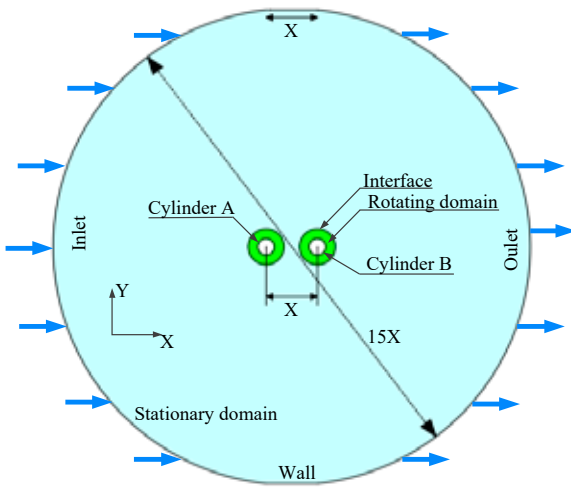


Fig. 4. Computational domain and boundary condition

The rotating cylinder with an endplate is shown in Fig.5 (a). The rotating cylinder with an endplate is shown. For the whole computational domain, the coupling unstructured and structured grids are adopted; to be specific, tetrahedral grids are used for the rotating domains and hexa-grids are

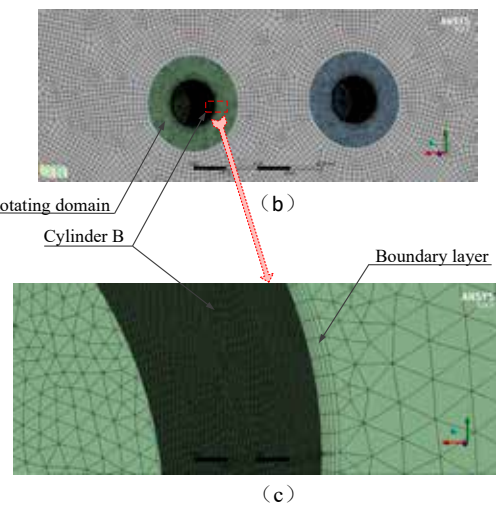
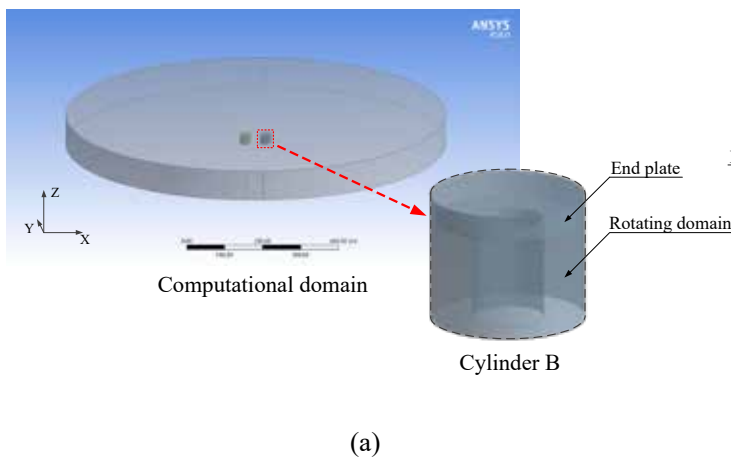


Fig. 5. Grid configuration for the cylinder

used for the whole domain. The $2*D$ range near the two cylinders forms the rotating domain, as shown in Fig. 5(b). The two rotating cylinders rotate clockwise. The surfaces of the two rotating cylinders are set as non-slip walls which have a certain roughness. The sliding grid is used in this rotating domain. As shown in Fig. 5(c), in order to simulate the rotation of the cylinder more accurately, a prismatic mesh layer is used on the wall of the rotating cylinder. There are five prism layers, with a layer growth rate of 1.2. Besides, the non-dimensional wall distance (y^+) is approximately equal to 1, which meets the requirements of the turbulence model; the blockage ratio of this model is about 1.6%. The left rotating cylinder is defined as cylinder A and the right rotating cylinder as cylinder B. In addition, the positive direction of the y -axis is the sailing direction of the ship and the port-wind is the focus of attention.

GRID INDEPENDENCE ANALYSIS

The grid independence was tested by using four grid densities of approximately 1,500,000, 2,000,000, 2,500,000, and 4,000,000 cells. The pressure coefficient C_p of cylinder A was used to compare different grids. The other verification simulations assumed that: the apparent wind angle is 90° , the environment wind is 10 m/s, the ship speed is 5 m/s, and the spin ratio α is 2.0. The instantaneous C_p is presented in Fig 6. The average C_p is listed in Table 2. When the grid reaches 2.5 million cells, further increasing the grid density has little effect on the results. When compared with the case of 4 million cells, the error of the C_p is less than 0.44%. Therefore, considering accuracy and efficiency, 2.5 million grids were selected for subsequent simulation.

Tab. 2. The average C_p of different grids

Grid number	Average C_p (30-60s)	Error of average- C_p
1,500,000	-2.00971	3.52%
2,000,000	-2.02827	2.63%
2,500,000	-2.07382	0.44%
4,000,000	-2.08309	0.00%

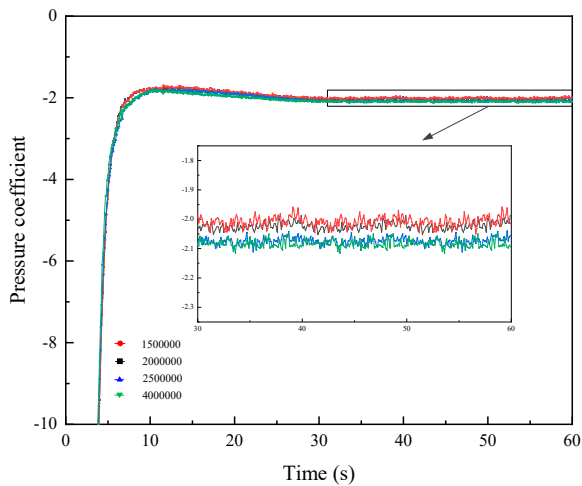


Fig. 6. Data curves of instantaneous C_p

COMPARISON OF EXPERIMENTAL DATA AND SIMULATION DATA

Comparison between simulation data and experimental data is shown in Fig. 7. Experimental data were obtained from Badalamenti et al. [31]. According to their research, the conditions selected for simulation were: the cylinder diameter (88.9 mm), cylinder length (450 mm), wind speed (7 m/s), diameter of end plate (177.8 mm), and selected spin ratios (0.0, 0.5, 1.0, 2.0 and 3.0, respectively). The lift coefficient and drag coefficient of the cylinder were compared. The errors between the simulation and experimental data are presented in Table 3. It can be seen that the numerical results were found to be a good match with the experimental data. The simulation settings in this study are the same as those used for simulation validation. Therefore, the numerical method is acceptable.

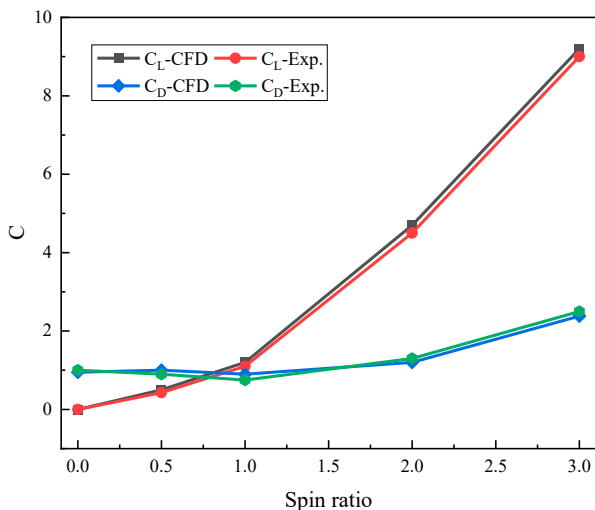


Fig. 7. Comparison of C_L and C_D for the numerical data and the experimental data

Tab. 3. C_L and C_D percentage error between numerical and experimental data

Spin ratio	0.0	0.5	1.0	2.0	3.0
C_L	/	16.2%	9.0%	4.4%	3.1%
C_D	5%	11.1%	20.0%	7.6%	4.8%

The aspect ratio of the rotor in the above experiment was 5, while the aspect ratio of the new rotor proposed in this study was 1.4. Then, in order to better test the accuracy of the simulation settings, rotors with similar aspect ratios were selected for comparison. The simulation results were compared with the results reported by De Marco et al. [32]. The conditions selected for simulation were: cylinder diameter (4 m), end plate diameter (8 m), cylinder length (14 m), and the angular speed of the rotor (10 rad/s). The results of the data comparison are shown in Fig. 8. The numerical data are close to the reference data and, therefore, the simulation settings are acceptable.

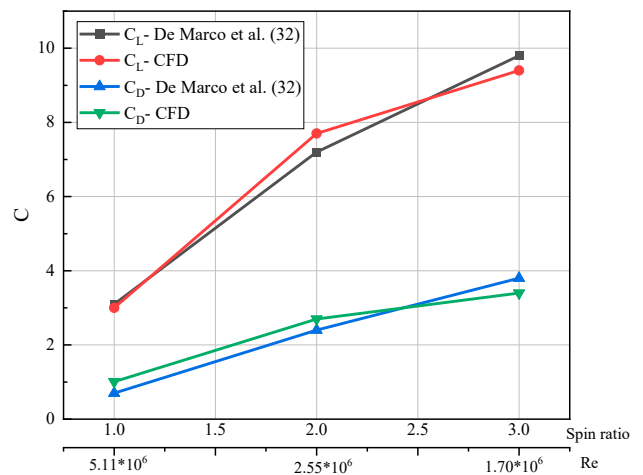


Fig. 8 Comparison of C_L and C_D for the numerical data and the reference data

ANALYSIS OF RESULTS

When the semi-submersible ship is sailing at sea, the two rotating cylinders are installed side by side at the stern. Its location is shown in Fig. 2(c_1). This is a typical condition when the ship is sailing. In order to verify the boosting effect of the rotating cylinders, the lift coefficients, drag coefficients and other parameters of the two rotating cylinders under different spin ratios were studied, when the apparent wind angle was 30° , 60° , 90° , 120° and 150° . The thrust contribution of the rotating cylinders was also studied. The section titled «Discussion of two rotating cylinders in different positions» below, briefly discusses and verifies the effect of distance on the performance of two rotating cylinders. The different positions of the two rotating cylinders on the deck are shown in Figs. 2(c_2)-(c_4).

DISCUSSION OF TWO ROTATING CYLINDERS SIDE BY SIDE

According to the relevant studies [33,34], the change of spin ratio and apparent wind angle will affect the boosting effect of the rotating cylinders. In order to explore the performance of rotating cylinders under different apparent wind angles and different spin ratios, the influence of the spin ratio on rotating cylinders under different apparent wind angles is discussed in this section.

The lift coefficient and drag coefficient

The lift coefficients (CL) and drag coefficients (CD) of two rotating cylinders at different spin ratios are given in Fig. 9. The lift coefficients of cylinder A and cylinder B are shown in Fig. 9(a) and (b), respectively. It can be seen that the spin ratio has an important effect on the performance of two rotating cylinders. The lift coefficients of the two rotating cylinders increase with the increase of the spin ratio. Secondly, by comparing the lift coefficients of the two rotating cylinders, it can be seen that the lift coefficient of cylinder B is less than that of cylinder A, under the same conditions. This may

be because cylinder B is partially immersed in the wake of cylinder A, so the lift coefficient of cylinder B is affected by cylinder A. In addition, the apparent wind angle has an effect on the two rotating cylinders. When the spin ratio of two cylinders is the same, the lift coefficient is the smallest when the apparent wind angle is 90° . The maximum lift coefficients of the two rotating cylinders are obtained at $\theta=150^\circ$ and $\alpha=3.0$. The maximum value of cylinder A is 11.98; the maximum value of cylinder B is 10.68.

Fig. 9(c) and (d) represent the drag coefficients of cylinder A and cylinder B, respectively. In Fig. 9(c), the effect of cylinder B leads to different variation trends of the drag coefficient of cylinder A with a change of spin ratio. When the apparent wind angle is 30° and 150° , as the spin ratio increases, the drag coefficient of cylinder A first increases and then decreases. The maximum value of drag coefficient is 2.26, at a spin ratio of 2.5. In addition, the drag coefficient of cylinder A, under the apparent wind angle of 90° , is the smallest, compared with other angles. In Fig. 9(d), the drag coefficient of cylinder B increases with the increase in spin ratio. When the apparent wind angle is 90° , the drag coefficient of cylinder B is much larger than that of other angles.

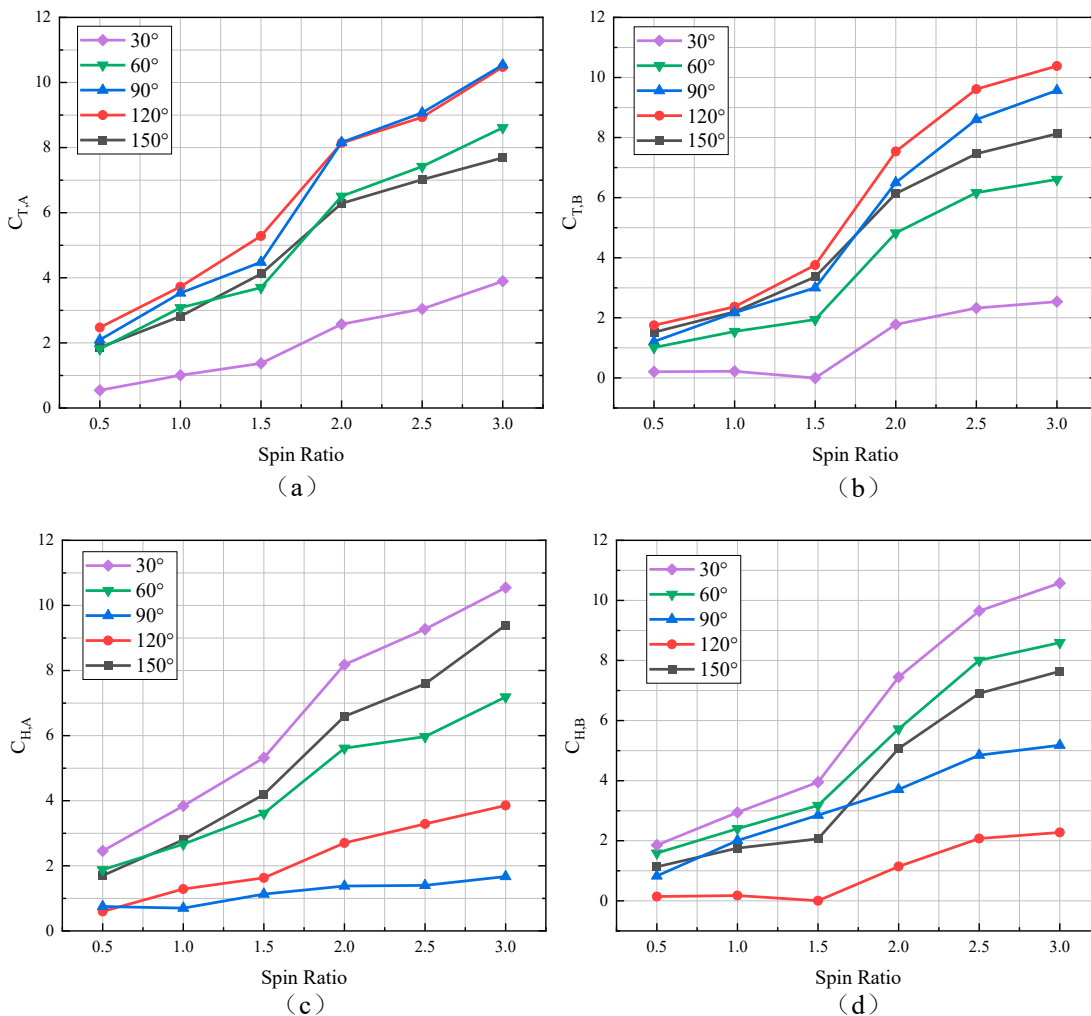


Fig. 9. Lift and drag coefficients for cylinder A (left) and cylinder B (right)

The thrust coefficient and heel coefficient

In order to express the thrust contribution of the rotating cylinder, intuitively, Fig. 10 shows the thrust coefficients and heel coefficients of cylinder A and cylinder B. According to Eqs. (2) and (3), the thrust and heel coefficients depend on the lift coefficient, the drag coefficient and the apparent wind angle. Fig. 10(a) and (b) show the thrust coefficients of cylinder A and cylinder B, respectively. It can be seen that the thrust coefficients of two rotating cylinders increase with the increase of the spin ratio. The maximum thrust coefficient is obtained at a spin ratio of 3.0. The maximum

thrust coefficient of cylinder A is 10.54 when the spin ratio is 3.0 and the apparent wind angle is 90°; the maximum thrust coefficient of cylinder B is 10.38 when the spin ratio is 3.0 and the wind angle is 120°. Fig 10(c) and (d) show the heel coefficients of cylinder A and cylinder B, respectively. It can be seen that the heel coefficients of two rotating cylinders increase with the increase of the spin ratio. In addition, it can be seen that the heel coefficient of cylinder A at the apparent wind angle $\theta=90^\circ$ is the smallest, compared with that of other angles; the heel coefficient of cylinder B at the apparent wind angle $\theta=120^\circ$ is smaller than that of other angles.

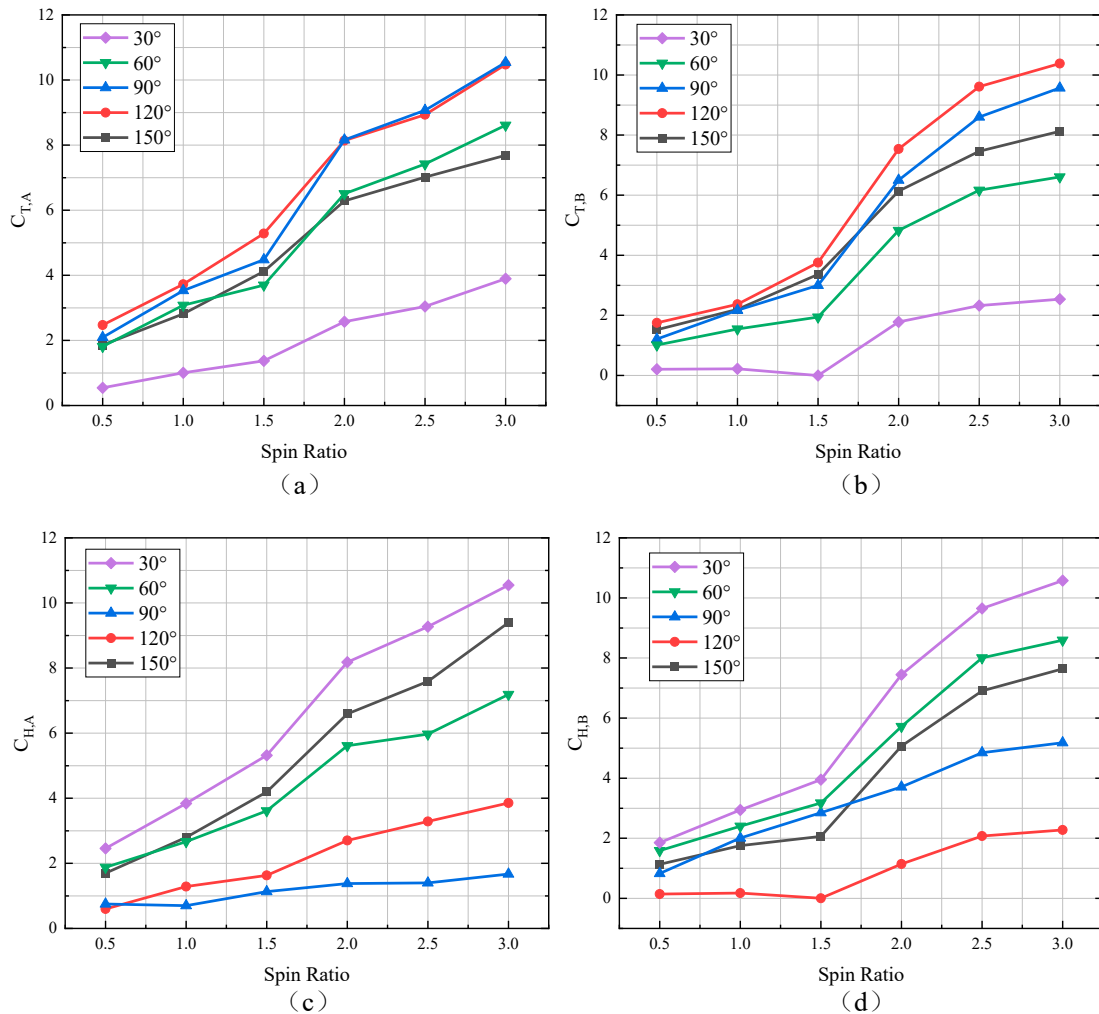


Fig. 10. Thrust and heel coefficients for cylinder A (left) and cylinder B (right)

The pressure distributions around the cylinders

For the purpose of analysing the pressure distributions around the two rotating cylinders for different spin ratios, the pressure contours with spin ratios of 0.5-3.0, at an apparent wind angle of 90°, are given, respectively. Fig. 11 shows the pressure area around two rotating cylinders in the mid-plane under different spin ratios. It was found that two areas of low-pressure appear on the top of the two rotating cylinders. The pressure differences in the rotating cylinders will produce

positive thrust to propel the ship. In addition, the pressure differences around the two rotating cylinders along the y-axis direction become larger with the increase in spin ratio. From the pressure graphs with spin ratios of 2.0, 2.5 and 3.0, the results show that the right side of cylinder B appears as a low-pressure area, due to the influence of cylinder A, and the low-pressure area becomes more obvious with the increasing spin ratio.

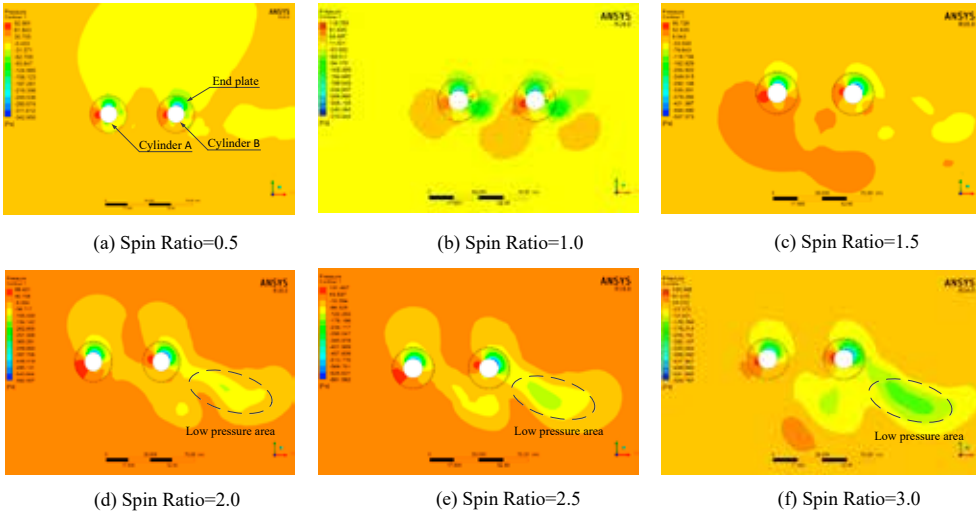


Fig. 11. Pressure distributions of the Flettner rotor system for different spin ratios

Thrust contribution of two cylinders

The total thrust provided by the two rotating cylinders at different apparent wind angles is shown in Fig. 12. The thrust contribution is the largest at an apparent wind angle of 120° and the smallest at an apparent wind angle of 30°, in the same spin ratio. In addition, the thrust of the rotating cylinder increases with the increase in spin ratio. The maximum thrust is obtained when the spin ratio is 3.0; to be more specific, maximum thrusts of 158 kN, 375 kN, 496 kN, 515 kN and 390 kN at apparent wind angles of 30°, 60°, 90°, 120° and 150°, respectively. The thrust of the rotating cylinder reaches its maximum at the apparent wind angle of 120°, because the drag generated by the rotating cylinder at this time will also provide part of the thrust for the ship. Therefore, when the apparent wind angle $\theta > 90^\circ$, a high drag is not a disadvantage.

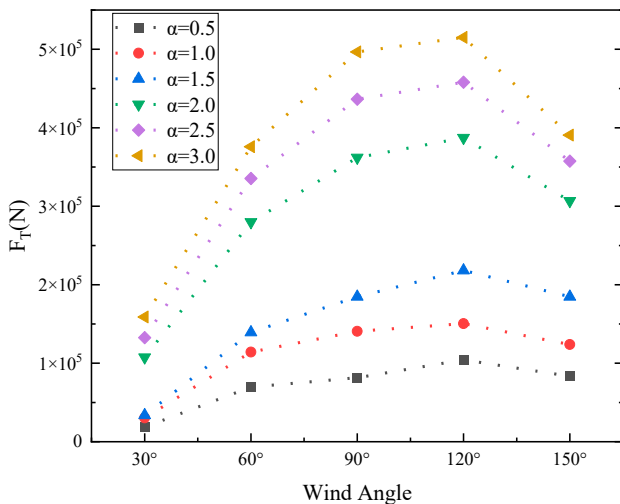


Fig. 12. The thrust contribution of the Flettner rotor system

Energy contribution of two cylinders

In order to evaluate the performance of the rotating cylinders, it is important to consider the thrust power (PT) and effective power (P_{ef}) of the rotating cylinders. Fig. 13 shows the total thrust power and total effective power of the two rotating cylinders at different spin ratios. The thrust power and effective power are calculated by Eqs. (6)-(8). In Fig. 13, at different apparent wind angles, the thrust power rises with the increase of the

spin ratio. The maximum thrust power is obtained at the spin ratio $\alpha=3.0$; to be more specific, maximum thrust power of 794 kW, 1879 kW, 2483 kW, 2575 kW and 1952 kW at apparent wind angles of 30°, 60°, 90°, 120° and 150°, respectively.

The effective power is determined by the motor consumption and the thrust power of the rotating cylinders. It provides more valuable information than thrust power. Fig. 13(a) shows the total effective power of the rotating cylinders under different spin ratios when the apparent wind angle is 30°. It can be seen that the maximum effective power reaches 241 kW at a spin ratio of 2.0. However, when the spin ratio is 3.0, the effective power is negative (which means that the thrust power is less than the power consumed by the motor), which is not good for the ship navigation. As shown in Figs. 13(b)-(e), the effective power first increases and then falls with the increase in spin ratio. In Fig. 13(b), when the spin ratio is 2.5 and the apparent wind angle is 60°, the maximum effective power is 1121 kW. The maximum effective power is 1626 kW at an apparent wind angle of 90° and under a spin ratio of 2.5. Similarly, when the apparent wind angle is 150°, the maximum effective power of the spin ratio $\alpha=2.0$ is 1237 kW. However, in Fig. 13(e), the maximum effective power corresponding to an apparent wind angle of 150° occurs at the spin ratio of 2.0, which is 1237 kW. Table 4 shows that the effective power of the two rotating cylinders can reach 65% when the apparent wind angle is 60°-150°. This proves that the thrust contribution of the rotating cylinders is far larger than the energy consumed by the motor.

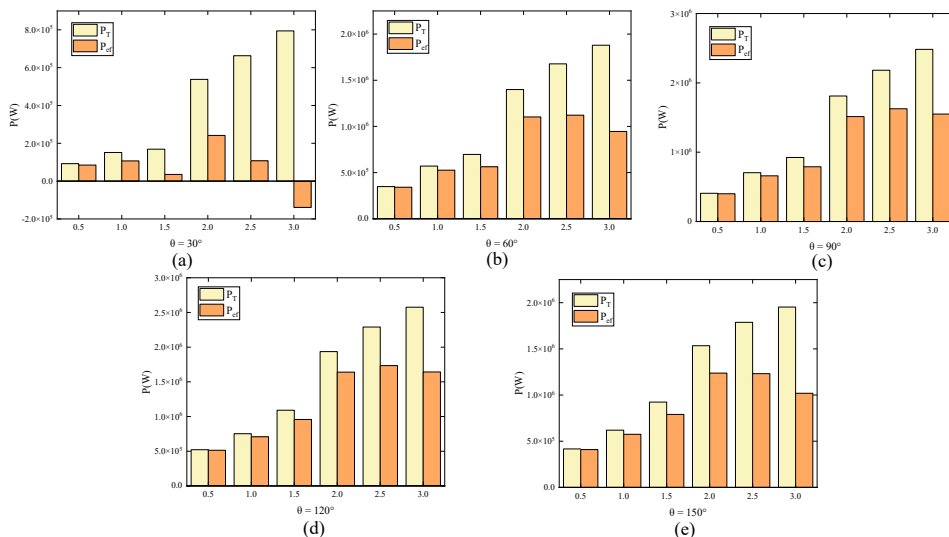


Fig. 13. The total thrust power (P_T) and total effective power (P_{ef}) of the Flettner rotor system

Tab. 4. Comparison of effective power

Apparent wind angle	Maximum effective power(W)	Spin ratio	Thrust power(W)	Effective power/Thrust power
30°	241703	2.0	538055	44%
60°	1121633	2.5	1677293	66%
90°	1626231	2.5	2181891	74%
120°	1734140	2.5	2289800	75%
150°	1237770	2.0	1534122	80%

DISCUSSION OF TWO ROTATING CYLINDERS IN DIFFERENT POSITIONS

Since the pontoons on the deck can move along the sliding rail, the position of the two rotating cylinders can be moved according to the direction of the wind, when the semi-submersible ship is sailing with no load or transporting small cargo. The position of the two rotating cylinders is shown in Figs. 2(c_2)-(c_4). In order to study the lift coefficients, drag coefficients and power values of the rotating cylinders at different

positions, the simulation condition is that the ship speed is 5 m/s and the environment wind speed is 10 m/s. The situation of apparent wind angle of 90° was selected, which is the most typical condition in semi-submersible ship navigation.

The lift coefficient and drag coefficient

Fig. 14 shows the point line graph of lift coefficients (CL), drag coefficients (CD) and lift-to-drag ratio (CL/CD) of two rotating cylinders at different positions. The spin ratio is still an important factor. The lift and drag coefficients of the two rotating cylinders increase with the increase of the spin ratio. In addition, when the spin ratio is 2.0-3.0, the lift coefficient of the cylinder A at a distance 7D, is larger than those at other positions. However, the lift coefficient of cylinder B is less than those at other positions. Figs. 14 (c) and (f) show the

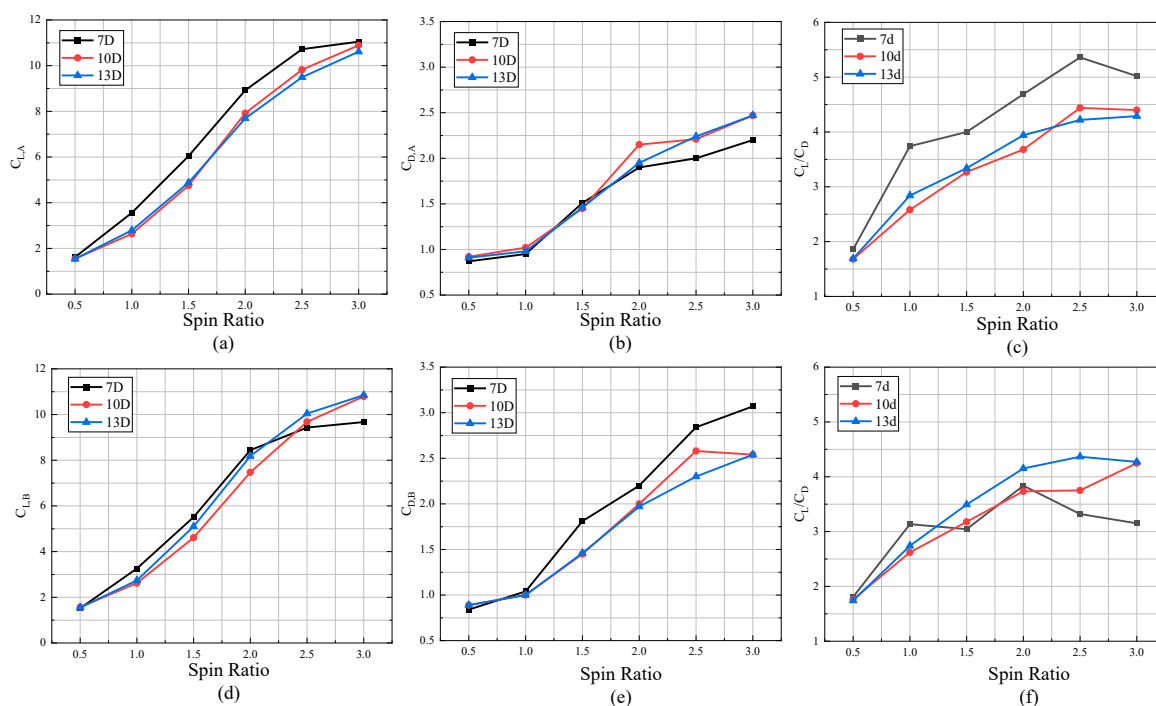


Fig. 14. Lift coefficient (a), drag coefficient (b) and lift-to-drag ratio (c) of cylinder A and lift coefficient (d), drag coefficient (e) and lift-to-drag ratio (f) of cylinder B at different positions

lift-to-drag ratios of rotating cylinders A and B, respectively. When the distance between the two rotating cylinders is 7D, there is interaction between the two rotating cylinders. The lift-to-drag ratio of cylinder B is less than that of cylinder A. When the distance between the two rotating cylinders is 10D and 13D, there is little difference in the lift-to-drag ratio of the two rotating cylinders, indicating that the influence between the two rotating cylinders is small at this distance.

Fig. 15 shows the pressure distributions at three positions with a spin ratio of 2.0. From the figure, it can be clearly seen that when the distance between the two rotating cylinders is 7D, there are two obvious low-pressure areas to the right of the two rotating cylinders. The pressure differences around the two rotating cylinders are 657 Pa along the y-axis direction. In addition to this, the pressure differences around the two rotating cylinders along the y-axis become smaller with the increase of distance. By comparing the pressure distributions, it can be found that distance is one of the important factors affecting the Magnus effect of rotating cylinders.

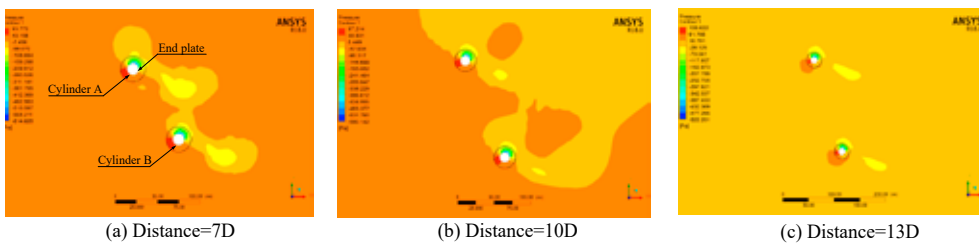


Fig. 15. Pressure distributions at different positions

Energy contribution

Fig. 16 shows the total thrust, the total thrust power and total effective power of the two rotating cylinders at different distances. The bar graph shows the total thrust power and total effective power of the rotating cylinders; the total thrust of two rotating cylinders is shown by the point line graph. It can be seen from the figure that the thrust of the two rotating cylinders increases with the increase in spin ratio. The thrust of two rotating cylinders is greatest when the distance between two cylinders is 7D and the spin ratio is 3.0. the maximum thrust is 511 kN. Similarly, when the distance is 10D and 13D, the maximum thrust reaches 535 kN and 529 kN, respectively. According to Eq. (6), it can be obtained that the maximum thrust power is 2558 kW, 2677 kW and 2649 kW at distances of 7D, 10D and 13D, respectively.

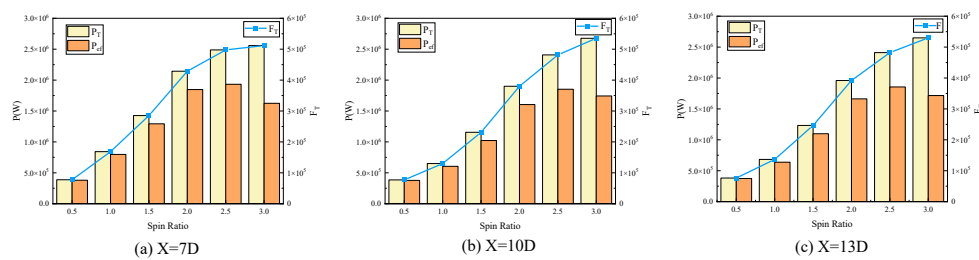


Fig. 16. The total thrust (FT), total thrust power (PT) and total effective power (Pef) of two rotating cylinders for different distances

By comparing the total effective power of two rotating cylinders at different positions, as the spin ratio increases, it can be found that the total effective power of the rotating cylinders first increases and then decreases. The effective power reaches the maximum at the spin ratio $\alpha=2.5$. When the distance is 7D, the maximum effective power is 1932 kW. When the distance is 10D, the maximum effective power is 1852 kW. Similarly, when the distance is 13D, the maximum effective power is 1855 kW.

CONCLUSIONS

In this study, the installation and use of a new type of Flettner rotor system is proposed; where the rotating cylinders envelope is on the outside of the pontoons. When side-winds occur, the Magnus force generated by the rotating cylinders will provide power for the navigation of the ship (based on the Magnus effect). A semi-submersible ship model with two rotating cylinders is established. Under different conditions, the two rotating cylinders are simulated by using Fluent software. The simulation results show that the new type of Flettner rotor system has a remarkable effect.

The main results that can be drawn are as follows:

1. This study compares the lift and thrust coefficients of two rotating cylinders when the two rotating cylinders are installed side by side. The lift coefficients of the rotating cylinders increase with the increase in spin ratio. The maximum lift coefficient occurs when the spin ratio is 3.0. In addition, the apparent wind angle also affects the performance of the rotating cylinders. The lift coefficients of the two rotating cylinders are at a minimum when the apparent wind angle is 90° ; the lift coefficients of the two rotating cylinders are at a maximum at an apparent wind angle of 150° . Therefore, the maximum lift coefficients of cylinder A and cylinder B are 11.98 and 10.68, respectively, at an apparent wind angle $\theta=150^\circ$ and spin ratio $\alpha=3.0$. Because thrust coefficient depends on the lift coefficient, the drag coefficient and the apparent wind angle, the maximum lift coefficient of the rotating cylinder does not mean that the thrust contribution

of the rotating cylinders reaches its peak value. The maximum thrust coefficient of cylinder A (corresponding to a spin ratio of 3.0) occurs when the apparent wind angle is 90° , which is 10.54; when the apparent wind angle is 120° and the spin ratio is 3.0, the maximum thrust coefficient of cylinder B is 10.38.

2. The pressure distributions of two rotating cylinders with different spin ratios and an apparent wind angle of 90° are compared. It can be seen that the pressure differences around the two rotating cylinders along the y-axis become larger with an increase in spin ratio. Under the conditions of the same spin ratio, it can be seen that, when the apparent wind angle is 120°, the total thrust of the two rotating cylinders reaches a peak value, which can reach 500 kN.

3. The thrust contribution of the two rotating cylinders increases with the increase in spin ratio. The maximum thrust power is 2575 kW at the apparent wind angle of 120° under a spin ratio of 3.0. Moreover, when the spin ratio increases, the effective power first increases and then decreases. When the apparent wind angle is 60°-120° and the spin ratio is 2.5, the maximum effective power is obtained. The maximum effective power in the other two apparent wind angles corresponds to the spin ratio of 2.0.

4. When the two rotating cylinders are in different positions, it is found that the lift coefficients of the two rotating cylinders increase with an increase of spin ratio. The maximum lift coefficient of cylinder A is obtained when the distance between the two rotating cylinders is 7D and the spin ratio is 3.0; the lift coefficient of the cylinder B is obtained when the distance between the two rotating cylinders is 13D and the spin ratio is 3.0. In addition, when the distance between the two rotating cylinders is 10D and the spin ratio is 3.0, the total thrust of the two cylinders is 530 kN, and the maximum thrust power is 2677 kW. By comparing the effective power of the two rotating cylinders at different positions, it is found that the maximum effective power is 1932 kW when the distance between the two rotating cylinders is 7D.

This study provides a useful reference for practical engineering applications.

ACKNOWLEDGEMENTS

This project was funded by the Natural Science Foundation of Shandong Province of China (ZR2021ME156).

REFERENCES

1. L. Zhu, B.L. Li, A. Li, W.X. Ji, Y. Qian, X.C. Lu and Z. Huang. 'Effects of fuel reforming on large-bore low-speed two-stroke dual fuel marine engine combined with EGR and injection strategy'. *International Journal of Hydrogen Energy*, 45, 2020. 29505-29517. doi: 10.1016/j.oceaneng.2019.01.026.
2. ICCT, The international maritime organization's initial greenhouse gas strategy. *Update Policy*, 2018. 3-4.
3. A. Half, L. Younes and T. Boersma, 'The likely implications of the new IMO standards on the shipping industry'. *Energy Policy*, 126, 2019. 277-286. doi: 10.1016/j.enpol.2018.11.033.
4. S.L. Wen, H. Lan, Y.Y. Hong, D.C. Yu, L.J. Zhang and P.Cheng. 'Allocation of ESS by interval optimization method considering impact of ship swinging on hybrid PV/diesel ship power system'. *Applied Energy*, 175, 2016. 158-167. doi: 10.1016/j.apenergy.2016.05.003.
5. F. Diab, H. Lan and S. Ali, 'Novel comparison study between the hybrid renewable energy systems on land and on ship'. *Renewable and Sustainable Energy Reviews*, 63, 2016. 452-463. doi: 10.1016/j.rser.2016.05.053.
6. P.C. Pan, Y.W. Sun, C.Q. Yuan, X.P. Yan and X.J. Tang. 'Research progress on ship power systems integrated with new energy sources: A review'. *Renewable and Sustainable Energy Reviews*, 144, 2021. 111048. doi: 10.1016/j.rser.2021.111048.
7. J.H. He, Y.H. Hu, J.J. Tang and S.Y. Xue. 'Research on sail aerodynamics performance and sail-assisted ship stability'. *Journal of Wind Engineering and Industrial Aerodynamics*, 146, 2015. 81-89. doi: 10.1016/j.jweia.2015.08.005.
8. L. Talluri, D.K. Nalianda and E. Giuliani, 'Techno economic and environmental assessment of Flettner rotors for marine propulsion'. *Ocean Engineering*, 154, 2018. 1-15. doi: 10.1016/j.oceaneng.2018.02.020.
9. N.J. Van Der Kolk, I. Akkerman, J.A. Keuning and R.H.M. Huijsmans. 'Part 2: Simulation methodology and numerical uncertainty for RANS-CFD for the hydrodynamics of wind-assisted ships operating at leeway angles'. *Ocean Engineering*, 201, 2020. 107024. doi: 10.1016/j.oceaneng.2020.107024.
10. Y. Ma, H.X. Bi, M.Q. Hu, Y.Z. Zheng and L.X. Gan. 'Hard sail optimization and energy efficiency enhancement for sail-assisted vessel'. *Ocean Engineering*, 173, 2019. 687-699. doi: 10.1016/j.oceaneng.2019.01.026.
11. R.H. Lu and J.W. Ringsberg. 'Ship energy performance study of three wind-assisted ship propulsion technologies including a parametric study of the Flettner rotor technology'. *Ships and Offshore Structures*, 15, 2020. 249-258. doi: https://doi.org/10.1080/17445302.2019.1612544. doi: 10.1080/17445302.2019.1612544.
12. F. Tillig and J.W. Ringsberg. 'Design, operation and analysis of wind-assisted cargo ships'. *Ocean Engineering*, 211, 2020. Article ID 107603. doi: 10.1016/j.oceaneng.2020.107603.
13. I.S. Seddiek and N.R. Ammar. 'Harnessing wind energy on merchant ships: case study Flettner rotors onboard bulk carriers'. *Environmental Science and Pollution Research*, 28, 2021. 32695-32707. doi: 10.1007/s11356-021-12791-3.

14. S. Pezzotti, V.N. Mora, A.S. Andres and S. Franchini. 'Experimental study of the Magnus effect in cylindrical bodies with 4, 6, 8 and 10 sides'. *Journal of Wind Engineering & Industrial Aerodynamics*, 197, 2020. 104065. doi: 10.1016/j.jweia.2019.104065.
15. L.C. Correa, J.M. Lenz, C.G. Ribeiro and F.A. Farret. 'Magnus Wind Turbine Emulator With MPPT by Cylinder Rotation Control'. *Journal of Dynamic Systems, Measurement, and Control*, 140, 2018. 101012. doi: 10.1115/1.4040212.
16. A. De Marco, S. Mancini, C. Pensa, G. Calise and F. De Luca. 'Flettner rotor concept for marine applications: a systematic study'. *International Journal of Rotating Machinery*. 2016. 12. Article ID 3458750. doi: 10.1155/2016/3458750.
17. B.Y. Li, R. Zhang, B.S. Zhang, Q.Q. Yang and C. Guo. 'An assisted propulsion device of vessel utilising wind energy based on Magnus effect'. *Applied Ocean Research*, 114 (2021), Article ID 102788. doi: 10.1016/j.apor.2021.102788.
18. G. Bordogna, S. Muggiasca, S. Giappino, M. Belloli, J.A. Keuning, R.H.M. Huijsmans and A.P. van 't Veer. 'Experiments on a Flettner rotor at critical and supercritical Reynolds numbers'. *Journal of Wind Engineering and Industrial Aerodynamics*, 188 (2019), 19–29. doi: 10.1016/j.jweia.2019.02.006.
19. G. Bordogna, S. Muggiasca, S. Giappino, M. Belloli, J.A. Keuning and R.H.M. Huijsmans. 'The effects of the aerodynamic interaction on the performance of two Flettner rotors'. *Journal of Wind Engineering and Industrial Aerodynamics*, 196, 2020. 104024. doi: 10.1016/j.jweia.2019.104024.
20. B.Y. Li, R. Zhang, Y.J. Li, B.S. Zhang and C. Guo. 'Study of a new type of Flettner rotor in merchant ships'. *Polish Maritime Research*, 109 (2021), 28-41. doi: 10.2478/pomr-2021-0003.
21. J. Seifert. 'A review of the Magnus effect in aeronautics'. *Progress in Aerospace Sciences*, 55, 2012. 17-45. doi: 10.1016/j.paerosci.2012.07.001.
22. X.Y. Liu, Y.X. Wang, J.J. Liang and S. Wang. 'CFD Analysis of Aerodynamic Characteristics of Ship's Wind-Assisted Rotor Sail. Navigation of China', doi: 1000-4653, 2019. 04-0046-05.
23. X.Y. Lu. 'Study on aerodynamic Performance of Vertical Magnus Wind Turbine'. University of Xiang Tan, May 2019.
24. A. Sedaghat, I. Samani, M. Ahmadi-Baloutaki, M.E.H. Assad and M. Gaith. 'Computational study on novel circulating aerofoils for use in Magnus wind turbine blades'. *Energy*, 91, 2015. 393-403. doi: 10.1016/j.energy.2015.08.058.
25. N.R. Ammar and I.S. Seddiek. 'Enhancing energy efficiency for new generations of containerized shipping'. *Ocean Engineering*, 215, 2020. 107887. doi: 10.1016/j.oceaneng.2020.107887.
26. M. Traut, P. Gilbert, C. Walsh, A. Bows, A. Filippone, P. Stansby and R. Wood. 'Propulsive power contribution of a kite and a Flettner rotor on selected shipping routes'. *Applied Energy*, 113, 2014. 362–372.
27. D. Moreira, N. Mathias, T. Morais. 'Dual flapping foil system for propulsion and harnessing wave energy: A 2D parametric study for unaligned foil configurations'. *Ocean Engineering*, 215 (2020), 107875. doi: 10.1016/j.oceaneng.2020.107875.
28. D. Wang and PL-F. Liu. 'An ISPH with $k-\epsilon$ closure for simulating turbulence under solitary waves'. *Coastal Engineering*, 157, 2020. 103657. doi: 10.1016/j.coastaleng.2020.103657.
29. B.S. Zhang, B.W. Song, Z.Y. Mao, W.L. Tian, B.Y. Li and B. Li. 'A novel parametric modeling method and optimal design for savonius wind turbines'. *Energies*. 10 (2017), 301. doi: 10.3390/en10030301.
30. D.J. Wang, K. Liu, P. Huo, S.Q. Qiu, J.W. Ye and F.L. Liang. 'Motions of an unmanned catamaran ship with fixed tandem hydrofoils in regular head waves'. *Journal of Marine Science and Technology*. 24, 2019. 705-719. doi: 10.1007/s00773-018-0583-x.
31. C. Badalamenti and S.A. Prince. 'Effects of endplates on a rotating cylinder in crossflow'. In *Proceedings of the 26th AIAA Applied Aerodynamics Conference*, Honolulu, Hawaii, USA, August 2008.
32. A. De Marco, S. Mancini, C. Pensa, 'Preliminary analysis for marine application of Flettner rotors' in *Proceedings of the 2nd International Symposium on Naval Architecture and Maritime (INT-NAM '14)*, Istanbul, Turkey, October 2014.
33. A. De Marco, S. Mancini, C. Pensa, R. Scognamiglio and L. Vittello. 'Marine application of Flettner rotors: numerical study on a systematic variation of geometric factor by doe approach'. In *Proceedings of the 6th International Conference on Computational Methods in Marine Engineering (MARINE'15)*, Rome, Italy, June 2015.
34. I.S. Seddiek and N.R. Ammar. 'Harnessing wind energy on merchant ships: case study Flettner rotors onboard bulk carriers'. *Environmental Science and Pollution Research*, 28, 2021. 32695–32707. doi: 10.1007/s11356-021-12791-3.

CONTACT WITH THE AUTHORS

Jingze Lv

College of Electromechanical Engineering,
Qingdao University of Science and Technology,
Qingdao 266061, Shandong, China,
CHINA

Yiqun Lin

College of Electromechanical Engineering,
Qingdao University of Science and Technology,
Qingdao 266061, Shandong, China,
CHINA

Rui Zhang

College of Electromechanical Engineering,
Qingdao University of Science and Technology,
Qingdao 266061, Shandong, China,
CHINA

Boyang Li

e-mail: qdlby@126.com

College of Electromechanical Engineering,
Qingdao University of Science and Technology,
Qingdao 266061, Shandong, China,
CHINA

Hualin Yang

College of Electromechanical Engineering,
Qingdao University of Science and Technology,
Qingdao 266061, Shandong, China,
CHINA

AN IMPROVED DYNAMIC SURFACE SLIDING MODE METHOD FOR AUTONOMOUS COOPERATIVE FORMATION CONTROL OF UNDERACTUATED USVS WITH COMPLEX MARINE ENVIRONMENT DISTURBANCES

Zaopeng Dong^{1,2,3} 

Shijie Qi^{1,3} 

Min Yu^{1,3*}

Zhengqi Zhang^{1,3} 

Haisheng Zhang^{1,3} 

Jiakang Li^{1,3}

Yang Liu^{1,3}

¹ Key Laboratory of High Performance Ship Technology (Wuhan University of Technology), Ministry of Education, Wuhan University of Technology, Wuhan, China

² Science and Technology on Underwater Vehicle Technology Laboratory, Harbin Engineering University, Harbin, China

³ School of Naval Architecture, Ocean and Energy Power Engineering, Wuhan University of Technology, Wuhan, China

* Corresponding author: yumin@whut.edu.cn (Min Yu)

ABSTRACT

In this paper, a novel dynamic surface sliding mode control (DSSMC) method, combined with a lateral velocity tracking differentiator (LVTD), is proposed for the cooperative formation control of underactuated unmanned surface vehicles (USVs) exposed to complex marine environment disturbances. Firstly, in view of the kinematic and dynamic models of USVs and the design idea of a virtual control law in a backstepping approach, the trajectory tracking control problem of USVs' cooperative formation is transformed into a stabilisation problem of the virtual control law of longitudinal and lateral velocities. Then, aiming at the problem of differential explosion caused by repeated derivation in the process of backstepping design, the first-order low-pass filter about the virtual longitudinal velocity and intermediate state quantity of position is constructed to replace differential calculations during the design of the control law, respectively. In order to reduce the steady-state error when stabilising the virtual lateral velocity control law, the integral term is introduced into the design of the sliding mode surface with a lateral velocity error, and then the second-order sliding mode surface with an integral is structured. In addition, due to the problem of controller oscillation and the role of the tracking differentiator (TD) in active disturbance rejection control (ADRC), the LVTD is designed to smooth the state quantity of lateral velocity. Subsequently, based on the dynamic model of USV under complex marine environment disturbances, the nonlinear disturbance observer is designed to observe the disturbances and compensate the control law. Finally, the whole cooperative formation system is proved to be uniformly and ultimately bounded, according to the Lyapunov stability theory, and the stability and validity of the method is also verified by the simulation results.

Keywords: underactuated USV, dynamic surface sliding mode control, lateral velocity tracking differentiator, nonlinear disturbance observer

INTRODUCTION

In recent years, marine science and technology has been developed, in order to explore the ocean [1, 2]. Meanwhile, because of the development and advancement of technologies in robotics and autonomous systems (RAS) [3], research on unmanned surface vessels (USVs) motion control has gradually become a hot topic [4-7], with USVs also playing an increasingly essential role in various fields, e.g. military defence, scientific research, environmental monitoring and so on [8-10]. However, with marine operations becoming more and more complex and diversified, a single USV cannot complete a mission well, owing to limitations such as limited information perception [11-13]. Consequently, cooperative formation control of USVs has aroused great attention in recent years, on account of the high fault tolerance, strong adaptability and robustness and cooperative formation control of underactuated USVs [14, 15].

The commonly used formation control strategies include the leader-follower method, behaviour-based method, virtual structure method and graph theory method. The leader-follower method is widely applied because it is simple and easy to use. The leader-follower method was combined with multi-layer neural network and adaptive robust techniques in [16], and the output feedback formation control problem for USVs with limited torque input was solved. In [17], a formation controller for a group of underactuated USVs was designed as an adaptive feedback control problem for a line of sight (LOS) based configuration of a leader and a follower. Design of the controller took time-varying constraints on the LOS and bearing angle into consideration and used asymmetric barrier Lyapunov functions. Similarly, the leader-follower method, LOS strategy and neural networks were used in [18], for designing the formation controller of a waterjet USV, exposed to unmodelled dynamics, environmental disturbances, input saturation, and output constraints. A USV formation approach, based on a distributed deep reinforcement learning algorithm, was proposed in [19], which made formations to arbitrarily increase the number of USVs or change formation forms. In [20], model predictive control was used to deal with vessel train formation (VTF) problems including cooperative collision avoidance and grouping of vessels; a single-layer serial iterative architecture was adopted in distributed formulation, for reducing communication requirements and improving robustness against failures. Both the unmeasurable velocity and external disturbances were estimated by a new finite-time extended state observer in [21] and derivatives of external disturbances for time need not be zero. Then a distributed finite-time formation controller was designed based on the above estimator. In [22] a sliding mode control approach and adaptive algorithms were applied to address the problem of the finite-time distributed formation control for USVs with model uncertainties, input saturation constraints and ocean disturbances. The unavailable system dynamics were approached by radial basis function neural networks (RBFNNs) and the minimum learning parameter (MLP) algorithm was adopted for simplifying

the calculations. Utilising the prescribed performance control method, neural network approximation, disturbance observers, dynamic surface control technique, and Lyapunov synthesis, a formation controller was designed to make USVs exposed to model uncertainties and time-varying external disturbances follow the desired trajectory in [23]. In [24], because the industrial applications of multi-marine vehicles systems needed to provide a realistic setup, a new collision-free distributed formation control method for underactuated USVs networks was proposed, which included a distributed coordination layer and a local fixed-time neural network control layer. An original fault tolerant leader-follower formation control project for a batch of underactuated USVs, which possessed partially known control input gain functions, was proposed in [25]. Simultaneously, the LOS range and angle tracking errors were demanded for constraint. In [26], in order to handle the leader-follower formation problem for several underactuated USVs when model uncertainties and environmental disturbances existed, a novel formation control scheme with robustness and adaptability, containing the MLP algorithm and the disturbance observer (DOB), was presented. An adaptive observer combined with neural networks was used to evaluate the velocity information of USVs and the unknown nonlinearities were estimated by neural networks in [27], solving the problem of connectivity preservation and collision avoidance among networked uncertain underactuated USVs with different communication ranges. In [28], on account of the problem for optimal trajectory tracking of a maritime autonomous surface ship (MASS), which was affected by inherent dynamic uncertainties and the time-varying external disturbances resulting from wind, waves and currents, the modified optimal adaptive super-twisting sliding mode control (OAST-SMC) algorithm was designed as a robust optimal adaptive strategy. Integrating sliding mode control and fuzzy control, a novel control scheme was presented in [29] and, in order to structure heterogeneous multi-agent unmanned formation systems mission requirements, an artificial potential field method and leader-follower method were used to solve the problem of unmanned aerial vehicle and unmanned surface vehicle (UAV-USV) formation motion control. In [30], because of a limited communication range, a distributed event-triggered tracking approach with robustness was proposed and the network connectivity and tracking performance of the formation system was guaranteed. In the meantime, in order to maintain connectivity of the formation system and avoid collisions with each other, a formation tracking controller of uncertain underactuated USVs (based on the leader-follower method) was designed by reducing connectivity-maintaining and collision-avoiding performance functions and constructing an obstacle avoidance strategy in the connectivity between the leader and followers in [31]. The paper by [32] presents an active disturbance rejection control (ADRC) and uncertain parameters, non-linearities, and external disturbances were all considered as parts of the disturbance, which is estimated in real-time by the Extended State Observer (ESO). Then the position and path-following control of a fully actuated

autonomous underwater vehicle (AUV) was solved. An efficient controller was designed through a backstepping technique for the case of full-state feedback in the presence of unknown external disturbances, and the dynamic positioning problem for autonomous surface ships was solved in [33]. In the meantime, the obtained control commands were distributed to each actuator of the overactuated vessel via unconstrained control allocation.

Summarising the above literature on cooperative formation control of USVs, the backstepping approach was adopted in most of the research and a lot of quantities needed to be derived during the design of a controller. However, a phenomenon known as ‘differential explosion’ can emerge after multiple derivatives, which makes the design process of the controller become complex and is unfavourable to engineering practice. Therefore, the novel dynamic surface sliding mode control (DSSMC) method in this paper is presented to solve this problem. The contributions of this paper are as follows: (i) After comprehensive consideration of the core idea for dynamic surface control, an improved sliding mode control method is applied to design a formation controller; (ii) Referring to the core idea of the backstepping approach, longitudinal velocity and lateral velocity virtual control laws are designed for the convenience of subsequent controller design; (iii) The integral term of lateral velocity error is introduced, to construct the second-order sliding surface with an integral for reducing steady-state error when stabilising the virtual lateral velocity; (iv) Considering the role of TD in ADRC, the lateral velocity tracking differentiator (LVTD) is designed to smooth the lateral velocity and avoid control law oscillation; (v) In order to approach marine environment disturbances and simplify the controller, the nonlinear disturbance observer, linked with a dynamic model of USV, is adopted to observe and compensate disturbances.

This paper is organised as follows. USV motion models and a description of a cooperative formation trajectory tracking control problem are arranged in Section 2. The control law is designed and the stability of the control law is proved in Section 3. In Section 4, simulation experiments are carried out, which verify the accuracy and effectiveness of the controller. Ultimately, some conclusions are formulated in Section 5.

PROBLEM FORMULATION

In order to design a USV formation controller, mathematical models of USV motion are formulated, which include kinematic and dynamic models. A problem with a USV formation model will be described in this section.

MATHEMATICAL MODELS OF USV

Supposing there are $N+1$ members in the system of USV formation, one is leader USV and the other N is a follower USV. According to [34], the kinematic models of USVs can be expressed as:

$$\boldsymbol{\eta}_j = \mathbf{R}(\psi_j)\mathbf{v}_j \quad (1)$$

Each USV is numbered by the subscript j ($j = k+1, k = 0 \dots N$), and where $\boldsymbol{\eta}_j = [x_j, y_j, \psi_j]^T$ and $\mathbf{v}_j = [u_j, v_j, r_j]^T$. (x_j, y_j) denotes the position coordinates of USV in the earth-fixed inertial frame; ψ_j is the heading angle; (u_j, v_j, r_j) represent the velocity vectors for the j th USV in the surge, sway and yaw directions in the body-fixed frame, respectively. $\mathbf{R}(\psi_j)$ is the rotation matrix of yaw, as follows:

$$\mathbf{R}(\psi_j) = \begin{bmatrix} \cos \psi_j & -\sin \psi_j & 0 \\ \sin \psi_j & \cos \psi_j & 0 \\ 0 & 0 & 1 \end{bmatrix}$$

The nonlinear dynamic model of USV with external environmental disturbances is described as:

$$\mathbf{M}_j \dot{\mathbf{v}}_j + \mathbf{C}(\mathbf{v}_j)\mathbf{v}_j + \mathbf{D}(\mathbf{v}_j)\mathbf{v}_j = \boldsymbol{\tau}_j + \mathbf{d}_j \quad (2)$$

where \mathbf{M}_j is the system inertia matrix (including added mass) of the j th USV; \mathbf{C}_j represents a Coriolis-centripetal matrix (including added mass); \mathbf{D}_j is the hydrodynamic damping coefficients matrix of the j th USV; and \mathbf{d}_j is the vector of environmental disturbance forces and moment acting on the j th USV:

$$\mathbf{M}_j = \begin{bmatrix} m_{1j} & 0 & 0 \\ 0 & m_{2j} & 0 \\ 0 & 0 & m_{3j} \end{bmatrix}, \mathbf{D}(\mathbf{v}_j) = \begin{bmatrix} d_{1j} & 0 & 0 \\ 0 & d_{2j} & 0 \\ 0 & 0 & d_{3j} \end{bmatrix}, \mathbf{C}(\mathbf{v}_j) = \begin{bmatrix} 0 & 0 & -m_{2j}v_j \\ 0 & 0 & m_{1j}u_j \\ m_{2j}v_j & -m_{1j}u_j & 0 \end{bmatrix}$$

$$\mathbf{d}_j = [d_{w_j}, d_{y_j}, d_{r_j}]^T$$

Equation (1) and (2) are unfolded and combined, and models of USV with three degrees of mathematical freedom can be obtained, as:

$$\begin{cases} \dot{x}_j = u_j \cos \psi_j - v_j \sin \psi_j \\ \dot{y}_j = u_j \sin \psi_j + v_j \cos \psi_j \\ \dot{\psi}_j = r_j \\ \dot{u}_j = \frac{m_{2j}}{m_{1j}} v_j r_j - \frac{d_{1j}}{m_{1j}} u_j + \frac{1}{m_{1j}} \tau_{uj} + \frac{1}{m_{1j}} d_{uj} \\ \dot{v}_j = -\frac{m_{1j}}{m_{2j}} u_j r_j - \frac{d_{2j}}{m_{2j}} v_j + \frac{1}{m_{2j}} d_{vj} \\ \dot{r}_j = \frac{m_{1j} - m_{2j}}{m_{3j}} u_j v_j - \frac{d_{3j}}{m_{3j}} r_j + \frac{1}{m_{3j}} \tau_{rj} + \frac{1}{m_{3j}} d_{rj} \end{cases} \quad (3)$$

DESCRIPTION OF COOPERATIVE FORMATION CONTROL OF USV

In order to simply and conveniently design a cooperative formation controller of a USV, the leader-follower method is adopted in this paper. The core of the leader-follower method means that one of this group is designated as the leader for all of the formation system and the remainder members are known as followers; moreover, the leader of the whole formation is tracked by followers in a certain relative position and attitude. The diagram of the cooperative formation model of USVs is established in the earth-fixed frame, as follows:

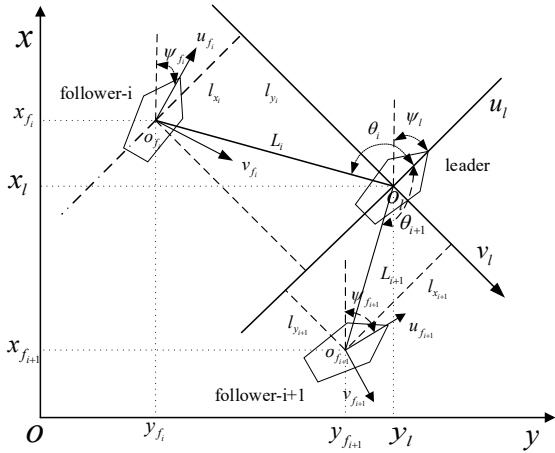


Fig. 1. Diagrammatic sketch of USVs formation

where (x_l, y_l, ψ_l) and $(x_{f_i}, y_{f_i}, \psi_{f_i})$ denote the position coordinates and heading angle of the leader USV and the i th ($i=1, 2, \dots, N-1$) follower in the earth-fixed frame, respectively; (u_l, v_l) and (u_{f_i}, v_{f_i}) represent the velocity vectors for the leader USV and the i th ($i=1, 2, \dots, N-1$) follower USV in the surge and sway directions in the body-fixed frame; (L_i, θ_i) ($\theta_i \in [-\pi, \pi]$, positive clockwise) are the distance and angle between the leader USV and the i th follower USV; (L_x, L_y) indicate the relative longitudinal and lateral distance between the leader USV and the i th follower USV in the leader-fixed frame.

According to the principle of the leader-follower method, when the USV formation is formulated, both L_i and θ_i are fixed values in the earth-fixed frame; meanwhile L_x and L_y are fixed values too. From Fig. 1, the desired relative longitudinal distance $L_{x,d}$ and lateral distance $L_{y,d}$ between the leader USV and the i th follower USV are as below:

$$\begin{cases} L_{x,d} = (x_{f,d} - x_l) \cos \psi_l + (y_{f,d} - y_l) \sin \psi_l \\ L_{y,d} = -(x_{f,d} - x_l) \sin \psi_l + (y_{f,d} - y_l) \cos \psi_l \end{cases} \quad (4)$$

Equation (4) can also be written as:

$$\begin{bmatrix} L_{x,d} \\ L_{y,d} \end{bmatrix} = \begin{bmatrix} \cos \psi_l & \sin \psi_l \\ -\sin \psi_l & \cos \psi_l \end{bmatrix} \begin{bmatrix} x_{f,d} - x_l \\ y_{f,d} - y_l \end{bmatrix} \quad (5)$$

The $L_{x,d}$ and $L_{y,d}$ are rotated from the body-fixed frame to the earth-fixed frame and the desired trajectory $(x_{f,d}, y_{f,d})$ of the i th follower USV in the earth-fixed frame can be obtained as:

$$\begin{cases} y_{f,d} = y_l + L_{y,d} \cos \psi_l + L_{x,d} \sin \psi_l \\ x_{f,d} = x_l + L_{x,d} \cos \psi_l - L_{y,d} \sin \psi_l \end{cases} \quad (6)$$

Therefore, the problem of the cooperative formation control of a group of USVs can be transformed into the trajectory tracking control of each USV in the group. Furthermore, the purpose of formation control can be changed as:

$$\begin{cases} \lim_{t \rightarrow \infty} \|x_{f_i} - x_{f,d}\| = 0 \\ \lim_{t \rightarrow \infty} \|y_{f_i} - y_{f,d}\| = 0 \end{cases} \quad (7)$$

CONTROLLER DESIGN

NONLINEAR DISTURBANCE OBSERVER

During navigation, USV formation systems are subject to unknown marine disturbances. In order to observe and compensate for disturbances, a nonlinear disturbance observer is designed [35] as follows:

$$\begin{cases} \dot{\hat{d}} = z + p(\theta, \dot{\theta}) \\ \dot{z} = -L(\theta, \dot{\theta})z + L(\theta, \dot{\theta})[G(\theta, \dot{\theta}) - T - p(\theta, \dot{\theta})] \end{cases} \quad (8)$$

Mathematical models of USV are combined with Eq. (8), as:

$$\begin{cases} \dot{\hat{d}}_j = \mathbf{Z}_j + \mathbf{L}_j \mathbf{M}_j \mathbf{v}_j \\ \dot{\mathbf{Z}}_j = -\mathbf{L}_j \hat{\mathbf{d}}_j - \mathbf{L}_j [-\mathbf{C}(\mathbf{v}_j) \mathbf{v}_j - \mathbf{D}(\mathbf{v}_j) \mathbf{v}_j + \boldsymbol{\tau}_j] \end{cases} \quad (9)$$

where $\mathbf{Z}_j = [Z_{ju}, Z_{jv}, Z_{jr}]^T$ is structural quantity; $\mathbf{L}_j = [L_{ju}, L_{jv}, L_{jr}]^T$ are the bandwidth parameters of the observer; and $\hat{\mathbf{d}}_j = [\hat{d}_{uj}, \hat{d}_{vj}, \hat{d}_{rj}]^T$ are observations of ocean disturbances.

Simultaneously, it must be considered that actual marine disturbances fluctuate slowly. In the following section, $\hat{\mathbf{d}}_j$ is assumed to be bounded and expressed as $|\hat{\mathbf{d}}_j| \leq \sigma$, ($\sigma \geq 0$). The error between observation and real disturbances is defined as:

$$\tilde{\mathbf{d}}_j = \hat{\mathbf{d}}_j - \mathbf{d}_j = [\hat{d}_{uj} - d_{uj}, \hat{d}_{vj} - d_{vj}, \hat{d}_{rj} - d_{rj}]^T \quad (10)$$

A derivation and simplification of Eq. (9) is:

$$\begin{aligned}\ddot{\mathbf{d}}_j &= \dot{\hat{\mathbf{d}}}_j - \dot{\mathbf{d}}_j \\ &= \dot{\mathbf{Z}}_i + \mathbf{L}_j \mathbf{M}_j \dot{\mathbf{v}}_j - \dot{\mathbf{d}}_j \\ &= -\mathbf{L}_j \hat{\mathbf{d}}_j - \mathbf{L}_j [-\mathbf{C}(\mathbf{v}_j) \mathbf{v}_j - \mathbf{D}(\mathbf{v}_j) \mathbf{v}_j + \boldsymbol{\tau}_j] + \mathbf{L}_j \mathbf{M}_j \dot{\mathbf{v}}_j - \dot{\mathbf{d}}_j \\ &= -\mathbf{L}_j \hat{\mathbf{d}}_j - \mathbf{L}_j [-\mathbf{C}(\mathbf{v}_j) \mathbf{v}_j - \mathbf{D}(\mathbf{v}_j) \mathbf{v}_j + \boldsymbol{\tau}_j - \mathbf{M}_j \dot{\mathbf{v}}_j] - \dot{\mathbf{d}}_j \\ &= -\mathbf{L}_j \hat{\mathbf{d}}_j + \mathbf{L}_j \mathbf{d}_j - \dot{\mathbf{d}}_j = -\mathbf{L}_j \tilde{\mathbf{d}}_j - \dot{\mathbf{d}}_j\end{aligned}\quad (11)$$

Based on the above assumption, the first order differential inequality on observation error can be gained as:

$$\dot{\tilde{\mathbf{d}}}_j + \mathbf{L}_j \tilde{\mathbf{d}}_j \leq \left| \dot{\mathbf{d}}_j \right| = \sigma \quad (12)$$

Equation (12) is solved as:

$$0 \leq \tilde{\mathbf{d}}_j(t) \leq \frac{\sigma}{\mathbf{L}_j} + [\tilde{\mathbf{d}}_j(0) - \frac{\sigma}{\mathbf{L}_j}] e^{-\mathbf{L}_j t} \quad (13)$$

According to Eq. (13), by selecting appropriate bandwidth parameters, the observation error can finally be stabilised.

DESIGN CONTROLLER OF FOLLOWER

The controller is designed in this part. Firstly, the virtual velocity control law can be obtained based on positive definite position error. Then, the surge force and yaw moment can be designed by stabilising the virtual velocity control law.

DESIGN VIRTUAL VELOCITY CONTROL LAW

The position error state quantity of the i th follower is defined as:

$$\begin{bmatrix} \mathbf{x}_{f_{j,e}} \\ \mathbf{y}_{f_{j,e}} \end{bmatrix} = \begin{bmatrix} \mathbf{x}_{f_i} - \mathbf{x}_{f_{j,d}} \\ \mathbf{y}_{f_i} - \mathbf{y}_{f_{j,d}} \end{bmatrix} \quad (14)$$

The derivation of Eq. (14) is as:

$$\begin{bmatrix} \dot{\mathbf{x}}_{f_{j,e}} \\ \dot{\mathbf{y}}_{f_{j,e}} \end{bmatrix} = \begin{bmatrix} \dot{\mathbf{x}}_{f_i} - \dot{\mathbf{x}}_{f_{j,d}} \\ \dot{\mathbf{y}}_{f_i} - \dot{\mathbf{y}}_{f_{j,d}} \end{bmatrix} = \begin{bmatrix} \cos(\psi_{f_i}) & -\sin(\psi_{f_i}) \\ \sin(\psi_{f_i}) & \cos(\psi_{f_i}) \end{bmatrix} \begin{bmatrix} \mathbf{u}_{f_i} \\ \mathbf{v}_{f_i} \end{bmatrix} - \begin{bmatrix} \dot{\mathbf{x}}_{f_{j,d}} \\ \dot{\mathbf{y}}_{f_{j,d}} \end{bmatrix} \quad (15)$$

The Lyapunov function is constructed as follows:

$$V_i = \frac{1}{2} \mathbf{x}_{f_{j,e}}^2 + \frac{1}{2} \mathbf{y}_{f_{j,e}}^2 \quad (16)$$

Derivation and simplification of Eq. (16) is as below:

$$\begin{aligned}\dot{V}_i &= \mathbf{x}_{f_{j,e}} \dot{\mathbf{x}}_{f_{j,e}} + \mathbf{y}_{f_{j,e}} \dot{\mathbf{y}}_{f_{j,e}} \\ &= \mathbf{x}_{f_{j,e}} (\mathbf{u}_{f_i} \cos \psi_{f_i} - \mathbf{v}_{f_i} \sin \psi_{f_i} - \dot{\mathbf{x}}_{f_{j,d}}) + \mathbf{y}_{f_{j,e}} (\mathbf{u}_{f_i} \sin \psi_{f_i} + \mathbf{v}_{f_i} \cos \psi_{f_i} - \dot{\mathbf{y}}_{f_{j,d}})\end{aligned}\quad (17)$$

Through the analysis of Eq. (17), virtual velocity control law $\alpha_{f_{j,u}}$ and $\alpha_{f_{j,v}}$ in the surge and sway directions, are devised as:

$$\begin{bmatrix} \alpha_{f_{j,u}} \\ \alpha_{f_{j,v}} \end{bmatrix} = \begin{bmatrix} \cos(\psi_{f_i}) & \sin(\psi_{f_i}) \\ -\sin(\psi_{f_i}) & \cos(\psi_{f_i}) \end{bmatrix} \begin{bmatrix} \dot{\mathbf{x}}_{f_{j,d}} - k_{1j} \mathbf{x}_{f_{j,e}} / \sqrt{\mathbf{x}_{f_{j,e}}^2 + \mathbf{y}_{f_{j,e}}^2 + C_{f_i}} \\ \dot{\mathbf{y}}_{f_{j,d}} - k_{2j} \mathbf{y}_{f_{j,e}} / \sqrt{\mathbf{x}_{f_{j,e}}^2 + \mathbf{y}_{f_{j,e}}^2 + C_{f_i}} \end{bmatrix} \quad (18)$$

where k_{1j} , k_{2j} , C_{f_i} are all positive numbers; and $\sqrt{\mathbf{x}_{f_{j,e}}^2 + \mathbf{y}_{f_{j,e}}^2 + C_{f_i}}$ is denoted by W_{f_i} .

DESIGN THE SURGE FORCE CONTROL LAW

The velocity error of the i th follower USV in the surge and sway directions are defined as $u_{f_{j,e}} = u_{f_i} - \alpha_{f_{j,u}}$, $v_{f_{j,e}} = v_{f_i} - \alpha_{f_{j,v}}$, respectively.

In order to reduce steady-state error, an integral term of $u_{f_{j,e}}$ is added to the sliding surface, when $u_{f_{j,e}}$ is stabilised and the surge force of the i th follower is designed. The integral first-order sliding surface is constructed as follows:

$$s_{1i} = u_{f_{j,e}} + \lambda_{1i} \int_0^t u_{f_{j,e}}(\tau) d\tau, \quad (\lambda_{1i} > 0) \quad (19)$$

substituting Eq. (3) into derivation of Eq. (19) as:

$$\begin{aligned}\dot{s}_{1i} &= \dot{u}_{f_{j,e}} + \lambda_{1i} u_{f_{j,e}} = \dot{u}_{f_i} - \dot{\alpha}_{f_{j,u}} + \lambda_{1i} u_{f_{j,e}} \\ &= \frac{m_{2j}}{m_{1j}} v_{f_i} r_{f_i} - \frac{d_{1j}}{m_{1j}} u_{f_i} + \frac{1}{m_{1j}} \tau_{f_{j,u}} + \frac{1}{m_{1j}} \tilde{\mathbf{d}}_{uj} - \dot{\alpha}_{f_{j,u}} + \lambda_{1i} u_{f_{j,e}}\end{aligned}\quad (20)$$

In order to avoid differential explosion, the first order low pass filter is applied. The new state quantity $X_{f_{j,u}}$ is introduced and defined as the output of the first order low pass filter. $\dot{\alpha}_{f_{j,u}}$ is replaced with a derivation of it. The mathematical expression is as follows [36]:

$$\begin{cases} T_{1i} \dot{X}_{f_{j,u}} + X_{f_{j,u}} = \alpha_{f_{j,u}} \\ X_{f_{j,u}}(0) = \alpha_{f_{j,u}}(0), \quad (T_{1i} > 0) \end{cases} \quad (21)$$

Equation (20) is obtained:

$$\dot{X}_{f_{j,u}} = (\alpha_{f_{j,u}} - X_{f_{j,u}}) / T_{1i} \quad (22)$$

In order to avoid the buffeting problem caused by designing the control law with a symbolic function, the reaching law of sliding mode control with hyperbolic tangent function is adopted in this paper.

$$\dot{s}_{1i} = -\varepsilon_{1i} \tanh(s_{1i}) - \eta_{1i} s_{1i}, \quad (\varepsilon_{1i} > 0, \eta_{1i} > 0) \quad (23)$$

Substituting Eq. (23) into Eq. (20), the surge force of the i th follower USV can be obtained as:

$$\tau_{f_{j,u}} = m_{1j} \left[-\frac{1}{m_{1j}} \tilde{\mathbf{d}}_{uj} - \frac{m_{2j}}{m_{1j}} v_{f_i} r_{f_i} + \frac{d_{1j}}{m_{1j}} u_{f_i} + \dot{X}_{f_{j,u}} - \lambda_{1i} u_{f_{j,e}} - \varepsilon_{1i} \tanh(s_{1i}) - \eta_{1i} s_{1i} \right] \quad (24)$$

DESIGN THE YAW MOMENT CONTROL LAW

Due to the underactuated characteristics of the research object and the lack of input in the sway direction, the second-order sliding surface of $v_{f_{ie}}$ is designed to make the yaw moment $\tau_{f_{fr}}$ appear. At the same time, in order to reduce steady-state error when tracking a straight trajectory, the integral term of $v_{f_{ie}}$ is introduced. The design of sliding surface is as follows:

$$s_{2_i} = \dot{v}_{f_{ie}} + \lambda_{2_i} v_{f_{ie}} + \lambda_{3_i} \int_0^t v_{f_{ie}} dt, \quad (\lambda_{2_i} > 0, \lambda_{3_i} > 0) \quad (25)$$

Derivations of Eq. (25) are:

$$\dot{s}_{2_i} = \ddot{v}_{f_{ie}} + \lambda_{2_i} \dot{v}_{f_{ie}} + \lambda_{3_i} v_{f_{ie}} = \ddot{v}_{f_i} - \ddot{\alpha}_{f_{iv}} + \lambda_{2_i} \dot{v}_{f_{ie}} + \lambda_{3_i} v_{f_{ie}} \quad (26)$$

For simplifying Eq. (26), derivations of Eq. (18) are needed as:

$$\begin{aligned} \dot{\alpha}_{f_{iv}} = & -r_{f_i} \alpha_{f_{iu}} - [\dot{x}_{f_{id}} - k_{1_i} (w_{f_i}^{-1} - w_{f_i}^{-3} x_{f_{ie}}^2) \dot{x}_{f_{ie}} + k_{1_i} w_{f_i}^{-3} x_{f_{ie}} y_{f_{ie}} \dot{y}_{f_{ie}}] \sin(\psi_{f_i}) \\ & + [\dot{y}_{f_{id}} - k_{2_i} (w_{f_i}^{-1} - w_{f_i}^{-3} y_{f_{ie}}^2) \dot{y}_{f_{ie}} + k_{2_i} w_{f_i}^{-3} x_{f_{ie}} y_{f_{ie}} \dot{x}_{f_{ie}}] \cos(\psi_{f_i}) \end{aligned} \quad (27)$$

The intermediate quantity is defined as:

$$\begin{aligned} p_{f_i} = & -[\dot{x}_{f_{id}} - k_{1_i} (w_{f_i}^{-1} - w_{f_i}^{-3} x_{f_{ie}}^2) \dot{x}_{f_{ie}} + k_{1_i} w_{f_i}^{-3} x_{f_{ie}} y_{f_{ie}} \dot{y}_{f_{ie}}] \sin(\psi_{f_i}) \\ & + [\dot{y}_{f_{id}} - k_{2_i} (w_{f_i}^{-1} - w_{f_i}^{-3} y_{f_{ie}}^2) \dot{y}_{f_{ie}} + k_{2_i} w_{f_i}^{-3} x_{f_{ie}} y_{f_{ie}} \dot{x}_{f_{ie}}] \cos(\psi_{f_i}) \end{aligned} \quad (28)$$

Similarly, the first order low pass filter of p_{f_i} is introduced, and p_{f_i} and \dot{p}_{f_i} are replaced with $X_{f_{ip}}$ and $\dot{X}_{f_{ip}}$, respectively. The mathematical expression is:

$$\begin{cases} T_{2_i} \dot{X}_{f_{ip}} + X_{f_{ip}} = p_{f_i} \\ X_{f_{ip}}(0) = p_{f_i}(0), \quad (T_{2_i} > 0) \end{cases} \quad (29)$$

Equation (29) is obtained:

$$\dot{X}_{f_{ip}} = (p_{f_i} - X_{f_{ip}}) / T_{2_i} \quad (30)$$

Then Eq. (27) can be simplified, as:

$$\dot{\alpha}_{f_{iv}} = X_{f_{ip}} - r_{f_i} \alpha_{f_{iu}} \quad (31)$$

Simultaneously, Eq. (26), (30) and (31) are solved as:

$$\dot{s}_{2_i} = \ddot{v}_{f_i} - \dot{X}_{f_{ip}} + \dot{r}_{f_i} \alpha_{f_{iu}} + r_{f_i} X_{f_{ip}} + \lambda_{2_i} \dot{v}_{f_{ie}} + \lambda_{3_i} v_{f_{ie}} \quad (32)$$

Similarly, the reaching law of sliding mode control is designed as:

$$\dot{s}_{2_i} = -\varepsilon_{2_i} \tanh(s_{2_i}) - \eta_{2_i} s_{2_i}, \quad (\varepsilon_{2_i} > 0, \eta_{2_i} > 0) \quad (33)$$

Eq. (32) and Eq. (33) are simplified, as follows:

$$\dot{r}_{f_i} = (-\dot{v}_{f_i} + \dot{X}_{f_{ip}} - r_{f_i} X_{f_{ip}} - \lambda_{2_i} \dot{v}_{f_{ie}} - \lambda_{3_i} v_{f_{ie}} - \varepsilon_{2_i} \tanh(s_{2_i}) - \eta_{2_i} s_{2_i}) / \alpha_{f_{iu}} \quad (34)$$

Owing to the drastic variation in \ddot{v}_{f_i} , the controller is not easily convergent. In order to smooth \dot{v}_{f_i} , LVTD is introduced and applied [35] and the discrete form is as below:

$$\begin{cases} x_{1_i}(k+1) = x_{1_i}(k) + hx_{2_i}(k) \\ x_{2_i}(k+1) = x_{2_i}(k) + h\{-rr_i^2[x_{1_i}(k) - \dot{v}_{f_i}(k)] - 2rr_i x_{2_i}(k)\} \end{cases} \quad (35)$$

where h is the time step size; rr_i are the control parameters of LVTD; and x_{1_i} and x_{2_i} are all output signals. \dot{v}_{f_i} is replaced with x_{1_i} and x_{2_i} is the differential of x_{1_i} which substitutes for \dot{v}_{f_i} . The yaw moment $\tau_{f_{fr}}$ of the i th follower can be obtained by simultaneously addressing Eq. (3), (34) and (35) as:

$$\begin{aligned} \tau_{f_{fr}} = & -(m_{1_j} - m_{2_j})u_{f_i} r_{f_i} + d_{3_j} r_{f_i} + m_{3_j} \dot{r}_{f_i} - \tilde{d}_{v_j} \\ = & -\tilde{d}_{v_j} - (m_{1_j} - m_{2_j})u_{f_i} r_{f_i} + d_{3_j} r_{f_i} \\ & + m_{3_j} (-x_{2_i} + \dot{X}_{f_{ip}} - r_{f_i} X_{f_{ip}} - \lambda_{2_i} \dot{v}_{f_{ie}} - \lambda_{3_i} v_{f_{ie}} - \varepsilon_{2_i} \tanh(s_{2_i}) - \eta_{2_i} s_{2_i}) / \alpha_{f_{iu}} \end{aligned} \quad (36)$$

STABILITY ANALYSIS

In this section, the stability of control law, Eq. (24) and (36), is proved. For the first order low pass filter introduced in the previous section, the filtering error is defined as:

$$\begin{cases} y_{1_i} = X_{f_{ip}} - \alpha_{f_{iu}} \\ y_{2_i} = X_{f_{ip}} - p_{f_i} \end{cases} \quad (37)$$

The derivation of Eq. (37), simultaneously with Eq. (22), (30), and (37), and simplifying, gives:

$$\begin{cases} \dot{y}_{1_i} = -\frac{y_{1_i}}{T_{1_i}} + \frac{\partial \alpha_{f_{iu}}}{\partial \dot{x}_{f_{id}}} \ddot{x}_{f_{id}} + \frac{\partial \alpha_{f_{iu}}}{\partial \dot{y}_{f_{id}}} \ddot{y}_{f_{id}} + \frac{\partial \alpha_{f_{iu}}}{\partial x_{f_{ie}}} \dot{x}_{f_{ie}} + \frac{\partial \alpha_{f_{iu}}}{\partial y_{f_{ie}}} \dot{y}_{f_{ie}} + \frac{\partial \alpha_{f_{iu}}}{\partial \psi_{f_i}} \dot{\psi}_{f_i} \\ \dot{y}_{2_i} = -\frac{y_{2_i}}{T_{2_i}} + \frac{\partial p_{f_i}}{\partial \dot{x}_{f_{id}}} \ddot{x}_{f_{id}} + \frac{\partial p_{f_i}}{\partial \dot{y}_{f_{id}}} \ddot{y}_{f_{id}} + \frac{\partial p_{f_i}}{\partial x_{f_{ie}}} \dot{x}_{f_{ie}} + \frac{\partial p_{f_i}}{\partial y_{f_{ie}}} \dot{y}_{f_{ie}} + \frac{\partial p_{f_i}}{\partial \psi_{f_i}} \dot{\psi}_{f_i} \end{cases} \quad (38)$$

The new quantities are defined as:

$$\begin{cases} \beta_{1_i} = \frac{\partial \alpha_{f_{iu}}}{\partial \dot{x}_{f_{id}}} \ddot{x}_{f_{id}} + \frac{\partial \alpha_{f_{iu}}}{\partial \dot{y}_{f_{id}}} \ddot{y}_{f_{id}} + \frac{\partial \alpha_{f_{iu}}}{\partial x_{f_{ie}}} \dot{x}_{f_{ie}} + \frac{\partial \alpha_{f_{iu}}}{\partial y_{f_{ie}}} \dot{y}_{f_{ie}} + \frac{\partial \alpha_{f_{iu}}}{\partial \psi_{f_i}} \dot{\psi}_{f_i} \\ \beta_{2_i} = \frac{\partial p_{f_i}}{\partial \dot{x}_{f_{id}}} \ddot{x}_{f_{id}} + \frac{\partial p_{f_i}}{\partial \dot{y}_{f_{id}}} \ddot{y}_{f_{id}} + \frac{\partial p_{f_i}}{\partial x_{f_{ie}}} \dot{x}_{f_{ie}} + \frac{\partial p_{f_i}}{\partial y_{f_{ie}}} \dot{y}_{f_{ie}} + \frac{\partial p_{f_i}}{\partial \psi_{f_i}} \dot{\psi}_{f_i} \end{cases} \quad (39)$$

where β_1 is a nonlinear continuous function, related to the position information of the USV. Because the position information is bounded, β_1 is also bounded. Hypothesis $N_{u_i} > 0$ is the upper bound of β_1 , then $\beta_1 < N_{u_i}$ holds. Similarly, β_2 is bounded, too. Supposing, $N_{p_i} > 0$ is the upper bound of β_2 , then $\beta_2 < N_{p_i}$ holds.

The stability of the control law designed in this paper is proved and the Lyapunov function is constructed as follows:

$$V_{1_i} = \frac{1}{2}s_{1_i}^2 + \frac{1}{2}y_{1_i}^2 + \frac{1}{2}s_{2_i}^2 + \frac{1}{2}y_{2_i}^2 + \frac{1}{2}x_{f_{i,e}}^2 + \frac{1}{2}y_{f_{i,e}}^2 \quad (40)$$

The derivation and simplification of Eq. (40) is:

$$\begin{aligned} \dot{V}_{1_i} &= s_{1_i}\dot{s}_{1_i} + y_{1_i}\dot{y}_{1_i} + s_{2_i}\dot{s}_{2_i} + y_{2_i}\dot{y}_{2_i} + x_{f_{i,e}}\dot{x}_{f_{i,e}} + y_{f_{i,e}}\dot{y}_{f_{i,e}} \\ &= s_{1_i}[-\varepsilon_{1_i} \tanh(s_{1_i}) - \eta_{1_i}s_{1_i}] + s_{2_i}[-\varepsilon_{2_i} \tanh(s_{2_i}) - \eta_{2_i}s_{2_i}] \\ &\quad + y_{1_i}\left(-\frac{y_{1_i}}{T_{1_i}} + \beta_{1_i}\right) + y_{2_i}\left(-\frac{y_{2_i}}{T_{2_i}} + \beta_{2_i}\right) + x_{f_{i,e}}\dot{x}_{f_{i,e}} + y_{f_{i,e}}\dot{y}_{f_{i,e}} \\ &\leq -\varepsilon_{1_i}|s_{1_i}| - \eta_{1_i}s_{1_i}^2 - \frac{y_{1_i}^2}{T_{1_i}} + y_{1_i}N_{u_i} - \varepsilon_{2_i}|s_{2_i}| - \eta_{2_i}s_{2_i}^2 - \frac{y_{2_i}^2}{T_{2_i}} + y_{2_i}N_{p_i} \\ &\quad - (k_{1_i}x_{f_{i,e}}^2 + k_{2_i}y_{f_{i,e}}^2) / w_{f_i} + \sqrt{x_{f_{i,e}}^2 + y_{f_{i,e}}^2} \sqrt{v_{f_{i,e}}^2 + u_{f_{i,e}}^2} \quad (41) \\ &\leq -\varepsilon_{1_i}|s_{1_i}| - \eta_{1_i}s_{1_i}^2 - \frac{y_{1_i}^2}{T_{1_i}} + (\alpha_{1_i}y_{1_i}^2 + \frac{N_{u_i}^2}{4\alpha_{1_i}}) - \varepsilon_{2_i}|s_{2_i}| - \eta_{2_i}s_{2_i}^2 - \frac{y_{2_i}^2}{T_{2_i}} + (\alpha_{2_i}y_{2_i}^2 + \frac{N_{p_i}^2}{4\alpha_{2_i}}) \\ &\quad - (k_{1_i}x_{f_{i,e}}^2 + k_{2_i}y_{f_{i,e}}^2) / w_{f_i} + \sqrt{x_{f_{i,e}}^2 + y_{f_{i,e}}^2} \sqrt{v_{f_{i,e}}^2 + u_{f_{i,e}}^2} \\ &\leq -\eta_{1_i}s_{1_i}^2 - (\frac{1}{T_{1_i}} - \alpha_{1_i})y_{1_i}^2 + \frac{N_{u_i}^2}{4\alpha_{1_i}} - \eta_{2_i}s_{2_i}^2 - (\frac{1}{T_{2_i}} - \alpha_{2_i})y_{2_i}^2 + \frac{N_{p_i}^2}{4\alpha_{2_i}} \\ &\quad - (k_{1_i}x_{f_{i,e}}^2 + k_{2_i}y_{f_{i,e}}^2) / w_{f_i} + \sqrt{x_{f_{i,e}}^2 + y_{f_{i,e}}^2} \sqrt{v_{f_{i,e}}^2 + u_{f_{i,e}}^2} \\ &\leq -\mu_{1_i}V_{1_i} + N_a \end{aligned}$$

where α_{1_i} and α_{2_i} are positive constants and μ_{1_i} and N_a are:

$$\begin{cases} \mu_{1_i} = \min(2\eta_{1_i}, \frac{2}{T_{1_i}} - 2\alpha_{1_i}, 2\eta_{2_i}, \frac{2}{T_{2_i}} - 2\alpha_{2_i}, \frac{2k_{1_i}}{w_{f_i}}, \frac{2k_{2_i}}{w_{f_i}}) \\ N_a = \frac{N_{u_i}^2}{4\alpha_{1_i}} + \frac{N_{p_i}^2}{4\alpha_{2_i}} + \sqrt{x_{f_{i,e}}^2 + y_{f_{i,e}}^2} \sqrt{v_{f_{i,e}}^2 + u_{f_{i,e}}^2} \end{cases} \quad (42)$$

Equation (41) is solved as:

$$0 \leq V_{1_i}(t) \leq N_a / \mu_{1_i} + [V_{1_i}(0) - N_a / \mu_{1_i}] e^{-\mu_{1_i}t} \quad (43)$$

To facilitate subsequent expressions, the new quantity is defined as follows:

$$\xi = [V_{1_i}(0) - N_a / \mu_{1_i}] e^{-\mu_{1_i}t} \quad (44)$$

From the above inequality, V_{1_i} is ultimately uniformly bounded. When the time is long enough, ξ tends to zero. Because N_a is bounded, at this point, the convergent limit of V_{1_i} is inclined to zero by choosing appropriate control

parameters. The position error, filtering error and sliding surface of formation system $x_{f_{i,e}}, y_{f_{i,e}}, y_{1_i}, y_{2_i}, s_{1_i}, s_{2_i}$ is, ultimately, uniformly bounded and convergent to zero. Therefore, the stability of control law Eq. (24) and (36) is proved and the above control goal of Eq. (7) can be achieved by the designed control law. The formation control of the USVs' formation system is then complete.

SIMULATION VERIFICATION

In order to further prove stability, effectiveness and general applicability of the formation controller designed above, the two cases including circular parallel formation and straight triangle formation are simulated by control law Eq. (24) and (36) in this section; the formation of three USVs are taken as examples. The parameters of the respective USV mathematical models [37] used in the simulation are as follows: $m_{11} = 25.8$, $m_{22} = 33.8$, $m_{33} = 2.76$, $d_{11} = 12 + 2.5|u|$, $d_{22} = 17 + 4.5|v|$, and $d_{33} = 0.5 + 0.1|r|$. The desired trajectory of the leader USV is given in the form of a parametric equation.

CIRCULAR PARALLEL FORMATION

The radius and frequency of the desired circular trajectory of the given leader USV are 20.00 m and 0.05 m, respectively. The mathematical equation is as follows:

$$\begin{cases} x_d = 20 \sin 0.05t \\ y_d = -20 \cos 0.05t \end{cases} \quad (45)$$

According to the actual ocean environment, the values of marine disturbances are chosen as: $d_j = [1 + 4 \sin(0.5t), 0.8 \sin(0.01t), 1 + 4 \sin(0.5t)]^T$.

Table 1 presents the formation information parameters.

Tab. 1. Formation information parameters

Follower USV	L / m	θ / rad
Follower USV 1	5	$\pi / 2$
Follower USV 2	5	$-\pi / 2$

The initial condition of leader USV, follower USV 1 and follower USV 2 are set as:

$$\begin{cases} [x_l(0), y_l(0), \psi_l(0), u_l(0), v_l(0), r_l(0)] = [-5 \text{ m}, -25 \text{ m}, 0 \text{ rad}, 0 \text{ m/s}, 0 \text{ m/s}, 0 \text{ rad/s}] \\ [x_{f_1}(0), y_{f_1}(0), \psi_{f_1}(0), u_{f_1}(0), v_{f_1}(0), r_{f_1}(0)] = [-6 \text{ m}, -22 \text{ m}, 0 \text{ rad}, 0 \text{ m/s}, 0 \text{ m/s}, 0 \text{ rad/s}] \\ [x_{f_2}(0), y_{f_2}(0), \psi_{f_2}(0), u_{f_2}(0), v_{f_2}(0), r_{f_2}(0)] = [-6 \text{ m}, -32 \text{ m}, 0 \text{ rad}, 0 \text{ m/s}, 0 \text{ m/s}, 0 \text{ rad/s}] \end{cases}$$

At the same time, during the simulation experiments, the restrictions on control thrust of the leader USV are: $\tau_{lu \max} = 30N$ and $\tau_{lr \max} = 20N$. The restrictions on control thrust of the follower USV 1 are: $\tau_{f_{1u} \max} = 30N$ and $\tau_{f_{1r} \max} = 20N$. Finally, the restrictions on control thrust

of the follower USV 2 are: $\tau_{f_2u\max} = 30N$ and $\tau_{f_2r\max} = 15N$. In addition, the changing rate of each USV is also limited, as follows: $d\tau_{lu\max} = 150N/s$, $d\tau_{lr\max} = 100N/s$, $d\tau_{f_1u\max} = 300N/s$, $d\tau_{f_1r\max} = 200N/s$, $d\tau_{f_2u\max} = 150N/s$ and $d\tau_{f_2r\max} = 100N/s$.

Table 2 presents the controller parameters.

Tab. 2. Controller parameters

	Leader USV	Follower USV 1	Follower USV 2
k_1	4.0	4.1	5.0
k_2	4.0	4.1	5.0
T_1	0.1	0.1	0.1
T_2	0.1	0.1	0.1
λ_1	0.0001	0.0001	0.0001
λ_2	25	30	28
λ_3	0.550	0.055	0.018
η_1	0.10	0.10	0.14
η_2	0.10	0.10	0.14
ε_1	0.010	0.010	0.016
ε_2	0.010	0.010	0.016
C	10	10	10

In order to explain the effect of the designed controller, the circular parallel formation trajectory tracking diagrams, state quantity convergence diagrams, disturbance observer diagrams, and control thrust diagrams are presented. Furthermore, in order to illustrate the role of LVTD for the controller and the whole formation system, circular parallel formation trajectory tracking diagrams without LVTD, control thrust diagrams without LVTD, and comparison diagrams of the position error of the leader USV (with and without LVTD) are shown. The simulation results are given in Figs. 2, 3, 4, 5 and 6.

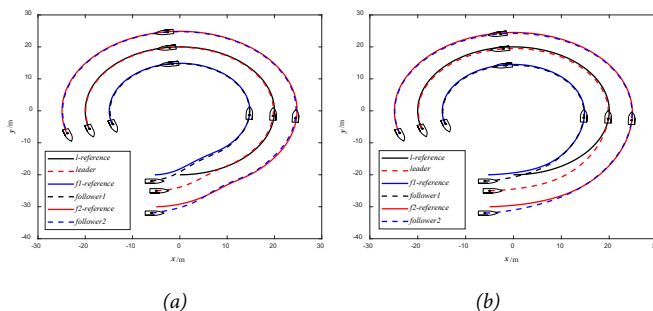


Fig. 2. Formation trajectory tracking results (a) with LVTD (b) without LVTD

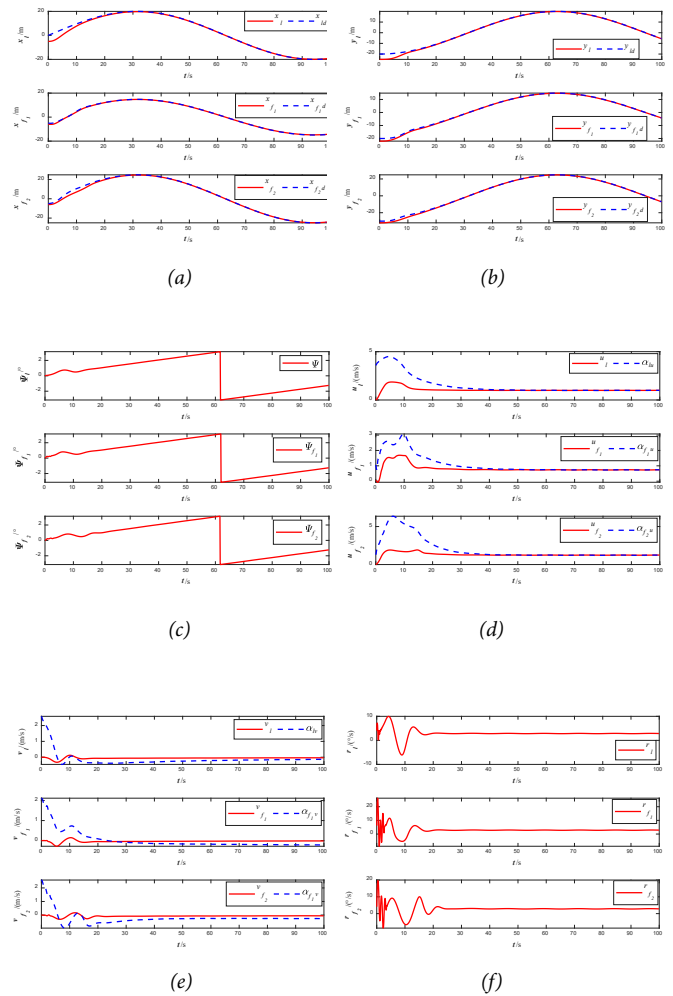


Fig. 3. The state quantities of the formation system with LVTD (a) longitudinal position (b) lateral position (c) heading angle (d) longitudinal velocity (e) lateral velocity (f) yawing angular velocity

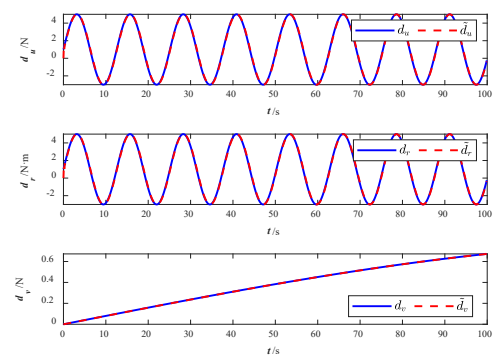


Fig. 4. Disturbance observer

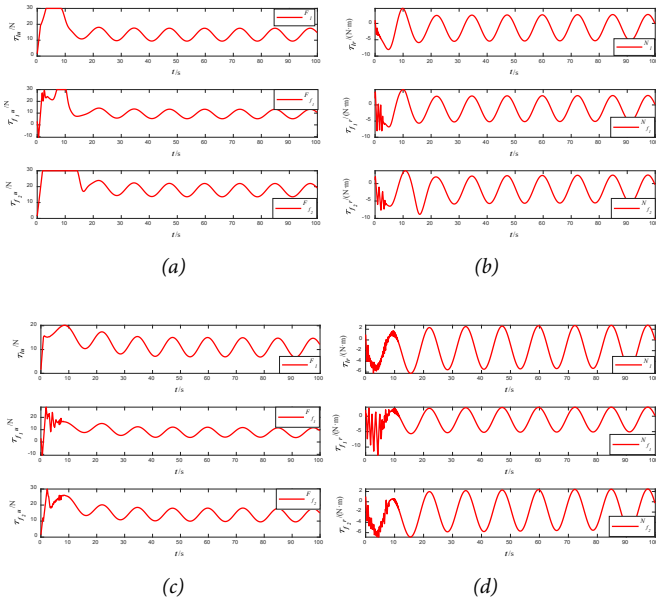


Fig. 5. Control thrust (a) the surge force with LVTD (b) the yaw moment with LVTD (c) the surge force without LVTD (d) the yaw moment without LVTD

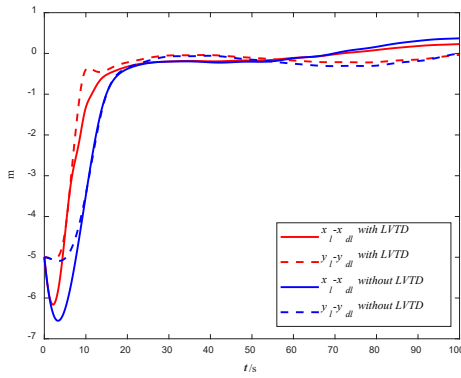


Fig. 6. Position error comparison of leader USV

STRAIGHT TRIANGLE FORMATION

The slope of the desired straight trajectory of the given leader USV is 0.5 and the mathematical formula is as follows:

$$\begin{cases} x_d = 0.5t \\ y_d = 0.25t \end{cases} \quad (46)$$

The values of marine disturbances are chosen to be the same as those above: $\mathbf{d}_j = [1 + 4 \sin(0.5t), 0.8 \sin(0.01t), 1 + 4 \sin(0.5t)]^T$.

Table 3 gives the formation information parameters.

Tab. 3. Formation information parameters

Follower USV	L / m	θ / rad
Follower USV 1	5	$5\pi / 12$
Follower USV 2	5	$-5\pi / 12$

The initial conditions of the leader USV, follower USV 1 and follower USV 2 are set as:

$$\begin{cases} [x_l(0), y_l(0), \psi_l(0), u_l(0), v_l(0), r_l(0)] = [0 \text{ m}, -4 \text{ m}, \pi / 2 \text{ rad}, 0 \text{ m/s}, 0 \text{ m/s}, 0 \text{ rad/s}] \\ [x_{f_1}(0), y_{f_1}(0), \psi_{f_1}(0), u_{f_1}(0), v_{f_1}(0), r_{f_1}(0)] = [-3 \text{ m}, -9 \text{ m}, \pi / 2 \text{ rad}, 0 \text{ m/s}, 0 \text{ m/s}, 0 \text{ rad/s}] \\ [x_{f_2}(0), y_{f_2}(0), \psi_{f_2}(0), u_{f_2}(0), v_{f_2}(0), r_{f_2}(0)] = [6 \text{ m}, -8 \text{ m}, \pi / 2 \text{ rad}, 0 \text{ m/s}, 0 \text{ m/s}, 0 \text{ rad/s}] \end{cases}$$

At the same time, during the simulation experiments, the restrictions on control thrust of the leader USV are: $\tau_{lu \max} = 30N$ and $\tau_{lr \max} = 10N$. The restrictions on control thrust of the follower USV 1 are: $\tau_{f_1u \max} = 40N$ and $\tau_{f_1r \max} = 20N$. Finally, the restrictions on control thrust of the follower USV 2 are: $\tau_{f_2u \max} = 40N$ and $\tau_{f_2r \max} = 15N$. In addition, the changing rate of each USV is also limited: $d\tau_{lu \max} = 350N/s$, $d\tau_{lr \max} = 120N/s$, $d\tau_{f_1u \max} = 350N/s$, $d\tau_{f_1r \max} = 180N/s$, $d\tau_{f_2u \max} = 320N/s$ and $d\tau_{f_2r \max} = 180N/s$.

Table 4 presents the controller parameters.

Tab. 4. Controller parameters

	Leader USV	Follower USV 1	Follower USV 2
k_1	4	6	6
k_2	10	12	12
T_1	0.10000	0.10000	0.00001
T_2	0.10000	0.10000	0.00001
λ_1	0.0001	0.0001	0.0001
λ_2	22	30	15
λ_3	18	20	15
η_1	0.1	0.1	0.1
η_2	0.10	0.02	0.02
ε_1	0.20	0.21	0.22
ε_2	0.20	0.21	0.22
C	10	10	10

Similarly, straight triangle formation trajectory tracking diagrams, state quantity convergence diagrams, disturbances observer diagrams, and control thrust diagrams are presented. The straight triangle formation trajectory tracking diagram without LVTD, control thrust diagram without LVTD, and

the comparison diagram of the position error of the leader USV with and without LVTD are also shown. The simulation results are given in Figs. 7, 8, 9, 10 and 11.

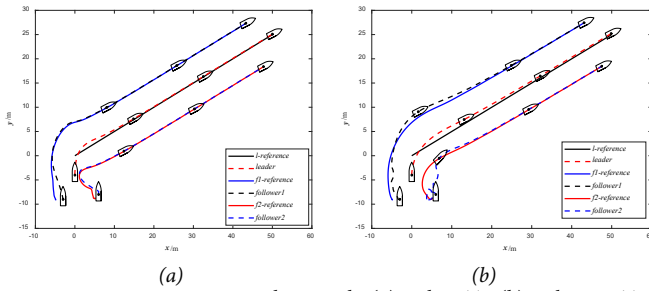


Fig. 7. Formation trajectory tracking results (a) with LVTD (b) without LVTD

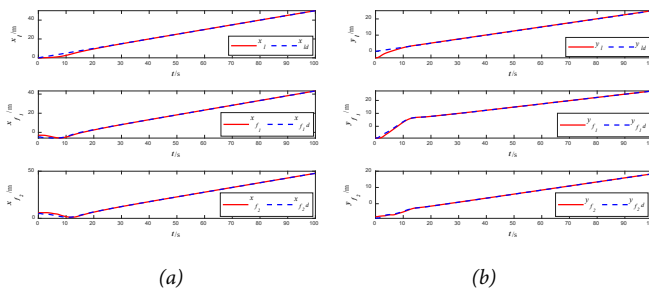


Fig. 8. The state quantities of formation system with LVTD (a) longitudinal position (b) lateral position (c) heading angle (d) longitudinal velocity (e) lateral velocity (f) yawing angular velocity

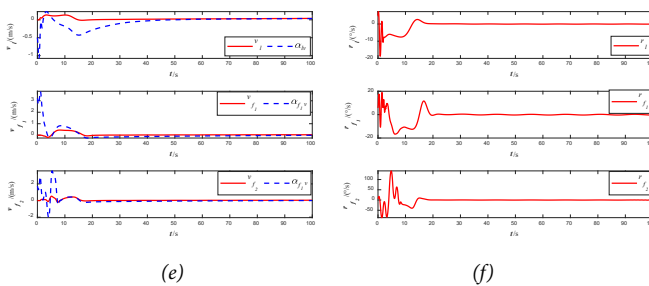


Fig. 8. The state quantities of formation system with LVTD (a) longitudinal position (b) lateral position (c) heading angle (d) longitudinal velocity (e) lateral velocity (f) yawing angular velocity

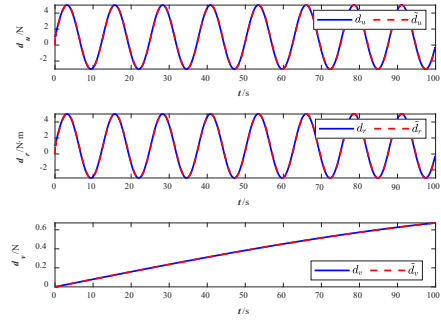


Fig. 9. Disturbances observer

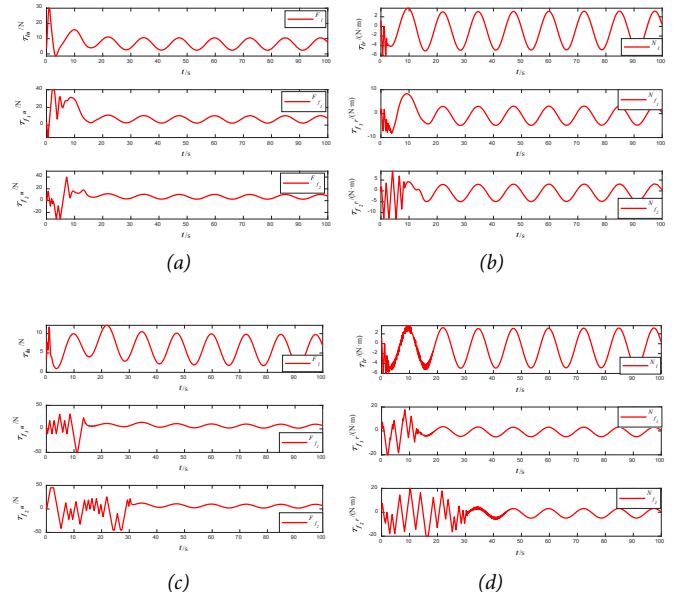


Fig. 10. Control thrust (a) the surge force with LVTD (b) the yaw moment with LVTD (c) the surge force without LVTD (d) the yaw moment without LVTD

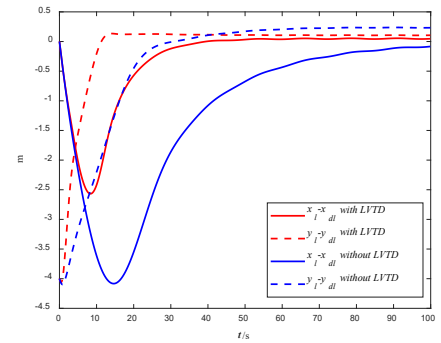


Fig. 11. Position error comparison of leader USV

From the simulation results of the above two cases with LVTD, the convergence time of the formation system is in the range 10~30 seconds; there is no instability or divergence after convergence, which also verifies that the control algorithm proposed in this paper is stable, reliable and effective. The formation trajectory tracking results shown in Fig. 2 and Fig. 7 are without compensation for lateral disturbance but the effect of formation tracking trajectory is still better,

which indicates a certain resistance to disturbance by the controller designed in this paper. In addition, the uncertainty of parameters in the USV mathematical models is considered in the simulation experiments; therefore, the robustness of the designed controller is proved. Figure 3 and Fig. 8 reveal that each state quantity of the USVs changes smoothly and slowly, except yawing angular velocity in Fig. 3(f) and Fig. 8(f). Because the positional error is relatively large during the initial stage of trajectory tracking, the rapidly changing control thrust is input for tracking the desired trajectory by each USV in the formation system as soon as possible; some fluctuation of yawing angular velocity is caused by this. Concurrently, this is also why the surge force and yaw moment in Fig. 5(a)-(b) and Fig. 10(a)-(b) fluctuate. Due to the integral term introduced when stabilising the lateral velocity error, the time taken to stabilise the lateral velocity is longer than other state quantities but the steady-state error is reduced, from Fig. 3(e) and Fig. 8(e). The situation where the nonlinear disturbance observer can observe the variable disturbance is proved in Fig. 4 and Fig. 9.

Through comparison of the simulation results with LVTD and those without LVTD (shown in Fig. 5 and Fig. 10), the oscillation of the controller is reduced due to the introduction of LVTD. Meanwhile, because of the excessive oscillation of the controller without LVTD, the stabilisation time of the formation system is longer and the steady-state error of the formation system is larger, which is indicated in Fig. 6 and Fig. 11. More specifically, from Fig. 6 it can be seen that the stability time of the formation system can be reduced by about 5-10 seconds and the steady-state error of position state quantity can be reduced by about 15 cm, by applying the controller with LVTD. This phenomenon is more obvious in the second case, as Fig. 11 shows that the stability time of the formation system can be reduced by about 50-60 seconds and the steady-state error of the position state quantity can also be reduced by about 15 cm by applying the controller with LVTD. The heading angle of the follower USVs changes greatly in the initial stage of the second case, so the oscillation of the controller without LVTD becomes more intense than the first case, which makes the practical trajectories of the follower USVs shown in Fig. 7(b) not smooth.

CONCLUSION

In this paper, an improved dynamic surface sliding mode control method, combined with tracking, is proposed for the cooperative formation control of underactuated USVs under complex marine environment disturbances. Firstly, based on the backstepping approach idea, the goal of formation control is changed and the virtual control law of longitudinal and lateral velocity is designed for the convenience of subsequent controller design. Then, the first-order low-pass filter about the virtual longitudinal velocity and intermediate state quantity of position is introduced during the stabilisation of the virtual control law of longitudinal and lateral velocity, respectively. Meanwhile, the problem of differential explosion

caused by repeated derivation is also solved well. Next, the lateral velocity error with an integral term is considered and introduced for constructing the second-order sliding mode surface, which reduces the steady-state error when stabilising the virtual lateral velocity control law. In addition, the LVTD is designed to smooth the state quantity of lateral velocity in view of the role of TD in ADRC, and the oscillation problem of the controller is successfully avoided. Moreover, combined with the dynamic model of USV, the nonlinear disturbance observer is designed for dealing with complex marine environment disturbances and compensating for them, which makes the design of the controller concise. Finally, the stability and effectiveness of the novel method are verified by Lyapunov stability theory and simulation experiments.

ACKNOWLEDGEMENTS

This work is supported by the Natural Science Foundation of China (Grant numbers 51709214, 51779052, 51809203); Stable Supporting Fund of Science and Technology on Underwater Vehicle Technology (Grant number JCKYS2022SXJQR-04); Innovative Research Foundation of Ship General Performance (Grant number 21822214).

REFERENCES

1. P.N.N. Thanh, P.M. Tom and H.P.H. Anh, 'A new approach for three-dimensional trajectory tracking control of under-actuated AUVs with model uncertainties,' *Ocean Engineering*, vol. 228, pp. 1-17, May. 2021. doi:10.1016/j.oceaneng.2021.108951.
2. P.J.B. Sanchez, F.P.G. Marquez, S. Govindara, A. But, B. Sportich, S. Marini, V. Jantara and M. Papaalias, 'Use of UIoT for offshore surveys through autonomous vehicles,' *Polish Maritime Research*, vol. 28, no. 3, pp. 175-189, Oct. 2021. doi:10.2478/pomr-2021-0044.
3. X.Y. Zhou, P. Wu, H.F. Zhang, W.H. Guo and Y.C. Liu, 'Learn to Navigate: Cooperative path planning for unmanned surface vehicles using deep reinforcement learning,' *IEEE Access*, vol. 7, pp. 165262-165278, Feb. 2019. doi:10.1109/ACCESS.2019.2953326.
4. H.B. Huang, M. Gong, Y.F. Zhuang, S. Sharma and D.G. Xu, 'A new guidance law for trajectory tracking of an underactuated unmanned surface vehicle with parameter perturbations,' *Ocean Engineering*, vol. 175, pp. 217-222, Mar. 2019. doi:10.1016/j.oceaneng. 2019.02.042.
5. L.G. Li, Z.Y. Pei, J.C. Jin and Y.S. Dai, 'Control of unmanned surface vehicle along the desired trajectory using improved line of sight and estimated sideslip angle,' *Polish Maritime Research*, vol. 28, no. 2, pp. 18-26, Jul. 2021. doi:10.2478/pomr-2021-0017.

6. S.S. Wang and Y.L. Tuo, 'Robust trajectory tracking control of underactuated surface vehicles with prescribed performance,' *Polish Maritime Research*, vol. 17, no. 4, pp. 148-156, Dec. 2020. doi:10.2478/pomr-2020-0075.
7. A. Stateczny and P. Burdziakowski, 'Universal autonomous control and management system for multipurpose unmanned surface vessel,' *Polish Maritime Research*, vol. 26, no. 1, pp. 30-39, Apr. 2019. doi:10.2478/pomr-2019-0004.
8. Z.P. Dong, Y. Liu, H. Wang and T. Qin, 'Method of cooperative formation control for underactuated USVs based on nonlinear backstepping and cascade system theory,' *Polish Maritime Research*, vol. 28, no. 1, pp. 149-162, Mar. 2021. doi:10.2478/pomr-2021-0014.
9. J.A. Gonzalez-Prieto, C. Perez-Collazo and Y. Singh, 'Adaptive integral sliding mode based course keeping control of unmanned surface vehicle,' *Journal of Marine Science and Engineering*, vol. 10, no. 1, pp. 1-20, Jan. 2022. doi:10.3390/jmse10010068.
10. J.Y. Zhuang, L. Zhang, Z.H. Qin, H.B. Sun, B. Wang and J. Cao, 'Motion control and collision avoidance algorithm for unmanned surface vehicle swarm in practical maritime environment,' *Polish Maritime Research*, vol. 26, no. 1, pp.107-116, Apr. 2019. doi:10.2478/pomr-2019-0012.
11. R.L. Miao, L.X. Wang and S. Pang, 'Coordination of distributed unmanned surface vehicles via model-based reinforcement learning methods,' *Applied Ocean Research*, vol. 122, pp. 1-15, May. 2022. doi:10.1016/j.apor.2022.103106.
12. L. Rowinski and M. Kaczmarczyk, 'Evaluation of effectiveness of waterjet propulsor for a small underwater vehicle,' *Polish Maritime Research*, vol. 28, no. 4, pp. 30-41, Jan. 2022. doi: 10.2478/pomr-2021-0047.
13. G.G. Tan, J. Zou, J.Y. Zhuang, L. Wan, H.B. Sun and Z.Y. Sun, 'Fast marching square method based intelligent navigation of the unmanned surface vehicle swarm in restricted waters,' *Applied Ocean Research*, vol. 95, pp. 1-15, Feb. 2020. doi:10.1016/j.apor.2019.102018.
14. H.N. Esfahani and R. Szlapczynski, 'Model predictive super-twisting sliding mode control for an autonomous surface vehicle,' *Polish Maritime Research*, vol. 26, no. 3, pp. 163-171, Sept. 2019. doi:10.2478/pomr-2019-0057.
15. X.L. Jiang and G.H. Xia, 'Sliding mode formation control of leaderless unmanned surface vehicles with environmental disturbances,' *Ocean Engineering*, vol. 244, pp. 1-9, Jan. 2022. doi:10.1016/j.oceaneng. 2021.110301.
16. K. Shojaei, 'Observer-based neural adaptive formation control of autonomous surface vessels with limited torque,' *Robotics and Autonomous Systems*, vol. 78, pp. 83-96, Apr. 2016. doi: 10.1016/j.robot.2016.01.005.
17. J. Ghommam and M. Saad, 'Adaptive leader-follower formation control of underactuated surface vessels under asymmetric range and bearing constraints,' *IEEE Transactions on Vehicular Technology*, vol. 67, no. 2, pp. 852-865, Feb. 2018. doi:10.1109/TVT.2017.2760367.
18. D.S. Wang and M.Y. Fu, 'Adaptive formation control for waterjet USV with input and output constraints based on bioinspired neurodynamics,' *IEEE Access*, vol. 7, pp. 165852-165861, Dec. 2019. doi:10.1109/ACCESS.2019.2953563.
19. S.W. Wang, F. Ma, X.P. Yan, P. Wu and Y.C. Liu, 'Adaptive and extendable control of unmanned surface vehicle formations using distributed deep reinforcement learning,' *Applied Ocean Research*, vol. 110, pp. 1-28, May. 2021. doi:10.1016/j.apor.2021.102590.
20. L.Y. Chen, H. Hopman and R.R. Negenborn, 'Distributed model predictive control for vessel train formations of cooperative multi-vessel systems,' *Transportation Research Part C-Emerging Technologies*, vol. 92, pp. 101-118, Jul. 2018. doi:10.1016/j.trc.2018.04.013.
21. M.Y. Fu and L.L. Yu, 'Finite-time extended state observer-based distributed formation control for marine surface vehicles with input saturation and disturbances,' *Ocean Engineering*, vol. 159, pp. 219-227, Jul. 2018. doi:10.1016/j.oceaneng.2018.04.016.
22. B. Huang, S. Song, C. Zhu, J. Li and B. Zhou, 'Finite-time distributed formation control for multiple unmanned surface vehicles with input saturation,' *Ocean Engineering*, vol. 233, pp. 1-14, Aug. 2021. doi:10.1016/j.oceaneng.2021.109158.
23. S.L. Dai, S.D. He, H. Lin and C. Wang, 'Platoon formation control with prescribed performance guarantees for USVs,' *IEEE Transactions on Industrial Electronics*, vol. 65, no. 5, pp. 4237-4246, May. 2018. doi:10.1109/TIE.2017.2758743.
24. J. Ghommam, M. Saad, F. Mnif and Q.M. Zhu, 'Guaranteed performance design for formation tracking and collision avoidance of multiple USVs with disturbances and unmodeled dynamics,' *IEEE Systems Journal*, vol. 15, no. 3, pp. 4346-4357, Sep. 2021. doi:10.1109/JSYST.2020.3019169.
25. X. Jin, 'Fault tolerant finite-time leader-follower formation control for autonomous surface vessels with LOS range and angle constraints,' *Automatica*, vol. 68, pp. 228-236, Jun. 2016. doi:10.1016/j.automatica.2016.01.064.
26. Y. Lu, G.Q. Zhang, Z.J. Sun and W.D. Zhang, 'Robust adaptive formation control of underactuated autonomous surface vessels based on MLP and DOB,' *Nonlinear*

- Dynamics, vol. 94, no. 1, pp. 503-519, Oct. 2018. doi:10.1007/s11071-018-4374-z.
27. B.S. Park and S.J. Yoo, 'Adaptive-observer-based formation tracking of networked uncertain underactuated surface vessels with connectivity preservation and collision avoidance,' *Journal of The Franklin Institute-Engineering and Applied Mathematics*, vol. 356, no. 15, pp. 7947-7966, Oct. 2019. doi:10.1016/j.jfranklin.2019.04.017.
 28. H.N. Esfahani, R. Szlapczynski and H. Ghaemi, 'High performance super-twisting sliding mode control for a maritime autonomous surface ship (MASS) using ADP-Based adaptive gains and time delay estimation,' *Ocean Engineering*, vol. 191, pp. 1-19, Nov. 2019. doi: 10.1016/j.oceaneng.2019.106526.
 29. K. Xue and T.Y. Wu, 'Distributed consensus of USVs under heterogeneous UAV-USV multi-agent systems cooperative control scheme,' *Journal of Marine Science and Engineering*, vol. 9, no. 11, pp. 1-20, Nov. 2021. doi:10.3390/jmse9111314.
 30. S.J. Yoo and B.S. Park, 'Guaranteed-connectivity-based distributed robust event-triggered tracking of multiple underactuated surface vessels with uncertain nonlinear dynamics,' *Nonlinear Dynamics*, vol. 99, no. 3, pp. 2233-2249, Feb. 2020. doi:10.1007/s11071-019-05432-5.
 31. B.S. Park and S.J. Yoo, 'Connectivity-maintaining and collision-avoiding performance function approach for robust leader-follower formation control of multiple uncertain underactuated surface vessels,' *Automatica*, vol. 127, pp. 1-10, May. 2021. doi:10.1016/j.automatica.2021.109501.
 32. H.C. Lamraoui and Q.D. Zhu, 'Path following control of fully actuated Autonomous underwater vehicle based on LADRC,' *Polish Maritime Research*, vol. 25, no. 4, pp. 39-48, Dec. 2018. doi:10.2478/pomr-2018-0130.
 33. M. Tomera and K. Podgorski, 'Control of dynamic positioning system with disturbance observer for autonomous marine surface vessels,' *Sensors*, vol. 21, no. 20, pp. 1-24, Oct. 2021. doi.org/10.3390/s21206723.
 34. T. Perez and T.I. Fossen, 'Kinematic models for maneuvering and sea keeping of marine vessels,' *Modeling, Identification and Control*, vol. 28, no. 1, pp. 19-30, Jan. 2007. doi: 10.4173/mic.2007.1.3.
 35. W.H. Chen, 'Disturbance observer based control for nonlinear systems,' *IEEE-ASME Transactions on Mechatronics*, vol. 9, no. 4, pp. 706-710, Dec. 2004. doi:10.1109/TMECH.2004.839034.
 36. J.Q. Han, 'From PID to active disturbance rejection control,' *IEEE Transactions on Industrial Electronics*, vol. 56, no. 3, pp. 900-906, Mar. 2009. doi:10.1109/TIE.2008.2011621.
 37. K.D. Do and J. Pan, 'Global robust adaptive path following of underactuated ships,' *Automatica*, vol. 42, no. 10, pp. 1713-1722, Oct. 2006. doi:10.1016/j.automatica.2006.04.026.

CONTACT WITH THE AUTHORS

Zaopeng Dong

Key Laboratory of High Performance Ship Technology
(Wuhan University of Technology), Ministry of Education,
Wuhan University of Technology, Wuhan;
Science and Technology on Underwater Vehicle Technology
Laboratory, Harbin Engineering University, Harbin, China;
School of Naval Architecture, Ocean and Energy Power
Engineering, Wuhan University of Technology, Wuhan
CHINA

Shijie Qi

Key Laboratory of High Performance Ship Technology
(Wuhan University of Technology), Ministry of Education,
Wuhan University of Technology, Wuhan;
School of Naval Architecture, Ocean and Energy Power
Engineering, Wuhan University of Technology, Wuhan
CHINA

Min Yu

e-mail: yumin@whut.edu.cn

Key Laboratory of High Performance Ship Technology
(Wuhan University of Technology), Ministry of Education,
Wuhan University of Technology, Wuhan;
School of Naval Architecture, Ocean and Energy Power
Engineering, Wuhan University of Technology, Wuhan,
CHINA

Zhengqi Zhang

Key Laboratory of High Performance Ship Technology
(Wuhan University of Technology), Ministry of Education,
Wuhan University of Technology, Wuhan
School of Naval Architecture, Ocean and Energy Power
Engineering, Wuhan University of Technology, Wuhan
CHINA

Haisheng Zhang

Key Laboratory of High Performance Ship Technology
(Wuhan University of Technology), Ministry of Education,
Wuhan University of Technology, Wuhan;
School of Naval Architecture, Ocean and Energy Power
Engineering, Wuhan University of Technology, Wuhan
CHINA

Jiakang Li,

Key Laboratory of High Performance Ship Technology
(Wuhan University of Technology), Ministry of Education,
Wuhan University of Technology, Wuhan;
School of Naval Architecture, Ocean and Energy Power
Engineering, Wuhan University of Technology, Wuhan
CHINA

Yang Liu

Key Laboratory of High Performance Ship Technology
(Wuhan University of Technology), Ministry of Education,
Wuhan University of Technology, Wuhan;
School of Naval Architecture, Ocean and Energy Power
Engineering, Wuhan University of Technology, Wuhan
CHINA

RESEARCH ON THE RISK CLASSIFICATION OF CRUISE SHIP FIRES BASED ON AN ATTENTION-BP NEURAL NETWORK

Zhenghua Xiong ¹

Bo Xiang ¹

Ye Chen ^{*} ²

Bin Chen ²

¹ Sichuan Communications Vocational and Technical College, Chengdu, China

² Wuhan University of Technology, China

* Corresponding author: 2654384978@qq.com (Y. Chen)

ABSTRACT

Due to the relatively closed environment, complex internal structure, and difficult evacuation of personnel, it is more difficult to prevent ship fires than land fires. In this paper, taking the large cruise ship as the research object, the physical model of a cruise cabin fire is established through PyroSim software, and the safety indexes such as smoke temperature, CO concentration, and visibility are numerically simulated. An Attention-BP neural network model is designed for realizing the intelligent identification of a cabin fire and dividing the risk level, which integrates the diagnosis results of multiple neural network models through the self-Attention mechanism and adaptively distributes the weight of each BP neural network model. The proposed model can provide decision-making reference for subsequent fire-fighting measures and personnel evacuation. Experimental results show that the proposed Attention-BP neural network model can effectively realize the early warning of the fire risk level. Compared with other machine learning algorithms, it has the highest stability and accuracy and reduces the uncertainty of early cabin fire warning.

Keywords: Cruise Fire; Simulation Modeling; Ensemble Learning; BP Neural Network

INTRODUCTION

Cruise tourism is a form of tourism that involves onboard activities and shore leisure on large passenger ships, with sea cruises being the main form [1]. Due to the complex internal structure, large number of cabins, and large passenger capacity of the cruise ship, the property and safety of the passengers can be greatly threatened if a fire breaks out. Therefore, it is very important to identify and classify the risk level of a fire in the cabin of the cruise ship, which can provide suggestions for the later implementation of fire-fighting measures and personnel evacuation.

The cruise cabin fire has the characteristics of the high possibility of the fire, the heavy load of the fire, low fire resistance

rating, serious fire losses, and low risk tolerance. Assessing the level of the fire is the key to implementing fire extinguishing measures and the evacuation of personnel in the later stage. The fire level is not accurately assessed according to certain information. It is necessary to monitor the parameters in the cabin and further judge the level of the cabin fire. Yoshidak et al. [1] built a three-story ship test channel to study and analyze the spread of flue gas in the channel during the fire and observed the change in the fire source, smoke exhaust, temperature, and pressure in the channel. Zhang [2] took a bulk carrier as an example, simulated the development process of the engine room fire, summarized the fire spread law by analyzing the simulation data, and used the Unity3D virtual reality engine to visualize the fire data, thereby strengthening the trainees' understanding

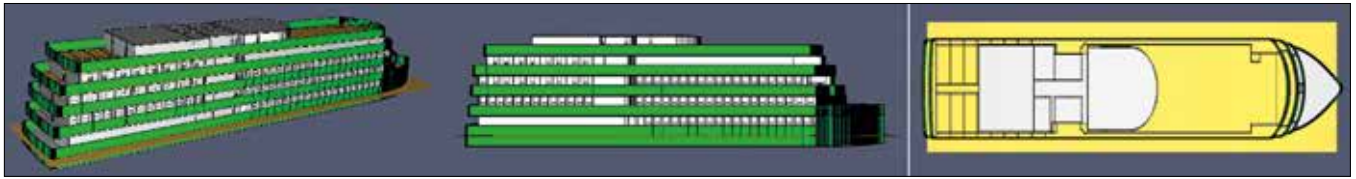


Fig. 1. Modeling diagram of the cruise cabin by using PyroSim

of the fire. Yang [3] studied a ship fire alarm system based on visual sensors that can detect flames and guide people to escape in the event of a fire. According to the monitoring of the cabin parameter information, how to determine the fire level is of great significance for the subsequent implementation of fire extinguishing measures and the evacuation of personnel.

The traditional fire model judgment level method is mainly based on the threshold set by the smoke, temperature, and other sensors to compare the values. The threshold judgment based on a single monitoring variable will be subject to errors caused by different factors such as the location of the ignition source, the combustion material, and the accuracy of the sensor. With the rapid development of machine learning technology, a fire class classification method based on multi-pass information fusion is proposed, which can extract features from cabin fire information in different scenarios and finally identify the fire class. Wu et al. [4] realized the monitoring of toxic and harmful gases in fire scenes based on machine learning. Wang [5] designed a ship fire secondary reasoning model based on a Back Propagation neural network (BP neural network) and Demspter Shafer evidence (D-s evidence) theory algorithm and built a ship fire intelligent alarm system based on the model. Wei et al. [6] proposed a rapid fire risk assessment method based on fuzzy mathematics and Support Vector Machine (SVM) algorithms. L. Jiang et al. [7] used multi-sensor information fusion methods to fuse at different levels to predict fire conditions. Xu et al. [8] established a BP neural network model to perform the real-time classification of fire hazard levels on ship compartments. Shi et al. [9] established a fuzzy comprehensive evaluation system to assess the level of fire risk.

Many parameters of fire change when a fire occurs, such as temperature, humidity, and gas concentration. It is difficult to accurately reflect the overall characteristics of the fire in a cruise cabin by the single fire characteristic information. Moreover, it is easy for the single fire information to be disturbed by the external environment, and the fire response is not sensitive enough, which might cause false alarms and missed alarms. In this paper, a novel Attention-BP neural network model based on the ensemble learning is proposed to classify the fire risk level of the cruise cabin. The proposed model integrates multiple BP neural network models to operate in parallel. The self-attention mechanism is introduced to adaptively calculate the weight of each individual model and fuse the diagnostic results of each model, which can improve the classification accuracy and reduce the uncertainty of the individual model. The proposed Attention-BP model can diagnose the fire risk level of the cruise cabin in real time and provide the basis for the subsequent fire-fighting measures and personnel evacuation.

THE SIMULATION OF THE FIRE PROCESS IN A CRUISE CABIN

Due to the high cost of cruise cabin fire experiments, it is difficult to conduct on-site experiments. In this paper, PyroSim software was used to simulate the development of cruise cabin fires [10]. By simulating the fire process with PyroSim software, the diffusion process of smoke during the whole fire process can be directly observed, and the curves of temperature, gas concentration, smoke, and personnel over time can be obtained.

CRUISE CABIN LAYOUT AND MODELING

In this paper, a cruise ship is selected as a simulation object. The total tonnage of the cruise ship is 4924 tons, the length is 135.20 m, and the width is 19.60 m. There are 5 decks in the passenger area, namely, the upper deck L1, walk deck L2, pilot deck L3, entertainment deck L4, and sun deck L5. The layout and structure of this real cruise ship cabin are very complex. This paper introduces the PyroSim software to simply model this ship cabin, and the three-dimensional view, front view and top view of this cruise ship are shown in Fig. 1.

All calculations in PyroSim must be calculated according to the grid. When using PyroSim to perform a numerical simulation of the fire in a cruise cabin, the cabin model needs to be meshed to determine the calculation area and the accuracy of the area grid. However, in the actual simulation work, as the mesh scheme becomes finer, the number of meshes will increase and the computing resources will cost more. The mesh setting will also lead to inaccurate simulation results. Therefore, the setting of the simulation grid size is the decisive factor in the accuracy and calculation time of the calculation simulation, and under the premise of ensuring the accuracy of the result, one must try to use thicker cells to save calculation resources and running time.

The determination of the grid size is related to the size of the fire source power, and the following formula is used to determine the size of the fire source feature diameter. Then, the range of the cell size is determined according to the relationship between the cell size and the fire source feature diameter.

$$D = \left(\frac{Q}{\rho C_p T g^{1/2}} \right)^{2/5} \quad (1)$$

where D is the characteristic diameter of the fire source (m), Q is the heat release rate of the fire source (kW), ρ is the air density (taken as 1.2 kg/m^3), C_p is the specific heat capacity of the air, (taken as 1.014 kJ/(kg.k)), T is the ambient temperature (293 K), and g is the acceleration of gravity (taken as 9.8 m/s^2).

According to the calculation results of the formula, and then comprehensively considering the impact of the simulation calculation running time and calculation accuracy, the uniform meshing method is used to set the size of each unit grid 0.5 m * 0.5 m * 0.5 m, and the entire cabin model is divided into 4 large calculation areas with a total of 974848 unit grids. The complete cabin model meshing diagram is shown in Fig. 2.

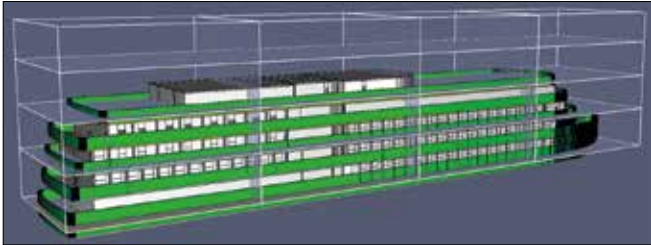


Fig. 2. Grid division of the cruise cabin model

SIMULATION OF FIRE SCENES

In this paper, the purpose of the fire simulation is to investigate the safe evacuation of personnel in a cabin fire, so the setting of the fire scene should be considered in terms of the safety of personnel evacuation. When designing a fire scene, it should be determined according to the principle of the most disadvantageous and the principle of the greatest probability. Combined with the internal structure and fire protection characteristics of the cruise cabin, four typical fire scenes are set, namely, the dining room on the 1st floor, a guest room on the 2nd floor, a business room on the 3rd floor, and the chess and card room on the 4th floor, as shown in Fig. 3.

In order to obtain more comprehensive simulation data during the occurrence of cabin fires, a total of 579 detectors were arranged in the model, which were divided into 4 groups for measuring temperature, visibility, and CO concentration located in L1, L2, L3, and L4, the detection points on each floor are mainly distributed near the burning room and on the ground of the main evacuation channel, and the distribution location of the detector is shown in Fig. 4.

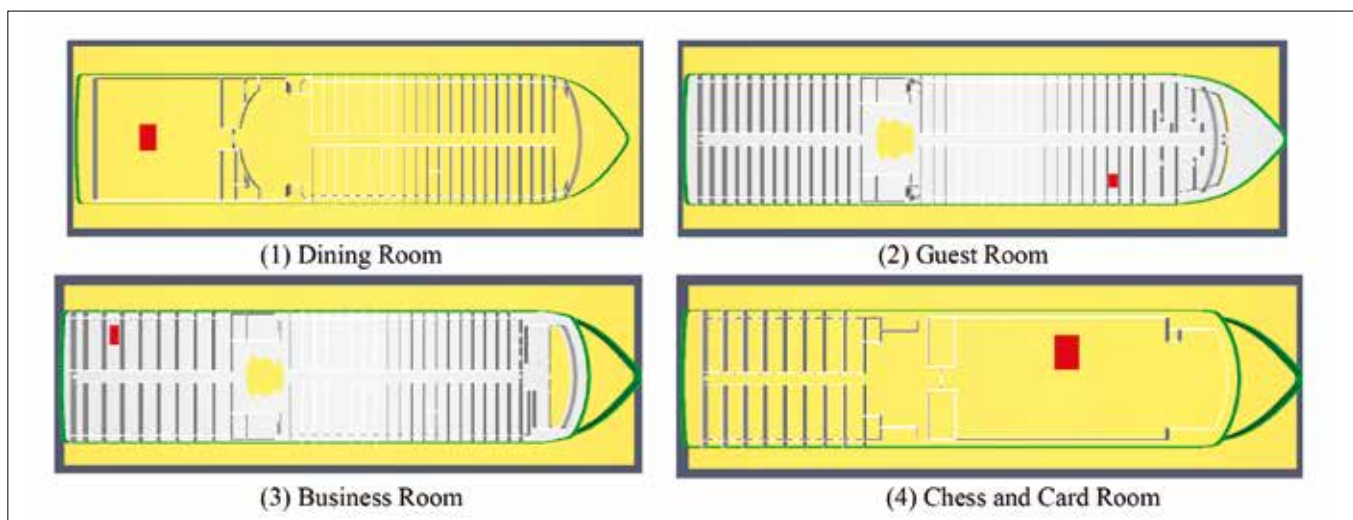


Fig. 3. Four fire points in the fire scene

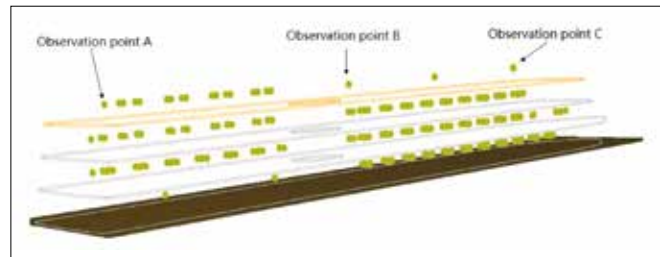


Fig. 4. Detector distribution diagram

In this paper, it is necessary to compare and analyze the visibility, the temperature, and the CO concentration at a 2.0 m height of the observation point in order to calculate the available safe evacuation time in different observation points. The limit time of human endurance for these three indicators is shown in Fig. 5. The minimum critical time of the three safety evaluation indicators is selected as the the available safe evacuation time of the observation point under each fire scenario.

CRUISE CABIN FIRE CLASSIFICATION MODEL

In this paper, the Attention-BP neural network based on the ensemble is proposed to realize the intelligent identification of the fire level in the cruise cabin, which can provide the basis for the subsequent fire-fighting measures and the personnel evacuation. The self-attention mechanism adopted in the Attention-BP neural network automatically learns the weights of the individual BP neural network model, which adaptively fuse multiple models and reduce the uncertainty of the individual model.

BP NEURAL NETWORK MODEL

The BP neural network is a multilayer feed-forward neural network trained according to an error inverse propagation algorithm. Fig. 6 shows a schematic diagram of a simple BP neural network with one input layer, implicit layer, and an output layer.

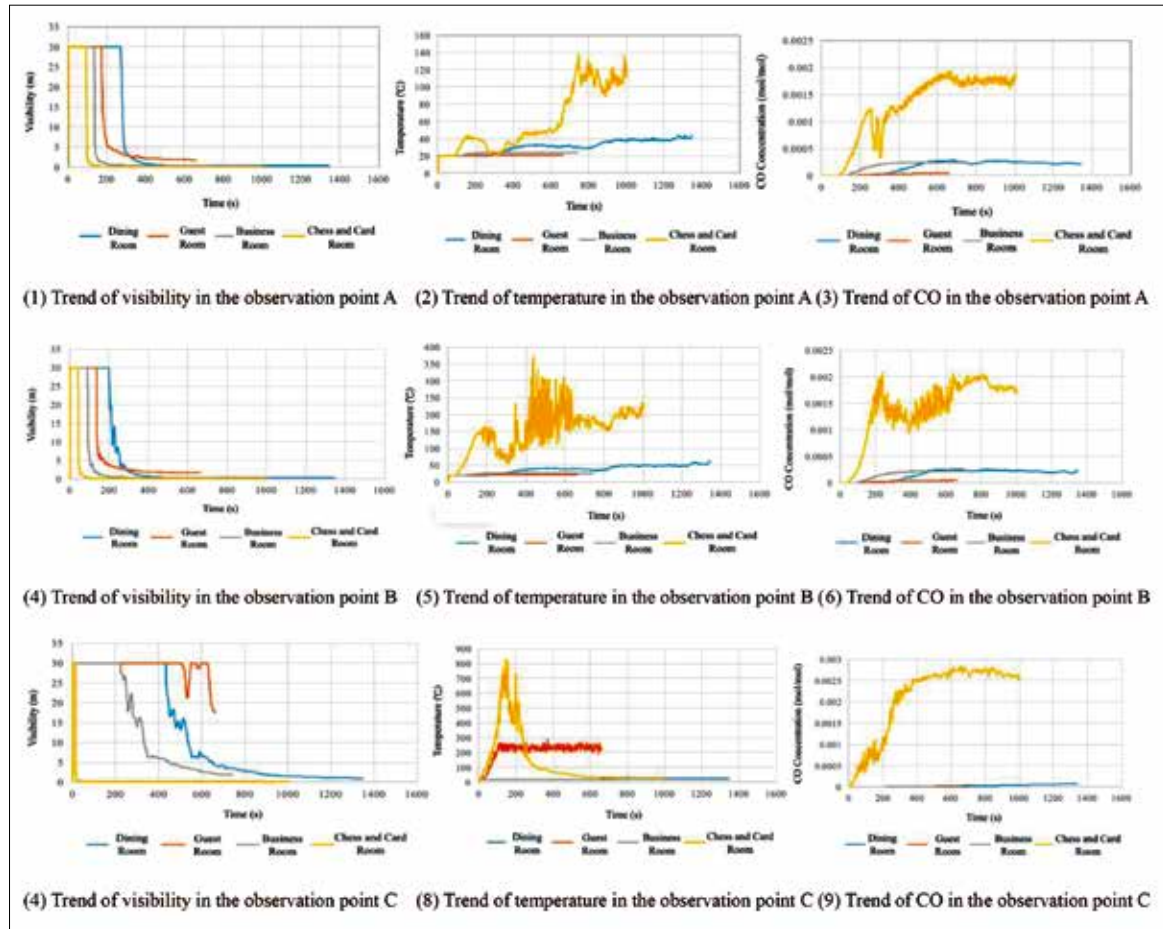


Fig. 5. Comparison of the trend of three safety indicators

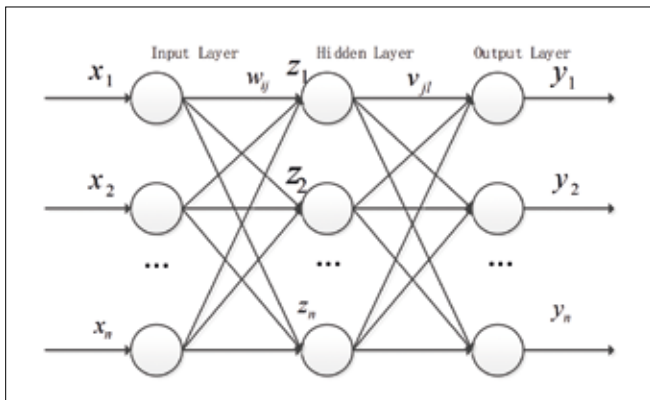


Fig. 6. BP neural network structure

The BP neural network has n inputs. The inputs are connected to the next layer by weights, and the output can be expressed as:

$$Z_j = f\left(\sum_i w_{ij} x_i - b_j\right) \quad (2)$$

where x_i is the input of the neuron, w_{ij} is the connection weight, b_j is the threshold of the neuron, z_j is the output of the neuron, and f represents a mapping function that maps the characteristics of the input node to another multidimensional space.

The mapping function is an activation function that extracts the characteristics of the input data nonlinearly through the

activation function and finally realizes the mining of nonlinear relationships in the data. Commonly used activation functions are divided into Sigmoid, Tanh, ReLU, etc. These activation functions perform nonlinear transformations of extracted features from each layer of neural networks.

The data are passed in by the input layer, and after being processed by the feature extraction and nonlinear transformation of the implicit layer, the result of the processing of the layer is the output. For the output, the error function is used to calculate the error of the output result and the expected value. The error function is:

$$E = \frac{1}{2} \sum_i (y_i - z_i)^2 = \frac{1}{2} \sum_i \left(y_i - f\left(\sum_j v_{ji} z_j - b_i\right) \right)^2 \quad (3)$$

where y_i is the true label value and v_{ji} is the eigenvalue extracted after nonlinear treatment by the hidden layer of the neural network.

The BP neural network uses backpropagation to calculate the resulting error E . The neuron node weights of each layer are adjusted and repeatedly trained until the error value reaches the expected error or the number of iterations is reached. A threshold is set to classify the input features using the network parameters at this time. The purpose of adjusting the network parameters is to make the network error E continuously decrease, and the weights of network can be determined when the error E is minimum. The amount of

adjustment is proportional to the decrease of the network error gradient, which is the process of finding the partial derivative. The formula is:

$$\frac{\partial E}{\partial \theta} = \frac{\partial}{\partial \theta} \sum_{k=1}^n (y - f(z_{jk} - b_j)) \quad (4)$$

where $\theta = (z, b)$ is the parameters of the network model and n is the number of neural elements. The update process of θ is:

$$\theta_i = \theta_i - l \cdot \frac{\partial E(\theta)}{\partial \theta} \quad (5)$$

where l represents the school rate of the model, which is the model hyper parameter that is set manually.

SELF-ATTENTION MECHANISMS

In the Attention-BP neural network model, the features extracted by each BP neural network are z_i . The features extracted by the various BP neural networks are correlated through the attention mechanism [12]. The weights of each BP neural network are calculated to obtain the importance of each extracted feature z_i :

$$(\partial_1, \partial_2, \dots, \partial_i) = att(z_1, z_2, \dots, z_i) \quad (6)$$

where ∂_i is the weights of each BP neural network model and $\partial_i \in R^{n \times 1}$ is the attention value of n nodes that output z_i .

The output is transformed using a nonlinear activation function to multiply z_i by a shared attention vector q point to obtain the final attention value w_i :

$$w_i = q^T \cdot \tanh(W \cdot z_i^T + b) \quad (7)$$

where W is the weight matrix of the attention mechanism and b is the bias vector.

The attention value ∂_i can be standardized by the Softmax function, and the formula is as follows:

$$\alpha_i = softmax(w_i) = \frac{\exp(w_i)}{\sum_{i=1}^n \exp(w_i)} \quad (8)$$

The model parameters z_i obtained by each BP neural network are fused through the attention value, ∂_i , and the final fusion feature value Z is obtained. Through the fusion of this characteristic parameter, the classification results can be made more accurate and reliable, and the formula is as follows:

$$Z = \alpha_1 \cdot z_1 + \alpha_2 \cdot z_2 \dots + \alpha_n \cdot z_n \quad (8)$$

FIRE CLASSIFICATION PROCESS BASED ON THE ATTENTION-BP NEURAL NETWORK

In this paper, a new type of Attention-BP neural network is designed for the classification of the risk level of a fire in a cruise cabin, and the structure of the network is shown in Fig. 7. The procedures can be summarized as follows:

(1) Data collection. The fire information data are collected through the smoke temperature sensor, CO concentration sensor, and the light transmittance sensor in the cabin.

(2) Data pre-processing. The acquired signals need to be standardized, and the datasets are divided into the training datasets and the testing datasets. The standardized data are fed into the BP neural network, and the standardized method selected in this paper is the Main-Max method. The collected data are normalized by the following formula:

$$x = \frac{x_{max} - \hat{x}}{x_{max} - x_{min}} \quad (10)$$

where \hat{x} is the original sample data, x_{max} is the maximum value in the sample data, and x_{min} is the minimum value in the sample data.

(3) Model training. The Attention-BP neural network model is constructed by the attention mechanism, and the normalized data training set is input into the integrated BP neural network model. The network model is trained, and the optimal network parameters are obtained after multiple iterations.

(4) Testing and verification. The trained Attention-BP neural network model is classified into the test set and the final classification results are obtained. The results are compared to the actual labels to verify the performance of the model.

(5) Online fire classification. The temperature, CO concentration, and particle size collected in real time are processed and input into the trained Attention-BP neural network model to classify the fire risk level of the cruise cabin.

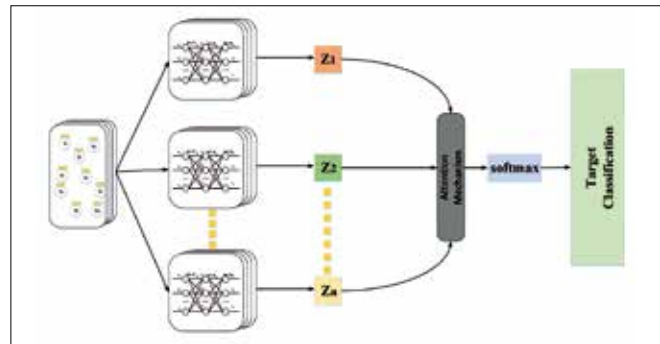


Fig. 7. Attention-BP neural network structure

EXPERIMENTAL VERIFICATION

CLASSIFICATION OF CRUISE CABIN FIRE CLASSES

Flue gas is a combustion product that is visibly suspended in the air due to pyrolysis and combustion, mainly including visible smoke particles and invisible combustion gases. The structure of the cruise ship cabin is complex, causing a wide variety of fire hazards. Once a fire occurs, it will quickly produce a large amount of smoke, which will pose a great threat to the safety of passengers. There are many factors affecting the safety of human life in the process of root fire development, and through the study of the characteristics of the fire spread and the analysis of the causes of death and injury due to the fire, the fire level can be classified. Considering the aspects of the temperature, visibility, and toxicity of the flue gas, the

Tab. 1. Classification of hazard classes in cruise cabins

	No impact (Hazard level 1)	Mild effects (Hazard level 2)	Moderate impact (Hazard level 3)	Serious impact (Hazard level 4)
Temperature	-40°C	40°C-60°C	60°C-90°C	90°C-
CO Concentration	-400 ppm	400-800 ppm	800-1200 ppm	1200 ppm-
Visibility	15 m or more	15-10 m	10-5 m	5 m or less
Physiological Symptoms	Less impact	The headache worsens and is dizziness, nausea life-threatening after 3 h	Within 30 min, dizziness, nausea, spasms; loss of consciousness within 2 h	Headache, dizziness, nausea within 20 min, death within 30 min

fire level is divided into 4 levels according to the physiological symptoms of the human body, as shown in Table 1.

NEURAL NETWORK STRUCTURE AND RESULTS ANALYSIS

The structure of the BP neural network will have an important impact on the classification results. The network structure parameters that affect the final classification results include the number of hidden layers, activation function, and the number of neurons. According to the characteristics of the fire data in this paper, the number of nodes entering the neural elements is 3, and the characteristics of the model input samples are temperature, CO concentration, and visibility. The number of nodes outputting neural elements is 4, which is the four fire hazard levels divided above. The number of hidden layers of the BP neural network and the number of neurons in the implicit layer are not guided by systematic theory, and their selection is mainly based on experience. In this paper, 8 kinds of network structures are designed for testing, and the designed network structure is shown in Table 2.

Tab. 2. BP neural network structure

Serial Number	Structure of the network and the number of neurons in the hidden layer
1	Input layer (3) + hidden layer 1 layer (15, Tanh) + hidden layer 2 layer (8, ReLU) + output layer (4, softmax)
2	Input layer (3) + hidden layer 1 layer (20, Tanh) + hidden layer 2 layer (10, ReLU) + output layer (4, softmax)
3	Input layer (3) + hidden layer 1 layer (15, ReLU) + hidden layer 2 layer (8, ReLU) + output layer (4, softmax)
4	Input layer (3) + hidden layer 1 layer (20, Sigmoid) + hidden layer 2 layer (10, Sigmoid) + output layer (4, softmax)
5	Input layer (3) + hidden layer 1 layer (20, Tanh) + hidden layer 2 layer (8, ReLU) + output layer (4, softmax)
6	Input layer (3) + hidden layer 1 layer (25, Tanh) + hidden layer 2 layer (15, Tanh) + hidden layer 3 (8, ReLU) + output layer (4, softmax)
7	Input layer (3) + hidden layer 1 layer (25, Sigmoid) + hidden layer 2 layer (15, Sigmoid) + hidden layer 3 layer (8, Sigmoid) + output layer (4, softmax)
8	Input layer (3) + hidden layer 1 (30, Tanh) + hidden layer 2 layer (15, ReLU) + hidden layer 3 (10, ReLU) + output layer (4, softmax)

Each network structure conducts 30 experiments and then takes the average of the 30 experimental results as the final accuracy of the network. The result is shown in Fig. 8. The BP

neural network with the sequence number 3 has the highest accuracy rate and uses the shortest model training time. The network structure is 3-15-8-4 and the activation function is ReLU. After analysis, it can be seen that the Sigmoid activation function is the worst effect. When the activation function is Tanh and ReLU, the model accuracy has improved to a certain extent. When the model uses the ReLU activation function, the training speed of the model will be greatly improved. This is because the convergence speed is fast when using the ReLU function, there is no need to calculate the index, and the gradient will not be saturated. When the hidden layer is 3 layers, the classification accuracy of the BP neural network begins to decline, indicating that the increment of the number of hidden layer and neurons will not improve the performance of the model. Considering that the classification model is aimed at the data set of three characteristics of temperature, CO concentration, and visibility collected in the cruise cabin, the data scale is not large, so the hidden layer of the BP neural network used in this paper is 2 layers.

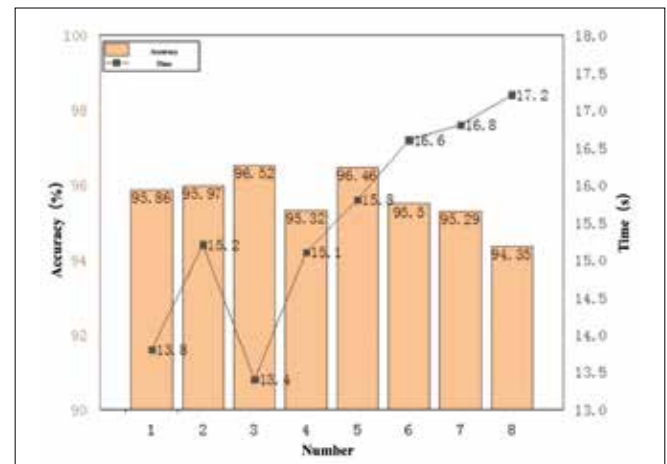


Fig. 8. Average accuracy and average training time under different network structures

In this paper, the BP neural network model uses the Adam optimizer. The initial iteration step is 1500 and the initial learning rate is 0.01. Fig. 9 shows the training and testing process of the BP neural network model. It can be concluded from Fig. 9(a) that during 250-600 iterations, the training process will fluctuate slightly, and then the training accuracy will continue to increase, while after 800 iterations, the test accuracy will not change significantly and even decrease

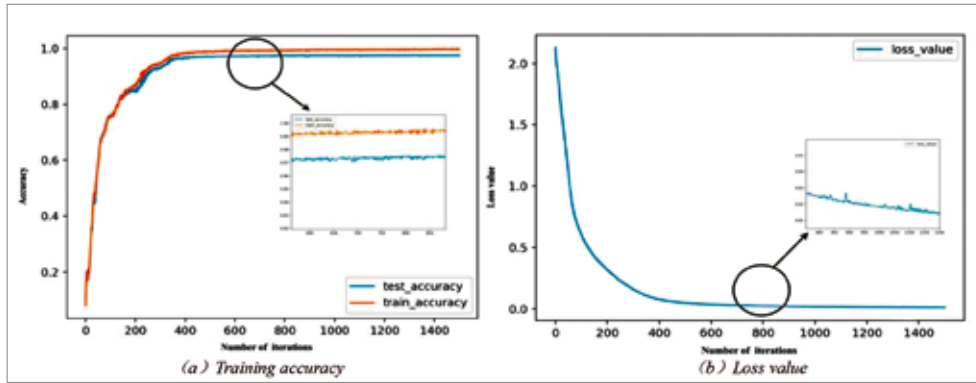


Fig. 9. Accuracy and loss in the training process

slightly. It can finally be determined that the number of iterations of this model is 800.

ALGORITHM COMPARISON

After determining the structure of an individual BP neural network in the previous section, it is of great significance to determine the number of a single BP neural network model in the integrated BP neural network model. The number of models can affect the quality of the final classification results. In this article, the number of BP neural network models is selected by searching {3,5,8,10}. The number of single models in the Attention-BP neural network can be determined from two aspects, the training time and classification accuracy. Table 3 shows the average classification accuracy and average training time under different model quantities. When the number of models increases, the classification accuracy of the integrated BP neural network also increases, but the calculation cost also increases gradually. When the number of models is 10, the training time of the Attention-BP neural network is up to 23.2 s. Through the average accuracy analysis, when the number of models is 5, 8, and 10, the classification accuracy of the Attention-BP neural network model is almost the same, which is about 1.5% higher than that when the number of models is 3. When the number of models is 8, the classification accuracy of the Attention-BP neural network model is the highest, but it is only 0.01% higher than that when the number of models is 5, but the training cost is greatly increased. Considering the two aspects of training time and accuracy, when the number of models is 5, the classification accuracy of the Attention-BP neural network model is higher (97.68%), and the training cost is relatively low. Therefore, the number of single models in the Attention-BP neural network model selected in this paper is 5.

Tab. 3. Accuracy rate and training time under different models

Number of BP neural network models	Average accuracy	Average training time
3	96.38%	19.1 s
5	97.68%	20.2 s
8	97.69%	21.4 s
10	96.55%	23.2 s

This paper compares the proposed model with other classification algorithms to verify the performance of the proposed Attention-BP neural network model. The comparison algorithms used are Support Vector Machine (SVM), Decision Tree (DT), K-Nearest Neighbor (KNN), Back Propagation Neural Network (BPNN), and Random Forest (RF). In order to quantify the classification performance of the different models, three performance indicators are introduced, including the recall rate (r), precision rate (p), and accuracy (α), which are defined as:

$$r = \frac{TP}{TP + FN} \quad (11)$$

$$p = \frac{TP}{TP + FP} \quad (12)$$

$$\alpha = \frac{TP + TN}{TP + TN + FP + FN} \quad (13)$$

where TP represents a positive sample that is correctly classified as a positive sample, FP is defined as the instance when a negative sample is misclassified as a positive sample, TN is when a positive sample is misclassified as a negative sample, and FN is a prediction that a negative sample is correctly classified as a negative sample.

Fig. 10 shows the performance of the different models. The proposed Attention-BP neural network model has the best performance in this paper. The average recall rate, precision rate, and accuracy of the proposed model can reach 97.83%, 97.54%, and 97.32%, respectively. Moreover, the stability is also higher than other algorithms. The RF model based on integrating multiple decision trees can achieve more generalized classification results and reduce the uncertainty of classification of a single model. Therefore, in this classification task of the fire risk, the performance of the RF model is higher than other simple classifiers, and its accuracy can reach 90.64%. The average recall rate, precision rate, and accuracy rate of a single BPNN model can reach 88.21%, 89.26%, and 88.51%, respectively, which are higher than classifiers such as SVM, KNN, and DT, but its performance is far lower than the Attention-BP neural network model. From the analysis of the classification performance and stability, it can be seen that the Attention-BP neural network model can provide high classification accuracy and stable diagnosis and is fully applicable to the classification of the cruise cabin fire risk level.

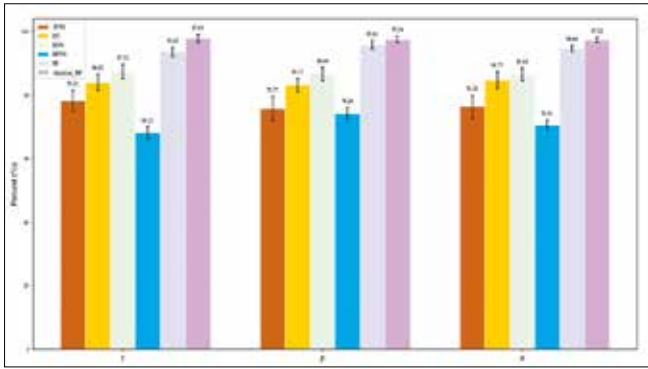


Fig. 10. Classification performance of different models

CONCLUSION

Based on the idea of integrated learning, this paper proposes an Attention-BP neural network structure for identifying the fire hazard level of cruise cabins. First of all, the cruise cabin fire development process was simulated by PyroSim software to achieve visibility, CO concentration, and temperature as three safety evaluation indicators. The fire hazard level is divided into four levels. The proposed Attention-BP neural network model is used to identify the fire level, which can realize the hazard level of the cabin in real time. After many experiments and comparison with other algorithms, it is proved that the recognition accuracy of the proposed model is high (reaching greater than 98%) and the classification stability is the best. Through the cruise cabin fire classification model, the operators on the cruise ship can understand the risk level of the fire, and then important guidance and suggestions can be provided for arranging fire extinguishing strategies and personnel evacuation measures.

REFERENCES

1. K. Yoshida, 'Full-scale model tests of smoke movement in ship passenger accommodations (first report)', Astm Special Technical Publication, 1998, (1336):163-171.
2. B. Zhang, 'Research on fire simulation and visualization application of ship engine room' [D], Wuhan University of Technology, 2018.
3. Yang Shusen, 'Research on ship fire alarm and escape strategy based on visual sensor' [D], Jiangsu University of Science and Technology, 2015
4. Z. Wu Zongkui, Y. Fan, 'Design of toxic and harmful gas monitoring system based on machine learning method', Fire Science and Technology, 2020, 39(11):1550-1553.
5. P. Wang, 'Research on control strategy of ship fire intelligent alarm system' [D], Harbin Engineering University, 2017.

6. Y.Y. Wei, J.Y. Zhang, J. Wang, 'Research on building fire risk fast assessment method based on fuzzy comprehensive evaluation and SVM', Procedia Engineering, 2018, 211:1141-1150.
7. L. Jiang, Y. Liu, Y. Li, et al. Fire prediction based on online sequence extreme learning machine[C]// 2017 7th IEEE International Conference on Electronics Information and Emergency Communication (ICEIEC). IEEE, 2017.
8. H. Xu, W. Yuan, M. Yu, 'Real-time classification of fire hazzard levels in ship cabins' [J], Ship Science and Technology, 2020, 42(19):72-77.
9. H. Shi, "A Fuzzy Approach to Building Fire Risk Assessment and Analysis," 2009 Third International Symposium on Intelligent Information Technology Application, 2009, pp. 606-609.
10. B. Chen, L. Shang, J. Sun, 'Simulation study on cabin fire and personnel evacuation of passenger ships', China Ship Repair, 2020, 33(06):34-38.
11. X. Wang, M. Zhu, D. Bo, et al. AM-GCN: Adaptive Multi-channel Graph Convolutional Networks[J]. ACM, 2020.

CONTACT WITH THE AUTHORS

Zhenghua Xiong

Sichuan Communications Vocational
and Technical College, Chengdu
CHINA

Bo Xiang

Sichuan Communications Vocational
and Technical College, Chengdu
CHINA

Ye Chen

Wuhan University of Technology
Wuhan
CHINA

Bin Chen

Wuhan University of Technology
Wuhan
CHINA

FUTURE SUSTAINABLE MARITIME SECTOR: FISHING CARRIERS AND THEIR ADOPTION TO THE ENVIRONMENTAL REGULATIONS. PART I

Viktor Yalama 
Olga Yakovleva* 
Volodymyr Trandafilov 
Mykhailo Khmelniuk 

Odesa National University of Technology, Refrigeration and Air-Conditioning Systems Department (RACS),
V.S. Martynovsky Institute of Refrigeration, Cryotechnologies and Ecoenergetics, Ukraine

* Corresponding author: RACS.olga.yakovleva@proton.me (Olga Yakovleva)

ABSTRACT

The study explored the legislative database for the maritime sector to be sustainable and have an intact blue economy. The problem for organizations with shipowners that have fishing boats older than 20 years is stated. Decision-making authorities face challenges nowadays. To be in the fleet for the next decade, shipowners for their ships should deploy energy efficiency projects for marine system retrofitting to improve energy efficiency and meet environmental regulations. The Ship Energy Efficiency Management Plan's development principles are discussed due to the current need for its deployment from 2021, so shipowners can contribute to the fast adoption of new regulations by the International Maritime Organization. In this work it is being offered to incorporate energy management issues with guidelines for upcoming regulations as well as those that are currently enforced. To improve energy efficiency, reduce environmental impact and cut fuel consumption costs, marine system retrofitting has been proposed. In this paper the focus is being put on studying energy management strengths and weaknesses which can lead to a qualitative understanding of the performance of the organizational structure, this work also focuses on the management settings concerning energy efficiency. If the organization wants to win by integrating energy policy, high-quality communication or promotion of energy efficiency issues should be employed. Marine plastic debris challenges fishing carriers on the African Union route. A possible beneficial solution for shipowners is discussed in this study.

Keywords: Maritime Sustainable Scenario Policy, Energy Management, Energy Efficiency, Fishing Carrier, Marine Plastic Debris

INTRODUCTION

According to the final communication from the commission to the European Parliament in May 2021 [1], a new approach to a sustainable blue economy has been discussed. The European Union (EU) implemented a directive on Maritime Spatial Planning in 2022, proposing cross-border cooperation as a key element of the EU policy and cooperation facilitated by the Commission. The key idea is to push the Member States forward in the direction of objectives integration of offshore

renewable energy development in their national spatial plans. Promoting renewable energy systems is the way to succeed.

In order to improve the existing situation balked with natural disasters and climate change, the EU Commission decided to continue the involvement of various types of investments as tools that can improve the desired relationship with important actors on the international arena. This is being done in order to achieve the EU sustainable development goals by implementing them into the blue economy. The Commission was forced to develop supply chains [2,3] for

empowering linkage between the blue economy and the Trade Policy, playing to the realization of the future Maritime Sustainable Scenario.

The maritime security strategy [4] and the associated action plan set out a cooperative response to modern dynamic world challenges concerning environmental security, environmental risks reduction, accidents, waste dumping, and illegal discharges and their prevention.

As 70% of the EU's external borders are maritime, the major part by the EU's trade in goods is carried by sea. Estimates show that the EU is the 3rd largest importer and the 5th largest producer in the fishing industry and aquaculture worldwide.

For ecosystem stability, blue economy value chains become global laying into the base of the world business that promotes required expertise, environmental action plans, and new rule of law according to Sustainable Fisheries Partnership. During the last decade, Asian countries and the African Union [5] have actively participated as maritime policy developers to secure the environment. The EU Commission will consider setting up an EU-Africa blue task force, which would support investments in a sustainable blue economy.

There are fishing carriers in use with the manufacturing year 2000.

How they can be adapted to the sustainable maritime blue economy?

Here come key challenges:

- to clear vision for adoption of maritime policy as a part of the sustainable scenario
- to improve energy efficiency;

MARINE PLASTIC DEBRIS

From the last decades, marine plastic debris has been a key issue worldwide causing countries and organisations to develop new action plans on how to solve the growing problem. Most marine debris is linked to human interaction with the maritime sector and originates on dry land [6]. According to Lebreton et al. [7], the 20 most polluted rivers in the world are responsible for two-thirds of all maritime sector debris. Corresponding to Ronkay et al. [8], about 18% of marine plastic debris officially originates in the fishing industry from altogether: fishing-related wastes like buoys, lines, nets, and other fishing gear, also from plastic wastes from human-related items like buckets, bottles, foamed polystyrene, bags/films, and miscellaneous plastics.

Dauvergne et al. [9] have made assumptions that plastic flowing into the oceans will double from 2010 to 2025, and that problem impacts both ocean pollution and the onboard systems' performance of many ships. As a result, governing plastic waste is a huge problem during its dispersal, durability as well as mobility.

International trade institutions do not make any contributions to problem-solving during the gap in their weaknesses. There are no well-adopted regulations according to control and monitor the regulation's executions by region. Also missing a business-oriented solution leads to growing

marine plastic pollution. Irresponsible consumers with resist government regulations as another reason for problems occurring. The executive branch is forced to perform sharp control by monitoring a situation and reporting to the government about its actions on a regular base. Legislative authority should encourage the industry to scale up local reforms in order to meet environmental regulatory requirements.

THE EUROPEAN GREEN DEAL

The European Green Deal (EGD) [10] is mobilizing the industry for a clean and circular economy, zero pollution, restoring ecosystem, sustainable and smart mobility. Policies intended for minimising harm to nature, biodiversity, and human wellbeing. The green transition plan rises up carbon emissions-cutting, cleaner energy sources adopting, as green technologies application to prevent environmental-related risks.

European Commission (EC) wants to reach targets by 2030: to reduce greenhouse gas emissions by 55% (from 1990 levels), to improve energy efficiency by 32.5%, and to increase renewable energy by 32%. In order to reach these targets on time, the EC created a dedicated action plan known as the EU Green Deal.

The EU enacted new regulations in order to meet the target of "zero" pollution (Net-Zero Law) [11]. International shipping [12] accounted for approximately 2% of global energy-related CO₂ emissions in 2019.

The International Maritime Organization (IMO) [13] has standardised regulations and put them in place for emissions control (air pollutants from ships) with its mandatory data collection systems as well as its mandatory energy-efficiency measures to reduce Greenhouse Gas (GHG) emissions. Ships passing through NO_x-Emission Control Areas (NO_x-ECAs) must adhere to mandatory engine standards or employ equivalent NO_x-Emission reduction technologies, as of January 1, 2021.

Energy efficiency-improving methods used together with environmental impact reduction methods are most desired for any energy efficiency project if it is required to meet a sustainable development scenario. Energy utilization (hot or cold) is a possibility to reduce both fuel consumption and carbon emissions along with improving energy efficiency. A research group from China [14] represented the cold energy utilization system as part of an energy-efficiency improvement program for LNG-powered container ships that lead to reducing carbon emissions. It can be a good option for shipowners to meet the International Maritime Organization requirements.

The energy efficiency analysis process (for ships), which is based on the energy quantity only, may lead to deceptive results. If we talk about a waste energy recovery that is intended for heating purposes, a ship can recover mostly all energy. It seems efficient from the energy viewpoint. At the same time, fully recovered waste heat from all available

(that can be produced by energy systems) on the ship doesn't indicate the existence of an efficient way of performing a recovering process. Using energy analysis, it is possible to determine the energy potential and boundary conditions for detecting the ineffectuality of the thermomechanical systems.

Bocheński and Kreft [15] proposed methods, using "probabilistic models" as tools for analysing various marine heating systems' solutions to determine the operational consequences associated with these solutions. Solutions and to develop a method for forecasting the parameters of the operational distribution of heat demand on cargo ships. In practice, it is common that errors leading to failing projects have mostly occurred during the design process. So, developing a new method that can contribute to improvements in the design process is desirable for the maritime sector. It can finally contribute to EGD.

During the pre-parametric design process of new ships, Turkish scientists, Okumuş at al. [16] proposed mathematical relationships (gradient boosting machine (GBM) regression algorithm) that can be used to estimate the power of the engines, emissions with prediction opportunities of the main engine and auxiliary engine power used to build "green" ships.

A Ukrainian research team, Kuznecov at al. [17] proposed the use of ejection cooling devices as part of the exhaust system to reduce NOx emissions in exhaust gases and to cut costs for the Selective Catalytic Reactor (SCR) maintenance in the exhaust system for the tanker with a deadweight of 45,564 t. Presented recommendations let shipowners both perform their work within environmental regulations and improve system efficiency.

System flexibility would allow the system to handle a variety of issues, in order to improve system performance that could lead to cost-effective shipping, cutting fuel consumption, and reducing environmental impact.

Abramowicz-Gerigk and Burciu [18] proposed new steering devices, including a dynamic coupling system and bow rotors on the pushed barges, to improve maneuverability and reduce the required maneuvering area for the push train that allows for operating the ship more efficiently.

REFRIGERATION TRANSPORT. REFRIGERANTS

Improving energy efficiency is a crucial issue for cold chain participants, refrigeration transport in particular.

The majority of refrigeration systems used on fishing vessels (fishing carriers) due to high vibration, together with hard operating conditions (storm) during refrigeration system performance, refrigerant leakage occurs and quite high that request to retrofit refrigeration systems to natural refrigerants in order to reduce Ozone Depletion Potential (ODP) and Global Warming Potential (GWP).

From the Cold Facts 2018, "25% of the Northern Prawn Fleet is still operating on Hydrochlorofluorocarbons (HCFC-22)". The start of the HFC refrigerants (hydrofluorocarbons) reduction phase under the Kigali Amendment to the Montreal

Protocol has affected fishing carriers. The fishing carrier refrigeration system configuration allows for a future transition to a natural refrigerant-charged system.

Montreal Protocol regulates Ozone Depleting Substances (ODS) which is included *Chlorofluorocarbons* (CFCs), and *hydrochlorofluorocarbons* (HCFCs) refrigerants. EU F-gas legislation regulates HFC refrigerants with high GWP value in order to replace halogenated hydrocarbons on the halogen-free is in charge for single working fluids: R717, R290, R600a, R170, R744, R718, R1270; and for mixtures: R600a/R290, R290/R170, R723 (NH₃ (60%) and dimethyl ether "DME" (40%)) at [19].

EU Commission presented regulations on substances that deplete the ozone layer for the maritime sector, pushing the maritime sector to deploy them. At the same time MARPOL - the International Convention for the Prevention of Pollution from Ships or Marine Pollution convention aims [20] to prevent pollution to the marine environment by ships from the following: ODS release to the air, installations on ships, ODS-containing equipment. Log Ozone Depleting Substances list is needed to be used to ensure suitable reception facilities for equipment when removed from ships. It is controlled by the International Maritime Organization. Parties to the Montreal Protocol recently decided that Technology and Economic Assessment Panel (TEAP) should engage with the International Civil Aviation Organisation (ICAO) and the IMO in order to identify the relevant alternatives currently available or in development to retrofit refrigeration systems that have a harmful environmental impact.

Energy efficiency together with energy security regulations contributes significantly to the problems in the environment within the maritime sector for ship manufacturers and owners.

ENERGY MANAGEMENT WITHIN ENERGY AUDIT

Each expert understands that not only system performance is a keystone but system management brings a lot of opportunities to improve energy efficiency as well. A qualitative sheet of investigation can allow judging the performance of organisational structure and management settings with regards to energy efficiency. At the same time, it can give us an idea of what further steps are possible to improve system performance.

Energy auditors execute commitments together with energy policy implementation and start to answer questions. Is there policy explicitness or not? Are there guidelines or not? Is there a policy that is not adopted? Is there adopted policy formally without a commitment from the management side? A recommended energy policy with an active commitment from the managerial.

Roles and staff responsibilities are under investigation as well. Energy auditors should go through delegation of responsibilities, answering a set of questions. Whether is it an informal "ad hoc" delegation of responsibilities or

not? Some delegations of responsibilities can have a place but can be unclear and can be with unstrict management involvement lines. It is recommended energy management is fully integrated into the organization with clear and strict line management accountability.

If targets and energy efficiency projects are in use, in this case, the expert focuses attention on the energy targets and invests in energy efficiency improvements. Only targets with low-cost initiatives are desirable to shipowners. System measurements with low and medium costs and a short payback period attract interest as well. The same energy management cost criteria are in use for the following cost reduction energy efficiency. Recommended way for targets and energy efficiency projects to perform life cycle cost analysis for energy efficiency investment evaluation together with carbon footprint reducing approach according to IMO requirement.

Energy performance should be monitored and analysed for significant energy use. Experts take into consideration: where is an accounting of energy consumption, whether is limited “ad hoc” tracing of energy consumption, whether is monthly monitoring with a set of limited sub-meters and cost reporting, whether is monthly monitoring and accounting based on the sub-meters with remote monitoring, whether it is associated with the company’s system? A recommended way for the owner is to make comprehensive energy performance monitoring which is entirely integrated with daily routine operations.

Without awareness and training, the quality of energy management is reduced. The expert goes through whether it is necessary for energy-related staff training to be provided. Energy auditors continue to answer on question list, whether it is engineers (technical staff) who rarely attend special courses or not, whether it is ad-hoc internal training for certain staff or not, and whether it is energy training for major system users or not. A recommendation to solve this problem is to perform appropriate and comprehensive staff training that is tailored to defined needs and requirements.

The communication part of energy management is an important issue.

The objectives of the study:

- To make a clear understanding of the development of a Ship Energy Efficiency Management Plan (SEEMP) and the need for its deployment with the Energy Efficiency Operational Indicator (EEOI), Energy Efficiency Existing Ship Index (EEXI), and the Carbon Intensity Indicator (CII)
- To reduce the environmental impact of the onboard systems
- To propose a solution for maritime plastic debris

SHIP ENERGY EFFICIENCY MANAGEMENT PLAN. MONITORING SHIP AND FLEET EFFICIENCY PERFORMANCE.

Deploying a Ship Energy Efficiency Management Plan (SEEMP) is one of the key objectives for companies and

shipowners. From the IMO energy efficiency measures [21], it is an “operational measure that establishes a mechanism to improve the energy efficiency of a ship cost-effectively”. The SEEMP offers an opportunity for shipping companies to manage ships efficiently and to manage fleet performance efficiently for the time required. Furthermore, the Energy Efficiency Operational Indicator (EEOI) might be used as a monitoring tool.

A SEEMP can be effectively used for environmental performance management, operational efficiency improvements, reducing emissions, and, moreover, cutting costs. According to SEEMP, the IMO pushes shipowners to contemplate new technologies and practices at each phase of the plan. Within MARPOL [22] additional regulatory tools, IMO has taken the lead on the following issues: improving energy efficiency and reducing GHG emissions. In 2021, the SEEMP regulations were adopted for all cargo, including the RoPax and cruise vessels, each weighing more than 5,000 GT. The key part of SEEMP (which will be enforced in 2023) is the issue of how to reach the required carbon intensity indicator

To develop SEEMP, the classical approach for energy management systems, according to standard ISO50001 listed in Table 1, can be used.

Tab. 1. Plan-Do-Check-Act specified for the maritime sector

Plan	To set ship and company-specific measures, HR development, and goal setting with key issues to reduce on-board administration. Include interconnection with company goals and processes, ship features within technical and operational areas, pieces of training, competence, and timetables
Do	To establish and deploy the required system that allows for each chosen measure to be rolled out affording to the SEEMP. The priority for a customer is that any existing system can use a mix of tools and processes, recording them to get opportunities for energy efficiency initiatives realization. Additional plans for responsibility role setting enhance the probability of sustainable activity being performed. A SEEMP can be a part of the Safety Management System which is mandated by the International Safety Management (ISM) Code [23]. It can be an additional initiative or broader energy management activity.
Check	In order to define monitoring system establishment using different tools, any form gained access may provide both qualitative and quantitative foundation for self-evaluation and successive performance reviews. The rule is using the right tool for the right place at the right time. Tools, systems, system elements, and processes are vital for achievement measurement and to ensure that improvement is sustained. A systematic approach for information management is in use in order to check system performance.
Act	This step allows for the completion of the cycle or for improvement by analysing the effectiveness of energy efficiency activities that were deployed. It can define options for improvements to processes as well as previous results that were/are reported to stakeholders. It will create awareness and trust within the energy efficiency improvement program as well as its activities. Include feedback on a regular basis to stakeholders using communication tools and plans validation.

While all cargo should use the SEEMP as the operational measure, shipowners must have a clear understanding of the proposed changes to better assist the IMO in its recommendation's realization.

The SEEMP deployment at a particular ship level is a part of the energy management policy. Assuming that a shipping company operates multiple ships, the corporation integrates a comprehensive energy management policy for all of the ships in its fleet. It can be a proper foundation for the SEEMP development as the operational measure for a specific type of ship.

The priority target of the SEEMP is to improve the ship's operating efficiency as a system for a long-term perspective, using required as well as optimized methods and techniques intended for energy efficiency improvements and fuel savings.

Both cutting costs for fuel and preventing environmental ship pollution releasing (strongly restricted by environmental regulations) are crucial issues for shipowners. The SEEMP helps with adopted methods to reduce fuel consumption and cut fuel costs. Proposing alternative fuels for use, that can cause less greenhouse gas emissions, the SEEMP does work according to requirements.

ENERGY EFFICIENCY OPERATIONAL INDICATOR (EEOI)

The energy efficiency operational indicator (EEOI) helps for measuring the fuel efficiency of the ship in operation. To assess the outcome of any changes in operation, it can be of great use for tracking improved voyage planning or changes in the maintenance of a ship's technical systems.

The data from the ship operation which can be attained from the ship's logbook, bridge log-book, engine log-boo, and deck log-book include official records using C_f is a non-dimensional conversion factor between fuel consumption and CO₂ emission. It is based on the carbon content proposed in [24]. Empirical analysis of ships from the Royal Belgian Shipowners' Association represents in detail analysis [25].

The EEOI for a voyage is defined as Eq. 1:

$$EEOI = \frac{\sum_j FC_j \times C_{Fj}}{m_{cargo} \times D} \quad (\text{Eq.1})$$

Where the average of the indicator for a period or a number of voyages is obtained, the indicator is calculated as Eq. 2:

$$\text{AverageEEOI} = \frac{\sum_i \sum_j (FC_{ij} \times C_{Fj})}{m_{cargo,i} \times D_i} \quad (\text{Eq.2})$$

j – the fuel type;

i – the voyage number;

FC_{ij} – the mass of fuel consumed j on voyage i ;

C_{Fj} – the fuel mass to CO₂ mass conversion factor for fuel j ;
 m_{cargo} – cargo carried (tons) or work done (number of TEU or passengers) or gross tonnes for passenger ship;
 D – the distance in nautical miles corresponding to the cargo of work done.

According to sustainable future maritime sector plans [26], “signatories to the Poseidon Principles for Marine Insurance have set the bar high on their ambition, not only in terms of measuring the climate alignment of their portfolio relative to a 100% CO₂ reduction goal by 2050 and aiming to align with the Paris Agreement in time but also the scope of the global fleet that this new initiative would include”. Shipping companies should be open to not only energy efficiency management together with energy management policy implementations but also to innovations which new technologies bring with them.

From investigating recent changes within regulations, it is derived and must be known that shipowners will adopt the Energy Efficiency Existing Ship Index (EEXI) and the Carbon Intensity Indicator (CII) for use in the near future. During the Marine Environment Protection Committee session [27] (MEPC 76) in 2021, the IMO realized amendments to MARPOL Annex VI, which represents the EEXI is applied to almost all oceangoing cargo and passenger ships weighing more than 400 gross tonnage. The regulations will into force by 2023.

EEXI together with CII incorporates a valuation of potential operational changes considering optimal energy efficiency technologies for energy efficiency improvements that are best suited for the ship under investigation.

MARINE PLASTIC DEBRIS

When the vessel is fully loaded, the level of seawater intake (for the refrigeration system) is below the level of the floating plastic debris in the ocean, which keeps the plastic from entering the system for a while. Due to the floating-level changing from a fully loaded to a completely unloaded fish carrier, plastic ends up in the sea chests during the water intake process and then it goes into the filters. While the fish carrier unloads, the time until the next maintenance for pre-filters, water pumps, water-cooled shell and tube condensers decreases.

During fish carrier routes in EU waters, the refrigeration system maintenance is scheduled for 1 time per month. The African Union route in comparison with EU route brings with cardinal changes to the maintenance time of onboard systems and refrigeration systems in particular. Technical parts work continuously. During water pump maintenance in Fig 1.it is possible to see marine plastic which is caused problems.



Fig. 1. System maintenance

Some types of plastic, including plastic bags (85% of marine plastic debris) and plastic bottle caps, pass through the filter. Plastic bags passing through the filter go to the system, which leads to the water pump run-out. The tube plate of the condenser is clogged, which leads to the water supply decreasing by 2 times. Due to the deviation of the water pump from the set parameters mode (plastic in the system) plus a clogged condenser tube sheet, the seawater supply at the condenser inlet is reduced to 20% of the main flow.

As a result, marine debris is not only harmful to the ocean ecosystem but also causes troubles with onboard systems. Shipowners try to solve their problems technically but any technical solution to manage plastic debris for an organization brings additional costs including systems maintenance costs.

RESULTS

The owner of the fishing carrier is trying to adapt their ship, which has installed a refrigeration system with HCFC-R22 refrigerant and is still operating within the existing regulations. After eight-ten years, the owner is planning to put out of use this ship. In order to meet new coming regulations that put strict requirements concerning energy systems' environmental impact. For an energy efficiency improvement program, it is being proposed to use refrigerants R290, R744, and R717 for the refrigeration system to reduce environmental impact, and global warming potential and to reach desired energy efficiency for system performance.

Not only energy audit is required to be done for energy efficiency program development but its deployment, considering energy management strengths and weaknesses.

After energy auditing, auditors derive energy potential to make a clear understanding of what energy can be saved

potentially or what system, system element, or process can be improved in order to improve system energy efficiency. Auditors go to the next step – energy efficiency improvements, energy savings program development, and transferring to the customer. After program realization, organization energy managers start to work continuously with energy efficiency issues expressed in the Action Plan, the plan of activities intended for energy efficiency improvements and energy savings. Energy managers during energy auditing should accurately go through energy management strengths and

weaknesses to make the analysis of how well energy efficiency issues can be managed within the organizational structure and management settings.

Adopting energy policy and having an active commitment from the managerial side, to fully integrate energy management requirements and rules, and being open to new energy efficiency projects can help to win extra for the organization. To carry staff training in order to define needs and requirements, and finally, to grand the efficient energy management with good communication concerning energy issues within organizational system inside and outside of it – these activities will lead the organization to become a leader in the market.

Regulations put to use SEEMP for each ship with a more than 400 GT from 2021. With a clear understanding of SEEMP development principles and its purpose shipowner can be ready for SEEMP adoption.

They will be used in the near future, and shipowners should have a sharp understanding that their ship can be put out of the fleet even before the desired term (following 8-10 years in the fleet) if the proposed program for improving energy efficiency is not implemented.

If an organization tries to meet the requirements of sustainable scenario development, blue economy, green ships programs deployment, within regulations, such move from shipowner side can create new opportunities for energy systems (refrigeration system as a part of) retrofits or modifications to look for new saving opportunities in improving energy efficiency. Arguing concerning environmental restrictions leads to nowhere.

Marine plastic debris is considered a problem, and through interviews with shipowners, it was derived that regional authorities must undertake harder control of the regulations which are currently enforced in the African Union. It is a pity, not much happens here. Marine plastic debris utilization hinders the marine refrigeration system

performance and maintenance time. It should be resolved by specified institutions not only for environmental regulation adoption control but sharp monitoring from the regional authority for illegal waste dumping to prevent it.

DISCUSSIONS

Marine transport is a key player in the food supply cold chain. From the second the temperature-sensitive fish is caught, the cold chain has to be maintained in each phase (from fishery to processing, from processing to a supermarket, and from supermarket to customer home) until the fish is lastly prepared for food.

In order to reduce fuel consumption, ship-owner can improve refrigeration system energy efficiency. To deploy sustainable development achievements and best practices within protecting the quality of the environment that can lead to stable ecosystems and support worldwide society for human well-being.

Shipowners of fish carriers should be interested in being informed about upcoming environmental regulations controlled by the International Maritime Organization and in making it easier for their quick adoption.

It is a crucial issue to have good energy management not only to deploy energy efficiency projects by retrofitting or optimizing systems in order to improve system performance, cut costs for fuel consumption and reduce the environmental impact. That is why improving communication within the organization (fast feedback from the project manager to occurring complications from the engineering stuff concerning energy efficiency issues) can create stronger management.

Old ships (more than 20 years in the fleet) need energy auditing for the possibility to be in use for the following ten years. Shipowner organization is a polish organization and conducts its own business from small orders around the EU to mostly African Union activity.

Using recommended refrigerants by the environmental regulations and the IMO for refrigeration systems leads to reducing their environmental impact.

Using a reward system for manufacturing (for reducing pollution) is a good encouragement to control environmental regulations execution for the Africa Union route.

CONCLUSIONS

A clear understanding of IMO regulations and requirements to adopt the Ship Energy Efficiency Management Plan can help organisations to work on a higher level with energy efficiency issues for their continuous improvements in order to cut costs.

Refrigeration system retrofitting is proposed for natural refrigerants (R290, R744, R717), which are approved by Montreal and Kiyoto protocols, the Kigali amendment, and other environmental regulations. By improving energy efficiency

with clever energy management and retrofitting marine refrigeration system shipowner gets new possibilities to get profitability.

Marine plastic debris utilisation and prevention of waste dumping should be controlled by regional authorities concerning the legislative base.

Fishing carriers are a part of the cold chain that cannot be removed easily due to their impact on food security. By integrating energy efficiency projects within the ship-owner organisation, it is possible to put in use old fishing carriers for eight-ten years more. During the following years, both the ship-owner organisation and African Union win from the proposed solution.

REFERENCES

1. European Commission, Brussels, "Communication from the commission to the European parliament, the council, the European economic and social committee, and the committee of the regions on a new approach for a sustainable blue economy in the EU Transforming the EU's Blue Economy for a Sustainable Future." COM(2021) 240 final, 2021. [Online] Available: <https://eur-lex.europa.eu/legal-content/EN/TXT/?uri=COM%3A2021%3A240%3AFIN> [Accessed: 28-Aug-2022].
2. T. Andersen, "Lloyd's register foundation," Lloyd's Register Foundation, 2022 [Online]. Available: <https://www.lrfoundation.org.uk/en/about-us/>. [Accessed: 28-Aug-2022].
3. Market Research. "Characteristics of Successful Sustainable Fishery Initiatives.," Wilderness market, September 2019 [Online] Available: <https://www.wildernessmarkets.com/category/market-research/> [Accessed: 28-Aug-2022]
4. Council of the European Union, "European Union maritime security strategy.," 11205/14, June 2014. [Online] Available: <https://data.consilium.europa.eu/doc/document/ST%2011205%202014%20INIT/EN/pdf> [Accessed: 28-Aug-2022]
5. African Union, "2050 Africa's Integrated Maritime Strategy (2050 Aim Strategy)" UNEP, 2012. [Online] Available: https://wedocs.unep.org/bitstream/handle/20.500.11822/11151/2050_aims_strategy.pdf [Accessed: 28-Aug-2022]
6. Plastics Europe, "Plastics Europe Annual Review 2017-2018.," Plastics Europe AISBL, May 2018. [Online] Available: https://issuu.com/plasticseuropeebook/docs/annualreport2018_plasticseurope_web. [Aug-2022]
7. L. Lebreton, B. Slat, F. Ferrari, B. Sainte-Rose, J. Aitken, R. Marthouse, S. Hajbane, S. Cunsolo, A. Schwarz, A. Levivier, K. Noble, P. Debeljak, H. Maral, R. Schoeneich-Argent, R. Brambini, and J. Reisser, "Evidence that the Great Pacific Garbage Patch is rapidly accumulating plastic," Sci.

- Rep., vol. 8, no. 1, 4666, march 2018. doi: 10.1038/s41598-018-22939-w [Accessed: 28-Aug-2022].
8. F. Ronkay, B. Molnar, D. Gere, and T. Czigany, "Plastic waste from marine environment: Demonstration of possible routes for recycling by different manufacturing technologies," *Waste Manag.*, vol. 119, pp. 101–110, 2021. doi: 10.1016/j.wasman.2020.09.029
 9. P. Dauvergne, "Why is the global governance of plastic failing the oceans?," *Glob. Environ. Change*, vol. 51, pp. 22–31, 2018. doi: 10.1016/j.gloenvcha.2018.05.002
 10. European Commission, "A European green deal," European Commission, October 2019. [Online]. Available: https://ec.europa.eu/info/strategy/priorities-2019-2024/european-green-deal_en. [Accessed: 28-Aug-2022].
 11. Regulation (EU) 2021/1119 of the European Parliament and of the Council of 30 June 2021 establishing the framework for achieving climate neutrality and amending Regulations (EC) No 401/2009 and (EU) 2018/1999, 'European Climate Law'. 2021. [Online] Available: <https://eur-lex.europa.eu/legal-content/EN/TXT/?uri=CELEX:32021R1119> [Accessed: 28-Aug-2022].
 12. J. Tattini, "Tracking International Shipping 2020," IEA, June 2020 [Online]. Available: <https://www.iea.org/reports/tracking-international-shipping-2020-2>. [Accessed: 28-Aug-2022]. [Accessed: 28-Aug-2022].
 13. International Maritime Organization, "Nitrogen Oxides (NOx) – Regulation 13," IMO, 2019. [Online]. Available: [https://www.imo.org/en/OurWork/Environment/Pages/Nitrogen-oxides-\(NOx\)-%E2%80%93-Regulation-13.aspx](https://www.imo.org/en/OurWork/Environment/Pages/Nitrogen-oxides-(NOx)-%E2%80%93-Regulation-13.aspx). [Accessed: 28-Aug-2022].
 14. Y. Li, B. Li, F. Deng, Q. Yang, and B. Zhang, "Research on the Application of Cold Energy of Largescale Lng-Powered Container Ships to Refrigerated Containers," *Polish Marit. Res.*, vol. 28, no. 4, 2022, doi: 10.2478/pomr-2021-0053.
 15. D. Bocheński and D. Kreft, "Cargo Ships' Heat Demand - Operational Experiment," *Polish Marit. Res.*, vol. 27, no. 4, 2020, doi: 10.2478/pomr-2020-0066.
 16. F. Okumuş, A. Ekmekçioglu, and S. S. Kara, "Modelling ships main and auxiliary engine powers with regression-based machine learning algorithms," *Polish Marit. Res.*, vol. 28, no. 1, 2021, doi: 10.2478/pomr-2021-0008.
 17. V. Kuznetsov, B. Dymo, S. Kuznetsova, M. Bondarenko, and A. Voloshyn, "Improvement of the cargo fleet vessels power plants ecological indexes by development of the exhaust gas systems," *Polish Marit. Res.*, vol. 28, no. 1, 2021, doi: 10.2478/pomr-2021-0009.
 18. T. Abramowicz-Gerigk and Z. Burciu, "Design and operational innovations in adapting the existing merchant river fleet to cost-effective shipping," *Polish Marit. Res.*, vol. 26, no. 4, 2020, doi: 10.2478/pomr-2019-0078.
 19. Bizer "R723 (NH3/DME) as an alternative to NH3," Bitzer.de. [Online]. Available: https://www.bitzer.de/shared_media/html/a-540/en-GB/160572427161557643.html. [Accessed: 28-Aug-2022].
 20. European Commission, "Regulation (EC) No 1005/2009 of the European Parliament and of the Council of 16 September 2009 on substances that deplete the ozone layer", SWD(2019) 406 final/2, EN, 2020. [Online] Available: https://ec.europa.eu/clima/system/files/2020-03/swd_2019_406_en.pdf [Accessed: 28-Aug-2022].
 21. Marinetrtraffic "MarineTraffic: Global Ship Tracking Intelligence," Marinetrtraffic.com, 2022 [Online]. Available: <https://www.marinetraffic.com/en/ais/home/centerx:21.1/centery:28.1/zoom:2>. [Accessed: 28-Aug-2022].
 22. International Maritime Organization, "MARPOL Consolidated Edition 2017". IMO. September 2020. pp.8 [Online] Available: https://wwwcdn.imo.org/localresources/en/publications/Documents/Supplements/English/QQQE520E_092020.pdf [Accessed: 28-Aug-2022].
 23. M.-V. Missing-Value, "The international safety management (ISM) code," in *Port State Control*, Z. O. Özçayır, Ed. Informa Law from Routledge, 2018, pp. 447–475.
 24. International Maritime Organization, "Guidelines for Voluntary Use of the Ship Energy Efficiency Operational Indicator (EEOI).", IMO. Ref. T5/1.01 MEPC.1/Circ.684. 2009. [Online] Available: https://wwwcdn.imo.org/localresources/en/OurWork/Environment/Documents/Technical%20and%20Operational%20Measures/MEPC.1_Circ.684_Guidelines%20for%20Voluntary%20use%20of%20EEOI.pdf [Accessed: 28-Aug-2022].
 25. S. Parker, C. Raucci, T. Smith, and L. Laffineur, "Understanding the Energy Efficiency Operational Indicator: An empirical analysis of ships from the Royal Belgian Shipowners' Association," *Seacargocharter.org*, 2015. [Online]. Available: <https://www.seacargocharter.org/wp-content/uploads/2020/10/UCL-2015-Understanding-the-Energy-Efficiency-Operational-Indicator-Main.pdf>. [Accessed: 28-Aug-2022].
 26. UCL, "Marine insurers shoot for goal, adopt principles including targets for zero-lifecycle GHG emissions," UCL Energy Institute, December 2021. [Online]. Available: <https://www.ucl.ac.uk/bartlett/energy/news/2021/dec/marine-insurers-shoot-goal-adopt-principles-including-targets-zero-lifecycle-ghg>. [Accessed: 28-Aug-2022].

27. International Maritime Organization, “Marine Environment Protection Committee (MEPC 76), 10 to 17 June 2021 (remote session),” IMO. [Online]. Available: <https://www.imo.org/en/MediaCentre/MeetingSummaries/Pages/MEPC76meetingsummary.aspx>. [Accessed: 28-Aug-2022].

CONTACT WITH THE AUTHORS

Viktor Yalama

Olga Yakovleva

Volodymyr Trandafilov

Mykhailo Khmelniuk

Odesa National University of Technology,
Refrigeration and Air-Conditioning Systems Department
(RACS), V.S. Martynovsky Institute of Refrigeration,
Cryotechnologies and Ecoenergetics
UKRAINE

FUTURE SUSTAINABLE MARITIME SECTOR: ENERGY EFFICIENCY IMPROVEMENT AND ENVIRONMENTAL IMPACT REDUCTION FOR FISHING CARRIERS OLDER THAN 20 YEARS IN THE FLEET PART II

Viktor Yalama 

Olga Yakovleva* 

Volodymyr Trandafilov 

Mykhailo Khmelniuk 

Odesa National University of Technology, Refrigeration and Air-Conditioning Systems Department (RACS), V.S. Martynovsky Institute of Refrigeration, Cryotechnologies and Ecoenergetics, Ukraine

* Corresponding author: RACS.olga.yakovleva@proton.me (Olga Yakovleva)

ABSTRACT

For the maritime sector to be sustainable and to have an intact blue economy, shipowners should be ready to implement Ship Energy Efficiency Management Plans alongside energy efficiency projects. The problem for organizations and shipowners having fishing carriers older than 20 years is highlighted and the following challenges arise for decision-making authorities. To keep such ships in the fleet for the next decade, shipowners should deploy energy efficiency projects for marine system retrofitting to improve energy efficiency and meet environmental regulations. An energy audit is performed and an energy efficiency program is proposed with guidelines for regulations that are currently coming into force. To improve energy efficiency, reduce the environmental impact, and cut fuel consumption costs, marine system retrofitting is done, in a particular case, with two options proposed. The first is a cascade refrigeration system with hydrocarbons and carbon dioxide, where the shipowner gains an energy efficiency improvement of about 20%. The second option is a two-stage refrigeration system with ammonium as the environmentally friendly refrigerant, which improves the energy efficiency by about 26%. Technical and economic issues have been discussed.

Keywords: Blue Economy, Energy Efficiency, Fishing Carrier, Vapor Compression Refrigeration Machine

INTRODUCTION

According to the final communication from the Commission to the European Parliament in May 2021 [1], a new approach to a sustainable blue economy has been discussed. The EU Directive on the Implementation of Maritime Spatial Planning in 2022 proposes cross-border cooperation as a key element of the EU policy. The cooperation is facilitated by the EU Commission to push the Member States closer to the integration of off-shore renewable energy development objectives in their national spatial plans, in order to promote the use of renewable energy systems.

Energy efficiency together with energy security regulations is a huge part of the issues concerning the environment within the maritime sector for ship manufacturers and owners.

There are still some reefers in the fleet (fish carriers) [2] that were manufactured in the year 2000 and the last decades of the 20th century.

How can they be adapted to the sustainable maritime blue economy?

Here the key challenges are as follows:

- to improve energy efficiency;
- to reduce fuel consumption;
- to reduce the environmental impact of onboard systems.

The Energy Efficiency Existing Ship Index (EEXI) together with the Carbon Intensity Indicator (CII) incorporates a valuation of potential operational changes considering optimal energy efficiency technologies for energy efficiency improvements that are best suited for the ship under investigation.

For potential operational changes, the following directions can be worked:

- Speed reduction across the ship fleet can reduce greenhouse gas (GHG) emissions.
- Ship sailing route assessments to define methods for *ship route* planning and *route* optimization as a part of *energy efficiency* [3].
- Onboard systems estimation to make technical modifications and reduce energy consumption.
- Cargo handling system estimation for seeking modification and optimization opportunities to reduce energy consumption.
- Sea water pump assessment to find the potential to reduce energy consumption.
- Variable frequency drives assessment to save energy and reduce GHG emissions in existing *ships based on the research of ABB marine* [4].
- Smart HVAC&R.

Performing energy quality analysis [5] contributes to the electric energy quality monitoring system to achieve green shipping for sustainable blue economy regulations.

Energy efficiency technologies [6-9] can be adapted to ship systems where there is high potential for cutting costs: air lubrication systems, wind-assisted propulsion [10] such as Flettner rotors, kite and sail propulsion, marine battery systems, or any energy storage systems [11], waste heat recovery systems [12-14] or energy recovery systems, exhaust gas cleaning systems [15] according to requirements set by maritime regulations, propeller efficiency retrofit, rudder efficiency retrofit, operated system or equipment auxiliary saving technologies to reduce energy consumption, shaft generators, engine tuning, trim optimization, coating or antifoul evaluation, cold ironing, HVAC&R to improve energy efficiency, and insulation improvements to reduce energy losses.

Refrigeration systems and refrigerants. In vapor refrigeration systems, natural refrigerants have been used in different industrial applications for some time. For marine refrigeration, R744 was used more often than R717 in marine applications. The key reason was the safety requirements, R744 being less toxic in comparison with R717. Despite the lower efficiency of R744, marine refrigeration systems were the most common solutions for onboard installations. Modern technology developments have made the R744 system economically competitive as well. Several of its thermodynamic properties are more valuable than the phasing-down of HFCs group refrigerants. As a result of the marine regulations in force, the demand for a transition to natural refrigerants is becoming more common in the maritime sector and other industries.

Addressing the first phase in global trends of refrigerants offered by the Montreal Protocol [16] and Kyoto Protocol [17], the next phases in the direction of environmentally friendly refrigerants have been performed. The global warming potential (GWP) and ozone depletion potential (ODP), which are regulated by the European Commission [18], confirm no bounds for natural refrigerants such as R717, and hydrocarbons (R290) as well as the carbon-dioxide based R744. Of these natural refrigerants, the last one has many additional advantages besides global environment safety. For applying carbon dioxide, local safety regulations for system maintenance and transport refrigeration are provided by [19] Bitzer and ASHRAE, as well as going through recommendations for the use of R744, being non-flammable as well as non-toxic and meeting the required safety class for refrigerants. Hence, the mass and compact sizing system characteristics, suitable for marine performance, are permitted for the development of refrigeration units intended for fishing vessels (fishing carriers) [20].

R290 hydrocarbons. These have a very low GWP=3. Systems with R290 have been in operation globally for many years. It is commonly used within compact systems with low charges – home refrigerators, self-contained commercial refrigeration equipment, and retrofitted automotive systems. The main hindrance to the use of R290 is its high flammability (A3 safety group). R290 is supplied to the automotive aftermarket sector and makes up about 15% of the Cold Food Chain (Australian research).

R717 (GWP=0) has been used as a common refrigerant throughout the 20th century, particularly for huge industrial plants intended for food processing. The European Commission (April 2022) proposed updating the EU F-Gas Regulation, opening up opportunities for the use of ammonia/ NH_3 (R717). For vapor compression refrigeration systems, R717 has a high latent heat as well as the highest refrigeration capacity per unit mass flow of all the refrigerants in current use. Since R717 has a low molar mass, it can have a higher particle velocity compared with other refrigerants, which enables small pipes to be used. While it is flammable and toxic, it is classified in the B2L safety group and additional safety measures are required.

The usage of R744 (GWP=1) in marine systems ceased in the 1950s, mostly due to technical complications that occurred and the reduced possibility to use synthetic working fluids that operate at lower working pressures. Nowadays, these problems have been solved, however, and there are applications for which R744 is the selected working fluid, such as for freezing applications, commercial refrigeration, etc.

These marine refrigeration systems contain 1000 kg of refrigerant. To make the engineering transition away from ODS refrigerant is one of the objectives that must be met. As for alternatives to ODS refrigerant, it has been proposed to develop an energy-efficient marine system with natural refrigerant in charge. A cascade refrigeration system (R290/R744) and a two-stage refrigeration system (R717) are proposed.

The study aims to adapt fishing carriers within a sustainable maritime sector according to the modern legislative base and IMO requirements.

The study objectives are as follows:

- To conduct an energy audit and offer a program to improve energy efficiency and reduce the environmental impact of the refrigeration system.
- To make an engineering transition away from the ODS refrigerant currently in use.

METHODS

As a result of the energy audit performed for the marine refrigeration system of the fish carrier of this study, the energy potential was identified and a program was proposed to improve its energy efficiency and reduce its environmental impact. Using natural refrigerants in both a cascade refrigeration system R290/R744 and two-stage R717 refrigeration system allows for meeting the requirements of maritime sector environmental regulations.

CASCADE SYSTEM R290 / R744

Technical data:

- Condensing temperature $t_{condens} = 30^{\circ}\text{C}$;
- Evaporating temperature $t_{evap} = -40^{\circ}\text{C}$;
- High-temperature R290 circuit, low-temperature R744 circuit.
- Cooling capacity (refrigeration effect) $Q_0 = 450 \text{ kW}$

It is essential to use a cascade refrigeration system when the difference between the temperature at which heat is rejected and the temperature at which refrigeration is required has a high value, in which case there is no possibility to find a single refrigerant with suitable properties.

The cascade refrigeration system works as two independent single-stage refrigeration machines, which are connected by an intermediate cascade heat exchanger. This system element connects the two refrigerant circuits thermally by working simultaneously as an evaporator and a condenser, where CO_2 condensation processes occur (as at the condenser) as the refrigerant of the R744 low-temperature circuit and evaporating processes occur when the refrigerant “boils off” (as at the evaporator) for the R290 high-temperature circuit.

In the high-temperature basin, R290 vapors are compressed in the high-temperature circuit (HTC) compressor and enter the condenser, where they are cooled, condensed, and supercooled down to the T_{13} temperature. Then the liquid refrigerant enters the regenerative heat exchanger, where it is supercooled due to the heat exchange process with the steam of low-temperature potential for the cascade heat exchanger. Refrigerant at the T_{14} temperature is throttled in the expansion valve, then the vapor-liquid mixture “boils off” in the cascade heat exchanger and through the regenerative heat exchanger, the refrigerant passes to the HTC compressor, and then the cycle repeats, as shown in Fig. 1.

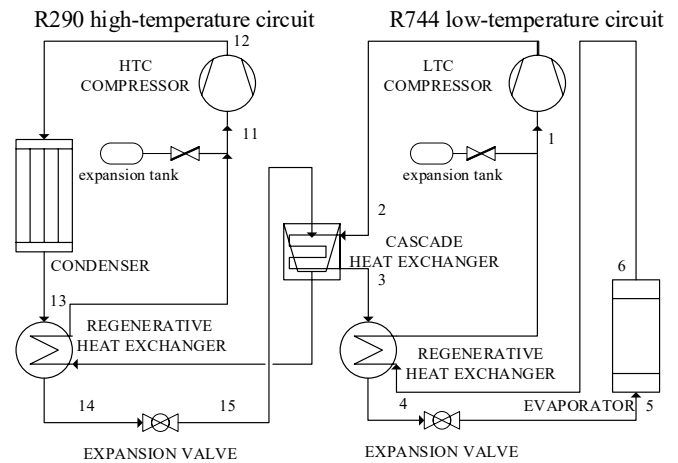


Fig. 1. Cascade refrigeration machine

In the low-temperature basin, R744 vapors are compressed in the LTC compressor and feed the cascade heat exchanger, where the R744 vapors are condensed. The liquid refrigerant is supercooled in the regenerative heat exchanger and enters the evaporator, where the refrigerant “boils off”, absorbing the latent heat from the object being cooled. The low-temperature steam is heated in the regenerative heat exchanger to the suction temperature T_1 . Refrigerant with temperature T_1 is fed to the LTC compressor. The cycle repeats.

When the machine is stopped for a long period, the temperature of the refrigerant becomes equal to the ambient temperature. The liquid refrigerant evaporates. Certainly, as the temperature rises, so does the pressure. Thus, a high saturation pressure is set in the machine, which corresponds to the ambient temperature. This pressure is quite high and can lead to serious problems when starting the compressor. Therefore, an expansion tank (balloon) is installed on the suction line of the compressor, which is switched on only when the machine is stopped.

The cascade refrigeration machine cycle is as follows:

- the intermediate temperature in the cascade heat exchanger is defined as:

$$T_{intermediate} := \sqrt{T_{condens_HTC} \times T_{evap_LTC}}, \text{ K} \quad (1)$$

where:

$T_{condens_HTC}$ – absolute condensing temperature of the high-temperature circuit, $T_{condens_HTC} = 303 \text{ K}$,

T_{evap_LTC} – absolute evaporating temperature of the low-temperature circuit,

$T_{evap_LTC} = 233 \text{ K}$, $T_{intermediate} = 265 \text{ K}$;

- evaporating temperature of the high-temperature circuit:

$$T_{evap_HTC} := \sqrt{T_{intermediate} - \Delta T}, \text{ K} \quad (2)$$

where: $\Delta T = 5 \text{ K}$, $T_{evap_LTC} = 260 \text{ K}$;

– condensing temperature of the low-temperature circuit:

$$T_{condens_LTC} := T_{intermediate} \div \Delta T, K \quad (3)$$

$$T_{condens_LTC} = 270 K;$$

- temperature overheating at the outlet of the compressor is 5 °C;
- the supercooling of the refrigerant in the condenser is 5 °C;
- the temperature of insufficient heat recovery is taken equal to 10 °C;
- regenerative heat exchanger efficiency $\eta = 0.8$.

THERMAL CALCULATION

The specific mass cooling capacity is calculated by:

$$q_{evap_LTC} = h_6 - h_5, kJ/kg \quad (4)$$

$$q_{evap_HTC} = h_{16} - h_{15}, kJ/kg \quad (5)$$

where h – enthalpy of nodes (Table 1).

The specific heat of condensation is determined by:

$$q_{condens_LTC} = h_2 - h_3, kJ/kg \quad (6)$$

$$q_{condens_HTC} = h_{12} - h_{13}, kJ/kg \quad (7)$$

The specific volumetric cooling capacity is calculated by:

$$q_v = q_{evap_LTC} \div V_1, kJ/m^3 \quad (8)$$

where V_1 is the refrigerant volume at the corresponding nodes in the circuit, m^3/kg .

The refrigerant mass flow rate through the low-temperature circuit:

$$\dot{m}_{LTC} := Q_{0_LTC} \div q_{0_LTC}, kg/s \quad (9)$$

where Q_{0_LTC} – system refrigeration capacity, kW.

The refrigerant mass flow rate through the high-temperature circuit is calculated using the heat balance equation for the cascade heat exchanger:

$$\dot{m}_{HTC} := \left(\dot{m}_{LTC} \times q_{0_LTC} \right) \div q_{0_HTC}, kg/s \quad (10)$$

Adiabatic work in the compressor:

$$W_{comp_LTC} := h_2 - h_1, kJ/kg \quad (11)$$

$$W_{comp_HTC} := h_{12} - h_{11}, kJ/kg \quad (12)$$

The actual displacement capacity (ADC) in the compressor:

$$V_{act.displ.capacity_LTC} := \dot{m}_{LTC} \times V_1, m^3/s \quad (13)$$

$$V_{act.displ.capacity_HTC} := \dot{m}_{HTC} \times V_1, m^3/s \quad (14)$$

External pressure ratio:

$$\pi_{external} = P_{condens} \div P_{evap} \quad (15)$$

In the standard range of refrigeration screw compressors, three values of the geometric compression ratio are adopted: for high-temperature and booster compressors $\varepsilon_{geometrical} = 2.6$ at $\pi_{external} \leq 4.0$; for the medium temperature $\varepsilon_{geometrical} = 4.0$ at $\pi_{external} \leq 8.0$; for low-temperature $\varepsilon_{geometrical} = 5.0$ at $\pi_{external} > 8.0$. $\varepsilon_{geometrical} = 2.6$ is chosen as the geometric compression ratio.

Theoretical compressor displacement:

$$V_{theoretical} = V_{actual} \div \lambda, m^3/s \quad (16)$$

where the feed rate of the screw compressor = 0.9 is found from [21] for the accepted brand of injected oil and the geometric compression ratio $\varepsilon_{geometrical} = 2,6$

To determine the power required to drive the compressor: Adiabatic:

$$N_{a_LTC} := \dot{m}_{LTC} \times W_{comp_LTC}, kW \quad (17)$$

$$N_{a_HTC} := \dot{m}_{HTC} \times W_{comp_HTC}, kW \quad (18)$$

Indicator:

$$N_{i_LTC} := N_{a_LTC} \div \eta_{i_LTC}, kW \quad (19)$$

$$N_{i_HTC} := N_{a_HTC} \div \eta_{i_HTC}, kW \quad (20)$$

where $\eta_{i_LTC}, \eta_{i_HTC}$ – indicator coefficient:

$$\eta_{i_LTC} := \lambda_{w_LTC} + b \times t_{evap_LTC} \quad (21)$$

$$\eta_{i_HTC} := \lambda_{w_HTC} + b \times t_{evap_HTC} \quad (22)$$

where b – factor ($b = 0.001$).

The indicator efficiency $\eta_{i_LTC}, \eta_{i_HTC}$ and effective efficiency $\eta_{effective}$ for a screw compressor operating with the injection of a small amount of liquid into the working cavities, mainly to reduce the temperature of the compressible medium, and a screw compressor with oil supplied to the working cavities, are found from the dependencies shown

in [21] depending on the geometric compression ratio $\varepsilon_{geometrical} = 2.6$.

The dependence of the effective efficiency for screw compressors on the external degree of pressure increase $\pi_{external}$ at various $\varepsilon_{geometrical}$ can be derived by the graphical method as well. The dependences of the mechanical efficiency of screw compressors of the types described above, as well as for a dry screw compressor, can be taken by the same method.

Power consumed by friction:

$$N_{friction_LTC} := V_{h_LTC} \times P_{friction}, kW \quad (23)$$

$$N_{friction_HTC} := V_{h_HTC} \times P_{friction}, kW \quad (24)$$

Effective power:

$$N_{e_LTC} := N_{friction_LTC} + N_{i_LTC}, kW \quad (25)$$

$$N_{e_HTC} := N_{friction_HTC} + N_{i_HTC}, kW \quad (26)$$

Coefficient of performance (COP):

a) Carnot cycle:

$$COP_c := T_{evap_LTC} \div (T_{condens_HTC} - T_{evap_LTC}) \quad (27)$$

b) theoretical:

$$COP_{theoretical} := q_{evap_LTC} \div (W_{compressor_HTC} - W_{compressor_LTC}) \quad (28)$$

c) actual:

$$COP_{actual} := Q_{evap_LTC} \div (N_{e_LTC} + N_{e_HTC}) \quad (29)$$

Thermodynamic perfection factor:

a) theoretical:

$$\eta_{theoretical} := COP_{theoretical} \div COP_c \quad (30)$$

b) actual:

$$\eta_{actual} := COP_{actual} \div COP_c \quad (31)$$

Theoretical refrigerant coefficient:

$$\varepsilon_{theoretical} := Q_{evap_LTC} \div (N_{a_LTC} + N_{a_HTC}) \quad (32)$$

REFRIGERATION SYSTEM HCFC-22

Technical data:

Cooling capacity $Q_0 = 450$ kW

Condensing temperature $t_k = 30$ °C;

Evaporating temperature $t_0 = -40$ °C;

Refrigerant – R22

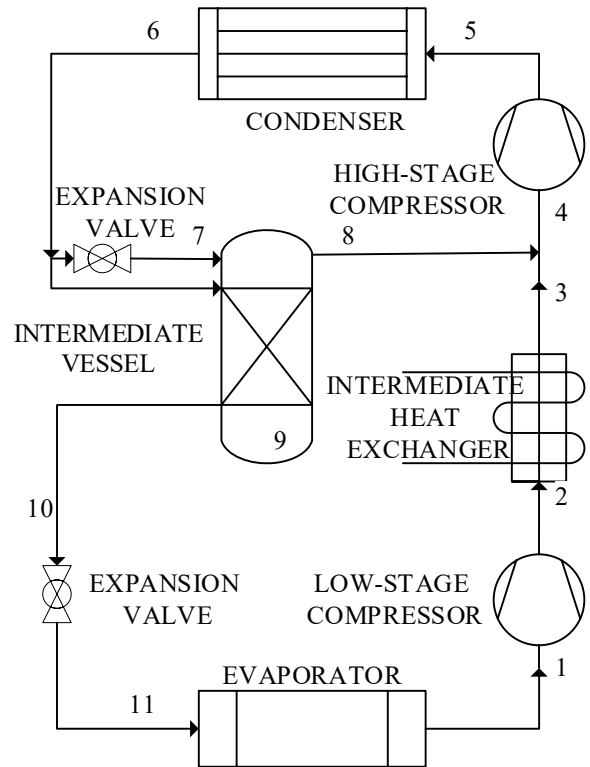


Fig. 2. Refrigeration system for two-stage refrigeration machine with one-time throttling and incomplete intermediate cooling

Tab. 1. Parameters in the corresponding nodes

№	1	2	3	4	5	6	7	8	9	10	11
p, bar	1.049	3.537	3.537	3.537	11.919	11.919	3.537	3.537	3.537	11.919	1.049
T, °C	-20	34.461	30	24	85	25	-10	-10	-10	-5	-40
h, kJ/kg	401	432	430	425	460	230	230	402	189	194	194
v, m³/kg	0.226	-	-	0.076	-	-	-	-	-	-	-

The average pressure of the high-stage compressor entering the suction:

$$P_{suction} \sqrt{11,9 \times 1,049} = 3,537 \text{ bar}$$

$$T_{suction} = -10^\circ \text{ C}$$

The refrigeration cycle parameters are calculated:

Specific cooling capacity:

$$q_{evap} = h_1 - h_{11} = 401 - 194 = 207 \text{ kJ/kg}$$

The mass flow of the high-pressure stage compressor m_{2_HPS} is greater than that of the low-pressure stage compressor m_{1_LPS} , since, in addition to the steam coming from the low-pressure stage compressor in the amount m_{1_LPS} , it also receives steam formed during the “boiling off” of the liquid in the economizer. The volumetric cooling capacity of the high-pressure compressor is about three times less due to the reduction in the volume of steam when compressed in the low-pressure compressor.

The mass supply of the compressor low-pressure stage, kg/s, is determined by the following:

$$\dot{m}_{1_LPS} = Q_{evap} \div q_{evap}, \text{ kg/s} \quad (33)$$

where Q_{evap} – cooling capacity, kW; q_{evap} – specific cooling capacity, kJ/kg;

The mass supply of the compressor high-pressure stage, kg/s, is determined by Eq. (34):

$$\dot{m}_{2_LPS} = \dot{m}_{1_LPS} \times \frac{h_8 - h_{10}}{h_8 - h_7}, \text{ kg/s} \quad (34)$$

To determine the parameters of node 4, the enthalpy for suction in the compressor high-pressure stage is as follows:

$$h_4 = h_8 + \frac{\dot{m}_{1_LPS} (h_3 - h_8)}{\dot{m}_{2_LPS}}, \text{ kJ/kg} \quad (35)$$

The specific work of the cycle, equal to the work of the low-pressure stage compressor:

$$w_1 = h_2 - h_1, \text{ kJ/kg} \quad (36)$$

The specific work of the cycle, equal to the work of the high-pressure stage compressor:

$$w_2 = h_5 - h_4, \text{ kJ/kg} \quad (37)$$

The specific load on the condenser:

$$h_{condenser} = h_5 - h_6, \text{ kJ/kg} \quad (38)$$

The coefficient of performance (theoretical):

$$COP_{theoretical} = q_{evap} / (w_1 - w_2) \quad (39)$$

The energy conversion factor of the cascade refrigeration unit of the Carnot cycle:

$$COP_c = T_{evap} / (T_{cond} - T_{evap}) \quad (40)$$

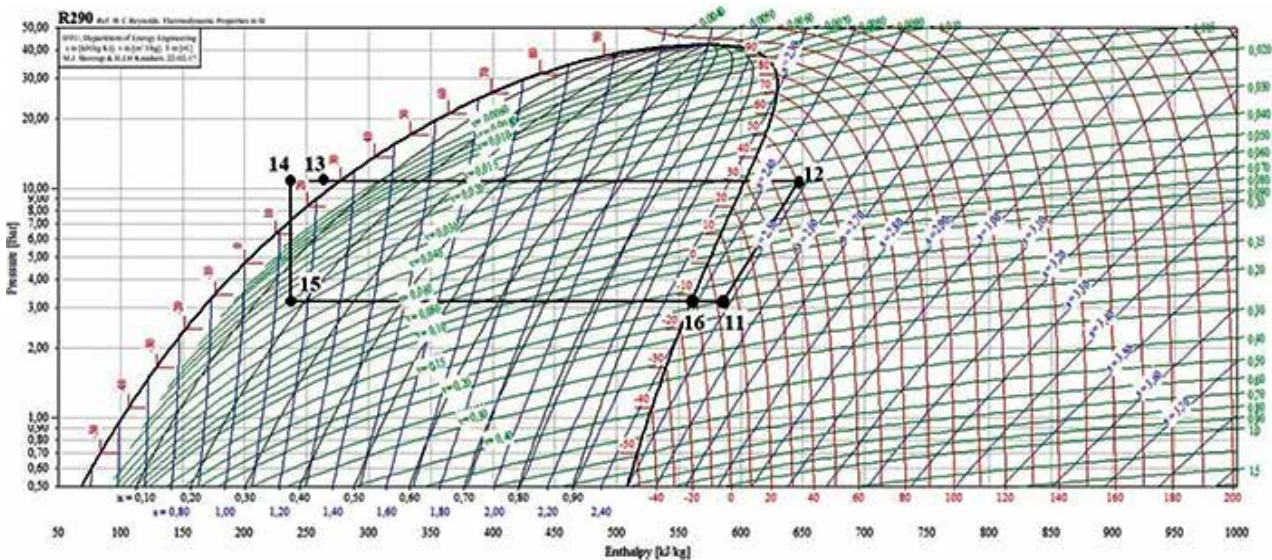
The thermodynamic perfection factor (theoretical) for the two-stage refrigeration system:

$$\eta_{theoretical} := COP_{theoretical} \div COP_c \quad (41)$$

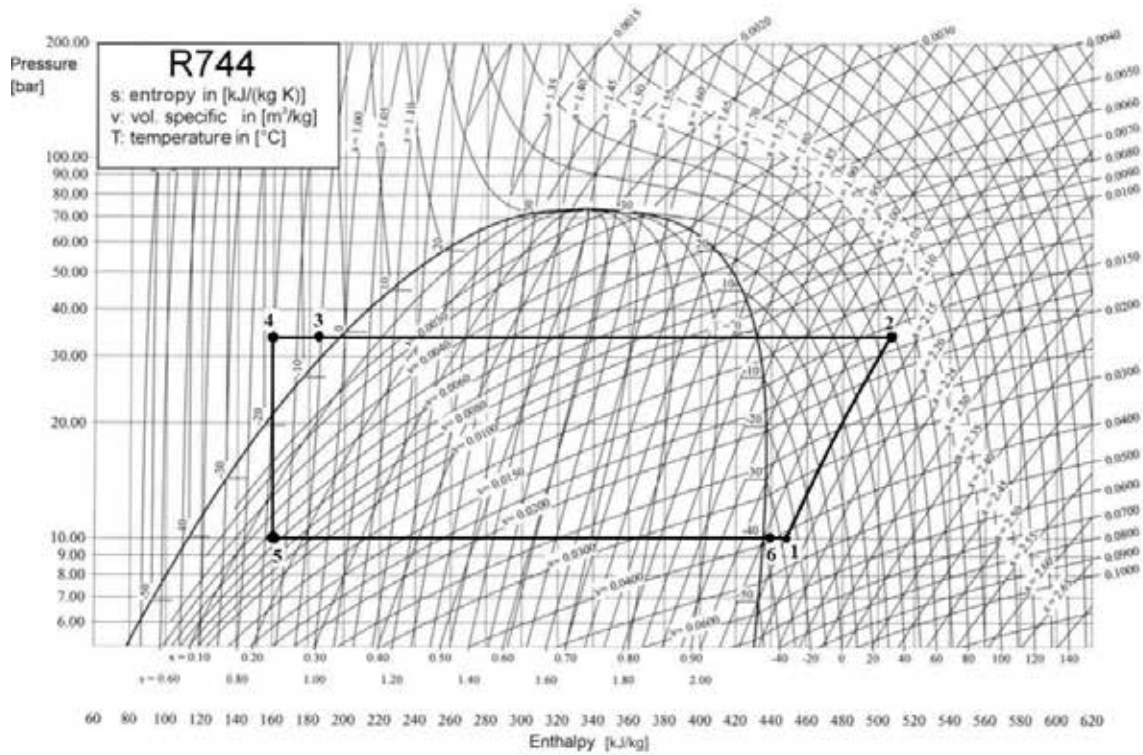
The full degree thermodynamic perfection factor (actual) for the cascade refrigeration system:

$$\eta_{actual} = COP_{actual}^n \div COP_c \quad (42)$$

The calculation for other refrigerants is done by analogy.



a) high-temperature cycle R290



b) low-temperature cycle R744

Fig. 3. Cascade refrigeration machine (a, b) R290 / R744 log P-h diagram.

RESULTS

The log P-h diagram is intended to determine the parameters of the nodes presented in Fig. 3, using CoolPack software for the simulation refrigeration system model.

The cascade refrigeration system thermodynamic processes:

- 11–12 adiabatic compression of refrigerant vapors by the LTC compressor;
- 12–13 isobaric condensation of refrigerant vapors in the condenser;
- 13–14 isobaric supercooling of liquid R290 in the “vapor-liquid” type regenerative heat exchanger;
- 14–15 isoenthalpy liquid throttling of refrigerant in the throttle valve;
- 15–16 isobaric evaporation of the vapor-liquid mixture into the cascade heat exchanger;
- 1–1 adiabatic vapor compression of the refrigerant vapor by the HTC compressor;
- 2–3 isobaric condensation of refrigerant vapors in the cascade heat exchanger;
- 3–4 isobaric supercooling of liquid R744 in the “vapor-liquid” type regenerative heat exchanger;
- 4–5 isoenthalpy throttling of liquid refrigerant in the throttle valve;
- 5–6 isobaric evaporation of vapor-liquid mixture in the cascade heat exchanger.

Tab. 2. Node parameters for cascade refrigeration system

High-temperature circuit						
Node number	11	12	13	14	15	16
p, bar	3.204	10.75	10.75	10.75	3.204	3.204
T, °C	3	50.4	25	15	-12	-12
h, kJ/kg	585.641	646.543	264	237.572	237.572	560
v, m ³ /kg	0.15					
Low-temperature circuit						
Node number	1	2	3	4	5	6
p, bar	10	33	33	33	10	10
T, °C	-25	58	-7	-17	-40	-35
h, kJ/kg	450	507	184	161	161	436
v, m ³ /kg	0.041					

Tab. 3. Thermal calculation results

Parameter	Value	Parameter	Value	Parameter	Value
q_{evap_LTC} kJ/kg	275	$V_{act.displ.capacity_HTC}$ m ³ /sec	0.246	$N_{friction_HTC}$ kWt	15.1
q_{evap_HTC} kJ/kg	322	λ_H	0.82	N_{e_LTC} kW	117.7
$q_{condens_LTC}$ kJ/kg	323	λ_w	0.81	N_{e_HTC} kW	132.9
$q_{condens_HTC}$ kJ/kg	382	V_{h_LTC} m ³ /sec	0.081	COP_c	3.33
q_v kJ/m ³	6707	V_{h_HTC} m ³ /sec	0.303	$COP_{theoretical}$	2.33
\dot{m}_{LTC} kg/sec	1.63	N_{a_LCT} kW	93.3	COP_{actual}	1.79
\dot{m}_{HTC} kg/sec	1.64	N_{a_HCT} kW	99.8	$\eta_{theoretical}$	0.701
W_{comp_LTC} kJ/kg	57	N_{i_LTC} kW	113.6	η_{actual}	0.539
W_{comp_HTC} kJ/kg	61	N_{i_HTC} kW	117.7	$\mathcal{E}_{theoretical}$	2.23
$V_{act.displ.capacity_LTC}$ m ³ /sec	0.067	$N_{friction_LTC}$ kW	4.1		

REFRIGERATION SYSTEM WITH HCFC-R22

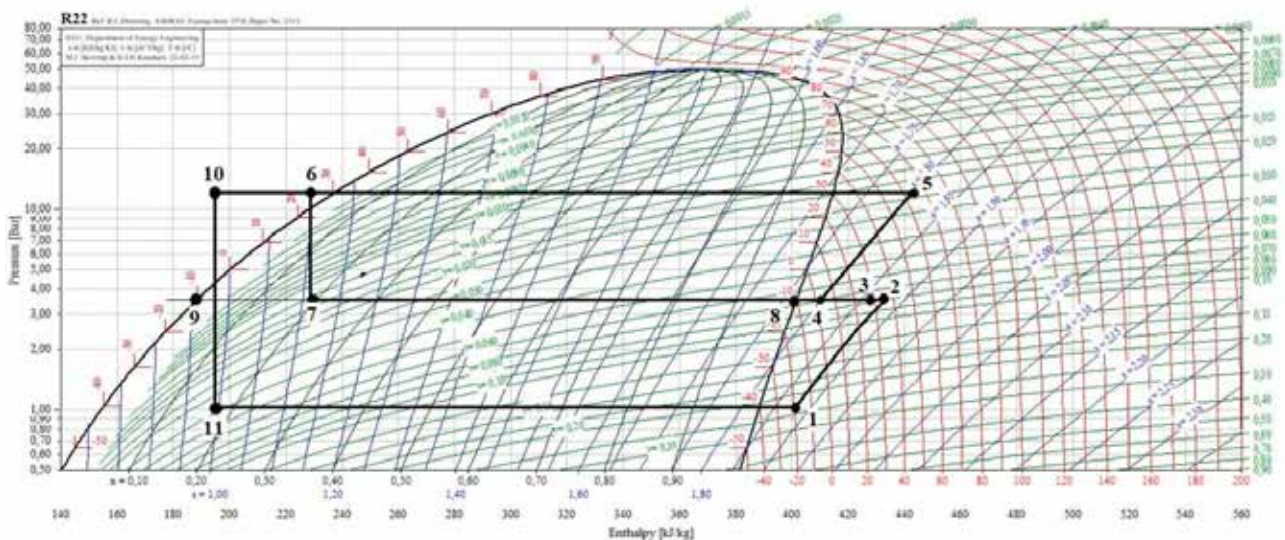


Fig. 4. Two-stage refrigeration machine R22 log P-h diagram using CoolPack software

Refrigeration system thermodynamic processes:
 1 – 2 adiabatic compression in the high-pressure stage compressor from P_0 to $P_{\text{superheat}}$;
 2 – 3 removing superheated steam in the intermediate heat exchanger, $P_{\text{superheat}} = \text{const}$;
 3 – 4 suction steam superheat in the high-pressure stage compressor, $P_{\text{superheat}} = \text{const}$;
 4 – 5 adiabatic compression in the high-pressure stage compressor from $P_{\text{superheat}}$ to P_{condens} ;
 5 – 6 condensing processes occurring in the condenser for $P_{\text{condens}} = \text{const}$, $t_{\text{condens}} = \text{const}$;
 6 – 7 throttling expansion valve 1 from P_{condens} to $P_{\text{superheat}}$ for $h = \text{const}$;
 7 – 8 “boiling off” in the intermediate vessel for $P_{\text{superheat}} = \text{const}$ and $\text{superheat} = \text{const}$;
 6 – 10 liquid subcooling in the coil in the intermediate vessel for $P_{\text{condens}} = \text{const}$;
 10 – 11 throttling in the expansion valve 2 from P_{condens} to P_0 for $h = \text{const}$;
 11 – 1 “boiling off” of refrigerant in the evaporator for $P_0 = \text{const}$, $t_0 = \text{const}$.

We summarize the results of the calculations for all the proposed alternative refrigerants in a table.

Tab. 4. Result for refrigeration systems

Parameter	R22 one-stage	R22 two-stage	Cascade R290/R744	R717 two-stage
q_{evap} , kJ/kg	170	207	275	1110
W_{comp} , kJ/kg	68	66	117	380
q_v , kJ/m ³	754	914	6707	634
N_a , kW	180	160	193	156
N_i , kW	300	230	250	236
$COP_{\text{theoretical}}$	2.5	3.11	2.33	2.92
COP_{actual}	1.5	1.95	1.8	1.9
$\eta_{\text{theoretical}}$	0.75	0.935	0.7	0.877
η_{actual}	0.45	0.587	0.54	0.571

Capital costs for the cascade refrigeration system (R290/R744) are presented in Table 5.

Tab. 5. Equipment cost for cascade refrigeration system

#	Equipment and its characteristics	Unit	Quantity	Cost per single unit, euro	Overall cost, euro
1	Compressor	piece	4	60000-70000	130000
2	Condenser	piece	2	9250	18500
3	Heat exchanger	piece	2	2050	4100
4	Cascade heat exchanger	piece	1	3000	3000

#	Equipment and its characteristics	Unit	Quantity	Cost per single unit, euro	Overall cost, euro
Total cost of equipment		155600 euro			
Cost of other equipment 10%		44896 euro			
Estimated cost of equipment		138767 euro			
Packaging costs and transporting costs 15%		20815 euro			
Assembly costs 20%		27753 euro			
Total		201213 euro			

Tab. 6. Cost of equipment and refrigerants for the two-stage ammonia refrigeration system and the regular one-stage vapor compression refrigeration system

Equipment for two-stage marine system R717 and one-stage marine system HCFC-22	Cost for two-stage marine system R717	Cost for one-stage marine system HCFC-22
Shut-off, control, and automatic valves	1105 euro	18674 euro
Pipes	2306 euro	6841 euro
Brazed plate heat exchangers	224 euro	-
Lamellar heat-exchange collapsible devices	3401 euro	-
Shell and tube heat exchangers	-	3729 euro
Compressor	90780 euro	119629 euro
Receiver	210 euro	521 euro
Pumps	1041euro	1320 euro
Air coolers	8063 euro	13150 euro
Refrigerants		
R717- 0.9t	737 euro	-
Heat transfer medium - 9.28t	12067 euro	-
Oil	56 euro	130 euro
HCFC-22 - 2t	-	1450 euro
Technical maintenance per year		
Filters, spare parts of compressor and pump replacement, etc.	931 euro	1737 euro
Total	116694 euro	169397 euro

DISCUSSION

The one-stage vapor compression refrigeration system is the object of an energy audit investigation. The owner of the fishing carrier is trying to adapt its ship which has installed a refrigeration system with HCFC-R22 refrigerant still operating in compliance with the existing regulations in force. After 8–10 years, the owner is planning to withdraw the ship from service. In order to meet the expected new regulations, which impose strict requirements concerning the environmental impact of on-board systems, an energy audit has been performed for the marine system, and the energy potential was derived. A program is proposed to

improve the marine system's energy efficiency and reduce its environmental impact. For the energy efficiency improvement program, two refrigeration systems have been chosen: a cascade refrigeration system R290/R744 which can improve the marine system's efficiency by about 20% and reduce its environmental impact because it uses natural refrigerants that do not harm the environment; and a two-stage refrigeration system R717 that can contribute still greater efficiency up to 26% and reduce the environmental impact due to its use of ammonium with GWP=0.

From the economic perspective, if we look at the capital costs, the two-stage vapor compression refrigeration system with R717 as the refrigerant requires 26% less investment than the cascade refrigeration system R290/R744.

Each of the proposed refrigeration systems can not only lead to energy savings and satisfy the environmental regulations requirements, but also cut the costs for fuel consumption and reduce the environmental impact.

Not only is an energy audit by professionals in the area of interest who have experience in the projects and competencies required for the development and deployment of a good energy efficiency program, but also energy management from the shipowner's side should be implemented to enable additional savings by the organization.

To look for extra steps that can be implemented for system performance improvements, to adopt an energy policy and ensure active commitment from the managerial side, to fully integrate energy management requirements and rules, to be open to new energy efficiency projects to make further gains, to train staff to define the needs and requirements, and finally, to enhance the efficient energy management with good communication concerning energy issues both within the organizational system and outside it – all these activities will enable the organization to become a leader in the market.

Guidelines are offered on how to develop a Ship Energy Efficiency Management Plan for future understanding and its subsequent deployment concerning the current regulations that each ship with a gross tonnage of more than 400 ton must comply with from 2021. By studying the development principles and purpose of such an SEEMP, the shipowner can be ready for its use, including an energy efficiency operational indicator, the existing energy efficiency ship index, and a carbon intensity indicator. These will be in use in the very near future and shipowners should have a clear understanding that their ship may be excluded from the fleet even before the desired term (after 8–10 years in the fleet) if the proposed program for improving energy efficiency is not implemented.

For a sustainable blue economy for the maritime sector, green ships programs, within the existing regulations, create new opportunities for on-board system retrofits or modernization and can prompt shipowners to move forward and to look for new savings opportunities through improved energy efficiency, at the same time as addressing new environmental restrictions.

CONCLUSIONS

Marine transport is a key player in the food supply cold chain. To improve communication within an organization concerning energy efficiency issues, not only to deploy energy efficiency projects by retrofitting or optimizing onboard systems to improve systems performance, to cut fuel costs, and reduce the environmental impact, it is crucial to have good energy management.

An energy audit has been performed. On the basis of the derived energy potential, a program for energy efficiency improvements and environmental impact reduction was offered for fishing carrier owners. This paper presents marine system retrofitting for a vapor compression refrigeration system with the HCFC-22 refrigerant in current use. An engineering transition away from ODS refrigerant is proposed for natural refrigerants (R290, R744, R717) which are approved by the Montreal and Kyoto protocols, the Kigali amendment, and other environmental regulations that are in force.

Shipowners can benefit from energy efficiency improvements of 20% to 26% from marine system retrofitting, as well as cutting the costs for fuel consumption.

By integrating energy efficiency projects, the organization may be able to retain fishing carriers in the fleet for 8–10 years longer as an effective part of the cold chain for African Union food security, and to contribute to maritime and security strategy problem-solving.

REFERENCES

1. *Europa.eu*. [Online]. Available: <https://eur-lex.europa.eu/legal-content/EN/TXT/PDF/?uri=CELEX:52021DC0240&rid=1>. [Accessed: 28 Aug 2022].
2. "MarineTraffic: Global Ship Tracking Intelligence," *Marinetraffic.com*. [Online]. Available: <https://www.marinetraffic.com/en/ais/home/centerx:21.1/centery:28.1/zoom:2>. [Accessed: 28 Aug 2022].
3. F. Tillig, W. Mao, and J. W. Ringsberg, "Systems modelling for energy-efficient shipping," *Transportportal.se*. [Online]. Available: <https://www.transportportal.se/Energieffektivitet/Systems%20modellering%20for%20energy-efficient%20shipping.pdf>. [Accessed: 28 Aug 2022].
4. Rasanen, J.-E.; Schreiber, E.W. Using Variable Frequency Drives (VSD) to save energy and reduce emissions in newbuilds and existing ships, Energy efficient solutions, White Paper, *ABB Marine and Cranes*. Available online: https://library.e.abb.com/public/a2bd960ccd43d82ac1257b0200442327/VFD%20EnergyEfficiency_Rasanen_Schreiber_ABB_27%2004%202012.pdf [Accessed: 30 Sep 2022].
5. S. Dallas, "Power quality analysis for greener shipping by implementing an on-board electric power quality

- monitoring system,” *J. Mar. Eng. Technol.*, vol. 21, no. 3, pp. 125–135, 2022, doi: 10.1080/20464177.2019.1658281
6. M. Jaurola, A. Hedin, S. Tikkanen, and K. Huhtala, “Optimising design and power management in energy-efficient marine vessel power systems: a literature review,” *J. Mar. Eng. Technol.*, vol. 18, no. 2, pp. 92–101, 2019, doi: 10.1080/20464177.2018.1505584
 7. I. Gospić, I. Glavan, I. Poljak, and V. Mrzljak, “Energy, economic and environmental effects of the marine diesel engine trigeneration energy systems,” *J. Mar. Sci. Eng.*, vol. 9, no. 7, p. 773, 2021, <https://doi.org/10.3390/jmse9070773>
 8. V. Palomba, G. E. Dino, R. Ghirlando, C. Micallef, and A. Frazzica, “Decarbonising the shipping sector: A critical analysis on the application of waste heat for refrigeration in fishing vessels,” *Appl. Sci. (Basel)*, vol. 9, no. 23, p. 5143, 2019, doi:10.3390/app9235143
 9. S. Du, “Thermal analysis of a forced flow diffusion absorption refrigeration system for fishing-boat exhaust waste heat utilization,” *Front. Energy Res.*, vol. 9, 2021, doi: 10.3389/fenrg.2021.761135
 10. Miro Petković, Marko Zubčić, Maja Krčum, Ivan Pavić “Wind assisted ship propulsion technologies – can they help in emissions reduction?,” *Nase More*, vol. 68, no. 2, pp. 102–109, 2021, doi:10.17818/NM/2021/2.6
 11. D. Karkosiński, W. A. Rosiński, P. Deinrych, and S. Potrykus, “Onboard energy storage and power management systems for all-electric cargo vessel concept,” *Energies*, vol. 14, no. 4, p. 1048, 2021, <https://doi.org/10.3390/en14041048>
 12. O. Farhat, J. Faraj, F. Hachem, C. Castelain, and M. Khaled, “A recent review on waste heat recovery methodologies and applications: Comprehensive review, critical analysis and potential recommendations,” *Cleaner Engineering and Technology*, vol. 6, no. 100387, p. 100387, 2022, <https://doi.org/10.1016/j.clet.2021.100387>.
 13. J. Zhemin and Y. Yuxin, “Analysis of waste heat utilization of ship main engine,” *E3S Web Conf.*, vol. 165, p. 06027, 2020, <https://doi.org/10.1051/e3sconf/202016506027>
 14. Y. A. Chaboki, A. Khoshgard, G. Salehi, and F. Fazelpour, “Thermoeconomic analysis of a new waste heat recovery system for large marine diesel engine and comparison with two other configurations,” *Energy Sources Recovery Util. Environ. Eff.*, pp. 1–26, 2020, doi: 10.1080/15567036.2020.1781298
 15. L. Mihanović, M. Jelić, G. Radica, and N. Račić, “Experimental investigation of marine engine exhaust emissions,” *Energy Sources Recovery Util. Environ. Eff.*, pp. 1–14, 2021, doi: 10.1080/15567036.2021.2013344
 16. UN Environment, “About Montreal protocol,” *Ozonaction*, 29 Oct 2018. [Online]. Available: <https://www.unep.org/ozonaction/who-we-are/about-montreal-protocol>. [Accessed: 28 Aug 2022].
 17. *Unfccc.int*, 1998. [Online]. Available: <https://unfccc.int/resource/docs/cop3/07a01.pdf>. [Accessed: 28 Aug 2022].
 18. *Europa.eu*. [Online]. Available: https://ec.europa.eu/clima/system/files/2020-03/swd_2019_406_en.pdf. [Accessed: 28 Aug 2022].
 19. “REFRIGERANT REPORT 21,” *Bitzer-refrigerantreport.com*. [Online]. Available: https://www.bitzer-refrigerantreport.com/fileadmin/Content/01_Startseite/A-501-21_EN.pdf. [Accessed: 28 Aug 2022].
 20. J. Bodys, J. Smolka, and K. Banasiak, “Design and simulations of refrigerated sea water chillers with CO2 ejector pumps for marine applications in hot climates,” International Institute of Refrigeration (IIR), 2018, <http://dx.doi.org/10.18462/iir.gl.2018.1244>
 21. A. N. Noskov, Thermal and structural calculation of a refrigeration screw compressor: Educational and methodological manual. *ITMO University*, 2015.

CONTACT WITH THE AUTHORS

Viktor Yalama

Olga Yakovleva*

Volodymyr Trandafilov

Mykhailo Khmelniuk

Odesa National University of Technology,
Refrigeration and Air-Conditioning Systems Department
(RACS), V.S. Martynovsky Institute of Refrigeration,
Cryotechnologies and Ecoenergetics
UKRAINE

JACKING AND ENERGY CONSUMPTION CONTROL OVER NETWORK FOR JACK-UP RIG: SIMULATION AND EXPERIMENT

Viet-Dung Do  ^{1,2}

Xuan-Kien Dang  ¹ *

Tien-Dat Tran  ¹

Thi Duyen-Anh Pham ¹

¹ Artificial Intelligent Transportation Research Group, Ho Chi Minh City University of Transport, Vietnam

² Dong An Polytechnic, Vietnam

* Corresponding author: kien.dang@ut.edu.vn (Xuan-Kien Dang)

ABSTRACT

Oil and gas projects differ from regular investment projects in that they are frequently large-scale, categorised as vital national projects, highly technological, and associated with significant risks. Drilling rigs are a crucial component of the oil and gas sector and the majority of the systems and equipment aboard drilling rigs are operated automatically. Consequently, it is crucial to address the topic of an advanced control theory for off-shore systems. Network technology connected to control is progressively being used to replace outdated technologies, together with other contemporary technologies. In this study, we examine how to adapt a networked control jacking system to the effects of internal and external disturbances with a time delay, using a Fuzzy controller (FC)-based particle swarm optimisation. To demonstrate the benefit of the proposed approach, the developed Fuzzy Particle Swarm Optimisation (FPSO) controller is compared with the fuzzy controller. Finally, the results from simulations and experiments utilising Matlab software and embedded systems demonstrate the suitability of the proposed approach.

Keywords: Networked control system, Environmental forces, Energy consumption, Fuzzy Particle swarm optimization, Jacking system, Time-delay

INTRODUCTION

In the role of exploiting oil and gas from below the oceans, several locations are planned for numerous small-scale drilling rigs, all of which are connected to, and communicate with, one another (for example, the Dai Hung 01 and Dai Hung 02 rigs in the Vietnam's continental shelf). Typically, one rig will serve as the operations centre, fully outfitted with monitoring technology for the other dependent rigs and manned by people, as shown in Fig. 1. The other, smaller, rigs are known as 'slavers' and the majority of them are automated, being run by a central rig with no operator. Underground power lines link the slavers, the majority of which do not yet include wireless monitoring,

control systems or network control. The fundamental cause of this is that the control algorithms have not encountered the safety expectations required when the system is controlled over a network. As a result, experts still attempt to remotely operate systems and equipment that are located offshore. The model must be tested and analysed in simulated environments before being applied in natural settings.

Jack-up platforms have been used for drilling, workover, and offshore oil and gas exploration for many years. In the process of jacking up a Jack-up Rig (JuR), there are numerous approaches [1-4] to controlling stability and reducing the forces that affect them. Even though each approach has its advantages, the study of intelligent control algorithms continually pushes

experts to find theoretical and practical solutions to help the system run more consistently and securely, and to carry out many more tasks than were previously conceivable. Many academics are devoted to developing improved technology and artificial intelligence because of the exceptional benefits that may be possible [5–10]. Fuzzy [5], Hybrid Fuzzy [6], Fuzzy Adaptive [7], Neural Network [8], Genetic Algorithm (GA) [9], and Particle Swarm Optimisation (PSO) [10] are a few of the recommended advanced control approaches that have demonstrated their efficacy and stability. In addition, there has been a lack of investigation into utilising existing control theory to improve the performance and efficacy of controllers, particularly complex systems or systems controlled through networks. The stability and continuity of the system is greatly influenced by time-delay and disturbances. Therefore, the method of control based on randomness also takes network technology, transmission speed, and packet drop-out data into consideration.

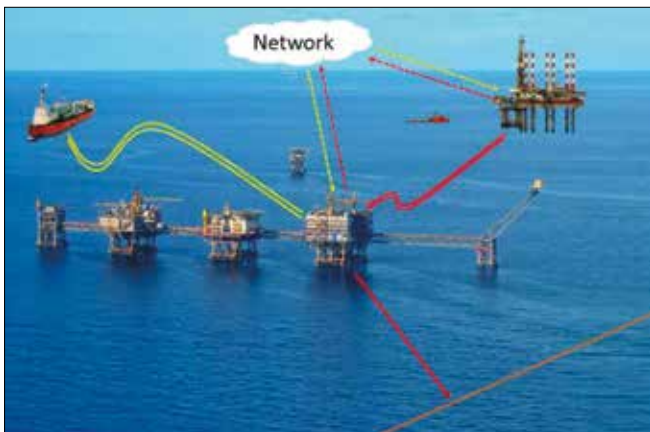


Fig. 1. The idea of network control systems for a Jack up Rig in off-shore systems

Recent literature has achieved a lot of innovative results, with respect to Fuzzy Control (FC) [6-7], which copes with problems of unpredictability, disturbance, and time-delay. This method was developed based on natural language; it can produce estimates that are more accurate and reflect the true nature of the issues. The fuzzy controller may be adjusted appropriately, and in an efficient manner, because of the use of metaheuristic algorithms, like the PSO. By using this method, the FLC may be easily adjusted to provide the appropriate performance without the need for extensive traditional testing. Within the limitations of a class of switching signals with typical dead-time, the FC technique maintains all closed-loop signals. It is also believed that the Adaptive Fuzzy Control (AFC) is a useful strategy for enhancing the performance of the fuzzy controller, particularly for Self-Adaptive Fuzzy Control (SAFC) [11–13], FPSO [14]. On the other hand, to improve the SAFC's flexibility and stability, optimum algorithms like GA and PSO are being researched and used in conjunction with fuzzy logic. Concerning networked control systems, FC is used to approximate the unknown nonlinear characteristics occurring in the system, while the Pade approximation was launched to handle network-induced delays [15]. In addition, model free fuzzy adaptive control has also

been proposed for networks and, in this case, the controller can track the reference trajectory satisfactorily, even in the presence of unmeasured disturbances and network-induced time delays [16]. It should be noted that, these factors motivated us to choose to employ the innovative technique for the JuR's jacking networked system, as it must operate in difficult environmental and network conditions.

Automated controllers are not essential in the process of constructing rigs in Vietnam and networked control is also not a key issue in the study. Considering that the fuzzy system may approximate a nonlinear composition, the hierarchical fuzzy model is an excellent technique for the JuR, with unexpected effects of time-delays and disturbances. To solve the mentioned problems, we proposed the PSO-based FC to improve the performance of the JuR's jacking networked control system by simulation. However, experimental validation of the proposed controller on the model is necessary in order to deploy the research outcome to the offshore industry. The study's main contributions include the following:

- (1) Developing a mathematical model of the Jacking system (JS) and incorporating it into a networked model.
- (2) Outlining a networked control model with the FPSO controller, considering the fact that the conventional controller designed for the JS is not that practical in light of disturbances and time-delays, including network issues.
- (3) Simulating and testing the FPSO controller in the model was contrasted with the other controller, to demonstrate the novelty of the proposed strategy.

The structure of this paper is as follows. Section 2 presents the mathematical model of the JS-included network and Section 3 analyses the factors which are already impacted, such as internal and external load and networked-induced delay. The FPSO control strategies are outlined in Section 4. Discussion of the simulation and experimental studies is presented in Section 5 and the study's concluding remarks are addressed in Section 6.

MATHEMATICAL MODEL OF THE JACKING CONTROL SYSTEM

The two most popular techniques for static or dynamic analysis of the JuR are the direct finite-element methodology [17] and the simple beam approach [18]. In the first approach, the rig is viewed as a spatial lattice frame structure with the forces and displacements in each member taken into account. In the other approach, the entire rig is replaced by a uniform beam carrying a lumped mass, designed to allow its static or dynamic behaviour to be predicted using straightforward theoretical formulas. The first technique is too complex to supply essential design knowledge, while the second is too straightforward to offer reliable information, hence neither should be used in the early phases of design. Because of this, it is simple to derive the equations of motion for the JuR by first determining the equations of motion for each leg and the upper hull separately, then integrating them, while enforcing the constraints of deformation compatibility and

As a similar type of networked control system (NCS), the insight diagram of the FPSO control through the network is presented in Fig. 2. The fuzzy system includes the double-inputs p_e , dp_e/dt , and single-output τ^* [7], and the fuzzy rule comprises a set of IF-THEN forms within θ^i :

$$\text{If } \sigma_1 \text{ is } K_1^i, \dots, \sigma_n \text{ is } K_n^i \text{ then } \tau^* \text{ is } \theta^i \quad (11)$$

Therein, $K_1^i, K_2^i, \dots, K_n^i \in R^h$ and are the input variables and output variables of the fuzzy system [7], respectively. By using the fuzzy system with the fuzzy rule (11), the Max-Prod inference rule, the singleton fuzzifier, the product inference engine and centre average defuzzifier, the output response τ^* is defined as follows:

$$\tau^*(\sigma) = \frac{\sum_{i=1}^m \theta^i [\prod_{j=1}^n \mu_{K_j^i}(\sigma_j)]}{\sum_{i=1}^m [\prod_{j=1}^n \mu_{K_j^i}(\sigma_j)]} \quad (12)$$

for $\mu_{K_j^i}(\sigma)$ expresses the membership functions (MFs) with m as the number of fuzzy rules. We get

$$T^{*T} = [\bar{\tau}^{*1}, \bar{\tau}^{*2}, \dots, \bar{\tau}^{*m}]^T \in R^m \quad (13)$$

as the vector of the fuzzy parameter. The fuzzy basis functions with ϕ are written as

$$\phi_i(\sigma) = \frac{\sum_{i=1}^m \theta^i [\prod_{j=1}^n \mu_{K_j^i}(\sigma_j)]}{\sum_{i=1}^m [\prod_{j=1}^n \mu_{K_j^i}(\sigma_j)]} \quad (14)$$

and notate $\phi_i(\sigma) = [\phi_1(\sigma), \phi_2(\sigma), \dots, \phi_m(\sigma)]^T$ as the fuzzy basis function vector. Then, the fuzzy system (12) is able to represent the linear parametric form as:

$$\tau^*(\sigma) = T^T \phi(\sigma). \quad (15)$$

Lemma 1 [21]: Let $\varphi(\sigma)$ be a continuous function defined on a compact set $\Omega \subset R^n$. Then, for any constant $\xi < 0$, there exists a fuzzy system $\tau^*(\sigma)$ in the form of Eq. (12), as

$$\sup_{\sigma \in \Omega} |\varphi(\sigma) - T^{*T} \phi(\sigma)| \leq \xi \quad (16)$$

By *Lemma 1*, the nonlinear function $\varphi(\sigma)$ can be approximated as

$$\phi(\sigma, T^*) = T^{*T} \phi(\sigma). \quad (17)$$

Define

$$T^{**} = \arg \min_{T^* \in \Omega} [\sup_{x \in Z} |\phi(\sigma) - \phi(\sigma, T^*)|] \quad (18)$$

where Z and Ω are compact regions for σ and T^* , respectively. Consequently, the minimum approximation error is determined as:

$$\xi = \phi(\sigma) - T^{**T} \phi(\sigma). \quad (19)$$

The demonstration in [21] indicates that the control system is asymptotically stable with the *Lemma 1* after attaining Eq. (19). PSO is tasked with identifying the appropriate fuzzy

set parameters that meet the requirements within Remark 1 and Remark 2 below:

Remark 1: Finding convergence for the best algorithms is a time-consuming task. There are several parameters that need to be tuned as the computing speed rapidly decreases.

Remark 2: The optimal parameter quality depends on the number of generations and the fitness function value $f_{FP}(t)$. If a small value is used, the convergence value is local. However, in the case of using the large value, the processing time will be slow.

Consequently, in order to increase processing speed (Remark 1) and ensure optimal parameter quality (Remark 2), a limit function approximates the goal value in Eq. (20) for quality relative to the target but, also, in a smaller space and with fewer occurrences. The fitness function value and the number of individuals are guaranteed, as in Eq. (21) and (22).

$$\lim_{t \rightarrow \infty} \|\tilde{f}_{FP}\| = \lim_{t \rightarrow \infty} \|f_{FP}^0 - f_{FP}\| = 0 \quad (20)$$

Concerning the relation between the importance of fitness and iteration constraints [22], the fitness function value and the number of individuals are guaranteed, as in Eq. (21) and (22).

$$iter_m^{min} \leq iter_m \leq iter_m^{max} \quad (21)$$

$$f_{FP}^{min} \leq f_{FP} \leq f_{FP}^{max} \quad (22)$$

In particular, PSO aims to identify the best MFs value, in order to help increase processing speed. Therefore, Algorithm 1 is used to make decisions regarding coefficient γ_i based on the PSO algorithm [10], in order to enhance control quality in a time-varying situation.

Algorithm 1: Dynamically learned PSO algorithm for proposed FPSO	
1	Initialize the position $\gamma_{ij}^p(t)$ and the velocity $v_{ij}(t)$ randomly.
2	Initialize correction coefficient γ_i ($\gamma_1, \gamma_2, \gamma_3, \gamma_4$).
3	while $iter_m^{min} \leq iter_m \leq iter_m^{max}$ do
4	for each iteration l do
5	update the profits of $\gamma_{ij}^p(t)$ and $\gamma_{ij}^{cp}(t)$ using Eqs. (23) and (24)
	$\gamma_{ij}^p(t+1) = \begin{cases} \gamma_{ij}^p(t), & \text{if } J(\gamma_{ij}^p(t+1)) \geq J(\gamma_{ij}^p(t)) \\ \gamma_{ij}^p(t+1), & \text{otherwise} \end{cases} \quad (23)$
	$\gamma_{ij}^{cp}(t+1) = \arg \min_{\gamma_{ij}^p} J(\gamma_{ij}^p(t+1)), 1 \leq i \leq s \quad (24)$
6	initialize the particle attribute $v_{ij}(k)$ using Eq. (25)
	$v_{ij}(t+1) = w(k)v_{ij}(t) + c_1r_1[\gamma_{ij}^{cp}(t) - \gamma_{ij}^p(t)] + c_2r_2[\gamma_{ij}^{cp}(t) - \gamma_{ij}^p(t)] \quad (25)$
	for
	$w(g) = \frac{(iter_{max} - g)(w_{max} - w_{min})}{iter_{max}} + w_{min} \quad (26)$
7	determine a new point $\gamma_{ij}^p(t)$ using Eq. (27)
	$\gamma_{ij}^p(t+1) = \gamma_{ij}^p(t) + v_{ij}(t+1) \quad (27)$
8	use the new coefficient $\gamma_{ij}^p(t)$ to correct the amplitude profits of the MFs, then define a fitness condition according to Eq. (28).
	$f_{FP}(t) = \int_0^{\infty} t p_e(t) dt$ guaranteed fitness constraints $f_{FP}^{min} \leq f_{FP} \leq f_{FP}^{max}$ (28)
9	compare the latest profits of the MFs to the termination condition. If the convergence condition is not satisfied, increase l and go back to Step 5.
10	end
11	end

The implementation of particle swarm optimisation (PSO) is simple and computationally effective. In our scenario, the membership functions' centres, widths, and weights are contained in the particles. The dimension of particles is determined by the number of parameters. The PSO is applied off-line to tune the membership functions. The FPSO

performance is defined as:

$$\tau_p^*(\sigma) = \frac{\sum_{i=1}^m \theta^i [\prod_{j=1}^n \mu_{K_{vj}^i}(\sigma_j)]}{\sum_{i=1}^m [\prod_{j=1}^n \mu_{K_{vj}^i}(\sigma_j)]}, \quad (29)$$

where $\mu_{K^i}(\sigma_i) = [\gamma_1(K_1^1, K_1^2, \dots, K_1^i)]$ expresses the error fuzzy set $p_e(t)$, $\mu_{K^i}(\sigma_i) = [\gamma_2(K_2^1, K_2^2, \dots, K_2^i)]$, indicates the error-velocity fuzzy set dp_e/dt , and $\theta^i = [(\gamma_3 + \gamma_4/s)(\theta^1, \theta^2, \dots, \theta^i)]$ are the so-called 'output fuzzy set' $\tau_p^*(\sigma)$. Then, $\phi_y(\sigma) = [\phi_y^1, \phi_y^2, \dots, \phi_y^m] \in R^m$ represents the fuzzy basis vector as

$$\phi_y(\sigma) = \frac{[\prod_{j=1}^n \mu_{K_{vj}^i}(\sigma)]}{\sum_{i=1}^m [\prod_{j=1}^n \mu_{K_{vj}^i}(\sigma)]}. \quad (30)$$

The PSO algorithm modifies the values of the fuzzy set with coefficient $\gamma_i(\gamma_1, \gamma_2, \gamma_3, \gamma_4)$ to define the best correction coefficient γ_i . An extremely high value of the control force might cause an imbalance in the JuR's overall energy system. The issue of energy consumption must be addressed, to achieve optimal management, and our goal is to use the least amount of energy possible while also boosting the amount of continuous electric supply that is required. In light of this, the desire may be summarised as follows [22]:

$$\text{Maximise}(\alpha_{uc} \vartheta_{\tau_{pc}^*} + \alpha_{es} \vartheta_{es}) \in [0,1], \quad (31)$$

where $\vartheta_{\tau_{pc}^*}$ is the stable electric coefficient and ϑ_{es} is the energy savings coefficient. $\alpha_{\tau_{pc}^*}$ and α_{es} define weights for stable electric and energy saving, respectively, setting $\alpha_{\tau_{pc}^*} + \alpha_{es} = 1$. Hence, the increase ϑ_{es} is proportional to the decrease in energy consumption U_e :

$$\vartheta_{es} \propto \frac{1}{U_e}. \quad (32)$$

The gains in energy savings can be expressed as [22]:

$$\vartheta_{es}(\tau_p^*) = \left(1 - \left(\frac{U_0 - U_{min}}{\Delta U}\right)^2\right) \in [0,1]. \quad (33)$$

Obviously, the energy system should guarantee that optimal condition (U_0) approaches the lowest possible energy consumption and ϑ_{es} increases, resulting in the greatest energy savings. In other words, we want to find U_0 values that will give the optimisation function in Eq. (33) the best value possible. However, higher values of $\tau_{p0}^*(\sigma)$ will result in a loss in the energy component, i.e. higher values of $\tau_{p0}^*(\sigma)$ causes $U_0 \rightarrow U_{max}$ and, thus, $\frac{U_0 - U_{min}}{\Delta U} \rightarrow 1$, which results in losing the gain in the energy component. Equation (33) achieves our intended goal of balancing stable electric and energy consumption. The constraints are specified as:

$$0 \leq U_{min} \leq U_0 \leq U_{max}. \quad (34)$$

Related to the time-delay problem, the response of the NCS will be lowered by the network-induced delay, causing errors in the data transmission process $e^{-d_{cas}}$ [27-28]. Typically, the delay of the control signal d_{ca} transmits to the JuR dynamic model. Therefore, the signal $\tilde{\tau}_p(\sigma)$ of the FPSO controller transmits information over the network as follows:

$$\tilde{\tau}_p(\sigma) = \tau_p^*(\sigma)e^{-d_{cas}} \quad (35)$$

The sensor-to-controller delay causes an error in the JS response ($e^{-d_{cas}}$), giving

$$p_j(s) = p_j^*(s)e^{-d_{cas}} \quad (36)$$

From Eqs. (35) and (36), the problems of d_{sc} and d_{ca} reduce the quality of the jacking system control over the network. So, the control force and torque vectors at each truss leg are rewritten as

$$\tilde{\tau}_p = [\tilde{\tau}_{pA}, \tilde{\tau}_{pB}, \tilde{\tau}_{pC}]^T \quad (37)$$

The control signals of each actuator consist of two components: amplitude and direction of force. The control force vectors from the thrust allocation to the actuator are determined as follows:

$$F_i = [\tilde{\tau}_p^T, \alpha^T]^T \in R^{2r} \quad (39)$$

EXPERIMENTAL MODEL DESIGN

MECHANICAL POWERTRAIN AND EMBEDDED SYSTEM DESIGN

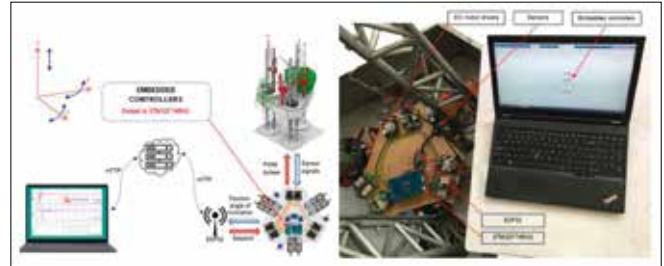


Fig. 3. Overall structure of UT-JuR 01

The position state variable of the JuR-hull served as the foundation for the experimental model, identified as UT-JuR 01, and is described in detail in Fig. 3. This integrated controller compares the instantaneous position signal to the desired position, to determine the incorrect location. The controller then uses the inaccurate number as a starting point to calculate the motor's lifting force to raise the JuR-hull to the designed position. The main components and functions of the UT-JuR 01 model are as follows:

- The 24 VDC power supplies voltage power to the control modules. A 24 VDC to 5 VDC voltage converter was used to power the STM32F746NG and ESP32 central processors, a 24 VDC to 3.3 VDC voltage converter to power the sensor block (IMU MPU6050 and Encoder), and a 24 VDC to 12 VDC voltage converter to power the DC Drivers block.
- The mounted IMU sensor monitored the platform inclination while the displacement sensor (Encoder) measured the location of the JuR-hull at the legs. The central processor STM32F746NG received feedback signals through an ADC converter circuit. Besides this, the supervisor station received the feedback values from the NCS via the ESP32 module.

- The central processor STM32F746NG computed the control force values based on the errors between the desired position and the actual position. This control signal was converted to a PWM pulse, to manage the speed and direction of the DC motors (via the DC Drivers) and to raise and lower the JuR-hull to the desired position.

CONTROL ALGORITHM

The testing control process in the UT-JuR 01 was performed in accordance with Algorithm 2. The ESP32 module received the feedback signal of the JuR's real position throughout this process and sent the data it contained to the supervisor station over the network. The supervisor station, on the other hand, employed the HTTP protocol to retrieve data.

```

Algorithm 2: Control over the network
1 Initialise JuR desired position  $p_d$ , inclination angle, speed and bit number of data transfer.
2 Initialise collection date of set-points (ESP32: Position and angle of inclination).
3 Initialise disturbance filter.
4 while Desired position do
5   for each control cycle do
6     (a) Determining position erroneous  $p_e$ .
7     (b) Using the Fuzzy PSO strategy to compute the control force  $\tau_p^*(\sigma)$ .
8     (c) Converting the output control signal to PWM pulse for DC motors.
9     (d) Defining the JuR actual position  $p_j$  using sensors (Encoder, IMU, distance).
10    (e) Transferring the JuR operation data to the cloud (ESP32: Position and inclination angle).
11    (f) Comparing the latest JuR position  $p_j$  to the termination condition  $p_d$ . If the JuR position is not satisfied, increase control cycle and go back to Step 6.
12  end
13 end

```

SIMULATION AND EXPERIMENTAL EVALUATION

SIMULATION RESULTS

In order to evaluate the efficacy of the suggested approach, this paper performed and compared simulations between the FPSO controller and the fuzzy controller [24], utilising the TamDao05 JuR model parameters that were used in this work at 1:100 scale. Matlab 2019a software was also used to simulate the controller and was developed using the same ambient variables and jacking system specifications [14], with reference to the environmental effect factors. Using the *m.file* that connects

to Simulink, the PSO algorithm finds the fuzzy controller's optimum, to have the best convergence on the control.

The response time of the JuR employing the FPSO controller is faster than the FC by approximately 3.5 s, in the case of the simulation without environmental influences (shown in Fig. 4(a)). Additionally, the fluctuation amplitude is around 0.12 cm less than the conventional solution. The comparable results indicate that the FPSO solution satisfies the criteria and this controller can guarantee the JuR model's high response quality in NCS circumstances. Besides this, the JuR-hull position's stability under changing weather conditions in the case of the JS is guaranteed by the FPSO controller. Figure 4(b) demonstrates that employing the proposed FPSO results in fluctuations that are 0.22 cm lower and 3.4 seconds faster than when using the FC controller. The performance of the jacking system using the FC controller meets the control requirements, in the case without environmental impacts, but does not achieve the requirements in the case with environmental impacts. However, the FPSO gave a satisfactory performance in all simulation scenarios.

Tab. 1. A response comparison of several controllers for simulation outcomes.

Simulation scenarios	Response time		Fluctuation		Overshoot	
	Fuzzy	FPSO	Fuzzy	FPSO	Fuzzy	FPSO
0 cm – 10 cm	5.5 s	3.5 s	0.45 cm	0.22 cm	4.0 cm	4.5 cm
0 cm – 30 cm	7.0 s	4.5 s	0.50 cm	0.25 cm	5.5 cm	6.5 cm
0 cm – 30 cm – 60 cm	6.5 s	4.5 s	0.55 cm	0.35 cm	6.0 cm	6.5 cm

In circumstances when the truss body was elevated and lowered by 0-10 cm (scenario 1), 0-30 cm (scenario 2), and 0-30-60 cm (scenario 3), Table 1 displays the comparative findings (scenario 3). The FPSO solution responds faster than the original FC approach [24], with response times of 2.0 s, 2.5 s, and 2.0 s for scenarios 1, 2, and 3, respectively. Besides this, the fluctuation amplitude of the FPSO solution is 0.22 cm, 0.25 cm, and 0.35 cm in three scenarios, which is lower than the case of using an FC controller, thereby verifying the quality of the proposed solution. Positive results indicate that the

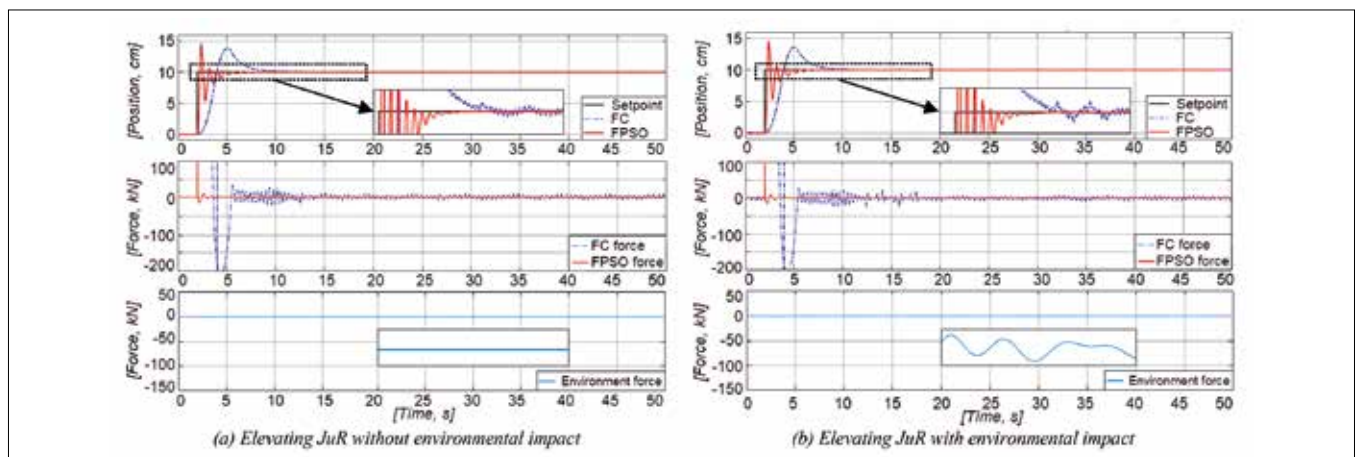


Fig. 4. FPSO controller simulation results compared with FC using control over the network

proposed approach offers better response quality than the FC controller due to the optimal correction coefficient. The FPSO approach with the energy consumption function restrictions (34), guarantees that the cost overshoot value is always within allowable limits when the network control environment influences the control process and causes errors $e^{-d_{cas}}$, $e^{-d_{scs}}$. Last but not least, the proposed controller FPSO can adapt to the environmental impact by optimal adjustment of the control parameter (the coefficient γ). However, the proposed algorithms need to test other actual conditions, in order to verify the advantages in the future.

RESULTS

Testing of the UT-JuR 01-embedded experimental model was carried out in two scenarios, the operating parameters of the

UT-JuR 01 were updated online (to the database using the ESP32 module), and the supervisory station continuously retrieved data to synthesize commands. The obtained experimental results are shown in Fig. 5 and Fig. 6. The experimental process was carried out in the two scenarios below:

- Scenario 1: The jacking lifts the JuR-hull from position 0 cm to 30 cm and maintains status in 580 seconds;
- Scenario 2: The JuR-hull is raised to a position of 60 cm from the reference position of 30 cm and maintains status in 580 seconds.

The fluctuation amplitude of the low JuR's legs is 1.35 cm (4.5%) for case 1 and 1.25 cm (2.1%) for case 2. Consequently, the results show that the FPSO solution, controlled via NCS, meets the quality requirements of 6%. The response time for the first case is 120 s and 135 s for the second case. The minimum response time for fluctuation stopping reaches the

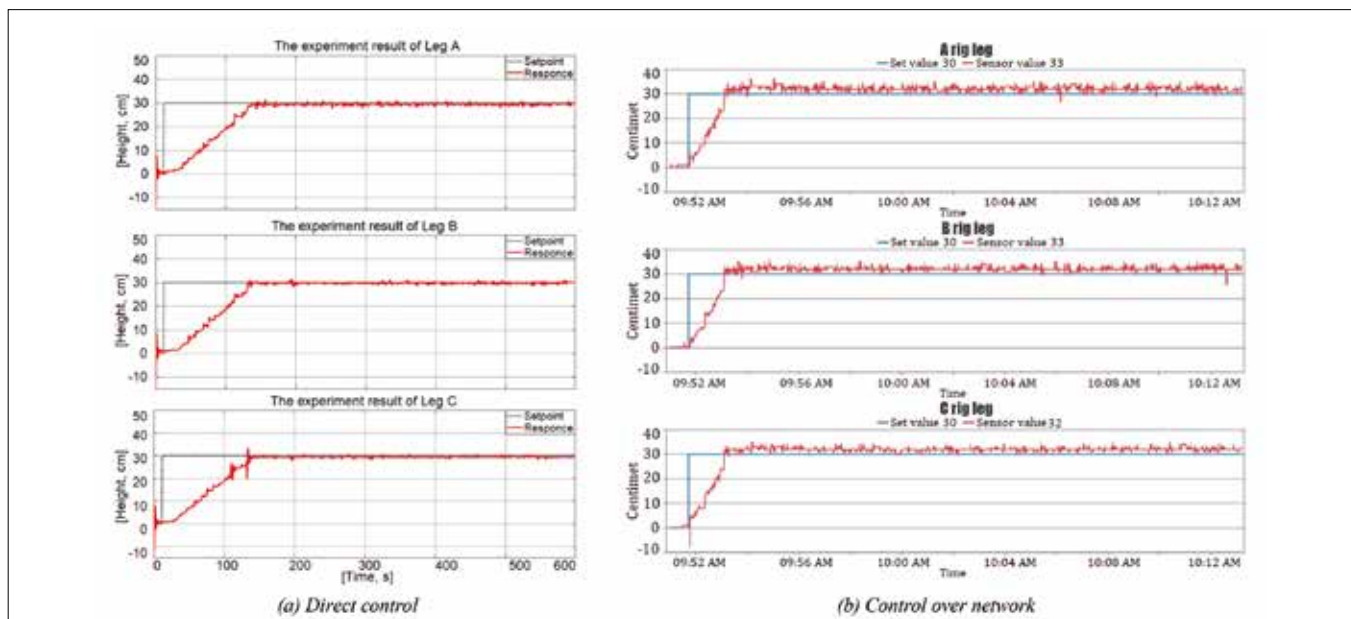


Fig. 5. Results of an experiment to move the JuR from a position of 0 cm to 30 cm

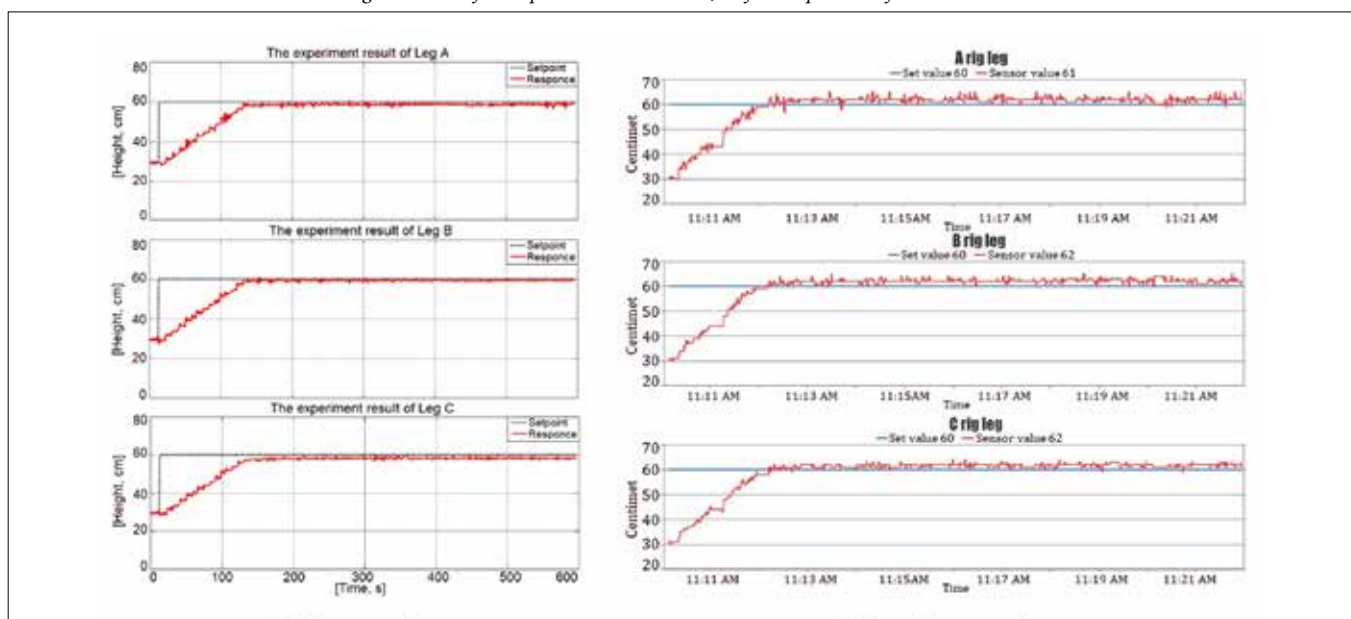


Fig. 6. Results of an experiment to move the JuR from a position of 30 cm to 60 cm

equilibrium value in 4.0 to 5.0 s, in experimental cases within the allowable limit (5.5 s). The direct control test (Figs. 5a and 6a) and over network control (Figs. 5b and 6b) yield identical findings.

Tab. 2. A response comparison of several solutions for experimental outcomes.

Experimental scenarios	Solution		Leg A	Leg B	Leg C	Centre of JuR
30–60 cm	Direct control Control network	over	59.55 60.60	59.75 60.85	59.60 61.05	59.65 60.65
30–80 cm	Direct control Control network	over	79.25 80.65	79.35 81.20	79.30 81.25	79.25 81.15

NB: All measurements are in cm

Table 2 provides further information comparing the testing scenario (30-60 cm and 30-80 cm) response outcomes for leg position and rig centre, while carrying out further control of the model using the network, demonstrating the precision of the data transfer technique used to operate the rig over the network. To meet the quality requirements, the position divergence amplitude, comparing the direct control and the networked control of the 30-60 cm scenario, is between 0.45 cm and 1.10 cm. In the 30-80 cm scenario, position divergence amplitude is between 0.85 cm and 1.40 cm. Compared to direct control, control over network outcomes guaranteed the quality of the system's reaction. Furthermore, the response exhibits duplicated values (displayed as a straight line) at some locations due to the slow speed of data transfer and delays.

CONCLUSION

This paper includes a brief discussion of the JuRs' system design, particularly in the jacking system. Employing an analysis of the JuR's motions along the axis, the mathematical modelling of the jacking system is developed. Additionally, it is thought that the PSO algorithm is a suitable approach for fuzzy adaptive control systems, to improve the performance of the fuzzy controller. Evidence of the proposed FPSO's simulation and experimental performance compared with the Fuzzy controller in the case of the control-induced network, showed the enhanced flexibility and stability of the approach. By using mathematical justifications, the energy system would do well to ensure that the optimal condition (U_0) approaches the lowest possible energy consumption; Eq. (33) achieves our goal of balancing stable electricity and energy consumption. Finally, the UT-JuR 01 model's experimental validation of the problem of energy conservation has not yet been completely tested and evaluated, despite careful analysis.

REFERENCES

1. J.T. Yi, F. Liu, T.B. Zhang, Z.Z. Qiu, and X.Y. Zhang, "Determination of the ultimate consolidation settlement of jack-up spudcan footings embedded in clays," *Ocean Eng.*, vol. 236, pp. 1-13, 2021, doi: 10.1016/j.oceaneng.2021.109509.
2. Q. Yin, J. Yang, G. Xu, R. Xie, M. Tyagi, L. Li, X. Zhou, N. Hu, G. Tong, C. Fu, and D. Pang, "Field experimental investigation of punch-through for different operational conditions during the jack-up rig spudcan penetration in sand overlying clay," *J. Petroleum Sci. Eng.*, vol. 195, pp. 1-21, 2020, doi: 10.1016/j.petrol.2020.107823.
3. F. Wang, W. Xiao, Y. Yao, Q. Liu, and C. Li, "An Analytical Procedure to Predict Transverse Vibration Response of Jack-Up Riser under the Random Wave Load," *Shock and Vibration*, vol. 2020, pp. 1-9, 2020, doi: 10.1155/2020/5072989.
4. Y. Xie, J. Huang, X. Li, X. Tian, G. Liu, and D. Leng, "Experimental study on hydrodynamic characteristics of three truss-type legs of jack-up offshore platform," *Ocean Eng.*, vol. 234, pp. 1-15, 2021, doi: 10.1016/j.oceaneng.2021.109305.
5. M. Pająk, L. Muślewski, B. Landowski, and A. Grządziela, "Fuzzy Identification of the Reliability State of the Mine Detecting Ship Propulsion System," *Polish Marit. Res.*, vol. 26, no. 1, pp. 55-64, 2019, doi: 10.2478/pomr-2019-0007.
6. M. Pashna, R. Yusof, Z.H. Ismail, T. Namerikawa, and S. Yazdani, "Autonomous multi-robot tracking system for oil spills on sea surface based on hybrid fuzzy distribution and potential field approach," *Ocean Eng.* vol. 207, pp.1-11, 2020, doi: 10.1016/j.oceaneng.2020.107238.
7. X.K. Dang, V.D. Do, and X.P. Nguyen, "Robust Adaptive Fuzzy Control using Genetic Algorithm for Dynamic Positioning System," *IEEE Access*, vol. 8, pp. 222077–222092, 2020, doi: 10.1109/ACCESS.2020.3043453.
8. T. Cepowski, P. Chorab, and D. Łozowicka, "Application of an Artificial Neural Network and Multiple Nonlinear Regression to Estimate Container Ship Length Between Perpendiculars," *Polish Marit. Res.*, vol. 28, no. 2, pp. 36-45, 2021, doi: 10.2478/pomr-2021-0019.
9. R. Zagan, I. Paprocka, M.G. Manea, and E. Manea, "Estimation of Ship Repair Time Using the Genetic Algorithm," *Polish Marit. Res.*, vol. 28, no. 3, pp. 88-99, 2021, doi: 10.2478/pomr-2021-0036.
10. L. Zhang, J. Sun, and C. Guo, "A Novel Multi-Objective Discrete Particle Swarm Optimisation with Elitist Perturbation for Reconfiguration of Ship Power System," *Polish Marit. Res.*, vol. 24, no. s3, pp.79-85, 2017, doi: 10.1515/pomr-2017-0108.

11. X. Gu and Q. Shen, "A self-adaptive fuzzy learning system for streaming data prediction," *Information Sci.*, vol. 579, pp. 623-647, 2021, doi: 10.1016/j.ins.2021.08.023.
12. S. Buzura, V. Dadarlat, B. Iancu, A. Peculea, E. Cebuc, and R. Kovacs, "Self-adaptive Fuzzy QoS Algorithm for a Distributed Control Plane with Application in SDWSN," 2020 IEEE International Conference on Automation, Quality and Testing, Robotics (AQTR), pp. 1-6, 2020, doi: 10.1109/AQTR49680.2020.9129922.
13. T. Vinu, S. Kumaravel, and S. Ashok, "Fuzzy Controller-Based Self-Adaptive Virtual Synchronous Machine for Microgrid Application," *IEEE Transactions on Energy Conversion*, vol. 36, no. 3, pp. 2427-2437, 2021, doi: 10.1109/TEC.2021.3057487.
14. T.D. Tran, V.D. Do, X.K. Dang, and B.L. Mai, "Improving the Control Performance of Jacking System of Jack-Up Rig Using Self-Adaptive Fuzzy Controller Based on Particle Swarm Optimisation," 8th EAI International Conference, INISCOM 2022, pp. 184-200, 2022, doi: 10.1007/978-3-031-08878-0_13.
15. C. Wu, J. Liu, X. Jing, H. Li, and L. Wu, "Adaptive Fuzzy Control for Nonlinear Networked Control Systems," *IEEE Transactions on Systems, Man, and Cybernetics: Systems*, vol. 47, no. 8, pp. 2420-2430, 2017, doi: 10.1109/TSMC.2017.2678760.
16. M.B. Kadri and S.M.K. Raazi, "Model Free Fuzzy Adaptive Control for Networked Control Systems," *Technology Forces J. Eng. Sci.*, vol. 2, no. 1, pp. 9-19, 2019.
17. W. Deng, X. Tian, X. Han, G. Liu, Y. Xie, and Z. Li, "Topology optimisation of jack-up offshore platform leg structure," *Proc. Inst. Mech. Engineers M, J. Eng. Maritime Environ*, vol. 235, no. 1, pp. 165-175, 2021, doi: 10.1177/1475090220928736.
18. Y.F. Fan and J.H. Wang, "Method to evaluate effect of spudcan penetration on adjacent jacket piles," *Appl. Ocean Res.*, vol. 106, pp. 1-14, 2021, doi: 10.1016/j.apor.2020.102436.
19. B. Rozmarynowski and W. Jesien, "Spectral Response of Stationary Jack-Up Platforms Loaded by Sea Waves and Wind using Perturbation Method" *Polish Marit. Res.*, vol.28, no. 4, pp.53-62, 2021, doi: 10.2478/pomr-2021-0049.
20. Z. Chao, H. Hong, B. Kaiming and Y. Xueyuan, "Dynamic amplification factors for a system with multiple-degrees-of-freedom," *Earthquake engineering and engineering vibration*, vol. 19, no. 2, pp. 363-375, 2000, doi: 10.1007/s11803-020-0567-9.
21. W. Min and Q. Liu, "An improved adaptive fuzzy backstepping control for nonlinear mechanical systems with mismatched uncertainties," *Automatika*, vol. 60, no. 1, pp. 1-10, 2019, doi: 10.1080/00051144.2018.1563357.
22. I. Ullah and D. Kim, "An Improved Optimisation Function for Maximising User Comfort with Minimum Energy Consumption in Smart Homes," *Energies*, vol. 10, no. 11, pp. 1818, 2017, doi: 10.3390/en10111818.
23. D.P. Kumar, "Particle Swarm Optimisation: The Foundation," *International Series in Operations Research & Management Science*, vol. 306, pp. 97-110, 2021, doi: 10.1007/978-3-030-70281-6_6.
24. V.D. Do, X.K. Dang, and A.T. Le, "Fuzzy Adaptive Interactive Algorithm for Rig Balancing Optimisation," *International Conference on Recent Advances in Signal Processing, Telecommunication and Computing*, pp. 143-148, 2017, doi: 10.1109/SIGTELCOM.2017.7849812.
25. K.S. Ahmed, A.K. Keng, and K.C. Ghee, "Stress and stiffness analysis of a 7-teeth pinion/rack jacking system of an Offshore jack-up rig," *Eng. Failure Analysis*, vol. 115, pp. 104623, 2020, doi: 10.1016/j.engfailanal.2020.104623.
26. Z.M. Ghazi, I.S. Abbood, and F. Hejazi, "Dynamic evaluation of jack-up platform structure under wave, wind, earthquake and tsunami loads," *J. Ocean Eng. Sci.*, vol. 7, pp. 41-57, 2022, doi: 10.1016/j.joes.2021.04.005.
27. H.D. Tran, Z.H. Guan, X.K. Dang, X.M. Cheng, and F.S. Yuan, "A Normalized PID Controller in Networked Control Systems with Varying Time Delays," *ISA Transactions*, vol.52, pp. 592-599, 2013, doi: 10.1016/j.isatra.2013.05.005.
28. X.K. Dang, Z.H. Guan, T. Li, and D.X. Zhang, "Joint Smith Predictor and Neural Network Estimation Scheme for Compensating Randomly Varying Time-delay in Networked Control System," *The 24th Chinese Control and Decision Conference*, pp. 512-517, 2015, doi: 10.1109/CCDC.2012.6244077.

CONTACT WITH THE AUTHORS

Xuan-Kien Dang

e-mail: kien.dang@ut.edu.vn

Artificial Intelligent Transportation Research Group
Ho Chi Minh City University of Transport
VIETNAM

Tien-Dat Tran

Artificial Intelligent Transportation Research Group
Ho Chi Minh City University of Transport
VIETNAM

Thi Duyen-Anh Pham

Artificial Intelligent Transportation Research Group
Ho Chi Minh City University of Transport
VIETNAM

Viet-Dung Do

Artificial Intelligent Transportation Research Group
Ho Chi Minh City University of Transport
Dong An Polytechnic
VIETNAM

MATHEMATICAL MODELLING OF MARINE POWER PLANTS WITH THERMOCHEMICAL FUEL TREATMENT

Oleksandr Cherednichenko  ¹

Serhiy Serbin  ¹ *

Mykhaylo Tkach  ¹

Jerzy Kowalski  ²

Daifen Chen  ³

¹ Admiral Makarov National University of Shipbuilding, Nikolaev, Ukraine

² Gdansk University of Technology, Poland

³ Jiangsu University of Science and Technology, China

* Corresponding author: serbin1958@gmail.com (S. Serbin)

ABSTRACT

The article considers the methodological aspects of the theoretical investigation of marine power plants with thermochemical fuel treatment. The results of the study of the complex influence of temperature, pressure, and the ratio of steam / base fuel on the thermochemical treatment efficiency are presented. The adequacy of the obtained regression dependences was confirmed by the physical modelling of thermochemical fuel treatment processes. For a gas turbine power complex with a thermochemical fuel treatment system, the characteristics of the power equipment were determined separately with further merging of the obtained results and a combination of material and energy flow models. Algorithms, which provide settings for the mathematical models of structural and functional blocks, the optimisation of thermochemical energy transformations, and verification of developed models according to the indicators of existing gas turbine engines, were created. The influence of mechanical energy consumption during the organisation of thermochemical processing of fuel on the efficiency of thermochemical recuperation is analysed.

Keywords: marine power plants, thermochemical fuel treatment system, gas turbine engine, mathematical modeling

INTRODUCTION

Global trends in the energy efficiency of fuel resources, minimising emissions of CO₂, NO_x, and other harmful substances, require the adaptation of promising energy-saving technologies to marine energetics [1, 2].

The known technology of thermochemical treatment of fuels by the regeneration of secondary energy resources of heat engines is a set of processes resulting in an increase in the enthalpy of energy boosters (a mixture of hydrocarbon fuels and oxidants), due to the endothermic conversion process of base fuel using secondary heat engine energy resources [3-6].

The use of thermochemical recuperation in the gas turbine engines (GTE) of a simple and steam-injected gas turbine

(STIG) cycle, as well as combined diesel-gas turbine power generating units, is very promising [7]. Such installations provide for thermochemical recuperation of the GTE exhaust gases by steam conversion of hydrocarbon fuels. In this case, conversion products are used as fuel [8, 9].

The variety of scheme solutions for the composition of a marine power plant, and a wide range of power equipment parameters, requires the identification of the relationships of components using mathematical modelling.

Functional decomposition allows the presentation of an energy module with thermochemical systems of recuperation (TCSR) of secondary energy resources in the form of a set of subsystems. In turn, each subsystem is formed as a set of units (superchargers, reactors, etc.) and groups of units united

Symbols and abbreviations

G	mass flow rate, kg/s
H_U	lower heat of combustion, kJ/kg
I	electric current, A
L	length, m
M	mass, kg
N	power, MW
p	pressure, MPa
s/bf	steam/fuel ratio, kg/kg
T	time, s
T, Θ	temperature, K
ε	comparative error
Δ	absolute error
η	efficiency
C	base fuel compressor
CC	combustion chamber
DP	desalination plant
GTE	gas turbine engines
HPC	high-pressure compressor
HPT	high-pressure turbine
HRSG	heat-recovery steam generator

LPC	low-pressure compressor
LPT	low-pressure turbine
PT	power turbine
R	reactor
STIG	steam-injected gas turbine
TCSR	thermochemical systems of recuperation

Indexes

<i>air</i>	air
<i>B</i>	base hydrocarbon fuel
<i>C</i>	conversion products
<i>calc</i>	calculations
<i>exp</i>	experimental data
<i>fix</i>	fixed parameters
<i>fuel</i>	fuel
<i>G</i>	exhaust gas
<i>max</i>	maximum allowable parameters
<i>min</i>	minimum allowable parameters
<i>R</i>	rational parameters
<i>THR</i>	parameters of the thermochemical fuel treatment

by a certain functional feature (gas turbine engine, internal combustion engine, etc.) [10].

Mathematical models of blocks, and groups of blocks, that form the mathematical model of the subsystem are usually a system of nonlinear algebraic equations.

In the mathematical modelling of new technologies, it is expedient to use the modular approach (Sequential Modular, SM) [11]. Equations for each unit (such as a thermochemical reactor) are solved using individual algorithms. In this case, for all calculation modules, a predetermined logical sequence of calculations is followed. The advantages of this approach to finding rational solutions are:

- the ability to test computational algorithms with subsequent verification of the results separately for some blocks or groups of blocks;
- a modular structure allows new blocks to be added easily and existing ones to be upgraded;
- relative simplicity and solution transparency allow easy verification of the original data for compliance and completeness.

An example of the use of this approach is the software for physicochemical processes modelling, which is implemented in the software package Aspen Plus [12, 13].

Mathematical modelling provides an opportunity to identify the range of effective use of promising fuels and their thermochemical treatment by the recuperation of secondary energy resources of marine power plants. Verification of the basic mathematical model provisions requires the physical modelling of individual processes of thermochemical fuel treatment.

IDENTIFICATION OF THE INVESTIGATION OBJECT

An energy module with thermochemical systems for the recuperation of secondary energy resources can be presented as a set of subsystems:

- an energy subsystem in which the chemical energy of the fuel is converted into mechanical, electrical, and thermal energy;
- subsystems of thermochemical recuperation and energy conversion.

The subsystem of thermochemical recuperation and energy conversion consists of two parts:

- a heat recovery circuit, which is designed to supply heat to the secondary energy engine resources to consumers of the thermochemical energy conversion circuit; and
- the circuit of thermochemical energy conversion, which can be performed in the form of a unit of thermochemical fuel treatment.

The modelling of physicochemical processes in blocks, groups of blocks, and the subsystems themselves is based on the fundamental laws of conservation of energy and mass. For the mathematical description of the processes of physical and chemical transformations, the equations of material and energy balances are used, which are closed by additional relations that take into consideration the features of a particular process.

The approaches formed in [14] propose to determine the minimum value of the calculated error in the mathematical modelling of processes in the selected class of phenomena, to confirm the acceptability of the selected model. It is proposed to use comparative error as a universal indicator [15, 16]:

$$\varepsilon = \Delta u_{pmm} / S \leq [(z^I - \beta^I) / N_{SI} + [(z^{II} - \beta^{II}) / (z^I - \beta^I)]], \quad (1)$$

where Δu_{pmm} is the dimensionless model error during the determination of the dimensionless variable u ; S is the range of values of the dimensionless studied variable u ; z^I is the total number of dimensionless physical variables in the chosen class of phenomena; β^I is the number of primary physical variables; z^{II} is the given number of selected physical dimensional variables; β^{II} is the number of the primary physical dimensional variables; and N_{SI} is the largest number of dimensionless complexes.

In the study of energy conversion processes in power plants, of the seven main variables of the SI system (L – length, M – mass, T – time, I – electric current, Θ – temperature, J – light intensity, F – the amount of substance) only three main ones are used (L , M , and Θ) and the fourth T is used for non-stationary processes. The processes of thermochemical transformations require additional consideration of F .

Achievable minimum comparative error in modelling energy conversion processes in power plants lies in a wide range of values (Table 1): from 0.004756, for stationary heat and mass transfer processes, to 0.13307, for modelling non-stationary heat transfer processes taking into consideration thermochemical transformations.

Thus, it is expedient to consider stationary conditions in the mathematical modelling of processes in the energy module with thermochemical systems, for the recuperation of secondary energy resources. On the one hand, this narrows the value of the results obtained, on the other hand, it allows obtaining the correct characteristics of power equipment.

Tab. 1. Achievable minimum comparative error according to different classes of phenomena

Class of phenomena	Description of the phenomena	Minimum comparative error ε_{min}
LM Θ	Stationary heat and mass transfer process	0.00476
LM Θ F	Stationary process of heat and mass transfer taking into consideration thermochemical transformations	0.01458
LMT Θ	Non-stationary process of heat and mass transfer	0.04457
LMT Θ F	Non-stationary process of heat and mass transfer taking into consideration thermochemical transformations	0.13307

Procedures for the verification and optimisation of processes in the energy module equipment with thermochemical energy conversion require adjustment of the heat engine model. Thus, when studying the efficiency of thermochemical fuel treatment by recuperating the gas turbine engine waste heat, the following characteristics are most often considered: effective power, specific fuel consumption, inlet turbine temperature, gas temperature at the engine outlet, and the rate of recuperation (regeneration).

In the case of modelling the internal combustion engine, the main parameters are: effective power, specific fuel consumption,

average effective pressure, maximum combustion pressure, and maximum combustion temperature.

A variety of fuels can be used as a base energy source, which requires the development of algorithms for the preliminary assessment of the effectiveness of thermochemical technologies for fuel of a specific composition and verification. Further adjustment of heat engine models need to take into consideration the existing limitations and requirements for modern or future models.

DETERMINATION OF RATIONAL PARAMETERS OF THERMOCHEMICAL FUEL TREATMENT

Thermochemical fuel treatment can be carried out using a wide range of technologies [6, 17, 18]:

- recuperation by decomposition (thermal dissociation);
- steam reforming;
- partial recuperation by autothermal reforming (where part of the feed undergoes catalytic combustion in the presence of oxygen);
- dry reforming (where the exhaust gas is used to reform the feed);
- plasma reforming (where reforming processes are carried out using low-temperature plasma).

In preliminary studies, the authors analysed the possibility of using the presented technologies. Steam conversion of hydrocarbons using exhaust gas utilisation in heat engines was selected for further research. The selection was made according to several criteria, primarily based on the assessment of the temperature level of the reaction, the increase in calorific value and the value of the utilised heat flow, as well as the amount of obtained hydrogen, the heat of the reaction, and others.

The coefficient of increase of the heat of combustion for base fuel is chosen as the main criterion for an estimation of energy efficiency in thermochemical processing. The proposed criterion is defined as [7]:

$$\bar{H}_U = \frac{\Delta H_U}{H_U^B}, \quad (2)$$

where $\Delta H_U = H_U^C - H_U^B$ is the difference between the lower heat of combustion of the conversion products H_U^C (kJ/kg) and the base hydrocarbon fuel H_U^B (kJ/kg).

The calorific value of the components of the synthesis gas (obtained during the conversion) is converted to 1 kg of base fuel.

A further algorithm for determining the rational parameters of the thermochemical fuel treatment by recuperating secondary energy resources, provides the following. For fixed values of the pressure p_{THR} of the thermochemical treatment, the composition of thermochemical treatment products is calculated, followed by the estimation of the heat of combustion H_U . The coefficient of increase of the heat of combustion \bar{H}_U is then determined, as a function of the temperature T_{THR} of the thermochemical treatment and steam / fuel ratio s/bf :

$$\left\{ \begin{array}{l} \bar{H}_{U_{1\dots l}}^1 = f(T_{THR_{1\dots m}}, s/bf_{1\dots n}), p_{THR_1} = const\ 1 \\ \bar{H}_{U_{1\dots l}}^2 = f(T_{THR_{1\dots m}}, s/bf_{1\dots n}), p_{THR_1} = const\ 2 \\ \bar{H}_{U_{1\dots l}}^3 = f(T_{THR_{1\dots m}}, s/bf_{1\dots n}), p_{THR_1} = const\ 3 \\ \bar{H}_{U_{1\dots l}}^k = f(T_{THR_{1\dots m}}, s/bf_{1\dots n}), p_{THR_1} = const\ k, \end{array} \right. \quad (3)$$

where k is the number of fixed pressure values; m is the number of fixed temperature values; n is the number of fixed values of the ratio s/bf ; and $l = m \cdot n$ is the number of calculated values of \bar{H}_U .

Generalising the influence of the s/bf ratio on the increase in the heat of combustion, under conditions of variation of the parameter $T_{THR} = var$ and a fixed value $p_{THR} = const$, allows us to parametrically represent the results in the form of graphical dependencies, an example of which is given in Fig. 1a.

For each fixed value of pressure at a fixed value of temperature and variable value of the steam / fuel ratio, the local maximum \bar{H}_U^R which corresponds to a certain rational value of the parameter s/bf^R , was determined (Fig. 1b).

The mathematical description of parametric dependencies for thermochemical conversion processes is presented in the form of a system of equations:

$$\left\{ \begin{array}{l} \bar{H}^{R623}_{U_1} = f(s/bf^{R623}), p_{THR_1} = const\ 1 \\ \bar{H}^{R1123}_{U_1} = f(s/bf^{R1123}), p_{THR_1} = const\ 1 \\ \bar{H}^{R623}_{U_2} = f(s/bf^{R623}), p_{THR_2} = const\ 2 \\ \bar{H}^{R1123}_{U_2} = f(s/bf^{R1123}), p_{THR_2} = const\ 2 \\ \bar{H}^{R623}_{U_3} = f(s/bf^{R623}), p_{THR_3} = const\ 3 \\ \bar{H}^{R1123}_{U_3} = f(s/bf^{R1123}), p_{THR_3} = const\ 3 \\ \bar{H}^{R623}_{U_4} = f(s/bf^{R623}), p_{THR_4} = const\ 4 \\ \bar{H}^{R1123}_{U_4} = f(s/bf^{R1123}), p_{THR_4} = const\ 4 \end{array} \right. \quad (4)$$

The obtained value \bar{H}_U^R , is the maximum achievable value of the coefficient of increase of the heat of combustion.

For each fixed value of pressure, the regression dependence of the maximum achievable value of the coefficient of increase of the heat of combustion on temperature as a polynomial function was determined:

$$\left\{ \begin{array}{l} \bar{H}_{U_1}^R = c_{11} \cdot T_{THR}^4 - c_{21} \cdot T_{THR}^3 + c_{31} \cdot T_{THR}^2 - c_{41} \cdot T_{THR} + d_1, \\ p_{THR_1} = const\ 1; \\ \bar{H}_{U_2}^R = c_{12} \cdot T_{THR}^4 - c_{22} \cdot T_{THR}^3 + c_{32} \cdot T_{THR}^2 - c_{42} \cdot T_{THR} + d_2, \\ p_{THR_2} = const\ 2; \\ \bar{H}_{U_n}^R = c_{1n} \cdot T_{THR}^4 - c_{2n} \cdot T_{THR}^3 + c_{3n} \cdot T_{THR}^2 - c_{4n} \cdot T_{THR} + d_n, \\ p_{THR_n} = const\ n. \end{array} \right. \quad (5)$$

The dependence of the coefficients of the polynomial function $\bar{H}_U^R = f(T_{THR}, p_{THR})$ on the pressure was established by regression analysis methods:

$$\bar{H}_U^R = a_1 \cdot T_{THR}^4 - a_2 \cdot T_{THR}^3 + a_3 \cdot T_{THR}^2 - a_4 \cdot T_{THR} + b, \quad (6)$$

where:

$$a_1 = -A_{11} \cdot p_{THR}^2 - A_{22} \cdot p_{THR} + B_1, a_2 = -A_{11} \cdot p_{THR}^2 - A_{22} \cdot p_{THR} + B_2,$$

$$a_3 = -A_{31} \cdot p_{THR}^2 - A_{32} \cdot p_{THR} + B_3, a_4 = -A_{41} \cdot p_{THR}^2 - A_{42} \cdot p_{THR} + B_4,$$

$$b = -A_b \cdot p_{THR}^2 - A_b \cdot p_{THR} + B_b.$$

The given algorithm allows the determination of the maximum achievable value of the coefficient of increase of the heat of combustion under the following restrictions: available levels of temperatures of secondary energy sources, admissible conversion pressure under conditions of conformity to the rational value of parameter s/bf^R .

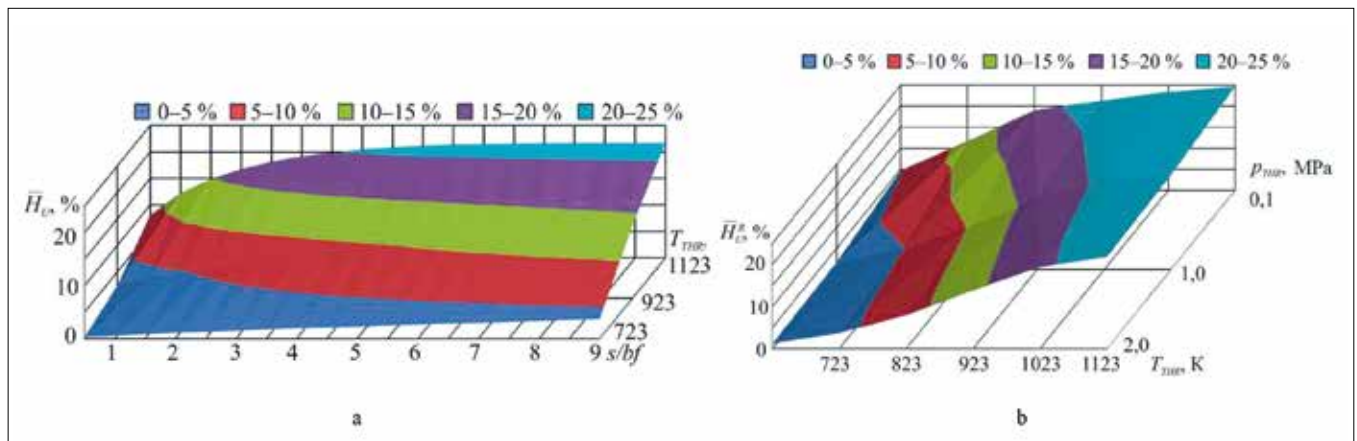


Fig. 1. Parametric dependences for thermochemical conversion processes: **a** – dependence $\bar{H}_U = f(T_{THR}, s/bf)$ for thermochemical treatment of natural gas at $p_{THR} = 2.0$ MPa; **b** – dependence $\bar{H}_U^R = f(T_{THR}, p_{THR}, s/bf^R)$ for thermochemical treatment of natural gas in the ranges of parameter changes: pressure 0.1–2.0 MPa; temperature 623–1123 K; steam / fuel ratio 0–9.

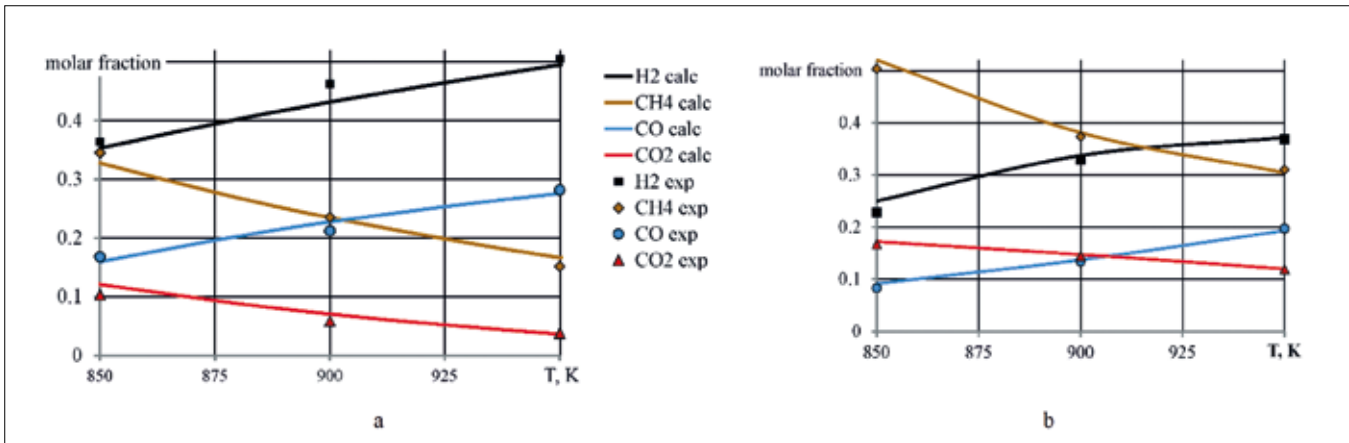


Fig. 2. Comparison of the results of experimental studies of the synthesis gas composition and the results of theoretical calculations for $s/bf=0.3$: **a** - $p_{THR} = 0.1$ MPa; **b** - $p_{THR} = 0.45$ MPa; H_2 calc, CH_4 calc, CO calc, CO_2 calc - theoretical calculations; H_2 exp, CH_4 exp, CO exp, CO_2 exp - experimental data

In order to verify the results of mathematical modelling, an experimental study of the energy efficiency of thermochemical fuel treatment processes at a pressure corresponding to the conditions of fuel gas feeding to heat engines was carried out.

A comparison of the results of experimental studies on synthesis gas composition [19] with theoretical calculations gives a satisfactory convergence of the values, which is not less than 92% (Fig. 2), and confirms the adequacy of the regression dependences $\bar{H}_U = f(T_{THR}, p_{THR}, s/bf)$.

According to the approaches proposed by the authors [7], the maximum allowable temperature of the endothermic reaction of fuel conversion T_{THR}^{max} is determined as:

$$T_{THR}^{max} = T_4 - \frac{\bar{H}_U \cdot H_U^B \cdot G_{fuel}}{G_G \cdot c_p} \quad (7)$$

where G_G is the exhaust gases flow rate; c_p is the mean mass heat capacity of the exhaust gases at a constant pressure in the relevant temperature range, and G_{fuel} is the mass fuel consumption.

According to calculations for the range of average gas temperatures behind marine gas turbine engines, 700-820 K, the maximum increase in the heat of combustion for modified gaseous hydrocarbon fuels, due to the thermochemical treatment of natural gas, is 8-12%, depending on process pressure.

Further studies of the effectiveness of thermochemical fuel treatment technology in marine energetics require the development of a mathematical model of a gas turbine energy complex with TCSR.

MATHEMATICAL MODELLING OF GAS TURBINE ENERGY COMPLEX WITH THERMOCHEMICAL FUEL TREATMENT SYSTEM

Mathematical models of gas turbine engines or internal combustion engines, when working as part of an energy module with thermochemical fuel treatment, must be adjusted to the selected basic characteristics. Therefore, mathematical

models of structural and functional blocks and groups of blocks contain calculation algorithms, including settings for specified characteristics.

Verification of the serial gas turbine engine model is based on the following characteristics:

- engine power N_{GT} is a fixed value N_{GT}^{fix} ;
- the maximum temperature behind the combustion chamber T_3 must not exceed the value T_3^{fix} .

When modelling processes in the energy module, the calculated values of the objective function $Y = f(x)$ must meet the conditions of the given tolerance for convergence ΔY^{tol} . In our case:

$$\Delta N_{GT} \leq N_{GT}^{tol} \dots \Delta T_3 \leq \Delta T_3^{tol}, \quad (8)$$

where $\Delta N_{GT} = |N_{GT} - N_{GT}^{fix}|$ and $\Delta T_3 = |T_3 - T_3^{fix}|$ are the absolute errors of parameter values.

It has been found that, other things being equal, for the objective function N_{GT} the main input variable is the amount of mass fuel consumption, i.e. $N_{GT} = f(G_{fuel})$. According to the objective function T_3 , the main input variable is the mass air flow, i.e. $T_3 = f(G_{air})$.

The correct setting of the initial parameters of input variables significantly reduces the calculation time and provides the required convergence for less iteration.

Wegstein's method [20] can be used as a method of convergence, according to which the results of the last two iterations were used to calculate the variable:

$$G_{fuel_k} = G_{fuel_{k-1}} - \frac{f(G_{fuel_{k-1}})(G_{fuel_{k-1}} - G_{fuel_{k-2}})}{f(G_{fuel_{k-1}}) - f(G_{fuel_{k-2}})};$$

$$G_{air_k} = G_{air_{k-1}} - \frac{f(G_{air_{k-1}})(G_{air_{k-1}} - G_{air_{k-2}})}{f(G_{air_{k-1}}) - f(G_{air_{k-2}})}. \quad (9)$$

Mathematical models of the gas turbine engine, recycling circuit, and thermochemical fuel treatment unit were created using the Aspen Plus physicochemical process modelling system. In our calculations, we used the following assumptions: all gases are treated as ideal gases; there is a chemical equilibrium in the reformer (the equilibrium value is a function

of temperature, pressure, composition of input gas, and steam to gas ratio). A Gibbs reactor in the Aspen® software is used to determine the composition of products in the reaction system. This reactor calculates the distribution of reaction products by minimising the Gibbs free energy of each of the existing elements in the reaction system. In [21], it is indicated that the results of computer modelling using this approach are confirmed by the data available from the industrial plant at the Puertollano petrochemical refinery.

The algorithm for calculating the parameters and characteristics of the gas turbine power complex with thermochemical fuel treatment contains three main stages (Fig. 3).

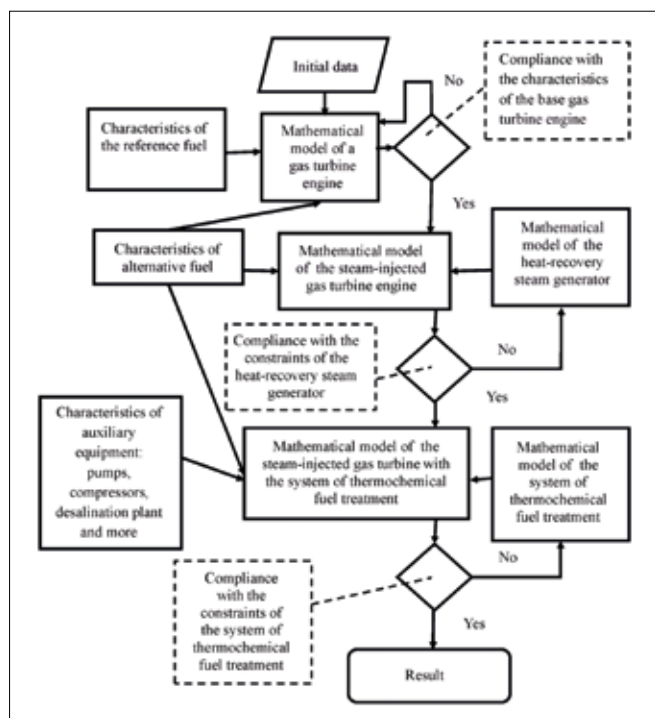


Fig. 3. Scheme of the algorithm for modelling processes in the energy module with thermochemical recuperation

The first stage involves adjusting the gas turbine engine model to the parameters of the serial engine at nominal operation mode: effective engine power, the gas temperature behind the combustion chamber, the rate of total pressure drop in the turbine or turbines, the rate of pressure increase in the compressor (compressors), mass air flow, and the mass consumption of reference fuel (e.g. methane). After verification of the model according to the parameters of the base engine, the model is adjusted to the operation of the gas turbine engine on alternative fuels.

In the second stage, the processes in the steam-injected gas turbine, created on the basis of the model of the first stage, are calculated.

The following parameters are defined:

- mass consumption of alternative fuels at a fixed value of power;
- steam productivity of the heat-recovery steam generator in the conditions of restrictions of the minimum temperature of the exhaust gases which is defined by the temperature of a dew point;

- change of mass air flow taking into consideration observance of the admissible temperature of gas behind the combustion chamber;
- the cost of mechanical energy to drive pressure change devices (pumps), which provide the necessary efficiency of the recycling system. At the third stage, the processes in the steam-injected gas turbine with the system of thermochemical fuel treatment are modelled.

The following parameters are defined:

- mass consumption of alternative fuels;
- the maximum achievable temperature of the fuel treatment process in the thermochemical reactor;
- steam productivity of the heat-recovery steam generator in the conditions of restrictions of the minimum temperature of the exhaust gases;
- change of mass air flow, taking into consideration observance of the admissible temperature of gas behind the combustion chamber;
- energy consumption in the desalination plant;
- the cost of mechanical energy to drive pressure change devices (pumps and compressors), which provide the necessary efficiency of recuperation and thermochemical fuel treatment systems.

In order to verify the adequacy of the proposed algorithms, mathematical modelling of the energy complex, based on the UGT 25000 gas turbine engine with a thermochemical fuel treatment system, was performed (Fig. 4). The GTE is a simple cycle dual-rotor turbine engine with a free power turbine (Table 2). The UGT 25000 is produced by the enterprise “Zorya-Mashproekt” (Ukraine) and designed for electric power generation, natural gas transportation and marine propulsion.

Tab. 2. Parameters of the UGT 25000

Parameters	Value
Number of compressors	2
Number of turbines	3
Turbine inlet temperature, K	1518
Compressor pressure ratio	21.8
Exhaust gas flow, kg/s	90
Exhaust temperature, K	763
Power, MW	27.5
Efficiency, %	36.5

The modelling provided for the operation of the turbocompressor unit in the nominal mode. We proposed the installation of a thermochemical reactor behind the power turbine of a serial gas turbine engine. The principle of operation was as follows. Synthesis gas from the thermochemical reactor was fed to the combustion chamber of the engine. In the reactor, due to the heat of the exhaust gases, the methane-steam mixture was heated and then steam reforming took place. Behind the reactor, the exhaust gas temperature has sufficient potential to produce recovery of the boiler steam required for the ‘steam reforming’ of the base fuel in the reactor. In the power module,

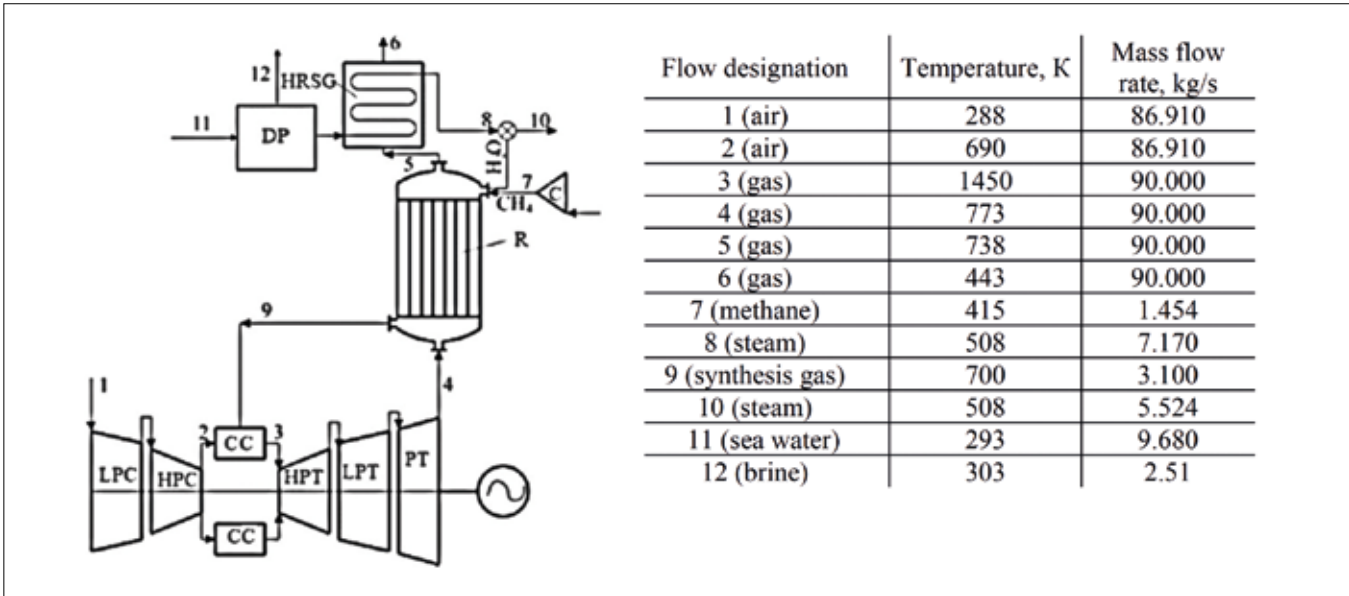


Fig. 4. – Design scheme of energy module with thermochemical fuel treatment based on UGT 25000: LPC – low-pressure compressor; HPC – high-pressure compressor; CC – combustion chamber; HPT – high-pressure turbine; LPT – low-pressure turbine; PT – power turbine; R – reactor; HRSG – heat-recovery steam generator; C – base fuel compressor; DP – desalination plant

similar to STIG cycle turbine units [22-23], water was removed from the cycle [24]. A desalination plant was provided to compensate for water losses [25]. In more detail, the scheme of thermochemical utilisation of the waste heat of a gas turbine engine by steam reforming of hydrocarbon fuel, the composition of the base fuel, and the main components of the synthesis gas were presented in [8].

The efficiency of the power module is accepted as a criterion:

$$\eta = (N_{GT} - \sum N_{add}) / (G_{fuel}^B \cdot H_U^B), \quad (10)$$

where N_{GT} is the mechanical power on the output shaft of the engine, kW; $\sum N_{add}$ is the power consumption for the driving of pumps and compressors, as well as for the needs of a desalination plant and other equipment of the thermochemical fuel treatment subsystem, kW; G_{fuel}^B is the base fuel consumption, kg/s; and H_U^B is the lower heat of combustion of base fuel, kJ/kg.

By mathematical modelling it was established that the use of thermochemical fuel treatment under steam reforming leads to the following changes in the basic cycle:

- increasing total pressure losses at the engine outlet due to total pressure losses in the reactor;
- increasing the amount of working fluid due to the injection of steam and synthesis gas into the combustion chamber;
- the recuperation of exhaust gas heat;
- power consumption for the driving of pumps and compressors, desalination plant and other auxiliary equipment of the thermochemical fuel treatment system.

An increase in the total pressure loss in the gas path, due to the thermochemical reactor, leads to a decrease in engine efficiency from 0.6-0.8% (absolute) and a decrease in specific power from 1.6-2.2% (higher values correspond to lower temperature value T_3).

Analysis of the results of the cycle calculation reveals an

increase in efficiency (Fig. 5) compared to the steam-injected gas turbine cycle. It should be assumed that synthesis gas is better able to stabilise combustion than the steam-fuel mixture used in the STIG cycle. It can be seen that, compared with the STIG cycle, the increase in the unit's efficiency due to the use of thermochemical fuel treatment in the temperature T_3 range of 1300–1700 K, is 0.5–4.5% (absolute), and the increase is greater, the higher the maximum cycle temperature. If we take the baseline for comparing a gas turbine unit with a traditional waste heat recovery system, in which the steam obtained in the exhaust gas boiler at a single pressure is used in a steam turbine [26], then the efficiency gain will be about 3.0-8.9% for the same temperature range of 1300-1700 K.

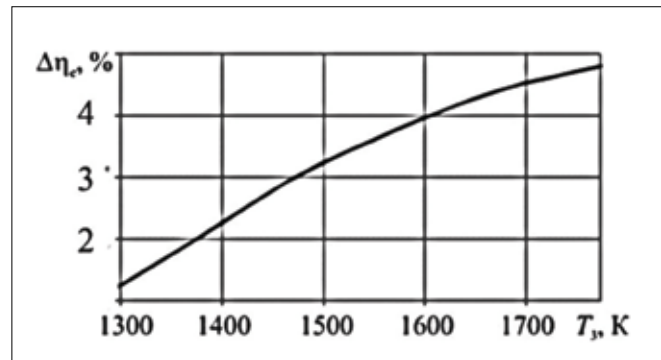


Fig. 5. Dependence of efficiency increase on the temperature behind the combustion chamber in comparison with the STIG cycle

As a result of endothermic reactions in the reactor, the amount of heat required for heating the methane-steam mixture and carrying out these reactions is removed from the exhaust gases. For the UGT 25000 engine at the given parameters, the part of the utilised heat makes 29% of the exhaust gases heat. In the total heat balance, this reduces the heat introduced into the cycle by the base fuel by 4.9%. Power consumption for the needs of the desalination plant is from 0.7-1.0% of the power of the energy

module and depends on the steam/fuel ratio. Experimental studies to determine the efficiency of thermochemical fuel processes [17] confirm the results of mathematical modelling, according to which, the expense of mechanical energy for the organisation of thermochemical fuel processes and the supply of modified products to the engine reduces the efficiency of thermochemical utilisation by 6-12%.

The efficiency of the gas turbine power module with a thermochemical natural gas treatment system with a thermochemical reactor behind a power turbine obtained by mathematical modelling methods shows that, at the relatively low levels of gas temperatures behind the combustion chamber (<1523 K) and the exhaust gases (700–820 K), steam conversion of natural gas due to the heat of exhaust gases is not efficient enough and can be compared with the STIG cycle. This coincides with the results of other researchers [27].

Comparison with the results of previous studies shows that the considered scheme of the power module with thermochemical fuel treatment based on serial GTE of the simple cycle with reactor behind a power turbine may be promising when using fuels such as methanol, ethanol, and associated gas with heavy hydrocarbons. The proposed scheme seems appropriate when the gas temperatures behind the combustion chamber of a serial marine GTE will be at least 1673 K.

FINAL CONCLUSIONS

The results of a comprehensive study of the characteristics of a gas turbine power module with a thermochemical treatment system are presented. The following results were obtained:

- to calculate the coefficient of increase of the heat of combustion within the given ranges of temperatures and pressures, regression dependences are proposed, which take into consideration the complex influences of temperature, pressure, and steam/base fuel ratio. The adequacy of the obtained regression dependences $\bar{H}_U = f(T_{THR}, p_{THR}, s/bf)$ was confirmed by physical modelling of thermochemical fuel treatment processes;
- according to the results of experimental studies, the expense of mechanical energy during thermochemical fuel treatment and injection of modified products into the engine, reduces the efficiency of thermochemical recuperation by 6-12%, which requires a rational selection of marine power plant scheme solutions;
- the proposed algorithms provide adjustments for the mathematical models of structural and functional blocks, optimisation of processes of thermochemical transformations, and verification of the developed models;
- for the range of average gas temperatures behind serial marine gas turbine engines 700-820 K, the maximum increase in the heat of combustion for modified gaseous hydrocarbon fuels is 8-12%;
- the mathematical modelling shows that, at the current level of serial marine gas turbine engines characteristics, the efficiency of the proposed power module increase is 2-3%, compared to the STIG cycle;
- the considered scheme of a thermochemical fuel treatment

system with a reactor behind a power turbine is quite effective when temperatures behind the combustion chamber are not lower than 1673 K;

- further work should study the effectiveness of the use of thermochemical technologies for the utilisation of secondary energy resources at partial operating modes of the installation.

REFERENCES

1. Lloyd's Register, QinetiQ and University of Strathclyde, 'Global Marine Technology Trends 2030', 2015. [Online]. Available: <https://www.lr.org/en/insights/global-marine-trends-2030/global-marine-technology-trends-2030/>.
2. UNCTAD, 'Review of Maritime Transport 2021: UNCTAD/RMT/2021', 2021. [Online]. Available: https://unctad.org/system/files/official-document/rmt2021_en_0.pdf.
3. W. Han, H. Jin, N. Zhang, and X. Zhang, 'Cascade Utilisation of Chemical Energy of Natural Gas in an Improved CRGT Cycle,' *Energy*, vol. 32, pp. 306–313, 2007. DOI: 10.1016/j.energy.2006.06.014.
4. N. Zhang and N. Lior, 'Use of Low/Mid-Temperature Solar Heat for Thermochemical Upgrading of Energy, Part I: Application to a Novel Chemically-Recuperated Gas-Turbine Power Generation (SOLRGT) System,' *J. Eng. Gas Turbines Power*, 134(7): 072301, 2012. DOI: 10.1115/1.4006083.
5. R. Carapellucci and L. Giordano, 'Upgrading Existing Gas-Steam Combined Cycle Power Plants Through Steam Injection and Methane Steam Reforming,' *Energy*, vol. 173, 229–243, 2019. DOI: 10.1016/j.energy.2019.02.046.
6. L. Tartakovskiy and M. Sheintuch, 'Fuel reforming in internal combustion engines,' *Progress in Energy and Combustion Science*, vol. 67, pp. 88-114, 2018. DOI 10.1016/j.peccs.2018.02.003 .
7. O. Cherednichenko and S. Serbin, 'Analysis of efficiency of the ship propulsion system with thermochemical recuperation of waste heat,' *J. Marine. Sci. Appl.*, vol. 17, pp. 122–130, 2018. DOI: 10.1007/s11804-018-0012-x .
8. O. Cherednichenko, S. Serbin, and M. Dzida, 'Investigation of the combustion processes in the gas turbine module of an FPSO operating on associated gas conversion products,' *Polish Maritime Research*, vol. 4, pp. 149–156, 2019. DOI: 10.2478/pomr-2019-0077.
9. O. Cherednichenko, S. Serbin, and M. Dzida, 'Application of Thermo-chemical Technologies for Conversion of Associated Gas in Diesel-Gas Turbine Installations for Oil and Gas Floating Units,' *Polish Maritime*, vol. 26(3), pp. 181-187,

2019. DOI: 10.2478/pomr-2019-0059.

MEES52427.2021.9598783.

10. H. Gaspar, A. Ross, D. Rhodes, and S. Erikstad, 'Handling Complexity Aspects in Conceptual Ship Design,' Int'l Maritime Design Conf., Glasgow, 2012. [Online]. Available: <https://www.semanticscholar.org/paper/Handling-aspects-of-complexity-in-conceptual-ship-Gaspar/1feb36a217217fb7acff86d609d71983536816a#related-papers>.
11. J. Caballero, M. Navarro, R. Femenia, and I. Grossmann, 'Integration of different models in the design of chemical processes: Application to the design of a power plant,' *Applied Energy*, vol. 124, pp. 256–273, 2014. DOI: 10.1016/j.apenergy.2014.03.018.
12. J. Haydary, *Chemical Process Design and Simulation: Aspen Plus and Aspen Hysys Applications*. Bratislava : John Wiley & Sons, 2018. 448 p.
13. K.I.M. Al-Malah, *Aspen Plus: Chemical Engineering Applications*. Hoboken; New Jersey, John Wiley & Sons Inc, 2016. 656 p.
14. C.-J. Kat and P.S. Els, 'Validation metric based on relative error,' *Mathematical and Computer Modelling of Dynamical Systems: Methods, Tools and Applications in Engineering and Related Sciences*, vol. 18 (5), pp. 487 – 520, 2012. DOI: <https://www.tandfonline.com/doi/full/10.1080/13873954.2012.663392>.
15. L. Brillouin, *Science and Information Theory*. 2nd edn. Dover Books on Physics, Courier Corporation, 2013. Available at: <https://www.perlego.com/book/112582/science-and-information-theory-second-edition-pdf>.
16. B. Menin, 'Information Measure Approach for Calculating Model Uncertainty of Physical Phenomena,' *American Journal of Computational and Applied Mathematics*, vol. 7(1), pp. 11-24, 2017. DOI: 10.5923/j.ajcam.20170701.02.
17. I.B. Matveev, S.I. Serbin, 'Theoretical and experimental investigations of the plasma-assisted combustion and reformation system,' *IEEE Transactions on Plasma Science*, vol. 38(12 Part 1), pp. 3306–3312, 2010. DOI: 10.1109/TPS.2010.2063713.
18. S.I. Serbin, I.B. Matveev, and G.B. Mostipanencko, 'Plasma-Assisted Reforming of Natural Gas for GTL: Part II - Modelling of the Methane-Oxygen Reformer,' *IEEE Transactions on Plasma Science*, vol. 43(12), pp. 3964–3968, 2015. DOI: 10.1109/TPS.2015.2438174.
19. O. Cherednichenko, M. Tkach and S. Dotsenko, 'Experimental Study of Processes in the Elements of Thermochemical Fuel Treatment Systems of Integrated Power Generating Units,' 2021 IEEE International Conference on Modern Electrical and Energy Systems (MEES), pp. 1 - 4, 2021. DOI: 10.1109/MEES52427.2021.9598783.
20. V.M. Verbuck, and D.I. Milman, 'Veckstein's method as a modification of the transversal method,' *USSR Computational Mathematics and Mathematical Physics*, vol. 17(2), pp. 215–216, 2017.
21. F.J. Durán, F. Dorado, and I. Sanchez-Silva, 'Exergetic and Economic Improvement for a Steam Methane-Reforming Industrial Plant: Simulation Tool,' *Energies* vol. 13, pp. 3807, 2020. <https://doi.org/10.3390/en13153807>.
22. S. Serbin, A. Mostipanencko, and I. Matveev, 'Investigation of the Working Processes in a Gas Turbine Combustor with Steam Injection,' *Proceedings of the ASME/JSME 8th Thermal Engineering Joint Conference, AJTEC2011-44042, T20012*, pp.1-6, 2011. DOI: <https://doi.org/10.1115/AJTEC2011-44042>.
23. S. Serbin and K. Burunsuz, 'Numerical study of the parameters of a gas turbine combustion chamber with steam injection operating on distillate fuel,' *International Journal of Turbo and Jet Engines*. Published online by De Gruyter, September 17, 2020. DOI: <https://doi.org/10.1515/tjeng-2020-0029>.
24. H.K. Kayadelen and U. Yasin, 'Thermoeconomic evaluation of simple, intercooled, STIG, and ISTIG cycles,' *International Journal of Energy Research*, vol. 42.12, pp. 3780-3802, 2018. DOI: <https://doi.org/10.1002/er.4101>.
25. Wärtsilä Water & Waste, www.wartsila.com, 2019. [Online]. Available: <https://www.wartsila.com/marine/build/fresh-water-generation/wartsila-reverse-osmosis>.
26. G.F. Romanovsky, N.V. Washchilenko, and S.I. Serbin, 'Theoretical basis for the design of marine gas turbine units,' *Mikolayiv: USMTU*, 304 p., 2003 (in Ukraine).
27. F. Pan, H. Zheng, Q. Liu, and R. Yang, 'Design and performance calculations of chemically recuperated gas turbine on ship,' *Proceedings of the Institution of Mechanical Engineers, Part A: Journal of Power and Energy*, vol. 227(8), pp. 908–918, 2013. DOI: 10.1177/0957650913498081.

CONTACT WITH THE AUTHORS

Oleksandr Cherednichenko

Admiral Makarov National University of Shipbuilding
Nikolaev
UKRAINE

Serhiy Serbin

e-mail: serbin1958@gmail.com

Admiral Makarov National University of Shipbuilding
Nikolaev
UKRAINE

Mykhaylo Tkach

Admiral Makarov National University of Shipbuilding
Nikolaev
UKRAINE

Jerzy Kowalski

Gdansk University of Technology
POLAND

Daifen Chen

Jiangsu University of Science and Technologym
CHINA

STUDIES ON THE EFFECTS OF COLD STARTS OF THE SHIP MAIN ENGINE

Andrzej Adamkiewicz 

Maritime University of Szczecin, Poland

Janusz Fydrych 

Briese Berederung, Hamburg, Poland

Jan Drzewieniecki* 

Maritime University of Szczecin, Poland

* Corresponding author: j.drzewieniecki@am.szczecin.pl (Jan Drzewieniecki)

ABSTRACT

This article presents the influence of various ship's operational conditions occurring during manoeuvres related to entering and leaving the ports and mooring operations. Frequent starts and stops of the ship's propulsion unit are then required, which affect the variability of the energetic loads of the ship's power plant, causing accelerated, non-design wear of the ship's main propulsion engine. The effects of cold start-ups of the main ship engine are the subject of this study. Conditions of the engine inlet valve damage process are discussed. The physics of the degradation process leading to air inlet valve damage was considered. Laboratory tests of structure continuity and their results are discussed, and the valve material defects were excluded as the cause of the damage. The causes of repeated damage to the inlet air valves were identified. The effectiveness of the performed corrective measures was confirmed by a documented control test of the engine start-up. The article is a utilitarian premise for the requirements of the Classification Society.

Keywords: cold start-ups, damage, inlet valves, main engine, ship

INTRODUCTION

Marine engines are complex technical systems undergoing constant modifications in terms of design as well as modes of operation. The said modifications are due to constantly emerging requirements concerning reliability, marine environment protection, and conservation of natural resources related to fuel and raw materials used in the production of marine engines. Consequently, both engine designers and users of the said engines face new challenges.

With the ultimate aim of meeting the requirements, the design process includes various actions that, among others, are taken in order to:

- reduce emission of pollutants from engine exhaust [1, 2, 3, 4, 5];

- use new ecological fuels [6, 7, 8];
- develop new operating principles for ship propulsion [9, 10, 11].

In terms of operation of marine engines, the undertaken actions are aimed, among others, at:

- reduction of fuel and lubricating oil consumption [12, 13, 14];
- operational diagnosis and prevention of component wear [15, 16].

One of the most pressing issues to be addressed in the process of marine engines operation is the reduction of structural component wear due to cold starts of the ship main engine.

In the operation process, there are various technical and energetic conditions of the ship propulsion power. The run

and character of these processes significantly depend on the decisions and actions of the crew. Therefore, the process of ship engine maintenance should be considered as being dependent on crew competence and operational proceedings. Real operational conditions of the ship propulsion power system are always different from the designed ones, and the achieved energy condition of the engine is the result of all vectors of control and disturbances in a given technical condition of engine serviceability [17, 18, 19, 20].

Procedurally correct preparation of the ship engine room to work, according to the principles of the accepted operational strategy and the requirements of the engine manufacturer, and, thus, the main propulsion power system is a basic initial condition of ship operation. In particular, ship manoeuvring in a port is a dynamic transient process, significantly deviating from the steady state of sailing at sea, which is a consequence of multiple and rapid changes of the main engine load. Thus, the elements of the engine are subjected to larger and more frequent changes in mechanical loads and thermal stresses, creating more difficult and demanding operating conditions [20, 21, 22].

Operating the main propulsion power system when its energy condition deviates from the design one, contributes to an increase in the probability of accelerated wear, the occurrence of malfunctions, up to eventual failure and breakdown [17, 23, 24].

The ship main engine is responsible for keeping the ship in motion in all operational conditions: during sea passage, in port and in limited water passage, as well as at anchor and in port. Continuity of ship operation in all operational states provides for steady operational conditions and also transient processes, acceleration and load deceleration, as well as engine shutdown. For the purpose of this study, operational documentations of a container ship and a cement carrier were used. Mutual relations of the steady condition operation time to the number of manoeuvres are shown in Fig. 1. During 102 h of sailing of a container ship in a month, 44 start-ups were made during the manoeuvres, while on a cement carrier, 20 start-ups were made during 112 h of manoeuvres.



Fig. 1. Total times of operating states of a container ship and a cement carrier realized in one month [own source].

The recorded number of cold start-ups caused degradation of the elements of tribological nodes of the main engine elements, and in particular, it caused damage to the charging air inlet-valve [25, 26, 27, 28, 29]. Their number and recurrence made it necessary to determine the reasons for the valve

malfunctions and failures in order to counteract and reduce the number of valve failures associated with the negative effects of cold starts of the engine. Repeated repairs became a burden in the operation and maintenance process, excluded ships from the transport service schedule, and increased costs. Therefore, in order to counteract this phenomenon, the need to analyse the consequences of ship engine cold start-ups arose.

In addition to the above, the effect of cold start-ups on air inlet-valves has a significant influence on the engine performance and emissions from diesel engines. Therefore, the consequences of this effect should also be taken into account as they significantly contribute to pollutant emissions in coastal waters [30].

Failure of each engine inlet valve is an individual event, insufficiently recognized in technical literature, both scientific and professional, and limited even in the technical and operation documentation of an engine. This has generated research interests in this area. In the available scientific technical literature, no references to this type of damage to intake valves have been found.

STUDY OBJECT

Repeated difficulties of starting the main engine operation, start-ups, unstable operation in the initial period after the start-up attempt, and recurrent damage to engine elements were observed in the operating practice. Fig. 2 shows the deviations from the mean value of the combustion pressure during the initial phase of the engine start-up.

The runs were recorded using an electronic indicator LEMAG Premet C XL made by LEHMANN & Michels GmbH and equipped with the WPREMET software, enabling the analysis of the measurement results. In Fig. 2, at the time of observation, three units 4, 5, and 8 in operation showed differences of several percent from the average value of the combustion pressure, three other units 1, 2, and 6 initiated operation, while two units did not start the combustion process at all, creating differences in the load of the piston-crank systems.



Fig. 2. Deviations from the mean value of the combustion pressure at the beginning of the first stage of the engine start-up.

Frequent lack of readiness of the main engine to start correct operation and recurrence of this type of damage point to the existence of systemic disturbances in the correctness of the engine start-up process.

This process occurs with irregular frequency and causes different forms of tribological wear of inlet valves. Fig. 3 shows endoscopic images of a damaged inlet valve mounted in the cylinder head of a Deutz 68M628 main power engine of 1715 kW.



Fig. 3. View of a defective inlet valve of the Deutz 68M628 main power engine.

The study of the causes and effects of the main engine damage was carried out on the basis of the operational experience of the ship propulsion plant operation, passive and active operational experiment, ship post-failure and shipowner's documentation, and the results of metallographic and scanning laboratory tests.

DETERMINANTS OF THE DAMAGE PROCESS OF THE SHIP MAIN ENGINE INLET-VALVES

The subject of the research comprised: the thermal condition of the engine and the engine room before starting the ship propulsion plant, including values of the temperature of the main working process media and the processes accompanying the main engine start-up.

On the basis of the analysis of the events in transient processes, it was assumed that the decisive influence on the main engine serviceability, Z , is exerted by imposing factors, according to the relation

$$Z(f) = f[t(\tau), \delta(\tau), l] \quad (1)$$

where:

- $t(\tau)$ – thermal factor,
- $\delta(\tau)$ – mechanical factor resulting from the dynamics of engine load changes,
- τ – time of intensity of transition processes,
- l – factor resulting from human activity including servicing during operation

The consequence of the superposition of such interactions is the mechanical violation of the continuity of the structure, with such consequences of wear processes as loss of materials and changes in the shape geometry of mating elements of the main engine. This kind of damage is a result of various mechanical and thermal loads of varied value and time, occurring at the initial stage of the main engine transient start-up process.

Ship engine start-up is performed with the participation of energy from an external source, which is compressed air from the start-up installation. The energy of compressed air during start-up is converted into kinetic energy of a back and forth movement of a piston-crank system of the engine, causing the heating of the fuel-air mixture in the combustion chamber to temperature T_2 at the stage of compression [17, 19].

$$T_2 = T_1 \varepsilon^{n_1 - 1} > T_{sz} \quad (2)$$

where:

- T_1 – air temperature at the beginning of the compression stroke,
- T_2 – air temperature at the end of the compression stroke,
- ε – compression ratio,
- n_1 – compression polytrope exponent in a cylinder, higher than the self-ignition temperature T_{sz}

The compression polytrope exponent n_1 is highly dependent on the crankshaft speed n . Increasing the compression time of the air in the combustion chamber favours heat exchange with the walls of the combustion chamber, which results in insufficient heating of the fuel-air mixture, cooled by the start-up air, expanding in the start-up valve. Thus, the process of self-ignition is significantly hindered because the rotational speed of the crankshaft is determined by the pressure of the start-up air and internal resistance of the engine kinematic system. In the case of an unsuccessful start, the main engine requires more starting air to be supplied in order for the fuel-air mixture in the combustion chambers of individual cylinders to self-ignite. In such a situation, the air supply time is extended, which promotes additional cooling of the combustion chamber. After a failed start, the main engine start-up is automatically repeated; thus, further cooling of the combustion chamber takes place. In this way, temperature gradients are created in the valve material, favouring circumferential microcracking of the inlet valves, as shown in Fig. 4 [18, 31, 32].

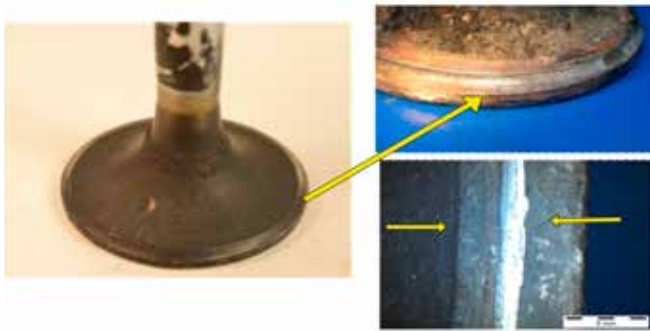


Fig. 4. Location of microcracks on the inlet valve:
a – view of the valve with peripheral microcracks on the inlet valve;
b – enlargement of a valve with visible microcracks;
c – enlargement of circumferential cracking of a disc.

If the equation (2) is not met, starting a diesel engine is difficult and sometimes impossible. Damage to the air inlet-valves generated by cold start-ups is only identified during scheduled engine overhauls if it does not cause extensive damage to the mating parts beforehand.

LABORATORY TESTING OF THE INLET-VALVE STRUCTURE

Two inlet-valves were randomly selected to study the effects of cold starts on the engine. The first valve was removed from the engine after 450 h of operation, while the second one was removed from the engine after it was damaged. Both valves were subjected to non-destructive macroscopic, microscopic, and metallographic examination [31, 32].

MACROSCOPIC TESTING

Organoleptic examination of the first valve revealed a bent stem and scratches in its upper part. These proved the existence of resistance to motion in the valve stem guide and defective operation of the “rotocap”. The second valve also had a bent stem and a partly broken off head. The view of the tested valves is shown in Fig. 5.



Fig. 5. View of studied damaged valves.

On both valves, circumferential cracks were located at the bottom, as shown in Fig. 4a.

The examined separation surfaces (scrap) of the damaged valve show two different breakthroughs in Fig. 6. The first breakthrough (1) shows furrow lines characteristic of fatigue scrap. The second breakthrough (2) is the separation scrap that resulted from the sudden breaking off of the part of the valve that was no longer cohesive. The nature of the scraps indicates that the process of destruction progresses over time.

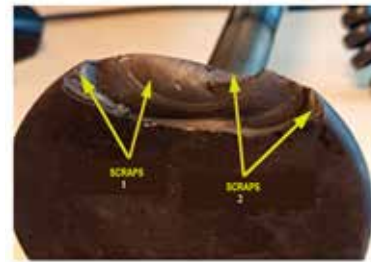


Fig. 6. View of the place of separation of the missing part of the inlet valve with visible separation lines: 1- fatigue scrap; 2 - separation scrap.

MICROSCOPIC TESTING

During the visual inspection of the examined valves, a micro-crack was found, which was the beginning of the propagation of further destruction proceedings. The microcrack was a result of thermal stresses that occurred in the second phase of the cold engine start-up [28, 31, 32]. The crack expansion was probably caused by a cyclic action of varying mechanical loads resulting from the repetition of transient engine operating states. The location of the micro-crack is shown in Fig. 7 [32].

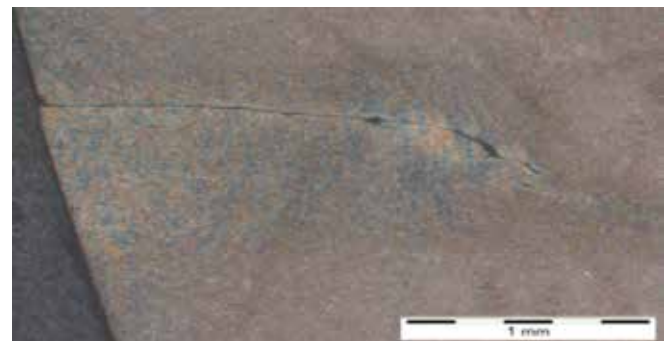


Fig. 7. View of a microcrack on the working surface of the damaged valve 2.

Circumferential cracks in the valve head found during examination using scanning electron microscopy revealed the formation of areas of local corrosion at the microcrack site, as shown in Fig. 8 [32].

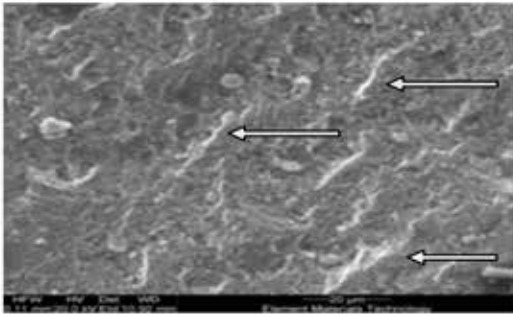


Fig. 8. Microscopic image of the surface of the tested valve.

At the same time, the structure of the valve material at the place of the fracture showed lines formed by fatigue crack growth. This phenomenon is documented by the electron microscope image shown in Fig. 9 [32].

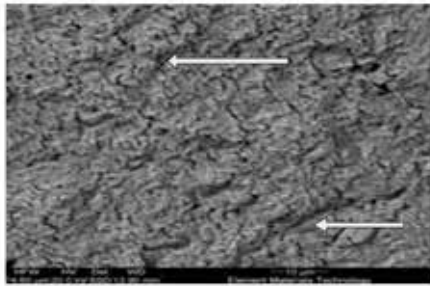


Fig. 9. Scanning electron microscope image of the surface of a cracked valve.

The revealed microcracks are the result of thermal stresses occurring during the process of exchange of the working medium [17].

METALLOGRAPHIC TESTING

For metallographic testing, a section of the head material, shown in Fig. 10 [31], was taken.



Fig. 10. View of valve 1 and a section of a valve for metallographic examination.

Examination of the valve revealed a tempered martensitic microstructure typical of the material of this type of valve [31]. The test results ruled out a material defect in the tested valve and, thus, excluded it as the cause of the failure. No deviations were found in the place of the fracture (scrap) and in the fragment away from it.

The Vickers hardness measurement of the tested valve head confirmed the required hardness of the valve material, while

the measurement of the valve thickness and angles showed that the permissible thickness loss exceeded the design value by 1 mm. This indicates repeated regeneration of the valve by grinding-in. The measurement of the valve thickness is shown in Fig. 11 [31], and the angle measurement location is shown in Fig. 12 [31].



Fig. 11. Valve thickness measurement in the faying section.

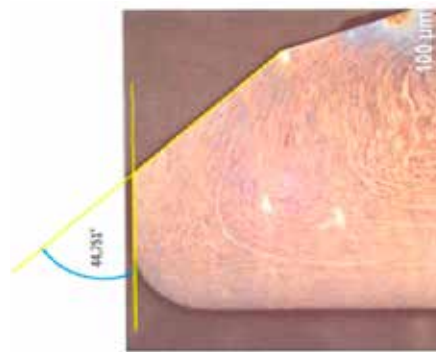


Fig. 12. Angle of faying face inclination measurement.

IDENTIFYING CAUSES OF DAMAGE

The causes generating damage to inlet-valves, bearing pans, and fuel apparatus are a consequence of various conditions resulting from the operational realities of the main propulsion power plant including cold starts of the engine [18, 22]. These causes are grouped according to the similarity of their destructive impact.

MALFUNCTION OF THE MAIN ENGINE HEATING SYSTEM

When the ship is stationary in port, the main engine should be heated by heating water in a circuit bypassing the heat exchanger. The temperature of the heating water and, thus, of the engine when it is not working should be in the range of 50–55 °C to ensure correct ignition during the engine start-up and its further operation. At the beginning of the research, as a result of the initial recognition of the heating water temperature and the quality of the circulating

oil purifying system and, consequently, the engine energy state, it was found that the temperature of the heating water and, therefore, the temperature of the engine before the start-up was only 20–25 °C. Starting of the engine in such a defined energy condition is known as the so-called “cold start”. The correct temperature of the low-temperature cooling circuit (LT – Low Temperature) of 60 °C, compliant with the operational documentation, was established only after 20 min of engine work at its load corresponding to about 50% of its nominal power. Looking for the correctness of the process course, Fig. 13 shows comparative diagrams of the engine cooling water temperature variation as a function of load. Diagrams were made during shop tests, by the crew of the ship, and for the purpose of verifying the engine cooling circuit functionality during the manoeuvres and sea passage (after the transient start-up process).

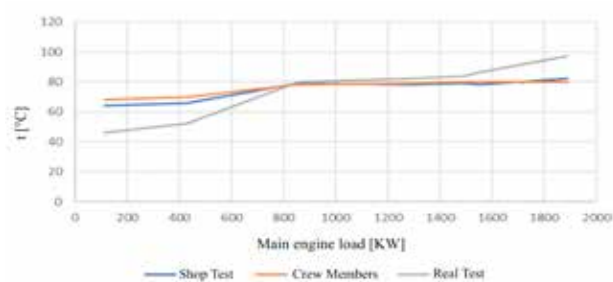


Fig. 13. Dependence of cooling water temperature on the main engine load: blue line - measurement from engine shop tests; red line - measurement taken by the crew; grey line - measurement taken for the sake of the case study.

To ensure the design operating conditions of the studied engine, the inlet cooling water temperature must not be lower than 60 °C. The inlet water temperature measurements made for the research in Fig. 13 show a lower temperature, while the outlet water temperature took correct values in the range of 78–82 °C.

Fig. 14 shows the variation of the engine cooling water temperature measured for the present study, from the value of the heating starting level during engine idling and port exit manoeuvres to the design value of the continuous operating temperature with the engine loaded at its nominal power. The relationship indicates that the water temperature at the beginning of the start-up is too low, reaching the correct value only after 20 min of operation with the engine load of 80% of its nominal power. The dotted line in the figure, reflecting the trend of the temperature change, confirms the correct operation of the automatic engine cooling system.

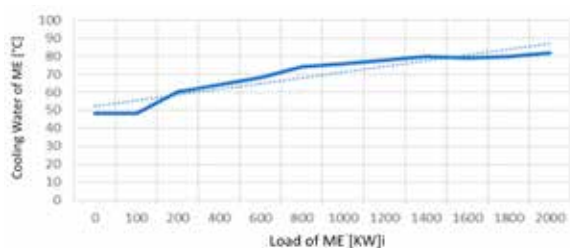


Fig. 14. Changes in the cooling water temperature as a function of engine power.

UNBALANCED ENGINE UNIT LOADS

In the case of an underheated main engine, underheated fuel injection pumps are the natural

consequence. This caused deterioration of the operating conditions of the barrel/plunger of the injection pumps and, consequently, the organization of the combustible mixture. The underheated engine operated unstably with a temporary reduction in speed and fuel delivery rate. Fig. 15 shows a run of the rotational speed and a representative of the fuel dose recorded during the engine start-up with the help of the Norris type control system.

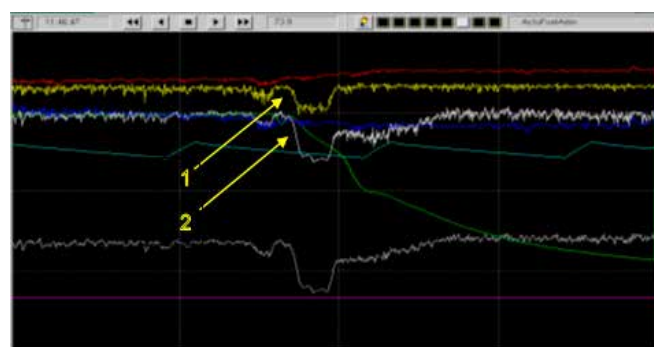


Fig. 15. Runs of the monitored parameters of the main engine operation during start-up: 1 - engine speed, 2 - fuel dose equivalent (Actual Fuel Admin).

An examination of the run of the start-up and the initial phase of engine operation showed an uneven distribution of loads on individual units. Lack of balancing of unit loads significantly hinders the start-up and the start of stable engine work and, thus, its ability to accept the load. The cylinder imbalance that is occurring, represented by the compression pressure, is shown in Fig. 16, with the distribution of the combustion pressure difference between the units.

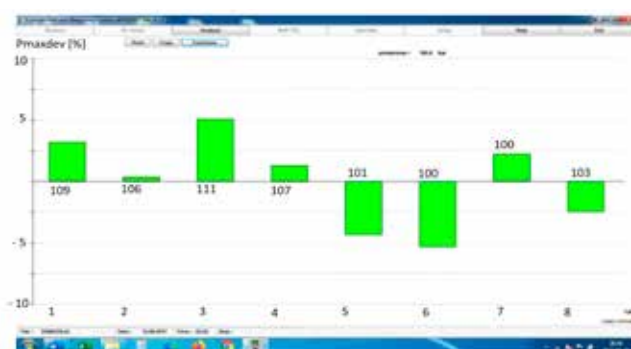


Fig. 16. Deviations from the mean value of the combustion pressure at the beginning of the second stage of engine start-up.

Temporary disengage/operation off of individual injection pumps from work was also observed. It disappeared after the energy condition of the main propulsion power plant had stabilized. Indicator tests of the combustion process and engine load condition were carried out using the LEMAG Premet C XL electronic indicator equipped with

the WPREMET software, enabling the real-time measurement of combustion pressures. Disturbances in the operation of the fuel system of individual injection pumps in the form of combustion pressure runs of the fuel-air mixture are shown in Fig. 17.

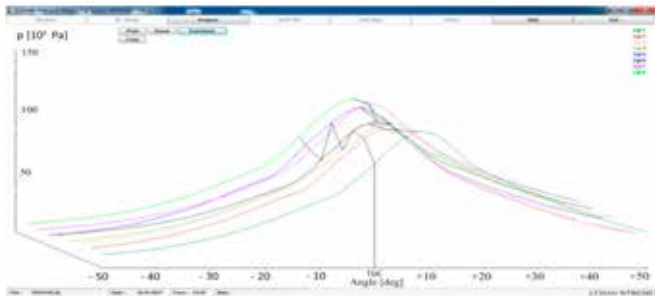


Fig. 17. Runs of combustion pressure in the first stage of the main engine operation as a function of the crankshaft rotation angle.

The combustion pressure runs for each cylinder showed significant differences. Identified by means of a diagram (Fig. 17), the hanging-up selected injection pump, disassembled for verification of its technical condition, revealed local traces of scuffing (B) and overheating in the form of a dark purple discoloration of the surface layer, as shown in Fig. 18.



Fig. 18. Local traces of scuffing on the barrel/plunger injection pump.

The revealed precision pair scuffing, manifested by pump hang-ups, is the result of the engine starting when the engine elements are at too low of a temperature during a cold start-up.

LUBRICATING OIL AT TOO LOW OF A TEMPERATURE

Starting the main engine when oil temperatures in the lubrication system are too low is difficult and sometimes even impossible. Frequently, if the main engine circulating oil is not purified long enough at standstill, it cannot be heated up to the required temperature by running the circulating pumps, removing sludge and possible water, and thus, heating up the engine crankshaft to the required temperature is not possible [18].

When the oil temperature is lowered, its rheological properties change. The viscosity of the engine lubricating oil increases and the resistance of the crankshaft movement increases. Oil with a higher viscosity does not reach all the motion pairs to the required extent. These conditions make it difficult to create an oil wedge in the hydrodynamic lubrication of the crankshaft bearings at the beginning of a start-up, which in turn leads to bearing pan damage. An

example of such damage to the crankshaft bearing pan of the engine under study is shown in Fig. 19.



Fig. 19. View of the damaged surface layer of the crankshaft bearing pan.

Diagnosing bearing shell wear is only possible during periodic inspections of piston-crank systems. Determination of the causes of wear depends on the correct assessment of the type of damage to the working surface of the slide bearings and their surface layer and the assessment of the quality of operation of the oil system.

Routinely during operation, causes of this type of wear are not associated with cold engine start-ups or underheated lubricating oil.

CORRECTIVE ACTIONS RESULTING FROM RESEARCH CONCLUSIONS

On the basis of the partial conclusions from the research, corrective actions were carried out during stay in port and verified during start-ups and registration of initial periods of engine work. Cooperation of the engine start-up time controller with the crankshaft speed meter was verified. Temperature controllers of the engine heating water and the state of the non-return valve at the connection of the engine heating and cooling circuits were corrected. Operation of the thermoregulatory valve adjuster in the engine circulating oil purifier system was adjusted.

The automatic setting of the starting fuel dose was adjusted. Settings of the injection pumps (fuel doses) and the moment of starting the fuel injection were corrected. The correction was made on three injection pumps with the use of a fuel dose corrector, included in the equipment of the injection pumps. The correctness of the timing phases of the mutual angle of rotation of the crankshaft and the camshaft was checked using an electronic meter.

Ship installations were tested during the engine preparation for operation. Temperature values of the heating water and lubricating oil were in accordance with the operation manual of the tested engine, i.e., temperatures of the heating water and lubricating oil were 50 °C and 45 °C, respectively.

After taking the corrective measures, control tests of the main engine preparation for starting and its start-ups were carried out in accordance with the technical and operational manual [19]. The engine start-ups proceeded and continued correctly. The start-up took place after a single feeding of the starting air with a small decrease in the air pressure in the starting air system.

The performed corrective actions balanced the load distribution across the engine units to some extent, as shown by the engine indicator graph in Fig. 20.

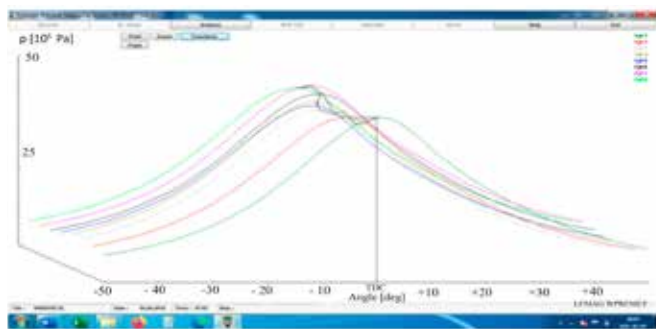


Fig. 20. Combustion pressure runs in the ship main power engine as a function of the crankshaft rotation angle, after correction actions, taken at the load of 50% of the nominal engine power.

The recorded runs of the pressure show more balanced loading of individual piston-crank systems. The effectiveness of the performed corrective actions, taking into account the conclusions of the conducted tests as fully as possible, was confirmed by the successful control tests of the engine start-up and its further operation without unscheduled repairs and valve damage.

FINAL REMARKS

Damage to each engine inlet-valve is an individual “random” event, not repeatable in nature, with different physics of the phenomenon course, although it most frequently occurs as a result of the so-called “cold starts” of the engine. The causes generating damage to the inlet valves and fuel system are the consequences of various conditions often resulting from random operational realities of the ship main propulsion system, e.g., cold starts of the engine and a periodically occurring phenomenon of pumping-up in its turbocharging system [33]. Superimposition of variable loads during manoeuvres on such a condition poses a threat to the stable operation of the power system and, thus, to the safety of navigation during the ship manoeuvres and subsequent sea passage.

The results of the conducted start-up tests and the procedure for assessing the effectiveness of engine work during normal operation confirmed the correctness of the applied methods for evaluating the causes of accelerated tribological wear and damage to engine elements as well as the validity of the undertaken predictive corrective actions in the applied operational strategy.

REFERENCES

1. Z. Yang, Q. Tan, and P. Geng, “Combustion and emissions investigation on low-speed two-stroke marine diesel engine with low sulfur diesel fuel,” *Polish Marit. Res.*, vol. 26, no. 1, p. 153-161, 2019, doi: 10.2478/pomr-2019-0017.
2. C. G. Rodriguez, M. I. Lamas, J. D. Rodriguez, and A. Abbas, “Analysis of the pre-injection system of a marine diesel engine through multiple-criteria decision-making and artificial neural networks,” *Polish Marit. Res.*, vol. 28, no. 4, p. 88-96, 2022, doi: 10.2478/pomr-2021-0051.
3. M. H. Ghaemi, “Performance and emission modelling and simulation of marine diesel engines using publicly available engine data,” *Polish Marit. Res.*, vol. 28, no. 4, p. 53-62, 2022, doi: 10.2478/pomr-2021-0050.
4. Z. Korczewski, “Test method for determining the chemical emissions of a marine diesel engine exhaust in operation,” *Polish Marit. Res.*, vol. 28, no. 3, p. 76-87, 2021, doi: 10.2478/pomr-2021-0035.
5. A. Tuan Hoang *et al.*, “A review on application of artificial neural network (ANN) for performance and emission characteristics of diesel engine fueled with biodiesel-based fuels,” *Sustain. Energy Technol. Assessments*, vol. 47, p. 360-386, Oct. 2021, doi: 10.1016/j.seta.2021.101416.
6. W. Zeńczak and A. K. Gromadzińska, “Preliminary analysis of the use of solid biofuels in a ship’s power system,” *Polish Marit. Res.*, vol. 27, no. 4, p. 67-79, 2020, doi: 10.2478/pomr-2020-0067.
7. A. T. Hoang, S. Nizetic, A. I. Ölçer, and H. C. Ong, “Synthesis pathway and combustion mechanism of a sustainable biofuel 2,5-dimethylfuran: Progress and prospective,” *Fuel*, vol. 286, p. 119337, 2021, doi: 10.1016/j.fuel.2020.119337.
8. DNV GL Maritime, Environmental advisory, “Methanol as marine fuel: Environmental benefits, technology readiness, and economic feasibility,” Report No.: 2015-1197, Rev. 2, 2016.
9. X. Gu, G. Jiang, Z. Guo, and S. Ding, “Design and experiment of low-pressure gas supply system for dual fuel engine,” *Polish Marit. Res.*, vol. 27, no. 2, p. 76-84, 2020, doi: 10.2478/pomr-2020-0029.
10. R. Zhao *et al.*, “A numerical and experimental study of marine hydrogen-natural gas-diesel tri-fuel engines,” *Polish Marit. Res.*, vol. 27, no. 4, p. 80-90, 2020, doi: 10.2478/pomr-2020-0068.
11. J. Kropiwnicki, “Application of Stirling engine type alpha powered by the recovery energy on vessels,” *Polish*

- Marit. Res.*, vol. 27, no. 1, p. 96-106, 2020, doi: 10.2478/pomr-2020-0010.
12. K. Rudzki and W. Tarełko, "A decision-making system supporting selection of commanded outputs for a ship's propulsion system with a controllable pitch propeller," *Ocean Eng.*, vol. 126, p. 254-264, 2016, doi: 10.1016/j.oceaneng.2016.09.018.
 13. H. Zeraatgar and M. H. Ghaemi, "The analysis of overall ship fuel consumption in acceleration manoeuvre using hull-propeller-engine interaction principles and governor features," *Polish Marit. Res.*, vol. 26, no. 1, p. 162-173, 2019, doi: 10.2478/pomr-2019-0018.
 14. Młynarczak and K. Rudzki, "Optimisation of the topping-up process of lubricating oil in medium-speed marine engines," *Polish Marit. Res.*, vol. 28, no. 2, p. 78-84, 2021, doi: 10.2478/pomr-2021-0024.
 15. J. Girtler, "A concept of determining the relation between load and wear of tribological systems of ship main selfignition engines by using probabilistic approach," *Polish Marit. Res.*, vol. 25, no. 4, p. 130-138, 2018, doi: 10.2478/pomr-2018-0139.
 16. P. Puzdrowska, "Diagnostic information analysis of quickly changing temperature of exhaust gas from marine diesel engine part i single factor analysis," *Polish Marit. Res.*, vol. 28, no. 4, p. 97-106, 2022, doi: 10.2478/pomr-2021-0052.
 17. P. Drożdźiel, "Impact of selected operation conditions of a car combustion engine on its start-up parameters," *Maintenance and Reliability*, vol. 4, p. 22-30, 2003, Polish Scientific and Technical Exploitation Society, Warsaw, doi: 10.17531/ein.
 18. MS Motorservice International GmbH, "Valve failures and their causes," (50003976-13), [Online]. Available: <https://www.ms-motorservice.com/>. [Accessed: June. 10, 2022].
 19. I. Piotrowski and K. Witkowski, "Operation of marine internal combustion engines," (in Polish), Foundation for the Development of Maritime University in Gdynia, 2012.
 20. J.K. Włodarski, "Operating states of marine internal combustion engines," (in Polish), Publishing House of Maritime University in Gdynia, 1990.
 21. A. Adamkiewicz and J. Fydrych, "Operational verification of ship Main Power System element choice – case study," *Journal of KONES Powertrain and Transport*, vol. 26 no.4 2019, doi: 10.2478/kones-2019-0120.
 22. A. Adamkiewicz and J. Fydrych, "Operation parameter monitoring as a condition to controlling the operation main power system," *Journal of Polish CIMAC*, vol. 3 no.1 Gdańsk 2008, ISSN 1231 – 3998, ISBN 83 – 900666 – 2 – 9.
 23. A. Bejger and J. Drzewieniecki, "The use of acoustic emission to diagnosis of fuel injection pumps of marine diesel engines. Chapter 2 - Analysis of operational problems occurring in fuel injection pump," *Energies*, vol. 12, no. 4, p. 4661, 2019. doi: 10.3390/en12244661.
 24. L. Chybowski, "Explosions in the starting air systems of marine engines. Causes, prevention and minimization of effects," (in Polish), Scientific Publisher of the Maritime University of Szczecin 2022.
 25. M. Brauss and J. Hiltz, "Diesel engine valve failures," *Conference: 56th Meeting of the Society for Machinery Failure Prevention Technology Virginia Beach, USA 2002*. Available: <https://www.researchgate.net/publication/275641222>. [Accessed: June. 10, 2022].
 26. Diesel Pro Power, „Engine valves — What do they do and how to correct failure,” [Online]. Available: <https://dieselpro.com/blog/engine-valves-what-do-they-do-and-how-to-correct-failure/>. [Accessed: June. 10, 2022].
 27. A. Göksenli and B. Eryürek, "Failure analysis of diesel engine intake valve," *Key Engineering Materials*, vol. 385-387, 2008. doi: 10.4028/www.scientific.net/KEM.385-387.29.
 28. A. Hornik, "Modeling of thermal loads of the seat-supercharged valve assembly compression ignition engine," (in Polish), Ph.D. [Dissertation], Silesian University of Technology Gliwice 2010.
 29. R. Lewis, "Wear of diesel engine inlet valves and seats," Ph.D. [Dissertation], Department of Mechanical Engineering. University of Sheffield, 2000.
 30. T. Chu Vanac, A. Zared, et al. "Effect of cold start on engine performance and emissions from diesel engines using IMO-Compliant distillate fuels," *Environmental Pollution*, vol. 255, Part 2, p. 113260, 2019.
 31. A. Frede and G. Noorman, "Untersuchung eines Einlassventils mit Tellerbruch," Markisches Werk GmbH; report no. IR Brise KHD628 20190327, test report 2019. A. Frede. and G.
 32. M. van der Laars, "Investigation of a filed inlet valve," Wartsila Element Materials Laboratory Raport no. ERO025247P Research report, 24.08.2018.
 33. O. Stolp, "Turbocharger surging. Facts and counter measures," ABB Hamburg 2012.

CONTACT WITH THE AUTHORS

Andrzej Adamkiewicz

Maritime University of Szczecin
ul. Wały Chrobrego 1-2
70-500 Szczecin
POLAND

Janusz Fydrych

Briese Berederung, Hamburg
POLAND

Jan Drzewieniecki

e-mail: j.drzewieniecki@am.szczecin.pl

Maritime University of Szczecin
ul. Wały Chrobrego 1-2
70-500 Szczecin
POLAND

NUMERICAL STUDY OF THE EJECTION COOLING MECHANISM OF VENTILATION FOR A MARINE GAS TURBINE ENCLOSURE

Hong Shi^{1*}

Qianwei Zhang¹

Meinan Liu¹

Kaijie Yang²

Jie Yuan²

¹ Jiangsu University of Science and Technology; China

² Nanjing University of Aeronautics & Astronautics; China

* Corresponding author: shihong@nuaa.edu.cn (Hong Shi)

ABSTRACT

A marine gas turbine enclosure must be designed to prevent overheating of the electrical and engine control components as well as diluting potential fuel leaks. In order to achieve an optimal enclosure design, a numerical study of the ventilation-ejection cooling mechanism of a gas turbine enclosure is carried out in this paper. The evaluation index of the ejection cooling performance is first proposed and the algorithm of numerical simulation is verified. On this basis, orthogonal combinations of structural parameters are carried out for the expansion angle α of the lobed nozzle and the spacing S between the outlet plane of the lobed nozzle and the inlet plane of the mixing tube. The flow and the temperature distribution inside the enclosure are analysed under different operating conditions. The results show that the influence of the lobed nozzle expansion angle α and the spacing S on the performance is not a single-valued function but the two influencing factors are mutually constrained and influenced by each other. For any spacing, the combined coefficient is optimal for the expansion angle $\alpha = 30^\circ$. When the expansion angle $\alpha = 45^\circ$ and the spacing $S = 100$ mm, the combined coefficient and the temperature distribution inside the enclosure are optimal at the same time.

Keywords: Gas Turbine Enclosure, Ejecting Cooling, Ventilation, CFD

INTRODUCTION

A large marine gas turbine is one of the important energy conversion and transfer devices for ships. Gas turbines can use different types of fuel and emit fewer pollutants [1]. In addition, the heat from gas turbine exhaust gas can be further utilised in the thermochemical reactor and steam generator, and the water extracted from the exhaust gas can be reused for steam injection in the gas turbine cycle [2-4]. All of this makes gas turbines for marine use more competitive. Presently, the most common large marine gas turbine is the General Electric LM2500, with subsequent modifications, such as the LM2500+ and LM2500+G4. The marine gas turbines have an enclosure design with mechanical drives and other

auxiliary components inside the enclosure. The enclosure not only isolates and protects the gas turbine from the external environment, but also reduces the impact of gas turbine operating noise and allows for easy maintenance and storage [5-7]. However, the closed working environment also makes it necessary to design a ventilation and cooling system for the gas turbine enclosure, to boost the power and efficiency of the gas turbine [8].

The ventilation and cooling system of a marine gas turbine enclosure prevents overheating of electrical and engine control components, as well as diluting potential fuel leaks, to eliminate stagnant areas that could lead to ignition in the cowling [9,10]. Conversely, excessive ventilation airflow may not only lead to unnecessary engine heat loss and excessive auxiliary power

requirements [11], but it may also result in excessive mixing tube outlet flow rates and, thus, additional installation costs. Therefore, optimum design of the enclosure ventilation and cooling must be based on an appropriate ventilation flow rate and temperature distribution. Traditionally, forced cooling ventilation is mostly used for cooling the enclosure, with fans providing the appropriate ventilation flow at the air inlet, which has more energy consumption in marine use. In contrast to forced cooling ventilation, ejection cooling does not require the installation of special cooling equipment and can save space in the ship design. In addition, exhaust noise can be suppressed and the intensity of infrared radiation reduced when using ejector airflow to cool the enclosure. Therefore, ejection cooling will be more widely used in marine gas turbine enclosure ventilation systems in the future [12]. However, current scholarly research is focused on forced cooling ventilation. CFD (Computational Fluid Dynamics) numerical simulations and experiments are used to obtain the distribution of airflow velocity and temperature inside the enclosure, as well as airflow organisation in the event of a gas leak [13-15]. Although there are relatively few references on the use of ejection cooling to reduce the internal temperature of gas turbine enclosures, ejecting systems have been studied relatively extensively for other applications.

Numerous studies have focused on the design of the lobed nozzle ejector and its matching with the mixing tube. Maqsood and Birk [16,17] investigated the ejecting performance of a bent ejector with a long elliptical cross-sectional area, a subsonic air-air bending ejector and an annular induced diffuser. Hu et al. [18] used PIV experiments to investigate the vortex structure and degree of turbulence in the near field of an ejector caused by a lobed nozzle. The results showed that the laminar area of the lobed nozzle is shorter and the smaller scale turbulent structures appear earlier, and are more extensive, than in the circular nozzle. Nastase and Meslem [19] found that a lobed nozzle without an expansion angle allows the improvement of mixing in the generated stream compared to a circular ejector. A lobed nozzle with an expansion angle reaches four times the entrainment of a circular ejector. Sheng [20] investigated the effect of different lobed peak spoilers on ejector performance (such as the entrainment coefficient, mixing efficiency and total pressure recovery coefficient). Varga et al. [21] found that the nozzle outlet plane influences both the critical back pressure and the entrainment coefficient. An optimum distance exists between the nozzle outlet plane and the mixing tube inlet, to allow for maximum entrainment of the secondary stream.

In summary, the lobed nozzle ejector itself and the matching of the ejector with other devices has been relatively well studied by relevant scholars. Most of the research focuses on the optimisation of the entrainment coefficient, with the objective of reducing the mainstream temperature and weakening the infrared radiation intensity, and less on the temperature distribution and pressure loss within the enclosure assembly. Although the ejection cooling is mainly based on the ejecting principle, the design objective is not only to improve the air entrainment coefficient and reduce

the total pressure loss of the ejection cooling system, but also to avoid localised high temperatures in the enclosure. Therefore, the results of the above-mentioned research on ejectors cannot be simply extended to the ventilation and cooling system of the gas turbine enclosure.

Accordingly, this paper takes a marine gas turbine enclosure as the research object and proposes evaluation indexes for the cooling performance of the enclosure. The orthogonal combination method is used to obtain the ejection cooling effect under different structure parameters. Furthermore, the mechanism analysis of the flow field and temperature distribution is carried out. Finally, the optimal ventilation and cooling solution is obtained, based on the multi-objective evaluation.

GEOMETRICAL AND METHODOLOGY

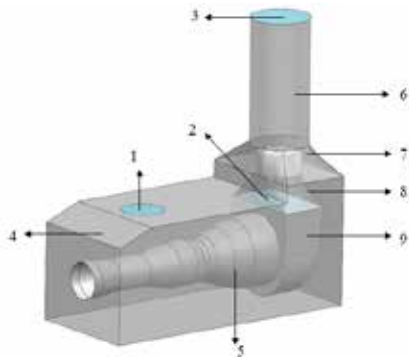
GEOMETRICAL MODEL AND BOUNDARY CONDITION

In this paper, the ejection cooling system of a marine gas turbine was studied and a geometrical model established. Due to the complexity of the actual model and the limitations of computing resources, the influence of the auxiliary equipment and the piping arrangement in the enclosure were not considered when building the geometrical model. Fig.1 shows a geometrical model reflecting the main features of the gas turbine casing.

The *Realizable k-ε* turbulence model was used in the CFD numerical simulation. Meanwhile, the equations of mass, momentum, turbulence kinetic energy and dissipation rate were solved using the SIMPLE (Semi-Implicit Method for Pressure Linked Equation) algorithm. The airflow properties were taken to be those for an ideal gas and the temperature was defined in sections, according to the state of the gas turbine operation. The surface of the high-temperature components of the gas turbine was coated with thermal protection material and the gas turbine casing set up as a slip-free wall, with an emissivity of 0.9 [22].

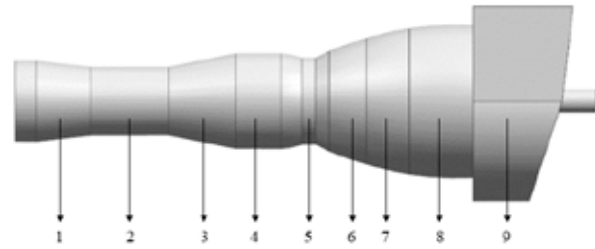
Furthermore, the exhaust plenum outlet was set up as a mass flow inlet with a mass flow rate of 27.8 kg/s and temperature of 782 K. The cooling inlet was set up as a pressure inlet with a temperature of 300 K and a pressure of 0 Pa. The mixing tube outlet was set up as a pressure outlet with a temperature of 300 K and a pressure of 1000 Pa.

Fig.2 shows the structure of the lobed nozzle ejector and the ejection cooling system.



(a) Enclosure geometrical model:

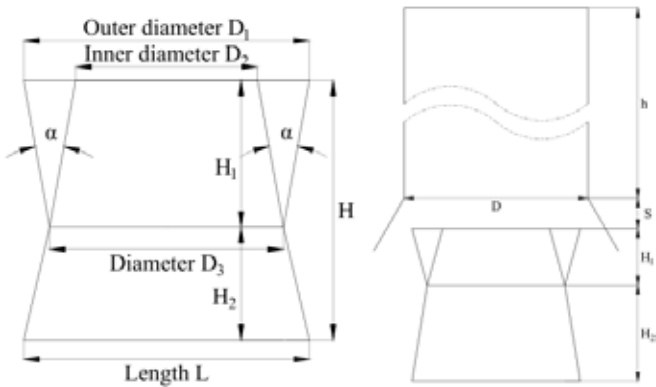
- 1 - Cooling inlet (Secondary stream inlet);
- 2 - Exhaust plenum outlet (Mainstream inlet);
- 3 - Mixing tube outlet (Mixed streams outlet);
- 4 - Gas turbine enclosure;
- 5 - Gas turbine casing;
- 6 - Mixing tube;
- 7 - Transition section (Between the mixing tube and the enclosure);
- 8 - Lobed nozzle ejector;
- 9 - Exhaust plenum.



(b) Gas turbine casing geometrical model:

- 1 - Inlet section 350 K;
- 2 - Low pressure air compressor 400 K;
- 3 - High pressure air compressor 550 K;
- 4 - Combustion 600 K;
- 5 - Aft combustion chamber 500 K;
- 6 - Transition section 700 K;
- 7 - Power turbine 400 K;
- 8 - Aft power turbine 400 K;
- 9 - Exhaust plenum 390 K.

Fig. 1. Geometrical model



(a) Lobed nozzle ejector

(b) Ejection cooling system

Fig. 2. Schematic of the structure

The lobed nozzle expansion angle α and the spacing S between the outlet of the lobed nozzle and the inlet of the mixing tube were set up as an orthogonal combination of structural parameters. Unlike traditional lobed nozzle ejectors, the lobed nozzle ejector studied in this paper consisted of a lobed nozzle section (H_1) and a square-to-circle section (H_2), as shown in Fig.2(a). As the exhaust plenum outlet plane is square, the lobed nozzle needed to be designed with a square-to-circle section, to connect the square plane of the exhaust plenum outlet to the circle plane at the bottom of the lobed nozzle.

It should be noted that, because the lobed nozzle ejector and the gas turbine enclosure were matched to each other, the total height (H) of the lobed nozzle ejector remained constant during the structural analysis of the lobed nozzle ejector. Therefore, when designing different expansion angles α by varying the lobed nozzle height (H_1), the change in lobed nozzle height (H_1) caused a change in the height of the square-to-circle height (H_2). There is a matching relationship between the two sections.

As shown in Fig.2(b), the spacing between the outlet of the lobed nozzle ejector and the inlet of the mixing tube is S . Specifically, $S < 0$ mm means that the ejector outlet is inside the mixing tube. $S = 0$ mm means that the ejector outlet is in the same plane as the mixing tube inlet. $S > 0$ mm means that there is a distance between the ejector outlet and the mixing tube inlet.

The fixed parameters of the ejector and mixing tube structure were designed as shown in Table.1.

Tab. 1. Fixed parameters

Design content		Parameter settings	
Ejector	Ejector	Total height	1000 mm
	Lobed nozzle section (H_1)	Outlet area	591323 mm ²
		Width of the lobe	100 mm
		Outer diameter (D_1)/ Inner diameter (D_2)	$D_1 = 1100$ mm, $D_2 = 700$ mm
		Diameter of the bottom circular surface (D_3)	900 mm
		Number of the lobe	10 (Evenly distributed by circumference)
Square-to-circle section (H_2)	Exhaust plenum outlet plane	1100 mm × 2000 mm	
Mixing tube	Diameter (D)	1200 mm	

Based on the fixed parameters in Table 1, orthogonal combinations were performed for four different lobed nozzle expansion angles α and six different spacings S , for a total of 24 combinations. Specifically, the expansion angle α of Case 1 - Case 6 was 20° and the spacings were: -100 mm, 0 mm, 100 mm, 200 mm, 400 mm, 500 mm, respectively. The expansion angle α for Case 7 - Case 12 was 30° and

the spacings were as above. The expansion angle α for Case 13 - Case 18 was 45° and the spacings were as before. The expansion angle α for Case 19 - Case 24 was 60° and the spacings were as above.

EVALUATION INDICATORS

System Performance Indicators

Due to space limitations in the ship, it is difficult to achieve the optimum mixing tube lengths for the ejector design. At the same time, considering the mixing loss between the mainstream and secondary streams, the maximum entrainment coefficient should not be pursued while meeting the cooling requirements of the gas turbine enclosure [23]. The entrainment coefficient and pressure are closely related to the temperature field. Therefore, in the actual program selection process, the flow field calculation can be performed first, to obtain a series of cases that meet the requirements, and then temperature field checks can be carried out. This method makes the calculation relatively efficient.

In this paper, the entrainment coefficient was combined with the pressure loss coefficient in the flow field calculation, to obtain the combined coefficient, and it was used as an evaluation indicator for the flow characteristics of the ejection cooling system. The implication of the combined coefficient is that a better system performance should provide a higher entrainment coefficient at a lower pressure loss. The equation is as follows:

$$\text{Combined coefficient} = \frac{\text{Entrainment coefficient}}{\text{Pressure loss coefficient}} \quad (1)$$

– Entrainment coefficient

The entrainment coefficient is a dimensionless coefficient that indicates the entrainment capacity of the ejection cooling system, and is defined as follows:

$$n = \frac{G_2}{G_1} \quad (2)$$

where G_1 is the mass flow rate of the mainstream, and G_2 is the mass flow rate of the secondary stream.

– Pressure loss coefficient

The pressure loss coefficient is a dimensionless coefficient which indicates the flow loss in the ejection cooling system and is expressed as follows:

$$\Pi = \frac{P_1 - P_2}{q} \quad (3)$$

where P_1 is the total pressure at the outlet of the exhaust plenum, P_2 is the total pressure at the outlet of the mixing tube, and q is the dynamic pressure at the outlet of the exhaust plenum.

Temperature Indicators

The air temperature in a typical plane within the enclosure needs to be less than 82°C (355 K) during operations [24]. It should be noted that, due to the high temperature of the gas turbine casing, it is difficult to significantly reduce the temperature in the section near the gas turbine casing by ejection cooling alone. Therefore, the temperature in the section near the gas turbine casing does not have to be considered within the required temperature indicators.

ALGORITHM VALIDATION

In order to ensure the reliability of the numerical simulations in this paper, a geometric model was built based on the parameters in the literature [25]. For the numerical simulation, the experimental system was simplified and only the lobed nozzle section was retained, as shown in Fig.3. Specifically, the outer diameter of the outlet plane of the lobed nozzle is 108.0 mm, the inner diameter is 54.0 mm, and the diameter of the inlet plane is 70 mm. The height of the lobed nozzle is 73 mm, the width of each lobe is 7.2 mm, and the number of lobes is 12. The boundary conditions of the numerical simulation were based on the experiments in the literature. Specifically, the mainstream inlet was set as the velocity inlet with a velocity of 21 m/s and a temperature of 620 K. The secondary stream inlet and the mixing outlet were simultaneously set as pressure boundaries, with an ambient pressure and a temperature of 300 K. The results of the experiments and simulations are shown in Fig.4.

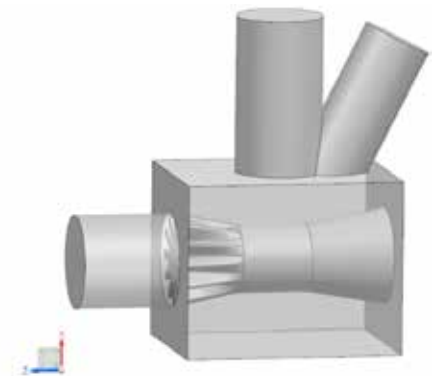


Fig. 3. Geometric model

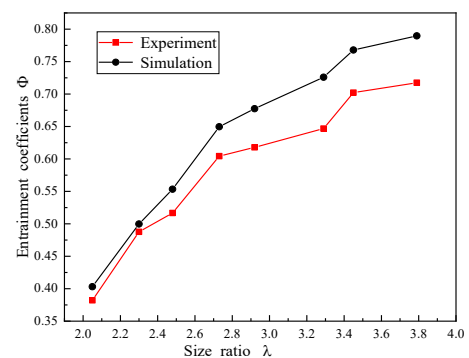


Fig. 4. Experiments and simulations

As shown in Fig.4, the simulation results are slightly higher than the experimental results. The main reason for this is that, in the experiments, the mainstream inlet of the lobed nozzle ejector is equipped with piping in front of it, which may lead to a non-uniform distribution of the mainstream velocity. In the simulations, however, the mainstream velocity is designed to be uniformly distributed. Therefore, there is a difference between the simulated and experimental mainstream inlets. Because the difference in the results of the entrainment coefficient in the experiments and simulations is less than 10%, for different size ratios, and the variation trend is relatively consistent, the numerical simulation of the ejector (in this paper) has some reliability and can be used for subsequent studies.

MESH INDEPENDENCE

An unstructured polyhedral mesh was created for the geometric model, with mesh refinement in more complex areas, such as the inlet and outlet of the model and the lobed nozzle ejector. At the same time, a boundary layer was created on the mixing tube and the gas turbine casing. In order to ensure that the results were independent of the number of meshes, when analysing the performance of the system, the geometric model of Case 3 ($\alpha = 20^\circ$, $S = 100$ mm) was chosen to create meshes of five different diameters. The effect of different diameters of meshes on the performance of the system was analysed using the total pressure of the mainstream inlet and the average temperature of the central plane as indicators. The results are shown in Table 2.

Tab. 2. Mesh independence validation

Number of meshes	2.05 million	3.37 million	4.70 million	5.88 million	6.75 million
Total pressure of the mainstream inlet (Pa)	3549.7	3684.4	3744.3	3748.4	3746.9
Average temperature of the central plane (K)	313.4	315.1	315.6	315.7	315.6

As shown in Table 2, when the number of meshes reaches 4.70 million, the total pressure at the mainstream inlet and the average temperature at the central plane hardly change as the mesh number increases. Considering the speed of the simulation and the accuracy of the results, a mesh with the number of 4.70 million was chosen for the subsequent simulations in this paper.

SIMULATION AND RESULTS

COMBINED COEFFICIENT

Fig.5 shows the variation pattern of the combined coefficient with the lobed nozzle expansion angle α and spacing S .

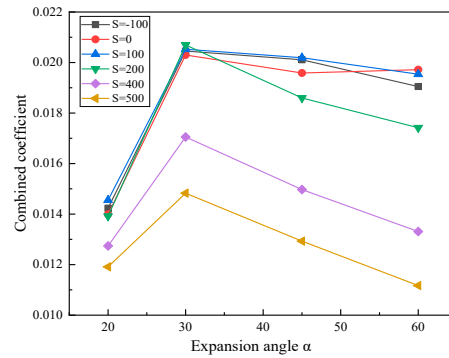


Fig. 5. Combined coefficient variation pattern

As shown in Fig.5, with the increase of the expansion angle α , the combined coefficient first increases and then decreases. When the expansion angle $\alpha = 20^\circ$, the ejector structure results in a high total pressure loss and, therefore, the combined coefficient remains low. For any spacing, the combined coefficient is optimal for the expansion angle $\alpha = 30^\circ$. Of the 24 cases, the four cases with the best combined coefficients are Case 7 ($\alpha = 30^\circ$, $S = -100$ mm), Case 9 ($\alpha = 30^\circ$, $S = 100$ mm), Case 10 ($\alpha = 30^\circ$, $S = 200$ mm), and Case 15 ($\alpha = 45^\circ$, $S = 100$ mm), with Case 10 having the best combined coefficient of them all. The following is a specific analysis, in terms of both the entrainment coefficient and the pressure loss coefficient.

Entrainment Coefficient

Fig.6 shows the variation pattern of the entrainment coefficient with the expansion angle α and spacing S .

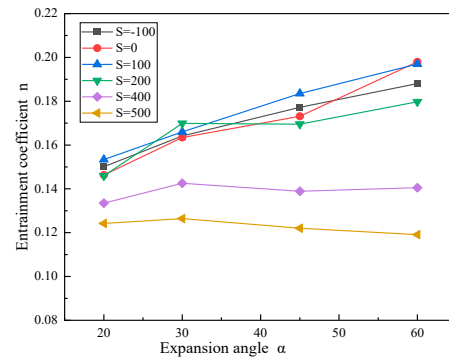


Fig. 6. Entrainment coefficient variation pattern

From Fig.6, it can be seen that there are two trends in the entrainment coefficient, with different expansion angles α and spacing S .

(1) When the spacing $S \leq 100$ mm, the entrainment coefficient increases with increasing expansion angle α .

In order to further study the mechanism of the effect of the expansion angle α on the entrainment coefficient, the velocity distribution and stream-wise vortices are specifically analysed for a spacing $S = 0$ mm. Fig.7 shows the velocity distribution of the ejector.

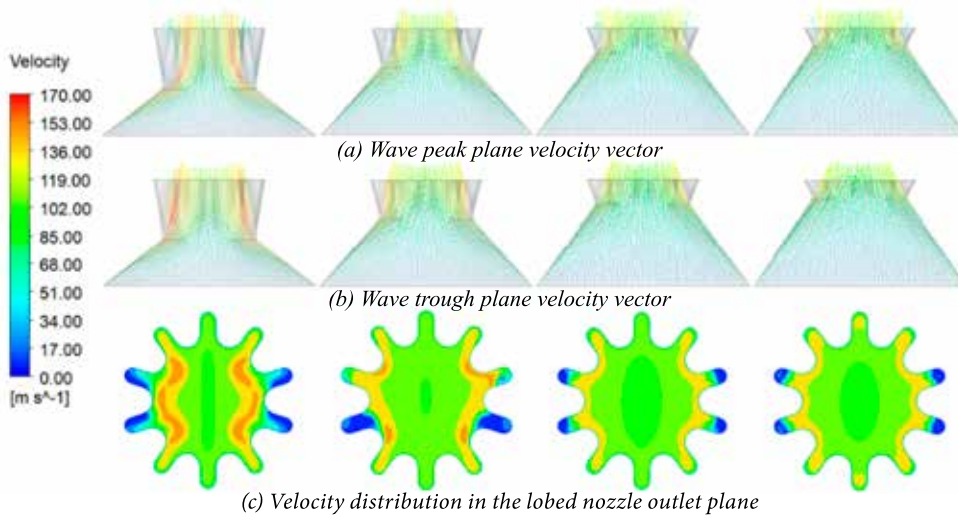


Fig. 7. Velocity of the lobed nozzle ejector plane
(From left to right : 20°, 30°, 45°, 60°)

As shown in Fig.7, due to the influence of the square-to-circle section (H_2) of the ejector, the mainstream velocity distribution within the ejector is not uniform and localised high velocity areas can exist near the walls. When the expansion angle $\alpha = 20^\circ$, the height of the square-to-circle section (H_2) is the smallest, the deformation in the length direction is the most intense, and the backflow area at the lobe boundary is larger. As the expansion angle α increases, the height of the square-to-circle section (H_2) gradually increases, and the deformation between the length direction of the exhaust plenum outlet and the circle plane at the bottom of the lobed nozzle is gradually eased. Meanwhile, the velocity of the mainstream gradually decreases along the walls and the velocity distribution inside the ejector tends to be uniform. In addition, as the height of the lobed nozzle section (H_1) gradually decreases, the backflow area within the lobed nozzle also gradually decreases and the utilisation of the mainstream gradually increases. Thus, as the expansion angle α increases, the entrainment coefficient gradually rises.

(2) When the spacing $S \geq 200$ mm, the entrainment coefficient fluctuates with increasing expansion angle α .

Taking the expansion angle $\alpha = 45^\circ$ as an example, Fig.8 shows the velocity vector in the inlet area of the mixing tube for spacings of 200 mm, 400 mm, and 500 mm.

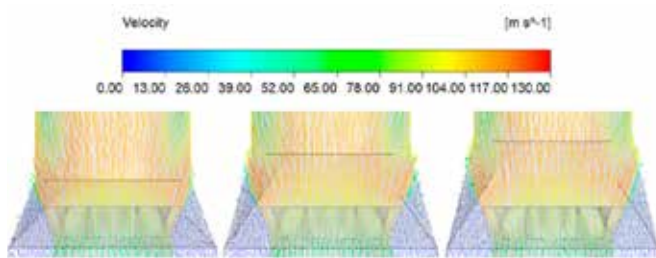


Fig. 8. Velocity vector in the mixing tube inlet area
(From left to right : 200 mm, 400 mm, 500 mm)

As shown in Fig.8, when the spacing $S = 200$ mm, the mainstream begins to diffuse fully as it reaches the mixing tube inlet, with a small proportion of the mainstream impacting the wall of the transition section in front of the mixing tube inlet. These block the passage of the secondary stream into the mixing tube and the wall of the transition section has an inclined angle, which causes the secondary stream to randomly return to the interior of the enclosure, thus reducing the entrainment coefficient.

When the expansion angle α changes, the impact point of the mainstream and transition section changes, resulting in fluctuations in the entrainment coefficient. However, when the spacing $S = 200$ mm, there is relatively little backflow and so the entrainment coefficient remains at a high level.

As the spacing S increases further, the passage from the ejector outlet plane to the inlet plane of the mixing tube gradually widens and the mainstream is fully diffused before it reaches the inlet of the mixing tube. The impact of the mainstream on the transition section wall reduces the utilisation of the mainstream and blocks the passage of the secondary stream, making the backflow of the secondary stream more serious. Therefore, the entrainment coefficient is generally low when the spacing S is large. The degree of backflow and passage blockage of the secondary stream depends on the matching relationship between the expansion angle α and the mixing tube. As the structure of the ejector and the transition section in front of the mixing tube do not vary in a univariate manner, the entrainment coefficient fluctuates with the expansion angle α , but does not vary significantly.

Pressure Loss Coefficient

Fig.9 shows the variation pattern of the pressure loss coefficient with the lobed nozzle expansion angle α and the spacing S .

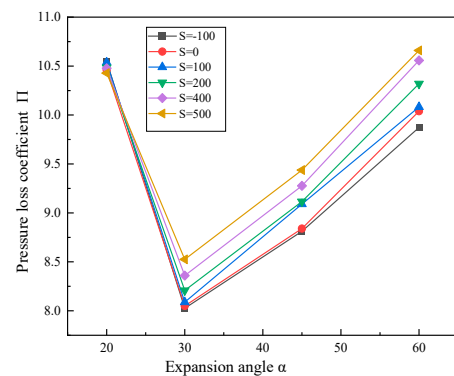


Fig. 9. Pressure loss coefficient variation pattern

As can be seen from Fig. 9, the pressure loss coefficient follows the same trend at different spacings. This means that, as the expansion angle α increases, the pressure loss coefficient at any spacing S shows a tendency to decrease and then increase. Specifically, the pressure loss coefficient decreases rapidly as the expansion angle α increases from 20° to 30° . As the expansion angle α increases further, the pressure loss coefficient gradually increases.

In order to further study the mechanism of the effect of the expansion angle α on the pressure loss coefficient, a pressure loss table is presented, for specific analysis. Using the spacing $S = 0$ mm as an example, Table 3 shows the total pressure loss of the ejection cooling system.

Tab. 3. Total pressure loss in the ejection cooling system

Spacing (S) / mm	Expansion angle (α)	Total pressure loss inside the ejector / Pa			Total pressure loss in the ejection cooling system / Pa		
		Lobed nozzle section (H ₁)	Square-to-circle section (H ₂)	Total pressure loss	Exhaust plenum outlet plane	Mixing tube outlet plane	Total pressure loss
0	20°	553.49	400.08	953.57	3719.74	1910.49	1809.25
	30°	303.87	164.73	468.60	3418.68	1923.11	1495.57
	45°	295.37	124.29	419.66	3454.36	1932.77	1521.59
	60°	327.39	100.80	428.19	3693.55	1971.37	1722.18

As can be seen from Table 3, two important mechanisms contribute to the total pressure loss in the ejector. These are: non-uniformity of the mainstream velocity, due to the sharp geometrical deformation of the square-to-circle part (H₂) of the ejector, and intense mixing, due to the enhanced entrainment capacity. Specifically, as the expansion angle α increases, the total pressure loss in the square-to-circle section

(H₂) gradually decreases. At an expansion angle $\alpha = 20^\circ$, the total pressure loss in the square-to-circle section (H₂) is the highest, at approximately 400.08 Pa. The main reason for this is that the square-to-circle section (H₂) achieves a sharp square to circle transition at a relatively short height. The large change in geometry leads to a non-uniform mainstream velocity which, in turn, leads to large pressure loss. As the square-to-circle section (H₂) gradually increases, the deformation is gradually eased and the local pressure loss is reduced. However, when the expansion angle $\alpha = 60^\circ$, the entrainment capacity increases significantly and the energy consumed by the entrained secondary stream also increases significantly, resulting in a higher total pressure loss in the lobed nozzle section (H₁).

TEMPERATURE DISTRIBUTION

For the study of the gas turbine ejection cooling system, in addition to obtaining a better combined coefficient, it is equally important to reduce the high temperature areas inside the enclosure. Therefore, this section provides a specific analysis of the temperature distribution in typical planes inside the enclosure for the four cases with the better combined coefficients. Fig.10 shows the temperature distribution in typical planes inside the enclosure for each of the four cases.

As shown in Fig.10, the airflow enters the enclosure from the cooling inlet and flows to the gas turbine casing surface and, subsequently, along the gas turbine surface below. Therefore, the temperature of the airflow directly below the cooling inlet is lower. As the space inside the enclosure increases, the airflow velocity gradually decreases and, combined with the radiation from the high temperature of the gas turbine casing surface, the airflow is further heated inside the enclosure.

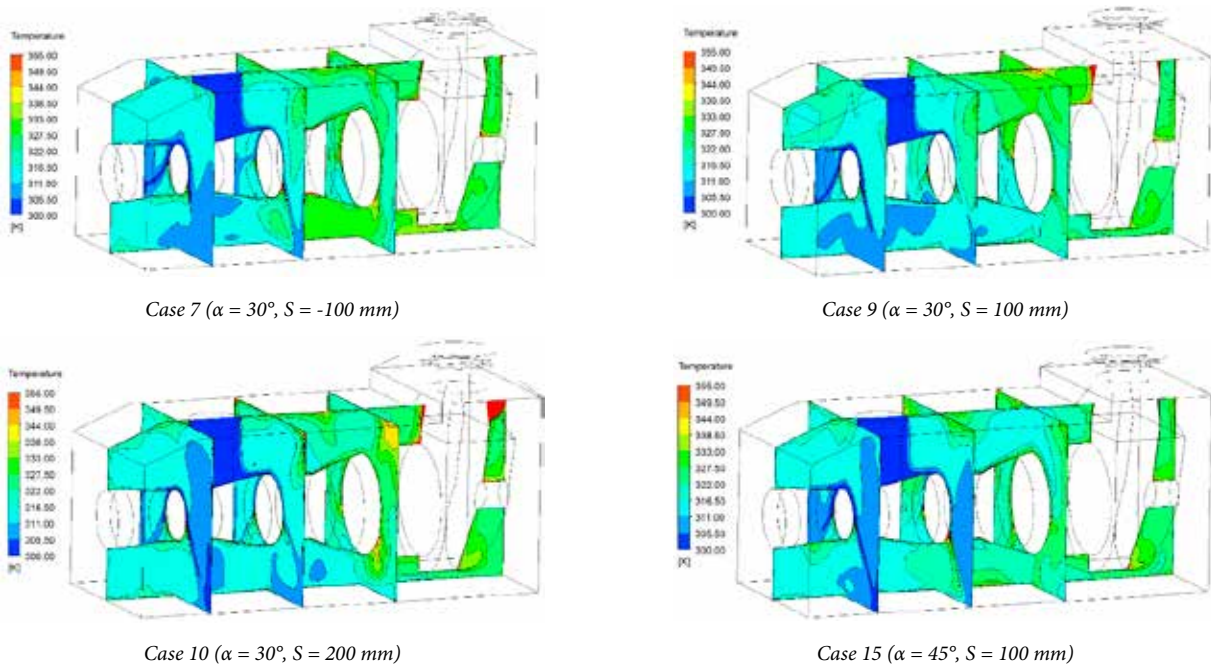


Fig. 10. Temperature distribution in typical planes

However, in Case 7, Case 9 and Case 10, there are localised areas with high temperatures on the top wall of the enclosure. This is because, as the spacing S increases, the backflow near the ejector inside the enclosure gradually becomes more serious. At the same time, more high temperature areas are generated inside the enclosure. In Case 15, the relatively high entrainment coefficient results in relatively high airflow velocities inside the enclosure and a relatively low temperature in the enclosure, with no high temperature areas inside the enclosure. On balance, Case 15 is the preferred option.

CONCLUSION

In this paper, a numerical study was carried out on the ventilation and cooling system of a gas turbine enclosure. The analysis focused on the effects of different expansion angles α and the spacing S between the lobed nozzle outlet plane and the mixing tube inlet plane on the ventilation and cooling performance. The combined coefficients of the ejection cooling system and the temperature distribution inside the enclosure under different design parameters were obtained and analysed specifically. The specific findings of this paper are as follows.

(1) The influence of the expansion angle α and the spacing S on performance is not a single-valued function, but the two influencing factors are mutually constrained and influenced by each other. The main reason for this is that the mixing tube in the enclosure and the square-to-circle section (H_2) interfere with the performance of the ejector, which differs significantly from a conventional ejector.

(2) The sharp reduction in height of the square-to-circle section (H_2) leads to the existence of a low velocity backflow area in the lobed nozzle, causing a blocking effect on the mainstream. However, as the expansion angle α increases, the backflow area within the lobed nozzle gradually decreases, and the utilisation of the mainstream gradually increases, more secondary streams can be entrained.

(3) For any spacing, the optimal combined coefficient is obtained for an expansion angle $\alpha = 30^\circ$. However, in the case of the better solution, there may still be localised high temperature areas inside the enclosure. So, four cases with the best combined coefficients are selected before the local temperature distribution analysis, namely Case 7, Case 9, Case 10 and Case 15. Through comparison and analysis, Case 15 has a better combined coefficient and there are no high temperature areas inside the enclosure, therefore Case 15 is the preferred option.

REFERENCES

1. N.R. Ammar and A. Farag, "CFD Modeling of Syngas Combustion and Emissions for Marine Gas Turbine Applications" Polish Maritime Research, vol.23, no.3, pp.39-49, 2016. doi: 10.1515/pomr-2016-0030.

2. O. Cherednichenko, S. Serbin, and M. Dzida, "Application of Thermo-chemical Technologies for Conversion of Associated Gas in Diesel-Gas Turbine Installations for Oil and Gas Floating Units," Polish Maritime Research, vol. 26, no. 3, 2019. doi: 10.2478/pomr-2019-0059.
3. S. Serbin, K. Burunsuz, M. Dzida, J. Kowalski, and D. Chen, "Investigation of Ecological Parameters of a Gas Turbine Combustion Chamber with Steam Injection for the Floating Production, Storage, and Offloading Vessel," International Journal of Energy and Environmental Engineering, 2021. doi: 10.1007/s40095-021-00433-w.
4. S. Serbin, N. Washchilenko, M. Dzida, and J. Kowalski, "Parametric Analysis of the Efficiency of the Combined Gas-Steam Turbine Unit of a Hybrid Cycle for the FPSO Vessel," Polish Maritime Research, vol. 28, no. 4, 2022. doi: 10.2478/pomr-2021-0054.
5. O. Kyrylash, V. Kostyuk, A. Smirnov, D. Tkachenko, and I.Loboda, "Mathematical Simulation of the Gas Turbine Packages Thermal State." Proceedings of the ASME Turbo Expo 2018: Turbomachinery Technical Conference and Exposition. vol.5C, Oslo, Norway. June 11-15, 2018. doi: 10.1115/GT2018-77194.
6. J. Kowalski, F. Di Mare, S. Theis, A. Wiedermann, M. Lange, and R. Mailach, "Investigation of the Ventilation Flow in a Gas Turbine Package Enclosure." European Conference on Turbomachinery Fluid Dynamics and Thermodynamics, 2019. doi: 10.29008/ETC2019-438.
7. A. Corsini, G. Delibra, M. Giovannelli, G. Lucherini, S. Minotti, S. Rossin, and L. Tieghi, «Prediction of Ventilation Effectiveness for LM9000 Package with Machine Learning.» Proceedings of the ASME Turbo Expo 2020: Turbomachinery Technical Conference and Exposition. vol.9. Virtual, online. September 21-25, 2020. doi: 10.1115/GT2020-14916.
8. Z. Domachowski, and M. Dzida, "Applicability of Inlet Air Fogging to Marine Gas Turbine" Polish Maritime Research, vol.26, no.1, pp.15-19, 2019. doi: 10.2478/pomr-2019-0002.
9. International Standard ISO 21789:2009 Gas Turbine Applications – Safety, International Organisation for Standardization, 2009.
10. G. Lucherini, V. Michelassi, and S. Minotti, "The Impact of Model Assumptions on the CFD Assisted Design of Gas Turbine Packages." Proceedings of the ASME Turbo Expo 2019: Turbomachinery Technical Conference and Exposition. vol.9. USA. June 17-21, 2019. doi: 10.1115/GT2019-90871.
11. R. Yerram, R. Watkins, and B. Ponnuraj, "Aeroderivative Gas Turbine Enclosure Ventilation System." Proceedings of the ASME Turbo Expo 2021: Turbomachinery Technical Conference and Exposition. vol.2C. Virtual, online. June 7-11, 2021. doi: /10.1115/GT2021-59136.

12. D.M. Li, L. Wang, X.Y. Wen, and S.D. Cao, "Numerical Simulation and Experimental Study of Marine Combustion Engine Exhaust Ejector." *Thermal Power Engineering*, vol.17, no.3, pp.226-230, 2002. doi: 10.3969/j.issn.1001-2060.2002.03.002.
13. B. Ponnuraj, B. Sultanian, A. Novori, and P. Pecchi, "3D CFD Analysis of an Industrial Gas Turbine Compartment Ventilation System." *Proceedings of the ASME 2003 International Mechanical Engineering Congress and Exposition. Heat Transfer*, vol.2. Washington, DC, USA. November 15–21, 2003. pp. 67-76. ASME. doi: 10.1115/IMECE2003-41672.
14. E. Graf, T. Luce, and F. Willett, "Design Improvements Suggested by Computational Flow and Thermal Analyses for the Cooling of Marine Gas Turbine Enclosures." *Proceedings of the ASME Turbo Expo 2005: Power for Land, Sea, and Air*. vol.5. Reno, Nevada, USA. June 6-9, 2005. pp. 587-593. doi: 10.1115/GT2005-68574.
15. G. Lucherini, S. Minotti, G. Ragni, and F. Bologna, "Experimental and Numerical Investigation on Gas Turbine Package Scale Model." *Proceedings of the ASME Turbo Expo 2018: Turbomachinery Technical Conference and Exposition*. vol.9. Oslo, Norway. June 11-15, 2018. doi: 10.1115/GT2018-75694.
16. A. Maqsood, and A.M. Birk, "Effect of a Bend on the Performance of an Oblong Ejector." *Proceedings of the ASME Turbo Expo 2007: Power for Land, Sea, and Air*. vol.6. Montreal, Canada. May 14-17, 2007. pp.37-45. doi: 10.1115/GT2007-27851.
17. A. Maqsood, and A.M. Birk, "Effect of Entraining Diffuser on the Performance of Bent Exhaust Ejectors." *Proceedings of the ASME Turbo Expo 2010: Power for Land, Sea, and Air*. vol.7. Glasgow, UK. June 14-18, 2010. pp.2793-2802. doi: 10.1115/GT2010-23499.
18. H. Hu, T. Saga, T. Kobayashi, and N. Taniguchi, "Research on the Vortical and Turbulent Structures in the Lobed Jet Flow Using Laser Induced Fluorescence and Particle Image Velocimetry Techniques." *Measurement Science & Technology*, vol.11, no.6, p.698, 2000. doi: 10.1088/0957-0233/11/6/313.
19. I. Nastase and A. Meslem, "Passive Control of Jet Flows Using Lobed Nozzle Geometries." *Mecanique Et Industries*, vol.8, no.2, pp.101-109, 2007. doi: 10.1051/meca:2007027.
20. Z.Q. Sheng, "Jet Mixing of Lobed Nozzles with Spoilers Located at Lobe Peaks." *Applied Thermal Engineering*, vol.119, pp.165-175, 2017. doi: 10.1016/j.applthermaleng.2017.03.048.
21. S. Varga, A.C. Oliveira, and B. Diaconu, "Influence of Geometrical Factors on Steam Ejector Performance – A Numerical Assessment." *International Journal of Refrigeration*, vol.32, no.7, pp.1694-1701, 2009. doi: 10.1016/j.ijrefrig.2009.05.009.
22. Z.B. Zhang, X.Y. Zhang, B.B. Li, and P. Sun, "Optimal Design of Cooling Structure of an Industrial Type Gas Turbine Enclosure Mount." *Thermal Science and Technology*, vol.5, no.7, 2016. doi: 10.13738/j.issn.1671-8097.2016.05.013.
23. Y.L. Han, "Numerical Simulation and Experimental Study of Marine Gas Turbine Exhaust Ejector." *Diss. Harbin Engineering University*, 2005, doi: 10.7666/d.y780039.
24. H. Bagheri and D. Vahidi, "Ventilation of Gas Turbine Package Enclosures: Design Evaluation Procedure." *25th International Conference on Offshore Mechanics and Arctic Engineering*, 2006.
25. Y.H. Liu, "Experimental Study and Numerical Simulation of Wave Flap Induced Mixer in Hot and Cold State." *Diss. Nanjing University of Aeronautics and Astronautics*, 2000. doi: 10.7666/d.y400568.

CONTACT WITH THE AUTHORS

Hong Shi

Jiangsu University of Science and Technology;
College of Energy & Power Engineering; Zhenjiang,
CHINA

Qianwei Zhang

Jiangsu University of Science and Technology;
College of Energy & Power Engineering; Zhenjiang,
CHINA

Meinan Liu

Jiangsu University of Science and Technology;
College of Energy & Power Engineering; Zhenjiang,
CHINA

Kaijie Yang

Nanjing University of Aeronautics & Astronautics;
Key Laboratory of Aircraft environment control
and life support, MIIT; Nanjing,
CHINA

Jie Yuan

Nanjing University of Aeronautics & Astronautics;
Key Laboratory of Aircraft environment control
and life support, MIIT; Nanjing,
CHINA

MONITORING THE PERFORMANCE OF A SHIP'S MAIN ENGINE BASED ON BIG DATA TECHNOLOGY

Meng Liang* 

Shanghai Dianji University, Business School, Shanghai, China

Mingzhi Chen

Shanghai Maritime University, Merchant Marine College and Shanghai Engineering Research Center of Ship Intelligent Maintenance and Energy Efficiency, China

* Corresponding author: liangmeng02@163.com (Meng Liang)

ABSTRACT

Under the recent background of 'Green Shipping' and rising fuel prices, it is very important to reduce the fuel consumption rate of ships, which is directly affected by the performance of the main engine. A reasonable maintenance schedule can optimise the performance of the main engine. However, a traditional maintenance schedule is based on the navigation distance and time, ignoring many other factors, such as a harsh working environments and frequently changing operating conditions, which will lead to faster performance degradation. In this study, a real-time evaluation method combing big data of ship energy efficiency with physics-based analysis is proposed to judge the degradation of main engine performance and assist in determining the maintenance schedule. Firstly, based on the developed ship energy efficiency big data platform, the distribution statistics and comparison of different operating states are carried out. Gaussian mixture model (GMM) and Density-Based Spatial Clustering of Applications with Noise (DBSCAN) are used to cluster the data and the high-density data areas are obtained as the analysis points. Then, the data of the analysis points are polynomial fitted, by the least square method, to obtain the propulsion characteristics curves, load characteristic curves, and speed characteristic curves, which can be used to observe the performance degradation of the main engine. The results show that this method can effectively monitor the degradation degree of the main engine performance, and is of great significance to fuel efficiency improvements and greenhouse gas (GHG) emissions reduction.

Keywords: Big data of ship energy efficiency, Main engine, Performance evaluation, Cluster analysis, Mechanism analysis

INTRODUCTION

Ocean transport is vital for global trade and more than 90% of international cargo is transported by the international shipping industry [1]. Despite its significance, however, the great amount of fuel consumption and air pollutants caused by the shipping industry are more and more severe. The main air pollutants caused by shipping include nitrogen oxides (NO_x), sulphur oxides (SO_x), harmful particulate matter (PM), and greenhouse gas (mainly CO₂). According to the publications of the International Maritime Organisation (IMO), international shipping accounts for 14-31%, 4-10%, and 2-3% of the total worldwide global emissions of NO_x, SO_x, and CO₂, respectively [2].

The IMO has issued a series of regulations to restrict the emission of air pollutants from shipping because they are aware of the seriousness of the problem. The shipping industry has also taken a series of measures to reduce emissions. The scrubber system is an alternative measure to reduce SO_x emissions, although it requires a large amount of cabin space, is complex and expensive to operate [3]. An SCR (Selective Catalytic Reduction) reactor can be used for reducing NO_x emissions. However, carbon capture and other CO₂ emission reduction equipment are far less mature than scrubber systems and SCR reactors and not commonly used. Alternative fuels, such as biofuels and hydrogen, are promising developments but there are still some concerns about their storage, technology maturity, and safety mitigation measures

in the current situation. Therefore, reducing fuel consumption remains the top priority in controlling greenhouse gas (GHG) emissions for ships in service.

Meanwhile, IMO has put forward more and more regulations concerning CO₂ emissions from ships, prompting international shipping companies to put in place technological and operational measures. In 2011, the Energy Efficiency Design Index (EEDI) [4] was proposed to urge shipping companies to meet basic energy efficiency requirements when building new ships and the Ship Energy Efficiency Management Plan (SEEMP) [5] was put forward in the same year (specific ship operational measures to reduce emissions). In late 2020, IMO approved the MARPOL Annex VI amendment, which requires all existing ships to satisfy both the Efficiency Existing Ship Index (EEXI) and Carbon Intensity Indicator (CII) requirements, as well [6]. This represents the IMO's follow-up action plan for reducing GHG emissions from international shipping vessels up to 2050. Since exhaust gas emission is difficult to measure directly, and is generally proportional to fuel consumption, the regulation for European ships' Monitoring, Reporting, and Verification (MRV) provides indirect monitoring through the ship's fuel consumption [7].

For a ship, the consumption of fuel mainly depends on two factors: the operating efficiency of the main propulsion system and the motion resistance [8]. Król summarised the current technical status of propeller system design and operation with the installation of energy-saving devices [9]. Puzdrowska paid attention to the problem of low controllability of marine medium and high-speed engines during operation, and proposed measures for quickly controlling the temperature of exhaust gas [10]. Król presented a simplified lifting surface method in propeller design [11]. Rudzki et al. proposed a decision-making system to select commands for the ship's propulsion system with a controllable pitch propeller [12]. Varbanets et al. provided a method to accurately measure the top dead centre (TDC) [13]. All of the above studies have laid an important foundation for performance improvements in ship propulsion systems.

It is widely known that the main engine is the main propulsion system overcoming the total resistance from the cargo dead weight, draft, trim, sea weather, etc. [14], to propel the ship forward. The main engine produces the original thrust through fuel consumption and pushes the propeller through a series of transmission devices to overcome the resistance [15]. As the original power of a ship, the performance of the main engine directly affects the fuel consumption rate. Customising a scientific maintenance schedule for the main engine can guarantee its good performance. However, a traditional maintenance schedule usually relies on the total navigation distance or time, without the consideration of many other environmental factors such as humidity, oscillatory working conditions, the switching of operating conditions, or weather changes on the voyage, etc.

This study aims to evaluate the performance degradation of the main engine in real-time through big data of navigation processes, such as ship fuel consumption, marine main engine

status, ship status, and cargo loading status. The maintenance schedule, based on the results analysed, considers more factors and is more in line with the actual circumstances. To analyse the behaviour of marine diesel engines in different unsteady states (e.g. determining fuel consumption rate), Ghaemi proposed a goal-based mathematical model and provided a method for determining the model parameters through the available data provided by the engine manufacturer [16]. However, data are still limited.

As one of the most traditional industries, the shipping industry still relies more on intuition than on data [17]. A small amount of original voyage data comes from the ship's noon report, but this data has many flaws, such as manual recording errors, long time intervals, and small amounts of data acquisition, which is not conducive to subsequent analysis [18]. Fortunately, the Internet of Things (IoT), data transmission technology, and big-data technology under the background of 'Industry 4.0', provide a promising approach for voyage data collection and transmission [19]. Fan et al. designed a multi-source information system to collect data related to a ship's energy consumption and navigation environment [20]. Deng et al. analysed and predicted the energy efficiency of ships, based on 6G communication technology, which can access the data in real-time [21]. Both of them focused on inland river ships. Tacjana et al. monitored the heat exchanger in a steam power plant through machine learning algorithms, which shows that machine learning is a measure worthy of research and application [22]. Witkowska et al. presented a multi-dimensional nonlinear dynamic positioning (DP) controller, which adopts the adaptive vector back-stepping method and Radial Basis Function (RBF) artificial neural network [23]. Facing a huge amount of data, it is necessary to choose the most appropriate data handling technology. Data cleaning is the first and most important step, avoiding the waste of analysis resources, or even the 'Garbage in, garbage out' phenomenon [24]. Perera et al. proposed a new digital model and built a data handling framework with pre-processing and post-processing units, based on the proposed digital model [25]. Raptodimos et al. proposed an integrated method based on an artificial neural network (ANN), which applies cross-clustering and self-organising mapping to cluster data, and then realises the main engine fault diagnosis [26]. Vanem et al. used unsupervised machine learning technology to analyse sensor data and monitor marine diesel engine anomalies [27]. Perera et al. introduced the expectation maximisation (EM) algorithm and Gaussian Mixture Models (GMMs) for the main engine speed-power clustering; analysis showed that data could be divided into three clustering centres [28]. Perera et al. studied the clustering methods again and obtained great relationships between ship performance and navigation information by principal component analysis (PCA) [29]. Yan et al. proposed the application of a distributed parallel K-means clustering algorithm for path division. Later, they used the Map Reduce-based k-average algorithm to analyse the environmental factors of different route segments [30, 31]. Adland et al. evaluated the effect of hull fouling on fuel consumption,

by regression analysis of daily fuel consumption and ship speed [32]. However, the influence of the decrease in diesel engine performance on the increase in fuel consumption was ignored.

In summary, most of the previous studies focused on the application of big data to consider the impact of environmental factors on ship energy efficiency and adopted intelligent algorithms, to assist ship fuel-saving decisions. However, the energy efficiency caused by the degradation of diesel engine performance and the impact of operating conditions on diesel engine performance is widely ignored and most of the black box models were adopted, so the analysis results were difficult to explain clearly. For energy efficiency monitoring and optimisation models, we need to balance the complexity of the model with the interpretability of the results. Based on this, models are usually classified as black box models or white box models. The black box model focuses on high precision of input and output. The white box model is characterised by physical characteristics, focusing on the interaction and logical relationship between various factors. The grey box model lies between the white box model and the black box model and has both advantages [33].

This study demonstrates a ship energy efficiency big data platform, based on the Beidou system, and some functional modules of the platform have also been described in previous work [18, 34]. This paper focuses on the functional modules, including data statistics, clustering, and engine performance analysis. A method of main engine performance evaluation is proposed, based on two years' of monitoring data from an operational ship. Using data statistics, machine learning, and physics-based methods, the comparison curves of diesel engine performance under different working conditions were obtained as the basis of the main engine performance evaluation.

Compared with previous studies, the contributions of this paper are:

- This study makes up for the fact that there are few applications of big data to evaluate the ship's main engine performance in previous studies.

- Previous studies have typically used only one of two approaches: unsupervised machine learning or physics-based analysis. This paper adopts the idea of the grey box model and combines the two methods to consider the accuracy and interpretability of the analysis results.
- The ship energy efficiency big data platform constructed in this study is universal and can also provide information support for energy-saving decisions of other diesel propulsion ships.

The rest of this paper is organised as follows: the description of the platform framework, techniques, and approaches is presented in Section II; data distribution statistics for the main engine operating situation are presented in Section III; the data cluster for the operational data is presented in Section IV; and the analysis results are presented in Section V. The conclusion is provided in Section VI.

DESCRIPTION OF PLATFORM FRAMEWORK, TECHNIQUES, AND APPROACHES

OVERALL FRAMEWORK OF BIG DATA PLATFORM

The framework of the big data platform is shown in Fig. 1. The on-board database records the main engine status, ship status, and ship loading status in real-time. In addition, it records the fuel consumption of the main engine from the high-precision mass flow meter. On the user interface of the on-board software, relevant monitoring data and curves are displayed, as well as the energy flow. Through the Beidou system, the data is transmitted to the onshore database in real time. Ship managers can carry out statistical analysis, clustering, polynomial curve fitting, and physics-based analysis with the collected data. The analysis results can be used as the basis for evaluating the energy efficiency of the ship and the performance of the main engine, which helps to make fuel-saving decisions and maintenance plans.

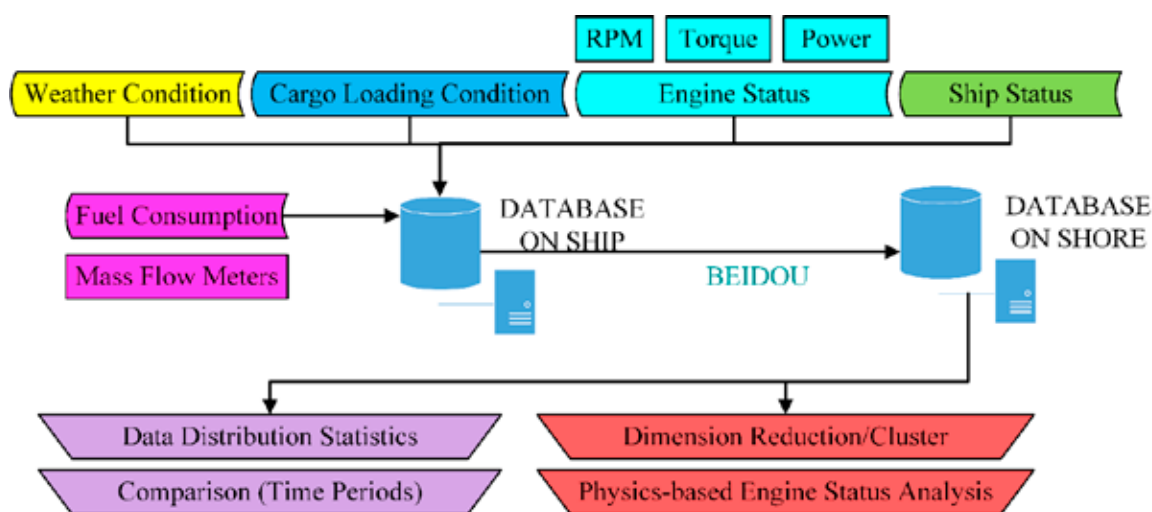


Fig. 1. Framework of big data platform

The on-board sensors measure the fuel consumption, main engine status, ship status, and ship loading status in real-time. Table 1 details some relevant data descriptions. The data comes from different systems and their acquisition frequency is not the same. The fuel consumption is read from the mass flow meter each second, using the RS485 communication device. The data on the engine status is sent out from the monitoring and alarm system every 30 seconds, via the Ethernet communication. Data such as ship speed and draft, relative wind speed and direction are read from the system on the bridge with the serial communication, and their frequency is about 10 seconds. To integrate all the systems with the same intervals, our platform records data every minute. Data from the sensors with a frequency greater than one minute are averaged, which also acts as a filter. In addition to the mean data, the standard deviation of high-frequency data is also calculated and recorded. The data is flagged as being abnormal if the standard deviation is higher than a certain threshold.

Tab. 1. Data Description

Categories	Items	Unit	Description
Fuel Consumption Rate	MEActFOCon	kg/h	fuel consumption rate
Main Engine Status	MERPM	r/min	main engine shaft speed
	METorque	kN*m	main engine shaft torque
	MEShaftPow	kW	main engine shaft power
Ship Status	ShipSpdToWater	knot	ship's water-referenced speed
	ShipSlip	%	slip ratio of propeller
Cargo Loading Status	ShipDraft	m	ship's draft

The MESFOC_kw is the specific fuel consumption of the main engine, see Eq. (1). Its unit is g/kWh. It shows how much fuel a diesel engine needs to produce 1 kW of power in one hour. This index can also reflect the economic performance of the engine and can be used for the analysis of engine performance degradation. Eq. (1) is affected by the lower calorific value (LCV) of the fuel. The ship studied in this work used marine diesel oil (MDO) and heavy fuel oil (HFO), which have different LCVs. However, when using HFO, marine engineers use the same type of fuel. For this concern, the platform automatically distinguishes two kinds of oil, with their different operating temperatures, to reduce the operations of engineers. Density is also recorded from the flow meter, for manual inspection. When the engine was running on HFO, this accounts for most of the available data. It is assumed that the used HFO has the same LCV in the current study, and the platform may also add a field to record the LCV for further consideration in future studies.

$$MESFOC_{kw} = \frac{MEActFOCon}{MEShaftPow} * 1000 \quad (1)$$

The propeller's slip rate is an important factor that characterises the main engine load; it is called ShipSlip in the system. The ShipSlip is calculated by Eq. (2), which is determined by the water reference speed v_s and the shaft speed n_{ME} . In Eq. (2), H is the pitch of the propeller, which is the distance that the propeller advances when it rotates one revolution.

$$ShipSlip = (1 - v_s * \frac{1852}{n_{ME}} * H * 60) * 100 \quad (2)$$

Since the vast majority of vessels use diesel engines, the matter of their efficient and safe operation is an ongoing issue [36]. A big data platform was installed on a 2400 TEU container ship in October 2019 and the data obtained from January 1st to July 31st, 2020, as well as the same period in 2021. These are taken as an example to illustrate the effectiveness of the proposed method. The ship uses a two-stroke low-speed diesel engine (MAN B&W 7S60ME-C10.5, MCR: 13,700 kW * 97 r/min) as the main engine. The main engine directly drives the fixed pitch propeller. The propeller has four blades and an average pitch of 6.134 m. Three diesel generators, one exhaust gas boiler, and one oil-fired boiler are installed on the ship.

Based on these energy efficiency-related data, approaches such as numerical distribution statistics, machine learning, and physics-based analysis were used for engine performance analysis.

In the data pre-processing, the data were removed while the vessel was at berth. The system on the bridge sometimes does not send data because the system may be shut down. These data were also removed. In this work, the performance of the engine under stable operation was studied, so only the data of specific fuel consumption in the range of 160-260 g/(kW*h) was kept. Table 2 shows a sample of the values of the variables.

Tab. 2. A sample of the values

PCDate	PCTime	MEActFOCons	MESFOC_kw	MESFOC_nmile	ShipSpdToWater
2020/5/24	9:01:00	1496.718	190	83.76997	17.867
MERpm	METorque	MEShaftPow	WindSpd	WindDir	Latitude
86	875.833	7877.5	29.017	239	10.50 N
ShipSpd	ShipHeel	ShipTrim	ShipDraft	ShipSlip	Longitude
17.651	0.29	0.382	8.651	-2.79775	126.00 E

DESCRIPTION OF TECHNIQUES

The platform applied data statistics, clustering, and curve fitting to fulfil the study.

Numerical Distribution Statistics

Statistics aim to extrapolate the ships' overall running and operating situations, based on the data. The analysis and comparison of data distribution are helpful to understanding the difference in working conditions of different ships or the same ship at different times. In numerical distribution statistics, the probability mass function (PMF) is a normalised histogram that shows the frequency of occurrence of each value, typically for discrete variables. The good performance of PMF needs to deal with the grouping interval, while the cumulative distribution function (CDF) does not, and it can explain the difference between the distributions more clearly. PMF and CDF are both applied to the data distribution. As in Eq. (3) and Eq. (4), the PMF of the value x in the set X is the probability of x in X , while the CDF of the value x in the set X is the cumulative probability of the values in X that are less than x .

$$pmf_x(x) = P(X = x) \quad (3)$$

$$cdf_x(x) = P(X \leq x) \quad (4)$$

Data Clustering

The basic idea of clustering is to construct k data clusters for a given data set with n samples. Generally, $k \leq n$; each cluster contains at least one sample and each sample only belongs to one cluster. Clustering methods divide data into k clusters, based on data distance or probability density models. In this paper, two different methods were used in the clustering process: the Gaussian mixture model (GMM) and density-based noise application spatial clustering (DBSCAN). The GMM is based on the assumption that the data conforms to the Gaussian statistical model and iteratively improves the parameters of the estimated model by using the Expectation-Maximisation (EM) algorithm. The algorithm can obtain the mean and covariance matrix of the clusters and get the weights of different clusters. When predicting the cluster category of a sample, the probability that the sample belongs to different clusters can be estimated. The GMM algorithm needs to input the number of clusters first, and then iteratively converges to the centre of the data cluster.

DBSCAN is a density-based clustering algorithm [35]. It can divide the region with a high-enough density into clusters and find cluster shapes in the noise data. DBSCAN describes the compactness of the sample set based on data density. Parameters (EPS, min_samples) are used to describe the compactness of the sample distribution in the neighbourhoods. Wherein, 'EPS' describes the small distance of neighbourhoods belonging to the same cluster, and 'min_samples' describes the minimum number of samples in the cluster.

If the number of samples included in the 'EPS' neighbourhood of sample x_i is not less than 'min_samples',

i.e. $|N_{EPS}(x_i)| \geq \text{min_samples}$, then x_i is called the core point. Otherwise, if $|N_{EPS}(x_i)| < \text{min_samples}$, then x_i may be in the neighbourhood of other core points, which is called a boundary point. If x_i is neither a core point nor a boundary point, it is a noise point. The DBSCAN algorithm also defines the concepts of density direct, density reachable, and density connected. The basic process of the DBSCAN clustering algorithm is to determine all the core points according to the parameters (EPS, min_samples). It needs to find the sample with the highest density to generate a cluster and repeat the process to divide the data samples.

In this paper, we used Python-based Scikit-Learn to perform DBSCAN and GMM clustering algorithms on the pre-processed data, to find 'clusters' [37].

Polynomial curve fitting

Polynomial fitting is used to find the unknown parameters in the empirical formula dominated by a known law or model hypothesis through several known points. For example, given a function $f(\mathbf{x}; a_0, a_1, a_2, \dots, a_m) = a_0 + a_1x_1 + a_2x_2 + \dots + a_mx_m$. \mathbf{x} represents an m -dimensional sample vector. a_0, a_1, \dots, a_m are the parameters to be determined. In general, given a set of samples $(\mathbf{x}_1, \mathbf{x}_2, \dots, \mathbf{x}_n)$ whose measured function values are (y_1, y_2, \dots, y_n) , it is possible to determine (a_1, a_2, \dots, a_m) by the least square method. A polynomial curve fit, as in Eq. (5) and (6), finds the parameter that minimises the squared value of the deviation between the output of the function and the measured value.

$$f(\mathbf{x}; a_0, a_1, \dots, a_m) = a_0 + a_1x_1 + \dots + a_mx_m \quad (5)$$

$$\arg \min_{a_0, a_1, \dots, a_m} \sum_{i=1}^n [f(\mathbf{x}_i; a_0, a_1, \dots, a_m) - y_i]^2 \quad (6)$$

The least square method is used to perform polynomial curve-fitting on the relationship between ME shaft speed - ME shaft power, ME shaft power - MESFOC_kw, and ME shaft speed - MESFOC_kw to further study the characteristics of the engine.

Physics-based Analysis

The effective power and specific fuel consumption of the main engine changes with the operating conditions of the diesel engine. The system carries out the performance evaluation of the main engine from three kinds of curves, which are the propulsion characteristics curve, the load characteristics curve, and the speed characteristics curve. The relationship between the main engine shaft power MEShaftPow and the main engine shaft speed MERPM during a ship's operation is cubic. This relationship is the propulsion characteristic of the main engine. The data of main engine shaft power, shaft speed, and specific fuel consumption rate MESFOC_kw are filtered in the cluster centres. The relationships between MEShaftPow - MESFOC_kw and MERPM - MESFOC_kw, which are the load and speed characteristics of the main engine, are obtained through data query and curve fitting by a self-developed software, written in C#.

DATA DISTRIBUTION STATISTICS FOR THE MAIN ENGINE OPERATING SITUATION

Using the method of distribution statistics, the two periods from January 1 to July 31 in 2020, and the same period in 2021, are taken as the comparison periods to compare the main engine status and the cargo loading status.

COMPARISON OF THE OPERATING STATUS OF THE MAIN ENGINE

Fig. 2 to Fig. 4 show the PMF and CDF of main engine shaft speed MERPM, main engine shaft power MESHaftPow and ship water reference speed ShipSpdToWater during the observation period. It can be seen that the MERPM is often set at 47, 62, 77, 80, and 85 r/min on board and the MESHaftPow is also concentrated in the corresponding section. While the ship is sailing at sea, most of the load of the main engine comes from overcoming the navigation resistance under still water and part of the power is affected by wind, current, wave, and cargo loading, etc. The ship usually needs to attain a certain speed to transfer goods in time. However, at the same ship speed, the ship resistance also changes with the weather and loading conditions. Therefore, the shaft power of the main engine fluctuates with the shipload. As shown in Fig. 4, the ship water reference speed ShipSpdToWater has three obvious operation centres: 9.0, 12.5, and 16.0 knots.

It can also be seen from Fig. 2 to Fig.4 that the recorded main engine shaft speed MERPM and main engine shaft power MESHaftPow are more often in the high load range in 2021, than in the same period in 2020, so the ship's speed also increases. This is due to the increased volume of containers in 2021 and the need for vessels to speed up their cargo turnover.

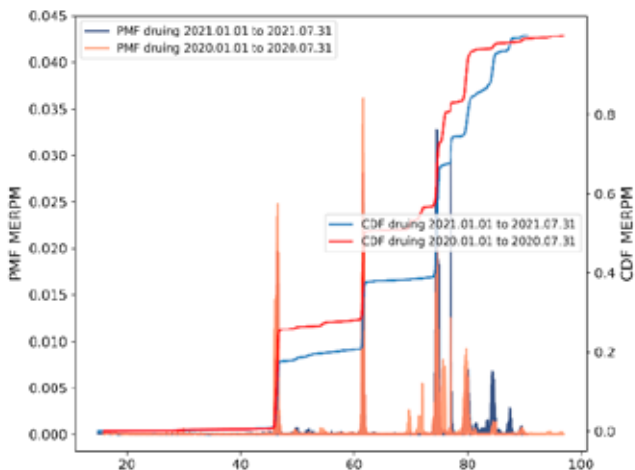


Fig. 2. PMF and CDF of main engine shaft speed (comparison between 2020 and 2021)

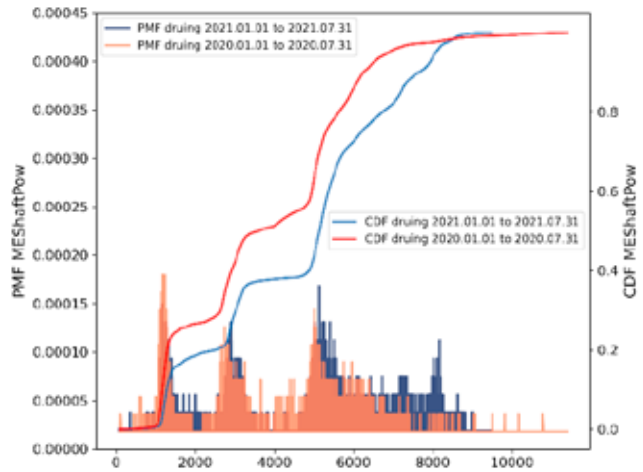


Fig. 3. PMF and CDF of main engine shaft power (comparison between 2020 and 2021)

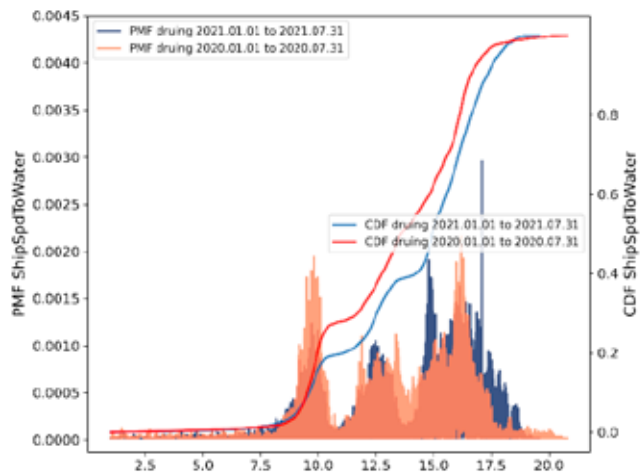


Fig. 4. PMF and CDF of water referenced ship speed (comparison between 2020 and 2021)

However, as shown in Fig. 5, the specific fuel consumption of the main engine MESFOC_kw in 2021 is more inclined to the left than that in the same period in 2020. That is to say, the specific fuel consumption is relatively low in 2021 because the main engine runs more in the high-power area in 2021 than that in 2020. It is hard to identify the engine performance degradation by the data statistics, which needs to be further studied from the engine load characteristics.

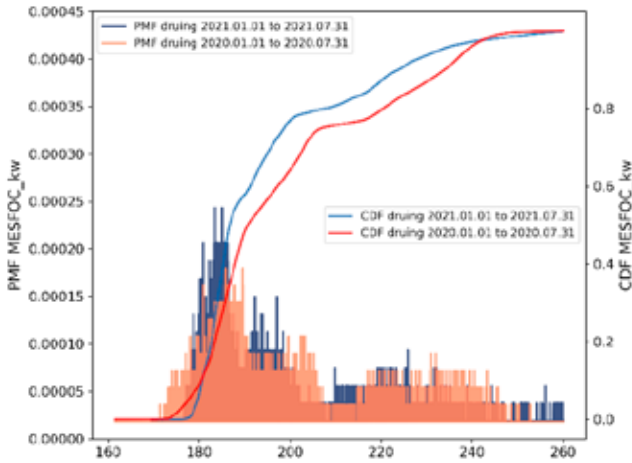


Fig. 5. PMF and CDF of main engine specific fuel consumption (comparison between 2020 and 2021)

COMPARISON OF SHIP BALLAST STATUS AND SHIP LOADING STATUS

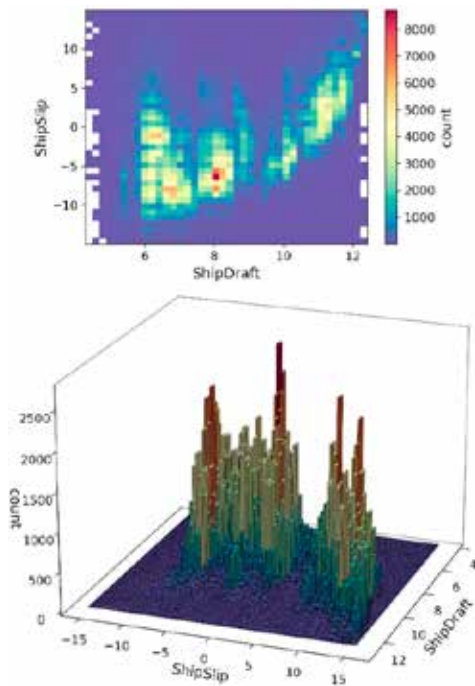


Fig. 6. Ship draft and propeller slip ratio (January 1st-July 31st, 2020)

Fig. 6 and Fig. 7 show the ship's draft ShipDraft and propeller slip ratio ShipSlip from January 1 to July 31 2020, and 2021, respectively. They show that the region of the ship's draft with the most data in 2020 is 8 m, while the region with the most data in 2021 is 11 m. The ship's draft significantly increases because the cargo volume of the ship in 2021 is significantly higher than that in the same period in 2020. In addition, both Fig.6 and Fig.7 show that, with the increase

of the ship's draft, the propeller slip ratio increases as well, due to the increase of the ship's resistance.

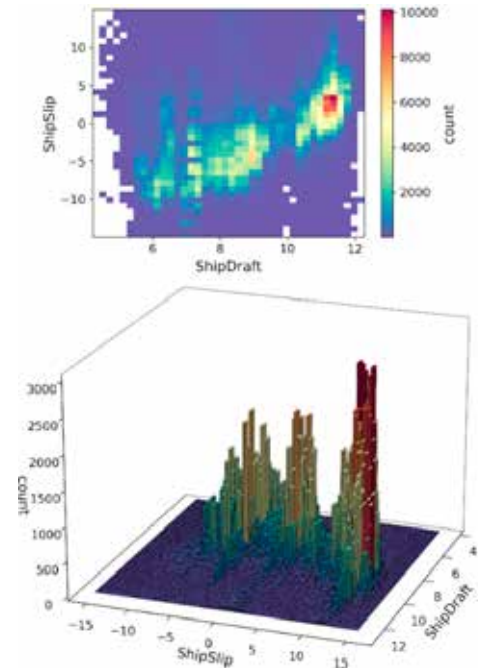


Fig. 7. Ship draft and propeller slip ratio (January 1st-July 31st, 2021)

The data in June 2020 is screened to show the ship draft effect on the main engine's load. In a month, the affect of the fouling of the ship's hull on the result is low. In the same period, the weather condition is similar. In addition, the relative wind speed is limited to the range 12-18 knots. The relationship between the main engine speed and the shaft power of the ship under ballast and full load conditions was studied. The data when the main engine runs in a stable manner is obtained. Under the ballast condition, the data of the ship's draft range is 6-7 m, and the data of the ship's draft range is 10.5-11.5 m under the full load condition. If two or more of the same data are at nearly the same engine speed, they are averaged at intervals of 0.2 *r/min* of engine speed. Fig. 8 shows the results. When the ship is in a ballast state, the data points of the main engine shaft speed and power are displayed as purple triangles; when the ship is fully loaded, they are displayed as yellow circles. On the same horizontal axis, the yellow circles are slightly higher than the purple triangles on the vertical axis. Loading cargo will increase the propeller slip ratio, leading to an increase in the load of the main engine. The average shaft speed of the ship at full load is 65.71 *r/min* and the required average shaft power is 4529.73 kW. The average shaft speed of the ship in ballast is 67.30 *r/min* and the required average shaft power is 4247.38 kW. Cargo loading causes the average shaft speed to decrease by 1.59 *r/min*, while the average power increases by 282.34 kW.

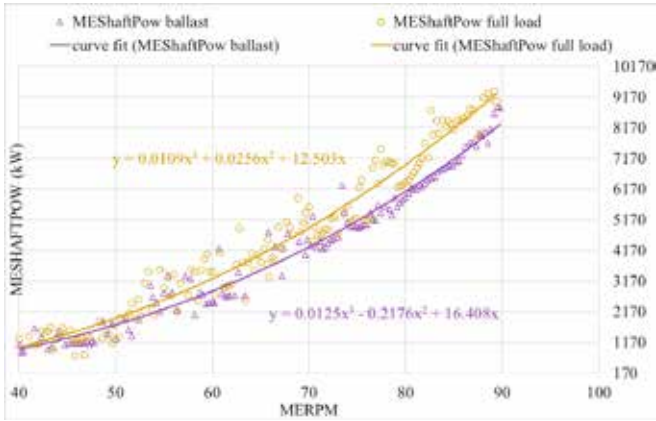


Fig.8 . Propulsion characteristics curves of the main engine (comparison under the ship in ballast and full load conditions)

CLUSTER OF OPERATION DATA

The pre-processed data distribution can be displayed as variable histograms. Fig. 9, Fig. 10, and Fig. 11 show the histograms of energy efficiency-related variables of the main engine with all data, ballast state data, and full load state data, respectively. In the figures, the horizontal axis is the variables' area and the vertical axis is the variables' count. The histogram results show that all variables are within a reasonable range. Moreover, the main engine mainly operates in the three power centres.

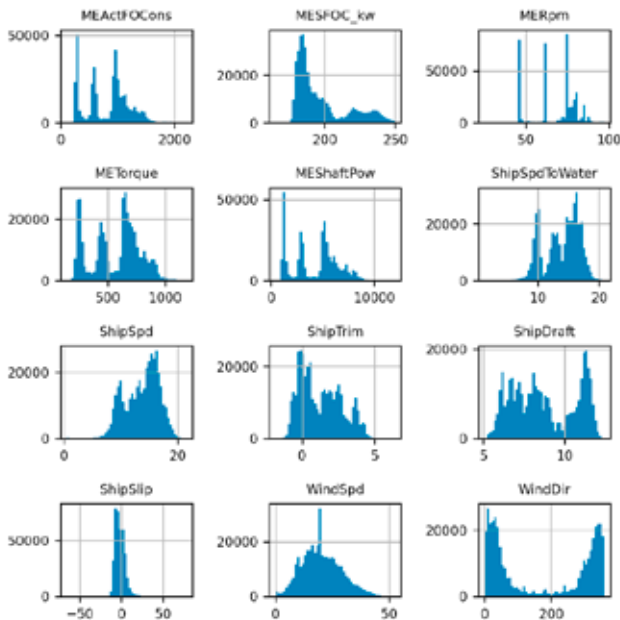


Fig. 9. Histogram of variables after data pre-processing (all data)

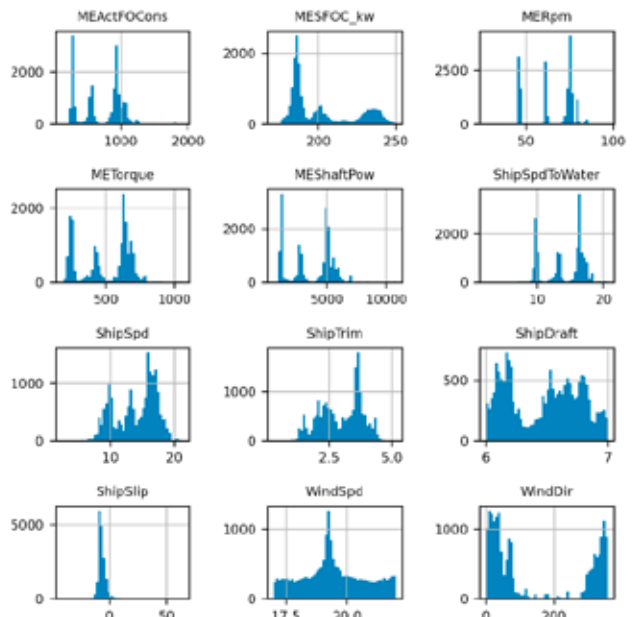


Fig. 10. Histogram of variables after data pre-processing under ballast state (relative wind speed in 12-18 knots and ship draft in 6-7 m)

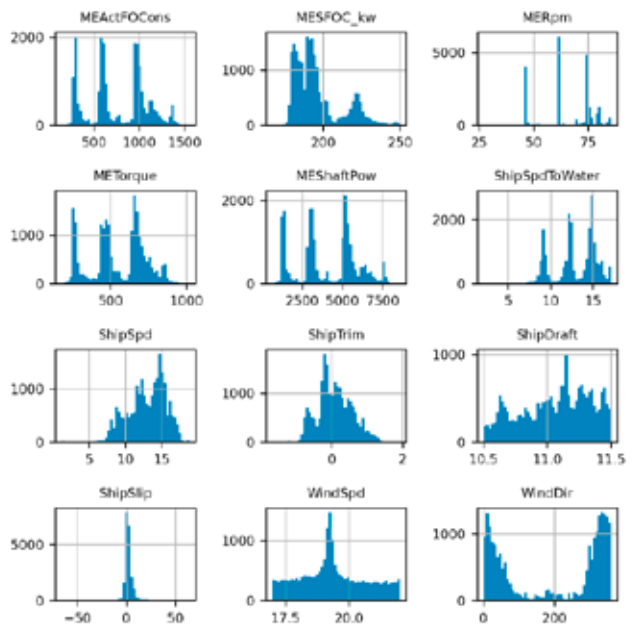


Fig. 11. Histogram of variables after data pre-processing under full load state (relative wind speed in 12-18 knots and ship draft in 10.5-11.5 m)

To explore the correlation between variables, we conducted Pearson correlation tests on them. Fig. 12 shows the Pearson correlation between all variables. It can be seen that the fuel consumption rate of the main engine is not only closely related to the state of the main engine but also has a certain correlation with the ship's draft, trim, and relative wind speed. Although this correlation is small, it should also be considered in the study. The ship's trim is highly related to the ship's draft. To further consider factors such as ship loading status

and weather conditions, the study further selects the same relative wind speed range to cluster similar weather. Data are also constrained under full load and ballast conditions, to remove the effects of vessel loading variations.

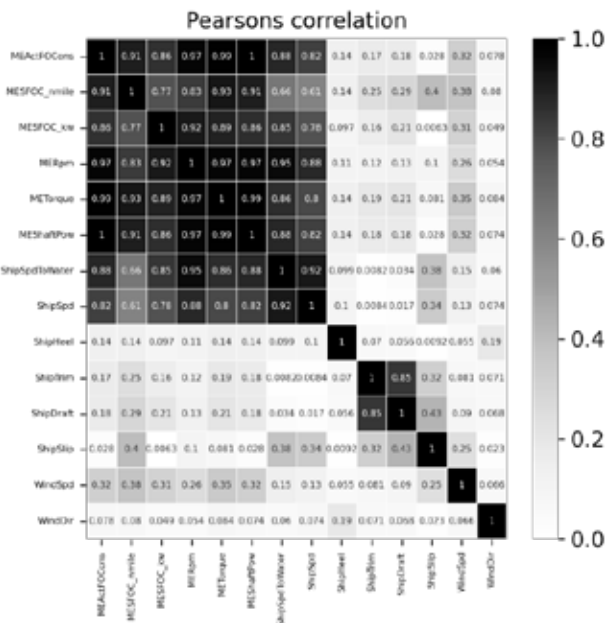


Fig. 12 Pearson correlation of the data (all data)

In this study, GMM and DBSCAN were combined for data clustering analysis. The general idea is to set the neighbourhood size (EPS) of DBSCAN to 3 and the minimum number of samples in the neighbourhood (min_samples) to 6, in order to obtain the frequent operation area of the main engine. Then GMM is applied to the cluster analysis of five variables (engine shaft speed MERPM, engine shaft power MEShaftPow, engine fuel consumption rate MEActFOCon, the specific fuel consumption of the main engine MESFOC, and water reference speed ShipSpdToWater) and three cluster centres are obtained. To consider the effects of the ship's loading status, weather conditions, and other factors, on the performance of the main engine, the cluster analysis was carried out on all data, ballast state data, and full load data, respectively.

Cluster analysis of all data

The cluster analysis results of all data are shown in Table 3 and Fig. 13-16. The three dark blue data clusters in Fig. 13 show the areas where the main engine often runs. Table 3 shows the three clustering centres and the clustering results are very consistent with the statistical analysis of data distribution. For a more intuitive display, Fig. 14 is a visualisation of three-dimensional data clusters of shaft speed, power, and fuel consumption rate, Fig. 15 displays two-dimensional data clusters of shaft speed and shaft power, and Fig. 16 is a visualisation of two-dimensional data clusters of water reference speed and shaft power.

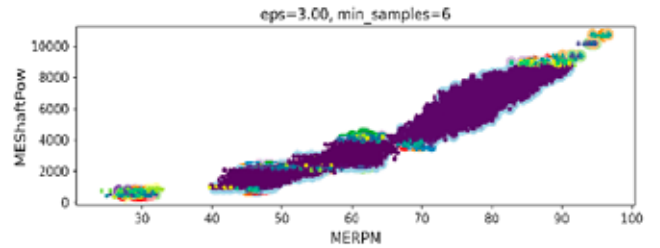


Fig. 13. Clustering analysis of shaft speed and power by DBSCAN in all states

Tab. 3. Clustering centre (All data)

Cluster centre	MERPM (r/min)	MEShaftPow (kW)	MEActFOCon (kg/h)	MESFOC (g/kw*h)	ShipSpdToWater (knot)
Cluster centre 1	46.56	1294.62	293.04	227.80	9.53
Cluster centre 2	78.10	6096.09	1123.29	184.68	16.07
Cluster centre 3	61.48	2970.05	591.04	199.43	12.60

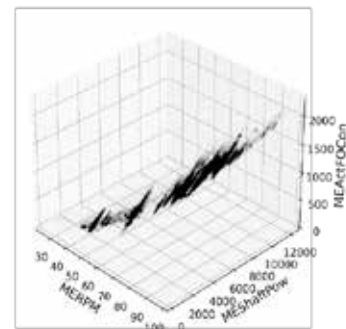


Fig. 14. Clustering analysis of shaft speed, power and fuel consumption rate by GMM in all states

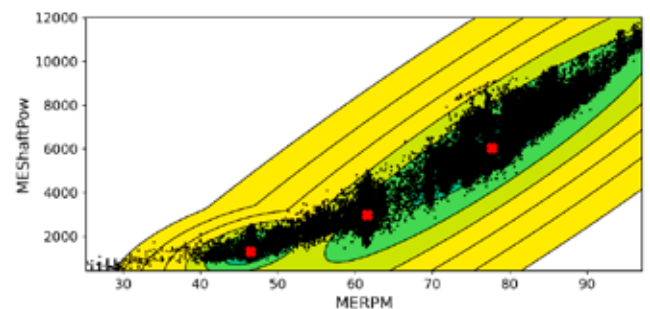


Fig. 15. Clustering analysis of shaft speed and power by GMM of all data

MECHANISM ANALYSIS RESULTS

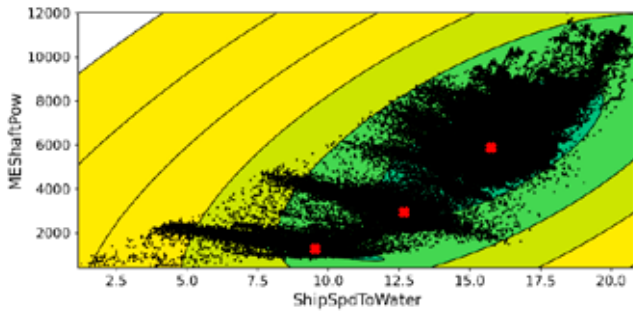


Fig. 16. Clustering analysis of water referenced ship speed and shaft power by GMM of all data

Clustering analysis of data under ballast and full load conditions

With the same steps (DBSCAN is used to determine three clusters and GMM is used to determine the cluster centres of key variables) and settings (EPS = 3, min_samples = 6), cluster analysis was performed on the data of ships with ballast and full load state, respectively. The cluster centres obtained from the analysis are shown in Tables 4 and 5.

Tab. 4. Clustering centre (data under relative wind speed in 12-18 knots and ballast state)

Cluster centre	MERPM (r/min)	MEShaftPow (kW)	MEActFOCon (kg/h)	MESFOC (g/kw ^h)	ShipSpdToWater (knot)
Cluster centre 1	46.42	1194.62	293.04	234.04	9.84
Cluster centre 2	76.83	5469.11	1013.31	185.63	16.80
Cluster centre 3	60.46	2708.24	548.33	203.84	12.73

Tab. 5. Clustering centre (data under relative wind speed in 12-18 knots and full load state)

Cluster centre	MERPM (r/min)	MEShaftPow (kW)	MEActFOCon (kg/h)	MESFOC (g/kw ^h)	ShipSpdToWater (knot)
Cluster centre 1	46.86	1433.69	314.81	221.08	9.10
Cluster centre 2	76.37	5779.90	1072.69	186.00	15.06
Cluster centre 3	61.57	3085.68	604.20	196.02	12.14

These cluster centres are areas with large amounts of data. They can be used to set the fuel consumption rate and the shaft speed in the mechanism analysis of the speed characteristic curve and the load characteristic curve.

In the three clustering centres, we applied the polynomial curve fitting to fit the relationship between the key indicators of the main engine. Firstly, we took the three cluster centres of shaft speed MERPM generated by GMM as the set value for the data query and fitted the curve to obtain the relationship between MEShaftPow - MESFOC_kw of the main engine, which is the load characteristic curve. Then we took the fuel consumption rate MEActFOCon of cluster centre 2 as the set value for the data query, and fitted the curve to obtain the relationship between MERPM - MESFOC_kw, i.e. the speed characteristic curve. These characteristic curves help us to understand the changing trends of the main engine performance.

COMPARISON OF MAIN ENGINE LOAD CHARACTERISTIC CURVES IN TWO PERIODS

Fig. 17 and 18 are the correlation diagrams of MEShaftPow - MESFOC_kw at the cluster centres under ballast and full load states, respectively. Fig. 17 and 18 both show that the main engine's specific fuel consumption MESFOC_kw in 2021 was higher than that in 2020. Tables 6 and 7 list the average main engine shaft power (average MEShaftPow) and the average specific fuel consumption (average MESFOC_kw) of the load characteristic curves in 2020 and 2021. In summary, the data of both ballast and full load conditions show that the specific fuel consumption rate of the engine has increased due to engine degradation. The parent engine test data in the manual shows that the specific fuel consumption rate at 50% MCR is 167.8 g/kWh, and the testing fuel LCV is 42009.20 kJ/kg. The measured data of the engine in actual operation is higher than the engine test. The measured data is reasonable since the actual operating conditions are more severe.

Tab. 5. Average MEShaftPow and MESFOC_kw (load characteristic curves under ballast state)

Cluster centre	2020		2021	
	MEShaftPow	MESFOC_kw	MEShaftPow	MESFOC_kw
Cluster centre 1	11.66% MCR	222.28 g/kWh	11.01% MCR	224.01 g/kWh
Cluster centre 2	39.93% MCR	185.90 g/kWh	39.84% MCR	186.73 g/kWh
Cluster centre 3	22.00% MCR	199.66 g/kWh	22.04% MCR	205.08 g/kWh

Tab. 6. Average MEShaftPow and MESFOC_kw (load characteristic curves under full load state)

Cluster centre	2020		2021	
	MEShaftPow	MESFOC_kw	MEShaftPow	MESFOC_kw
Cluster centre 1	14.07% MCR	213.43 g/kWh	13.98% MCR	215.80 g/kWh
Cluster centre 2	47.66% MCR	183.78 g/kWh	47.27% MCR	185.94 g/kWh
Cluster centre 3	25.03% MCR	194.26 g/kWh	25.00% MCR	195.37 g/kWh

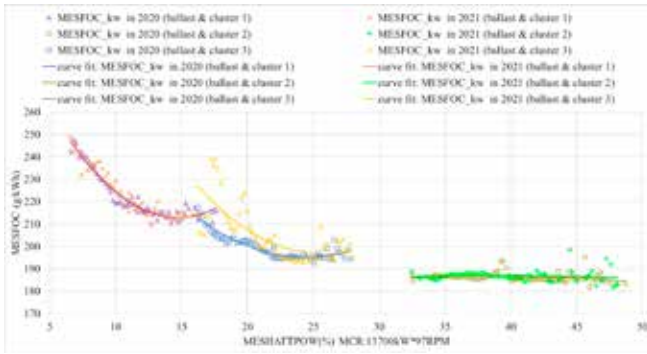


Fig. 17. Load characteristic curve of main engine shaft power - specific fuel consumption at cluster centres of ballast state

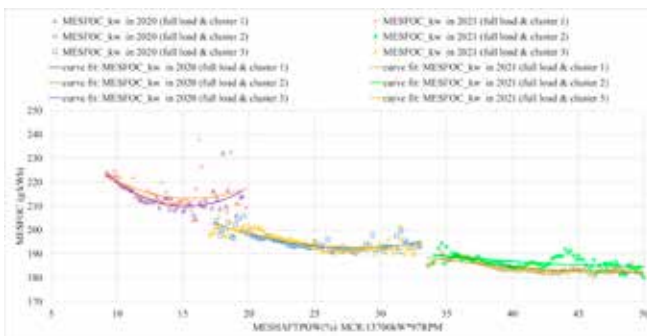


Fig. 18. Load characteristic curve of main engine shaft power - specific fuel consumption at cluster centres of full load state

COMPARISON OF MAIN ENGINE SPEED CHARACTERISTIC CURVES IN TWO PERIODS

The speed characteristic curves of the ship in the ballast and full load states, during the comparison periods, are created at cluster centre 2, as shown in Fig. 19.

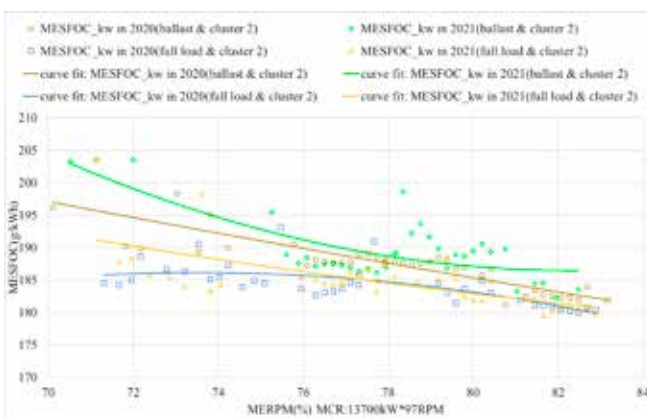


Fig. 19. Speed characteristic curve of main engine shaft speed - specific fuel consumption at cluster centre 2 of ballast & full load states

The MEActFOCon of cluster centre 2 in the full load state is 1072.69 kg/h, while that in the ballast state is 1013.31 kg/h. At the query point, the engine load in the full load state is a little higher than in the ballast state, and so MESFOC_kw

of the speed characteristic curve in the full load state is a little lower than that in the ballast state. Although the results also show that the specific fuel consumption rate in 2021 was higher than in 2020, the amount of data in the speed characteristic curve is still relatively small, and it is necessary to collect more data for further research.

CONCLUSION

This paper presents a main engine performance monitoring method based on energy efficiency big data. The method combines distribution statistics, clustering, and polynomial curve fitting to obtain the propulsion characteristics and load characteristic curves, as the basis of performance degradation monitoring and maintenance schedule of the main engine. The test results show that this method can effectively monitor the degradation of engine performance.

This research can be used as an important basis for creating a maintenance schedule for main marine engines. In the future, the ship maintenance schedule can be determined automatically, by developing the ship's intelligent energy efficiency system, which should consist of various autonomous technologies, such as machine learning (ML) and artificial intelligence (AI) technologies, assisting in intelligent monitoring, forecasting, and making auxiliary fuel-saving decisions.

ACKNOWLEDGMENT

This work was supported in part by the National Natural Science Foundation of China (52001195, 61873161) and the Science & Technology Commission of Shanghai Municipality and Shanghai Engineering Research Center of Ship Intelligent Maintenance and Energy Efficiency (20DZ2252300).

REFERENCES

1. B. Qiao, W. He, Y. Tian, Y. Liu, O. Cai, and Y. Li, "Ship emission reduction effect evaluation of air pollution control countermeasures," *Transportation Research Procedia*, vol. 25, pp. 3606-3618, 2017, doi: 10.1016/j.trpro.2017.05.325.
2. F. Jasper, H. Shinichi et al., "Fourth IMO Greenhouse Gas Study 2020," *International Maritime Organisation (IMO)*, London, UK, 2020.
3. V. Kuznetsov, B. Dymo, S. Kuznetsova, M. Bondarenko, and A. Voloshyn, "Improvement of the cargo fleet vessels power plants ecological indexes by development of the exhaust gas systems," *Polish Maritime Research*, vol. 28, pp. 97-104, 2021, doi: 10.2478/pomr-2021-0009.
4. I. Ančić and A. Šestan, "Influence of the required EEDI reduction factor on the CO₂ emission from bulk carriers,"

- Energy Policy*, vol. 84, pp. 107-116, 2015, doi: 10.1016/j.enpol.2015.04.031.
5. E.K. Hansen, H.B. Rasmussen, and M. Lützen, "Making shipping more carbon-friendly? Exploring ship energy efficiency management plans in legislation and practice," *Energy Research & Social Science*, vol. 65, pp. 101459, 2020, doi: 10.1016/j.erss.2020.101459.
 6. M. Kalajdžić, M. Vasilev, and N. Momčilović, "Power Reduction Considerations for Bulk Carriers with respect to Novel Energy Efficiency Regulations," *Brodogradnja: Teorija i praksa brodogradnje i pomorske tehnike*, vol. 73, pp. 79-92, 2022, doi: 10.21278/brod72205.
 7. L. Fedi, "The Monitoring, Reporting and Verification of Ships' Carbon Dioxide Emissions: A European Substantial Policy Measure towards Accurate and Transparent Carbon Dioxide Quantification," *Ocean Yearbook Online*, vol. 31, pp. 381-417, 2017, doi: 10.1163/22116001-03101015.
 8. W. Tarełko, "The effect of hull biofouling on parameters characterising ship propulsion system efficiency," *Polish Maritime Research*, vol. 21, pp. 27-34, 2014, doi: 10.2478/pomr-2014-0038.
 9. P. Król, «Hydrodynamic state of art review: rotor-stator marine propulsor systems design,» *Polish Maritime Research*, vol. 28, pp. 72-82, 2021, doi: 10.2478/pomr-2021-0007.
 10. P. Puzdrowska, «Diagnostic information analysis of quickly changing temperature of exhaust gas from marine diesel engine. Part i single factor analysis,» *Polish Maritime Research*, vol. 28, pp. 97-106, 2021, doi: 10.2478/pomr-2021-0052.
 11. P. Król, "Blade section profile array lifting surface design method for marine screw propeller blade," *Polish Maritime Research*, vol. 26, pp. 134-141, 2019, doi: 10.2478/pomr-2019-0075.
 12. K. Rudzki and W. Tarełko, "A decision-making system supporting selection of commanded outputs for a ship's propulsion system with a controllable pitch propeller," *Ocean Engineering*, vol. 126, pp. 254-264, 2016, doi: 10.1016/j.oceaneng.2016.09.018
 13. R. Varbanets, V. Zalozh, A. Shakhov, I. Savelieva, and V. Piterska, "Determination of top dead centre location based on the marine diesel engine indicator diagram analysis," *Diagnostyka*, vol. 21, pp. 51-60, 2020, doi: 10.29354/diag/116585.
 14. S. Park, S. W. Park, S. H. Rhee, S. B. Lee, J. E. Choi, and S. H. Kang, "Investigation on the wall function implementation for the prediction of ship resistance," *International Journal of Naval Architecture and Ocean Engineering*, vol. 5, pp. 33-46, 2013, doi: 10.2478/IJNAOE-2013-0116.
 15. M.B. Samsul, "Blade cup method for cavitation reduction in marine propellers," *Polish Maritime Research*, 2021, doi: 10.2478/pomr-2021-0021, doi: 10.2478/pomr-2021-0021.
 16. M.H. Ghaemi, "Performance and emission modelling and simulation of marine diesel engines using publicly available engine data," *Polish Maritime Research*, vol. 28, pp. 63-87, 2021, doi: 10.2478/pomr-2021-0050.
 17. B.D. Brouer, C.V. Karsten, and D. Pisinger, "Big data optimisation in maritime logistics," *Big data optimisation: Recent developments and challenges*. Springer, Cham, vol. 18, pp. 319-344, 2016, doi: 10.1007/978-3-319-30265-2_14.
 18. X. Zeng and M. Chen, "A Novel Big Data Collection System for Ship Energy Efficiency Monitoring and Analysis Based on BeiDou System," *Journal of Advanced Transportation*, vol. 2021, pp.1-10, 2021, doi: 10.1155/2021/9914720.
 19. I. Zaman, K. Pazouki, R. Norman, S. Younessi, and S. Coleman, "Challenges and opportunities of big data analytics for upcoming regulations and future transformation of the shipping industry," *Procedia engineering*, vol. 194, pp. 537-544, 2017, doi: 10.1016/j.proeng.2017.08.182.
 20. A. Fan, X. Yan, and Q. Yin, "A multisource information system for monitoring and improving ship energy efficiency," *Journal of Coastal Research*, vol.32, pp. 1235-1245, 2016, doi: 10.2112/JCOASTRES-D-15-00234.1.
 21. J. Deng, J. Zeng, S. Mai, B. Jin, B. Yuan, Y. You. S. Lu, and M. Yang, «Analysis and prediction of ship energy efficiency using 6G big data internet of things and artificial intelligence technology,» *International Journal of System Assurance Engineering and Management*, vol. 12, pp. 824-834, 2021, doi: 10.1007/s13198-021-01116-9.
 22. T. Niksa-Rynkiewicz, N. Szewczuk-Krypa, A. Witkowska, K. Cpałka, M. Zalański, and A. Cader, "Monitoring regenerative heat exchanger in steam power plant by making use of the recurrent neural network," *Journal of Artificial Intelligence and Soft Computing Research*, vol. 11, pp. 143-155, 2021, doi: 10.2478/jaiscr-2021-0009.
 23. A. Witkowska and T. Niksa-Rynkiewicz, «Dynamically positioned ship steering making use of backstepping method and artificial neural networks,» *Polish Maritime Research*, vol. 25, pp. 5-12, 2018, doi: 10.2478/pomr-2018-0126.
 24. S. García, J. Luengo, and F. Herrera, "Data preprocessing in data mining," *Cham, Switzerland: Springer International Publishing*, vol. 72, pp. 59-139, 2015, doi: 10.1007/978-3-319-10247-4.

25. L.P. Perera and B. Mo, "Ship performance and navigation information under high-dimensional digital models," *Journal of Marine Science and Technology*, vol. 25(1), pp. 59-139, 2020, doi: 10.1007/978-3-319-10247-4.
26. Y. Raptodimos and I. Lazakis, "Using artificial neural network-self-organising map for data clustering of marine engine condition monitoring applications," *Ships and Offshore Structures*, vol. 13, pp. 649-656, 2018, doi: 10.1080/17445302.2018.1443694.
27. E. Vanem and A. Brandsæter, "Unsupervised anomaly detection based on clustering methods and sensor data on a marine diesel engine," *Journal of Marine Engineering & Technology*, vol. 20, pp. 217-234, 2021, doi: 10.1080/20464177.2019.1633223.
28. L. P. Perera, and B. Mo, "Data analytics for capturing marine engine operating regions for ship performance monitoring," *International Conference on Offshore Mechanics and Arctic Engineering*, American Society of Mechanical Engineers, 2016, Vol. 49989, doi: 10.1115/OMAE2016-54168
29. L. P. Perera, and B. Mo, "Marine engine operating regions under principal component analysis to evaluate ship performance and navigation behaviour," *IFAC-PapersOnLine*, vol. 49(23), pp. 512-517, 2016, doi: 10.1016/j.ifacol.2016.10.487.
30. X. Yan, K. Wang, Y. Yuan, X. Jiang, and R. R. Negenborn, "Energy-efficient shipping: An application of big data analysis for optimizing engine speed of inland ships considering multiple environmental factors," *Ocean Engineering*, vol. 169, pp. 457-468, 2018, doi: 10.1016/j.oceaneng.2018.08.050.
31. K. Wang, X. Yan, Y. Yuan, X. Jiang, G. Lodewijks, and R. R. Negenborn, «Study on route division for ship energy efficiency optimisation based on big environment data,» *2017 4th International Conference on Transportation Information and Safety (ICTIS), IEEE*, pp. 111-116, 2017, doi: 10.1109/ICTIS.2017.8047752.
32. R. Adland, P. Cariou, H. Jia, and F. C. Wolff, "The energy efficiency effects of periodic ship hull cleaning," *Journal of Cleaner Production*, vol. 178, pp. 1-13, 2018, doi: 10.1016/j.jclepro.2017.12.247.
33. O. Loyola-Gonzalez, "Black box vs. white-box: Understanding their advantages and weaknesses from a practical point of view," *IEEE Access*, vol. 7, pp. 154096-154113, 2019, doi: 10.1109/ACCESS.2019.2949286.
34. X. Zeng, M. Chen, H. Li and X. Wu, "A Data-Driven Intelligent Energy Efficiency Management System for Ships," *IEEE Intelligent Transportation Systems Magazine*, doi: 10.1109/MITS.2022.3153491.
35. M. Ester, H. P. Kriegel, J. Sander, and X. Xu, "A density-based algorithm for discovering clusters in large spatial databases with noise," *kdd*, vol. 96, pp. 226-231, 1996.
36. R. Varbanets, V. Klymenko, O. Fomin, V. Pištěk, P. Kučera, D. Minchev, A. Khrulev, and V. Zalozh, "Acoustic method for estimation of marine low-speed engine turbocharger parameters," *Journal of Marine Science and Engineering*, vol. 9, 2021, doi: 10.3390/jmse9030321.
37. A. Géron, "Hands-on Machine Learning with Scikit-Learn and TensorFlow: Concepts, Tools, and Techniques to Build Intelligent Systems". *Sebastopol, CA, USA: O'Reilly Media*, 2017.

CONTACT WITH THE AUTHORS

Meng Liang

e-mail: liangmeng02@163.com

Shanghai Dianji University, Business School,
Shanghai
CHINA

Mingzhi Chen

Shanghai Maritime University,
Merchant Marine College and Shanghai Engineering
Research Center of Ship Intelligent Maintenance
and Energy Efficiency, Shanghai
CHINA

OPTIMIZATION MODEL TO MANAGE SHIP FUEL CONSUMPTION AND NAVIGATION TIME

Krzysztof Rudzki  ¹ *

Piotr Gomulka  ^{2,3}

Anh Tuan Hoang  ⁴

¹ Gdynia Maritime University, Poland

² Gdansk University of Technology, Poland

³ Demen Engineering Gdansk, Poland

⁴ HUTECH University, Ho Chi Minh City, Viet Nam

* Corresponding author: k.rudzki@wm.umg.edu.pl (K. Rudzki)

ABSTRACT

Owners of vessels are interested in the lowest possible operating costs. These costs are mainly related to fuel consumption during navigation. To manage it rationally, the main decision-making problem is selecting the proper parameters of the ship's propulsion system during navigation. In practice, operators of ships equipped with controllable pitch propellers controlled in manual mode make a selection of the commanded outputs based on their own knowledge, intuition, and all accessible information regarding sea conditions. In many cases, their decisions are unreasonable or incorrect. Therefore, it would be desirable to support their decision-making in selecting the commanded outputs. For this reason, we have decided to develop a decision support system in the form of an expert system. This computer-aided system supports the selection of the commanded outputs of the ship's propulsion system. The most important component of this system is the two-criteria optimization model, allowing the rational management of the ship fuel consumption and navigation time.

Keywords: expert system, optimization model, ship fuel consumption, time of navigation

INTRODUCTION

Rational management of resources is the most important challenge facing our civilization in the modern world. It is also the fundamental postulate of the micro-economy. The immediate reason why various economic operators must behave rationally is the rarity and depletion of accessible resources. In the management of industrial processes, the operators use various resources, such as:

- human resources - people with their knowledge and practical skills,
- natural resources - land with its riches (hydrocarbons), water, air,

– artefact resources - tools, machines, buildings, financial resources.

The problem of rational resource management also affects the maritime industry, including the fleet carrying out maritime transport tasks. Owners of vessels such as commercial, passenger and fishing vessels, tugs, etc. are interested in the lowest possible operating costs. These costs are mainly related to the use of material resources, e.g. fuel consumption during navigation and the navigation time to reach the required destination. To manage these resources rationally, the main decision-making problem is selecting the proper parameters of the ship's propulsion system during navigation. This, in turn, can be reformulated as an issue of the optimal selection of the

operating parameters (called the commanded output) of the ship's propulsion system, containing a source of mechanical power (engines), and propulsors transforming this power into propulsive force. The set-up of the propulsion system depends on the vessel size and type of operation.

In practice, two main types of propulsors are used for the propulsion of vessels: fixed pitch propellers (FPP) and controllable pitch propellers (CPP). A fixed pitch propeller is a propulsor with the pitch fixed. To increase or reduce the vessel speed, the propeller's rotational speed is increased or reduced. A CPP varies the angle of each blade (pitch) to control the amount of thrust produced by the propulsor. To increase or reduce the vessel's speed, the CPP pitch is altered. In the variable load conditions of navigation, this property allows for optimum use of the ship's engine power by selecting the propeller thrust force according to the ship hull resistances and operation in the area of maximum efficiency of the ship's propulsion system.

The CPP type of propulsor is most common on vessels where it is necessary to sail efficiently at two different load conditions, i.e. towing or running free, and on ships that sail to ports with limited or no tug assistance. Therefore, a CPP can mostly be used on tugs, cruise ships, ferries, cargo and fishing vessels. The pitch and rotational speed of the CPP may be controlled independently of one another, or together through a speed/pitch ratio controller. There are two modes of setting up commanded outputs:

- programmed control mode, when the speed/pitch ratio controller is utilized,
- remote manual mode, when the CPP pitch and rotational speed are controlled separately.

The programmed control mode of propulsion control automatically provides the optimum pitch and rotational speed combination for any given speed. The speed/pitch ratio controller calculates the CPP pitch and rotational speed that are required to achieve the desired ship speed under ideal conditions.

The remote manual mode is used in vessels that operate mainly in different load conditions, for example harbour tugs, fishing vessels, and sailing vessels running under an engine. Selection of the commanded outputs of their ship's propulsion system is made by setting up both the engine rotational speed and the CPP pitch. Combinations of two manipulated commanded outputs to realize the desired ship motion are very complex and complicated. Moreover, the permissible ranges for these outputs are limited by the maximum speed to be obtained from the ship engine and by the minimum speed ensuring the vessel's maneuverability. These ranges are not fixed and depend primarily on sea conditions, in particular the wind speed and direction and the sea current.

As was mentioned earlier, to manage ship fuel consumption and the navigation time to reach the required destination rationally, it is necessary to select proper commanded outputs of the propulsion system, that is, the engine rotational speed and the CPP pitch. To illustrate these relationships, we consider three options:

- moderate fuel-efficient navigation and ship speed is desirable,

- navigation with the lowest fuel consumption is desirable, whereas the time to reach the required destination is not important,
- navigation at the highest possible speed is desirable (e.g. in an emergency); in this case, fuel consumption is not taken into account.

In the presented options, both resources to be managed, that is, the fuel consumption and navigation time, are opposed to each other. In our opinion, it is desirable to find a compromise solution that will allow us to plan navigation more flexibly. In practice, the operators of ships equipped with the CPP controlled in manual mode make a selection of the commanded outputs based on their own knowledge, intuition, and all accessible information regarding sea conditions. In many cases, their decisions are unreasonable or incorrect. Therefore, it would be desirable to support their decision-making in selecting the commanded outputs.

For this reason, we have decided to develop a decision support system in the form of an expert system. This computer-aided system supports the selection of the commanded outputs of the ship's propulsion system. The most important component of this system is the two-criteria optimization model, allowing the rational management of the ship's fuel consumption and navigation time.

LITERATURE REVIEW

In the bibliographic resources available, there are many publications that present the application of optimization methods to various maritime problems. These methods have been used for various aspects of the maritime industry as well as different stages of the life cycle of vessels, including, *inter alia*, optimization of:

- routes and schedules of merchant ships from the point of view of travel time to the destination and fuel consumption,
- design of offshore floating units, including the design of the ship's hull and propulsion,
- ship's operation and maintenance.

To compete with large consortia and attract new customers, many shipping companies have started consolidating their efforts. Therefore, these companies need to develop new strategies for planning efficient routes and ship schedules. Some decisions that must be taken by shipping companies are contradictory in their nature. However, the existing models presented in the literature usually combine conflicting objectives into a single objective function, which aims to minimize costs. Such an approach does not allow the conflicting nature of certain cost elements to be taken into account, which additionally reduces the possibilities for analyzing relevant compromise solutions.

To avoid this shortcoming, the study [1] proposed a multi-objective mixed non-linear optimization model for the vessel scheduling problem that took all the main cost components presented in the literature into account and divided them into two opposite groups. The original nonlinear model was linearized by discretizing the vessel sailing speed reciprocal.

The Global Multi-Objective Optimization Algorithm was developed to obtain the Pareto Front vessel schedules.

The paper [2] presents the optimization of the ship's shipping route based on the dynamic programming method. The optimization was carried out in accordance with the minimum fuel consumption strategy, taking into account the ship's movements due to sea conditions. The ship's voyage was parameterized as a multi-stage decision-making process to formulate a dynamic programming optimization problem. Waves and wind conditions were estimated for each route segment based on weather forecasting maps, then seakeeping related indexes and fuel oil consumption were computed taking into account wave-induced ship motions and added resistance.

In [3] the authors pointed out that the majority of published works on the optimization of the ship's shipping route almost exclusively use a single-objective optimization approach, making it practically impossible to successfully achieve safety and economy-related goals. Their method represents an attempt to develop such solutions by applying an evolutionary multi-objective optimization to pursue three objectives: minimization of the risk of collision, minimization of fuel consumption due to collision avoidance maneuvers, and minimization of the extra time spent on collision avoidance maneuvers with regard to autonomous surface ships.

Instead, a similar method of optimization but with regard to the sailboats in [4] has been used.

Issues concerning multi-objective optimization of offshore floating units, including the design of the ship's hull and propulsion are presented in many publications as well. For example, in [5] shipping companies spend good efforts in improving the operational energy efficiency of existing ships. Accurate fuel consumption prediction model is a prerequisite of such operational improvements. Existing grey-box models (GBMs a genetic algorithm-based gray-box model for predicting the ship's fuel consumption based on ship operation data was proposed. The methodology of model development consists of a ship's fuel consumption modeling procedure based on the basic principles of the ship's propulsion, a GA-based estimation procedure, and a performance assessment procedure. According to the paper's authors, the proposed model provides a more reliable relationship between the fuel consumption rate of the ship and the factors affecting it than existing models. Unfortunately, this model has two major deficiencies: it has been tested for only one ship and neglects the impact of hull and propeller biofouling.

The authors of the paper [6] proposed the use of different methods of single- and multi-objective optimization of the specific characteristics of a liner shipping service. In particular, they proposed a multi-objective optimization model based on maximizing profit, minimizing CO₂ emissions and minimizing SO_x emissions, for which all components of the substitute objective function are a function of the ship's speed.

Many publications, in turn, are dedicated to issues of the ship's design process, in a particular selection of the optimal shape of a hull, the geometry of a propeller, or the cooperation of the hull-propeller system.

The parametric design and multi-objective optimization of ships under uncertainty applying the Holistic Optimization Design Approach are presented in [7]. The developed optimization procedure begins with setting up a detailed parametric model that captures both the external and internal geometric characteristics of the ship, along with the integration of several numerical tools. This allowed the evaluation of a multitude of merit functions and design constraints, all as part of the optimization problem.

Multi-objective surrogate-based hull-form optimization using high-fidelity Reynolds-Averaged Navier-Stokes Equations is presented in [8], whereas computational fluid dynamics-based hull form optimization using the approximation method is reported in [9] and [10]. To quickly obtain practical ship forms with good resistance performance, the optimal design method of ship forms by using the non-linear programming method is presented in [11].

A global view for the multi-objective combinatorial optimization (MOCO) problems in ship design, where the main focus is on evolutionary computation, particularly genetic algorithms, and posterior evaluation of Pareto-optimal solutions, is presented in [12]. A two-stage hybrid approach is proposed for an extremely hard MOCO problem in ship design, the subdivision arrangement of a ROPAX vessel. A multi-objective genetic algorithm technique is employed in the first stage, which enables the combinatorial tree to be explored, resulting in better solutions for the MOCO problem in a reasonable processing time. In the second stage, a classical multiple attribute making technique is used to determine the ranking order of the Pareto-optimal solutions. The application of the proposed approach was explained through a real case study from ship design.

Attempts are also made to use multi-objective optimization methods to design the ship room arrangement. For example, a method combining systematic layout planning and a genetic algorithm to optimize the cabin placement within ships is presented in [13], [14], [15], whereas application of the particle swarm algorithm to optimize the ship's vertical passage layout problem is presented in [16].

The optimal ship power plant solutions for different fuel types by applying cost, emission, and safety objectives based on the product life-cycle are analyzed in [17]. For this purpose, a two-objective optimization method was used to determine the optimal configurations of the cruise ship's power plant, taking into account the actual operational profile of the ship and several design parameters of its energy system. The results obtained showed, inter alia, that the cruise ship's power plants with dual-fueled engines working with natural gas show lower life-cycle costs and emissions while demonstrating a level of system safety comparable to the basic configuration of a power plant.

The design method proposed in [18] provides a comprehensive approach to multi-objective optimization of the hull-propeller system of a ship. Two objective functions, i.e. lifetime fuel consumption and operating cost functions, are taken into account. An evolutionary algorithm based on NSGA-II was adopted. The results showed that the proposed method is

the right and effective approach to finding Pareto optimal solutions distributed uniformly and is able to improve both of the objective functions significantly and other performances of the system.

The paper [19] presents a parametric model of the ship's propeller geometry which, in combination with the nondominated sorting genetic algorithm II, was used to optimize the ship's propeller profiles. The radial distribution functions of the propeller pitch and other propeller components were varied. According to the authors of this paper, the optimization procedure presented can provide a well-balanced starting point for the design of high-efficiency propellers, while meeting the conflicting requirements on cavitation inception and other factors characterizing the operation of the propeller.

The work [20] presents ideas and an assessment of two methods using evolutionary algorithm techniques to optimize the marine propeller from the point of view of its cavitation. The particle swarm optimization (PSO) algorithm was used in the multi-objective optimization. Three PSO algorithms were developed and tested to optimize four design solutions of marine propellers for different types of ships. The results were evaluated by a study of the generation medians and the Pareto front development.

In [21] Multi-objective Particle Swarm Optimization was applied to achieve the effective shape of the ship's propeller. Maximizing efficiency and minimizing cavitation were chosen as partial optimization objectives.

The paper [22] proposes a design solution for a high-speed ship propeller. A specially developed optimization procedure was used and the necessary data were obtained from studies of reduction models carried out in the towing tank. The propeller design is solved using a multi-objective approach to numerical optimization and combines the Boundary Elements Method, a viscous flow solver based on the Reynolds-Averaged Navier-Stokes Equations approximation, a parametric 3D description of the blade, and a genetic algorithm.

Relatively few publications are available related to the multi-objective optimization of the ship's operation and maintenance problems. For instance, a hybrid multi-criteria decision making and optimization approach to the issue of support-and-repair ship allocation on a deep-sea route is presented in [23]. This approach was based on an aggregation of evaluation information of quantitative criteria (i.e. weight and economics) and qualitative criteria (i.e. reparability, reliability, and convenience). The authors built a mathematical model of the allocation of this equipment in the form of a mixed-integer nonlinear model. A removal strategy based on a greedy algorithm modifies impossible solutions. According to the authors, the proposed method achieves better solution accuracy and global search performance than three widely used penalty-based methods by several test instances generated randomly. The NSGA-II algorithm based multi-objective optimization approach to arrive at an optimum maintenance plan for the vast variety of machinery to improve the average reliability of a ship's operations at sea at minimum cost is presented in [24].

The analysis carried out here of the issues related to the application of multi-objective optimization methods to the

various problems that arise in the operation and design of ships shows that:

- this concerns a wide range of maritime industry areas, for instance: optimizing the ship's routes and schedules [1]-[6], design of the ship's arrangement [7], [12]-[17], hull and propeller shape [8]-[12], optimizing the ship's hull and propeller cooperation [18]-[22], and optimizing the maintenance process [23], [24],
- these methods are based on analytical models, for example [1], [17], [25] or numerical models, for example [12], [19], [22], and in the majority, they are parametric studies, where data were obtained from the ship's historical logs or specifications of the existing ships,
- these methods used various optimization algorithms, for example: exact algorithms in [1], [17], [25], approximation algorithms in [9], and metaheuristic algorithms (evolutionary algorithm [18]; genetic algorithm [13], [14] [15]; particle swarm optimization [16], [20]).

Unfortunately, from the perspective of the problem discussed in this paper, i.e., supporting the selection of the commanded outputs of the ship's propulsion system, the literature review performed found no methods based on data collected during the planned sea trials regarding ship fuel consumption and speed prediction.

COMPUTER-AIDED SYSTEM SUPPORTING THE SELECTION OF THE COMMANDED OUTPUTS

In the most general sense, selection of the commanded outputs considered as the decision-making problem can be formulated as follows: *what should be the CPP rotational speed and pitch to ensure both the desired fuel consumption necessary for the ship's propulsion and the ship's speed for the observed meteorological conditions at sea.*

To build an expert system supporting the selection of the commanded outputs, it is necessary to pre-define the form of functions connecting the presented parameters. The form of these functions is very important because it determines the further actions associated with the essential elements of the developed decision support system, including data acquisition and function mapping. The analysis presented in [26] showed that the most useful solution to do this is the use of a mathematical apparatus based on artificial neural networks (ANNs) and the theory of multi-criteria optimization.

The developed expert system supporting the selection of the commanded outputs consists of the following main components:

- a data acquisition module,
- a module of the ANN functions, and
- a module of the commanded output selection.

Data acquisition module

The main tasks of the data acquisition module are:

- determination of the developed system variables,
- acquisition and collection of relevant data necessary for the building of the ANN functions.

In line with the postulate for rational use of resources, the fuel consumption necessary for the ship's propulsion and the

ship's speed were taken as the system output variables.

As the system input variables, the following factors were taken into account:

- the operating parameters of the CPP, namely its rotational speed and pitch,
- the parameters affecting the ship's motion, the values of which are subjected to change with variations in sea conditions.

For the building of the ANN functions, the following variables were taken into account (Table 1):

- input variables: ship's engine rotational speed, CPP pitch, wind direction, wind speed, state of the sea, tidal current direction, and tidal current speed,
- output variables: hourly fuel consumption rate and instantaneous ship speed over the ground.

To verify the correct selection of the commanded outputs, the torsional torque of the drive shaft was used as the constraint in the optimization module. Therefore, it was decided to measure a torque on the driveshaft to determine: a torque and minimum engine rotational speed values when friction clutch slipping is detected, and the maximum torque value when exceeding the permissible gear oil temperature is observed during long-term operation of the ship's propulsion system.

A detailed analysis of the factors affecting the ship motion and the method of selecting the system variables are presented in [26] and [27].

To collect the relevant data necessary for the construction of the ANN functions, we conducted a dedicated experiment at sea on a ship equipped with a two-blade CPP. The experiment was carried out on the ship Pogoria launched in 1980. Her length overall is 40.59 meters and her width is 8 meters. Pogoria's propulsion system consists of a 255 kW main engine, which drives a CPP with a 356 rpm nominal rotational speed through a 1:4.5 reduction gear ratio. This experiment was conducted with the engine as the main source of power (without using sails) for various conditions at sea. To obtain suitable data, we used various navigational and meteorological instruments

aboard the ship, and a specially developed measuring device for measuring fuel consumption and shaft torque.

The data necessary for building the ANN functions were obtained from 315 observations carried out during sea trials that lasted nearly two years. A total of 18 variables were recorded and 11 variables were used to construct the ANN functions. The remaining parameters were used to check and verify the correctness of the collected data. The experiment resulted in a dataset that was converted to the output and input values of the ANN models.

More information concerning the measuring devices and procedures of the sea trials can be found in [27], and the detailed description of the tested vessel in [28].

During the long-running sea trials, it was noted that the occurrence of hull biofouling has a significant impact on ship speed reduction. Therefore, we decided to include this factor as an additional input variable named 'time since the last docking of the ship' (Table 1). More information regarding the biofouling phenomenon and the influence of the biofilm layer on the ship hull resistance is presented in [29].

The module of ANN functions

As was mentioned, to build a computer-aided system supporting the selection of the commanded outputs, it is necessary to build ANN functions connecting the selected input and output variables. Such functions allow us to solve problems formulated not very well formally and, to replace the 'manual' process of building functions with a network learning process. In [30] Authors stated that the ANN model could supply a relatively high determination coefficient as compared between predicted results and experimental data, showing that the ANN model could have a good ability to predict the engine behaviors with an accuracy higher than 95%.

The STATISTICA software was used to assess the quality of the collected dataset necessary for the construction of the ANN models. A central agglomeration procedure and six combinatorial methods were used to analyze the correctness of the factor space

Tab. 1. Variables used in two-criteria optimization model

Type of variable	Variable name	Variable identifier	Ranges of variable		Observed values (taken into account in optimization simulation)
			min	max	
Decision-making variables (commanded outputs)	rotational engine speed [rpm]	X_1	from 1000 to 1800 with steps of 50		
	pitch of CPP [pitch scale]	X_2	from 2 to 18 with steps of 1		
Observed variables (conditions of sea and ship hull)	wind direction angle in relation to the longitudinal axis of the ship [°]	X_3	-90	90	-90
	wind speed [knot]	X_4	0	40	17
	state of the sea [degree in Douglas scale]	X_5	0	10	4
	tidal current direction angle in relation to the longitudinal axis of the ship [°]	X_6	-90	90	-15
	tidal current speed [knot]	X_7	0	10	1
	time since the last docking of the ship [months]	X_8	0	24	8
Output variables	hourly fuel consumption rate [dm ³ /h]	X_{1obs}	2	60	to be calculated
	instantaneous speed over the ground [knot]	X_{2obs}	2	12	

structure. In the considered space, all data were separated by the metrics that proved their appropriate selection [31].

As a rule, the data processed employing the ANN techniques are derived from observations and therefore they cannot be entered into networks directly. For this reason, data preparation by using the normalization and standardization techniques to rescale the input and output variables prior to training neural network models was applied. In particular, a linear normalization with a 10% stock in the range of 0.1 to 0.9 for data with positive variable values and -0.9 to 0.9 for data with negative variables values, respectively, was used. Normalization in this way allows data to be extrapolated, that is, to go beyond the range of observed values, e.g., greater than the observed values of the wind speed or sea state.

To build the ANN models, we used the MATLAB software package and carried out many actions required by the ANN techniques and namely:

- division of the data set into three sets (training, testing, and validation),
- determination of the ANN model architecture (choosing the number of hidden layers and epochs of network learning),
- assessment of the ANN model quality (using MATLAB regression plots that displayed the network outputs with respect to targets for training, validation, and testing sets).

Following the suggestions presented in [32], two networks were created for output variables, that is, for the hourly fuel consumption rate and instantaneous ship speed over the ground respectively. In both cases Multilayer Perceptron (MLP) networks were implemented with the following structures:

- eight neurons in the input layer, representing the input variables for both ANN models,
- two hidden layers with different numbers of neurons, and
- one neuron in the output layer representing the output variables separately for each of the ANN models.

These two networks differ only in the number of neurons in their hidden layers.

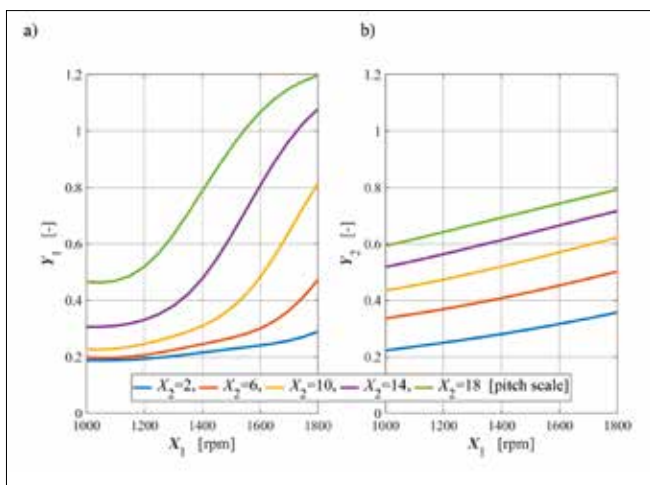


Fig. 1. Relationships between the decision-making variable X_1 'rotational speed of the engine' and the normalized output variables: a) Y_1 'normalized hourly fuel consumption rate'; b) Y_2 'normalized instantaneous speed over the ground' (for values of the observed variables presented in Table 1)

The quality of the received networks was proved using MATLAB regression plots. In both cases, the quality of fit is reasonably good for all datasets, with R^2 values above 0.95. More detailed information regarding the application of artificial neural networks for modeling ship speed and fuel consumption can be found in [31]. Examples of the relationships between the output variables and input variables of the received ANN functions for both the entire range of decision-making variable values and the selected meteorological sea conditions presented in Table 1 are shown in Fig. 1 and 2.

The conducted analysis of the modeling results for both ANN models of the MLP type allowed us to assert that:

- **although the data obtained from sea trials have inherently discrete values, they let us set up the neural networks result in continuous functions,**
- **the networks built are well matched to the real data, as evidenced by the relatively high correlation coefficients and the lack of so-called 'sigmoid-cliffs' [33],**
- **there are some problems in matching with the sea trial observations, especially in areas where relatively few data have been collected or a lack of them is observed.**

Information regarding the constructed ANN functions is saved as a matrix and stored in the computer memory as a set of a weight factor matrix assigned to all neuron inputs, from which the obtained networks consist of information about the structure of the connections between neurons in each layer. The size of such a matrix is very large.

Taking into account the above statements, we have decided to apply the ANN functions developed to build a module of two-criteria optimization allowing for the management of both the ship fuel consumption and the navigation time through selecting the commanded outputs.

The module of the commanded output selection

As was mentioned earlier, to support a selection of the commanded outputs of the ship's propulsion system, we have developed a decision support system in the form of

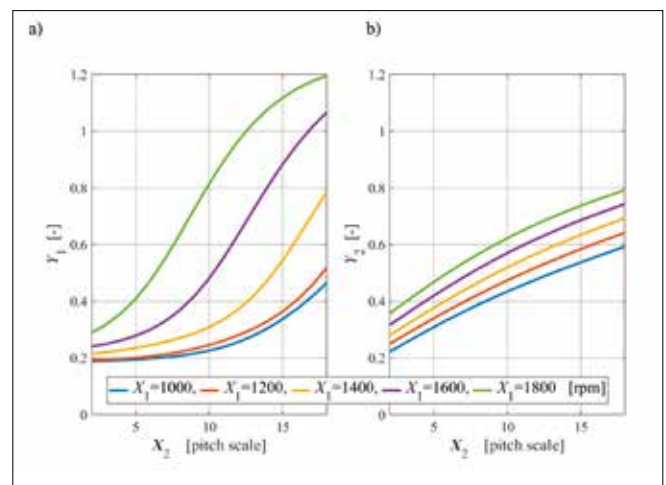


Fig. 2. Relationships between the decision-making variable X_2 'pitch of the propeller' and the normalized output variables: a) Y_1 'normalized hourly fuel consumption rate'; b) Y_2 'normalized instantaneous speed over the ground' (for values of the observed variables presented in Table 1)

a computer-aided system. The developed system allowed the selection of the decision-making variables (the commanded outputs) that should ensure that the ship reaches the required destination with reasonable fuel consumption. Moreover, we assumed that the most appropriate way to build such a system is through the use of two-objective optimization methods based on ANN functions. Thus, the developed ANN functions were used as criterion functions in the considered module of the commanded output selection.

The general idea of the module of the commanded output selection is presented in Fig. 3 in the form of a 'black box'. In it, three inputs interact with the process of commanded output selection and produce two outputs.

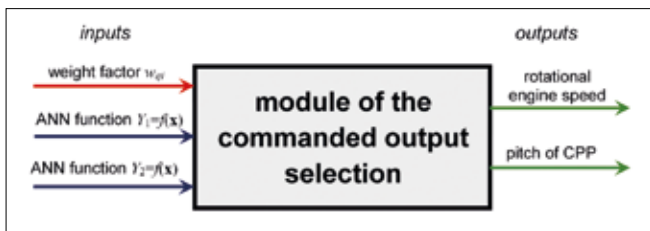


Fig. 3. Module of the commanded output selection in the form of a 'black box' (\mathbf{x} - a vector of the input observed variables in ANN function development)

Two inputs refer to the received ANN functions $Y_1=f(\mathbf{x})$ and $Y_2=f(\mathbf{x})$ respectively, whereas the third input is a set of weight factors w_{qi} of the optimization function. On the other hand, two outputs specify values of the commanded output selection, i.e. the desirable values of the ship engine rotational speed X_1 and CPP pitch X_2 .

To build the commanded output selection module, we have developed the mathematical optimization model of the considered two-objective optimization problem. In general, it consists of an objective function and a set of constraints in the form of a system of equations or inequalities.

The objective function of two-objective optimization

As was mentioned, both the developed ANN functions $Y_1=f(\mathbf{x})$ and $Y_2=f(\mathbf{x})$ will be used as criterion functions in the two-objective optimization. The values of the first criterion should be as small as possible. This is connected with fuel consumption, whereas the values of the second criterion should be as large as possible because it is related to wasted navigation time. Therefore, the Weighted Sum Method was used as the substitute objective function Z in the proposed two-objective optimization. This method minimizes a positively weighted convex sum of both the selected criterion functions. The essence of this substitute objective function Z_{sof} is to assign appropriate weights w_{qi} to both criteria Y_1 and Y_2 , then adding the products of the weights and criteria values:

$$Z_{sof} = w_{q1} \cdot Y_{N1} + (1 - w_{q1}) \cdot Y_{N2} \rightarrow MIN \quad (1)$$

$$0 \leq w_{qi} \leq 1 \quad (2)$$

$$w_{q1} + w_{q2} = 1 \quad (3)$$

where:

- Z_{sof} - the substitute objective function of a two-objective optimization problem,
- Y_1 - the normalized hourly fuel consumption rate,
- Y_2 - the normalized instantaneous speed over the ground,
- w_{q1} - the weight factor of criterion 1,
- w_{q2} - the weight factor of criterion 2.

The accepted form of this function is in accordance with the logic of managing the ship fuel consumption and navigation time to reach the required destination, and it is intuitively understandable and decision-maker-friendly for ship operators. Moreover, the adoption of this approach is recommended in many publications dealing with issues of multi-criteria optimization, for example in [34], [35].

When the Weighted Sum Method is used, the calculation is performed by gradually changing the values of the weights, which leads to a better understanding of the relationship between the selected criteria.

In the considered module of the commanded output selection, the ANN functions were used as criterion functions. Unfortunately, the graphic charts of both the selected criterion functions have consistent slopes (Fig. 1 and 2). Therefore, the substitute objective function Z_{sof} (Eq. 1) was modified by introducing a new output variable Y_{lss} representing the loss of ship speed:

$$Y_{lss} = Y_{2max} - Y_{2obs} \quad (4)$$

where:

- Y_{lss} - the output variable expressing the loss of ship speed,
- Y_{2max} - the maximal instantaneous ship speed over the ground read from the measuring device,
- Y_{2obs} - the instantaneous speed over the ground read from the measuring device.

As already mentioned, the normalization and standardization techniques were applied to rescale the input and output variables prior to training the neural network models. In particular, a linear normalization was used across the range from 0 to 1 for positive values of the variables Y_2 , which means that $Y_{2max} = 1$ and

$$Y_{Nlss} = 1 - Y_2 \quad (5)$$

where:

- Y_{Nlss} - the normalized output variable expressing the loss of ship speed,
- Y_2 - the normalized variable Y_{2obs} .

In this case, the normalized criterion function Y_{Nlss} (representing the loss of speed by the ship) has a slope opposite to the normalized criterion function Y_1 characterizing the fuel consumption (Fig. 4).

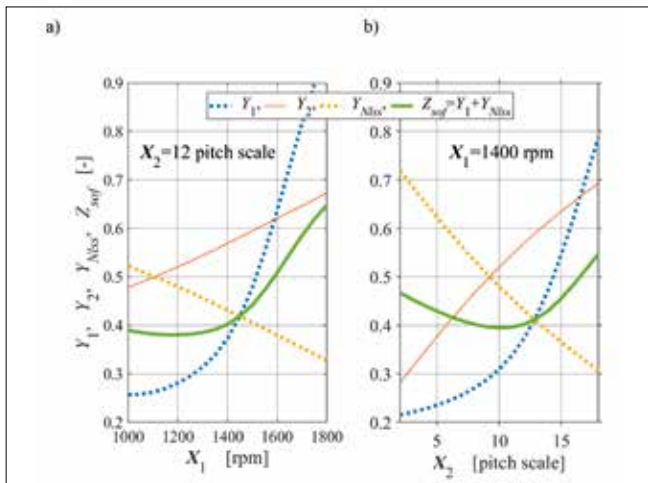


Fig. 4. Relationships between the normalized output variables $Y_1, Y_2, Y_{N1s}, Z_{sof}$ and: a) the decision-making variable X_1 'rotational speed of the engine'; b) the decision-making variable X_2 'pitch of the propeller' (for values of the observed variables presented in Table 1)

After performing the appropriate substitutions and transformations, the substitute objective function Z takes the following form:

$$Z_{sof} = 1 + w_{q1}(Y_{N1} - 1) + (w_{q2} - 1)Y_{N2} \rightarrow MIN \quad (6)$$

This is a convex function where the minimum occurs (Fig. 4). This is a purely technical approach that facilitates graphical analysis of the optimization results and does not change the results of the optimization in any way.

Set of acceptable solutions

One of the important stages in the development of the optimization model is the determination of a set of acceptable solutions. In the general case, this set imposes inequality and equality constraints on possible solutions. In the considered module of the commanded output selection, the set of acceptable solutions includes constraints imposed on:

$$1000 \leq n \leq 1800 \text{ [rpm]} \quad (7)$$

The decision-making variable X_1 'rotational speed of the engine' is controlled remotely by the first lever, which changes the positions of the control rod of the engine inline injector. The command values are read as indications n of the rpm indicator (with 50 rpm accuracy) as standard equipment of the propulsion engine system. The allowable ranges for these values set the first inequality optimization constraint:

$$2 \leq H \leq 18 \text{ [pitch scale]} \quad (8)$$

- decision-making variables,
- permissible operating ranges of the ship's propulsion system. In the first case, the operating ranges of the ship engine rotational speed and the pitch of the CPP set the optimization constraints on the values of the decision-making variables, that is, the commanded outputs. These constraints are directly related to the working principles of mechanisms controlling the settings of the engine rotational speed and the CPP pitch. The ship operator controls the rotational speed of the engine (and consequently, the shaft speed) and the CPP using two command levers situated on the navigation bridge (Fig. 5a). These levers remotely control the engine injector pumps and the angles of the CPP blades. An example of the blade angle is shown in Fig. 5b.

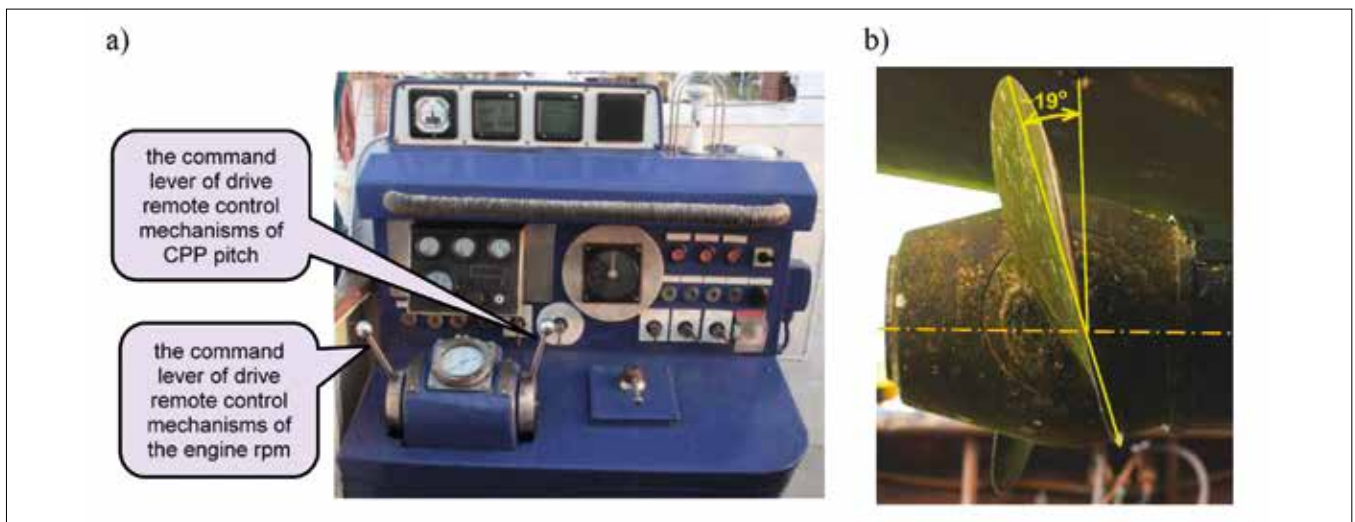


Fig. 5. Mechanisms controlling settings of the engine rotational speed and CPP pitch: a) command levers; b) example of the CPP blade angle

Nevertheless, there is no direct relation between the position of the command lever and the engine rotational speed. This is due to the fact that setting the rotational speed may correspond to different positions of the control rod of the inline injector pumps depending on the current load. The current load, in turn, depends on the orientation of the CPP blades to the propeller hub. Therefore, to control the current load of the ship engine, we introduce the shaft torque M as the next optimization constraint.

In general, the operating range of the engine is determined as follows:

$$M_{min} \leq m \leq M_{max} \quad (9)$$

where:

- M – the current value of the torque on the ship’s propulsion shaft,
- M_{min} – the minimal permissible value on the ship’s propulsion shaft,
- M_{max} – the maximum permissible torque value on the ship’s propulsion shaft.

The minimum permissible torque M_{min} is determined by the minimum torque required to overcome resistance in the engine, gear, shaft bearings and CPP with the zero pitch angle.

As a rule, the maximum permissible torque is determined based on characteristics called the engine operating ranges. Unfortunately, we do not have any access to such characteristics. Therefore, the torque values were read from strain gauges mounted on the ship’s propeller shaft by wireless transfer of the signal [26].

To determine the relationships between the torque M and the command outputs, separate functions were built using ANN techniques. To develop these functions, the same approach and observations were used as those used to develop the ANN functions (Fig. 6).

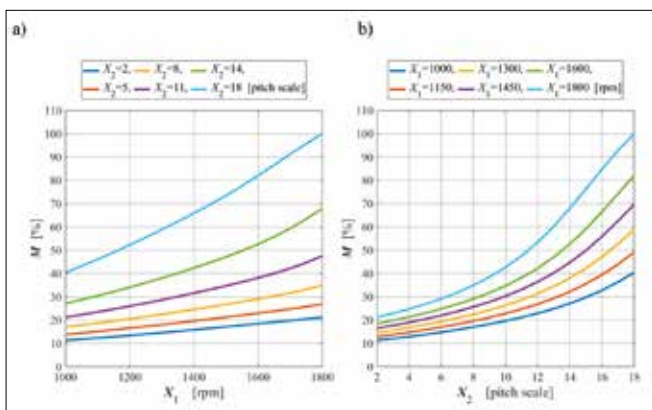


Fig. 6. The relationships between shaft torque M and: a) ‘rotational speed of the engine’; b) ‘pitch of the CPP’ (for values of the observed variables presented in Table 1)

The minimum maneuvering speed of the ship v_{min} was selected as the additional constraint. Based on years of ship operator experience, we have taken into account the following inequality as the optimization constraint:

$$v_{min} \leq 2 \text{ knots} \quad (10)$$

This minimal ship speed plays an important role in avoiding possible damage resulting from collisions, contact with berths or other ships.

Two-criteria optimization algorithm

The two-criteria optimization algorithm procedure (Fig. 7) was created based on the mathematical optimization model developed, including both the objective function and the set of acceptable solutions.

To determine the optimum values of the output commands, the complete search method was used. This method was selected because of the small number of possible combinations of commanded outputs, that is, combinations of the decision-making variables X_1 ‘rotational speed of the engine’ and X_2 ‘pitch of the CPP’ respectively. This resulted in 289 combinations of possible settings of the commanded outputs. For each combination, the minimal values of the objective function were calculated.

To prevent the selection of an unacceptable solution, we applied a special technical approach based on significant enlarging of the value of the substitute objective function Z . In such case, this value Z was multiplied by a rate called the ‘penalty factor’.

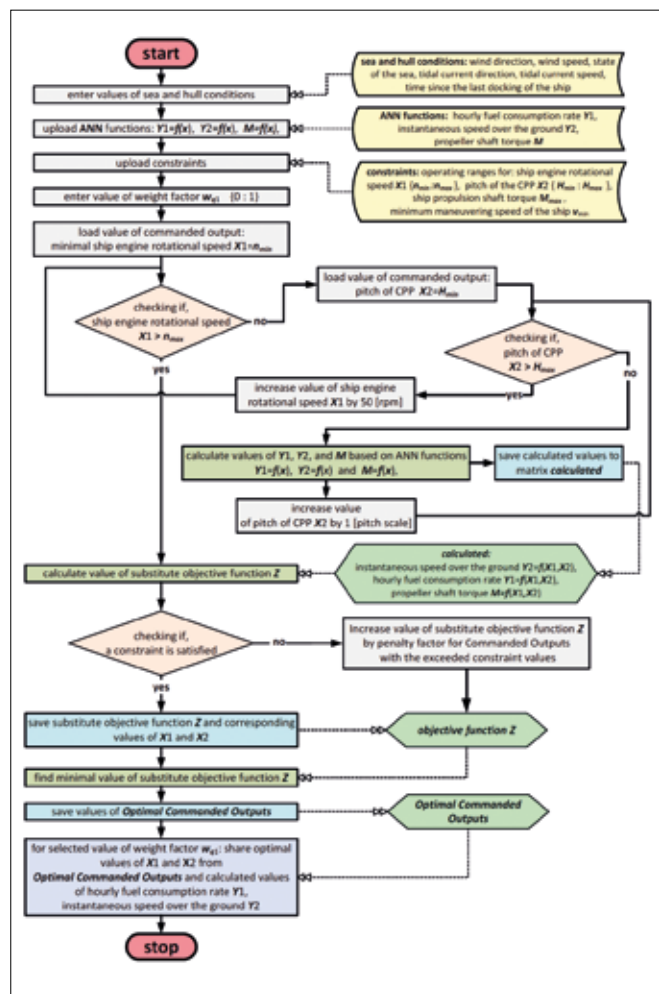


Fig. 7. Algorithm procedure of two-objective optimization

Optimization calculations were performed using standard mathematical functions and mathematical operations on matrices of the MATLAB package.

RESULTS AND DISCUSSION

To validate the correctness of the form of the substitute objective function Z_{sof} (Eq. 6), it was investigated before basic optimization calculations. An example of such an investigation is presented in Fig. 8 as the 3D plot where this function is mapped by the surface in a tradeoff curve form. The calculation was performed for the weight factors $w_{q1} = w_{q2} = 0.5$ for the entire ranges of the decision-making variables X_1 and X_2 , taking into account the selected meteorological sea conditions presented in Table 1. The function obtained has a long, narrow, and bent shaped flat valley, where the minimum of the substitute objective function Z occurs. For other meteorological data, similar 3D plots were obtained that confirmed that the substitute objective function was chosen correctly.

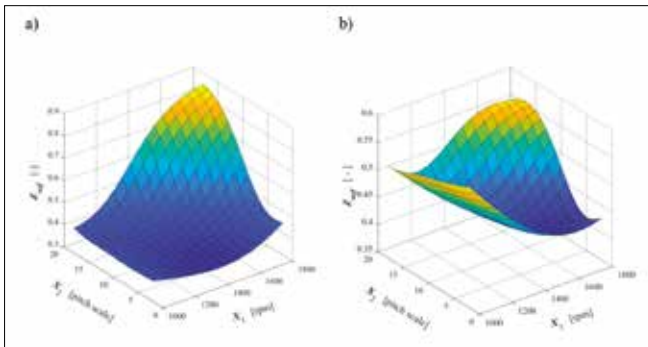


Fig. 8. Three-dimensional visualization of relationships between the substitute objective function Z and both the decision-making variables X_1 'rotational speed of the engine' and X_2 'pitch of the propeller': a) $w_{q1} = 0.35$; b) $w_{q1} = 0.65$ (for values of the observed variables presented in Table 1)

In our research, we performed calculations to carry out the analysis of the substitute objective function values for weight factors w_{qi} changing from 0 to 1 with a step of 0.1 for the various meteorological conditions and the entire range of decision variables X_1 and X_2 based on the developed two-criteria optimization algorithm procedure (Fig. 7).

Some examples of the results obtained by the optimization calculations are presented in Fig. 9 in the form of 2D graphs. All calculations were performed for selected weight factor values $w_{q1} = 0.2, 0.4, 0.6,$ and 0.8 and selected meteorological and hull conditions presented in Table 1. The curves shown in the 2D graphs have marked points demonstrating the minima of the substitute objective function Z_{sof} .

In some cases, these points lie at the graph edges due to the constraint (Eq. 7) imposed on the decision-making variable X_1 , which limits the allowable ranges of the ship engine speed. For example, in cases of the decision-making variable value of a pitch of the CPP:

- X_2 equals 2, the allowable maximum engine speed moved the substitute objective function minimum to the graph left edge (Fig. 8b),
- X_2 equals 14, the allowable minimum engine speed moved

the substitute objective function minimum to the graph right edge (Fig. 8c).

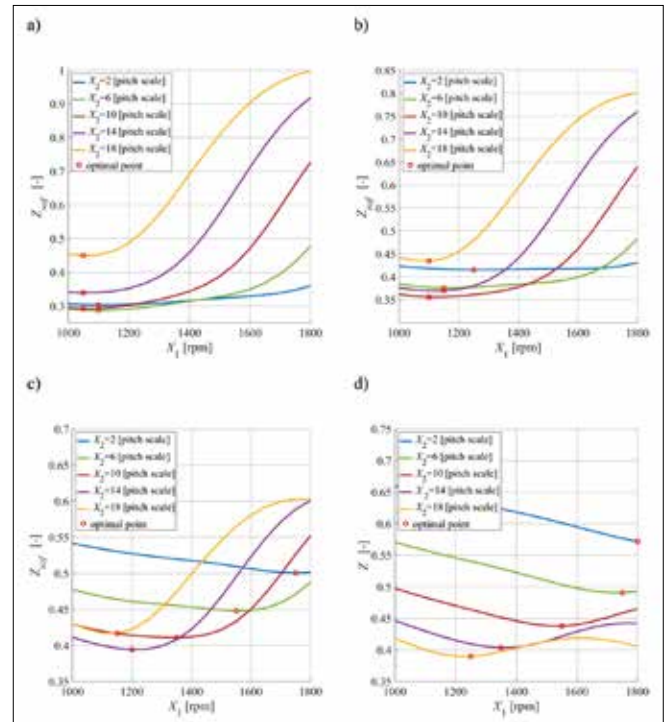


Fig. 9. The substitute objective function Z for values of the observed variables presented in Table 1 for the whole ranges of decision-making variables: rotational speed of the engine X_1 and pitch of CPP X_2 in relation to the weight factors: a) $w_{q1} = 0.2/0.8$; b) $w_{q1} = 0.4/0.6$; c) $w_{q1} = 0.6/0.4$ and, d) $w_{q1} = 0.8/0.2$.

Table 2 presents the estimated values of the output variables Y_1 (hourly fuel consumption rate) and Y_2 (instantaneous speed over the ground), together with the estimated value of the torque on the ship's propulsion shaft. These were calculated based on the developed algorithm procedure of two-criteria optimization presented in Fig. 7:

- for the optimal values of the command outputs (rotational speed of the engine and pitch of the CPP),
- for the weight factors w_{qi} from 0 to 1 with a step of 0.1, and
- taking into account the selected meteorological conditions presented in Table 1.

Based on the optimization simulations and analysis of the obtained results carried out, we can state that the developed two-criteria optimization model strongly supports the selection of the commanded outputs of the considered ship's propulsion system. The minimum values of the substitute optimization function Z_{sof} (Eq. 6) occur for most of the range of decision-making variables (commanded outputs). However, in the case of selection of the border values of the weight factor close to 0 or 1, the minimum values of this function are moved to the left or right periphery of its parts due to the imposed constraints.

It is clear that with a weight factor of 0 or 1, the considered two-criteria optimization problem comes down to the issue of single-criterion optimization. Then the minimum hourly fuel consumption rate or maximum ship speed over the ground should be sought.

Tab. 2. Observed values of resource use predicted by the two-criterion optimization model

Weight factor w_{qi}	Optimal values of commanded outputs		Observed values of resource use		
	Optimal setting of rotational speed of the engine	Optimal setting of pitch of the CPP	Hourly fuel consumption rate	Instantaneous speed over the ground	Torque as a percentage of nominal torque
[-]	[rpm]	[pitch scale]	[dm ³ /h]	[knot]	[%]
0.0	1050	3	10.76	2.22	12.30
0.1	1100	5	11.01	3.14	15.48
0.2	1100	7	11.45	3.90	18.38
0.3	1100	9	12.26	4.61	21.82
0.4	1100	11	13.71	5.27	26.04
0.5	1200	12	15.69	5.89	32.11
0.6	1200	14	18.38	6.49	39.40
0.7	1250	15	21.54	6.95	46.78
0.8	1300	16	26.64	7.41	55.86
0.9	1500	18	51.10	8.65	89.19
1.0	1800	15	60.62	8.92	92.69

In addition, for the given meteorological conditions and adjacent values of the weight factors, the two-criteria optimization model provides different combinations of the optimal values for the commanded outputs. Moreover, the estimated values of the output variables Y_{1obs} (hourly fuel consumption rate) and Y_{2obs} (instantaneous speed over the ground) are close to each other. This allows the introduction of additional optimization criteria, e.g. harmful pollutants contained in the exhaust gases emitted from the ship engine (NO_x, CO₂, ppm, etc.).

CONCLUSIONS AND FINAL REMARKS

Based on the results obtained, we can conclude that the developed model of two-objective optimization supporting a selection of commanded outputs for a ship's propulsion system:

- allowed us to develop an expert system that, in turn, supports a setting of the commanded outputs that ensures the set time to reach the required destination with rational fuel consumption,
- has minimum values of its substitute objective function for the vast majority of the range of decision-making variables, which makes it very useful for optimal selection of both the pitch and rotational speed of the CPP.

Moreover, the developed decision-making system:

- allows the selection of the commanded outputs in the dialogue between the decision-maker and the computer, where the decision-maker takes the appropriate decisions, and the computer processes the collected data and makes

available a proposal for the selection of the commanded outputs,

- ensures cooperation with other systems used in the ship operation to receive the actual data,
- provides the possibility of continuously updating the parameters of the decision-making system resulting from the acquisition of the new data.

The developed methodology can also be applied to other types of vessels with a similar design solution to their propulsion systems. Developing such a system requires an experiment to be performed in the form of sea trials for the acquisition of new data specific to the tested vessel.

During the study, it was noted that, for some meteorological and operational conditions and adjacent values of the weight factors, the developed system provides various combinations of optimal commanded outputs and for which the projected values of the output variables (ship speed and fuel consumption) are close enough. Therefore, there is an opportunity to introduce additional optimization criteria, e.g. emissions of harmful pollutants (NO_x, CO₂, pollutant concentration) from the ship engine. This issue sets the direction for further research.

The research findings were also used in practice. Since the ship's operator did not allow the use of the installed measuring apparatus (torque meter, fuel consumption meter) outside the prescribed sea trial period, it was dismantled. Therefore, it was not possible to continue operating the computer system to select the proper parameters of the ship's propulsion system during navigation to the present date. To use the research findings, a special assisting table was drawn up for the ship operators. This table contained the ranges of the typical observed variable values and the corresponding commanded outputs, ensuring optimal values of both the ship speed and the fuel consumption values.

In the opinion of the shipowner of the tested ship, a noticeable reduction in fuel consumption was observed. Of course, this is only a qualitative opinion and cannot be considered as a reliable scientific confirmation of the results of the research findings.

REFERENCES

1. M. A. Dulebenets, "A comprehensive multi-objective optimization model for the vessel scheduling problem in liner shipping," *Int. J. Prod. Econ.*, 2018, doi: 10.1016/j.ijpe.2017.10.027.
2. R. Zaccone, E. Ottaviani, M. Figari, and M. Altosole, "Ship voyage optimization for safe and energy-efficient navigation: A dynamic programming approach," *Ocean Eng.*, 2018, doi: 10.1016/j.oceaneng.2018.01.100.
3. R. Szlarczyński and H. Ghaemi, "Framework of an evolutionary multi-objective optimisation method for planning a safe trajectory for a marine autonomous surface ship," *Polish Marit. Res.*, 2020, doi: 10.2478/pomr-2019-0068.

4. E. Sobiecka, R. Szlaczynski, and M. Zyczkowski, "Evolutionary multi-objective weather routing of sailboats," *Polish Marit. Res.*, 2020, doi: 10.2478/pomr-2020-0054.
5. L. Yang, G. Chen, N. G. M. Rytter, J. Zhao, and D. Yang, "A genetic algorithm-based grey-box model for ship fuel consumption prediction towards sustainable shipping," *Ann. Oper. Res.*, 2019, doi: 10.1007/s10479-019-03183-5.
6. A. Cheaitou and P. Cariou, "Greening of maritime transportation: a multi-objective optimization approach," *Ann. Oper. Res.*, 2019, doi: 10.1007/s10479-018-2786-2.
7. A. Priftis, E. Boulougouris, O. Turan, and G. Atzampos, "Multi-objective robust early stage ship design optimisation under uncertainty utilising surrogate models," *Ocean Eng.*, 2020, doi: 10.1016/j.oceaneng.2019.106850.
8. T. P. Scholcz and C. H. J. Veldhuis, "Multi-objective surrogate based hull-form optimization using high-fidelity rans computations," 2017.
9. S. Zhang, B. Zhang, T. Tezdogan, L. Xu, and Y. Lai, "Computational fluid dynamics-based hull form optimization using approximation method," *Eng. Appl. Comput. Fluid Mech.*, 2018, doi: 10.1080/19942060.2017.1343751.
10. J. Čerka et al., "Optimization of the research vessel hull form by using numerical simulaton," *Ocean Eng.*, 2017, doi: 10.1016/j.oceaneng.2017.04.040.
11. Z. Baoji, "Research on Ship Hull Optimisation of High-Speed Ship Based on Viscous Flow/Potential Flow Theory," *Polish Marit. Res.*, 2020, doi: 10.2478/pomr-2020-0002.
12. A. I. Ölçer, "A hybrid approach for multi-objective combinatorial optimisation problems in ship design and shipping," *Comput. Oper. Res.*, 2008, doi: 10.1016/j.cor.2006.12.010.
13. S. Su, Y. Zheng, J. Xu, and T. Wang, "Cabin Placement Layout Optimisation Based on Systematic Layout Planning and Genetic Algorithm," *Polish Marit. Res.*, 2020, doi: 10.2478/pomr-2020-0017.
14. Y.L. Wang, C. Wang, and Y. Lin, "Ship cabin layout optimization design based on the improved genetic algorithm method," 2013, doi: 10.4028/www.scientific.net/AMM.300-301.146.
15. J. Li, H. Guo, S. Zhang, X. Wu, and L. Shi, "Optimum Design of Ship Cabin Equipment Layout Based on SLP Method and Genetic Algorithm," *Math. Probl. Eng.*, 2019, doi: 10.1155/2019/9492583.
16. X. Liu, Z. Liu, S. Yu, and T. Gong, "Adapted particle swarm optimization algorithm-based layout design optimization of passenger car cockpit for enhancing ergonomic reliability," *Adv. Mech. Eng.*, 2019, doi: 10.1177/1687814019837808.
17. V. Bolbot, N. L. Trivyza, G. Theotokatos, E. Boulougouris, A. Rentizelas, and D. Vassalos, "Cruise ships power plant optimisation and comparative analysis," *Energy*, 2020, doi: 10.1016/j.energy.2020.117061.
18. H. Ghassemi and H. Zakerdoost, "Ship hull-propeller system optimization based on the multi-objective evolutionary algorithm," *Proc. Inst. Mech. Eng. Part C J. Mech. Eng. Sci.*, 2017, doi: 10.1177/0954406215616655.
19. John Huisman; Evert-Jan Foeth, "Automated multi-objective optimization of ship propellers," 2017.
20. F. Vesting and R. E. Bensow, "Particle swarm optimization: an alternative in marine propeller optimization?," *Eng. Optim.*, 2018, doi: 10.1080/0305215X.2017.1302438.
21. S. Mirjalili, A. Lewis, and S. A. M. Mirjalili, "Multi-objective optimisation of marine propellers," 2015, doi: 10.1016/j.procs.2015.05.504.
22. S. Gaggero et al., "Efficient and multi-objective cavitating propeller optimization: An application to a high-speed craft," *Appl. Ocean Res.*, 2017, doi: 10.1016/j.apor.2017.01.018.
23. R. Zhao, X. Xie, and W. Yu, "Repair equipment allocation problem for a support-and-repair ship on a deep sea: A hybrid multi-criteria decision making and optimization approach," *Expert Syst. Appl.*, 2020, doi: 10.1016/j.eswa.2020.113658.
24. A. K. Verma, A. Srividya, A. Rana, and S. K. Khattri, "Optimization of maintenance scheduling of ship borne machinery for improved reliability and reduced cost," *Int. J. Reliab. Qual. Saf. Eng.*, 2012, doi: 10.1142/S0218539312500143.
25. Y. Zhao, Y. Fan, J. Zhou, and H. Kuang, "Bi-objective optimization of vessel speed and route for sustainable coastal shipping under the regulations of emission control areas," *Sustain.*, 2019, doi: 10.3390/su11226281.
26. K. Rudzki, "Two-objective optimization of engine ship propulsion settings with controllable pitch propeller using artificial neural networks," Gdynia Maritime University, 2014.
27. K. Rudzki and W. Tarelko, "A decision-making system supporting selection of commanded outputs for a ship's propulsion system with a controllable pitch propeller," *Ocean Eng.*, 2016, doi: 10.1016/j.oceaneng.2016.09.018.
28. J. Kozak and W. Tarełko, "Case study of masts damage of the sail training vessel POGORIA," *Engineering Failure Analysis*. 2011, doi: 10.1016/j.engfailanal.2010.11.016.

29. W. Tarełko, "The effect of hull biofouling on parameters characterising ship propulsion system efficiency," *Polish Marit. Res.*, 2014, doi: 10.2478/pomr-2014-0038.
30. A. Tuan Hoang et al., "A review on application of artificial neural network (ANN) for performance and emission characteristics of diesel engine fueled with biodiesel-based fuels," *Sustain. Energy Technol. Assessments*, vol. 47, p. 101416, Oct. 2021, doi: 10.1016/j.seta.2021.101416.
31. W. Tarełko and K. Rudzki, "Applying artificial neural networks for modelling ship speed and fuel consumption," *Neural Computing and Applications*. 2020, doi: 10.1007/s00521-020-05111-2.
32. R. Tadeusiewicz, "Neural network as a tool for medical signals filtering, diagnosis aid, therapy assistance and forecasting improving," 2009, doi: 10.1007/978-3-642-03882-2-406.
33. R. Matignon, "Neural Network Modeling using SAS Enterprise Miner," *AuthorHouse, London*, 2005.
34. J. Andersson, "A survey of multiobjective optimization in engineering design," 2000.
35. R. T. Marler and J. S. Arora, "Survey of multi-objective optimization methods for engineering," *Structural and Multidisciplinary Optimization*. 2004, doi: 10.1007/s00158-003-0368-6.

CONTACT WITH THE AUTHORS

Krzysztof Rudzki

Gdynia Maritime University
Faculty of Marine Engineering
Gdynia
POLAND

Piotr Gomulka

Gdańsk University of Technology
Narutowicza 11/12
80-233 Gdańsk
POLAND

Anh Tuan Hoang

HUTECH University
Ho Chi Minh City
VIET NAM

AN INNOVATIVE METHOD OF MEASURING THE EXTENSION OF THE PISTON ROD IN HYDRAULIC CYLINDERS, ESPECIALLY LARGE ONES USED IN THE SHIPBUILDING AND OFFSHORE INDUSTRY

Paweł Dymarski* 

Gdansk University of Technology, Institute of Naval Architecture and Ocean Engineering, Poland

Czesław Dymarski 

Gdansk University of Technology, Institute of Naval Architecture and Ocean Engineering, Poland,

Piotr Grymajło

Poland

* Corresponding author: pawdymar@pg.edu.pl (Paweł Dymarski)

ABSTRACT

The article presents the results of selected works related to the wider subject of research conducted at the Faculty of Mechanical Engineering and Shipbuilding at the Gdańsk University of Technology, regarding designing various on board devices with hydraulic drive for ships and other offshore facilities. One of the commonly used these mechanisms are hydraulic actuators with the measurement of the piston rod extension. The issue of precise measurement of the piston rod extension is extremely important in modern technologies of construction, assembly and precise displacement and positioning of large and heavy, both land and ocean engineering objects or structural elements with the use of several large hydraulic cylinders working in parallel. The article presents a one of two new patented P.425099 – A device for measuring the extension of a hydraulic cylinder piston rod. [1].

Keywords: hydraulic cylinders, piston rod extension measurement, roller rotation sensor

INTRODUCTION

The issue of precise measurement of the extension of a hydraulic cylinder piston rod is very important in the contemporary dynamic development of new machines and devices, especially automatic machines with hydraulic drive, requiring precise control of the process of their operation and protection against overload [2]. In the technical literature and on websites [3,4,5,6,7] you can find information with a general description of the principle of operation and the main technical and geometric parameters of this type of actuator, but usually without precise description of the piston rod extension measurement. Meanwhile, the development of

increasingly larger structures and devices, not only on land, but also on the sea, both installed and floating during the construction, assembly and operation of which, it is required to precisely move large and heavy elements with the help of several parallel actuators. An example of the need to use such actuators are various types of equipment for ships and platforms, including, for example, mechanisms for changing the reach of deck cranes, mechanisms for opening and closing and holding in a set position external and internal ramps and watertight doors, mechanisms for opening and closing various types of hatch covers, systems compensation of flooding of specialized equipment for offshore drilling and exploitation of deposits from floating objects, as well as ship equipment

for servicing offshore wind farms. In particular, devices for automatic piston extension measurement can be used during the installation process of floating wind turbines [8,9,10,11].

When using sliding motion machines in ocean engineering, an important issue is to solve the problem of proper sealing. The paper [12] presents an innovative solution of sealing with the use of magnetic fluid seals for reciprocating motion. On the other hand, the influence of water and mineral oil on mechanical losses in a hydraulic motor for offshore and marine applications is presented in [13].

The need for high precision during the above-described applications resulted in the development and creation of several methods of measuring the extension of the actuator piston rod and their application in practice. The results of their operation so far have allowed their producers to assess to some extent a number of important features of their operation, including mainly the method and precision of measurement, reliability, purchase and operation costs. Several of the most popular methods are presented and characterized in [3]. The solutions presented there usually use magnetostrictive sensors. A description of the basics of the measurement method is provided in [14]. They mainly differ in the location of the magnetostrictive sensor. When deciding on the measurement at the actuator design stage, the sensor can be integrated into the cylinder itself, but if the actuator already exists, the sensor is placed outside the cylinder, and the displacement measurement can be performed using draw wire sensors and magnetic or optical measuring rods or measuring tapes. A significant problem here was the design of the sensor and the routing of the signal outwards, as the cylinder housing bore is always a weak point as there is a high risk of oil leakage at higher operating pressures [15]. The above-mentioned measurement methods are characterized by considerable construction complexity, difficult access to sensors operating in variable pressure conditions and a high cost of execution and operation.



Fig. 1. Photo of the actuator with a magnetostrictive sensor located at the bottom of the cylinder

For a better visualization of the subject matter of the invention, Fig. 2 shows a drawing of an actuator without measuring device and with a relatively very large diameter of the piston rod in relation to the diameter of the cylinder ($d_r/D_c = 0,82$), which is usually used for difficult sea and land operations requiring precise movement of large, heavy

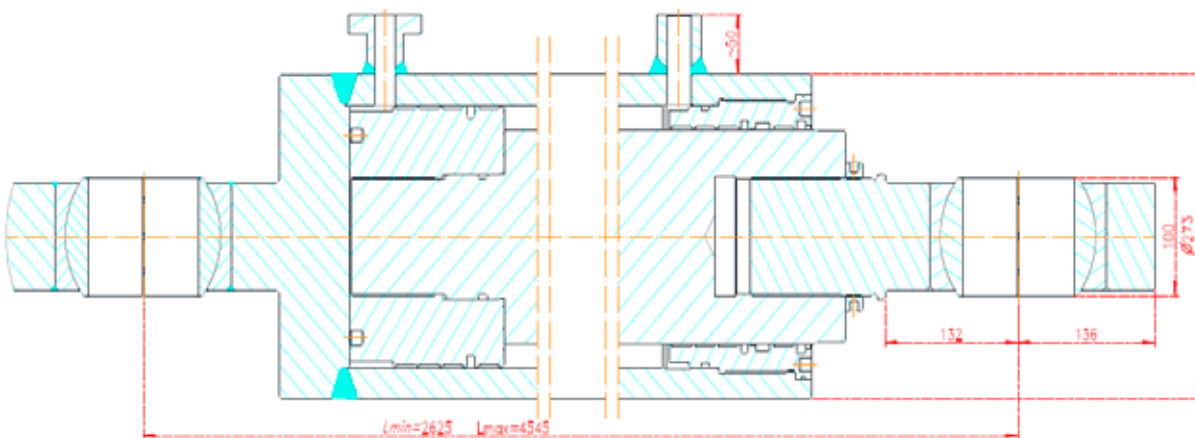


Fig. 2. Longitudinal cross-section a typical hydraulic cylinder, without a sensor for measuring the extension of the piston rod, which up to now often are used to move large and heavy elements with the help of several similar parallel mounted actuators.

objects by means of a set of several parallel working hydraulic cylinders. In these cylinders, the available space between the cylinder tube and the piston rod is smaller, which makes it difficult, but as shown in Fig. 3 and in Fig. 4, does not prevent the application of the method according to the invention shown when installed in such a cylinder. Magnetostrictive sensors are also widely used in robotics. Zhang et al describe the use of magnetostrictive tactile sensor array in robotic fingers [16]. The use of magnetostrictive sensors for precise botanical measurements is presented in [17]. Descriptions of Magnetostrictive Control Rod Position Identification applications are also presented in [18,19].

Another method of measuring the extension of the piston rod - using microwaves, developed by Dorneich and Fritton, was presented in the article [20]

AN EXAMPLE OF USING THE NEW MEASUREMENT METHOD

The method of measuring the actuator piston rod displacement, shown in Fig. 3, according to the invention, is characterized in that the measuring unit is placed in a closed pressureless chamber located in the cylinder body 1, but outside the working chambers, behind a partition 2 with elements guiding and sealing the piston rod 3. This cylindrical chamber is closed with a disc-shaped cover 4 screwed to the said partition 2. In the axis of the cover there is a cylindrical opening with a circumferential channel in which an elastic scraper 5 and sealing ring is mounted [21]. The diameter of this hole is slightly larger than the diameter of the piston rod, which allows it to move freely in relation to the cover while maintaining the tightness of the chamber with the measuring assembly. A body 8 with elements of

the measuring device is attached to the inner face of the cover 4 with screws or welded on. The body 8 has two arms, one larger and thicker, with a cylindrical opening. The axis of this hole is in a plane perpendicular to the axis of the cylinder. The hole houses an axle 9 with two cylindrical pivots of different diameters and a threaded end with a transverse slot for a screwdriver. This axle is mounted with a smaller pin in the body 8 arm and rigidly fixed to it with nuts 10. Two rolling bearings 12 are mounted on the journal with the larger diameter of this axle, with intervals determined by the length of the spacer sleeves 11. These bearings support a roller 13 made of a magnetic material, e.g. polyamide, and on the outer cylindrical surface it is advantageous to apply a layer 15 (sleeve) made of a more flexible material, e.g. rubber or other material with appropriate properties [7]. The geometrical parameters of the axles and the roller as well as their positions are selected in such a way that the roller with its cylindrical surface slightly presses the piston rod 3, so that the linear movement of the piston rod 3 in the cylinder causes the roller to rotate. A shallow, cylindrical recess in which a permanent magnet 16 is mounted is made on the front surface of the roller 13 along its axis of rotation. Opposite the face of the roller with the magnet 16, a printed plate 17 is attached to the second arm of the body 8, which is a very precise sensor of the angle of rotation of the magnetic poles rotating together with the roller of the magnet. During the operation of the actuator, the linear displacement of the piston rod will cause the rotating roller with the magnet to rotate along it, and thus generate signals in the printed board, which through the wires 18 connected to it reach the hermetic electrical connector 19 located in the cover 4 wall and through this connector are led to the computer or via an external cable to other control device.

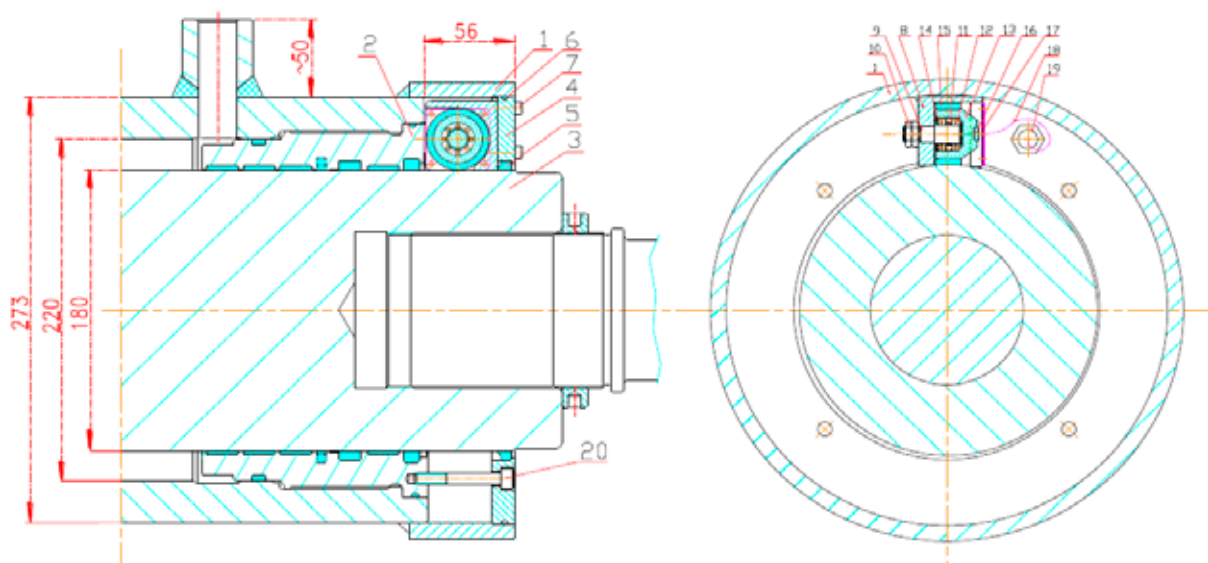


Fig. 3. longitudinal and cross section through the actuator showing the location of the gauge

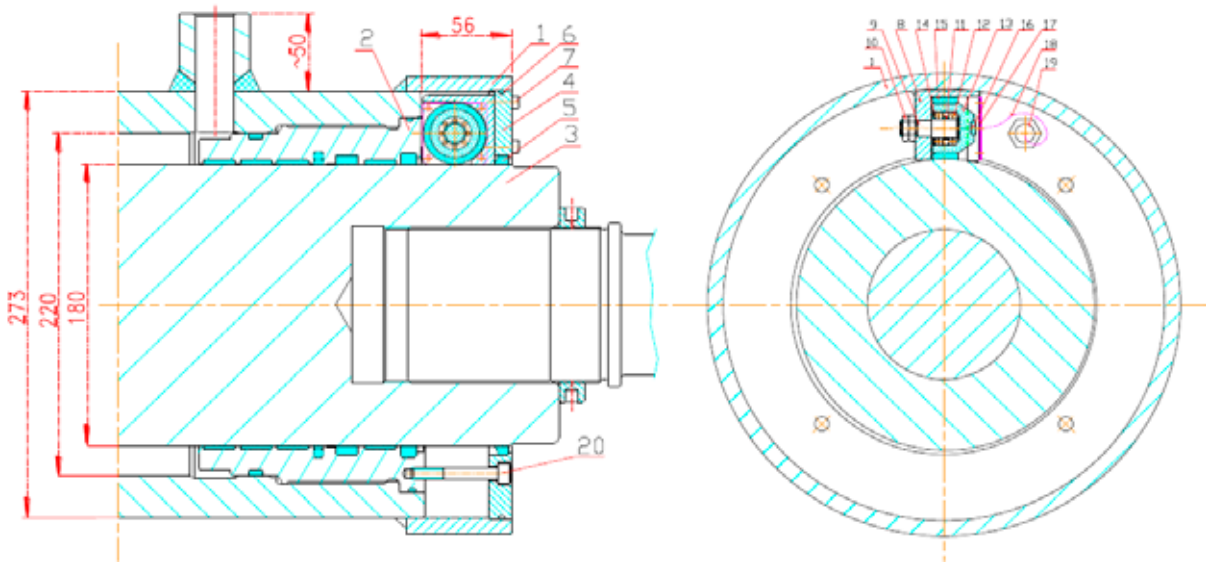


Fig. 3. Longitudinal and cross section through the actuator showing the location of the gauge

A preferred variant is to make an axle 9 with an eccentric pin for bearings with an eccentricity (values of the shift of the axis of this pin in relation to the pin mounting it in the body arm) equal, for example, to $e = 0.5$ mm. Such a solution allows in a very simple way, by changing the angular position of the axle 9 with the roller 13 in the body 8 arm, to precisely regulate the rolling radius within 1 mm and the value of pressure of the roller against the piston rod. This can be done by loosening the nuts 10 on the axle 9, and then turning the axle with a screwdriver to a certain angle and tightening the nuts again, thus locking the changed angular position of the axle. After such adjustment, it is only necessary to enter a new value of the roller radius into the computer program and check the accuracy of indications by fully extending and retracting the piston rod with a known displacement value.

The method according to the invention has several very significant advantages over the methods used so far, namely:

- enables continuous and very precise measurement of the length, direction and speed of the actuator's piston rod extension;
- it is structurally simple and therefore relatively reliable and cheap;
- the measuring unit is placed in a closed chamber, in which there are stable and relatively favorable working conditions, practically independent of very variable, especially in terms of pressure, conditions in the working chambers of the actuator, which is very important, especially for ensuring correct and long-term operation sensors;
- easy access to the measuring assembly without the need to disconnect the hydraulic actuator, requiring

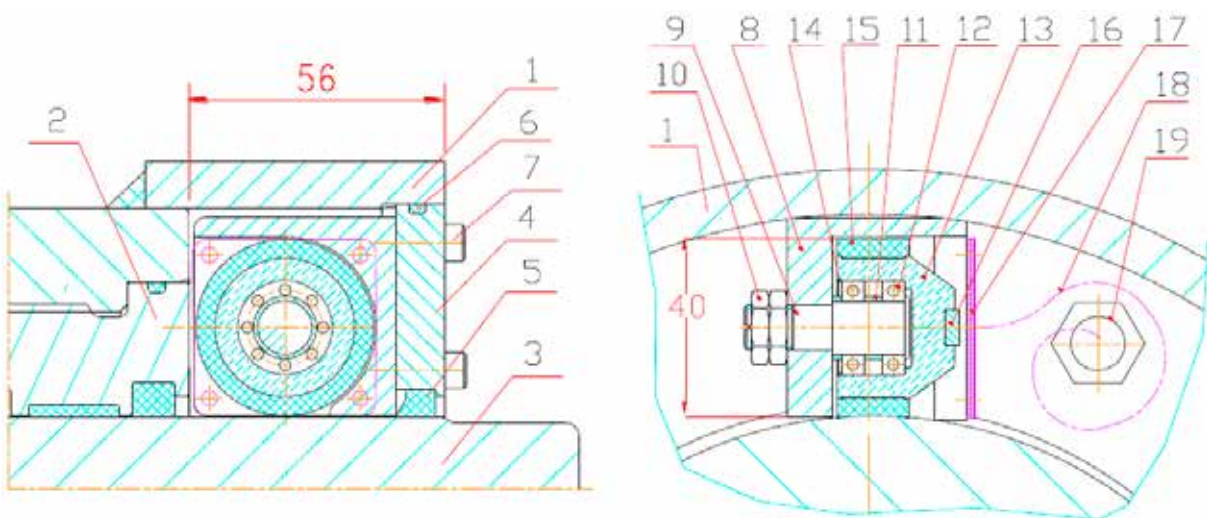


Fig. 4. A device for measuring the extension of the piston rod

only unscrewing the bolts 20 securing the cover 4 and extending the partial piston rod with the cover until the measuring assembly mounted on the inner wall of the cover is fully accessible, which greatly facilitates the control and adjustment of the assembly, and also possible replacement of its elements;

- in the variant with an eccentric axis, a simple and easy way to adjust the pressure of the roller against the piston rod and to introduce corrections to the measurement program, which will significantly extend the life of the roller even in the event of certain changes in the properties of the material from which it is made without the need to replace it with a new one.

Installing the inventive piston rod extension measurement assembly in this exemplary atypical cylinder required only a slight lengthening of the cylinder by welding ~ 60mm of the pipe section 1, and making the cover 4 and the sealing ring 6, which consequently increased the length of the cylinder by 56mm. Compared to the maximum length of this actuator, which is 4545 mm, this represents 1.2%.

SUMMARY

The method of measuring the extension of the actuator piston rod and the designed measuring unit presented in the article are original and patent pending. The authors of the article have not found such a solution in the available publications so far. The presented method of measuring the actuator piston rod extension is, according to the authors, relatively simple and accurate, it enables the device to operate in difficult conditions, without the risk of oil leakage. It allows easy access to measuring instruments and possible replacement of its components without the need to open the working space of the hydraulic cylinder. In order to confirm the above-mentioned advantages of this method, laboratory tests of the actuator were carried out with the presented measuring unit installed. The description of the Laboratory stand and the results of the tests carried out will be presented in the next article.

ACKNOWLEDGEMENT

The authors of the article would like to thank P.H.S Hydrotor S.A. for providing the actuator and construction of the test stand, as well as for the construction of a hydraulic power supply unit. The authors would also like to thank FESCH Feedback Engineering s.c. for the performance of laboratory tests of the measurement system prototype.

The project was financed from the regional programme for founding R&D services “μGrants R&D for enterprises” implemented by Excento Sp. z o.o. (special purpose vehicle of the Gdańsk University of Technology)

BIBLIOGRAPHY

1. P.425099, “A device for measuring the extension of a hydraulic cylinder piston rod “. Patent granted in 2021.
2. “Innovative Ship Relies on Smart Cylinders”, Power&Motion, Feb 1, 2003, <https://www.powermotiontech.com/sensors-software/controls-instrumentation/article/21883570/innovative-ship-relies-on-smart-cylinders>
3. P. Boughton, “Measuring the displacement of hydraulic cylinders”, Design Engineer – Instrumentation, 5th February 2013
4. <https://www.cpi-nj.com/hydraulic-cylinder-position-sensors/>
5. <https://www.cpi-nj.com/linear-position-sensors/>
6. EP1620702B1 patent, “Piston rod position detection system”
7. T. Vanthuyne, “An electrical thrust vector control system for the VEGA launcher”, Proceedings of 13th European space mechanisms and tribology symposium ESMATS’2009, Vienna, 23–25 September 2009 (ESA SP-670, July 2009).
8. Dymarski, C., Dymarski, P., & Żywicki, J. (2017). Technology Concept of TLP Platform Towing and Installation in Waters with Depth of 60 m. Polish Maritime Research, 24(s1), 59-66. <https://doi.org/10.1515/pomr-2017-0022>
9. Dymarski, P., Dymarski, C., & Ciba, E. (2019). Stability Analysis of the Floating Offshore Wind Turbine Support Structure of Cell Spar Type During its Installation. Polish Maritime Research, 26, 109-116. <https://doi.org/10.2478/pomr-2019-0072>
10. Ciba, E. (2021). Heave Motion Of A Vertical Cylinder With Heave Plates. Polish Maritime Research, 28, 42-47. <https://doi.org/10.2478/pomr-2021-0004>
11. Ciba, E., Dymarski, P., & Grygorowicz, M. (2022). Heave Plates with Holes for Floating Offshore Wind Turbines. Polish Maritime Research, 29, 26-33. <https://doi.org/10.2478/pomr-2022-0003>
12. Matuszewski, L. (2019). New Designs of Centrifugal Magnetic Fluid Seals for Rotating Shafts in Marine Technology. Polish Maritime Research, 26(2). <https://doi.org/10.2478/pomr-2019-0023>
13. Sliwiński, P. (2020). The Influence of Water and Mineral Oil on Mechanical Losses in a Hydraulic Motor for Offshore and Marine Applications. Polish Maritime Research, 27(2). <https://doi.org/10.2478/pomr-2020-0034>

14. E. Hristoforoua, A. Ktenab, „Magnetostriction and magnetostrictive materials for sensing applications”, *Journal of Magnetism and Magnetic Materials* 316 (2007) 372–378
15. “Linear displacement transducer isn’t limited by stroke”. *Power&Motion*, March 6, 2013, <https://www.powermotiontech.com/sensors-software/controls-instrumentation/article/21883571/linear-displacement-transducer-isnt-limited-by-stroke>
16. B. Zhang, B. Wang, Y. Li, W. Huang, Y. Li, “Magnetostrictive Tactile Sensor Array for Object Recognition”, *IEEE Transactions on Magnetics*, vol. 55, no. 7, July 2019
17. J.J. Beato-López, I. Royo-Silvestre, C. Gómez-Polo, “Micrometric non-contact position magnetoimpedance sensor”, *Journal of Magnetism and Magnetic Materials* 465 (2018) 489–494
18. Y.W. Park, H.W. Song, E.J. Yoo and J.W. Kim, “Concept and Numerical Verification of Magnetostrictive Control Rod Position Identification,” *The Korean Society of Mechanical Engineers Autumn Conference*, pp. 3672-3673, 2013.
19. E.J. Yoo, Y.W. Park, and M.D. Noh, “Characterization of Detection Signal for Sensing Coil Type in Magnetostrictive Control Rod Position Indicator,” *Proc. of KSPE Spring Conference*, pp. 219-219, 2016.
20. A. Dorneich, M. Fritton, “Microwave Position Sensor for Hydraulic Drives”, *30th Eurosensors Conference, EUROSENSORS 2016, Procedia Engineering* 168 (2016), pp. 1257–1260
21. A.S. Rana, R.S. Sayles, “An experimental study on the friction behaviour of aircraft hydraulic actuator elastomeric reciprocating seal”, *Tribol. Interface Eng. Ser.* 2005;48:507–515. doi: 10.1016/S0167-8922(05)80052-5.

CONTACT WITH THE AUTHORS

Paweł Dymarski

e-mail: pawdymar@pg.edu.pl

Gdansk University of Technology,
Institute of Naval Architecture
and Ocean Engineering, Gdansk
POLAND

Czesław Dymarski

Gdansk University of Technology,
Institute of Naval Architecture
and Ocean Engineering, Gdansk,
POLAND

INFLUENCE OF MATERIAL THICKNESS ON THE DUCTILE FRACTURE OF STEEL PLATES FOR SHIPBUILDING

Jakub Kowalski *

Janusz Kozak 

Gdansk University of Technology, Poland

* Corresponding author: jakkowal1@pg.edu.pl(J. Kowalski)

ABSTRACT

In the shipbuilding industry, the risk of brittle fractures is relatively high because some units operate in arctic or subarctic zones and use high thickness (up to 100 mm) steel plates in their structures. This risk is limited by employing certified materials with a specific impact strength, determined using the Charpy method (for a given design temperature) and by exercising control over the welding processes (technology qualification, production supervision, and non-destructive tests). However, for offshore constructions, such requirements may prove insufficient. For this reason, regulations employed in constructing offshore structures require conducting crack tip opening displacement (CTOD) tests for steel and welded joints with thicknesses exceeding 40 mm for high tensile strength steel and 50 mm for other steel types. Since classification codes do not accept the results of CTOD tests conducted on specimens of sub-sized dimensions, the problem of theoretically modelling the steel construction destruction process is of key importance, as laboratory tests for notched elements of considerable thickness (100 mm and higher) are costly and problems stemming from high loads and a wide range of recorded parameters are not uncommon. The aim of this research is to find a relationship between material thickness and CTOD value, by establishing and verifying a numerical model that allows recalculating a result obtained on a sub-size specimen to a full-size specimen for a ductile fracture mode. This work presents results and conclusions from numerical modelling and compares them with laboratory test results of the elastic-plastic properties of high thickness steel, typically used in offshore applications.

Keywords: ductility, toughness, plasticity, CTOD

INTRODUCTION

Ductility is used as a measure of a material's resistance to cracking. In the shipbuilding industry, the Charpy method is usually used. This test is a strictly quantitative method and is performed on small, standardised specimens, usually with the dimensions 10 x 10 x 55 mm. As a measure of a material's toughness, the energy absorbed when breaking a specimen, by striking it with a pendulum hammer into a notched specimen,

is determined. The test result is satisfactory if the average absorbed energy is greater than the reference value for a given type of steel at a particular temperature. Although it has some advantages, like price and time required to perform the test, the Charpy method presents several disadvantages: the specimen has a standardised size which is independent of thickness, the test results only deliver a number without any information about the failure mode, the notch in the test specimen is cut mechanically and its geometry depends on the shape of the

cutter used (which changes with time and produces different notch shapes). For this reason, alternative methods were investigated to assess material ductility.

In the early 1920s a new branch of science came into being: fracture mechanics. Depending on fracture type, three main parameters were introduced (Fig. 1):

- Stress intensity factor (SIF), denoted as K , was proposed by Griffith [1] for the brittle fracture mode.
- Crack Tip Opening Displacement (CTOD), was proposed by Wells [2] for the mixed (ductile and brittle) fracture mode.
- J-integral, proposed by Rice [3], for the ductile fracture mode. J-integral can also be used for elastic analysis of the stress intensity factor.

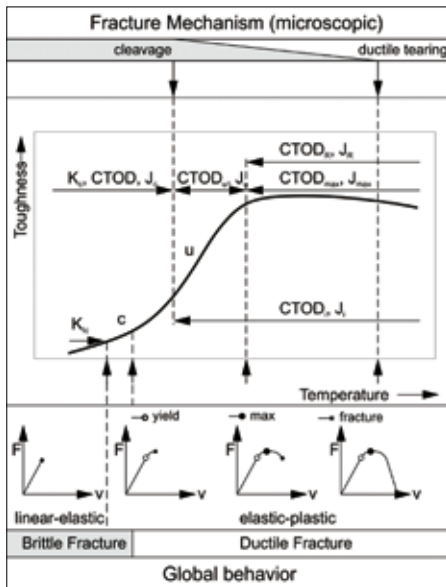


Fig. 1. Fracture mechanics factors and their applicability to fracture process descriptions [4]

This paper focused on CTOD, due to the fact that this factor is required by classification societies standards [5-8]. The fundamentals of the CTOD test are based on breaking a specimen with a full thickness of the material, subject to verification. The specimen has a preliminary, mechanically cut notch, which then develops (through fatigue processes) to such a size that the effects of mechanical treatment stay far from the front of the fatigue notch and the shape of the notch front is repeatable for each specimen. To check this repeatability, the results of the test are verified after the specimen is fully fractured and only accepted if the proportion of the fatigue fracture front is properly verified. There are a few types of specimens defined in the standards [9-11], which differ in terms of shape, type of loading and, different stress states in front of the crack tip. The most commonly used are: compact specimens (straight-notch and stepped-notch), which are in tension and bending at the same time, bending specimens with a single notch SNE(B), and tension specimens with a single edge notch SNE(T). The dimensions of the specimens depend on the thickness of the material to be tested and the specimen type. The CTOD values obtained for different specimen types vary. Results obtained for SNE(B) specimens are more conservative compared with

SEN(T) specimens [12]. Current rules for shipbuilding [5-8] require CTOD tests on SEN(B) specimens with a recommended section geometry $B \times W$ ($W=2B$), where B is the thickness of the material, see Fig. 2. The principle of the CTOD test for a ductile material and bent specimen is shown in Fig. 2.

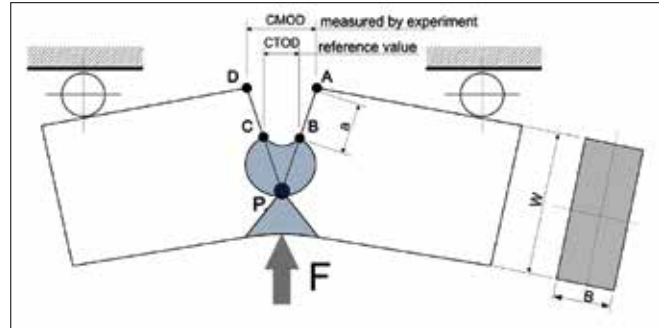


Fig. 2. Principle of the CTOD test

CTOD is a geometric value that can be defined as follows.

$$\delta_T = \frac{r_y (W - a) AD}{r_y (W - a) + a} = \frac{r_y (W - a) \delta_M}{r_y (W - a) + a} \quad (1)$$

where r_y is a coefficient:

$$r_y = \frac{CBa}{(W - a)(AD - CB)} \quad (2)$$

Coefficient r_y usually takes values in the range 0.38–0.46 [13]. The effect of stable tearing (crack extension), which is characteristic of ductile fractures, is not included in Eq. (1) for CTOD calculations.

The equations for CTOD evaluation, which were introduced into the standards [9–11], are still being improved. The equations in [9], for the SNE(B) specimen type (see Eq. (3)) are based on the geometry of the specimen, relative crack length, plastic component of CMOD (see Fig. 2) and the maximum value of force. A different approach is presented in ASTM [10] and ISO [11], where an energy-based concept is the basis for CTOD evaluation. Recent research by Kawabata et al. [14] and Khor [15] resulted in modification of the CTOD formulas in the ISO 12135 standard, 2021 edition.

The requirement that specimen thickness B should be equal to (or almost equal, due to technological issues connected with specimen preparation) the tested material's thickness, in the case of thick materials, causes problems. As has been mentioned before, specimen dimensions depend on the material's thickness. For example, for 100 mm thick material (specimen type SNE(B)), the recommended specimen geometry ($B \times 2B$) dimensions will be equal to: length 920 mm x breadth 100 mm x width 200 mm, and the mass of the specimen will be approximately 145 kg. Such a specimen requires strength machines with high load capacities and it is very difficult to operate this during the testing procedure. This is the reason why the investigation of the influence of specimen size on CTOD test results has been performed. Some authors have pointed out that the toughness value of materials is influenced by factors like specimen size and thickness, loading rate and crack depth. These factors influence both the toughness value and the transition temperature, see Fig. 3 [16].

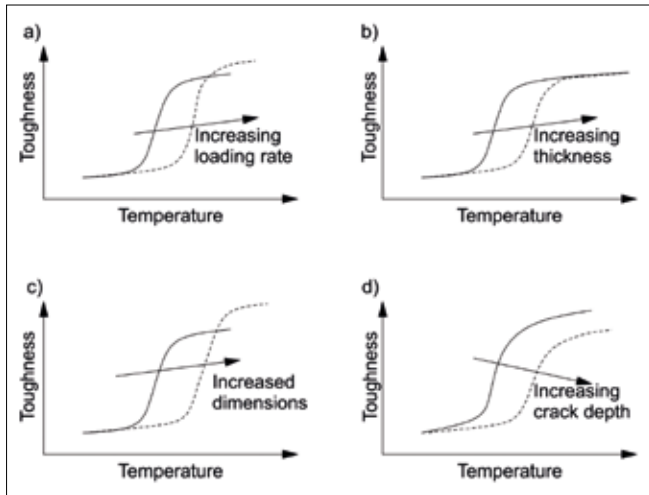


Fig. 3. Effect of loading rate (a), thickness (b), specimen dimension (c) and crack depth (d) on ductile-to-brittle transition curves [16]

Gough [17] proposed that CTOD and J values increase with specimen size (based on laboratory test results). Palombo, Sandon and Marco [18] showed that CTOD increases with specimen size but decreases with temperature (Fig. 3c). Kowalski and Kozak [19] investigated and described the influence of crack depth, as a linear function (Fig. 3d), on CTOD value. Kowalski [20] showed differences in the influence of specimen thickness and notch depth on CTOD value.

These examples show that the problem has been discussed, mainly qualitatively. In this paper, we attempt to quantify the influence of specimen size on the CTOD value for steel, based on numerical calculations, which model material behaviour in the ductile failure process, and verified by natural scale laboratory test results.

RESEARCH METHODOLOGY

The idea of this research was to study the influence of material thickness on toughness (see Fig. 2c). The test was carried out according to the standards for the CTOD test [9, 11], based on three-point bending specimens SNE(B). The test was planned assuming a changing specimen width, with constant geometrical proportions and keeping a_0/W (where a_0 is an initial crack length) constant and equal to 0.60. Three specimens were tested for each thickness. The geometry and masses of the tested specimens are presented in Fig. 4. Specimens were denoted as W60, W80, W100, and W120, where the number is a height of the specimen in mm.

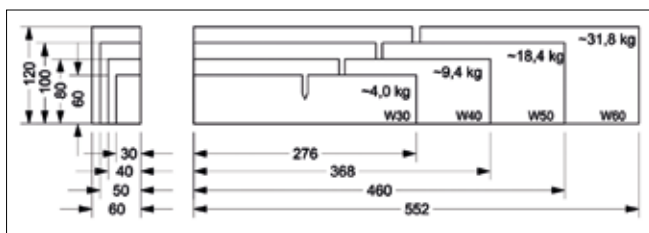


Fig.4. Dimension and mass of the specimen

All specimens (including specimens for tensile testing) were cut from one plate made of NV E36 DNV PT.2 CH2 SEC.1:2016 high tensile steel for shipbuilding, with the mechanical properties presented in Table 1 and the chemical composition given in Table 2.

Tab. 1. Material properties of tested steel

Tensile test result				
Yield point, R_e [N/mm ²]	Ultimate strength, R_m [N/mm ²]	Elongation, A_{50} [%]	Elastic modulus, E [GPa]	
398	537	29	215	
Impact test result, size 10 x 10 x 55, type KV, Longitudinal [J]				
	1	2	3	4
temp +20°C	146	133	121	133
temp -40°C	210	202	209	207

Tab. 2. Chemical composite of tested steel

C	Si	Mn	P	S	Al	Nb
0.161	0.46	1.50	0.012	0.002	0.031	0.042
V	Ti	Cu	Cr	Ni	Mo	Ca
0.052	0.005	0.016	0.50	0.040	0.006	0.002

Mechanical properties were determined by in-house testing on an upgraded ZD-40 Pu machine (force measurement accuracy $\pm 1\%$ of the measured value). Elongation was measured using an Epsilon 2543-050M-025M-ST extensometer with a 50 mm measuring base. The extensometer allowed measurement up to the point of specimen rupture with an accuracy of ± 0.001 mm. Specimens with a circular cross-section, 10 ± 0.1 mm in diameter, were used for the test. The specimen was tested under tensile stress at a strain rate $\dot{\epsilon} = 0.0044$ 1/s. The tensile curve is presented in Fig. 5.

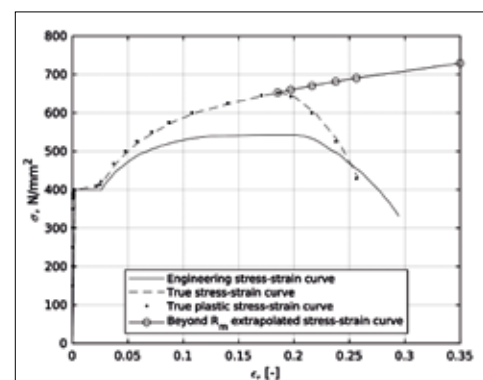


Fig. 5. Tensile testing results expressed in the form of engineering and true stresses

NUMERICAL ANALYSIS

The aim of the modelling was to find the relationship between specimen thickness and CTOD value. Due to the double symmetry of the specimens, a quarter of the volume and

corresponding supports were modelled. The simplification of assuming no friction between the supports and the specimen was employed in the process. True stress – strain plastic curve, extrapolated beyond R_m was used. The material model containing ductile damage mechanisms, based on strain and stress triaxiality, was also used. A time-domain simulation was conducted using an explicit method. A standardised, physical CTOD test was performed in the displacement control mode. The same situation took place for numerical simulation.

The problem was modelled with Abaqus CAE software. The mesh size in critical regions was 0.5 mm for all models, which was a good compromise between result quality and computation time. In the neighbourhood of the crack, a C3D8R element was applied. For the biggest specimen, changing the mesh size in the critical region to 0.25 mm made the recalculated CTOD result different by -3.6%, in comparison to a mesh size of 0.5 mm. Force vs. CMOD (Crack Mouth Opening Displacement) plots for different element sizes are presented in Fig 6. Significant results of mesh convergence analysis are presented in Table 3.

Tab. 3. Summary of element size study

Element size in crack tip region, [mm]	F_m , [kN]	V_p , [mm]	δ_c , [mm]	F_m error [%]	V_p error [%]	δ_c error [%]	Normalised computation time, [-]
0.25	200.4	15.81	3.45	1.3	-4.0	-3.6	22.15
0.50	197.8	16.47	3.58	0.0	0.0	0.0	1.0
0.60	211.5	17.63	3.84	6.9	7.0	7.3	0.68
1.00	223.1	17.97	3.93	12.8	9.1	9.6	0.09

Where:

- F_m – Maximum force for a test which exhibits a maximum force plateau, N;
- V_p – plastic component of CMOD, mm;
- δ_c – CTOD, calculated in accordance with Eq. (3), mm;
- F_m error – F_m error in relation to the 0.5 mm element size mesh, [%].

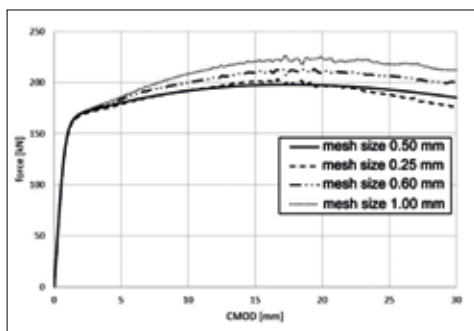


Fig. 6. Force vs. CMOD plots for various element sizes

Detailed information on modelling the material fracture description, the calibration of the model and its verification

are presented in [19] and [21]. Fig. 7 presents the typical output from simulations with stress distribution along the crack.

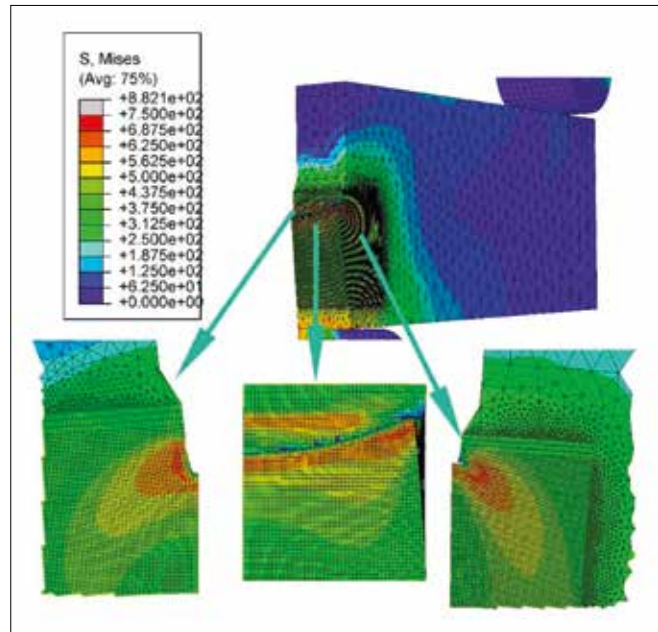


Fig. 7 Model of 3-point bending specimen with subsequent destruction

LABORATORY TESTS

The tests were performed on a dedicated stand with measurements of load, displacement and crack opening displacement (COD). Fig. 8 presents the sizes of the tested specimens (from W30 to W60). Force was measured by a 250 kN load cell with 1% accuracy. For COD measurement, an Epsilon 3541-010M-120M-LT COD gauge was used. The resolution of this gauge is 0.001 mm and the permissible error cannot exceed 0.5%. Before the CTOD test started, fatigue pre-cracks were generated into the specimen. The maximum pre-crack force for a given specimen size was calculated in accordance with (BSI 1991) and (ISO 2016). Force values calculated in accordance with BS 7448 (BSI 1991) were lower than those in accordance with ISO 12135 (ISO 2016) and so they were chosen. Calculated R (fatigue force ratio) was equal to 0.1 for each case.

The second stage (after pre-cracking) of testing CTOD was the process of breaking. Fig. 9 shows a W100 specimen on the test stand during the test.

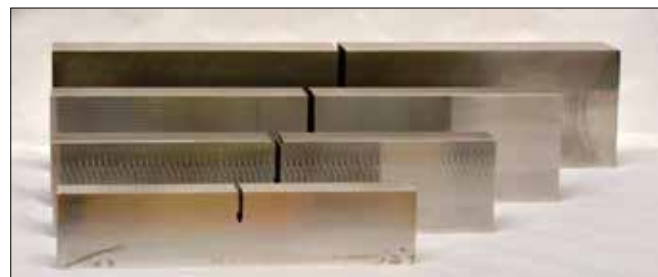


Fig. 8 Set of specimens representing the full spectrum of thicknesses applied



Fig. 9. W100 Specimen during laboratory testing—breaking phase

After the process of breaking, as the third stage of the test, the specimen was separated into two parts to open the cracking plane for real a_0 value measurement. We used a standard procedure and a detailed description is available in [9-11]. The final stage of quality control for the results was to check if the assumed numerical calculations from the ductile damage mechanism were appropriate for this case. For this purpose, a scanning electron microscope (SEM) investigation was performed and the results are shown in Fig. 10.

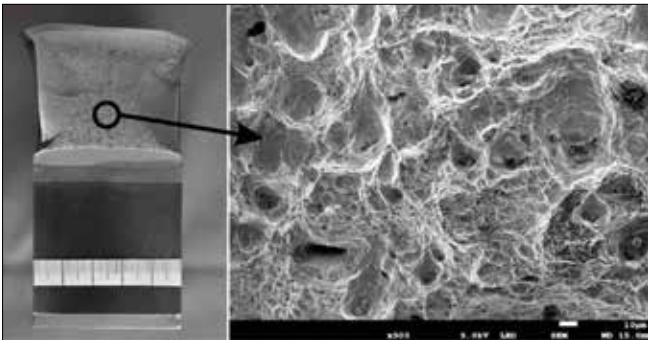


Fig. 10. SEM investigation results—ductile failure mode. Shear lips were formed during the final stage of specimen breaking—after data acquisition stopped

One can see that the failure mechanism was ductile, as was expected. Voids are clearly seen. The applied numerical failure model was phenomenologically correct.

RESULTS AND DISCUSSION

Results from both the numerical simulation and laboratory testing were processed in exactly the same way, using the CMOD vs. force records and procedure described in [9] and [11]. The following formula was used as a method for CTOD calculation for three-point bend specimens:

$$\delta_T = \left[\frac{FS}{BW^{1.5}} f\left(\frac{a_0}{W}\right) \right]^2 \frac{(1-\nu^2)}{2R_{p02}E} + \frac{0.4(W-a_0)V_p}{0.4W+0.6a_0+z} \quad (3)$$

where F is the force, N; $f(a_0/W)$ is the stress intensity factor coefficient, [-]; σ_{RP02} is the proof strength at 0.2% plastic elongation, N/mm²; ν is the Poisson ratio for steel, $\nu = 0.3$; [-], V_p is as defined before, mm; and z is the initial distance of the

notch opening gauge measurement position from the notched edge of the specimen, $z = 0$, in mm.

A comparison of the test results with FEM calculation results, for a 100 mm wide specimen, is presented in Fig. 11.

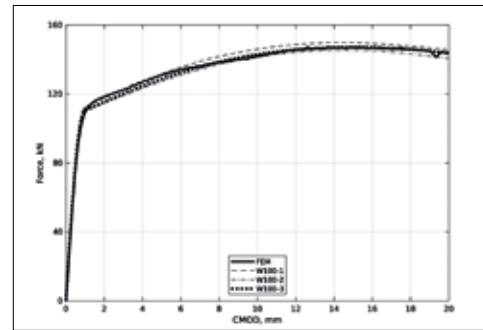


Fig. 11. Comparison of test results (W-100-1,2,3) with FEM calculation results for a specimen width of 100 mm

The results of the numerical simulation and laboratory tests are presented in Table 4 and Table 5. Both sets of results are in good agreement. The difference between FEM and average laboratory values for W60, W80, W100 and W120 are 0.0%, 1.2%, 0.7% and 4.5%, respectively. For the first three cases, the results of FE calculations and laboratory tests can be treated as being equal. The last one is noticeable because a lower value was obtained in the FE calculation; thus, the results are conservative and can be used safely.

Tab. 4. FEM results summary

Specimen	B, mm	W, mm	a_0/W , [-]	δ , mm
FEM B30	30	60	0.60	2.01
FEM B40	40	80	0.60	2.55
FEM B50	50	100	0.60	3.12
FEM B60	60	120	0.60	3.58

Table 5. Laboratory test results summary

Specimen	B, mm	W, mm	a_0/W , [-]	δ , mm	δ_{av} , mm
W60	29.98	60.17	0.63	1.97	2.01
	30.02	60.15	0.60	2.04	
W80	39.77	80.05	0.60	2.63	2.58
	40.02	80.17	0.60	2.52	
	40.10	80.12	0.60	2.59	
W100	59.26	100.37	0.59	3.17	3.10
	59.35	100.32	0.59	3.08	
	59.65	100.23	0.60	3.04	
W120	59.90	120.17	0.60	3.77	3.75
	60.10	119.73	0.60	3.74	
	60.10	120.08	0.60	3.74	

The test results and FEM calculations for the whole of the tested series are presented in Fig. 12.

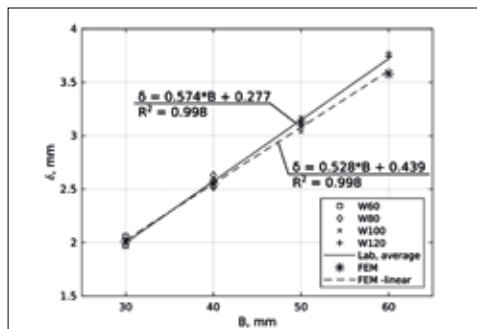


Fig. 12 Test results and FEM calculations for the whole program of tests

The results presented in Fig. 12 are almost linear in character, with a significant influence of specimen thickness on critical crack opening displacement. Linear approximations for laboratory test results, as well as FEM analysis, are presented in Fig. 12. Such equations can be used for assessing CTOD for other material thicknesses.

CONCLUSIONS

- Numerical simulations, verified by laboratory testing, prove the influence of specimen size on CTOD value. The model of plastic flow presented in this paper gave acceptably accurate results. However, future research should take into account the latest methods to define stress flow after necking.
- The results obtained by numerical modelling present an almost linear relationship between the size of the specimen and CTOD value.
- Laboratory verification tests confirmed the truth of this relationship and good numerical and experimental result compliance was obtained. Thus, the presented and properly calibrated numerical model can be used for evaluating scale effects in CTOD tests.
- The research was conducted at a constant room temperature, which means that ductile failure was assumed, for a particular steel grade with a constant a_0/W ratio. Thus, the presented procedure is limited to certain test conditions.
- The next step for improving the numerical model is to verify the crack extension process during the numerical simulation. It should allow reliable evaluation of the influence of specimen size on CTOD. The problem, which is still open, is to quantify the size effect (thickness of material) on the Ductile-To-Brittle Transition Curve.

ACKNOWLEDGEMENTS

The computing tasks, utilising Abaqus software, presented in this paper were carried out within a research grant at the Centre of Informatics Tricity Academic Supercomputer & Network.

REFERENCES

1. A. Griffith, 'The phenomena of rupture and flow in solids', *Philosophical Transactions*, vol. 221, pp. 163–198, 1920.
2. A. Wells, 'Application of fracture mechanics at and beyond general yield, Report No. M13/63', *British Welding Journal*, pp. 563–590, 1963.
3. J. R. Rice, 'A Path Independent Integral and the Approximate Analysis of Strain Concentration by Notches and Cracks', *J Appl Mech*, vol. 35, no. 2, pp. 379–386, Jun. 1968, doi: 10.1115/1.3601206.
4. W. Dahl and P. Langenberg, 'Fracture Toughness of Metallic Materials', in *Encyclopaedia of Materials: Science and Technology (Second Edition)*, 2001, pp. 3336–3340.
5. DNV, *RULES FOR CLASSIFICATION, Ships, Part 2 Materials and welding, Chapter 1 General requirements for materials and fabrication*. DNV AS, 2022.
6. Standards Norway, *NORSOK STANDARD M-101, Structural steel fabrication*, 5th ed. Lysaker, 2011.
7. DNV, *DNV OFFSHORE STANDARDS, DNV-OS-B101, Metallic materials*. DNV AV, 2021. [Online]. Available: <https://rules.dnv.com/docs/pdf/DNV/OS/2021-07/DNV-OS-B101.pdf>
8. Polski Rejestr Statków, *Rules For Classification and Construction on sea-going ships, Part IX, Materials and Welding*. Gdańsk: PRS, 2021. [Online]. Available: https://www.prs.pl/uploads/mor_p9.pdf
9. BSI, *BS 7448-1:1991 - Fracture mechanics toughness tests. Method for determination of K_{Ic}, critical CTOD and critical J values of metallic materials*. London: BSI, 1991.
10. ASTM International, 'ASTM E1820 - 18a Standard Test Method for Measurement of Fracture Toughness', 2018.
11. ISO, *ISO 12135:2016 Metallic materials — Unified method of test for the determination of quasistatic fracture toughness*. Geneva, 2016.
12. P. L. Moore and A. M. Crintea, 'Single edge notched tension (SENT) testing at low temperatures', *Proceedings of the Biennial International Pipeline Conference, IPC*, vol. 3, 2016, doi: 10.1115/IPC201664021.
13. A. Neimitz, *Mechanika Pękania*. Warszawa: Wydawnictwo Naukowe PWN, 1998.
14. T. Kawabata, T. Tagawa, T. Sakimoto, Y. Kayamori, M. Ohata, Y. Yamashita, E. Tamura, H. Yoshinari, S. Aihara, F. Minami, H. Mimura, Y. Hagihara, 'Proposal for a new CTOD

calculation formula', *Eng Fract Mech*, vol. 159, pp. 16–34, 2016, doi: 10.1016/j.engfracmech.2016.03.019.

15. W. L. Khor, 'A CTOD equation based on the rigid rotational factor with the consideration of crack tip blunting due to strain hardening for SEN(B)', *Fatigue Fract Eng Mater Struct*, vol. 42, no. 7, pp. 1622–1630, Jul. 2019, doi: 10.1111/ffe.13005.
16. F. C. Campbell, 'Fatigue and Fracture: Understanding the Basics'. 2012.
17. J. Morrison and J. P. Gough, 'Specimen size and orientation effects on the toughness of steel weldments', *Journal of Engineering Materials and Technology, Transactions of the ASME*, vol. 111, no. 3, pp. 270–277, 1989, doi: 10.1115/1.3226466.
18. M. Palombo, S. Sandon, and M. de Marco, 'An Evaluation of Size Effect in CTOD-SENB Fracture Toughness Tests', *Procedia Eng*, vol. 109, pp. 55–64, 2015, doi: 10.1016/j.proeng.2015.06.207.
19. J. Kowalski and J. Kozak, 'The Effect of Notch Depth on CTOD Values in Fracture Tests of Structural Steel Elements', *Polish Maritime Research*, vol. 25, no. 2, 2018, doi: 10.2478/pomr-2018-0058.
20. J. Kowalski, 'Experimental and Numerical Investigation on Specimen Geometry Effect on the CTOD Value for VL-E36 Shipbuilding Steel', *Polish Maritime Research*, vol. 28, no. 3, 2021, doi: 10.2478/pomr-2021-0038.
21. J. Kowalski and J. Kozak, 'Numerical Model of Plastic Destruction of Thick Steel Structural Elements', *Polish Maritime Research*, vol. 25, no. 2, pp. 78–84, 2018, doi: 10.2478/pomr-2018-0057.

CONTACT WITH THE AUTHORS

Jakub Kowalski

e-mail: jakkowal1@pg.edu.pl

Gdańsk University of Technology
Narutowicza 11/12
80-233 Gdańsk
POLAND

Janusz Kozak

Gdańsk University of Technology
Institute of Naval Architecture and Ocean Engineering
Narutowicza 11/12
80-233 Gdańsk
POLAND

APPLICATION OF THE CORROSION TESTER IN CORROSION TESTS USING THE ACOUSTIC EMISSION METHOD

Krzysztof Emilianowicz *

Milena Supernak 

Agnieszka Ossowska 

Gdansk University of Technology, Poland

* Corresponding author: krzysztof.emilianowicz@pg.edu.pl (K. Emilianowicz)

ABSTRACT

The article presents an innovative method of corrosion tests using the acoustic emission method and the corrosion tester. The problem of corrosion occurring in ballast tanks and tanks carrying petroleum products is discussed. The acoustic method is presented which, due to the use of a unique corrosion tester, is used to monitor the course of corrosion processes in steel. The principle of operation of the corrosion tester, its construction and its use in Non Destructive Testing (NDT) are described in detail. Corrosion test results, obtained with the use of a corrosion tester, are presented. An analysis and a short discussion of the obtained results are given. The results of both the acoustic and metallographic tests prove the possibility of detecting material damage occurring during the operation of the corrosion tester, allowing determination of the course and type of corrosion damage.

Keywords: corrosion, hull steels, acoustic emission, corrosion tester.

INTRODUCTION

CORROSION

Corrosion is the phenomenon of spontaneous destruction of a material as a result of its interaction with the environment. This is caused by process, such as a chemical transformation of the material or deterioration of its physical properties. The surrounding environment is primarily the atmosphere and the solution with which the material is in contact. Until recently, corrosion was only associated with the oxidation of metals and their alloys, which were not resistant to oxidising agents. We are currently observing a growing interest in the corrosion of concrete polymers, semiconductors, vitreous materials, etc.

In addition to the usual corrosive environments (water, soil, humid atmosphere or industrial), microbiological systems, non-aqueous environments (petrochemistry), molten salts and metals (nuclear energy) are of increasing interest. It follows that corrosion means all phenomena related to the environment, both natural and artificial. Corrosion failure is one of the main causes of material loss. Economic losses due to metal corrosion are estimated at nearly 3-4% [1] of Gross National Income (depending on the country), with the largest proportion being iron alloys. It is estimated that 30% of the annually produced alloys of this metal are used only for the replacement of corroded elements. This should include costs related to downtime due to breakdowns or temporary protection measures. The task of corrosion engineering is to minimise and slow down this process.

Corrosion is most often classified [2-14] according to the material and environment in which it works, e.g. corrosion in a humid environment, corrosion in molten salts, gas corrosion, corrosion in non-aqueous liquids, corrosion in molten metals. Due to the type and structure of the materials, we can distinguish between: corrosion of active metals and their alloys, corrosion of passivating metals, corrosion of precious metals and their alloys, corrosion of organic polymers, corrosion of silicate materials, corrosion of modern materials and corrosion of concrete.

- There are three basic types of corrosion:
- Uniform corrosion,
- Pitting corrosion,
- Electrochemical corrosion.

The corrosion mechanism of various materials depends on the type of environment and the type of electrical conductivity at the metal-environment phase border. Corrosion is electrochemical for materials with high conductivity, while for those with low or no conductivity, corrosion occurs as a chemical or physicochemical process. Electrically conductive materials in various environments undergo electrochemical corrosion due to the formation of corrosive micro-cells. The mechanism of generating potentials in a wet environment is analogous to that in galvanic cells [9, 11].

ACOUSTIC EMISSION METHOD

One of the non-destructive testing methods [15-19] is acoustic emission, which determines the momentary generation of elastic waves caused by the process or the release of energy in a given material. Corrosion occurs in both cases. The acoustic emission method is a passive non-destructive testing method. The advantages of this method are:

- the possibility of inspecting individual elements of the structure,
- the possibility of examining and monitoring the entire large facility,
- the possibility of conducting real-time and continuous monitoring,
- the possibility of locating the sources of acoustic emission signals generated by damage or defects in the material, and
- the possibility of observing the processes at the place of their formation.

The processes accompanied by acoustic emission include changes at both the macro and micro level. Examples include:

- corrosion,
- plastic deformation,
- leaks in tanks or pipelines,
- delamination of coatings, and
- chemical reactions.

Acoustic emissions (AE) are sonic signals accompanying a change in the structure of the material during a sudden release of stored internal energy or by the process of formation of temporary elastic waves [5-13,15-18]. As the wave travels through the material, in the event of a defect, the wave is dispersed and reflected. This phenomenon is called an event and an acoustic wave is emitted, which is created as a result

of the released internal energy. A wave formed in this way (Fig. 1(a) and Fig. 1(b)) is registered by the acoustic sensor. In the case of pitting corrosion monitoring, events arise from cracks in the passive layer that form on the surface of the corrosive metal. The events that become the source of wave emissions may be low-energy or high-energy events and determine the progress of pitting formation.

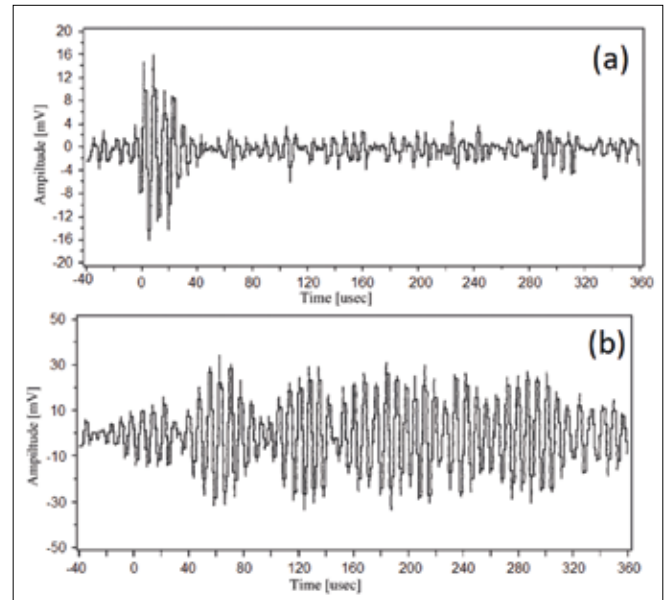


Fig. 1. Run of (a) short wave, (b) reflected wave [26].

The acoustic emission signal is characterised by such parameters as: energy, amplitude, number of crossings of the discrimination threshold, rise time and duration of the acoustic signal (Fig. 2).

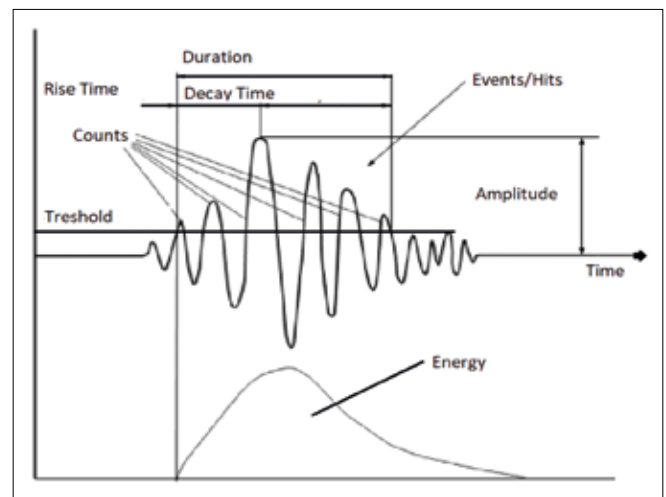


Fig. 2. A single acoustic emission signal [17].

The diagram of the acoustic emission test is shown in Fig. 3. Because of the AE system software, it is possible to visualise the registered measurement data in real time. When several sensors are used, with appropriate software algorithms, it is possible to locate the energy source of the acoustic emission

on the basis of the difference in the time the wave reaches individual sensors.

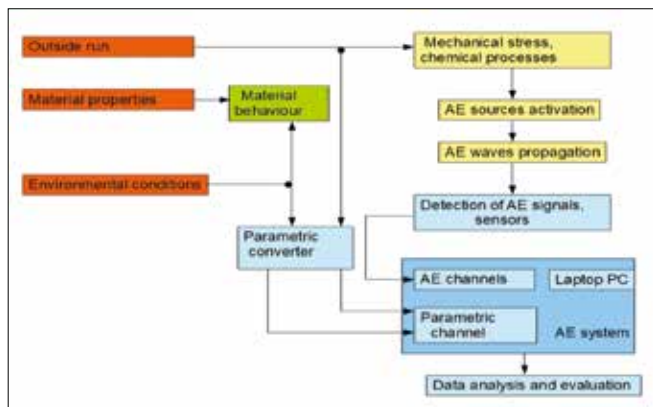


Fig. 3. Diagram showing the acoustic emission system in operation.

Currently, this method is globally recognised [20-23] as being appropriate for the periodic testing of large devices, e.g. in the petrochemical or shipbuilding industry. The above-mentioned method complements other methods of non-destructive testing (NDT) very well. This allows for a more accurate assessment and verification of the detected damage.

MATERIALS AND METHODS

MATERIAL

Hull steel of category A was used in the tests, according to the classification in PRS (Polish Ship Registry) [24], from which the elements of both the measuring tank and the corrosion tester were made. Hull steels are normal (NSS) and high strength (HSS) steels, which are used in the production of structural elements used in the construction of hull elements of ships. There are several varieties. According to the classification of the Polish Register of Shipping (PRS), normal strength steels are divided into categories A, B, D, and E, while the abbreviations AH, BH, HE and HF 32, 36 and 40 describe constantly increasing strength, respectively (e.g. AH32). Hull steel of category A is one of the most commonly used steels in shipbuilding. Because of its excellent mechanical properties, chemical composition and welding properties, it can be used in the construction of ship sections, including the construction of tanks (e.g. ballast, cofferdam, etc.).

Normal strength hull steels (NSS) are characterised by a yield point of 235 MPa, while its maximum tensile limit varies from 400 to 520 MPa, depending on the category. An important criterion when selecting the operation of the hull steel, especially at low temperatures, is the fracture toughness test. For normal strength category A hull steel, the impact strength at room temperature (+20 degrees Celsius) should not be less than 27 J or 20 J (depending on the rolling direction of the test sample). For category B, the work of breaking a sample with a thickness of up to 50 mm should not be less than 27 J (20 J at a temperature of 0°C) and for steel D and E, it should be

the same, at temperatures of -20°C and -40°C, respectively. The mechanical properties may also be influenced by the additional thermo-mechanical treatment of the hull steel, the so-called 'delivery condition'. It is estimated that about 30% of all hull steels in the world are put into service after machining, most often in the controlled rolling (CR) condition and the thermo-plasticised (TMCP) condition.

The chemical composition of hull steels is very important for both their mechanical properties, such as tensile strength, and weldability. These factors may change, depending on the type and quantity of the alloying elements present in the composition of this steel. The main alloying elements are Manganese (Mn) and silicon (Si), the addition of which, not only increases the mechanical properties but also allows the removal of harmful elements, e.g. sulphur (Mn in an amount above 0.8%). The addition of 0.4% silicon assists deoxidation of the steel and also increases its plasticity and elasticity due to the strengthening of ferrite in the structure. Other alloying elements are: vanadium, aluminium, niobium, titanium, copper, molybdenum, chromium and nickel. The latter has a particularly significant impact on not only the mechanical properties, but also some physical properties. The addition of molybdenum, together with chromium and manganese, for example, increases the hardenability, yield point and tensile strength of the steel. Nickel, on the other hand, significantly improves the brittle transition temperature, shifting it towards lower values. The undesirable elements are mainly sulphur and phosphorus, the amount of which should not exceed 0.0035% in the alloy. Oxygen is also an undesirable element as it can have a negative effect on the plasticity or strength of the steel during the setting process. Therefore, the main deoxidisers are silicon and aluminium.

RESEARCH PROCESS

The research was divided into two stages. The purpose of the first was to collect the acoustic signal from the corrosion tester attached to one of the walls of the measuring tank made of hull steel of category A. The second stage consisted of carrying out metallographic inspections (macroscopic and microscopic examinations using an optical microscope, by KEYENS) of the corrosion damage on the surface of the tested corrosion tester, and estimating the size of this damage.

After assembling the measuring set and flooding the corrosion tester with a corrosive mixture (the chemical composition is given in Table 1), the purpose of which is to catalyse and initiate the corrosion processes taking place in the reaction tank of the corrosion tester, the corrosion tester was mounted on the inner wall of the measuring tank, as shown in Fig. 4. Then, with the use of magnetic grippers, VS-75 (which frequency range from 30 to 120 kHz while peak is 75 kHz) type measuring sensors with EP 34 preamplifiers and VS-150 RIC (operating in frequency range from 100 to 450 kHz while peak is 150 kHz) sensors were attached to the walls of the measuring tank. The VS-75 and VS 150 RIC sensors were connected (using cables) to the AMSY-5 measuring system (produced by Vallen Systeme GmbH company) used for acoustic analysis. After

completion of the test, the corrosion tester was dismantled and thoroughly dried. Any loose corrosion products deposited during the test were removed from the surface of the stopper of the reaction cylinder. The prepared plug was then subjected to metallographic examination using a KEYENS microscope.

Tab. 1. The corrosion solution composition used during the tests.

Position	Mixture component	Mass concentration
1	H ₂ SO ₄	10
2	HNO ₃	10
3	NaCl	3

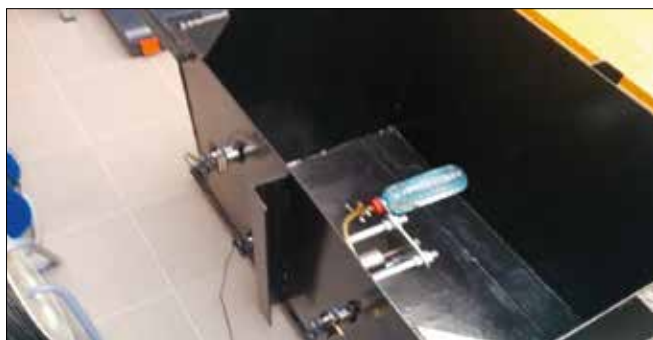


Fig. 4. Corrosion test tank with the KE-2 corrosion tester attached and the VS75-V and VS150 RIC acoustic sensors installed.

EQUIPMENT

For corrosion tests using the acoustic emission method, AMSY-5 measuring equipment from Vallen GmBH was used, together with a set of acoustic sensors (Fig. 5), the KE-2 (given name for corrosion tester according to patent no. P.431331) corrosion tester (shown in Fig. 5), a corrosion test tank made of hull steel of category A, and corrosive solution (Table 1). All elements of the measurement set are summarised in Table 2.

CORROSION TESTER KE-2

This device allows simulation of the corrosion processes taking place at the test site. As a result, the acoustic emission monitoring system is able to separate the tester from the background noise, as well as locating the place of its attachment with a high probability. This type of corrosion tester should be constructed based on certain criteria:

- it must be made of a material that will be as close as possible to that from the test site,
- it must have a significantly active contact surface with the tested surface, so that the corrosion signal coming from the tester is captured by sensors located on this surface, which will significantly improve the location and allow for better 'audibility' of the signal against noise coming from outside the test area,
- the size of the tester must be sufficiently appropriate to be delivered and placed in the place of the test,
- the composition of the corrosive solution must be selected in such a way as to reflect the corrosion process in real conditions as faithfully as possible, but strong enough



Fig. 5. Acoustic sensors, type VS-75V i VS-150 RIC, used during the tests.

Tab. 2. List of elements used during the tests.

Position	Test Equipment	Number of pieces
1	Corrosion test tank	1
2	Corrosion tester	1
3	Measuring equipment (AMSY-5 from Vallen GMBH company)	1
4	Acoustic sensors: type VS-75-V with pre-amplifiers	4
5	Acoustic sensors: type VS 150 RIC	2
6	Magnetic grippers	6
7	Cables	6

to simulate the given conditions in the shortest possible time. In the case of laboratory tests, or if we are not limited in time, a solution can be exactly the same as the one in the environment whose destructive process on a given surface is to be observed. Otherwise, the process must be accelerated by adding appropriate catalysing factors,

- the tester must be built in such a way that it is tight and does not initiate corrosion at the test site and, when working, especially with an unstable corrosive solution, it is safe for both the user and the environment.

The above criteria are met by the KE-2 corrosion tester (Fig. 6.), which is used during corrosion measurements and accompanying acoustic events monitored by the VALEN system. It can be used to study both corrosion phenomena, occurring at a constant ambient temperature, and phenomena occurring at elevated temperatures, including in gases. It aims to collect the necessary data, which may help to build a better classifier in the future, and this will translate into better detectability of the corrosion process itself in real conditions.



Fig. 6. The KE-2 corrosion tester with some of its elements.

RESULTS AND DISCUSSION

ACOUSTIC TESTS

The corrosion tester includes a reaction cylinder, among other things - constructed of ordinary hull steel of category A. The chemical composition of this steel is shown in Table 3. It is typical steel used in shipbuilding. The choice of this material is not accidental as it is this steel that is used to make tanks for the transport of crude oil and petroleum products, which are the subject of the research. The most realistic representation of the research conditions on tankers was the aim. Because of this solution, it was possible to simulate the corrosion process and record the acoustic signal coming from it without damaging the actual tank.

Tab. 3. Chemical composition of the material (Hull Steel of Category A according to PRS Classification) of the reaction cylinder *

Element	C _{max}	Mn _{max}	Si _{max}	Al _{min}
Share in [%]	0.23	2.50	0.50	0.04

* The table does not include the sulphur and phosphorus content, which are impurities, according to the requirements they should not exceed 0.035% of the composition.

Before the acoustic test itself, all components of the corrosion tester were well cleaned. After removing all impurities, the reaction cylinder and stopper were degreased with ethyl alcohol. Then, the corrosion processes in the tester were initiated, commencing with flooding the tester reaction tank with the corrosive solution (Table 1) to 1/3 of its volume. After placing and mounting the tester in the tank (Fig. 4) and connecting the VS150 RIC and VS75 sensors with preamplifiers, the AMSY-5 acoustic emission system was activated and the recording of the acoustic signal was started. The signal recording from the moment of flooding to its completion was about 30 minutes. The results of this measurement are presented in Fig. 7 and Fig. 8.

The presented test results prove the possibility of continuous detection of acoustic signals from the corrosion tester. It gives a stable and clear 50 dB signal that stands out clearly from the rest of the acoustic background during the measurement, which

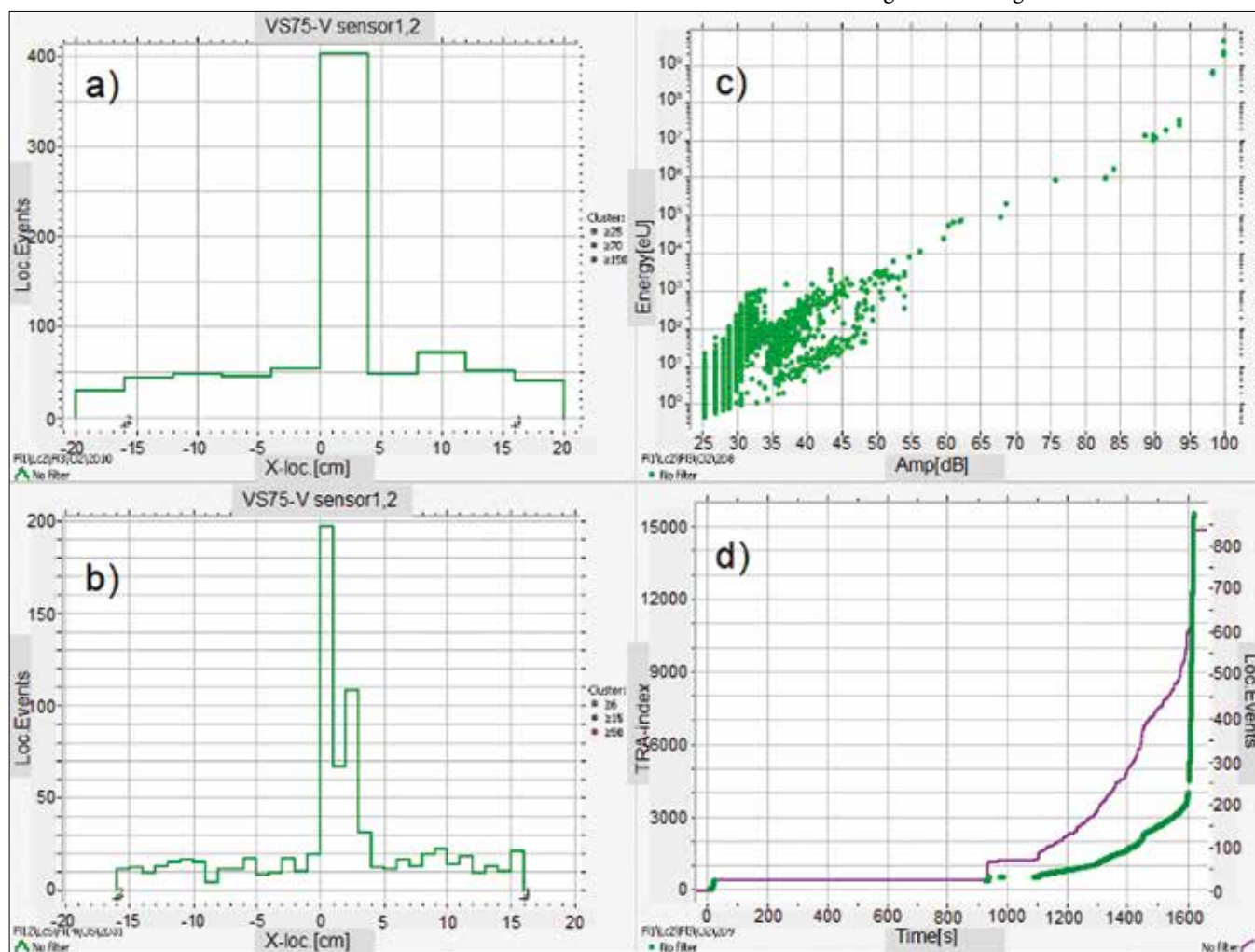


Fig. 7 The KE-2 corrosion tester and its background detectability for VS 75-V sensors, a), b) - the relationship between the location of the tester in relation to the sensors and the number of events recorded by the system, c) the dependence of the signal amplitude given in decibels (dB) to the released energy, d) graph of the measurement time and the number of events.

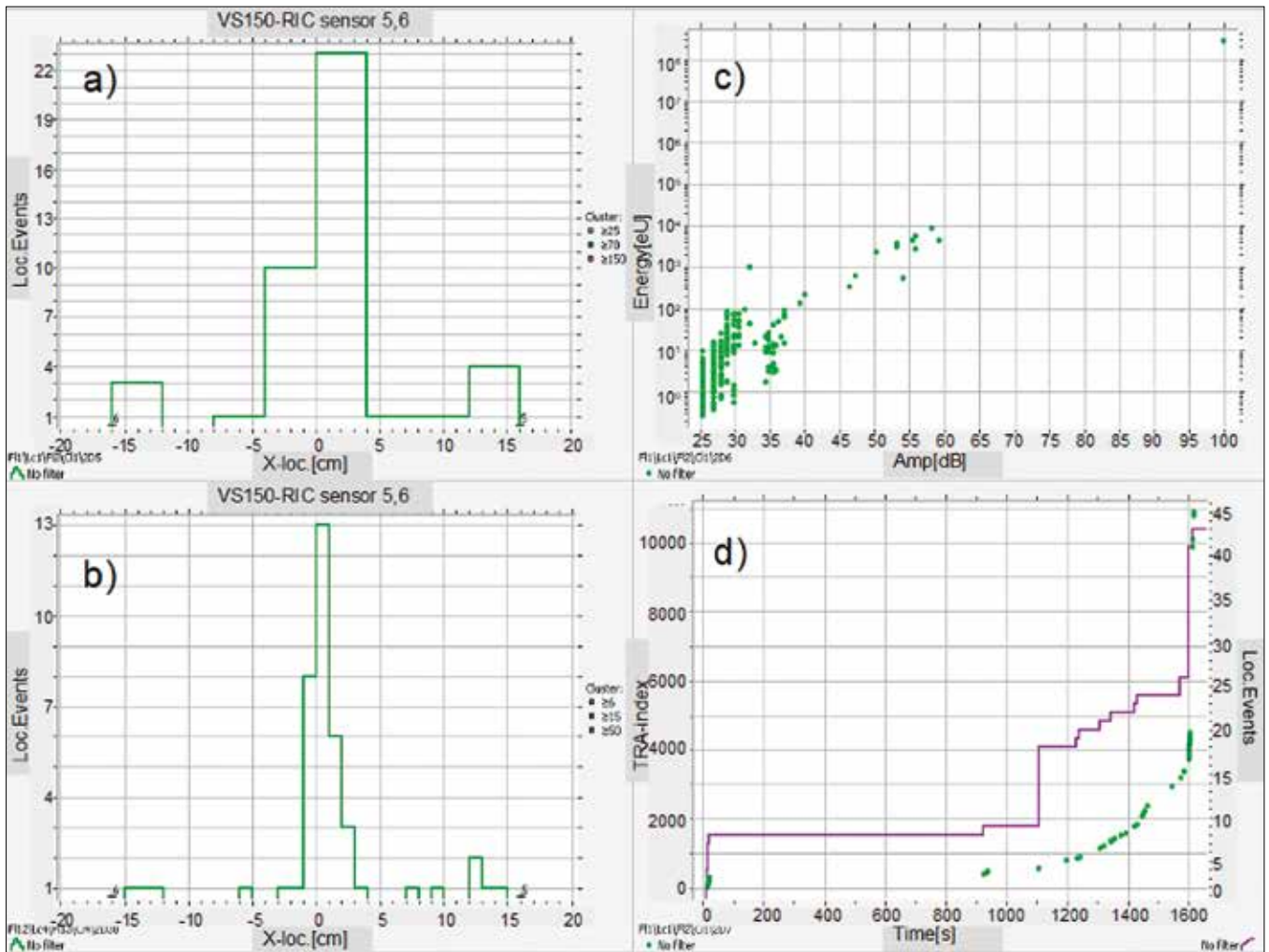


Fig. 8. The KE-2 corrosion tester and its detectability for VS150-RIC sensors. a), b). dependence between the location of the tester in relation to the sensors and the number of events recorded by the system, c) dependence of the signal amplitude in decibels (dB) to the released energy, d) dependence of the measurement time of the number of events

fluctuates around 20-30 dB, as shown in the graphs (Fig. 7c and 8c). This is a similar result to that found by [25], which is characteristic for the amplitude of the signal originating from corrosion occurring in steels in seawater. The corrosion signal obtained in the laboratory during corrosion tests also corresponds to the amplitude of the signal obtained during further tests carried out on real objects [26]. It can be observed that the tester is visible against the background noise coming from the laboratory. A clearly visible increase in energy in the places where the acoustic sensors of both VS75-V and VS150-RIC are attached, can also be observed. This proves not only the possibility of detecting the signal coming from the corrosion tester, but also the possibility of its partial localisation, which is very well illustrated in the graphs in Fig. 7a, 7b, 8a and 8b.

METALLOGRAPHIC TESTS

Figures 9 and 10 present the results of metallographic testing of the plug covering the tester's reaction cylinder. The profile of the plug's surface shows extensive corrosion damage along the cross-section up to a certain point. Once that is exceeded,

the damage that occurs is very small. This is due to the way the corrosion tester is attached to the tank during the test. After careful examination of the photographs, a distinct line can be seen between the corrosive solution and the air trapped in the rest of the tester's reaction cylinder (Fig. 10).

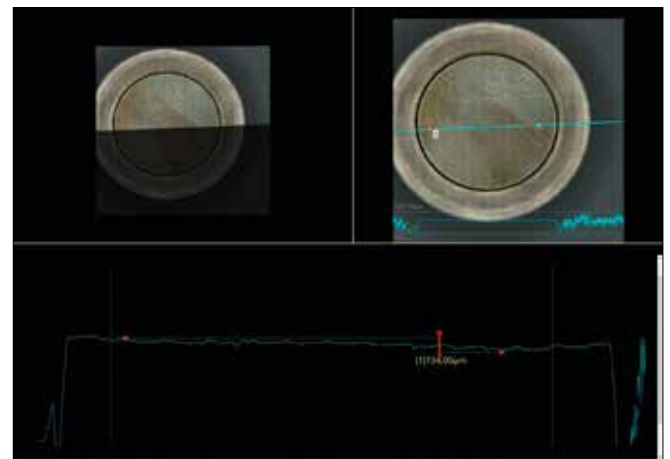


Fig. 9. The profile of the cylinder plug surface after the corrosion test.

It can be seen that, in part of the contact between the solution and the corrosive gas, the corrosion losses are interconnected pits, extending along the line of immersion of the cork of the reaction cylinder in the corrosive solution. Their depth, as shown in Fig. 10, is different. The greatest value of the depth, about 107-134 μm , is achieved in the chambers of the phase contact. The largest and most extensive complex of corrosion pits can be observed in Fig. 10. The photographs make up the cork profile and were built on the basis of the conceptual image stitching method implemented in the KEYENS optical microscope software. The magnification of a single photo was about 20 times (Fig. 9). Points 1 to 6 (Fig. 10) show a fragment of the plug surface corresponding to the measurement points of the profile cross-section and show the depths of the corrosion cavities collected in various places of the resulting corrosion pitting complex. The deepest pit in the complex has a depth of 110 μm , while the smallest has a depth of 0.32 μm . It should be mentioned that both pits presented in Fig. 9 and Fig. 10 were only selected as examples and do not show the full scope of the observed corrosion degradation of the material on the measured plug.

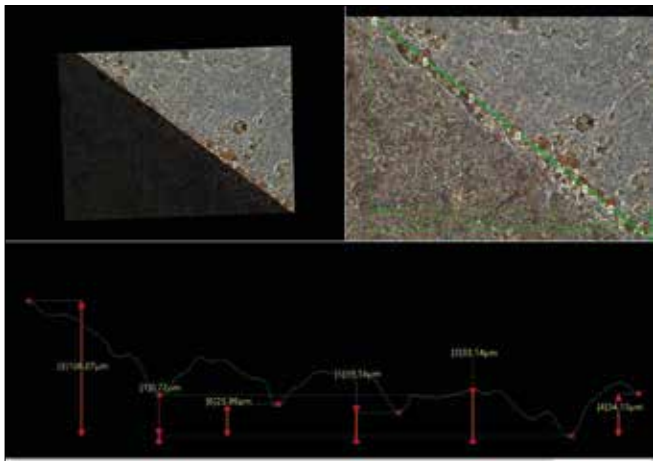


Fig. 10. The surface profile of the greatest corrosion damage observed on the surface of the plug from the reaction cylinder. As you can see in the photograph, the shape of this damage is extensive and consists of many pits connected with both. The deepest corrosion cavity is about 110 μm deep and the smallest is about 0.32 μm .

SUMMARY

The results clearly indicate that the corrosion processes taking place in the reaction cylinder of the corrosion tester are reflected in the course of the acoustic signal obtained during the test. It is also evident, from metallographic studies, that the corrosion process is most intense along the immersion line (the gas-solution phase contact). This may suggest that the main measure of corrosion is electrochemical and general. On the surface of the tested material, it should also be noticed that slight corrosion pits in the submerged part of the tester may suggest the initiation of pitting corrosion.

CONCLUSIONS

Analysing the results obtained during the laboratory testing of the tank using the acoustic emission method with the use of a corrosion tester, the following conclusions can be made.

- Corrosion Tester KE-2, as assumed, gives a stable acoustic signal under accelerated corrosion conditions and is locatable by the AMSY-5 acoustic system.
- The acoustic signal from the corrosion tester is clearly visible against the background noise in the environment, even in the absence of additional signal filtering. It should be noted, however, that this signal is catalysed by means of a corrosive solution and the actual character of corrosion in sea water or in a tank, therefore, may have a slightly different character.

The metallographic testing of the plug surface and the acoustic analysis of the corrosion process in the KE-2 corrosion tester clearly show that, apart from the standard uniform corrosion, we also deal with pitting corrosion at a later stage of progressive corrosion damage. Moreover. It could also be noted that the acoustic events shown by the acquisition system correspond to the formulation of the corrosion pits shown in the metallographic studies.

REFERENCES

1. M. Fahad Sheikh, K. Kamal, F. Rafique, S. Sabir, H. Zaheer, K. Khan, "Corrosion detection and severity level prediction using acoustic emission and machine learning based approach" *Ain Shams Engineering Journal*, vol. 12, pp. 3891-3903, 2021. doi: <https://doi.org/10.1016/j.asej.2021.03.024>
2. C. U. Grosse, M. Ohtsu, T. Shiotani, D. G. Aggelis, *Acoustic Emission Testing: Basics for Research – Applications in Engineering*, Springer, 2021.
3. S. Li, Z. Liang, L. Zhang, "Corrosion evaluation of prestressed high-strength steel wires with impressed current cathodic protection based on acoustic emission technique" *Structural Control & Health Monitoring*, vol. 31, pp. 1-14, January 2022. doi: <https://doi.org/10.1002/stc.2934>
4. L. Calabrese, M. Galeano, E. Proverbio, D. Di Pietro, F. Cappuccini, A. Donato, "Monitoring of 13% Cr martensitic stainless steel corrosion in chloridesolution in presence of thiosulphate by acoustic emission technique" *Corr. Science*, vol. 111, pp. 151-161, 2016. doi: <https://doi.org/10.1016/j.corsci.2016.05.010>
5. H. Tian, X. Wang, Z. Cui, Q. Lua, L. Wang, L. Lei, Y. Li, D.Zhang, "Electrochemical corrosion, hydrogen permeation and stress corrosion cracking behavior of E690 steel in thiosulfate-containing artificial seawater" *Corr. Science*, vol. 144, pp. 145-162, Nov. 2018. doi: <https://doi.org/10.1016/j.corsci.2018.08.048>

6. J. Kovac, A. Legat, B. Zajec, T. Kosec, E. Govekar, "Detection and characterisation of stainless steel SCC by the analysis of crack related acoustic emission" *Ultrasonics*, vol. 62, pp. 312-322, Sept. 2015. doi: <https://doi.org/10.1016/j.ultras.2015.06.005>
7. D. Li, W. Yang, W. Zhang, "Cluster analysis of stress corrosion mechanisms for steel wires used in bridge cables through acoustic emission particle swarm optimization" *Ultrasonics*, vol. 77, pp. 23-31, May. 2017. doi: <https://doi.org/10.1016/j.ultras.2017.01.012>
8. C. Jirarungsatian, A. Prateepasen, "Pitting and uniform corrosion source recognition using acoustic emission parameters" *Corr. Science*, vol. 52, pp. 187-197, Jan. 2010. doi: <https://doi.org/10.1016/j.corsci.2009.09.001>
9. J. Xu, X. Wu, E.-H. Han, "Acoustic emission response of sensitized 304 stainless steel during intergranular corrosion and stress corrosion cracking" *Corr. Science*, vol. 73, pp. 262-273, Aug. 2013. doi: <https://doi.org/10.1016/j.corsci.2013.04.014>
10. J. Kovac, C. Alaux, T. J. Marrow, E. Govekar, A. Legat, "Correlations of electrochemical noise, acoustic emission and complementary monitoring techniques during intergranular stress-corrosion cracking of austenitic stainless steel" *Corr. Science*, vol. 52, pp. 2015-2025, Jun. 2010. Doi: <https://doi.org/10.1016/j.corsci.2010.02.035>
11. G. Du, J. Li, W.K. Wang, C. Jiang, S.Z. Song, "Detection and characterisation of stress-corrosion cracking on 304 stainless steel by electrochemical noise and acoustic emission techniques" *Corr. Science*, vol. 53, pp. 2918-2926, Sept. 2011. doi: <https://doi.org/10.1016/j.corsci.2011.05.030>
12. M. Breimesser, S. Ritter, H.-P. Seifert, S. Virtanen, T. Suter, "Application of the electrochemical microcapillary technique to study intergranular stress corrosion cracking of austenitic stainless steel on the micrometre scale" *Corr. Science*, vol. 55, pp. 126-132, Feb. 2012. Doi: <https://doi.org/10.1016/j.corsci.2011.10.011>
13. A.A. Oskuie, T. Shahrabi, A. Shahriari, E. Saebnoori, "Electrochemical impedance spectroscopy analysis of X70 pipeline steel stress corrosion cracking in high pH carbonate solution" *Corr. Science*, vol. 61, pp. 111-122, Aug. 2012. doi: <https://doi.org/10.1016/j.corsci.2012.04.024>
14. K. Wu, J.-W. Byeon, "Morphological estimation of pitting corrosion on vertically positioned 304 stainless steel using acoustic-emission duration parameter" *Corr. Science*, vol. 148, pp. 331-337, Mar. 2019. doi: <https://doi.org/10.1016/j.corsci.2018.12.031>
15. M. Breimesser, S. Ritter, H.-P. Seifert, T. Suter, S. Virtanen, "Application of electrochemical noise to monitor stress corrosion cracking of stainless steel in tetrathionate solution under constant load" *Corr. Science*, vol. 63, pp. 129-139, Oct. 2012. doi: <https://doi.org/10.1016/j.corsci.2012.05.017>
16. L. Calabrese, G. Campanella, E. Proverbio, "Identification of corrosion mechanisms by univariate and multivariate statistical analysis during long term acoustic emission monitoring on a pre-stressed concrete beam" *Corr. Science*, vol. 73, pp. 161-171, Aug. 2013. doi: <https://doi.org/10.1016/j.corsci.2013.03.032>
17. I. Baran, "Acoustic Emission (AE) - AE Method of technical devices testing," *Institute of Fundamental Technological Research, XXV non-destructive material testing seminar*, Zakopane Mar. 20-22, 2019. doi: 10.26357/BNiD.2019.017
18. F. Delaunois, A. Tshimombo, V. Stanciu, V. Vitry, "Monitoring of chloride stress corrosion cracking of austenitic stainless steel: identification of the phases of the corrosion process and use of a modified accelerated test" *Corr. Science*, vol. 110, pp. 273-283, Sept. 2016. doi: <https://doi.org/10.1016/j.corsci.2016.04.038>
19. Z. Zhanga, X. Wu, J. Tan, "In-situ monitoring of stress corrosion cracking of 304 stainless steel in high temperature water by analyzing acoustic emission waveform" *Corr. Science*, vol. 146, pp. 90-98, Jan. 2019. doi: <https://doi.org/10.1016/j.corsci.2018.10.022>
20. Z. Zhang, Z. Zhang, J. Tan, X. Wu, "Quantitatively related acoustic emission signal with stress corrosion crack growth rate of sensitized 304 stainless steel in high-temperature water" *Corr. Science*, vol. 157, pp. 79-86, Aug. 2019. Doi: <https://doi.org/10.1016/j.corsci.2019.05.030>
21. J. Cuadra, P.A. Vanniamparambil, D. Servansky, I. Bartoli, A. Kontsos, "Acoustic emission source modeling using a data-driven approach" *Journal of Sound and Vibration*, vol. 341, pp. 222-236, Apr. 2015. doi: <https://doi.org/10.1016/j.jsv.2014.12.021>
22. K. He, Z. Xia, Y. Si, Q. Lu, Y. Peng, "Noise Reduction of Welding Crack AE Signal Based on EMD and Wavelet Packet" *Sensors*, vol. 20, pp. 761-773, Jan. 2020. doi: <https://doi.org/10.3390/s20030761>
23. L. Calabrese, M. Gleano, E. Proveribbio, D. Di Pietro, A. Donato, F. Cappuccini, "Advanced signal analysis applied to discriminate different corrosion forms by acoustic emission data" *32Th Conference on Acoustic Emission Testing*, Prague 2016. [Online]. Available: https://www.ndt.net/article/ewgae2016/papers/65_paper.pdf
24. *Rules for the Classification and Construction of Naval Ships part IX: Materials and Welding*, Polish Register of Shipping, 2021

25. Y. Zheng, Y. Zhou, Y. Zhou, T. Pan, L. Sun, D. Liu, "Localized corrosion induced damage monitoring of large-scale RC piles using acoustic emission technique in the marine environment" *Construction and Building Materials*, vol. 243, pp. 1-17, May. 2020. doi: <https://doi.org/10.1016/j.conbuildmat.2020.118270>
26. K. Emilianowicz, "Monitoring of underdeck corrosion by using acoustic emission method" *Polish Maritime Research*, vol. 81, pp. 54-61, Mar. 2014. doi: <https://doi.org/10.2478/pomr-2014-0008>

CONTACT WITH THE AUTHORS

Krzysztof Emilianowicz

e-mail: krzysztof.emilianowicz@pg.edu.pl

Gdańsk University of Technology
Faculty of Mechanical Engineering and Ship Technology
Narutowicza 11/12
80-233 Gdańsk
POLAND

Milena Supernak

Gdańsk University of Technology
Institute of Naval Architecture and Ocean Engineering
Narutowicza 11/12
80-233 Gdańsk
POLAND

Agnieszka Ossowska

Gdańsk University of Technology
Faculty of Mechanical Engineering and Ship Technology
Narutowicza 11/12
80-233 Gdańsk
POLAND

A METHOD FOR THE INTERPRETATION OF SONAR DATA RECORDED DURING AUTONOMOUS UNDERWATER VEHICLE MISSIONS

Mariusz Zieja ^{1, *}

Wojciech Wawrzyński ²

Justyna Tomaszewska ³

Norbert Sigiel ⁴

¹ Air Force of Technology, Warsaw, Poland

² Warsaw University of Technology, Poland

³ Military University of Aviation, Dęblin, Poland

⁴ MCM Squadron, Gdansk, Poland

* Corresponding author: mariusz.zieja@itwl.pl (M. Zieja)

ABSTRACT

Image acquisition from autonomous underwater vehicles (AUVs) is useful for mapping objects on the seabed. However, there are few studies on the interpretation of data collected with side-scan sonar during autonomous underwater vehicle missions. By recording the seabed with 3D multibeam sonar, a large number of survey points can be obtained. The collected data are processed using applications based on remote sensing image processing. The data collected during AUV missions (or other sonar carriers) needs to be pre-processed to reach the proper effectiveness level. This process includes corrections of signal amplification (Time Varying Gain, or TVG) and geometric distortions of sonar images (Slant Range Corrections). It should be mentioned that, when carrying out the interpretation process for structures on the sea floor, sonar users need to understand the process of visualising seabed projections and depressions, as well as the resolution limitations of the sonar sensors.

Keywords: onar technologies; sea floor monitoring; autonomous underwater systems.

INTRODUCTION

During both world wars, tens of thousands of sea mines were laid in the Baltic Sea, a significant number of which still remain on the seabed and pose a significant threat to shipping and the marine environment. According to the Baltic Marine Environment Protection Commission 'HELCOM', during World War II alone, some 40,000 tonnes of chemical ammunition was also dumped into Baltic waters.

The environment will deteriorate because of the length of time the objects have been on the seabed, the associated progressive corrosion and poor water exchange in the Baltic Sea. The location of these objects, and their protection or destruction, is a significant challenge for the countries around the Baltic Sea. Due to rapidly developing autonomous

systems, there are new possibilities for detecting, classifying and identifying the threat. For this reason, the exploration of marine waters is extremely necessary since, in many areas (particularly those difficult to access by humans), the level of the threat is still unknown. Therefore, in order to expand the explored areas, data are collected from sensors mounted on underwater vehicles. Image acquisition from underwater vehicles is useful for mapping objects on the seabed [1]. The data collected in this way make it possible to identify objects on the seabed, such as sunken ships. Having accurate maps of the seabed is important to ensure safe transport. Therefore, more and more attention is being paid to the development of rapid methods for object detection and the monitoring of possible obstacles in maritime transport routes [2] increasing attention is being paid to the development of effective methods for the

detection and monitoring of possible obstacles on the transport route. Bathymetric laser scanners record the full waveform reflected from the object (target). Modern developments in obtaining spatially correct digital data from side-scan sonar systems have resulted in images that can, subsequently, be processed, enhanced, and quantified. With appropriate processing, these acoustic images can be made to resemble easily recognisable optical photographs.

The first operators of Synthetic Aperture Sonar (SAS) were military users. In particular, they are used in large areas where small, low-signature bottom mines need to be detected and classified in a short amount of time and with sufficiently high resolution [3]. The technology also has a number of other potential applications, including seabed exploration, underwater archaeology, mapping debris, and search and rescue operations.

Vehicles used for seabed exploration can be divided into two main groups: manned and unmanned operating vehicles. Within unmanned underwater vehicles (UUV), two groups can be distinguished: Remotely Operated Vehicles (ROV) and Autonomous Underwater Vehicles (AUV). AUVs can be classified as: underwater glider, underwater propeller AUV and biomimetic AUV [4]. The main differences between the different types of UUVs, such as ROV and AUV, lie in their mode of operation. The first is remotely controlled and the second is highly automated and carries out tasks independently. In some cases, only second-class vehicles are regarded as autonomous robots.

Each of these platforms has various imaging and mapping capabilities, appropriate for specific scales and tasks [5]. They gain the necessary information through on-board sensors and systems. Every AUV, in its most basic form, must have a navigation system, a propulsion system and a dry, watertight environment for placing on-board components. In addition, an AUV is typically equipped with systems and components such as a diving system, microcontroller, attitude control, power supply and sonar [6]. By providing a synthetic aperture, the sonar is able to overcome physical limitations and achieve higher resolution, compared to side-scan sonar (SSS), which is a different technique for obtaining underwater images. In order for the sonar to work properly, the UUV must move less than one-half the physical length of the antenna between pings (a pulse of sound created by active sonar). By moving slightly less, overlapping data can be used to estimate the platform's movement with an incredible degree of accuracy. The maximum reachable coverage using SAS is, therefore, inversely proportional to the platform speed. This means that the area coverage rate is dependent of speed and directly coupled to the length of the receiver array. Acoustic cameras (sonars) are the most suitable sensors because they provide acoustic images with more precision than other sensors, even in turbid water [7]. The most popular configuration of sonar sensors used to monitor underwater obstacles is a forward-looking sonar (FLS) [8] with one of the most popular configurations being forward looking sonar (FLS). A Gaussian Particle Filter (GPF), based on the tracking approach, is used to more accurately identify objects to solve the problem of persistently tracking multiple

targets in a noisy environment. It is based on the nature of acoustic-visual images and modified signal filtering, as well as growing regional segmentation methods to improve image processing performance. Secondly, a generalised regression neural network is adopted to evaluate multiple features of target regions and the representation of feature subsets is developed to improve tracking performance [9]. Recently, one of the methods used for underwater image reconstruction is analysing data from 3D optical sensors. Together with distributed scalable big data, storage and artificial intelligence in automated 3D metrology is a powerful tool in the investigation of the seabed [10].

Although sonar data displayed on a screen can be interpreted by inexperienced operators, the effectiveness of the whole operation can be significantly increased when users of the sonar systems have a basic knowledge. Effective sonar record interpretation requires taking into account many factors, including complex processes of data collection and environmental restrictions, as well as platform characteristics. The article includes recommendations and guidance for operators, which are helpful during sonar record interpretation, and mainly focuses on the data obtained during autonomous underwater vehicle (AUV) missions. Previous works related to the subject mostly cover the aspects of side scan sonar data received using towed sonars [11, 12]. However, the basic principles of sonar operation are the same. There are some differences concerning the sonar records acquired during AUV missions, which will be described in this paper. The first section covers the characteristics of side scan sonar geometry. The second section describes characteristic sonar record disruptions and AUV mission planning aspects. The last sections are dedicated to the proper interpretation of objects and sea bottom structures. This work includes examples of sonar records of real objects.

RELATED WORKS

Researchers have acknowledged a growing interest in the interpretation of AUV imagery in various disciplines, e.g. maritime archaeology, geology and military applications. One of the last explored methods is automatic target recognition for small autonomous vehicles with the usage of efficient deep learning algorithms. As Topple and Fawcett [13] pointed out, advances in deep learning have managed object detection using data from a variety of sensor types. This was achieved by adapting neural network-based models trained on large datasets from natural images, which are commonly applied to the remote sensing (RS) domain through transfer learning. Unfortunately, the limitations of small hardware, such as computational performance and battery power, reduce the possibility of running deep learning models on board. Standard pre-trained object detection models include large conventional neural networks requiring tens to hundreds of billions of floating-point operations to distinguish multiple object classes in natural images. Indeed, such large models may be too complex for the tasks performed by sonar. Consequently, [13]

proposed the MiNet system, which was successfully deployed aboard the Ocean Server Iver small AUV during the REBOOT sea trials and predicted the width, length and class of objects detected in sonar images within minutes of the completion of each mission stage.

In another method described by Yu et al. [14] the first step in side-scan sonar (SSS, side-scan radar data was used (the method consisting of four main steps) to visualise the data. Firstly, the raw SSS data were analysed to obtain a greyscale image and the blind zone boundary of the image was obtained using a threshold method. Secondly, the noise characteristics of the image were analysed and the de-noising algorithm optimised to effectively remove high-frequency noise. Then, spatial-temporal matching calculations were performed for each port and starboard ping and the accurate coordinates of the first bottom returns were obtained by extreme value detection. Finally, automatic and accurate bottom line detection was performed according to the smooth processing of the coordinate sequence of the first bottom returns.

In Zhang et al. [15] the point target reference spectrum (PTRS, the authors described multi-receiver synthetic aperture sonar and proposed a new method for providing high-resolution images in systems. In the proposed method, the point target reference spectrum (PTRS), azimuth modulation, and coupling term were deduced based on an accurate time delay. This modification of the PTRS method has an advantage over the traditional one, in which algorithms are still exploited.

The image generation method presented by Chen et al. [16] was based on a retinex algorithm using a two-sided filtering process, colour pre-correction, estimated reflectivity and dynamic range. Compensation, colour compensation and other processes realise the accurate perception of underwater targets using an extended Kalman filter (EKF) and spatial feedback linear transformation matrix. The target range method was used to solve the joint angles of the manipulators and target tracking and grasping were then completed. Underwater experiments showed that the algorithm not only improved the dynamic stability of AUVs but also ensured the grasping accuracy of the underwater robot and optimised the control performance of the system.

Considering that de-noising and detection of underwater sonar images are crucial for proper image interpretation, Wang et al. [17] proposed a new adaptive approach to address this issue. Firstly, an adaptive method for de-noising non-local spatial information based on the golden ratio was proposed and, secondly, a new adaptive cultural algorithm (NACA) was offered to precisely and quickly complete the process of detection. The next step was the development of image generation and interpretation, as an alternative for the fuzzy clustering method and Markov segmentation algorithm. Although their results were satisfactory, the processing procedures are quite complex and computationally costly.

Last but not least, the advanced Automatic Target Recognition (ATR) method applied by Isaacs [18], for unexploded ordnance (UXO) detection and classification using sonar data from open ocean survey sites, should be mentioned. The classic paradigm of anomaly detection in

images breaks down in cluttered and noisy environments. After an upgrade, and when more robust object detection is performed using an in-situ weighted highlight-shadow detector, features are generated on geometric moments in the imaging domain and, finally, classification is performed using an Ada-boosted decision tree classifier. This method is widely used for military purposes.

Sonar data processing is also one of the daily responsibilities of the research centre at the NATO Centre for Maritime Research and Experimentation, which is working on the utilisation of robotics in minefields, to deliver doctrinally relevant autonomy and on-board intelligence. Research on improving the quality of image signals is being conducted by the Naval Undersea Warfare Center, Maritime Technologie und Forschung, the Centre for Maritime Research and Experimentation and the Atlantic Research Centre, among others.

SIDE SCAN SONAR GEOMETRY

Sonar signals are broadly classified as either passive or active. The sound waves generated by sea creatures, the motors of ships, or the sea itself (i.e. waves) are passive sonar signals, whereas radar signals are active sonar signals. With active signals, a sonar device (a sonar transducer) produces sounds and then analyses the echo. In this research, the data from SSS has been used. SSS is easily accessible and economic to use to get images of the seabed and underwater objects. Object and target detection based on SSS images has a wide diversity of applications for military purposes; it is increasingly used for the identification and categorisation of mines.

The images discussed in the following section were generated using an algorithm for AUV route generation, which was designed to reduce the time needed to prepare a mission plan, taking into account the environmental and vehicle-specific characteristics. This algorithm can be summarised in the following way:

- The starting point for the development of the programme was the data acquired during the research, concerning both the architecture of a given subsystem, its tactical data (manoeuvring elements, energy consumption, accuracy of geographic positioning during mission execution, etc.), as well as the characteristics of the operating environment (in this case, the Baltic Sea area).
- The main parameters entered in the algorithm were: geographical position of the area of operations, AUV Altitude, AUV Speed, Course, Water Depth, speed of sound propagation in water (SVP) and a theoretical range of the sonar.
- After entering the parameter values, the operator can generate a mission plan using three modes: planning based on sonar near/far ranges, planning based on AUV speed, or planning based on object detection probability.
- The process is then optimised. The optimal distribution of the search pattern and the optimal trajectory of the AUV should provide full area coverage. For the systems

equipped with side-looking sonars, the lawnmower pattern gives a possibility to cover the nadir gap below the sonar transducer. The distance between the mission plan line is determined by the sonar detection ranges, i.e. the maximum and the minimum. For the vehicle equipped with synthetic aperture sonar where the detection ranges depend mainly on vehicle speed, the minimum and maximum values can be determined experimentally for the specified AUV speed. The optimal trajectory of the autonomous vehicle can be determined by implementing the transformations from the projection of the geographic coordinates describing the area of operation into a mission plan, in a format acceptable by the manufacturer's software.

The key to the proper interpretation of collected data is knowledge concerning side scan sonar geometry and sonar carrier characteristics (Fig. 1). In the classic configuration, the sonar carrier moves along a known trajectory and through an antenna, which main azimuth leaf is perpendicular to the direction of the carrier's motion radiates the observed area with an acoustic wave [19]. The echo signals reflected from the object are returned to the antenna, where they are received, processed and presented on the screen of the operator's console. The delay time between the signal generation and reception determines the longitudinal resolution of presented images.

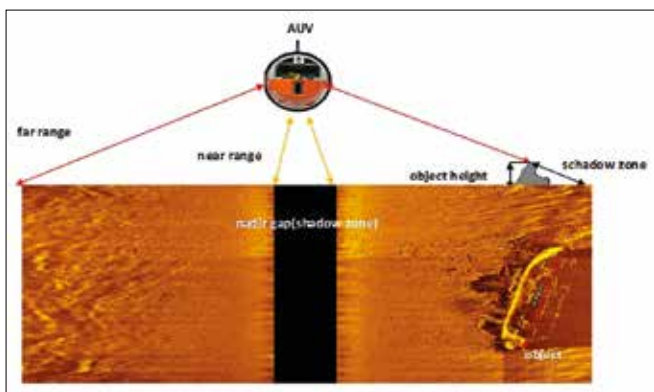


Fig. 1. Side-scan sonar geometry.

Assuming range gates of duration τ , the two seafloor objects O1 and O2 are separated by ΔR_g and will be resolved if their returns do not overlap in time (Fig. 2). The round-trip travel time for a pulse associated with the object at range R_s is given by [20]:

$$t = \frac{2R_s}{c}, \quad (1)$$

The incremental delay due to the proximate object O2 is:

$$t + \tau = \frac{2(R_s + \Delta R_s)}{c}, \quad (2)$$

where:

- c – is the propagation speed in the medium (e.g. seawater),
- τ – is the delay interval between the transmission and the reception of the pulse,
- R_s – is the instantaneous slant range measured from the sensor to a point on the seafloor,
- ΔR_s – is the range of the separation of the two seafloor objects O1 and O2.

A measure of the slant plane separability is obtained by subtracting Eq.(1) from Eq.(2), and is given by:

$$\tau = \frac{2\Delta R_s}{c}, \quad (3)$$

The relationship between ground-plane and slant-plane (Fig. 2 (left)) is approximated as:

$$\Delta R_g = \frac{\Delta R_s}{\cos\theta_g}, \quad (4)$$

where: θ_g is the grazing angle.

Therefore, two objects on the seafloor are fully resolvable if their ground separation satisfies:

$$\Delta R_g \geq \frac{c\tau}{2\cos\theta_g}, \quad (5)$$

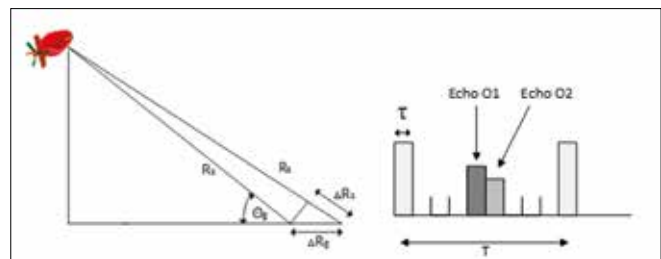


Fig. 2. Time domain representation of transmitted pulse and corresponding echoes [20] (Licensee IntechOpen).

Fig. 3 shows the slant-plane view of side-looking sonar with a projector of length D and azimuth beam width Θ_H . The parameters δ_a^{min} and δ_a^{max} correspond to the linear azimuth beam width at the minimum and maximum slant ranges, respectively. The half-power angular beam width of a uniformly weighted rectangular aperture of length D is given in by the approximate relationship [20]:

$$\Theta_H = \frac{\lambda}{D}, \quad (6)$$

where λ is the acoustic wavelength of the signal.

The resolution of a side looking sonar system at slant range distance R_s is given by:

$$\delta_a \cong \frac{R_s \lambda}{D}. \quad (7)$$

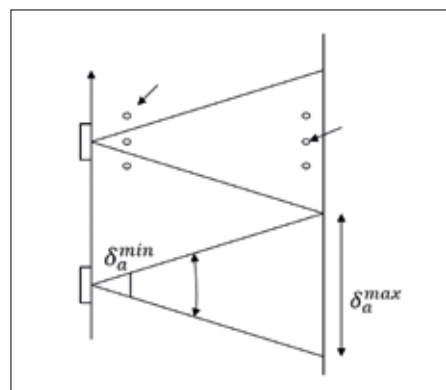


Fig. 3. Slant range, along-track SAS geometry with a beam spread as a function of slant-range [20] (Licensee IntechOpen).

In order to keep the resolution small as the range increases,

the frequency and/or the physical aperture length D must be increased. The azimuth resolution, however, will depend on the slant range [20].

Conventional sonar usually uses the same transducers to generate the signal and to receive the echo from an object. One of the examples of that solution is the GAVIA autonomous underwater vehicle, equipped with the conventional side looking sonar EDGETECH. New solutions have recently appeared, which separate the transmitter and receiver array, e.g. AUV HUGIN equipped with HiSAS sonar. In both cases, sonar image creation is connected with precise counting of the time between the signal generated by the transmitter and the echo received from the object in the water column or on the seabed. Nowadays, the systems equipped with synthetic aperture sonar technology provide possibilities to generate higher resolution images, which means higher quality of data, with the same pulse frequency (Fig. 4) [21].

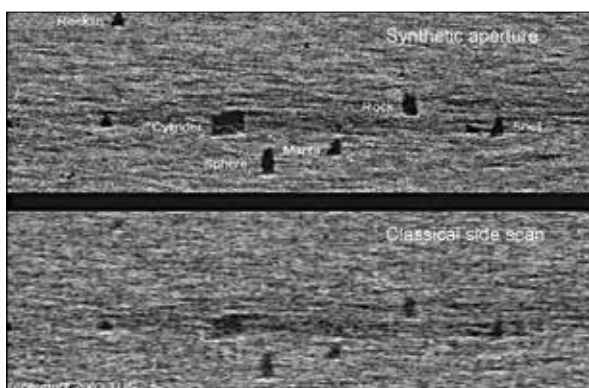


Fig. 4. Comparison of synthetic and classical side scan apertures for the equal sonar frequency [21] (copyright TUS).

FACTORS AFFECTING THE QUALITY OF SONAR DATA

The remote sensing modalities available for underwater purposes (acoustic methods) cover frequency ranges from a few Hz to a few MHz, and are the most widely used by far. Effective interpretation of the data results from a deep analysis of sonar images. The data collected during AUV missions, or other sonar carriers, need to be pre-processed to reach a proper effectiveness level [22] Polish Academy of Sciences Branch Lublin. All rights reserved. The paper includes a probabilistic method for evaluating the durability of components and device assemblies which operate under the impact of destructive processes. As a result of these processes, wear that causes deterioration of their cooperation conditions occurs. It is assumed that a component operates reliably when the wear does not exceed the acceptable (limit. This process includes corrections of the signal amplification (such as Time Varying Gain (TVG)) and geometric distortions of the sonar image (Slant Range Corrections (SRC)) [23, 24]. After SRC, the sonar images are geometrically corrected across-track; the along-track corrections account for the variations in platform speed. This process, called anamorphosis, produces an image in which the inter-pixel spacing is the same across-track and along-track [25].

Sound speed profile distribution in the water column is another source of geometric distortion, which is strictly connected with such factors as water temperature, pressure and salinity, and needs to be taken into account. These processes are the initial steps in data post-processing, which are conducted automatically without the operator's attention. Further corrections usually depend on the user's knowledge and experience and are enabled by dedicated programs for sonar record analysis, e.g. SeeTrack or Reflection. The operator can reach proper image enhancement by setting special filters, e.g. mean filter, median filter, or a palette of colours. These parameters can be selected and optimised by operators; however, there are many factors on which they have very limited influence. Characteristic distortions of sonar images result from acoustic pulse interaction with the water surface and these are presented in the following sections.

SIGNAL RETURNS FROM THE SEA SURFACE

The signal returns from the sea surface could be present in a sonar record when the sonar is closer to the surface than to the seabed. In that case, the acoustic pulse reflection from the surface will be faster than the echo from the bottom. Reflections from the surface will be present on the sonar image as an additional line. When the water surface is calm, only a thin line can be recognised. The distance between this line and the sonar is equal to the actual depth of an AUV or other sonar carrier. When the operation is conducted in different conditions, e.g. a rough sea, there is a high possibility of more extensive noise from waves, sometimes making interpretation of the data impossible. A characteristic distortion of a sonar image may also be generated by a ship's propellers. Taking safety into account during operations focusing on seabed research, there should not be any other units in the vicinity of the AUV during the mission. However, the distortion presented in Fig. 5 might appear as a result of the 'mother' ship unit being too close to the vehicle equipped with sonar. In most cases, the reason for shortening the distance between the AUV and the 'mother' ship is to improve the acoustic link capabilities. The operator should take that fact into account and keep a safe distance from the vehicle, greater than the sonar's farthest range. The distortion is visible as a white streak covering the proper data and can be generated by propellers, but also by buoys and other objects anchored in very strong currents.

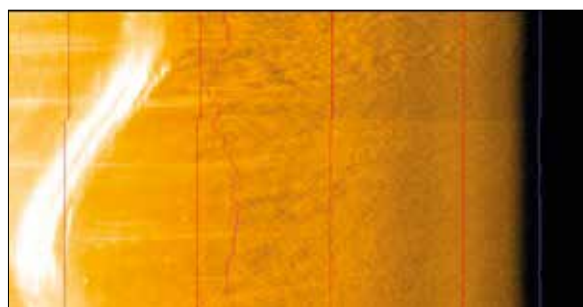


Fig. 5. Distortion of sonar record caused by a ship's propellers

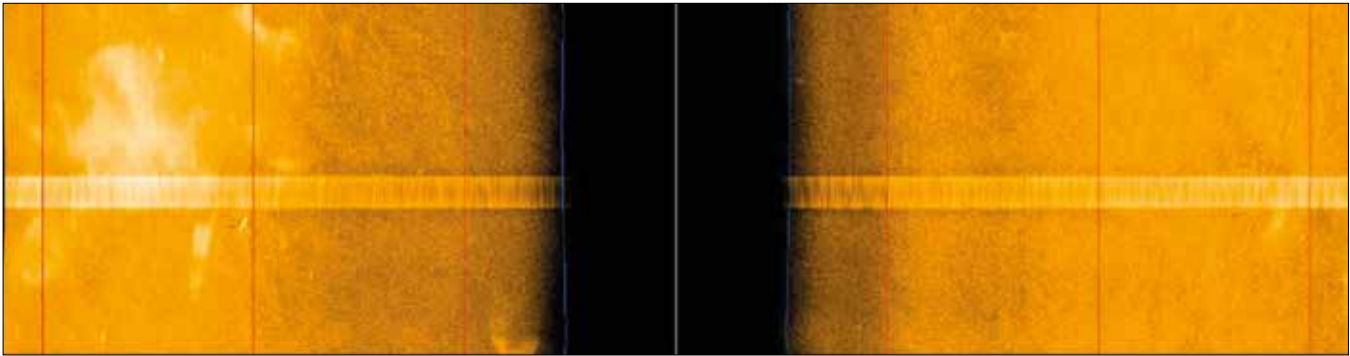


Fig. 6. Deformation of sonar image caused by environmental disruptions.

Multiple echoes from one object are another example of image disturbance. This situation is not very common and only takes place when special conditions are met, which include calm sea surfaces, shallow water areas and the presence of an object generating a very strong echo. Multiple echoes result from the different paths used by acoustic pulses to reach the object and return to the receiver. In normal conditions, the signals are moving along the way 'sonar-object-sonar'. When operating on a calm sea and shallow water, there is a possibility that additional echoes could be generated. This effect is a result of acoustic signal reflections from the surface. In that case, the signals are moving along the route: 'sonar-object-water-surface-sonar'.

Air bubbles appearing as an output of working propellers, leaking gases, and other environmental disruptions, might be another cause of obtaining improper data. When the intensity of these phenomena is very high, there is a possibility that all information from the assigned area could be lost (Fig. 6).

There may be additional restrictions relating to the specific hydrology of the area in which the operation is being conducted. One of these restrictions is connected with the sound speed profile distribution over the water column, which impacts the maximum and minimum sonar detection ranges. Fig. 7 shows that, despite the theoretical far range of sonar being equal to 180 m, useful data can only really be obtained up to 90 m from the transceiver. The other information presented on the screen does not allow operators to detect the objects of interest.

Degradation of the sonar range could appear in the area where the salty seawater is mixing with the freshwater from the rivers. The sound speed profile has a great impact on

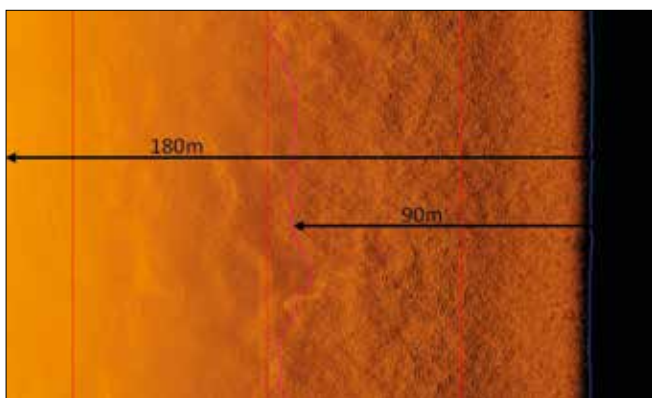


Fig. 7. Restrictions in the range of useful sonar data.

establishing sonar range. The main factor influencing the sound speed profile is temperature: a one-degree increase in water temperature results in increasing the speed of sound by 3.5 m/s. Increasing the salinity by 1 PSU causes an increase in the sound speed by 1.3 m/s, while pressure changing with the depth will increase the sound speed by 1.8 m/s for every 100 m [26]. The sound velocity value can be determined by Eq. (8) [27]:

$$C = 1449,2 + 4,6T - 0,55T^2 + 0,00029T^2 + (1,34 - 0,01T)(S - 35) + 0,016Z \quad (8)$$

where:

- C – speed of sound in water, expressed in metres per second;
- T – water temperature, expressed in degrees Celsius;
- S – salinity, in parts per thousand;
- Z – depths, in metres measured from the sea surface.

Most AUV operations require collecting and displaying data with 100% coverage of the area of interest. Full area coverage is crucial; for example, during mine countermeasure missions, confidence that all of the unexploded ordnance (UXO) has been found is an essential part of the whole mission. Taking that fact into account, the operator needs to adjust the mission plan to current environmental conditions and sonar capabilities, mainly with respect to near and far ranges. One of the most effective search patterns for an AUV vehicle equipped with side scan sonar is the 'lawnmower' pattern (Fig. 8).

The optimal distances between the mission plan lines can be determined by the equations:

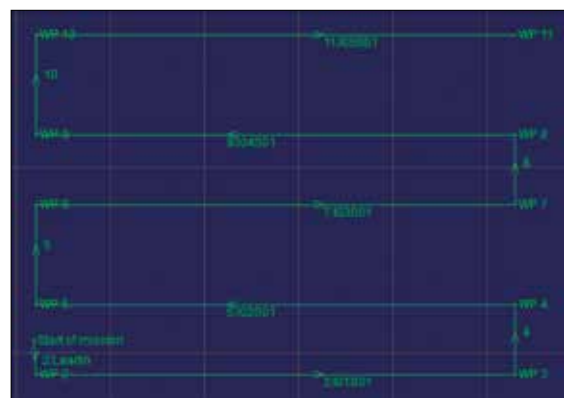


Fig. 8. AUV mission plan - lawnmower pattern tracks distribution.

$$D_{long} = 2 * R_{max} - SDNE_{AUV} - Overlap, \quad (9)$$

$$D_{short} = R_{max} - R_{min} - SDNE_{AUV} - Overlap, \quad (10)$$

where:

- D_{long} – long spacing between the mission plan lines;
- D_{short} – short spacing between the mission plan lines;
- R_{min} – near sonar range;
- R_{max} – far sonar range;
- $Overlap$ – parameter used to increase the confidence that full area coverage will be achieved during the mission;
- $SDNE_{AUV}$ – standard deviation of AUV navigational error.

For example, for the range values measured during this research and assuming a standard vehicle height above the bottom (i.e. 30 m), the determined values are presented in Table 1.

Tab. 1. Results of the calculation of the distance between the search strips of an AUV HUGIN vehicle.

Velocity [m/s]	The short spacing between the mission plan lines D_{short} [m].	The long spacing between the mission plan lines D [m].
1.5	138	350
2.0	83	240
2.5	58	174

The technique of distributing bands in such a way that each two neighbouring bands cover their own nadir zones makes it possible to achieve complete coverage of the area while ensuring high efficiency in the operations. The optimal selection of distances between individual lanes, taking into account the area of operation and vehicle and sonar parameters, is a complicated task which requires the consideration of many factors. Mistakes made at the planning stage may not only lead to the acquisition of poor quality data but also threaten the safety of equipment and people. In view of the above, it is important to automate the planning process and support operators, in order to ensure safety and efficiency of conducted operations.

RESTRICTIONS CONNECTED WITH SCREEN RESOLUTION AND SONAR DATA MOSAICKING PROCESS

Taking into account the efficiency of data analysis, especially during a mission focused on detecting and classifying small objects, the selection of proper monitor size and resolution, on which the data will be post-processed, is a crucial decision. Incorrect screen resolution and size could result in omitting objects, especially when the analysis is carried out over a long period of time by only one operator. Fig. 9 shows the same object presented on three different size screens and at

different resolutions. During operations focusing on searching for objects which have a well-known size, knowledge about current monitor settings helps to assess the real size of the detected structure and makes it possible to carry out proper classification.

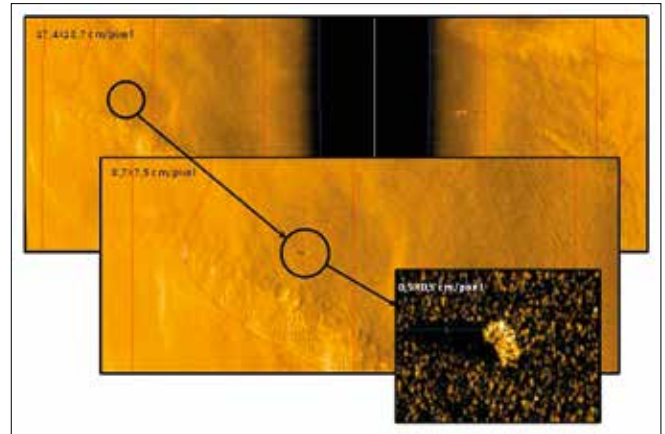


Fig. 9. Presentation of the same object at three different resolutions.

With the dynamic development of computers and informatics intended for the post-processing of hydrographic data, a new era in the field of digital sonar image (mosaic) generation has arrived. Nowadays, this process takes less time and is simplified, giving the user many devices to minimise and remove errors from the generated data. Despite the great improvements in data quality, the process of generating high-resolution mosaics is still burdened with many errors, which are the result of imperfections in sonar devices [28]. Fig. 10 presents the sonar image mosaicking errors caused by movement of the AUV during data collection.

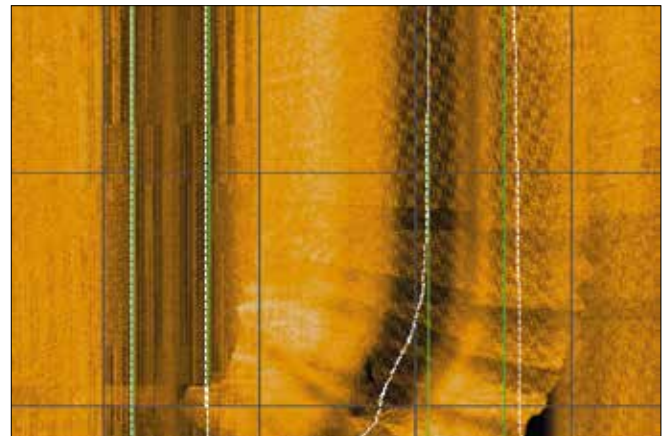


Fig. 10. Sonar image mosaicking errors caused by movement of the AUV during data collection.

VISUALISATION OF OBJECTS AND THEIR CHARACTERISTIC FEATURES

An object term is assigned to all structures recorded on the sonar screen, excluding the seabed and water surface. Objects can be located anywhere in the water space, starting from the bottom and ending at the water surface. The key factor that

helps to classify an object as a specific structure is its shadow and its presentation on the screen. During the AUV mission planning process, the operators need to focus on a few factors, which can have a great impact on further presentation of the objects. An AUV altitude affects the length of a sonar shadow and the projection of shadow on the sonar image. Shadow measurements give the operators additional possibilities for improving the classification process. These measurements are based on a simple calculation of shadow length and other dimensions of the echo (Fig. 11, Eq. (11)).

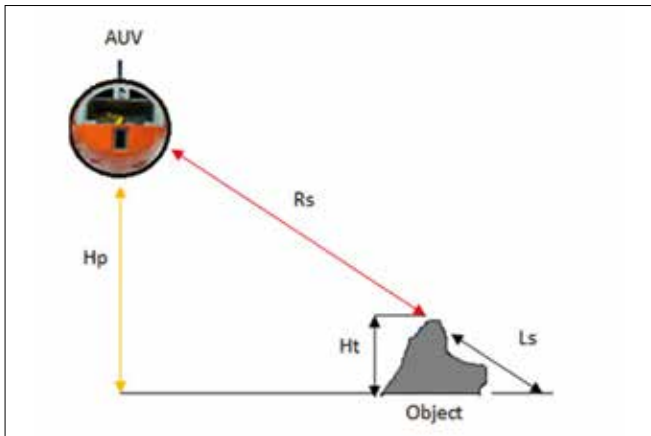


Fig. 11. Calculation concerning the height of an object based on its acoustic shadow.

$$H_t = \frac{H_p \cdot L_s}{R_s + L_s} \quad (11)$$

where:

- H_t – is the height of the object;
- L_s – is the length of the acoustic shadow;
- H_p – is the altitude of the vehicle;
- R_s – is the straight-line distance between the vehicle and the object (Slant Range) [29].

The acoustic shadow usually allows a larger amount of data to be obtained, compared to the direct reflections from an object. Fig. 12 shows that, even without the presence of a submarine kiosk on the screen, the shadow allows the operator to detect it and to measure its size.



Fig. 12. Acoustic shadow providing the possibility to assess the size of the submarine vessel's kiosk.

Manmade objects usually have clearly outlined edges, while natural objects are more rounded. It is highly recommended that attention be paid to the fact that some objects may generate a very strong echo but still do not have an acoustic shadow (Fig. 13). The presence of a shadow makes it possible to assess whether the echo which has been found is true or has only appeared as a result of multipath phenomena.



Fig. 13. Object which does not have an acoustic shadow but generates a very strong echo.

The acoustic shadow provides a possibility to verify the location of an object in the water column, which clarifies if the structure is lying at the bottom or is suspended somewhere higher in the water column. Fig. 14 shows an acoustic shadow which is separated from an object by a few metres.

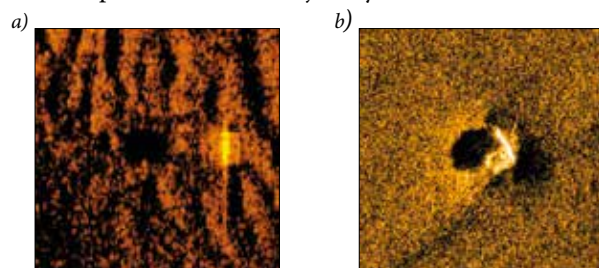


Fig. 14. Presentation of two objects, which are located: a) in the water column b) at the bottom.

When an object is located in the water column, but at a higher altitude than the autonomous vehicle, then there it is highly likely that its shadow will be invisible (Fig. 15).

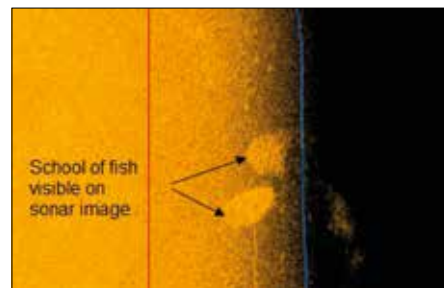


Fig. 15. School of fish visible on sonar image but not giving an acoustic shadow.

Usually, objects present stronger echoes than the bottom structure. However, an inverted presentation cannot be excluded. Some objects reflect less energy than the bottom around them. Fig. 16 presents a rubber wheel lying on a sandy bottom, an element that reflects less energy than more common objects on the sea floor.

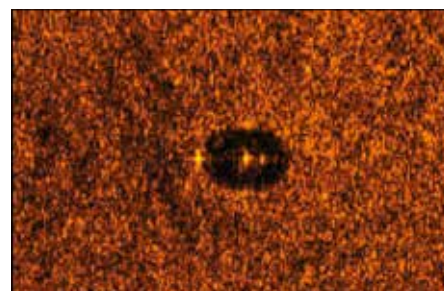


Fig. 16. Visualisation of rubber wheel, an element which produces weaker echo strength than other common objects on the sea floor.

The effectiveness of an AUV mission focused on collecting and analysing sonar data may be degraded due to the object characteristics or environmental factors, e.g. bottom composition. In that case, it is highly recommended to plan additional tracks, to observe the structure from other directions. An ideal solution, giving a more objective situational assessment, is to carry out the identification process by diverse or remotely operated vehicles (ROV) after detecting an object of interest. The experience gained during the aforementioned process helps the operators to increase their knowledge and efficiency of data analysis.

The visualisations of example objects are presented below (Fig. 17-18).

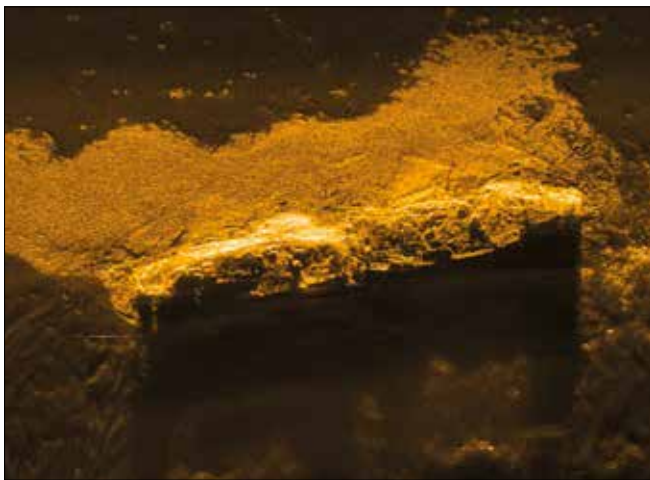


Fig. 17. Shipwreck surrounded by heavy fuel.

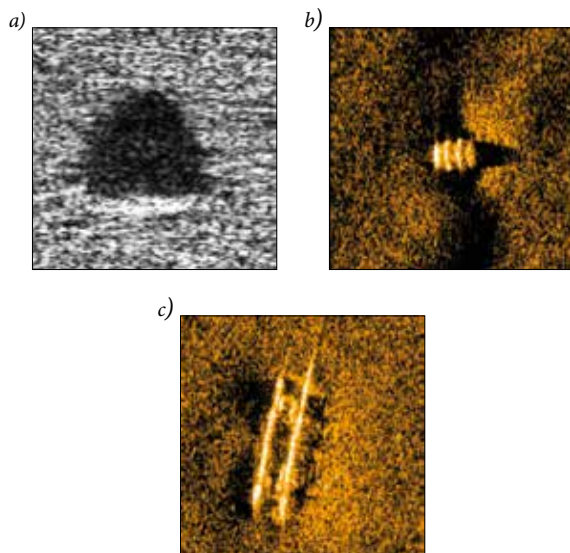


Fig. 18. Objects presented on sonar record: a) sea mine Manta type [21] b) barrel c) ladder.

PRESENTATION OF SEA FLOOR STRUCTURES ON SONAR IMAGES

Carrying out the interpretation process for sea floor structures, sonar users need to know about the process of visualisation of seabed projections and depressions. It may be

the case that the acoustic shadow (or 'black hole') is visible on the screen but there is no possibility of finding the object which generated this shadow. In that case, it is highly probable that the operator recognises the depression of the seabed. In that case, the energy generated from the transmitter is dispersed inside the depression and does not give a visible shadow. Examples of this situation usually appear when the seabed structure is folded or in areas with wells and boreholes (Fig. 19).

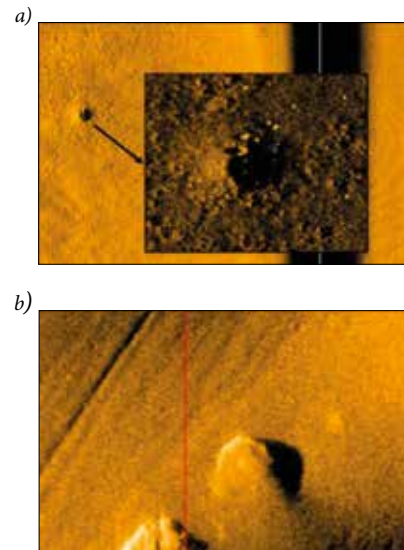


Fig. 19. a) Seabed depression visible on sonar record b) Seabed projection visible on sonar record.

A depression is usually presented on the sonar record with a strong echo on the outer part of the image, looking from the sonar side. The operator needs to consider how that image was generated, taking into account sonar beam characteristics, AUV movements and the basic principles associated with post-processed data. An acoustic shadow always appears behind the object; the opposite situation represents seabed depressions.

SUMMARY

It can be concluded that sonar imaging and processing is now an intensively explored topic. The use of autonomous vehicles for harbour and seaway traffic line monitoring is one of the most effective solutions, in terms of maintaining security awareness. This paper has contributed to the subject by presenting the concept of image reconstruction from data collected during AUV missions. For this purpose, a side-scan sonar, widely used to collect signals in aquatic environments, was used. With appropriate processing (including de-noising), collected data can be interpreted by inexperienced operators. However, it is highly recommended that users of sonar technology familiarise themselves with the methods and techniques that make that process more effective.

Although new techniques and programs provide dedicated solutions which help the process of data interpretation, the decisions regarding proper object classification still depend on the human factor. In order to ensure the correct assessment

and classification of objects on sonar imagery, the table below can be used.

Tab. 2. Sonar Contact Confidence Level Form

Sonar Contact Confidence Level					
Object no.	Shape	Shadow	Size	Echo Strength	Environment around object
Object 1					

New algorithms and programs, such as Automated Target Recognition (ATR) solutions, are still only advisory and the most appropriate mission analysis is based on the knowledge and experience of the operators [30, 31]. The paper presented includes guidelines and recommendations, which should be helpful for operators working with sonar data.

REFERENCES

1. P. Smith Menandro and A. Cardoso Bastos, "Seabed Mapping: A Brief History from Meaningful Words", *Geosciences*, vol. 10, no. 7, Art. no. 7, Jul. 2020, doi: 10.3390/geosciences10070273.
2. T. Kogut and K. Bakula, "Improvement of Full Waveform Airborne Laser Bathymetry Data Processing based on Waves of Neighbourhood Points", *Remote Sens.*, vol. 11, no. 10, Art. no. 10, Jan. 2019, doi: 10.3390/rs11101255.
3. M. Żokowski, M. Chodnicki, P. Krogulec, and N. Sigiel, "Procedures concerning preparations of autonomous underwater systems to operation focused on detection, classification and identification of mine like objects and ammunition", *J. KONBiN*, vol. 48, pp. 149–168, Dec. 2018, doi: 10.2478/jok-2018-0051.
4. S. Sivčev, J. Coleman, E. Omerdić, G. Dooly, and D. Toal, "Underwater manipulators: A review", *Ocean, Eng.*, vol. 163, pp. 431–450, Sep. 2018, doi: 10.1016/j.oceaneng.2018.06.018.
5. C. Roman and R. Mather, "Autonomous Underwater Vehicles as Tools for Deep-Submergence Archaeology", *Proc. Inst. Mech. Eng. Part M J. Eng. Marit. Environ.*, vol. 224, no. 4, pp. 327–340, Nov. 2010, doi: 10.1243/14750902JEME202.
6. L. A. Gonzalez, "Design, Modelling and Control of an Autonomous Underwater Vehicle", Bachelor of Engineering Honours Thesis 2004, The University of Western Australia, 2004.
7. Y. Ji, S. Kwak, A. Yamashita, and H. Asama, "Acoustic camera-based 3D measurement of underwater objects through automated extraction and association of feature points", *IEEE Int. Conf. Multisens. Fusion Integr. Intell. Syst.*, vol. 0, pp. 224–230, 2016, doi: 10.1109/MFI.2016.7849493.
8. W. Kazimierski and G. Zaniewicz, "Determination of Process Noise for Underwater Target Tracking with Forward Looking Sonar", *Remote Sens.*, vol. 13, no. 5, Art. no. 5, Jan. 2021, doi: 10.3390/rs13051014.
9. T. Zhang, S. Liu, X. He, H. Huang, and K. Hao, "Underwater Target Tracking Using Forward-Looking Sonar for Autonomous Underwater Vehicles", *Sensors*, vol. 20, no. 1, p. 102, Dec. 2019, doi: 10.3390/s20010102.
10. O. Y. Sergiyenko and V. V. Tyrsa, "3D Optical Machine Vision Sensors with Intelligent Data Management for Robotic Swarm Navigation Improvement", *IEEE Sens. J.*, vol. 21, no. 10, Art. no. 10, 2021, doi: 10.1109/JSEN.2020.3007856.
11. K. Bikonis, M. Moszyński, and Z. Lubniewski, "Application of Shape From Shading Technique for Side Scan Sonar Images", *Pol. Marit. Res.*, vol. 20, pp. 39–44, 2013, doi: 10.2478/pomr-2013-0033.
12. G. Grelowska, E. Kozaczka, and W. Szymczak, "Acoustic Imaging of Selected Areas of Gdansk Bay with the Aid of Parametric Echosounder and Side-Scan Sonar", *Pol. Marit. Res.*, vol. 24, no. 4, pp. 35–41, Dec. 2017, doi: 10.1515/pomr-2017-0133.
13. J. M. Topple and J. A. Fawcett, "MiNet: Efficient Deep Learning Automatic Target Recognition for Small Autonomous Vehicles", *IEEE Geosci. Remote Sens. Lett.*, vol. 18, no. 6, pp. 1014–1018, Jun. 2021, doi: 10.1109/LGRS.2020.2993652.
14. H. Yu, Z. Li, D. Li, and T. Shen, "Bottom Detection Method of Side-Scan Sonar Image for AUV Missions", *Complexity*, vol. 2020, pp. 1–9, Oct. 2020, doi: 10.1155/2020/8890410.
15. X. Zhang, C. Tan, and W. Ying, "An Imaging Algorithm for Multireceiver Synthetic Aperture Sonar", *Remote Sens.*, vol. 11, no. 6, Art. no. 6, Jan. 2019, doi: 10.3390/rs11060672.
16. W. Chen, L. Wang, Y. Zhang, X. Li, J. Liu, and W. Wang, "Anti-disturbance grabbing of underwater robot based on retinex image enhancement", *Chinese Automation Congress (CAC)*, Nov. 2019, pp. 2157–2162. doi: 10.1109/CAC48633.2019.8997332.
17. X. Wang, Q. Li, J. Yin, X. Han, and W. Hao, "An Adaptive De-noising and Detection Approach for Underwater Sonar Image", *Remote Sens.*, vol. 11, no. 4, Art. no. 4, Jan. 2019, doi: 10.3390/rs11040396.
18. J. C. Isaacs, "Sonar automatic target recognition for underwater UXO remediation," in *2015 IEEE Conference on Computer Vision and Pattern Recognition Workshops (CVPRW)*, Jun. 2015, pp. 134–140. doi: 10.1109/CVPRW.2015.7301307.
19. A. Waite, *Sonar for Practising Engineers*, 3 rd. Wiley: Hoboken, NJ, USA, 2002. Accessed: Jun. 15, 2021. [Online]. Available: <https://www.wiley.com/en-us/Sonar+for+Practising+Engineers%2C+3rd+Edition-p-9780471497509>

20. R. Heremans, Y. Dupont, and M. Acheroy, "Motion Compensation in High Resolution Synthetic Aperture Sonar (SAS) Images". IntechOpen, 2009. doi: 10.5772/39408.
21. F. Florin, F. Fohanno, I. Quidu, and J. Malkasse, "Synthetic Aperture and 3D Imaging for Mine Hunting Sonar", *Engineering*, 2004, Accessed: Jun. 11, 2021. [Online]. Available: /paper/Synthetic-Aperture-and-3D-Imaging-for-Mine-Hunting-Florin-Fohanno/0cff43ea7dc424e21b9ed83d256a2e25eda4a312
22. M. Zieja, M. Ważny, and S. Stępień, "Outline of a method for estimating the durability of components or device assemblies while maintaining the required reliability level", *Eksploat. Niezawodn. - Maint. Reliab.*, vol. 20, no. 2, 2018, doi: 10.17531/ein.2018.2.11.
23. D. T. Cobra, A. V. Oppenheim, and J. S. Jaffe, "Geometric distortions in Side-Scan Sonar images: A Procedure for their estimation and correction", *J. Ocean. Eng.*, vol. 17, no. 3, 1992.
24. M. Machado, P. Drews-Jr, P. Núñez, and S. Botelho, "Semantic Mapping on Underwater Environment Using Sonar Data". 2016. doi: 10.1109/LARS-SBR.2016.48.
25. P. Blondel, *The Handbook of Sidescan Sonar*. Berlin Heidelberg: Springer-Verlag, 2009. doi: 10.1007/978-3-540-49886-5.
26. K. H. Talib, M. Y. Othman, S. A. H. Sulaiman, M. A. M. Wazir, and A. Azizan, "Determination of speed of sound using empirical equations and SVP", in *2011 IEEE 7th International Colloquium on Signal Processing and its Applications*, 2011, pp. 252–256.
27. R. J. Urick, *Principles of Underwater Sound*, 3rd ed. Peninsula Pub, 1996. Accessed: Jun. 03, 2021. [Online]. Available: <https://www.abebooks.com/9780932146625/Principles-Underwater-Sound-3rd-Edition-0932146627/plp>
28. X. Shang, J. Zhao, and H. Zhang, "Automatic Overlapping Area Determination and Segmentation for Multiple Side Scan Sonar Images Mosaic", *IEEE J. Sel. Top. Appl. Earth Obs. Remote Sens.*, vol. 14, pp. 2886–2900, 2021, doi: 10.1109/JSTARS.2021.3061747.
29. J. Tęgowski and A. Zielinski, "Synthesis And Wavelet Analysis Of Side-Scan Sonar Sea Bottom Imagery", *Hydroacoustics*, vol. 9, 2006.
30. A. K. Mishra and B. Mulgrew, "Automatic target recognition" in *Encyclopedia of Aerospace Engineering*, R. Blockley and W. Shyy, Eds. Chichester, UK: John Wiley & Sons, Ltd, 2010, p. eae281. doi: 10.1002/9780470686652.eae281.
31. T. Praczyk, "Correction of Navigational Information Supplied to Biomimetic Autonomous Underwater Vehicle", *Pol. Marit. Res.*, vol. 25, no. 1, pp. 13–23, Mar. 2018, doi: 10.2478/pomr-2018-0002.

CONTACT WITH THE AUTHORS

Mariusz Zieja

e-mail: mariusz.zieja@itwl.pl

Air Force of Technology
Warsaw
POLAND

Wojciech Wawrzyński

Warsaw University of Technology
Warsaw
POLAND

Justyna Tomaszewska

Military University of Aviation
Dęblin
POLAND

Norbert Sigiel

MCM Squadron
Gdansk
POLAND